PROCEEDINGS OF
WORKSHOP XVI
THE DYNAMIC CHARACTERISTICS OF FAULTING
INFERRED FROM RECORDINGS OF STRONG GROUND MOTION
VOLUME II
Convened under Auspices of
NATIONAL EARTHQUAKE HAZARDS REDUCTION PROGRAM
Sponsored by
U.S. NUCLEAR REGULATORY COMMISSION
21-23 October 1981

CONFERENCES TO DATE

Conference I   Abnormal Animal Behavior Prior to Earthquakes, I
                      Not Open-Filed

Conference II   Experimental Studies of Rock Friction with
                      Application to Earthquake Prediction
                      Not Open-Filed

Conference III   Fault Mechanics and Its Relation to Earthquake
                      Prediction
                      Open-File No. 78-380

Conference IV   Use of Volunteers in the Earthquake Hazards
                      Reduction Program
                      Open-File No. 78-336

Conference V   Communicating Earthquake Hazard Reduction
                      Information
                      Open-File No. 78-933

Conference VI   Methodology for Identifying Seismic Gaps and
                      Soon-to-Break Gaps
                      Open-File No. 78-943

Conference VII   Stress and Strain Measurements Related to
                      Earthquake Prediction
                      Open-File No. 79-370

Conference VIII   Analysis of Actual Fault Zones in Bedrock
                      Open-File No. 79-1239

Conference IX   Magnitude of Deviatoric Stresses in the Earth's
                      Crust and Upper Mantle
                      Open-File No. 80-625

Conference X   Earthquake Hazards Along the Wasatch and
                      Sierra-Nevada Frontal Fault Zones
                      Open-File No. 80-801

Conference XI   Abnormal Animal Behavior Prior to Earthquakes, II
                      Open-File No. 80-453

Conference XII   Earthquake Prediction Information
                      Open-File No. 80-843

Conference XIII   Evaluation of Regional Seismic Hazards and Risk
                      Open-File No. 81-437

Workshop XVI   The Dynamic Characteristics of Faulting Inferred
                      from Recordings of Strong Ground Motion
                      Open-File No. 82-591

UNITED STATES

DEPARTMENT OF THE INTERIOR

GEOLOGICAL SURVEY

PROCEEDINGS OF

WORKSHOP XVI

THE DYNAMIC CHARACTERISTICS OF FAULTING

INFERRED FROM RECORDINGS OF STRONG GROUND MOTION

VOLUME II

Convened under Auspices of

NATIONAL EARTHQUAKE HAZARDS REDUCTION PROGRAM

Sponsored by

U.S. NUCLEAR REGULATORY COMMISSION

21-23 October 1981

Editor and Organizer

John Boatwright
U.S. Geological Survey
Menlo Park, CA 94025

Compiled by
Muriel Jacobson

Menlo Park, California

1982

TABLE OF CONTENTS

VOLUME I

VOLUME II

THE INFLUENCE OF RUPTURE VELOCITY AND SOURCE COMPLEXITY
ON THE RADIATION OF SEISMIC ENERGY

COMPUTATIONAL MODELS OF RUPTURE

THREE-DIMENSIONAL SIMULATION OF SPONTANEOUS RUPTURE:

THE EFFECT OF NON-UNIFORM PRESTRESS

by
Steven M. Day

Systems, Science and Software
P. O. Box 1620
La Jolla, CA 92038-1620
(714)453-0060

Abstract

We use a finite difference method to study crack propagation in a three-dimensional continuum, for conditions of both uniform and non-uniform prestress. The rupture criterion employed satisfies two fundamental physical requirements: it ensures finite stresses in the continuum and finite energy dissipation in crack extension. The finite-stress numerical simulations exhibit abrupt jumps in rupture velocity when sharp changes in prestress are encountered on the crack plane, behavior analogous to that predicted theoretically for two-dimensional, singular cracks. For uniform prestress conditions, the slip velocity function is approximately a low-pass filtered version of that of a singular, constant rupture velocity crack. For non-uniform prestress, spatial variations of peak slip velocity are strongly coupled to spatial variations of rupture velocity.

For uniform prestress and low cohesion, rupture velocity is predicted to exceed the S-wave velocity in directions for which Mode II (inplane) crack motion dominates. A sub-shear rupture velocity is predicted for directions of predominantly Mode III (antiplane) crack motion. Introduction of stress heterogeneities is sufficient, in each of the three cases studied, to reduce average rupture velocity to less than the S-velocity, but local super-shear rupture velocities can still occur in regions of high prestress. Rupture models with significant segments of super-shear propagation velocities may be consistent with seismic data for some large earthquakes, even where average rupture velocity can be reliably determined to be sub-shear.

INTRODUCTION

It is generally assumed that earthquake ground motion results from unstable slip accompanying a sudden drop in shear stress on a geologic fault. An important theoretical tool for studying such ground motion has been the so-called "dislocation" earthquake model. In this approach the earthquake is represented in terms of the displacement discontinuity, or "slip function," on the fault plane. The form of the slip function is generally chosen on an intuitive basis, without rigorous analysis of the time-dependent stresses acting in the focal region.

In contrast to dislocation models, "dynamic" earthquake models are those which take explicit account of the driving (tectonic) and resisting (frictional) stresses in the source region, and derive the resulting slip via the equations of motion. Such earthquake models generally lead to nonlinear, mixed boundary value problems requiring numerical methods for their solution. The three-dimensional case, in particular, presents formidable computational requirements.

In this study, we present numerical solutions for the rupture and slip histories predicted by a dynamic earthquake model. We consider various conditions of both uniform and nonuniform prestress. Our objective is to obtain an improved theoretical understanding of potential rupture propagation effects on earthquake ground motion. The earthquake is modeled as a spontaneously propagating shear crack in a three-dimensional continuum, with rupture growth governed by a slip-weakening failure criterion. The equations of motion are solved by a finite difference method.

A number of studies have treated the three-dimensional dynamic problem of a propagating shear fault, with the simplification that rupture velocity is specified a priori rather than being derived from a failure criterion. These results are reviewed by Das (1981) and Day (1982).

Numerical solutions for fixed rupture velocity dynamic faults have satisfactorily quantified some important three-dimensional geometrical effects such as the influence of fault width on the slip function. In the latter reference, for example, closed-form approximations are developed for the dependence of final slip, slip rise time, and slip velocity intensity (i.e., the strength of the crack-edge velocity singularity) on fault width and length. By means of such relationships, the fixed rupture velocity dynamic models help establish physical interpretations for the purely kinematic parameters associated with the more routinely used dislocation earthquake models (e.g., Swanger, et al., 1980).

Madariaga's (1977) analysis suggests that changes in rupture velocity of a propagating fault are the predominant source of high-frequency radiation. To gain a physical understanding of unsteady rupture propagation requires a "spontaneous rupture" dynamic model. That is, a failure criterion must be introduced into the numerical simulation so that rupture growth is determined as part of the dynamic solution. Spontaneous-rupture dynamic models have been studied in two dimensions, using both analytical solutions and numerical solutions. Freund (1979) provides a good review of this work.

Three-dimensional solutions for spontaneous shear cracks are very limited in number. Numerical solutions have been obtained by Day (1979), using the "slip-weakening" failure criterion (Ida, 1972; Andrews, 1976a), and by Das (1981) and Virieux and Madariaga (1982), using the "critical stress level" criterion (Das and Aki, 1977).

In this paper, we first describe the conceptual and experimental basis for the slip-weakening rupture model and point out some of the uncertainties involved in applying the model to the scale of geologic faulting. In the subsequent section, we apply the rupture model to obtain finite difference solutions for spontaneous rupture in a uniformly prestressed whole space. Then we turn to the effects of nonuniform prestress. We study finite difference simulations for three particular problems. In two cases, the prestress configuration consists of a single, isolated concentration of high stress on the fault plane. The third case consists of five separate stress concentrations, with intervening lower-stress areas.

Our focus in the present paper is on the rupture process itself, particularly the dependence of rupture velocity and slip velocity, respectively, on prestress and fault strength. Our intent is to identify specific phenomena associated with rupture propagation which may be important for defining the seismic radiation. We deliberately treat problems involving only simple geometries, and make no effort to simulate the full range of complexity which might be present in the earth.

An important further step will be to determine how the rupture phenomena identified in this study would be manifested in the radiated seismic signal. The slip histories obtained from the numerical solutions presented here are sufficient to synthesize the radiated wave field, and this issue will be considered in a subsequent report.

FAULT MODEL

The model of faulting employed here follows that described by Day (1982), except that rupture is spontaneous, not prescribed a priori as in that study. In particular, we retain the approximation that faulting is confined to a single plane and that the continuum is linearly elastic everywhere outside that plane. In this model, any inelastic response of the fault zone must be approximated through a (nonlinear) boundary condition on the fault plane. We will use the terms "failure" and "rupture" interchangeably to denote loss of strength of the fault zone, without prejudice as to whether the actual process of faulting in the earth more nearly resembles frictional sliding on a discrete fault plane or fracture of intact rock.

When an abrupt stress-drop is imposed on a crack in an otherwise linearly elastic continuum, the stress at the crack edge is singular. As pointed out by Andrews (1976a), this is true even though, in special cases, the traction acting on the crack plane may itself be non-singular. The basic assumption guiding our construction of a failure criterion is that material strength is finite so that shear stress concentrations near the crack edges must be bounded by some prescribed yield stress. As noted by Andrews, bounded stress must be accompanied by energy absorption at the rupture front as rupture extends.

One way to avoid the stress singuarity is to posit a "cohesive zone" just ahead of the crack edge in which slip is resisted by some distribution of cohesive tractions. Ida (1972) introduced the slip-weakening shear-crack model, in which the cohesive traction is assumed to depend only on the amount of slip across the crack. Ida analyzed the steady-state problem of a propagating, antiplane shear crack, for various functional forms of slip weakening. It was demonstrated that this model is equivalent to the Griffith criterion in its prediction of rupture growth, provided the zone over which the cohesive tractions act is small compared with the overall crack dimension. The specific fracture energy of the Griffith criterion was identified with the work done by the cohesive traction.

In this study, we employ the slip-weakening model in the form given by Andrews (1976a), and illustrated in Figure 1, with some obvious generalizations to three dimensions. The shear traction vector τ on the fault plane is limited in magnitude by a finite yield stress, τ_u, which is greater than, or equal to, the initial equilibrium value of traction, τ_0. Slip commences at a point when necessary to prevent the magnitude of τ from exceeding τ_u. This relative displacement is denoted $\underline{s}$, and has a path length denoted by
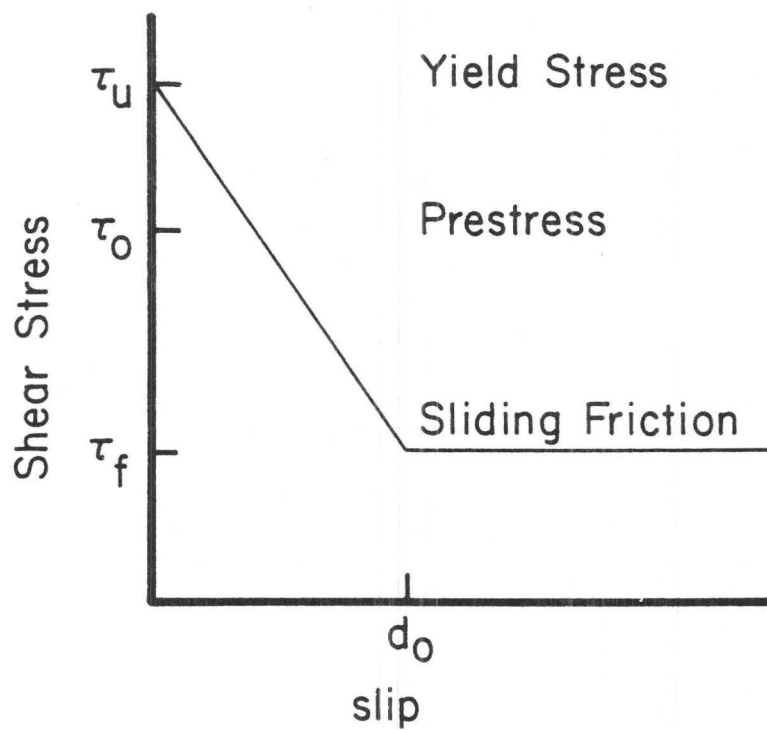
Figure 1.   Sketch of the slip-weakening model. The curve
represents the shear stress level on the fault
required to sustain sliding, as a function of the
slip path-length.

s, where s is given in differential form by $ds^2 = d\mathbf{s} \cdot d\mathbf{s}$. The slip is assumed to weaken the fault plane at that point, reducing the shear traction required to sustain sliding by an amount proportional to s. Finally, when s reaches a critical value, d_0, cohesion is considered to be destroyed, and further sliding occurs at a specified "dynamic friction" level, τ_f.

We will define the dynamic stress drop, $\Delta\tau$, to be the difference between the absolute values of shear prestress and sliding frictional stress,

$$\Delta\tau = \tau_0 - \tau_f \quad . \tag{1}$$

A second important quantity is a dimensionless ratio which Das and Aki (1977) call S, and which is a measure of how near the initial stress field is to failure. This ratio is defined by

$$S = \frac{\tau_u - \tau_0}{\Delta\tau} \quad , \tag{2}$$

and $S + 1$ represents the stress change which occurs across the rupture front, normalized to the dynamic stress drop.

This failure model satisfies the requirement that stress be everywhere finite. The energy dissipated in overcoming cohesion, per unit area encompassed by extension of the rupture, is denoted by 2γ. It is given by

$$2\gamma = \frac{1}{2} d_0 (\tau_u - \tau_f) \quad , \tag{3}$$

and γ can be interpreted as a specific fracture energy.

Laboratory measurements of rock friction show slip-weakening behavior of this type. Dieterich, et al. (1978) and Dieterich (1980) have measured time histories of shear stress and slip during unstable slip events induced on lapped sawcuts in large laboratory samples (granite blocks, with long dimension on the order of 1 meter). An example of these observations of unstable slip events, taken from the latter reference, is shown in Figure 2. Dieterich examined in detail the shear stress-displacement curves for several such events. He finds that the stress drop at the onset of rupture is not instantaneous. Instead, a finite slip of approximately 3 to 5 microns is required before the residual sliding friction level is reached. The intervening stress-displacement behavior is very similar to that assumed in Figure 1 (see, for example, Figure 6 of
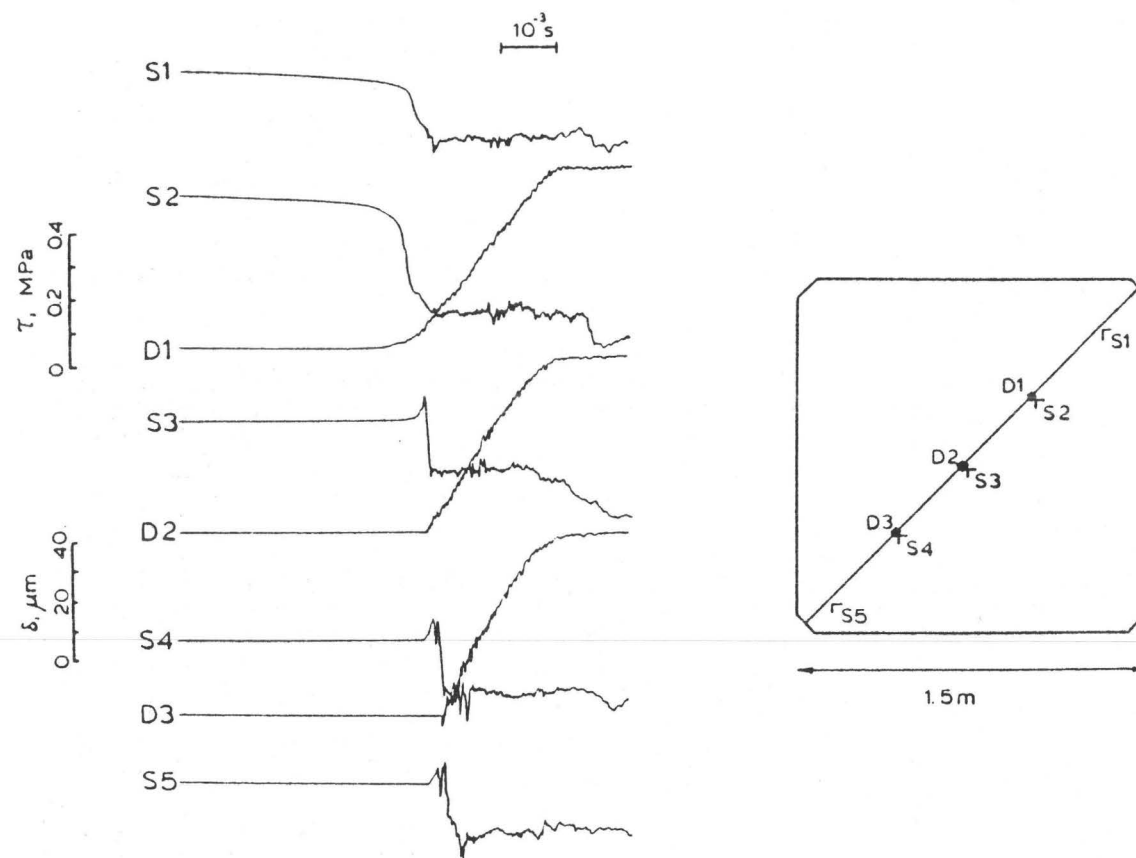
Figure 2. Laboratory measurements of fault shear stresses and relative displacements, versus time, for an unstable slip event in granite (from Dieterich, 1980).

Dieterich, 1980). These laboratory results lend support to the simple slip-weakening criterion as a reasonable model for unstable frictional sliding. We will proceed on the hypothesis that unstable frictional sliding, in turn, is a useful analogue for natural earthquakes with source dimensions on the order of hundreds to thousands of meters.

From Dieterich's data, reproduced in Figure 2, we can infer a representative value of S. This ratio lies in the range 0.0 to 0.5 for the five stress recordings shown, S1 through S5. In our numerical experiments with uniform prestress, we will examine rupture propagation for two values of S in this range, S = 0.2 and S = 0.5. We cannot be sure, of course, that these values are representative of actual earthquake faulting. In fact, the numerical results in the next section suggest that, on the average, cohesive stresses are probably somewhat larger than implied by these values of S.

We will also need an estimate for the fractional stress-drop, $\Delta\tau/\tau_0$. Laboratory stick-slip experiments in rock give values of $\Delta\tau/\tau_0$ of a few percent to a few tens of percent (e.g., Byerlee, 1967; Scholz, et al., 1972; Dieterich, et al. 1980). In our numerical simulations with uniform prestress, $\Delta\tau/\tau_0$ will be set to 0.1. Actually, for a given value of $\Delta\tau$, the value of $\Delta\tau/\tau_0$ has very little effect on the dynamic solution; it influences principally the amount of slip which occurs in the direction perpendicular to the prestress direction, and this slip component is usually small in any case. The main importance of estimating $\Delta\tau/\tau_0$, in the context of the slip-weakening model, is to guide our estimation of d_0.

Laboratory results give us few guidelines from which to estimate d_0, apart from the qualitative one that d_0 may be substantially larger for geologic faults than for laboratory faults since it appears to increase with surface roughness and gouge particle size (Dieterich, 1981). The numerical solutions for uniform stress will be nondimensionalized with respect to d_0. In the non-uniform stress simulations, however, we introduce a length scale into the problem; so we will have to assign numerical values to d_0. For the reason discussed below, we will use values of d_0 several orders of magnitude larger than the laboratory values, which range from roughly 2×10^{-6} meters to 2×10^{-4} meters (Dieterich, 1980).

If we are to retain the analogy to frictional sliding, relatively large values of d_0 appear to be required to prevent those stress components not relieved by slip on the fault from exceeding the failure stress. To see this, we perform a calculation

similar to one done by Andrews (1976a). For Mode III (antiplane strain) crack propagation, in which the shear stress component τ_{yz} is relieved on the plane y = zero, Ida and Aki (1972) give the following expression for the unrelieved component of shear stress on y = 0, τ_{xz}:

$$\tau_{xz} = \frac{\mu \dot{s}}{2}_R \qquad , \qquad (4)$$

where μ is the shear modulus, υ_R is the rupture velocity, and s is the slip rate. Ida (1972) obtained a numerical estimate of the peak value of $\dot{s}$ for an antiplane crack in which τ_{yz} is limited by the slip-weakening criterion. His result can be written as

$$Max(\dot{s}) \simeq .68 \frac{4V^2}{d_0 \upsilon_R} \qquad (5)$$

where V is the slip velocity intensity for the so-called "macroscopic", or "large-scale" solution. That is, V characterizes the crack-tip velocity for the corresponding singular crack problem, and is defined by

$$\dot{s} \sim V\xi^{-1/2} \qquad ,$$

where ξ is distance behind the crack tip, and ξ is small compared to the overall crack length, but still exceeds the length over which the cohesive stresses act.

Although Equations (4) and (5) were derived for the antiplane problem, we will assume that they also provide a rough estimate of maximum shear stress in the general case of a shear crack in three dimensions. Day (1981) determined V numerically for propagating rectangular shear cracks in three dimensions, and found that V is limited by the narrow dimension of the crack, W. Using his approximation for V,

$$V \simeq \frac{W}{2} \frac{\Delta\tau}{\mu} \upsilon_R \qquad ,$$

together with Equations (4) and (5), we find, very approximately,

$$Max. \ shear \ stress \simeq \frac{\Delta\tau W}{\mu d_0} \Delta\tau \ .$$

Therefore, to ensure that the maximum shear stress does not exceed τ_u, it is adequate that d_0 obey approximately

$$\frac{\Delta\tau W}{\mu d_0} < \tau_u / \Delta\tau \quad . \tag{6}$$

For example, for a fault width of 4 km, a dynamic stress-drop of 10 MPa (100 bars), shear modulus of 3.2×10^4 MPa, S of 0.5, and fractional stress-drop equal to 0.1, the inequality (6) is satisfied for d_0 of about 0.12 m or greater. This set of parameters would imply a fracture energy γ of about 4.5×10^5 Jm^{-2}, which happens to be very close to Aki's (1979) estimate of 4×10^5 Jm^{-2} for the specific fracture energy associated with stopping of rupture during the 1966 Parkfield earthquake.

The above considerations should roughly apply even if we acknowledge that failure is probably not strictly confined to a plane. Then the interpretation would be that large values of d_0 are necessary in order for the specific fracture energy (which is proportional to d_0 in our model) to adequately simulate energy loss through inelastic work in the continuum. It is obvious, however, that considerable uncertainty exists, both as to the numerical value and physical interpretation of the model parameter d_0.

UNIFORMLY PRESTRESSED FAULT

Problem Description. We use the slip-weakening model to simulate spontaneous rupture in a uniform whole space. The fault occupies the plane $z = 0$ and relieves the xz component of stress. Rupture starts at the origin and grows outward, and the fault slip is symmetric about both the x and y axes. The prestress, τ_0, strength, τ_u, frictional stress, τ_f, and the critical slip, d_0, are all constant on the plane $z = 0$. The continuum is a Poisson solid; that is, the ratio of the P-wave speed, α, to the S-wave speed, β, equals $\sqrt{3}$. The fractional stress drop, $\Delta\tau/\tau_0$, is 0.1, although variations of $\Delta\tau/\tau_0$ would have very little effect on the numerical solutions. We will consider two values of S, $S = 0.2$ and $S = 0.5$.

The relevant boundary value problems are solved using a three-dimensional finite difference method. The dynamic solution is explicitly time-stepped, and artificial viscosity is used to suppress any high-frequency oscillations in the solution caused by the numerical dispersion which is intrinsic to discrete numerical methods such as finite difference. As a further precaution, the slip velocity time-histories are post-processed with a low-pass filter to remove any significantly dispersed high-frequency components of the solution.

Rupture Inception. Once started in a uniform stress field, rupture proceeds spontaneously, without stopping, driven by the dynamic stress concentration at the fault edges. However, some additional mechanism is required to initiate rupture from the equilibrium prestress configuration. We might imagine, for example, that a relatively small area on the prospective fault plane has been weakened, and that the shear stress there falls from τ_0 to τ_f. This initial crack then slides stably under a slowly increasing tectonic load. Eventually, a situation develops which is analogous to the critical crack in elastic fracture mechanics, and accelerating crack growth ensues.

Our interest will be confined to the dynamics of faulting after the onset of instability, and we will not concern ourselves here with the quasi-static processes leading to instability. Instead, we will simply induce an instability artificially, as described later. However, in order to establish a fundamental length scale for the dynamic solution, it is useful to estimate the size of a critical static crack. For this purpose, we assume that the crack is initially circular. We further assume (only for the present purpose, however) that, at the onset of instability, the circular crack initially expands uniformly, retaining circular shape. To estimate the critical radius, r_c, we seek a balance

between strain energy release rate and the energy dissipation rate at the crack edge, per unit increase in the crack radius. We start with Neuber's (1937) solution for the static slip on a circular shear crack in a Poisson solid:

$$s_\infty(r) = \frac{24}{7\pi} \frac{\Delta\tau}{\mu} r_c \sqrt{1 - \frac{r^2}{r_c^2}} \quad , \qquad (7)$$

where s_∞ is the static slip, μ is the shear modulus, β is the shear wave speed, r_c is the crack radius, and r is the distance from the crack center. The total "available" energy, E, is defined as the drop in strain energy due to crack formation minus the work done against friction, and can be calculated from Equation (7):

$$E = \frac{8\Delta\tau^2 r_c^3}{7\mu} \quad . \qquad (8)$$

The slip-weakening mechanism dissipates energy Σ at the rupture front at the rate

$$\frac{d\Sigma}{dr_c} = \pi(S + 1) d_o r_c \qquad (9)$$

per unit increase in crack radius. The desired estimate of the critical radius is r_c such that $E-\Sigma$ is stationary, which gives

$$r_c = \frac{7\pi}{24} \frac{\mu(S + 1) d_o}{\Delta\tau} \quad . \qquad (10)$$

For our dynamic simulations, we have induced an instability through the artifice of enforcing, within the focal region, a minimum rupture velocity equal to half the shear speed β (Andrews, 1976b, used a similar method to start plane-strain shear cracks). The choice of this value for minimum rupture velocity is a compromise between approximating quasi-static crack inception (favored by rupture velocity approaching zero) and reducing computation time (favored by a high minimum rupture velocity).

Numerical Results for Rupture Velocity. Because of the spatial uniformity of the problem, there is no intrinsic length scale apart from the critical crack radius (Equation (10)). We will present the numerical results in nondimensional form using r_c as the fundamental length unit. Since the derivation of r_c is

approximate, however, we will ignore the numerical factor $7\pi/24$ in Equation (10). Then, distance x and time t, respectively, are given in terms of the nondimensional variables, x' and t', by

$$x = \frac{(S + 1)\, \mu d_0}{\Delta \tau}\, x'$$

$$t = \frac{(S + 1)\, \mu\, d_0}{\Delta \tau \beta}\, t' \tag{11}$$

Figure 3 shows contours of the rupture front at equal intervals of dimensionless time, t', for the two values of S. The rupture front is defined to enclose regions of the fault plane on which the slip has exceeded d_0. For both values of S, rupture propagation is most rapid in the direction of prestress, the x direction, and is least rapid in the y direction; this leads to roughly elliptical rupture fronts. The figure indicates that rupture acceleration is less rapid for the higher-strength case, S = 0.5, than for S = 0.2.

Figure 4 shows rupture velocities obtained from the numerical solutions along the two principal directions. The velocities are shown as functions of hypocentral distance, for both values of S. The initial, flat parts of the curves represent the minimum rupture velocity, $0.5\,\beta$. As the minimum is exceeded, rapid acceleration of the rupture front occurs. This begins on the x axis (prestress direction) at dimensionless distance of about 0.7, and begins at a slightly greater distance along the y axis.

In the y direction, the rupture velocity smoothly approaches the shear wave velocity; for S = 0.2, the rupture velocity reaches $0.95\,\beta$ by the time the fault has propagated a dimensionless distance of about 5. Increasing the strength increases the distance at which a given rupture velocity is achieved, as shown by the curve for S = 0.5.

In the x direction, acceleration is more rapid than in the y direction; for S = 0.2, the rupture reaches the shear wave velocity at $x' \approx 1.5$. For S = 0.5, the shear wave velocity is reached at $x' \approx 3.0$. The rupture velocity then levels off somewhat, before accelerating rapidly again toward the P-wave velocity, α. For S = 0.2, the rupture velocity reaches $0.9\,\alpha$ at $x' \approx 3.5$. The leveling off of the rupture velocity near the shear wave velocity is more pronounced for S = 0.5, and the acceleration toward the P velocity occurs at greater distance.
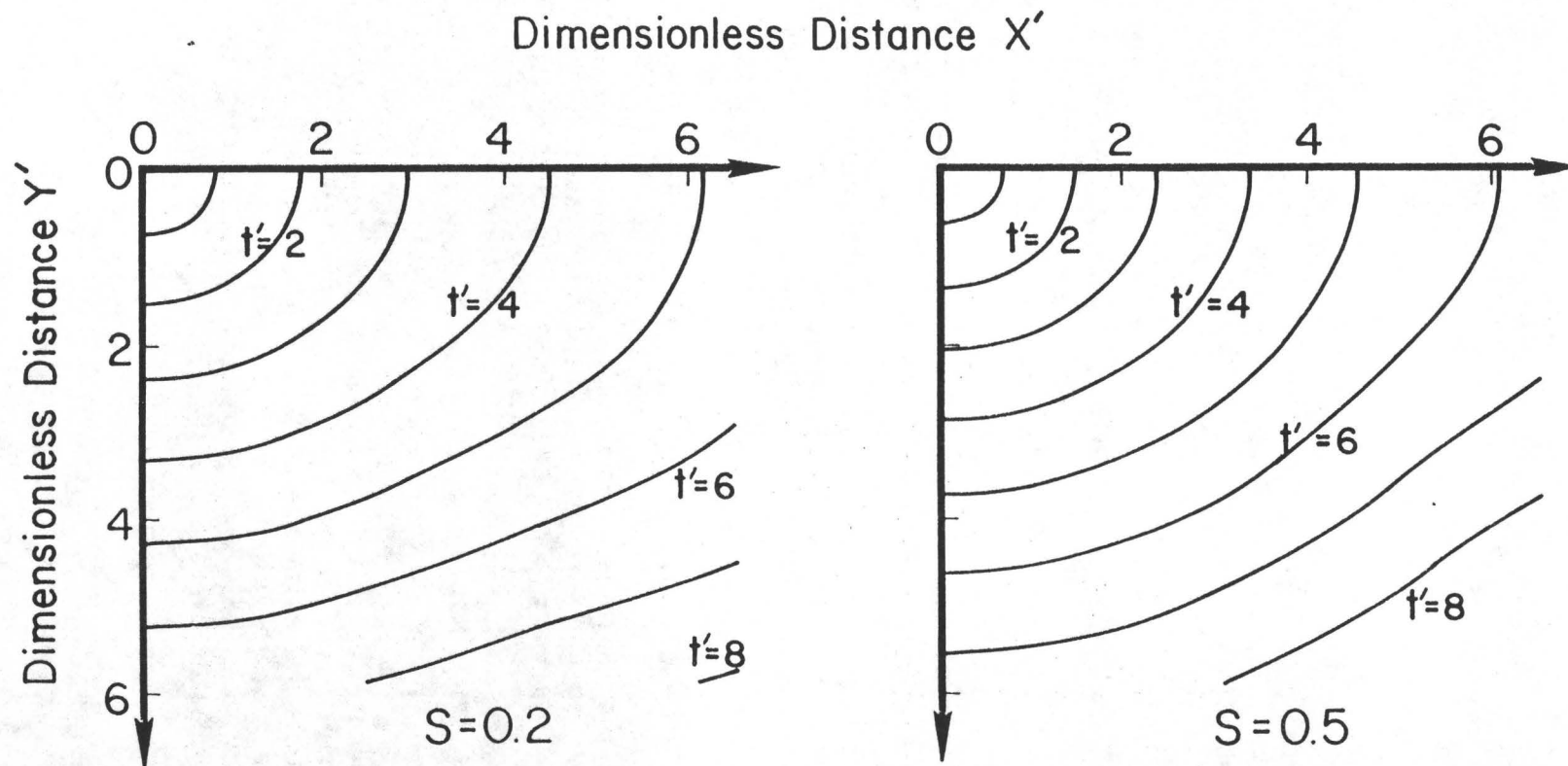
Figure 3.   Rupture front contours, at unit intervals of the dimensionless time, for the case of uniform prestress. The two cases represent numerical simulations performed for S = 0.2 and S = 0.5, respectively.

468
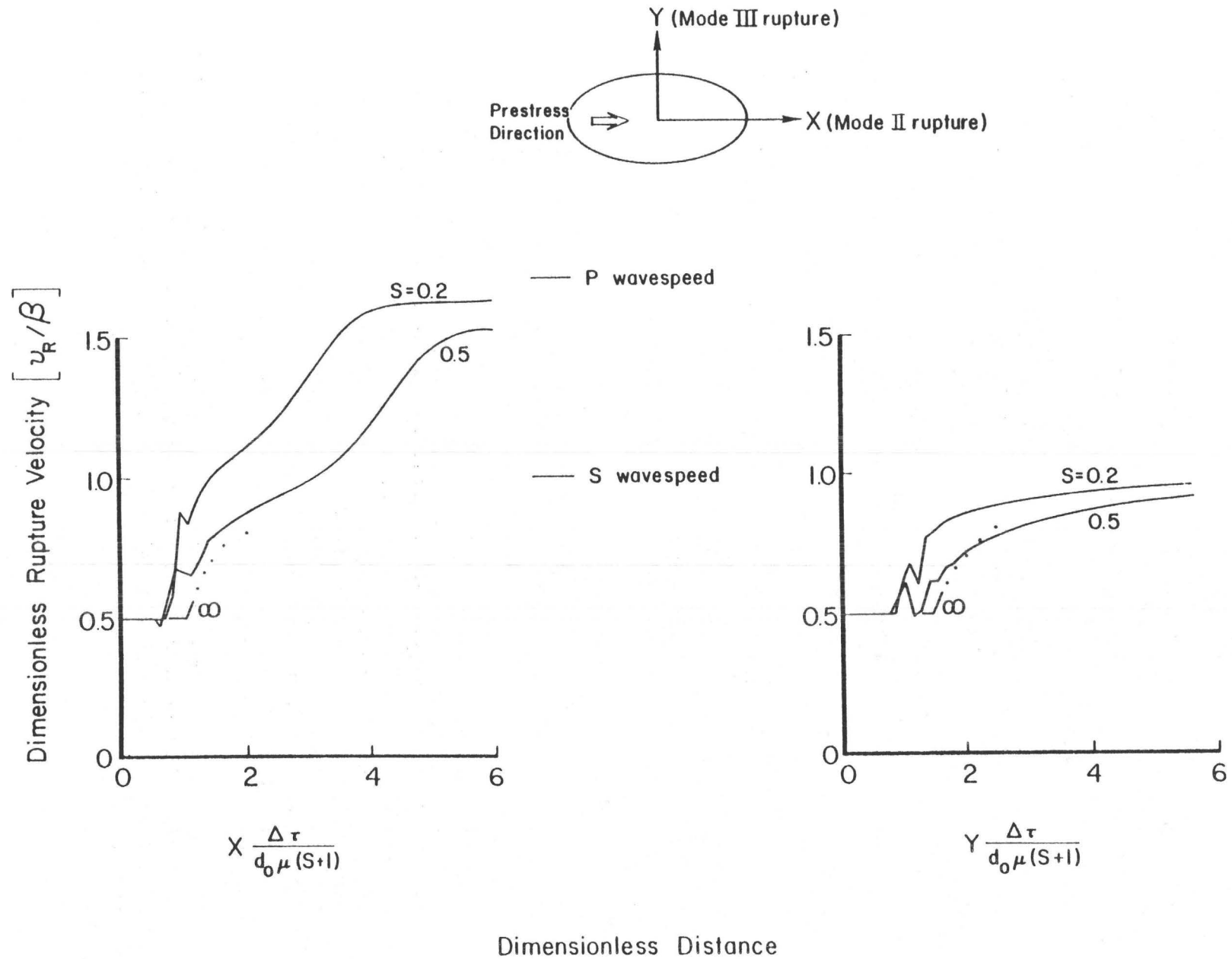
Figure 4. Rupture velocity as a function of dimensionless distance, for the case of uniform prestress. The solutions are shown along both the x axis (prestress direction) and the y axis. Numerical solutions are given for two finite values of the strength parameter S. Also shown is the analytic solution for the onset of spontaneous rupture in the singular case (S = ∞).

Also indicated in Figure 4 are the distances along the x and y axes, respectively, at which a singular crack (i.e., the case $S = \infty$), driven at $\upsilon_R = 0.5\ \beta$, first begins to accelerate spontaneously. These values are obtained analytically, using standard results for the energy release rate, G, at the edge of a circular crack growing at constant velocity (e.g., Richards, 1976). The energy release rate is a known function of crack radius, rupture velocity, and position on the rupture front; we simply equate G to twice the specific fracture energy, set the rupture velocity to 0.5 β, and solve for crack radius. As was the case for the two numerical solutions for finite S, the singular rupture front begins accelerating first along the x axis (the prestress direction), and last along the y axis.

Once the crack starts accelerating, the analytic results for $S = \infty$ no longer apply. The dotted lines suggest the expected behavior of the singular crack, based on the approximation of using the self-similar circular crack solution for G after the onset of accelerating rupture.

The most important aspect of Figures 3 and 4 is the prediction of rupture velocities exceeding the shear wave velocity for propagation in the direction of Mode II crack extension (x axis). On the other hand, rupture remains sub-shear in the direction of purely Mode III crack propagation (the y direction). Das (1981) has obtained similar results using the critical stress level criterion of failure.

The result that the Mode III rupture is sub-shear, but approaches the S-wave velocity asymptotically, agrees with two-dimensional analytical solutions for Mode III cracks (e.g., Kostrov, 1966). The prediction of super-shear rupture in the direction of prestress, for both S = 0.2 and S = 0.5, is in agreement with Burridge's (1973) two-dimensional analysis of Mode II rupture propagation for a finite-stress rupture criterion. The two-dimensional numerical solutions of Das and Aki (1977) and Andrews (1976b) also yield super-shear rupture velocities for values of S similar to those used here. Those studies have established, however, that for values of S exceeding approximately 1.63, Mode II rupture propagation is sub-shear. This result is expected to govern the three-dimensional solution, as well; so for substantially higher fault strength relative to $\Delta\tau$, rupture velocity is expected to be sub-shear in all directions.

Earlier we discussed some observations made by Dieterich of unstable slip events in granite blocks with dimensions on the order of a meter. Typical fault parameters observed in these experiments are (see Figure 2) $\Delta\tau \approx 0.2$ MPa, $S \approx 0.5$, and $d_0 \approx 3 \times 10^{-6}$ m.

Then, assuming $\mu \approx 3 \times 10^4$ MPa for granite, we find that a hypocentral distance of 1 meter corresponds to a dimensionless distance x' of about 1.5. From Figure 4, we see that this is well within the range of sub-shear rupture velocity for S = 0.5. Thus, the numerical solutions indicate that rupture velocities will usually be sub-shear for similar experiments on this scale. This prediction is sensitive to the value of S, however; for S = 0.2, for example, a 1 meter distance corresponds to x' = 1.8, which, according to Figure 4, is close to the distance for transition to super-shear rupture, for this value of S. It is conceivable, then, that rupture velocity measurements on this length scale will occasionally exceed β, for similarly prepared fault surfaces.

Numerical Results for Slip Velocity. Normalized slip velocities along the x and y axes are shown in Figure 5. These have been low-pass filtered to attenuate Fourier components with (nondimensional) periods shorter than about 0.6. The figure shows that the peak (low-passed) slip velocity increases with focal distance. The increase appears to be similar in form to the $\sqrt{r}$ increase found analytically for circular, fixed rupture velocity models (Kostrov, 1964). Peak slip velocity, at a given focal distance, is higher on the y axis than on the x axis. This azimuthal variation is qualitatively explained by the Burridge and Willis (1969) solution for the slip s on a self-similar, expanding elliptical crack:

$$s = C \frac{\Delta\tau\beta}{\mu} \left(t^2 - \frac{x^2}{\upsilon_x^2} - \frac{y^2}{\upsilon_y^2}\right)^{1/2} H\left(t^2 - \frac{x^2}{\upsilon_x^2} - \frac{y^2}{\upsilon_y^2}\right) \qquad (12)$$

where C is a constant and υ_x and υ_y are the rupture velocities in the x and y directions, respectively. This expression predicts that peak (low-passed) slip velocity, on the y axis will approach $(\upsilon_x/\upsilon_y)^{1/2}$ times the peak slip velocity at the same focal distance on the x axis. At x' = 5.7, this accounts for about half the observed difference in peak velocity between the two azimuths. The discrepancy is not surprising, considering that Equation (12) strictly applies only to singular cracks and for constant rupture velocities, with υ_x less than the Rayleigh wave velocity and υ_y less than the shear velocity.

The overall shapes of the slip velocity curves are similar to those for the self-similar solution (Equation (12)). That is, they are roughly low-pass filtered square-root singularities. In fact, the peak slip velocities in Figure 5 are very close to what one would predict from low-pass filtering the self-similar solution (which has singular stress) using the same short-period cutoff that
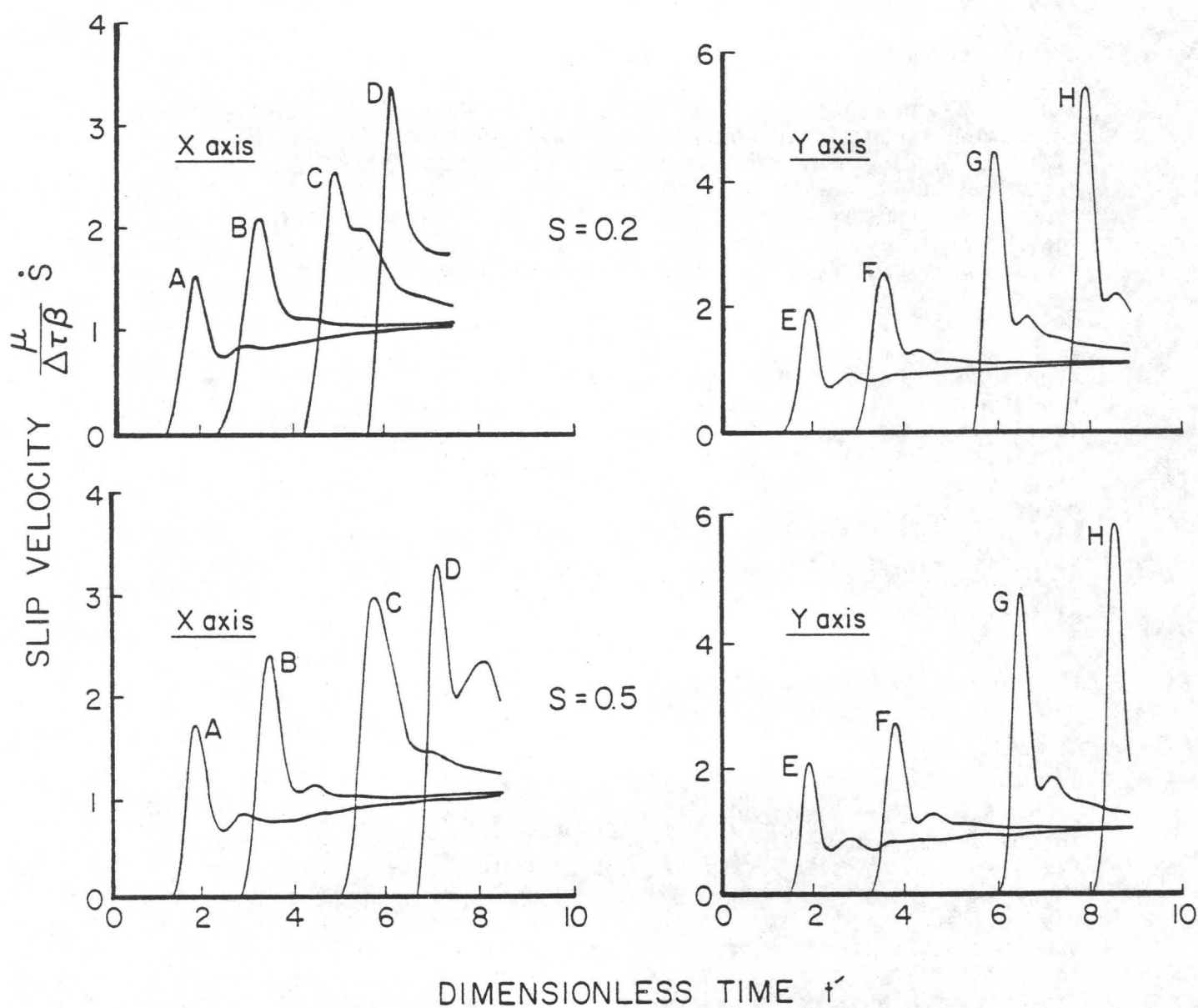
Figure 5. Slip velocity time histories for several points along the x and y axes, for the numerical simulations with uniform prestress. The time histories have been low-pass filtered, with a nondimensional cutoff period of 0.6.

was applied to our numerical solutions. The finite stress condition incorporated into the numerical solution apparently does not substantially reduce peak velocity, relative to singular-stress crack solutions, within the frequency band preserved by the present numerical solutions. Scaled to $\Delta\tau = 10$ MPa, $\mu = 3.24 \times 10^4$ MPa, $\beta = 3.46$ km/sec, and $(S + 1)d_0 = 0.12$ m, the upper frequency cutoff for these calculations would correspond to about 15 Hz, and the maximum hypocentral distance represented in Figure 5 would correspond to about 2.25 km.

These results show that the expression $(\tau_u - \tau_f)\beta/\mu$ does not necessarily provide a good estimate of peak slip velocity, as has been hypothesized previously (for example, Del Mar Technical Associates, 1978). Figure 5 shows peak slip velocities as high as five times this estimate, and these must be interpreted as lower bounds since the computed velocities have been low-pass filtered.

FAULTS WITH NON-UNIFORM PRESTRESS

Introduction. There is growing evidence that spatially inhomogeneous stress changes are a prevalent feature of shallow-focus earthquakes (for example, Hanks, 1974; Kanamori and Stewart, 1978; Hartzell and Brune, 1979; Bache, Lambert and Barker, 1980). Such variations in stress-drop, plus the likely variability of frictional strength along faults, may be expected to give rise to irregularities in rupture velocity. Madariaga's (1977) analysis suggests that such rupture velocity variations may be the predominant source of high-frequency radiation from propagating faults. Clearly, it is important to improve our understanding of rupture propagation and its relationship to non-uniformities in the stress field.

In this section, we describe numerical simulations of spontaneous rupture propagation in the presence of localized stress concentrations. Three particular problems are considered. In two cases, the prestress configuration consists of a single, isolated concentration of high shear stress on the fault plane. In both cases, the high-stress patch is embedded in a lower regional stress field. The third case consists of an array of five separate stress concentrations with intervening lower-stress zones.

The fault parameters used in the three simulations are given in Table 1. The strength, τ_u, sliding friction τ_f, and critical slip, d_0, are all held constant; only variations of τ_0 are considered. The elastic properties, for all three simulations, are $\alpha = 6.0$ km/sec, $\beta = 3.46$ km/sec, and $\mu = 3.24 \times 10^4$ MPa. In each case, rupture is induced in a high-stress region centered at the origin. The fault then propagates in the $z = 0$ plane, and relieves the x, z stress component. In Problems I and II, rupture growth was permitted to stop spontaneously. In Problem III, rupture growth decelerated considerably as it progressed into the low-stressed region, but still reached pre-specified strength barriers which delimited a 6 km x 18 km rectangular region.

Problem I. Figure 6 shows the geometry for Problem I. The high-stress patch ($\Delta\tau = 10$ MPa) is circular, with a radius of 1400 meters. Outside this radius, the fault plane is uniformly prestressed at the sliding friction level ($\Delta\tau = 0$).

Figure 7 shows rupture-front contours at 0.3 second intervals of time. The rupture accelerates rapidly over the prestressed patch, then abruptly decelerates as it breaks into the zero stress-drop region. In the y direction, deceleration is very abrupt, and the fault penetrates only about 150 meters beyond the edge of the stress concentration. In the x direction, however, the

Table 1.

FAULT PARAMETERS FOR NON-UNIFORM PRESTRESS SIMULATIONS

Problem Number	d_o (m)	τ_u (MPa)	τ_f (MPa)	Max τ_o (MPa)	Min τ_o (MPa)
I	0.10	102	90	100	90.0
II	0.10	102	90	100	92.5
III	0.08	102	90	100	92.5

Figure 6. Fault geometry for non-uniform prestress Problem I.

Figure 7. Rupture front contours obtained from the numerical solution
to Problem I. The rupture front is shown at 0.3 second
intervals. The fault stops spontaneously after 1.5 seconds.

fault penetrates about 500 meters into the low-stress region. After 1.5 seconds, rupture growth has ceased.

Figure 8 shows both peak slip velocity (low-passed, 5 Hz cutoff) and rupture velocity along the x axis. Rupture velocity accelerates rapidly throughout the stress concentration as we would predict on the basis of the uniform prestress solution. The shear wave velocity is reached at a hypocentral distance of about 800 meters, and rupture velocity is then super-shear until reaching the edge of the stress concentration. When the fault breaks into the lower-stress region, rupture velocity drops immediately to about 1 km/sec, and rupture growth finally stops spontaneously. The gradual stopping of rupture in a region of zero dynamic stress-drop is in qualitative agreement with the predictions of Husseini, et al. (1975), which were based on an antiplane strain crack model.

It is known, from the analytical results of Eshelby (1969), for example, that crack edges have no inertia, in the case of singular cracks. That is, rupture velocity responds instantaneously to changes in driving stress. The rupture velocity drops abruptly in our numerical solution as well, after rupturing through the stress concentration. Thus, the finite-stress numerical fault model exhibits a lack of inertia similar to that predicted by classical fracture mechanics.

The rupture velocity given in Figure 8 is the local, or "tangent", rupture velocity. That is, it is obtained from the gradient of rupture arrival time. While the tangent rupture velocity exceeds the shear wave velocity over a significant area of the fault, the average, or "secant", rupture velocity is always sub-shear in this problem. That is, at any point along the x axis, the hypocentral distance divided by rupture arrival time is less than β for this simulation.

Peak slip velocity roughly parallels the shape of the rupture velocity curve in Figure 8. The initial increase in peak slip velocity with hypocentral distance is expected from our results for the uniform prestress problem. When the rupture velocity decelerates after breaking through the stress concentration, the peak slip velocity also decreases.

Problem II. This case, sketched in Figure 9, differs from the previous one only in having a non-zero dynamic stress-drop ($\Delta\tau$ = 2.5 MPa) outside the area of stress concentration ($\Delta\tau$ = 10 MPa). Figure 10 shows rupture front contours for this case. Fault growth again stops spontaneously in this case. This spontaneous arrest of rupture occurs in spite of the fact that the prestress everywhere exceeds dynamic friction. As in the previous

Figure 8. Rupture velocity and peak slip velocity for Problem I, as functions of position along the x axis. Peak slip velocity is obtained from low-pass filtered (5 Hz cutoff) time histories of slip. The S-wave velocity is shown by a horizontal line, indicating that the local rupture velocity is slightly super-shear near the edge of the stress concentration.
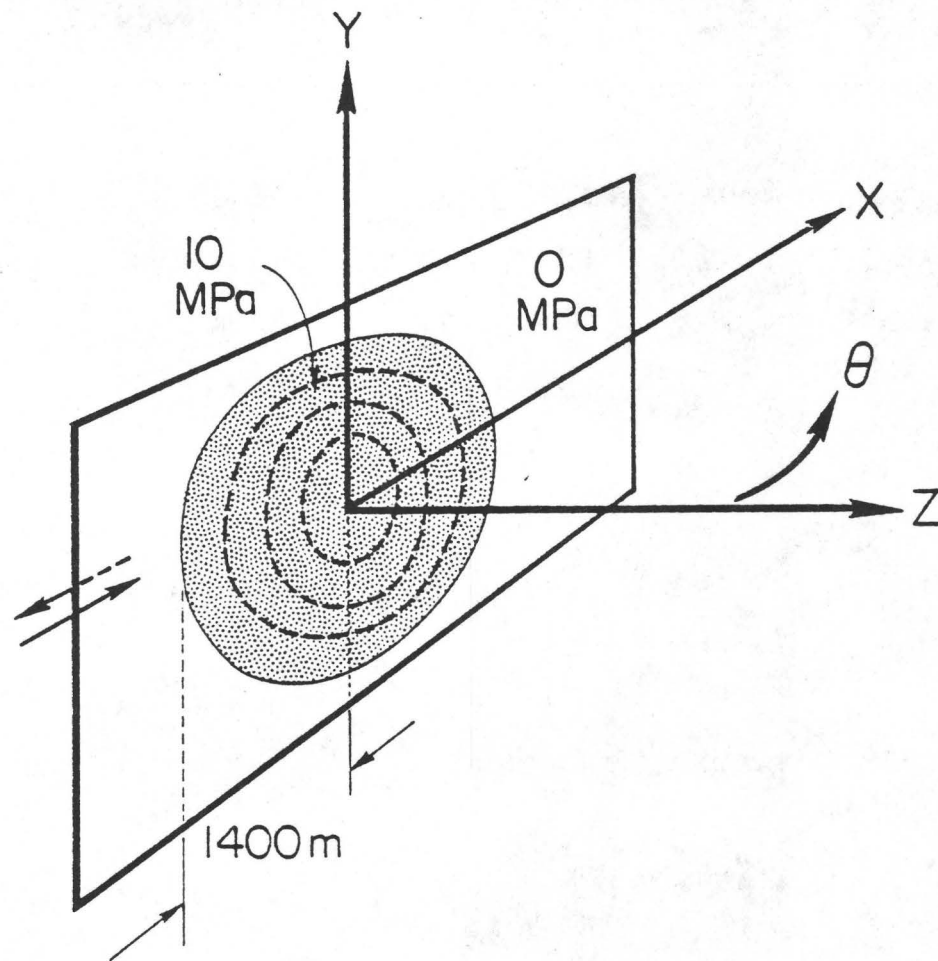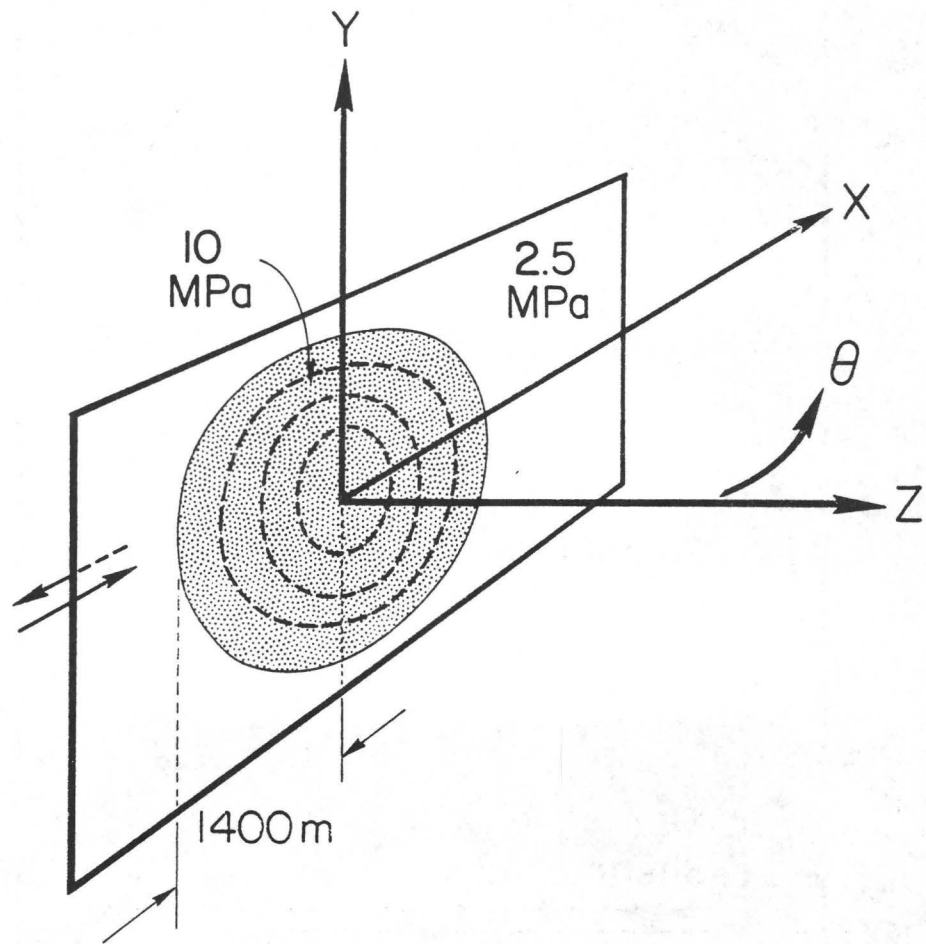
Figure 9. Fault geometry for non-uniform prestress, Problem II.
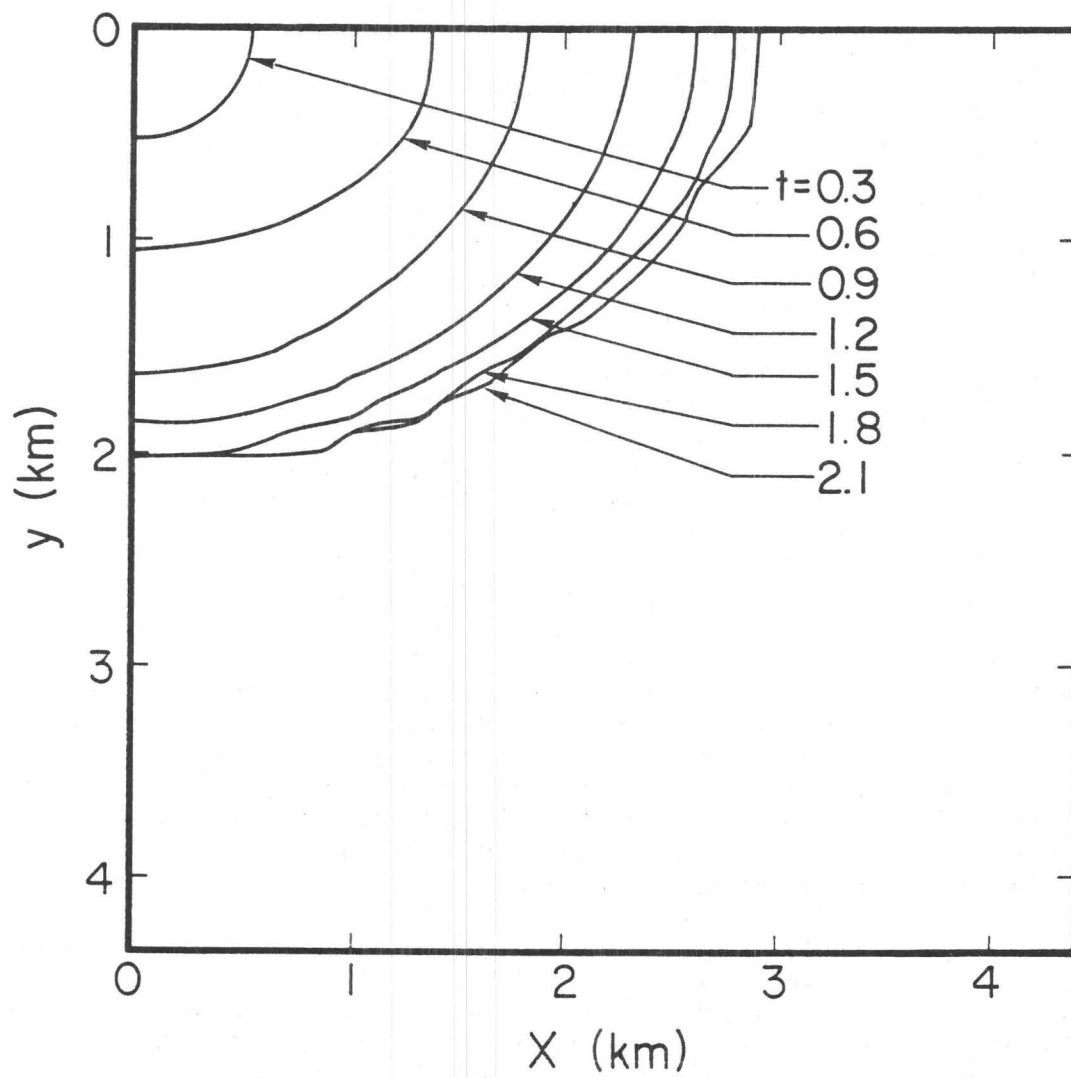
Figure 10. Rupture front contours obtained from the numerical solution to Problem II, shown at 0.3 second intervals. Fault growth stops spontaneously at approximately 2.1 seconds.

case, rupture growth decelerates outside the stress concentration, but overshoots further into the lower-stress region than was the case in Problem I. The overshoot distance is 600 meters in the y direction and 1500 meters in the x direction, compared to the stress concentraton radius of 1400 meters.

Rupture velocity and peak slip velocity along the x axis are shown in Figure 11. Local rupture velocity is super-shear near the edge of the stress concentration, peaking at about 4 km/sec, and drops abruptly to about 1 km/sec after breaking through the stress concentration. It then recovers to about 1.7 km/sec before smoothly decelerating to zero. Secant rupture velocity is everywhere sub-shear. The peak slip velocity mirrors this behavior of the local rupture velocity, again demonstrating the strong linkage between the two quantities.

Problem III. The problem geometry for this case is sketched in Figure 12. Each of the five high-stress areas ($\Delta\tau$ = 10 MPa) is square, with dimension 2250 meters, and they are symmetrically disposed about the hypocenter. The remainder of the plane is low-stressed ($\Delta\tau$ = 2.5 MPa), and each low-stress area between stress concentrations is 1050 meters in width.

Figure 13 shows the rupture front contours at 0.1 second intervals. A fairly complex pattern of rupture emerges. Along the y axis, for example, rupture stops shortly after 1 second. As rupture advances on the other parts of the fault plane, however, the stress concentration along the y axis increases, causing rupture propagation to recommence at about 1.8 seconds. Along the x axis, rupture accelerates rapidly as it breaks each high-stress patch, and decelerates between patches. At 1.1 seconds, and then again at 1.9 seconds, the rupture front "jumps", leaving unbroken areas behind, which subsequently break.

Figure 14 shows the peak slip velocities and rupture velocities along the x axis. The close relationship between maximum slip velocity and rupture velocity is especially evident here. The dashed portions of the rupture velocity curve represent regions that ruptured out of sequence as the rupture front jumped ahead to a high-stress patch.

We note that apparent local rupture velocities in excess of the P-wave velocity occur at the edges of the stress concentrations. Of course, the secant rupture velocity (hypocentral distance divided by rupture travel time) is everywhere less than the P-wave speed, as required by causality. On the other hand, the secant rupture velocity does slightly exceed the S-wave velocity at some intermediate points along the x axis. Over the entire fault
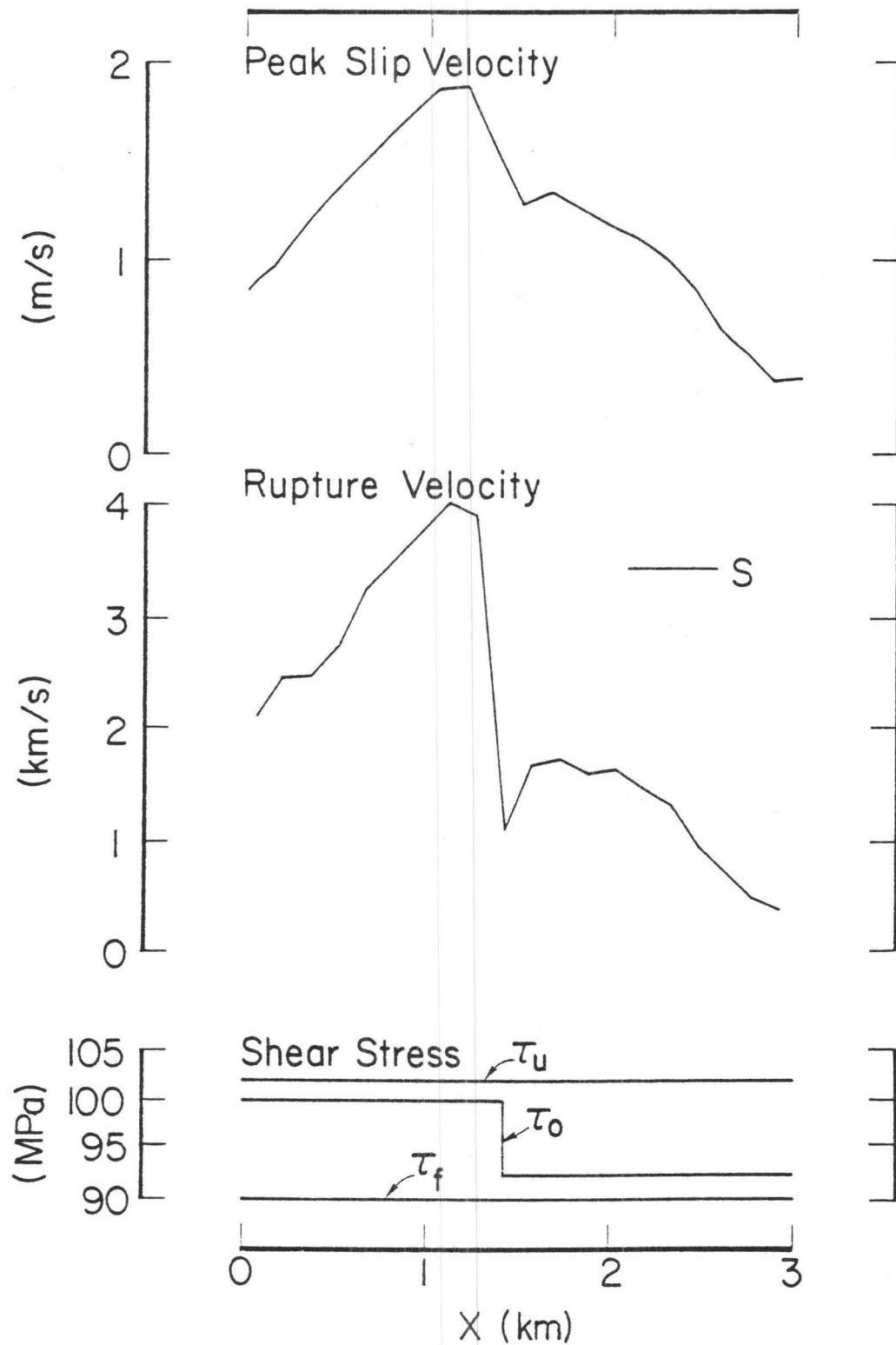
Figure 11. Rupture velocity and peak slip velocity for Problem II, as functions of position along the x axis. Peak slip velocity is obtained from low-passed (5 Hz cutoff) time histories.
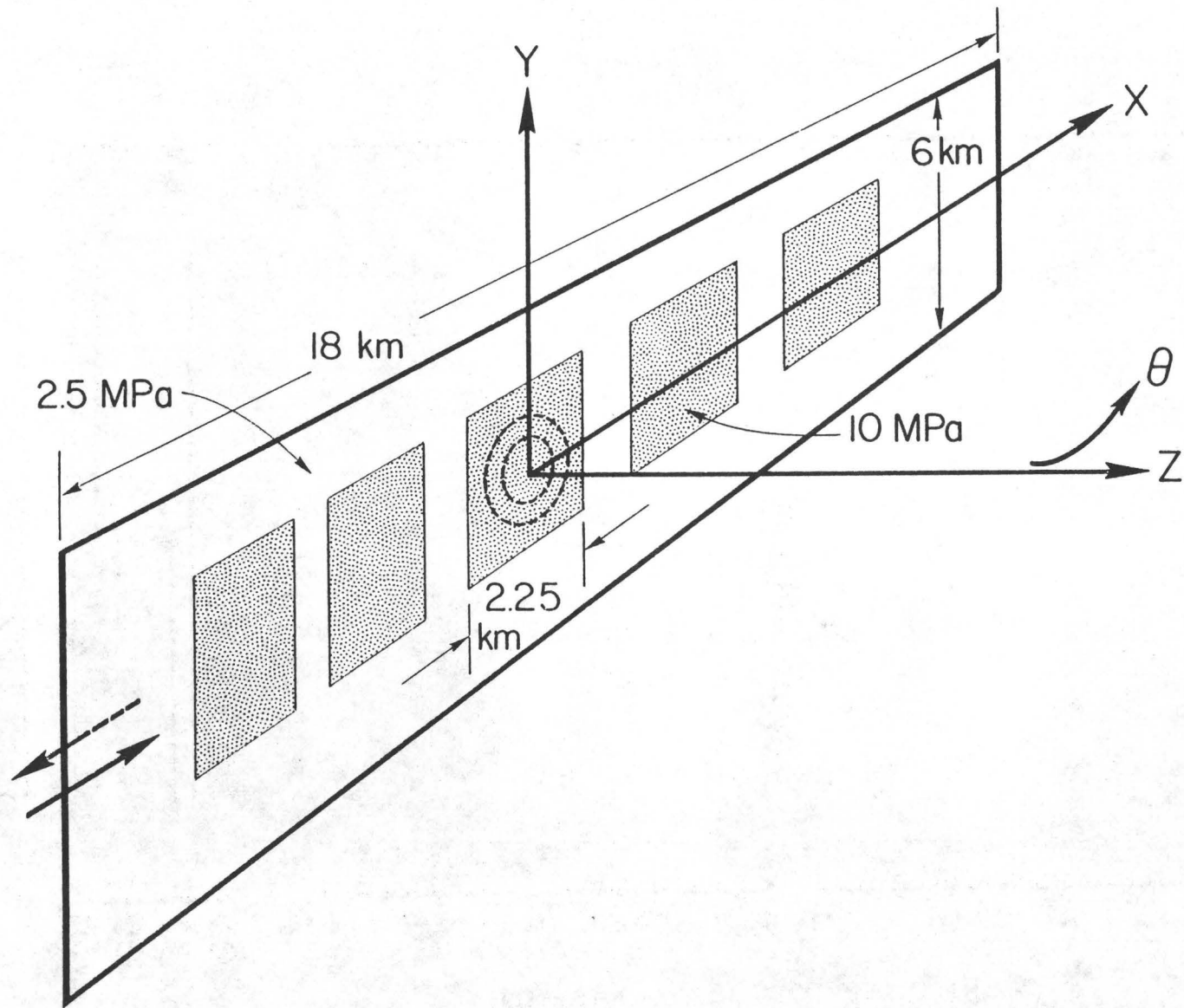
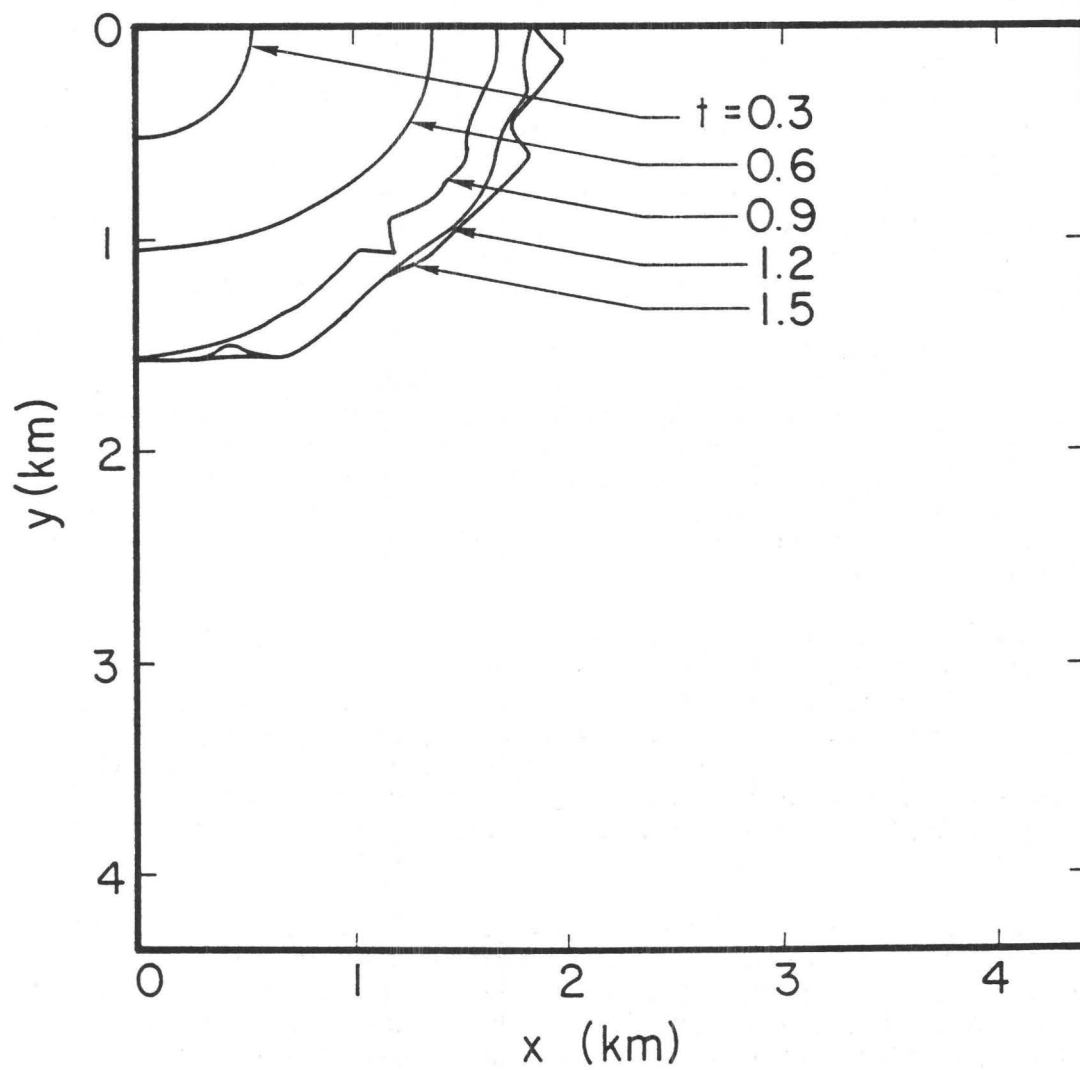Figure 12. Fault geometry for non-uniform prestress, Problem III.

484
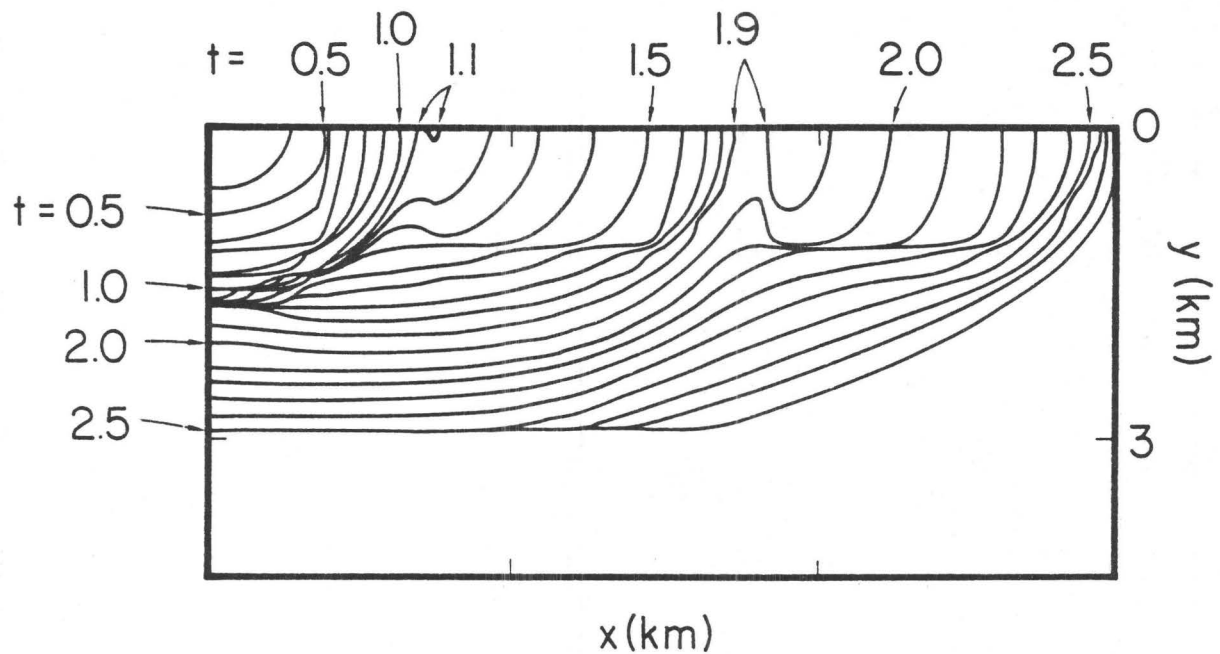
Figure 13. Rupture front contours obtained from the numerical solution to Problem III. Rupture front is shown at 0.1 second intervals. Contours at 1.1 seconds and 1.9 seconds indicate that the rupture has "jumped", with the slipping surface becoming temporarily multiply connected. Fault growth beyond x = 9 km and y = 3 km has been artificially inhibited by a strength barrier.
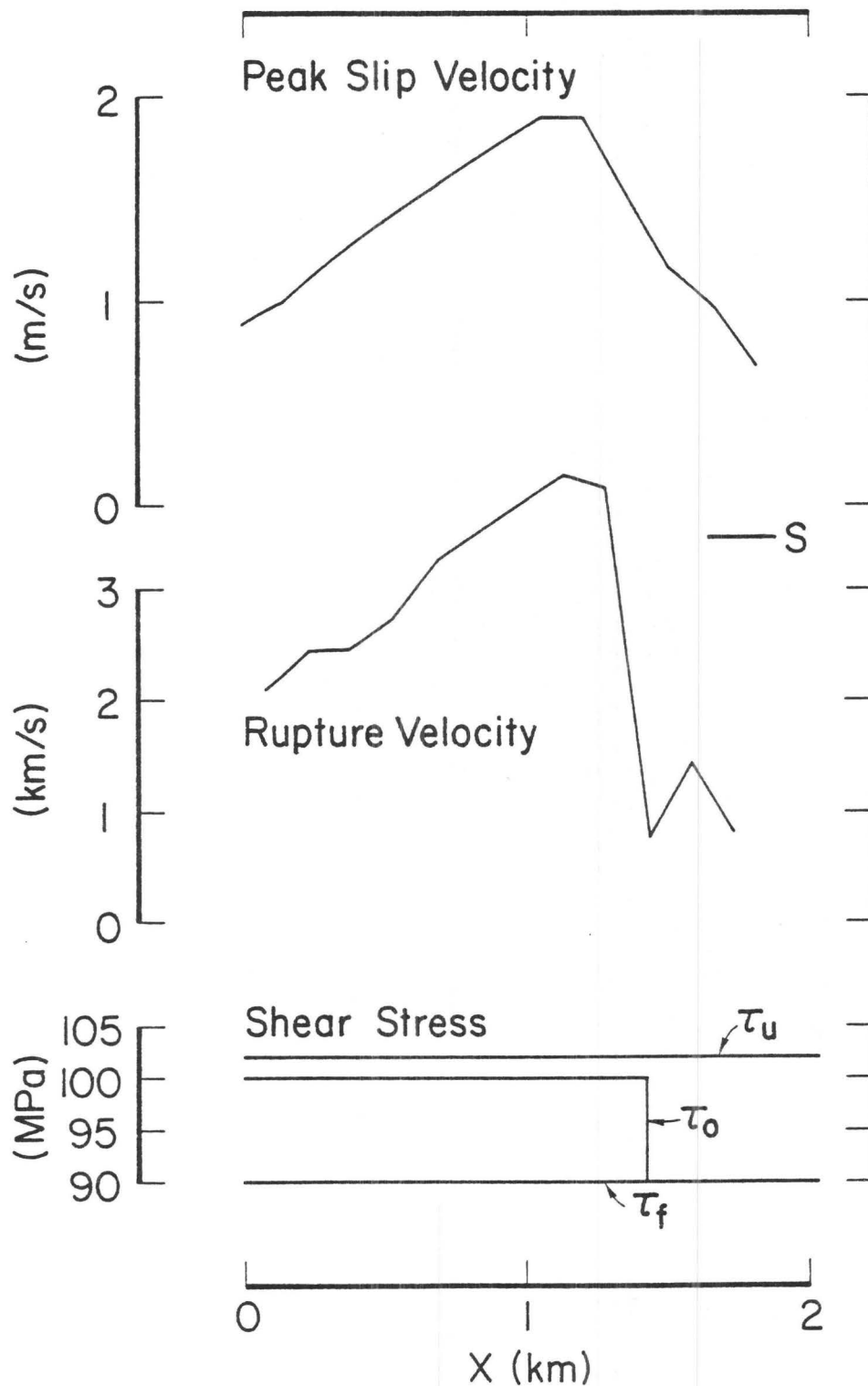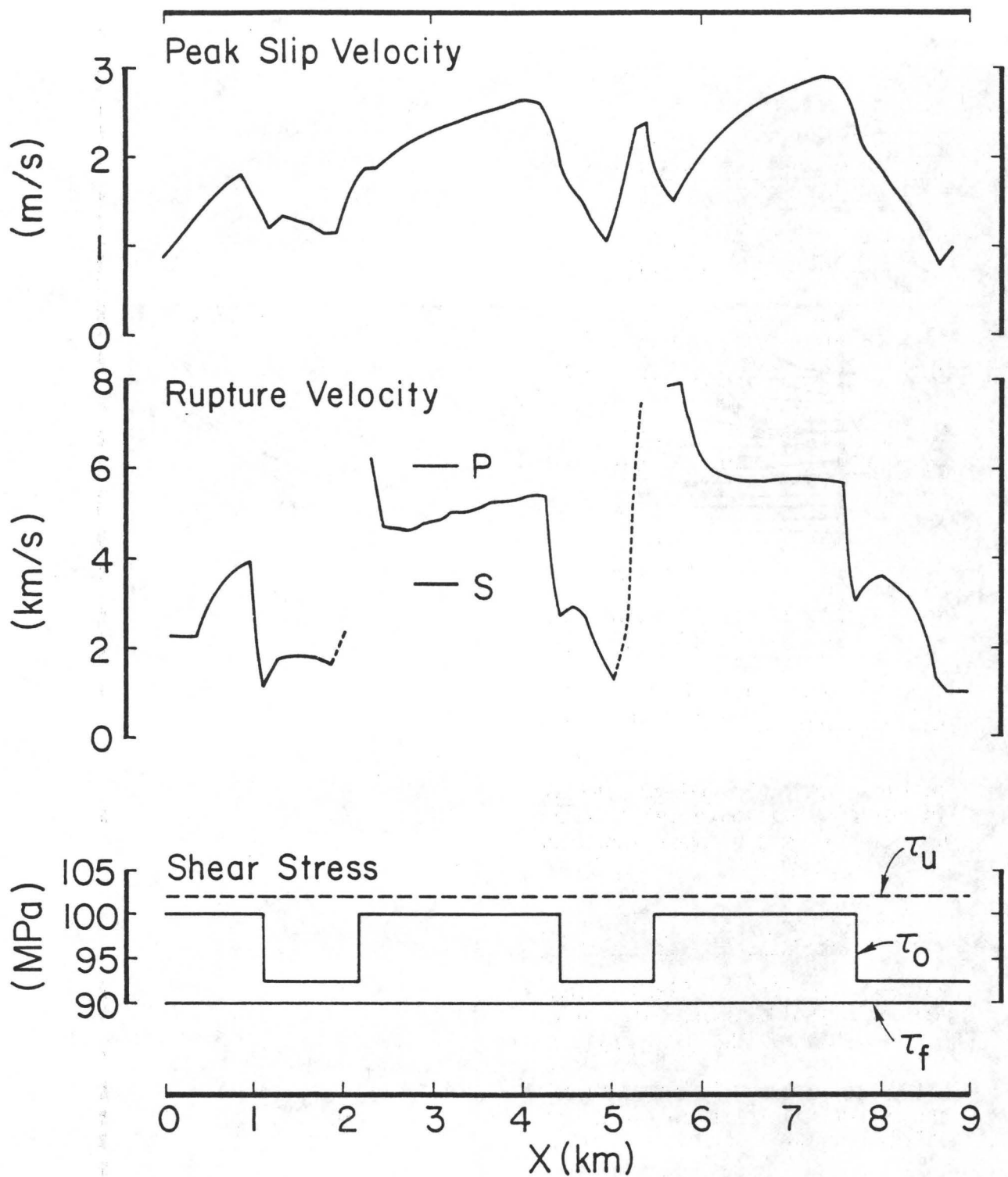
Figure 14. Rupture velocity and peak slip velocity for Problem III, as functions of position along the x axis. Peak slip velocity is obtained from low-passed (5 Hz) time histories. Dashed parts of the rupture velocity curve indicate regions which ruptured out of sequence. For example, rupture occurred at x = 5.6 km while the region between 5.0 and 5.6 km was still intact. The linkage between rupture velocity and peak slip velocity is particularly evident in this figure. Note that it is "local" rupture velocity which is plotted -- that is, the derivative of the rupture arrival time curve. Causality is not violated by those portions of the curve which exceed the P-wave velocity.

length, however, the secant rupture velocity is slightly sub-shear, equaling approximately 0.95 β.

The mean value of the dynamic stress-drop over the entire 6 x 18 km fault in Problem III is about 4.2 MPa. We have defined S for the uniform stress case as the ratio of the cohesive stress $(\tau_u - \tau_0)$ to the dynamic stress-drop $\Delta\tau$; if we take the ratio of spatial averages of these quantities for the non-uniform stresses of Problem III, we get a value of about 1.8. This value is considerably higher than the values for S of 0.2 and 0.5 used in the uniform prestress simulations. As a result, the average rupture velocity has been reduced from well above the shear wave speed for the uniform stress case to about 5 percent below the shear wave speed for the non-uniform prestress case. This result can be compared with the theoretical results cited earlier which predict sub-shear rupture velocity when S exceeds 1.63. It is interesting that the theoretical predictions, which were based on two-dimensional formulations and uniform stress conditions, are in reasonable accord with the gross average behavior of the three-dimensional, non-uniform stress model.

DISCUSSION

We have used a finite difference method to study crack propagation in a three-dimensional continuum, for conditions of both uniform and non-uniform prestress. The model of rupture which was employed satisfies two fundamental physical requirements: it ensures finite stresses in the continuum, and it dissipates energy in the course of crack extension. Furthermore, the rupture model agrees reasonably well with available laboratory measurements of unstable slip events although scaling of the model parameters to natural earthquakes presents large uncertainties.

In some respects, the behavior of our three-dimensional finite-stress numerical simulations resembles that predicted by two-dimensional singular-stress crack models. We observe an abrupt jump in rupture velocity after rupture of a stress concentration, for example, which agrees with the prediction of the singular theory that crack edges lack inertia (Eshelby, 1969). When the dynamic stress-drop outside the stress concentration was increased from 0 (Problem I) to 2.5 MPa (Problem II), the magnitude of the rupture velocity jump diminished slightly, but a finite jump still occurred instantaneously (within the resolution of the numerical solution).

Also foreshadowed by classical fracture mechanics, at least qualitatively, is the strong coupling which we find between rupture velocity and peak slip velocity for the non-uniformly prestressed fault simulations. Analytic solutions (for example, Freund, 1979) for the elastic field in the vicinity of a propagating crack-tip singularity give a slip velocity singularity whose intensity is proportional to two factors. The first of these is a functional of the whole rupture history of the crack, and can generally be found only from numerical solutions similar to ours; the second factor, however, increases monotonically with the instantaneous rupture velocity.

In other respects, the behavior of our finite-stress numerical simulations is quite different from the behavior of the singular models. An important result to emerge from this and earlier theoretical studies of finite-stress shear crack propagation (e.g., Burridge, 1973; Andrews, 1976b; Das and Aki, 1977; Burridge, Conn and Freund, 1979) is the recognition that rupture velocities in excess of the shear wave velocity may be possible when cohesive stresses are sufficiently low. In this study, we have established the applicability of the earlier two-dimensional results to the three-dimensional problem of mixed-mode shear crack propagation. Specifically, super-shear rupture velocity is predicted for low-cohesion cracks in directions for which Mode II (inplane) crack motion dominates, while sub-shear velocity is predicted for

directions of predominantly Mode III (antiplane) crack motion. Das (1981) has obtained a similar result using a different finite-stress rupture criterion (the "critical stress level" criterion) and a different numerical method (the boundary integral equation method).

The theoretical work cited above has demonstrated that rupture velocity becomes sub-shear if the cohesive stress is sufficiently high, i.e, if the dimensionless strength parameter S defined in the text is less than about 1.6. The numerical results presented here demonstrate that average rupture velocity can be reduced to the sub-shear level by another mechanism as well -- the introduction of stress heterogeneities. Furthermore, segments of a fault can rupture at super-shear velocity while the average rupture velocity remains sub-shear. The latter phenomenon was observed in all three of the non-uniform prestress simulations studied.

The numerical results indicate that the possibility of super-shear rupture velocity in rock depends on how near the average prestress is to some "failure" stress (which need not be identified with the laboratory strength as measured on small, homogeneous samples of intact rock). Thus, detailed study of rupture propagation velocity and its spatial variability, for a given event, could provide important information on the stress levels acting in the fault zone immediately prior to failure. Several studies have inferred super-shear rupture velocities for earthquakes (e.g., Kanamori, 1970; Douglas, Hudson and Marshall, 1981). These results may be evidence for prestress levels relatively close to failure. Super-shear rupture velocites have also been reported for laboratory stick-slip experiments (e.g., Wu, Thomson and Kuenzler, 1972; Johnson, Wu and Scholz, 1973). In the laboratory studies cited, stick-slip was preceded by stable sliding; it may be that the occurrences of super-shear rupture velocity reflect a weakened state associated with this stable sliding phase, rather than reflecting the static strength of the fault. On the other hand, Das and Scholz (1981) have cited evidence from earthquake aftershock occurrences, for several events, which suggests the presence of stress levels very close to failure even off the plane of main-shock faulting.

Most seismic studies of rupture velocity only estimate its average value. Thus, it is possible that a rupture mechanism analogous to our Problem III simulation occurs commonly in nature. That is, some fault segments in large earthquakes may rupture at super-shear velocities, even though most reported rupture velocity determinations are less than the shear wave velocity (e.g., Geller, 1976). In fact, Wu and Kanamori (1973) prefer such a mechanism for the 1965 Rat Island earthquake. They infer from seismic surface wave observations that the event had an average rupture velocity of 4 km/sec. At the same time, their analysis of seismic body waves

led to a multiple event interpretation; the inferred rupture velocities for the individual sub-events were in the range 5.1 to 6.7 km/sec, values approaching the P-wave velocity. Actually, our numerical simulations show that even supersonic (greater than the P velocity) rupture velocities may be physically admissible for individual sub-events of an earthquake, even though causality demands that its average rupture velocity be subsonic.

Even the relatively simple prestress configurations studied here result in fairly complex rupture histories. An important further step will be to examine their effect on the radiated seismic signal. The radiated wavefield can be synthesized using the slip histories obtained from these numerical simulations, and this issue will be considered in a subsequent study.

ACKNOWLEDGMENTS

REFERENCES

Aki, K. (1979). Characterization of barriers on an earthquake fault, J. Geophys. Res., 84, 6140–6148.

Andrews, D. J. (1976a). Rupture propagation with finite stress in antiplane strain, J. Geophys. Res., 81, 3575–3582.

Andrews, D. J. (1976b), Rupture velocity of plane strain shear cracks, J. Geophys. Res., 81, 5479–5687.

Bache, T. C., D. G. Lambert, and T. G. Barker (1980), A source model for the March 28, 1975 Pocatello Valley earthquake from time-domain modeling of teleseismic P-waves, Bull. Seism. Soc. Am., 70, 405–418.

Burridge, R. (1973). Admissible speeds for plane-strain self-similar shear cracks with friction but lacking cohesion, Geophys. J. R. Astr. Soc., 35, 439–455.

Burridge, R., G. Conn, and L. B. Freund (1979). The stability of a rapid Mode II shear crack with finite cohesive traction, J. Geophys. Res., 85, 2210–2222.

Burridge, R., and J. R. Willis (1969). The self-similar problem of the expanding elliptical crack in an anisotropic solid, Proc. Camb. Phil. Soc., 66, 443–468.

Byerlee, J. D. (1967). Frictional characteristics of granite under high confining pressures, J. Geophys. Res., 72, 3639–3648.

Das, S. (1981). Three-dimensional spontaneous rupture propagation and implications for the earthquake source mechanism, Geophys. J., 67, 375–393.

Das, S. and K. Aki (1977). A numerical study of two-dimensional spontaneous rupture propagation, Geophys. J. R., 50, 643–668.

Das, S. and C. H. Scholz (1981). Off-fault aftershock clusters caused by shear stress increase , Bull. Seism. Soc. Am., 71, 1669–1675.

Day, S. M. (1979). Three-dimensional finite difference simulation of fault dynamics, Final Report SSS-R-80-4295, Systems, Science and Software, La Jolla, California.

Day, S. M. (1982). Three-dimensional finite difference simulation of fault dynamics: Rectangular faults with fixed rupture velocity, Bull. Seism. Soc. Am. (in press).

Del Mar Technical Associates (1978). Simulation of earthquake ground motions for San Onofre Nuclear Generating Station Unit 1, Final report for Southern California Edison Company, submitted for review to the Nuclear Regulatory Commission.

Dieterich, J. H. (1980). Experimental and model study of fault constitutive properties, in Solid Earth Geophysics and Geotechnology, AMD-Vol. 42, ed. S. Nemat Nasser, American Society of Mechanical Engineers, New York.

Dieterich, J. H. (1981). Constitutive properties of faults with simulated gouge, Geophysical Monograph Series (J. Handin Festschrift), American Geophysical Union.

Dieterich, J. H., D. W. Barber, G. Conrad and Q. A. Gordon (1978). Preseismic slip in a large scale friction experiment, Proceedings of the 19th U.S. Rock mechanics Syposium, Mackay School of Mines, University of Nevada, Reno.

Douglas, A., J. A. Hudson, and P. D. Marshall (1981). Earthquake seismograms that show Doppler effects due to crack propagation, Geophys. J. R. Astr. Soc.m 64, 163-185.

Eshelby, J. D. (1969). The elastic field of a crack extending non-uniformly under general anti-plane loading, J. Mech. Phys. Solids, 17, 177-199.

Freund, L. B. (1979). The mechanics of dynamic shear crack propagation, J. Geophys. Res., 84, 2199-2209.

Geller, R. J. (1976). Scaling relations for earthquake source parameters and magnitudes, Bull. Seism. Soc. Am., 66, 1501-1523.

Hanks, T. C. (1974). The faulting mechanism of the San Fernando earthquake, J. Geophys. Res., 79, 1215-1229.

Hartzell, S. H., and J. N. Brune (1979). The Horse Canyon earthquake of August 2, 1975 -- Two-stage stress-release process in a strike-slip earthquake, Bull. Seism. Soc. Am., 69, 1161-1173.

Husseini, M. I., D. B. Jovanovich, M. R. Randall, and L. B. Freund (1975). The fracture energy of earthquakes, Geophys. J. R. Astr. Soc., 43, 367-385.

Ida, Y. (1972), Cohesive force across the tip of longitudinal-shear crack and Griffith's specific surface energy, J. Geophys. Res., 77, 3796-3805.

Ida, Y., and K. Aki (1972). Seismic source time function of propagating longitudinal-shear cracks, J. Geophys. Res., 77, 2034-2044.

Johnson, T., F. T. Wu, and C. H. Scholz (1973). Source parameters for stick-slip and for earthquakes, Science, 179, 278-280.

Kanamori, H. (1970). Synthesis of long-period surface waves and its application to earthquake source studies -- Kurile Islands earthquake of October 13, 1963, J. Geophys. Res., 75, 5011-5027.

Kanamori, H., and G. S. Stewart (1978). Seismological aspects of the Guatemala earthquake of February 4, 1976, J. Geophys. Res., 83, 3427-3434.

Kostrov, B. V. (1964). Self-similar problems of propagation of shear cracks, J. Appl. Math. Mech., 28, 1077-1087.

Kostrov, B. V. (1966). Unsteady propagation of longitudinal shear cracks, J. Appl. Math. Mech., 30, 1241-1248.

Madariaga, R, (1977). High-frequency radiation from crack0 (stress-drop) models of earthquake faulting, Geophys. J., 51, 625-651.

Neuber, H., (1937). Kerbspannungslehre, Springer-Verlag, Berlin; Theory of notch stresses: Principles for exact calculation of strength with reference to structural form and material, the Office of Tech. Info., AEC-tr-4547, 1958 (English translation).

Richards, P. G. (1976). Dynamic motions near an earthquake fault: A three-dimensional solution, Bull. Seism. Soc. Am., 66, 1-32.

Scholz, C. H., P. Molnar, and T. Johnson (1972). Detailed studies of frictional sliding of granite and implications for the earthquake mechanism, J. Geophys. Res., 77, 6392-6406.

Swanger, H. J., S. M. Day, J. R. Murphy, and R. Guzman (1980). State-of-the art study concerning near-field earthquake ground motion, Nuclear Regulatory Commission report NUREG/CR-1978, prepared by Systems, Science and Software.

Virieux, J., and R. Madariaga (1982). Dynamic faulting studied by a finite difference method, Bull. Seism. Soc. Am., in press.

Wu, F. T., and H. Kanamori (1973). Source mechanism of February 4, 1965, Rat Island earthquake, J. Geophys. Res., 78, 6082-6092.

Wu, F. T., K. C. Thomson, and H. Kuenzler (1972). Stick-slip propagation velocity and seismic source mechanism, Bull. Seism. Soc. Am., 62, 1621-1628.

REMARKS ON SEISMIC ENERGY RADIATION FROM SIMPLE SOURCES

By

J. W. Rudnicki

Department of Civil Engineering
The Technological Institute
Northwestern University
Evanston, Illinois 60201

(312) 492-7629

ABSTRACT

General expressions for energy radiated from seismic sources in linear elastic bodies are illustrated and clarified by examining the energy radiated from two simple sources: a spherically symmetric source and a constant stress drop (crack) fault model. Calculations with the spherical source demonstrate that the point source approximation for the radiated energy is not asymptotic in the sense that it does not approach the actual radiated energy for small source dimension. Comparison between the energies radiated from the spherical source for a ramp time function and for a modulated ramp demonstrate that the modulation is not effective in increasing the total radiated energy even though it does cause a peak in the spectrum of the farfield particle velocity at the characteristic frequency of the modulation. For $a/cT > 2$, where a is the radius of the spherical source, c is the wave speed and T is the rise time, the strain energy change overestimates the radiated energy by less than a factor of two. The simple fault model is used to examine further the circumstances for which the radiated energy can be predicted adequately from the knowledge of the difference between the static end states. The conditions given by Rudnicki and Freund (1981) are shown to generalize the assumption of Orowan (1960) that the final stress on the fault equals the dynamic friction stress.

INTRODUCTION

Rudnicki and Freund (1981) have recently examined representations for the energy radiated by seismic sources in linear elastic, isotropic, homogeneous solids. The purpose of this examination was to clarify the nature of seismic energy radiation and to illuminate its origin in seismic faulting without making any unnecessarily restrictive hypotheses about the source of radiation. Hence, farfield representations of the radiated energy were obtained for any source describable by a moment density tensor. Fault surface representations were obtained without making any assumptions about the behavior of the fault surface tractions and particle velocities or the relation between them.

In this paper, the meaning of the general expressions for radiated energy is illustrated and clarified by detailed examination of two very simple models of seismic sources: a spherically symmetric homogeneous source and a constant stress drop (crack) fault model with uniform fault surface tractions. A spherically symmetric source is obviously not an appropriate model for seismic faulting. Nevertheless, it has been frequently used to discuss radiated seismic energy (e.g. Yoshiyama, 1963; Bath, 1966; Randall, 1964, 1973) because simple evaluation of the radiated energy is possible. Although numerical analysis is routinely used to study more realistic fault models, the quantities necessary to evaluate the radiated energy, fault surface tractions and particle velocities or farfield particle velocities, are often difficult or expensive to compute accurately. More importantly, many of the general features of energy radiated from the spherical source model also apply to radiation from a fault although the details are, of course, different. In addition, an important advantage that the spherical source model has over many simple dislocation models, for example, that of Haskell (1964), is that the strain energy change is bounded so that it is possible to make a nontrivial assessment of the amount of energy radiated relative to the total amount available.

Because, as already noted, the geometry of the spherical source model is not appropriate for a realistic model of faulting, some features of energy radiation from constant stress drop (crack) models are also examined. Specifically, the results of Rudnicki and Freund (1981) concerning the circumstances in which the radiated energy can be estimated from the difference between the static end states are examined in terms of the simple fault model of Orowan (1960). It is shown that the conditions given by Rudnicki and Freund (1981) are a generalization of Orowan's (1960) assumption that the final stress on the fault equals the dynamic friction stress.

The paper begins by reviewing the results of Rudnicki and Freund (1981). Then, results on energy radiation from the spherical source and simple crack models are presented. Finally, the relation between a static estimate of radiated energy and some simple dynamic estimates used to interpret seismic observations is discussed.

RESULTS FROM RUDNICKI AND FREUND

Farfield Representations

Rudnicki and Freund (1981) adopt the following definition of radiated energy:

$$E_R = \int_{-\infty}^{\infty} \int_S [n_j \sigma_{ij} \dot{u}_i] \, dS dt \tag{1}$$

where u_i is the displacement measured from some initial static state, σ_{ij} is the stress associated with u_i, the superposed dot denotes the time rate of change, S is a spherical surface of radius r centered at the source, and $\underset{\sim}{n}$ is the unit normal to S directed toward the source. The integrand of (1) is the rate at which work is done by material inside S on material outside S. In general, the integral in (1) will depend on the radius r at which it is evaluated. However, for $r \gg \ell$, where ℓ is a characteristic source dimension, the stress and particle velocity for elastodynamic sources typically satisfy

$$\dot{u}_i = O(r^{-1}) , \quad \sigma_{ij} = O(r^{-1}) \tag{2}$$

as $r \to \infty$ in any fixed direction. Because the element of area dS can be written as $dS = r^2 d\Omega$ where $d\Omega$ is an element of solid angle, (1) can be expected to have a finite nonzero value as $r \to \infty$.

Although the representation (1) gives a clear conceptual meaning to radiated energy as the total energy flow from the source, it is not amenable to direct measurement. However, if in addition to (2), the stress and particle velocity are related by

$$\sigma_{ij} n_j + \rho (\underset{\sim}{n} \cdot \underset{\sim}{\dot{u}}) n_i c_d + \rho (\underset{\sim}{m} \cdot \underset{\sim}{\dot{u}}) m_i c_s = O(r^{-2}) \tag{3}$$

as $r \to \infty$ in any fixed direction, then the radiated energy can be expressed as

$$E_R = \int_{-\infty}^{\infty} \int_S \rho [c_d (\underset{\sim}{n} \cdot \underset{\sim}{\dot{u}})^2 + c_s (\underset{\sim}{m} \cdot \underset{\sim}{\dot{u}})^2] dS dt \tag{4}$$

where ρ is the density, c_d and c_s are the dilatational and shear wave speeds, respectively, and $\underset{\sim}{m}$ is the unit tangent vector to S in the direction of the shear traction on S, that is,

$$m_j (n_k \sigma_{k\ell} m_\ell) = n_i \sigma_{ij} - n_j (n_k \sigma_{k\ell} n_\ell) \text{ on } S.$$

Of course, (4) applies only for isotropic solids. Rudnicki and Freund (1981) demonstrate that (3) is satisfied for all sources that can be characterized by a moment density tensor.

The radiated energy, as represented by (4), can, at least in principle, be determined by observations. Farfield particle velocities can be observed and used to estimate the integral (4). Despite the practical difficulties that may be involved in such a procedure, it is significant that the radiated energy can be measured, since observations in the farfield are not sufficient, even in

principle, to reconstruct the complete spatial variation of the moment density tensor (Kostrov, 1968; Aki and Richards, 1980). The integral (4) can, of course, be estimated in the nearfield, but, in this case, the representation (4) is not equivalent to (1) and the interpretation of (4) as energy outflow from the source is lost. Note, however, that because farfield particle velocities and, hence, the radiated energy cannot, in general, be expressed in terms of the seismic moment tensor, one can infer that the radiated energy contains information that is not available even if the complete time variation of the seismic moment tensor is known. Furthermore, the Parseval identity can be used to express E_R in terms of the Fourier transforms of the particle velocities. These properties make the radiated energy an attractive quantity for characterizing seismic sources.

Practical difficulties that arise in making empirical estimates of E_R are, however, substantial. A good estimate requires that the particle velocities be observed over a sufficiently large angular range. Moreover, corrections for path effects, finite boundaries, and differing distances of observation points from the source must be made. Nevertheless, this procedure apparently was used by Gutenberg and Richter (1942) to establish a relationship between radiated energy and magnitude although several authors (e.g. Brune, 1970; Vassiliou and Kanamori, 1982) have remarked that the precise significance of this relationship is unclear. However, because of the difficulties mentioned, it may often be convenient to approximate the source as a point. More precisely, in the point source approximation attention is restricted to wavelengths that are very much greater than source dimensions. In this case, the radiated energy can be expressed in terms of the moment tensor $M_{ij}(t)$ and, in particular, Rudnicki and Freund (1981) have shown that the radiated energy is given by

$$60\pi\rho\ c_s^5\ E_R = (c_s/c_d)^5 \int_{-\infty}^{\infty} \left\{ 2\ddot{M}'_{ij}(\tau_d)\ddot{M}'_{ij}(\tau_d) + \frac{5}{3}\left[\ddot{M}_{kk}(\tau_d)\right]^2 \right\} dt$$

$$+ 3 \int_{-\infty}^{\infty} \ddot{M}'_{ij}(\tau_s)\ \ddot{M}'_{ij}(\tau_s)\ dt \tag{5}$$

where $\tau_d = t - r/c_d$, $\tau_s = t - r/c_s$ and $M'_{ij} = M_{ij} - \delta_{ij}M_{kk}/3$. For a fault source that is a planar surface S_F of sliding discontinuity, the only nonzero components of M_{ij} are $M_{12} = M_{21} = M(t)$ where

$$M(t) = \mu \int_{S_F} \Delta u(\xi_1,\xi_3,t)d\xi_1 d\xi_3 \ , \tag{6}$$

μ is the shear modulus and the coordinate axes have been chosen so that the slip Δu is in the x_1 direction and x_2 is normal to the fault plane. In this case (5) reduces to

$$E_R = \frac{1}{10\pi\rho c_s^5} \left\{ \int_{-\infty}^{\infty} \ddot{M}^2(t - r/c_s)dt + \frac{2}{3}(c_s/c_d)^5 \int_{-\infty}^{\infty} \ddot{M}^2(t - r/c_d)dt \right\} \tag{7}$$

Despite the simplicity of the point source approximation, calculations with the spherically symmetric source described later indicate that although this may be an adequate approximation for displacement values, it has deficiencies when applied to the radiated energy.

Fault Surface Representations

The previous expressions for the radiated energy (with the exception of (7)), apply for general types of sources and are useful for making estimates of the radiated energy from observations. To assess the physical origin of the radiated energy it is necessary to have representations that relate to the nonelastic processes at the source. If the source has the structure of a propagating crack, Rudnicki and Freund (1981), following Kostrov (1974), have shown that the radiated energy can be expressed as

$$E_R = -\Delta U - \int_{-\infty}^{\infty} \int_{S_F} \sigma_{ij} n_j \dot{u}_i \, dS dt - \int_{-\infty}^{\infty} F(t) \, dt \qquad (8)$$

where, for convenience, it has been assumed that the initial stress is zero (Rudnicki and Freund (1981) show that the initial stress does not contribute to the radiated energy). In (8) $\Delta U = U_{final} - U_{initial}$ is the change in strain energy of the body; the second term is the work of the fault surface tractions, where S_F is a surface coinciding with the fault surfaces (excluding the extending edges) and n_i is the unit normal pointing into the adjacent material; and $F(t)$ is the energy flux to the extending fault edges. More precisely, $F(t)$ is defined as (Freund, 1972a; Kostrov, 1974)

$$F(t) = \lim_{S_0 \to 0} \int_{S_0} \left\{ \sigma_{ij} n_j \dot{u}_i + \left[\frac{1}{2} \sigma_{ij} u_{ij} + \frac{1}{2} \rho \dot{u}_i \dot{u}_i \right] v \right\} dS \qquad (9)$$

where S_0 is a tube enclosing the fault edges and v is the local velocity of the fault edge. Although the strain energy change depends only on the static end states, the other two terms depend on the details of the dynamic rupture process. Hence, as is to be expected, E_R cannot, in general, be determined from the static end states.

If the fault extension occurs quasistatically, no energy is radiated and (8) reduces to an expression for the strain energy change

$$\Delta U = - \int_{-\infty}^{\infty} \int_{S_F} [\sigma_{ij} n_j \dot{u}_i]_0 \, dS dt - \int_{-\infty}^{\infty} F_0(t) \, dt \qquad (10)$$

where the subscript "0" denotes the value during quasistatic propagation. Subtracting (10) from (8) yields a revealing formula for the radiated energy:

$$E_R = \int_{-\infty}^{\infty} \int_{S_F} \{ [\, n_j \sigma_{ij} \dot{u}_i \,]_0 - [n_j \sigma_{ij} \dot{u}_i] \} \, dS dt + \int_{-\infty}^{\infty} [F_0(t) - F(t)] \, dt \quad (11)$$

The source of radiated energy is the difference in the work rate of the fault surface tractions during quasistatic and dynamic extension (first term) and the difference in the energy flux to the fault edge during quasistatic and dynamic extension (second term). An alternative expression for the radiated energy that is essentially the form given by Kostrov (1974, eq. 2.26) can be obtained by integration by parts of the first term in (11) (permissible because the fault surface tractions are bounded) and noting that the integrated portions vanish because the static end states are fixed. The result is

$$E_R = \int_{-\infty}^{\infty} \int_{S_F} \{ [n_j \dot{\sigma}_{ij} u_i] - [n_j \dot{\sigma}_{ij} u_i]_0 \} \, dS dt + \int_{-\infty}^{\infty} [F_0(t) - F(t)] \, dt \; . \quad (12)$$

This form makes evident that there is no contribution from the first term in (11) and (12) if the fault surface tractions are time independent. Also, if an average fault surface traction $(\sigma_{ij} n_j)_{ave}$ is defined by

$$\int_{-\infty}^{\infty} \int_{S_F} [\sigma_{ij} n_j \dot{u}_i]_0 \, dS dt = \int_{S_F} [(n_j \sigma_{ij})_{ave} u_i^{final}] \, dS \quad (13)$$

the first term in (11) can be rewritten using the relation

$$\int_{-\infty}^{\infty} \int_{S_F} [\sigma_{ij} n_j \dot{u}_i]_0 \, dS dt = \int_{-\infty}^{\infty} \int_{S_F} [(\sigma_{ij} n_j)_{ave} \dot{u}_i]_0 \, dS dt \; . \quad (14)$$

SPHERICALLY SYMMETRIC SOURCE

Consider a spherical source of radius a. If the source is homogeneous, the stress and particle velocities in the surrounding linear elastic material are identical to those that result from the application of a pressure p(t) to the boundary of a spherical cavity. The behavior of p(t) will, of course, depend on the nature of the physical processes in the source region, but here it suffices to assume that an appropriate pressure function can be inferred. Hence, it is only necessary to consider the response of the linear elastic region $r > a$ subject to the boundary condition

$$\sigma_r(a, t) = -p(t) \tag{15}$$

where $\sigma_r(r, t)$ is the radial component of stress. The only nonzero displacement is $u(r,t)$ in the radial direction and the radial stress is related to the displacement by the equation

$$\sigma_r = (\lambda + 2\mu) \left(\frac{\partial u}{\partial r} + 2\frac{u}{r} \right) - 4\mu \frac{u}{r} \tag{16}$$

where μ is the shear modulus and λ is the Lame constant. Thus, the definition of radiated energy (1) reduces to

$$E_R = 4\pi R^2 \int_{-\infty}^{\infty} \left[-\sigma_r(R,t)\dot{u}(R,t) \right] dt \tag{17}$$

where $R \gg a$.

For zero initial velocity and displacement and a pressure p(t) applied beginning at t = 0, the solution for the particle velocity has the following form

$$\dot{u}(r,t) = \frac{1}{\rho c} \frac{a}{r} \int_0^{t-(r-a)/c} \dot{p}(t')g(t-t'-(r-a)/c) \, dt' \tag{18}$$

where ρ is the density and $c = c_d$ is the dilatational wave speed. The function g is the particle velocity at $r = a$ due to sudden application of a pressure ρc (Achenbach (1973, p. 131) gives the potential φ for this case where $u = \partial\varphi/\partial r$)) and is given by

$$g(\tau) = \beta^{-1} e^{-\alpha c\tau/a} \left[(a/r-\alpha) \sin (\beta c\tau/a) + \beta \cos (\beta c\tau/a) \right] \tag{19}$$

where

$$\alpha = 2\mu/(\lambda + 2\mu) = (1-2\nu)/(1-\nu)$$

and $\beta^2 = 2\alpha - \alpha^2$. It can easily be verified that $\dot{u}(r,t)$ and $\sigma_r(r,t)$ satisfy (2) and that (3), which in this case reduces to

$$\sigma_r + \rho c \dot{u} = 0(r^{-2}) \tag{20}$$

as $r \to \infty$, is also satisfied. Consequently, the radiated energy can be expressed in the form (4) as

$$E_R = 4\pi R^2 \rho c \int_{-\infty}^{\infty} \dot{u}^2(R,t) \, dt \tag{21}$$

where the equivalence of (21) and (17) is exact in the limit as $R \to \infty$.

For a spherically symmetric source, the moment tensor is isotropic, that is,

$$M_{ij}(t) = M(t) \, \delta_{ij} \tag{22}$$

and $M(t)$ is related to $p(t)$ by

$$M(t) = \pi\mu^{-1}(\lambda + 2\mu)a^3 p(t) \tag{23}$$

(Aki and Richards, 1980, Vol. I, Problem 3.5). Consequently, the point source approximation for the radiated energy (5) reduces to

$$E_R = \frac{1}{4\pi(\lambda+2\mu)c^3} \int_{-\infty}^{\infty} \ddot{M}^2(t-r/c) \, dt \tag{24}$$

where the relation $(\lambda+2\mu) = \rho c^2$ has been used.

An alternate expression for the radiated energy, analogous to the fault surface representation (11), can be obtained by demanding that the rate of work at $r = a$ and at $r = R$ be equal to the rate of change of kinetic energy $\dot{K}$ and of strain energy $\dot{U}$ in the region $a < r < R$. This requirement is expressed as

$$4\pi R^2 \sigma_r(R,t)\dot{u}(R,t) - 4\pi a^2 \sigma_r(a,t)\dot{u}(a,t) = \dot{K} + \dot{U} \tag{25}$$

Integrating in time and recognizing that the kinetic energy vanishes in the initial and final states yield

$$E_R = 4\pi a^2 \int_{-\infty}^{\infty} p(t)\dot{u}(a,t)dt - \Delta U \tag{26}$$

where (15) and (17) have been used and ΔU is the difference between the strain energy in the initial and final states. For quasistatic application of $p(t)$, $E_R = 0$ (as can be verified by direct calculation from the quasistatic solution) and (26) reduces to

$$\Delta U = 4\pi a^2 \int_{-\infty}^{\infty} p(t)\dot{u}_0(a,t)dt \tag{27}$$

where, as before, the subscript "0" denotes the quasistatic value. The quasistatic solution for the displacement is

$$u_0(r,t) = p(t)a^3/4\mu r^2 \tag{28}$$

and, thus, the strain energy change is

$$\Delta U = p_\infty^2 \pi a^3/2\mu \tag{29}$$

where $p_\infty = \lim_{t \to \infty} p(t)$. Substituting (27) into (26) yields

$$E_R = 4\pi a^2 \int_{-\infty}^{\infty} p(t) \left[\dot{u}(a,t) - \dot{u}_0(a,t)\right] dt \tag{30}$$

The interpretation of (30) is similar to that of (11): energy is radiated because the particle velocity at the source boundary is different during quasistatic and dynamic response of the material. If (30) is integrated by parts the result is

$$E_R = 4\pi a^2 \int_{-\infty}^{\infty} \dot{p}(t) \left[u_0(a,t) - u(a,t)\right] dt \tag{31}$$

where the integrated portions vanish because $u_0(a,t) = u(a,t)$ in the initial and final states.

In the following subsections the radiated energy is determined for three specific choices of $p(t)$: an exponential increase, a ramp function, and a modulated ramp function. The first example is used to assess the accuracy of the point source approximation. The last two examples are compared to illustrate the effect on the radiated energy of enriching the high frequency portion of the particle velocity spectrum.

Example 1: Exponential Pressure Increase

Assume the pressure $p(t)$ is given by

$$p(t) = p_\infty(1 - e^{-t/T}) \tag{32}$$

where p_∞ is the final value of $p(t)$. The particle velocity can be evaluated from (18) and used to determine the radiated energy from either (21) or (26). The result for the radiated energy is

$$E_R = \frac{\pi}{2\mu} p_\infty^2 a^3 \frac{(a/cT)^2}{[a/cT) + \alpha]^2 + \beta^2} \tag{33}$$

and the radiation efficiency, defined as $\eta = E_R / \Delta U$, is plotted in Figure 1 for $\nu = 0.25$ as a function of a/cT. Note that as $T \to 0$, $p(t)$ approaches a step function and $\eta = 1$.

The exact expression for the radiated energy (33) can be compared with the result of the point source approximation by substituting (32) into (23) and evaluating the integral (24). The result is

$$(E_R)_{point} = \frac{M_\infty^2}{8\pi (\lambda + 2\mu) (cT)^3} \tag{34}$$

where $M_\infty = \pi \mu^{-1} (\lambda + 2\mu) a^3 p_\infty$. Because the strain energy change for a point source of fixed moment is infinite, the radiation efficiency of a point source is zero. The ratio of the energy radiated by the point source to the actual radiated energy is

$$\frac{(E_R)_{point}}{E_R} = (a/cT) [1 + (a/cT) + (2\alpha)^{-1} (a/cT)^2] \tag{35}$$

Examination of (35) reveals that the point source approximation yields a value for the radiated energy within 10% of the actual value only for a/cT in the range $0.52 \le a/cT \le 0.56$. Moreover, in contrast to the point source approximation to the particle velocities, which becomes more accurate as a/cT becomes small, the approximation for the radiated energy severely underestimates E_R for small values of a/cT.

Example 2: Ramp Function

For a ramp function increase in pressure, that is,

$$p(t) = P_\infty \begin{cases} t/T & , 0 < t < T \\ 1 & , t \ge T \end{cases} \tag{36}$$

the radiated energy is

$$E_R = \frac{\pi}{2\mu} p_\infty^2 a^3 \{\alpha^{-1}(a/cT)^2 [1-\beta^{-1} e^{-\alpha cT/a} (\alpha \sin \beta cT/a + \beta \cos \beta cT/a)] \} \tag{37}$$

The radiation efficiency is again plotted in Figure 1. The curve is qualitatively similar to that for the exponential time function although the initial rise of the ramp function is much steeper.

Example 3: Modulated Ramp Function

The pressure increase is assumed to have the form of the modulated ramp function used by Haskell (1964) for the displacement in his fault model:

$$p(t) = p_\infty \begin{cases} \frac{1}{T}\left[t - (T/2n\pi)\sin(2n\pi t/T)\right] & , \ 0 < t < T \\ 1 & , \ t > T \end{cases} \tag{38}$$

For $n = 0$, $p(t) = 0$ for $0 < t < T$ and for $n = \infty$ (38) reduces to the ramp function (36). The modulation produces a peak in the Fourier spectrum proportional to $(\omega - \omega_n)^{-2}$ where ω is Fourier frequency and $\omega_n = 2n\pi/T$. The evaluation of the radiated energy involves considerably more algebra than in the two previous examples but the final result can, nevertheless, be expressed in the following compact form

$$\frac{E_R}{(2\mu)^{-1}p_\infty^2 \pi a^3} = \frac{(2\alpha)(a/cT)\Omega^2}{(2\alpha - \Omega^2)^2 + 4\alpha^2\Omega^2}$$

$$+ \frac{(a/cT)^2}{\beta\alpha}\, \text{Im}\left\{ \frac{\Omega^4(\alpha + \imath\beta)}{[(-\alpha + \imath\beta)^2 + \Omega^2]^2}\left[1 - \exp\left((-\alpha + \imath\beta)\,cT/a\right)\right] \right\} \tag{39}$$

where $\Omega = 2n\pi(a/cT)$, $\imath = (-1)^{\frac{1}{2}}$, and Im $\{\ldots\}$ denotes the imaginary part of $\{\ldots\}$. This expression reduces to (37) for $n \to \infty$. Equation (39) is plotted in Figure 1 as a function of a/cT for several values of n. For $n \geq 3$, the curves cannot be distinguished from those for the ramp function pressure. Although the modulation of the ramp function has a significant effect on the Fourier spectrum of the particle velocity, amplifying the spectrum in the neighborhood of $\omega = \omega_n$, it is evident from Figure 1 that the overall effect on the radiated energy is relatively small. The greatest effect occurs for $n = 1$ and even in the steep portion of the curve, the difference in E_R is at most by a factor of two. Although it is not known whether this feature is shared by more realistic models of seismic faulting, it is consistent with the conclusion of an empirical study by Vassiliou and Kanamori (1982) of the spectral energy density of strong ground motion velocity records from three earthquakes. They conclude that most of the energy is radiated from the low frequency portion of the spectrum, that is, below 1 to 2 Hz.

If fault surface tractions are time-independent (so-called constant stress drop models), the first term in (11) or (12) vanishes so that the radiated energy is given by

$$E_R = \int_{-\infty}^{\infty} \{F_0(t) - F(t)\}\, dt \; . \tag{40}$$

This expression is a more general form of that derived by Husseini and Randall (1976) in their discussion of energy radiation from constant stress drop models. The energy flux to the fault edge $F(t)$ can be related to the dynamic energy release rate G by

$$F(t) = \oint G\, v\, ds \tag{41}$$

where the integral is taken around the fault edge and v is the local velocity of propagation. For semi-infinite cracks (or finite cracks prior to the arrival of reflected waves at the crack-tip) the function G has been shown (Atkinson and Eshelby, 1968; Freund, 1972b; Fossum and Freund, 1975) to have the form

$$G = G_0(\ell)\, g(v)$$

where $g(v)$ is a universal function of velocity (for a given mode of propagation) and $G_0(\ell)$ is the quasistatic energy release rate for a crack that instantaneously coincides with the actual crack. The function $g(v)$ satisfies $g(0) = 1$ and $g(c) = 0$ where $c = c_s$ in antiplane strain and $c = c_R$, the Rayleigh wave speed, in plane strain. For plane strain and antiplane strain, $g(v) \simeq 1 - v/c$. Because $g(v)$ decreases with velocity, E_R increases with velocity but, in contrast to the results for dislocations (Clifton and Markenscoff, 1981), approaches a finite limit as v approaches the limiting velocity. More specifically, for propagation near the limiting velocity, $F(t) \ll F_0(t)$ and the radiated energy can be approximated by

$$E_R = \int_{-\infty}^{\infty} F_0(t)\, dt \tag{43}$$

Using (10) to replace the right-hand side of (43) yields

$$E_R = -\Delta U - \int_{-\infty}^{\infty} \int_{S_F} [\sigma_{ij} n_j \dot{u}_i]_0 \, dS\, dt \tag{44}$$

Hence, the radiated energy is equal to the excess of the strain energy change over the work of the fault surface tractions during quasistatic fault propagation.

The meaning of this expression can be clarified by considering a simple model of faulting in which the shear stress drops from a uniform initial value τ_1 to a final value τ_0 over an area S where τ_0 is also uniform over S. Then the strain energy change is (e.g. Savage and Wood, 1971)

$$\Delta U = - (\tau_0 + \tau_1) \, \Delta \bar{u} \, S \tag{45}$$

where $\Delta \bar{u}$ is the average relative displacement. Because the tractions on the fault surface (excluding the extending edge) have been assumed to be time-independent, the traction must equal its final value τ_0. Thus, the second term in (44) is $\tau_0 \, S \, \Delta \bar{u}$ and the radiated energy is

$$E_R = \Delta \tau \, M_0 / 2\mu \tag{46}$$

where $\Delta \tau = \tau_1 - \tau_0$ is the static stress drop and M_0 is the final (static) value of the seismic moment (6). This estimate of the radiated energy is identical to that obtained by Orowan (1960) when the final stress on the fault is equal to the friction stress. An alternate derivation of (46) that illustrates the approach of Orowan (1960) can be obtained by neglecting the last term in (8) and assuming that the traction on the fault surface is equal to a uniform time-independent friction stress τ_f. With these assumptions (8) becomes

$$E_R = \frac{1}{2} (\tau_0 + \tau_1) \, \Delta \bar{u} S - \tau_f \, \Delta \bar{u} \, S \tag{47}$$

where τ_0 and τ_1 are again the final and initial values of fault surface traction. When $\tau_0 = \tau_f$, (47) reduces to (46).

The remarkable feature of (46) is that it is an estimate of the radiated energy that can be obtained entirely from knowledge of the static end states. In other words, equation (46) is a zero frequency estimate of the radiated energy. Some empirical evidence that (46) is a good approximation for large earthquakes has been given by Kanamori (1977). Specifically, Kanamori (1977) showed that for earthquakes having a rupture length of about 100 km, the energy calculated from the right hand side of (46) is a good approximation to the energy obtained from the magnitude and the Gutenberg-Richter energy magnitude relationship. To the extent that this relationship yields an accurate value for the radiated energy, Kanamori's (1977) results suggest that (46) is a good approximation.

Although the apparent propagation speed of faults is near the limiting velocity so that it is accurate to assume $F(t) \ll F_0(t)$, it seems unlikely that fault surface tractions are time-independent as necessary for (40). Perhaps the simplest example of a case in which the fault surface tractions are time-

dependent is the partial stress drop model of Brune (1970) and there seems to be no reason to rule out more complex time dependence. However, it is possible that the time dependence of fault surface tractions may cause high frequency energy radiation that does not substantially contribute to the total radiated energy. A study by Vassiliou and Kanamori (1982) of strong-motion velocity records from three California earthquakes suggests that even as close as 1 to 5 km from the fault, most of the contribution to the radiated energy is from velocity components below 1 to 2 Hz. in frequency.

Unfortunately, there have been no detailed numerical calculations to determine the accuracy of the approximation (46). However, the calculations for the spherical source model, summarized in Figure 1, suggest that for $a/cT > 2$, the strain energy change overestimates the radiated energy by less than a factor of two. Moreover, the enrichment of the high frequency portion of the spectrum by modulation of the ramp function was shown to have little effect on the over-all amount of radiated energy.

Some evidence that $F(t) \ll F_0(t)$ for many earthquakes can be inferred from critical values of G necessary to cause rupture. A frequently used fracture propagation criterion is that fracture occurs when $G = G_{crit}$ where, for simplicity, G_{crit} is usually assumed to be a constant or a function of position that reflects the resistance of material to fracture propagation. Values of G_{crit} summarized by Rudnicki (1980) range from $10\text{-}10^6$ J/m^2 with the lower end of the range appropriate for creep events and laboratory tensile tests and the higher end associated with earthquakes that fracture fresh or largely rehealed fractures. However, Rudnicki (1980) has pointed out that even the largest of these values, when multiplied by fault area, yields an energy that is orders of magnitude smaller than the energy calculated from the Gutenberg-Richter relationship for a magnitude appropriate to the fault area. Specifically, the ratio of the Gutenberg-Richter energy to fracture energy is estimated to be about 10^6 for a magnitude 8 earthquake and 10^2 for a magnitude 6. As pointed out by Kostrov (1974), the decrease in the ratio suggests that the fracture energy may be more significant for smaller earthquakes and laboratory size fractures. Consequently, these events may have significantly different energy radiation characteristics than larger earthquakes. Aki (1979) has noted, however, that the local values of G_{crit} may be much higher than the average over the fault. Nevertheless, the size scale associated with these locally high values may be such that the energy radiated from them is not a significant contribution to E_R.

In the last section, it was pointed out that, under certain circumstances, an estimate of the radiated energy from knowledge of the static end states is possible. Although one can, in theory, state precisely the circumstances when such an estimate will be accurate, identifying them in practice is difficult. In this discussion, the form of such an estimate is compared with two simple dynamic estimates that have been used to interpret seismological observations. For a circular fault of radius a, the estimate (46) for the radiated energy yields

$$E_R = \frac{7}{32} \frac{M_0^2}{\mu a^3} \tag{48}$$

where M_0 is the final (static) value of the moment.

A popular model for interpreting seismic observations is that of Brune (1970) which is based on the shape of the Fourier transform of the displacement. For the purposes of this discussion, it suffices to assume that the magnitude of the Fourier transform of the seismic moment is given by

$$| \tilde{M}(\omega) | = \frac{M_0}{\omega [1 + (\omega/\omega_0)^2]} \tag{49}$$

where ω_0 is the "corner frequency" and

$$\tilde{M}(\omega) = \int_{-\infty}^{\infty} e^{-\iota \omega t} M(t) \, dt .$$

(This assumption is equivalent to using the form of the farfield spectrum suggested by Brune (1970) and a double-couple radiation pattern.) The radiated energy can then be evaluated from (7) by using the Parseval relation and (49). The result, neglecting the small contribution from the dilatational waves, is

$$E_R = \frac{7}{32} \frac{M_0^2}{\mu a^3} \left[\frac{4}{35\pi} \left(\frac{a\omega_0}{c_s} \right)^3 \right] \tag{50}$$

Using values for the corner frequency suggested by Brune et al. (1979), that is,

$$\omega_0 \simeq 2\pi (c_s/3a) (1 \pm 0.5)$$

yields a numerical value for the term in brackets of 0.287 to 0.387.

Vassiliou and Kanamori (1982) have studied energy release for deep focus earthquakes by assuming that the farfield displacement time function is trapezoidal with a duration of T_d and a rise time T_r. If it is assumed that the height of

the trapezoid is proportional to M_0/T_d and that the radiation pattern is that for a double couple, the radiated energy is

$$E_R = \frac{7}{32} \frac{M_0^2}{\mu a^3} \left[\frac{32}{35\pi} \left(\frac{a}{c_s T_d} \right)^3 \frac{1}{\zeta(1-\zeta)^2} \right] \tag{51}$$

where $\zeta = T_r/T_d$. Vassiliou and Kanamori note the effect of ζ is small for $0.1 \leq \zeta \leq 0.5$. Using $\zeta = 0.2$, $T_d = a/v$ and a rupture velocity, $v = 0.75\, c_s$, yields a value of 0.959 for the term in brackets.

Note that both of the dynamic estimates of energy radiation have the same form as the static estimate (48), that is, they are proportional to the square of the seismic moment divided by the cube of the overall rupture length (although in the estimate of Vassiliou and Kanamori (1982) the rupture length enters in terms of the duration of the farfield time function). Moreover, the numerical factor in brackets in (51) is close to unity whereas that in (50) is equal to about one-third, which is not too greatly different. Randall (1973) has noted that a variety of estimates of seismic energy based on the form of the displacement spectrum, give similar results. However, a feature common to both Randall's estimates and those here is that rupture is characterized by a single characteristic dimension, the overall rupture length, as a result of assuming that rupture proceeds smoothly. There is, of course, ample evidence that rupture proceeds in a discontinuous fashion, controlled by the strength and distribution of barriers and asperities. No thorough analysis of the effects of discontinuous rupture on energy radiation has yet been given. An analysis by Haskell (1964) suggests that such incoherent rupture could increase the total radiated energy by a factor of three, but the interpretation of this result is complicated by the fact that the strain energy change, and hence the static estimate of the radiated energy, for this model is unbounded. If incoherent ruptures result primarily in high frequency energy the empirical results of Vassiliou and Kanamori (1982) suggest that such energy is not significant in altering the total amount of radiated energy. On the other hand, discontinuous ruptures have been shown to have a substantial effect on estimates of static parameters (e.g. Madariaga, 1979; Rice, 1980; Rudnicki and Kanamori, 1981) and, as a consequence, static estimates of the radiated energy would also be affected.

REFERENCES

Achenbach, J.D. (1973). Wave Propogation in Elastic Solids, North Holland, New York, 425 pp.

Aki, K. (1979). Characterization of barriers on an earthquake fault, J. Geophys. Res. 84, 6140-6148.

Aki, K. and P. G. Richards (1980). Quantitative Seismology: Theory and Methods, Vol. I, W. H. Freeman, San Francisco, 557 pp.

Atkinson, C. and J. D. Eshelby (1968). The flow of energy into the tip of a moving crack, J. Fracture Mech. 4, 3-8.

Bath, M. (1966). Earthquake energy and magnitude, in Physics and Chemistry of the Earth, L. H. Ahrens, Editor Pergamon Press, New York, 117-165.

Brune, J. N. (1970). Tectonic stress and the spectra of seismic shear waves from earthquakes, J. Geophys. Res. 75, 4997-5009.

Brune, J. N., R. J. Archuleta and S. Hartzell (1979). Far-field S-wave spectra, corner frequencies, and pulse shapes, J. Geophys. Res. 84, 2262-2272.

Clifton, R. and X. Markenscoff (1981). Elastic percursor decay and radiation from nonuniformly moving dislocations, J. Mech. Phys. Solids 29, 227-252.

Fossum, A. F. and L. B. Freund (1975). Nonuniformly moving shear crack model of a shallow focus earthquake mechanism, J. Geophys. Res. 80, 3343-3347.

Freund, L. B. (1972a). Energy flux into the tip of an extending crack in an elastic solid, J. Elast. 2, 341-349.

Freund, L. B. (1972b). Crack propagation in an elastic solid subjected to general loading -- I. Constant rate of extension, J. Mech. Phys. Solids 20, 129-140.

Gutenberg, B. and C. F. Richter (1942). Earthquake magnitude, intensity, energy and acceleration, Bull. Seism. Soc. Am. 32, 163-191.

Haskell, N. A. (1964). Total energy and energy spectral density of elastic wave radiation from propagating faults, Bull. Seism. Soc. Am. 54, 1811-1841.

Husseini, M. I. and M. J. Randall (1976). Rupture velocity and radiation efficiency, Bull. Seism. Soc. Am. 66, 1173-1187.

Kanamori, H. (1977). The energy release in great earthquakes, _J. Geophys._
Res. 82, 2981-2987.

Kanamori, H. and D. L. Anderson (1975). Theoretical basis of some empirical
relations in seismology, _Bull. Seism. Soc. Am._ 65, 1073-1095.

Kostrov, B. V. (1968). The inverse problem of the theory of tectonic
foci, _Izv. Earth Physics_ 9, 18-29.

Kostrov, B. V. (1974). Seismic moment and energy of earthquakes and seismic
flow of rock, _Izv. Earth Physics_ 1, 23-40.

Madariaga, R. (1979). On the relation between seismic moment and stress
drop in the presence of stress and strength heterogeneity, _J. Geophys._
Res. 84, 2243-2250.

Orowan, E. (1960). Mechanism of seismic faulting, _Geol. Soc. Am. Mem._ 79,
323-345.

Randall, M. J. (1964). Seismic energy generated by a sudden volume change,
Bull. Seism. Soc. Am. 54, 1291-1298.

Randall, M. J. (1973). Spectral theory of seismic sources, _Bull. Seism._
Soc. Am. 63, 1133-1144.

Rice, J. R. (1980). Mechanics of earthquake rupture, in Physics of the
Earth's Interior, Proceedings of the International School of Physics,
"Enrico Fermi", Italian Physical Society, Course LXX VII (1979,
Varenna on Lake Como, Italy) on Physics of the Earth's Interior,
A. M. Dziewonski and E. Boschi, Editors, North Holland Publishing
Company, 555-649.

Rudnicki, J. W. (1980). Fracture mechanics applied to the earth's crust,
in _Ann. Rev. Earth Planet. Sci._ 8, 489-525.

Rudnicki, J. W. and L. B. Freund (1981). On energy radiation from seismic
sources, _Bull. Seism. Soc. Am._ 71, 583-595.

Savage, J. C. and M. D. Wood (1971). The relation between apparent stress
and stress drop, _Bull. Seism. Soc. Am._ 61, 1381-1388.

Vassiliou, M. S. and H. Kanamori (1982). Energy release in deep focus
earthquakes, submitted to _Bull. Seism. Soc. Am._

Yoshiyama, R. (1963). Note on earthquake energy, _Bull. Earthquake Res._
Inst., Tokyo Univ. 41, 687-697.

The radiated energy E_R divided by the strain energy is plotted against a/cT where a is the radius of the spherical source, c is the dilatation wave speed, and T is the rise time. The results are shown for three forms of the pressure function: an exponential increase (32), a ramp function (36), and a modulated ramp (38), where n is the number of periods of superimposed sinusoidal oscillation. Results are shown for a value of Poisson's ratio $\nu = 0.25$.
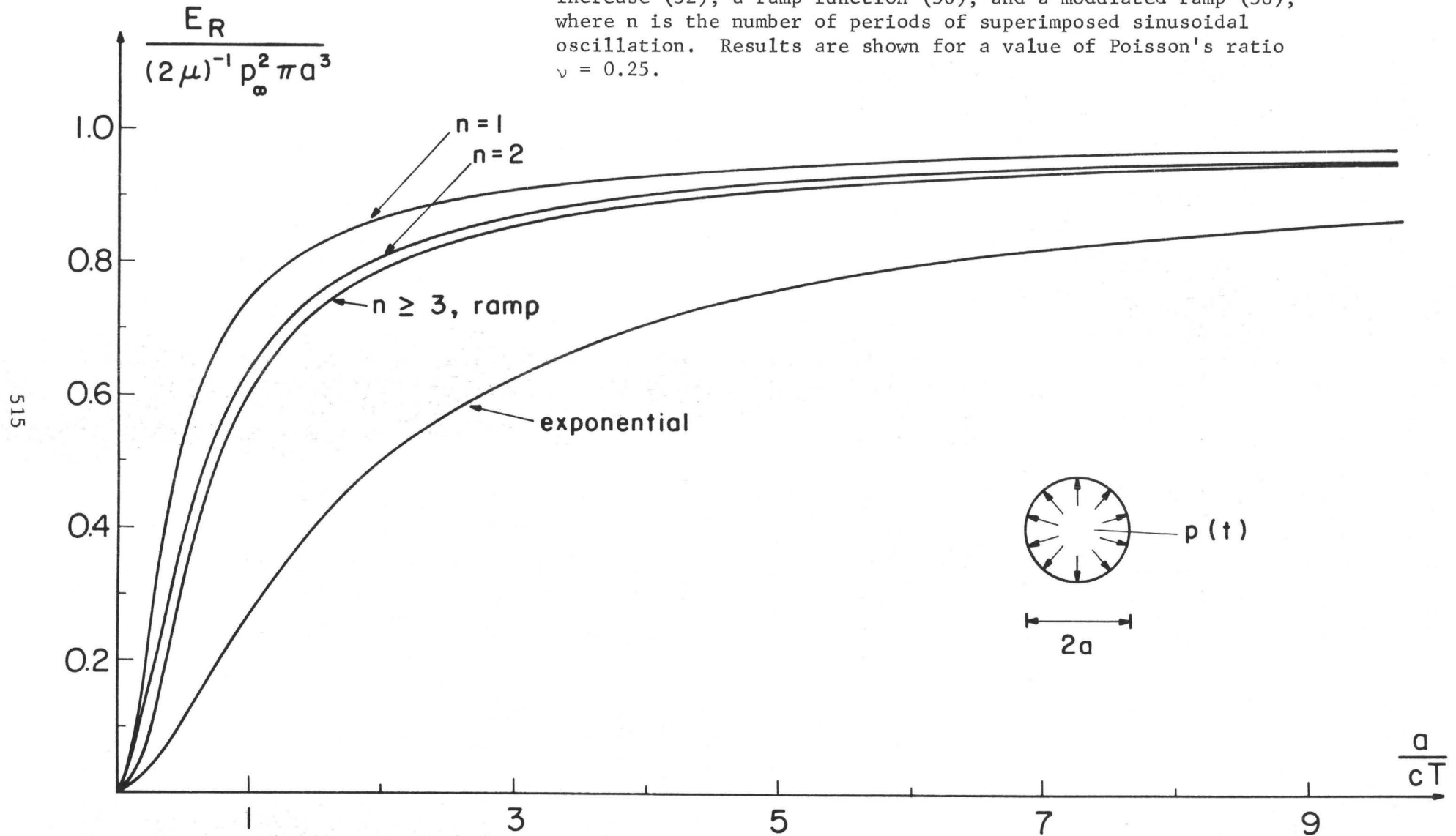
Figure 1

DYNAMIC CIRCULAR SYMMETRICAL AND ASYMMETRICAL CRACK MODELS

Jean VIRIEUX[*], Institut de Physique du Globe de Paris,
Université Paris VI, 75230 Paris Cedex 05, France.

[*] Present address : Laboratoire de Géodynamique, Tour 15, 1er étage,
4, pl. Jussieu - 75230 Paris Cedex 05, France (1)-336.25.25 Ext. 45-88

Abstract : Far-field radiations are investigated for dynamic circular cracks. We study symmetrical models where the center of the initial crack is also the center of the final one, and asymmetrical models where the center of the initial crack is at a given distance of the center of the final crack. We found two bursts of energy associated with stopping phases that control the width of the far-field pulse and the fall-off of the spectrum.

Three types of nucleation are considered for symmetrical models. The average corner frequency of S waves ν_o^s is related to the final source radius L by $\nu_o^s = 0.32 \, \beta/L$. The corner frequency of P waves is larger than ν_o^s by a factor of 1.25. The fall-off of the spectrum is of the order of $\nu^{-2.3}$. When the initial crack has a finite size, sharp initial phases are induced, filling the intermediate region of the spectrum and shifting slightly the corner frequencies to higher values.

Asymmetrical models are strongly radial dependent. An important directivity effect is shown, giving corner frequencies as high as $\nu_o^s = 0.60 \, \beta/L$ and $\nu_o^p = 0.90 \, \beta/L$ with a fall-off of the order of $\nu^{-2.8}$.

A-Introduction.

Crack models provide considerable insight into the process of shallow earthquakes. During the five past years, improvement in numerical methods allows complicated crack models to be studied. Madariaga (1976) has solved the dynamic circular faulting. The obtained dynamic features have been introduced in kinematic models by Boatwright (1980). Spontaneous rupture has been intensively studied (Das & Aki, 1977 ; Day, 1979 ; Miyatake, 1980 ; Das, 1981). Free surface effects have been included (Archuleta & Frazier, 1978 ; Miyatake, 1980). Heterogeneous behaviour has been simulated (Das & Aki, 1977 ; Miyatake, 1980).

In order to constrain source models by observations, an interesting problem is to study far-field radiation for circular symmetrical and asymmetrical crack models. After presenting the problem formulation, we study the Madariaga circular crack. Three different kinds of nucleation are investigated. By shifting the center of the nucleation, we destroy the symmetry and study the impact on the far-field pulse and spectrum.

B-Plane Crack Model.

To understand the influence of different geometries of the fault on the far-field radiation, we restrain our study to a particular set

of models that we present in this section and for which the mathematical formulation is simple. A more complete formulation can be found in Archuleta & Frazier (1978), for example. Let us introduce the medium with equations governing the wave propagation, boundary conditions applied at the edges of the medium (source included) and initial conditions at the beginning of the rupture. These are now discussed in the following sections.

1-Medium : We assume a linear, homogeneous, isotropic and infinite medium where elastodynamic equations which relate stress and displacement at a point M are given by the relations :

$$\rho \ddot{u}_i = \sigma_{ij'j} \qquad \text{equation of motion}$$

$$\sigma_{ij} = \lambda u_{k'k} \delta_{ij} + \mu(u_{i'j} + u_{j'i}) \qquad \text{Hooke's law}$$

2-Boundary conditions : Let us consider a plane crack and choose our coordinate frame so that the crack plane will be on the plane (xoy). On this plane, shear stress drops suddenly to a constant dynamic friction stress σ_f at a point M, after the passage of the rupture front. This failing in the linearity induces a discontinuous displacement, or slip, between the two surfaces of the crack S_1^+ and S_1^-. We complete our coordinate frame by taking S_1^+ on the positive side of the axis z. This is the only boundary condition to be applied in the infinite medium.

3-Initial conditions : The medium before the rupture is in equilibrium under a static shear stress $\sigma_{xz} = \sigma_s(x,y,z)$, with a zero velocity everywhere. We consider three different types of rupture nucleation.

A commonly used way to start rupture is the self-similar nucleation. At time t = 0, the crack starts from one point and propagates. The initial prestress σ_0 is uniform, making computation easier.

Another widely used nucleation is the instantaneous nucleation. At time t = 0, a crack of finite size appears and starts to propagate. Again the initial stress is uniform $\sigma_{xz} = \sigma_0$, but the model is non-causal.

The third type of nucleation, physically the most acceptable, is the static nucleation. A preexisting crack of finite size becomes unstable at time t = 0, and starts to propagate. The initial stress is the non-uniform static stress of the preexisting crack.

4-Propagation of the rupture : From its initial shape, the rupture expands at a constant rupture velocity v_r until its final shape. This is a kinematic description of the geometry where the acceleration is instantaneous. Theoretical work by Eshelby (1969) and previous work on spontaneous rupture by Das & Aki (1977), for example, indicate a quick acceleration to a terminal velocity and suggest that an instantaneous acceleration approximation is reasonnable. Less may be said about the deceleration because not much is known about the parameters that control it, and thus the stopping phases of the models discussed here may be too large.

5-Healing of the rupture : We suppose that the slip is mainly along
the x-direction of the shear prestress. This hypothesis is well suppor-
ted during the propagation of the rupture by the work of Miyatake (1980)
and Virieux & Madariaga (1982). During the stopping process, a small
amount of slip must occur along the y-direction because of the different
velocities of stopping phases. We neglect it and consider only the
component Δu_x of the slip and we note it Δu. When the slip velocity $\Delta \dot{u}$
at a point M reverses its sign, we set it to zero healing the crack at
this point.

6-Physical parameters - scaling : Because we assume one direction for
the slip, the only stress that enters in the problem is the stress
drop $\Delta \sigma = \sigma_o - \sigma_f$, where σ_o is the uniform prestress away from the
crack. If we call L the longest distance of the final crack edge from
its center and take the P-wave velocity to be α and the S-wave velocity β
with $\alpha = \sqrt{3}\,\beta$, we can define the following dimensionless quantities :

$$\text{Length :} \quad (x,y,z) = L\ (X,Y,Z)$$

$$\text{Time :} \quad t = L/\beta\ T$$

$$\text{Stress :} \quad \sigma = \Delta\sigma S$$

$$\text{Displacement :}\ u = L\ \Delta\sigma/\ \mu U$$

$$\text{Velocity :}\ \dot{u} = \beta\Delta\sigma/\ \mu U$$

$$\text{Moment :}\ m_o = L^3\ \Delta\sigma\ M_o$$

$$\text{Moment velocity :}\ m_o = L^2\ \Delta\sigma\beta M_o$$

Any dimensional results, that have the same ratio between the
initial crack and the final crack length, the same ratio v_r/β
and the same Poisson's ratio ($\alpha = \sqrt{3}\,\beta$), can be found from our results.

C-Slip Velocity Calculation.

The boundary problem in an infinite medium is transformed into a
mixed boundary problem in a half-space, by using the symmetry of the
plane crack. Then noting that S_2 is the complementary part of S_1 the
surface area of the crack plane, the boundary conditions become[1] :

$$\begin{cases} u_x = u_y = 0 \quad ; \quad \sigma_{zz} = 0 \qquad \text{on } S_2 \\ u_y = 0 \qquad\qquad ; \quad \sigma_{xz} = \sigma_f,\ \sigma_{zz} = 0 \quad \text{on } S_1 \end{cases}$$

Because the equations are linear, we can substract the uniform
prestress existing away from the crack, σ_o and also normalize to obtain
dimensionless boundary conditions :

$$\begin{cases} U_x = U_y = 0 \quad ; \quad S_{zz} = 0 \qquad \text{on } S_2 \\ U_y = 0 \quad ; \quad S_{xz} = -1\ ,\quad S_{zz} = 0 \quad \text{on } S_1 \end{cases}$$

We solve the mixed boundary problem using a finite difference method (Virieux & Madariaga, 1982) computing the slip velocity on the crack surface as a function of time.

We distinguish four types of behaviour in the slip velocity at one point (figure 1). Before the point M is reached by the crack, the slip velocity is zero. When the crack reaches this point, the slip velocity presents a singularity of the form $1/\sqrt{r}$, where r is the distance from the point M inside the crack to the crack edge. This singularity is related to the singularity of the stress outside the crack. The third type of behaviour occurs as the edge of the crack is moving away. The point M receives energy from every point around it and its slip velocity tends to a constant. When the point M becomes affected by the arrest of the rupture propagation, we have the fourth behaviour, characterized by a slowing of the slip velocity until the final stopping of sliding, called the healing phase. The relative importance of the four types of behaviour are highly dependent of the initial geometry of the crack, its time-evolution, its final geometry and the position of the point M.

Dynamic faulting simulated by our finite difference method exhibits all these features. Let us anticipate our results to illustrate the importance of geometry on time evolution, by showing healing phases for an asymmetric crack propagating at rupture velocity $v_r = 0.87\beta$ until it reaches its final shape. The healing phase does not start from where the rupture front first reaches the final rupture boundary. Although its slip velocity is slowed at first, it is nonetheless one of the last points to lock(figure 2).

D-Far-Field Body-Wave Radiation.

Since the Burridge & Knopoff paper of 1964, calculations of far-field P and S waves have been widely published (e.g. Aki & Richards, 1980 ; Madariaga, 1981). Information about the source slip velocity is contained in what it is defined as the far-field pulse .

$$\omega(\hat{R},t) = \mu \int_{\Sigma} \Delta\dot{u} \ (\vec{r},t + \frac{\vec{r} \cdot \hat{R}}{c}) \ dS$$

where $\dot{u}$ is the slip velocity in the x-direction, $\hat{R}$ is the unit vector pointing towards the observer (figure 3) and C is either P or S wave velocity. The frequency spectrum can be expressed as :

$$\omega(\hat{R},\nu) = \mu \int_{\Sigma} \Delta\dot{u}(\vec{r},\nu) e^{i\frac{2\pi\nu}{c}\hat{R}\cdot\vec{r}} \ dS$$

Knowing $\Delta\dot{u}(r,t)$ on our discrete fault surface as a function of time, we compute the Fourier transform $\Delta\dot{u}(r,\nu)$ for every point, and obtain the frequency spectrum in the direction of the observer as a shifted sum of $\Delta\dot{u}(r,\nu)$ over the fault surface. We filter our spectrum with a cosine filter to remove the effects of the spatial sampling interval. For P waves, a suitable cut-off frequency is $\nu_c^p = \alpha/4\,\Delta x$, where Δx is one spatial grid step and in effect we do not model frequencies higher than this. However applying a filter with the same effect on frequency content of S waves (with a cut-off frequency $\nu_c^s = \beta/6.93\,\Delta x$) gives small oscillations. We prefer to retain the maximum frequency content rather than applying heavier but still

comparable filters to both P and S waves.

On this basis we can discuss the properties of the far-field P and S wave forms and spectra. The spectrum $\omega(R,\nu)$ has a maximum at zero frequency because $\Delta \dot{u}$ does not change sign on the fault plane ; hence $\omega(R,0) = M_o$, the seismic moment. Because of the assumptions in section C, M_o is actually the M_{xz} component alone. At high frequencies, an asymptote of the form $\nu^{-\gamma}$ can be drawn with a corner frequency ν_o that is the intersection of this asymptote with the low frequency level. This high frequency fall-off is controlled by stopping phases. For a fall-off of ν^{-2}, stopping phases correspond to a slop discontinuity in the velocity pulse (Madariaga, 1981). The velocity time function and spectra are more sensitive to stopping phases. We therefore turn our attention to the far-field velocity behaviour and note that the velocity spectrum presents a maximum at a frequency that we identify with the corner frequency ν_o. Drawing a high frequency asymptote with confidence on the pulse spectrum is possible in our first model (similar to that of Madariaga, 1976). We find a fairly good agreement between this corner frequency and the one picked out from the velocity spectrum. Because finding corner frequency as a maximum of the velocity spectrum is easier, we retain this definition of the corner frequency for the other models.

E-Symmetrical Models.

In this section, the initial and final shapes of the crack are con-centric disks. Because the rupture velocity ($v_r = 0.87\beta$) is the same in any direction, the final circular edge is reached everywhere at the same time. That is why we call these models symmetrical. We present results for $\theta = 60°$ and $\phi = 0°$.

1-Self-similar nucleation - SM1 model : The initial crack has a zero radius at time t = 0. This model was studied by Madariaga (1976). Our results (figure 4) depart from Madariaga's ones for two reasons, in part as a consequence of the lower grid density used here. The first is the numerical difficulty in modelling self-similar behaviour when the crack radius is of the order of the spatial grid step. At the beginning, the form of the pulse is smoother than t^2 or, as an equivalent statement, the velocity pulse shows the linear time tendency only after a while. The second difficulty is our modelling of stopping phases, noted by small sticks in our figures. Because of our numerical high frequency limit and our discrete computation of far-field waves, the jump in velocity pulse and the slope discontinuity in pulse are smoothed out. So the time duration of the pulse is longer than that shown by Madaria-ga (1976).

The high frequency asymptote is selected as Brune & al (1979) did. However, for S waves, the corner frequency ν_o^s, picked out either from the pulse spectrum or from the velocity spectrum, is lower than the Brune one (1970). The P wave corner frequency ν^p is always higher than

520

the S wave corner frequency ν_o^s, since the width of the P wave pulse is narrower than the S wave pulse. We find :

$$\nu_o^p = 0.40 \ \beta/L \ = 0.23 \ \alpha/L$$

$$\nu_o^s = 0.32 \ \beta/L$$

The ratio of the two corner frequencies 1.25 is lower than the average value 1.5 found by Madariaga (1976) but still inside the interval [1.2, 1.7] of Hanks (1981). The high frequency asymptote has a slope of the order of −2.3, explained by the smoothness of stopping phases.

2-Instantaneous nucleation − SM2 model : This model presents the same over-all results as the SM1 model, except sharper initial phases coming from the finite size of the initial crack. We note extreme initial phases by small black triangles in our figures. Stopping phases are arriving at the observer, while initial phases from different points of the crack are still arriving (figure 5). This imbrication is related to the ratio of the starting and final radius. We choose a ratio of 0.5, in order to stress this point. Initial phases fill the intermediate range of the spectrum, but do not affect significantly corner frequencies and fall-off.

3-Static nucleation − SM3 model : We choose the same geometry as the SM2 model for comparison. The initial state of stress is the static stress of the preexisting crack. This model differs only by the greater importance of initial phases. We observe a distinguishable arrival for the last initial phase (figure 6). A slight shift of corner frequencies could be observed, but the fall-off is still the same − $\nu^{-2.3}$ behaviour.

F-ASYMMETRICAL MODELS.

The initial and final shapes of the crack are excentric disks, destroying the symmetry. We move the center of the nucleation to the positive side of the x-axis, with the proportions of the figure 2. Because of the asymmetry, we present results for $(\theta,\phi) = (60°,0°)$ and for $(\theta, \phi) = (60°,180°)$, corresponding to $(\theta, \phi) = (60°,0°)$ for symmetrical models. The rupture velocity is still $0.87 \ \beta$, and the arrest of the rupture takes some time to extend over the whole final crack edge.

1- Self-similar nucleation − AM1 model : This model has to be compared with the SM1 model. An important directivity effect is shown, arising from the time lag between stopping phases in different radial directions (figure 7 and figure 8). The pulse shape changes from a box shape ($\phi=0°$) to a narrow triangle shape ($\phi = 180°$). For S waves, we observe a shift of corner frequency from $0.30 \ \beta/L$ to $0.55 \ \beta/L$. And, for P waves, the shift is from $0.40 \ \beta/L$ to $0.75 \ \beta/L$.

2- Static nucleation − AM2 model : As for the SM2 and SM3 models, the finite size of the initial crack implies sharper initial phases that increase the directivity effect (figure 9 and figure 10). The S wave corner frequency shifts from a value $0.32 \ \beta/L$ to a value $0.60 \ \beta/L$. And the P wave corner frequency from a value $0.45 \ \beta/L$ to a value $0.90 \ \beta/L$. The fall-off has a slope close to −3.

G-CONCLUSION

Through this study, we present five different source models and the corresponding far-field radiations. We show that pulses and spectra are controlled by stopping phases. The impact of initial phases is small, even for the academic case where the size of the final crack is only twice the size of the initial one.

Azimuthal dependence allows average relations between the geometry of the source and physical parameters defined on the far-field radiation. Relation between the final length of the crack and the corner frequency is in agreement with the Brune's one, for symmetrical models.

However, for asymmetrical models, a strong radial effect destroys this relation. A consequent directivity effect changes the shape of the pulse from a 'box' shape towards a "narrow triangle' shape, doubling the corner frequency. It implies that the corner frequency has to be interpreted with great care. The relation with the length of the final crack is still adequate, but the determination of stress drop which depends critically on the corner frequency cannot be trusted.

REFERENCES –

Aki, K. and P.G. Richards (1980). Quantitative Seismology : Theory and methods, volumes I & II, W.H. Freeman and Company, San Francisco.

Archuleta, R.J. and G.A. Frazier (1978). Three-dimensional numerical simulations of dynamic faulting in a half space, Bull. Seism. Soc. Am. 68, 541-572.

Boatwright, J. (1980). A spectral theory for circular seismic sources ; simple estimates of source dimension, dynamic stress drop, and radiated energy, Bull. Seism. Soc. Am. 70, 1-27.

Burridge, R. and L. Knopoff (1964). Body force equivalents for seismic dislocations, Bull. Seism. Soc. Am. 64, 1789-1808.

Brune, J.N. (1970). Tectonic stress and the spectra of seismic shear waves from earthquakes, J. Geophys. Res. 75, 4997-5009.

Brune, J.N., R.J. Archuleta and S. Hartzell (1979). Far-field S-wave spectra, corner frequencies, and pulse shapes, J. Geophys. Res. 84, 2262-2272.

Das, S. and K. Aki (1977). Fault plane with barriers : a versatile earthquake model, J. Geophys. Res. 82, 5658-5670.

Das, S. (1980). A numerical method for determination of source time
    function for general 3-D rupture propagation, Geophys. Journ. Roy.
    astr. Soc. 62, 591-604.

Das, S. (1981). Three-dimensional spontaneous rupture propagation and
    implications for the earthquake source mechanism,Geophys.Journ. Roy.
    astr. Soc. 67, 375-393.

Day, S.M.(1979). Three-dimensional finite difference simulations of fault
    dynamics Systems, Science & Software Report SSS-R-80-4295.

Eshelby, J.D. (1969). The elastic field of a crack extending non-uniformly
    under general anti-plane loading, J. Mech. Phys. Solids, 17, 177-199.

Hanks, T. (1981). The corner frequency shift, earthquake source models
    and Q, Bull. Seism. Soc. Am. 71, 597-612.

Madariaga, R. (1976). Dynamics of an expanding circular fault, Bull.
    Seism. Soc. Am. 66, 639-666.

Madariaga, R. (1981). Dynamics of seismic sources, Advanced study Institutes
    Series, 71-96.

Miyatake (1980). Numerical simulations of earthquake source process by
    a three-dimensional crack mode. Part I - Rupture process, J. Phys.
    Earth, 28, 565-598.

Virieux, J. and R. Madariaga (1982). Dynamic faulting studied by a finite
    difference method. Bull. Seism. Soc. Am. 72, 345-369.

AM1 healing phases

nucleation point

X
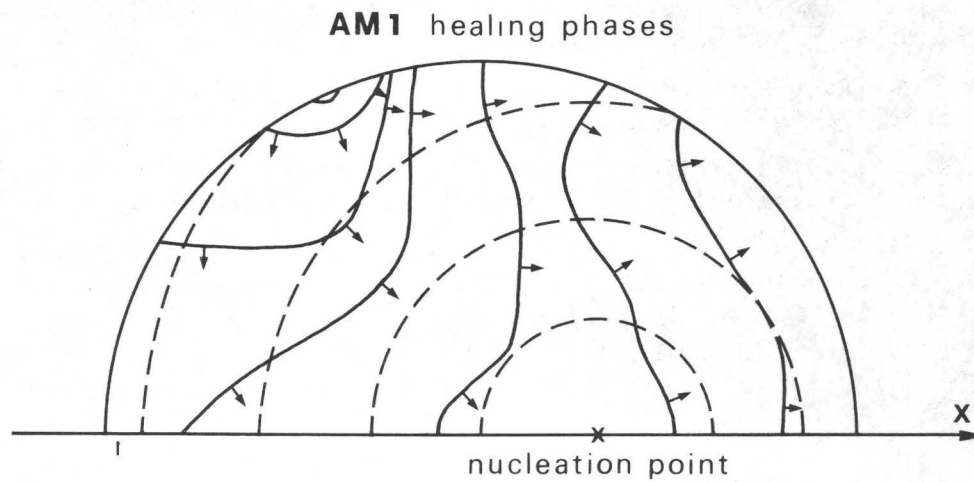
Figure 2: Healing phases for the AM1 model. Dotted lines are rupture front at different times. Continuous lines with small arrows are healing phases.
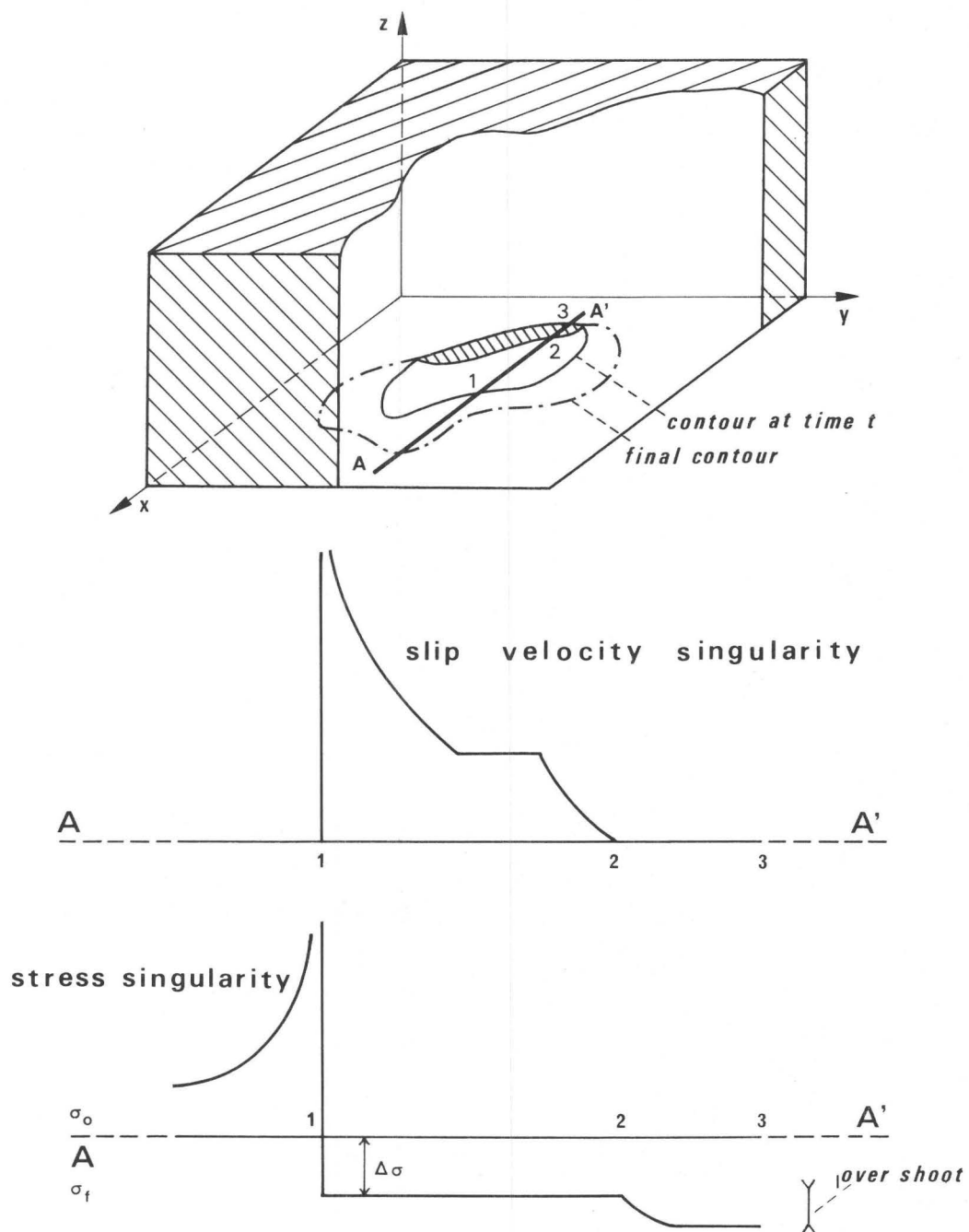
Figure 1: Behaviour of the slip velocity along a cross - section AA′ on the crack surface, associated with the behaviour of the stress.
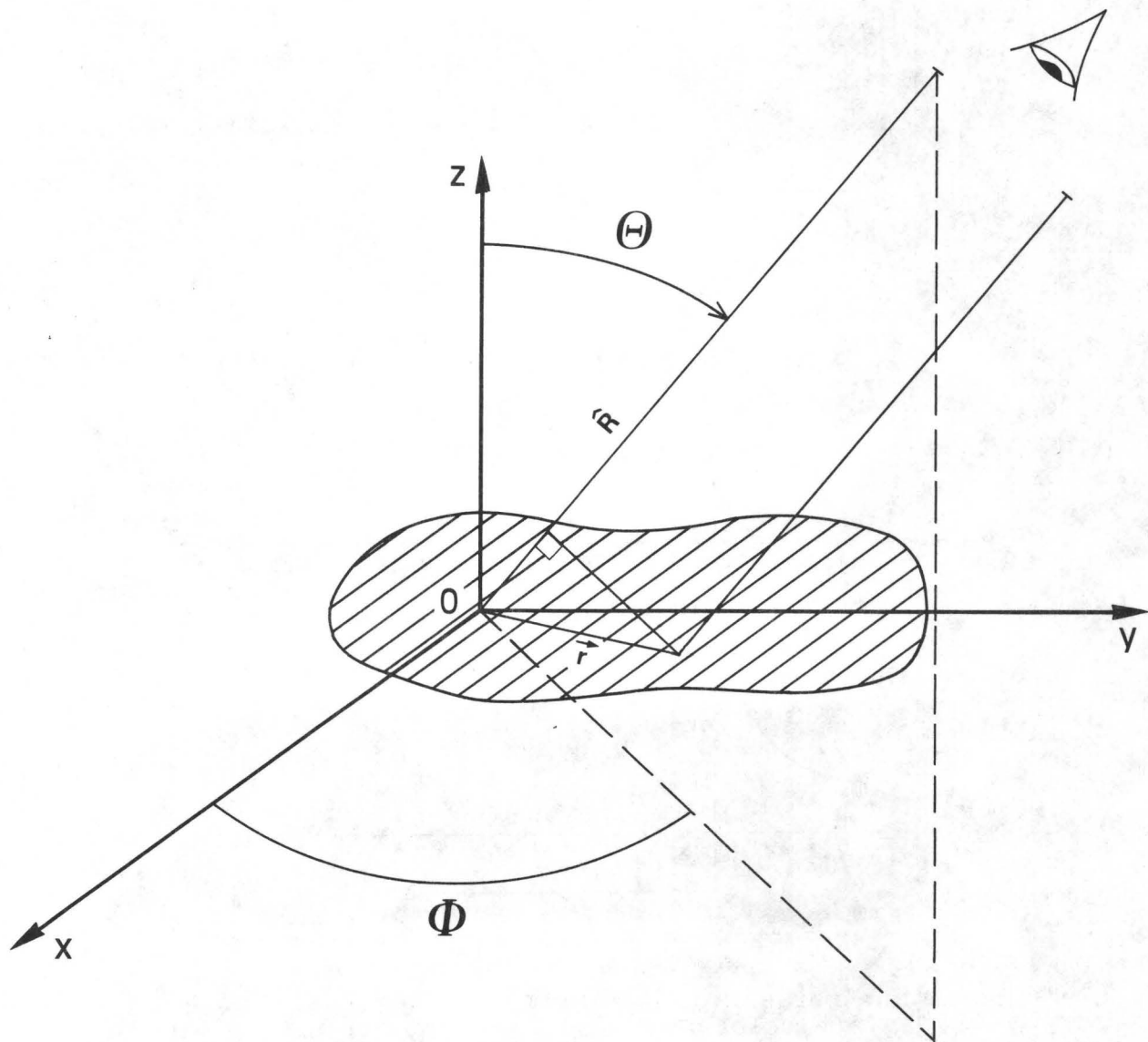
Figure 3 : Reference frame for far-field radiation

SM1
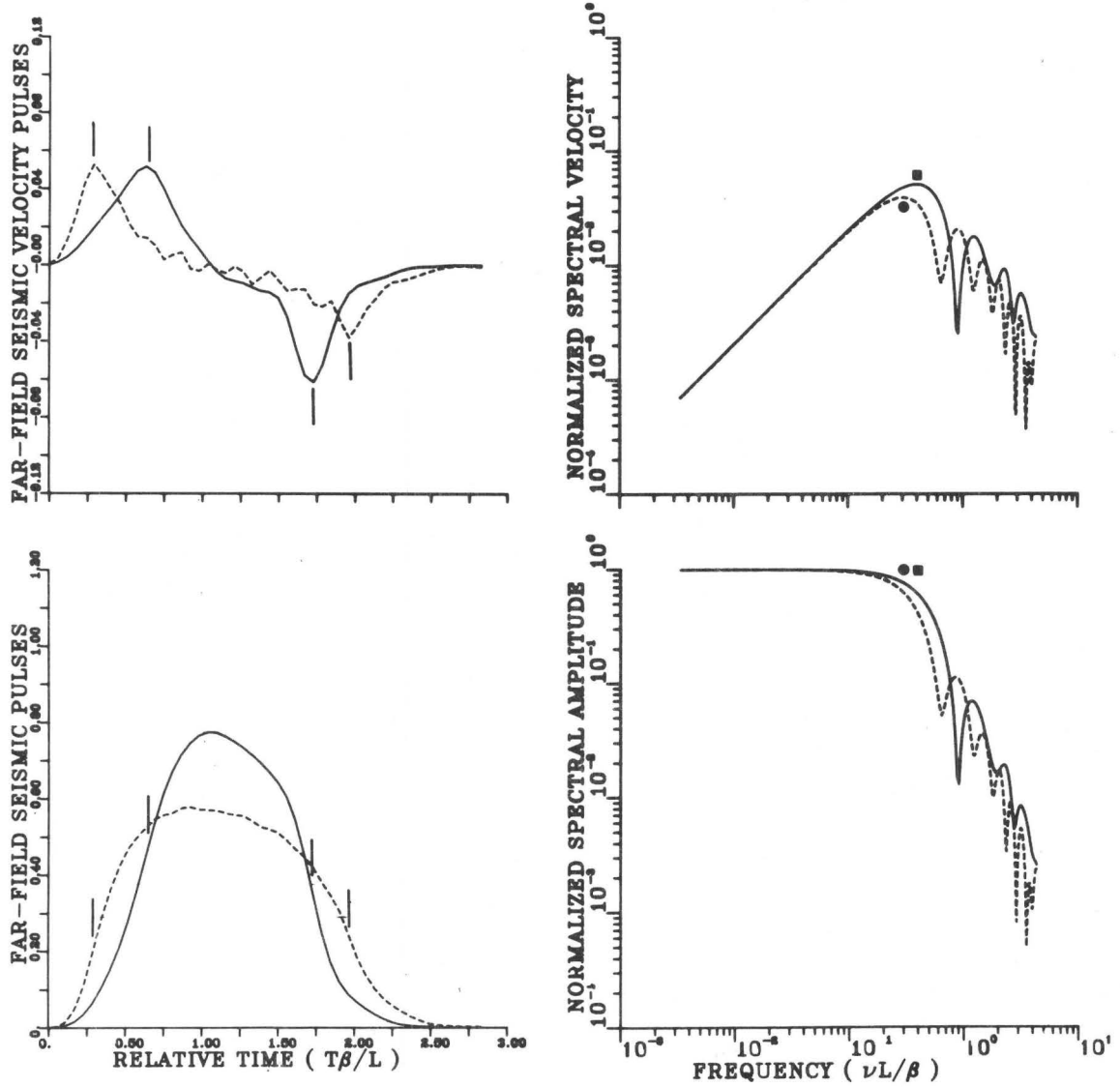
Figure 4: Far-field calculations for the SM1 model at $\theta=60°$ and $\varphi=0°$. Continuous line defines P wave results and dotted line S wave results. Spectra are normalized with the moment or the moment velocity. Pulses are scaled by a constant time integral. The P wave corner frequency is indicated by a full square, while the S wave corner frequency by a full circle. Stopping phases are noted by small vertical sticks.

SM2
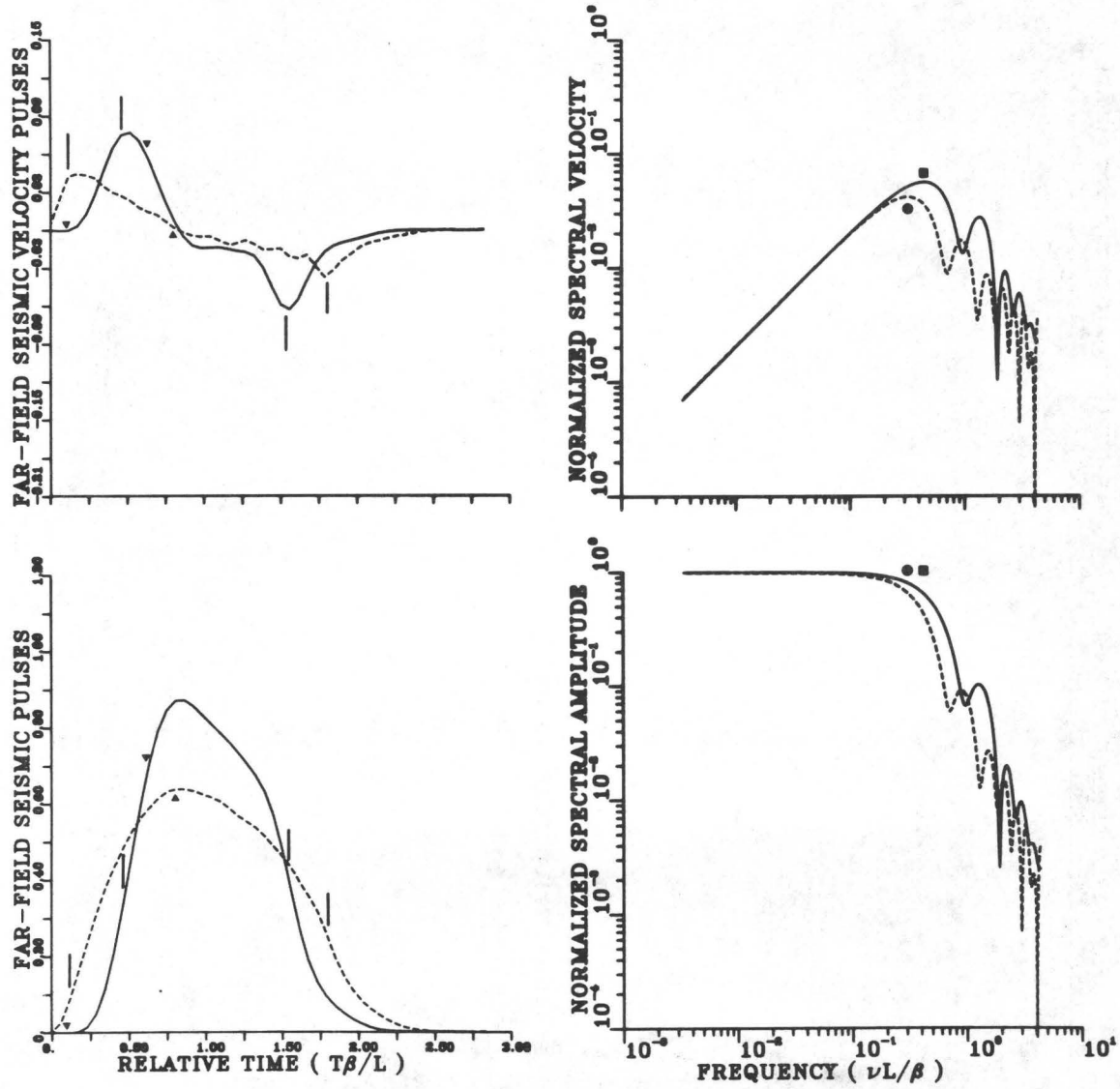
Figure 5: Far-field calculations for the SM2 model at $\theta = 60°$ and $\varphi = 0°$. Full small triangles represent initial phases. Other notations same as for figure 4.

SM 3
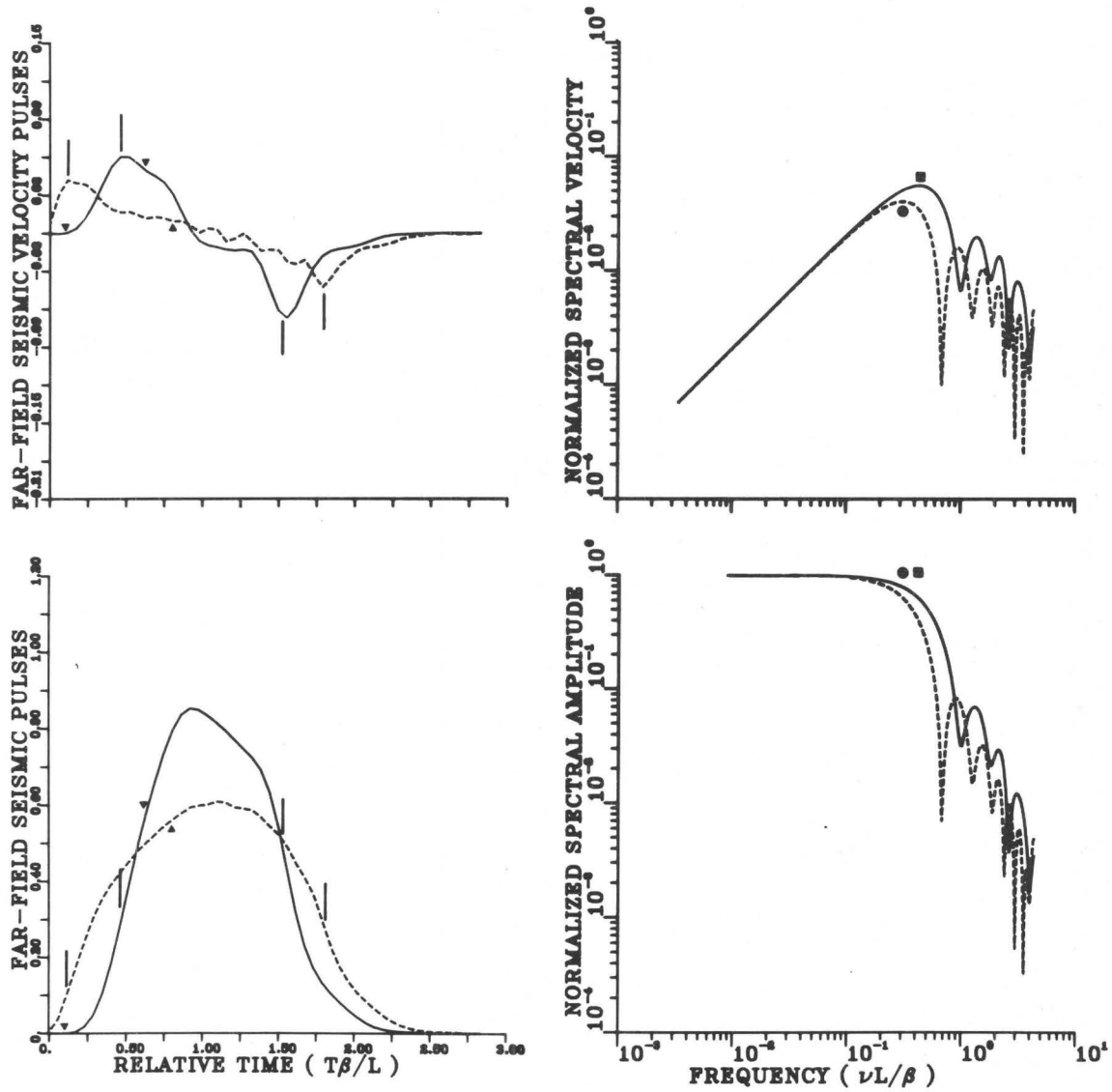
Figure 6 : Far-field calculations for the SM3 model at $\theta = 60°$ and $\varphi = 0°$. Same notations as figure 5.
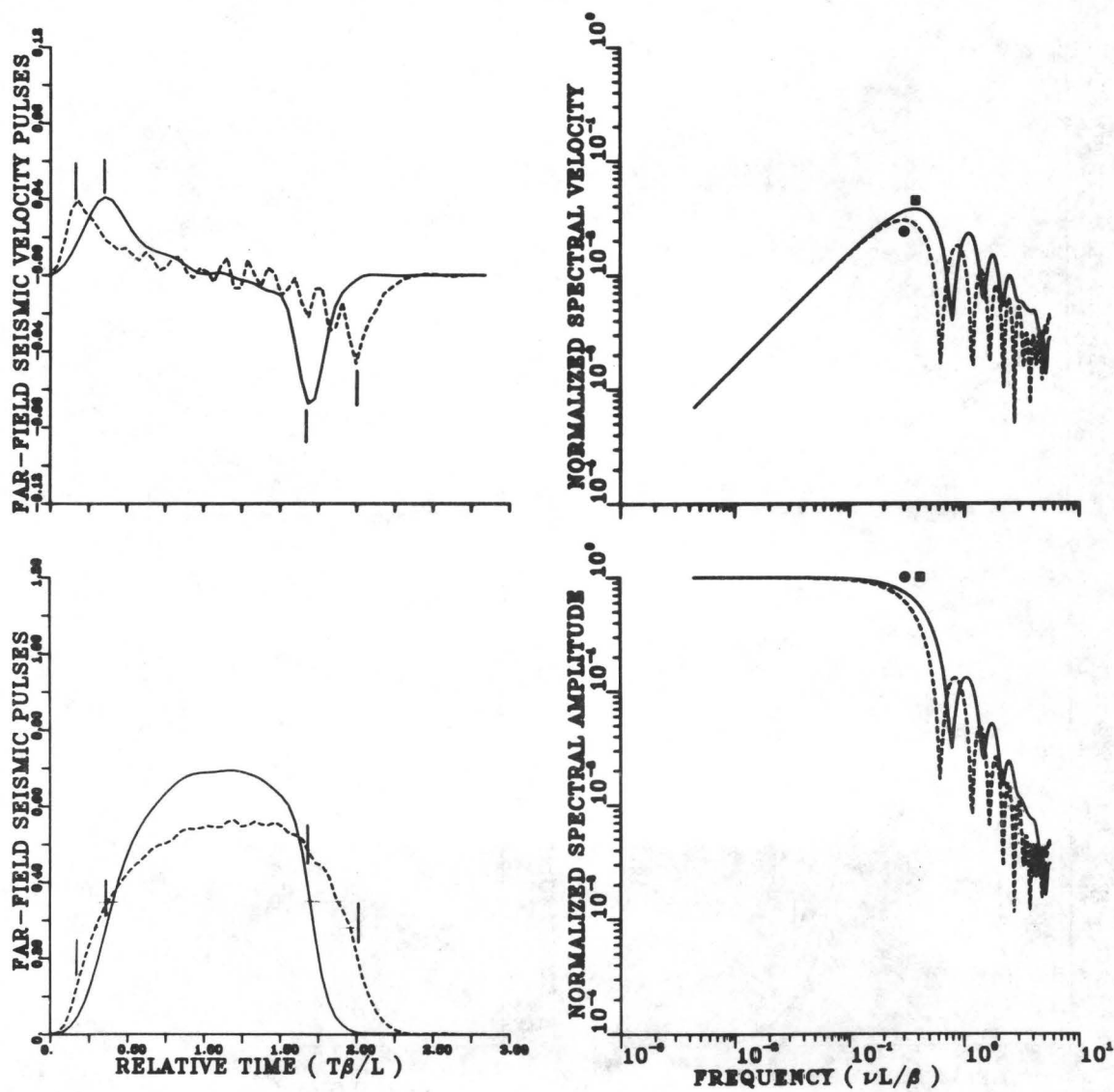
Figure 7 : Far-field calculations for the AM1 model at $\theta=60°$ and $\varphi=0°$. Same notations as figure 4.

A M 1
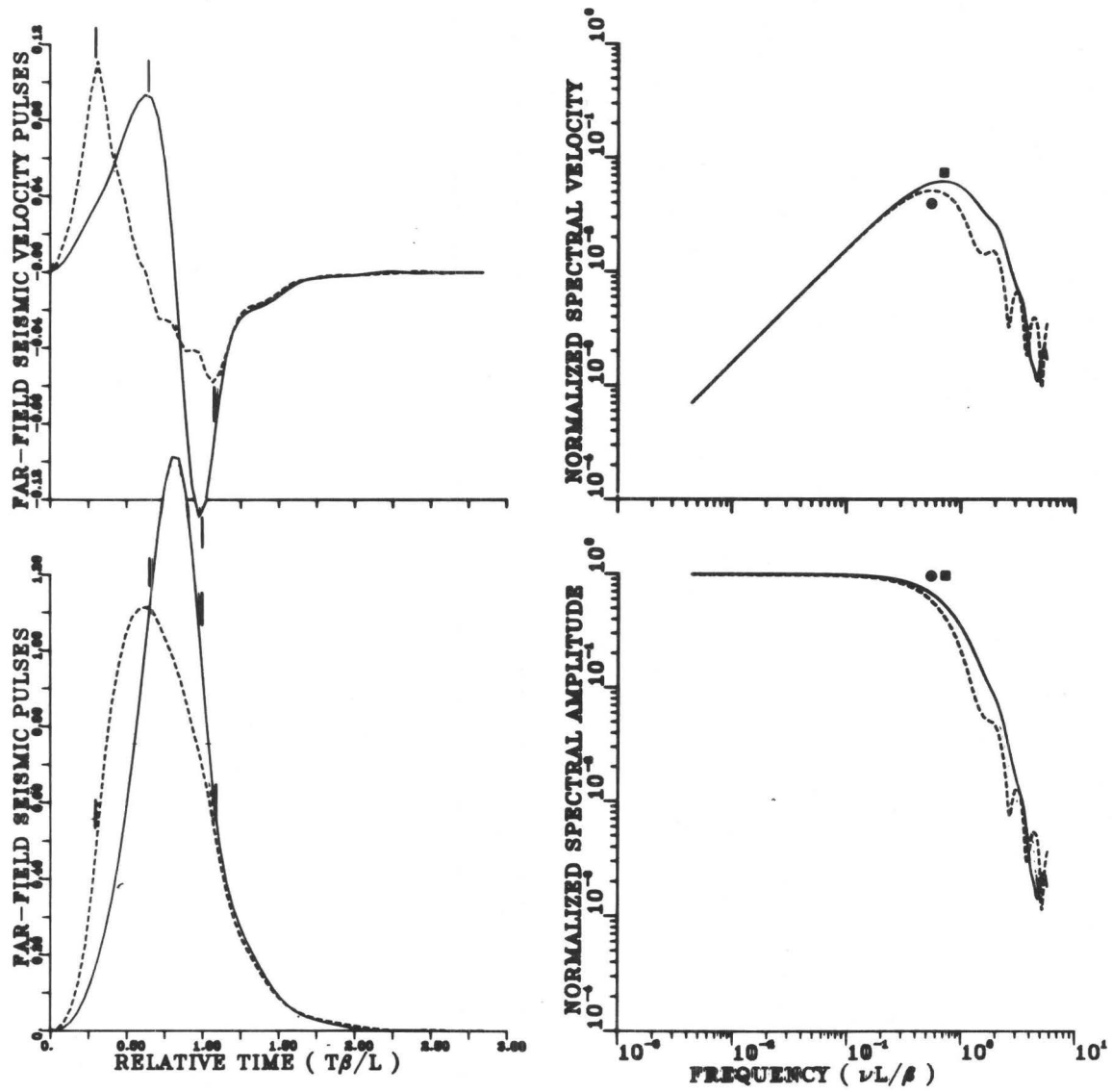
Figure 8 : Far-field calculations for the AM1 model at θ=60° and φ=180°. Same notations as figure 4.

531

AM 2

Figure 9 : Far-field calculations for the AM2 model at $\theta=60°$ and $\varphi=0°$. Same notations as figure 5.

532

A M 2
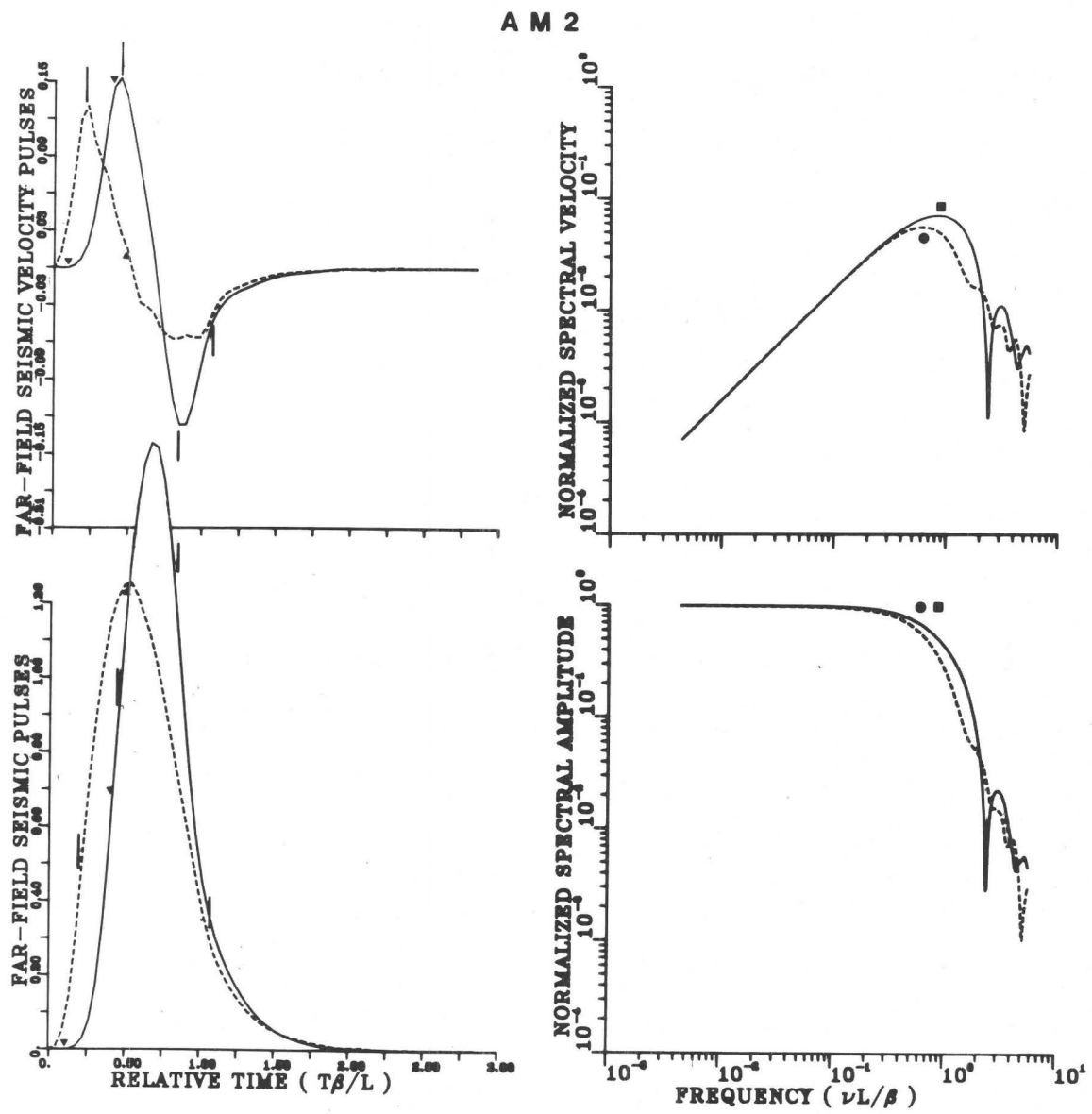
Figure 10 : Far-field calculations for the AM2 model at $\theta = 60°$ and $\varphi = 180°$. Same notations as figure 5.

PARAMETRIC STUDY OF NEAR-FIELD MOTIONS FOR
OBLIQUE-SLIP AND DIP-SLIP FAULT MODELS

by

John G. Anderson and J. Enrique Luco

ABSTRACT

The near-field motion on the surface of a uniform half-space for oblique-slip and dip-slip faults has been studied by the use of a dislocation model. The fault is modeled by an infinitely long buried dislocation of finite width; rupture propagates horizontally along the fault and past the observation points with a constant rupture velocity lower than the Rayleigh wave velocity. In addition to those parameters which control peak amplitudes near a vertical, strike-slip fault (depth of the top of the fault, horizontal rupture velocity), the dip of the fault plays an important role. The slip direction and the angle between the rupture front and the down-dip direction of the fault also become increasingly important in determining amplitudes of peak ground motions as the dip of the fault decreases from vertical to shallow angles.

Because this model leads to increased amplitudes of ground motions as the fault dip decreases, and based on the extent to which this model underestimates peak amplitudes in California for vertical strike-slip events, one may anticipate considerable regions with large peak accelerations (>1g) and peak velocities (>100 cm/sec) above thrust faults.

Institute of Geophysics and Planetary Physics, Scripps Institute of Oceanography, University of California, San Diego, La Jolla, California 92093 (J.G.A.).

Department of Applied Mechanics and Engineering Sciences, University of California, San Diego, La Jolla, California 92093 (J.E.L and J.G.A).

INTRODUCTION

This article is a continuation of the parametric study on strong ground motion which was initiated by Anderson and Luco (1982). The previous paper studied the effect of several parameters on the strong ground motion in the near field of a vertical strike-slip fault in a uniform half-space. The fault is modeled by an infinitely long buried dislocation of finite width; rupture propagates horizontally along the fault and past the observation points with a constant rupture velocity lower than the Rayleigh velocity. We now extend the previous results to dipping faults and to faults which include a dip-slip component of ground motion. Since Anderson and Luco (1982) thoroughly studied the strike-slip fault, our approach will be to begin with that case, and see what happens as we deviate from the pure strike slip. We will study the evolution of ground motion for cases which are intermediate between pure strike-slip and pure thrust, and then study the pure thrust case in more detail.

Previous parametric studies of three dimensional oblique-faulting or thrust-faulting in a half-space on a model of comparable complexity have apparently not been carried out. A number of two-dimensional models have been presented (Mal, 1972; Schafer, 1973; Brock, 1975; Niazi, 1975; Litehiser, 1976; Bouchon and Aki, 1977; Bouchon, 1978; Madariaga, 1980). These models assume that the rupture velocity along the horizontal dimension of the fault is infinite, in contrast to the model considered here which assumes a finite horizontal rupture velocity.

DESCRIPTION OF THE MODEL

The model derived by Luco and Anderson (1982) gives the ground motion near a fault of finite width and infinite length, which is embedded in a uniform half-space. Figure 1 illustrates the geometry of the fault model and the coordinate systems employed. The fault has a strike parallel to the x axis (Fig. 1A) and may have an arbitrary dip, γ, which is measured from the horizontal y axis. Faulting

occurs as a uniform shear dislocation between the depths $z_u \leqslant z \leqslant z_d$. For the general case of a fault with dip different from $90°$, the vertical projection of the fault to the free surface extends over the range $y_u \leqslant y \leqslant y_d$. The width of the fault is $W = \sqrt{(z_d - z_u)^2 + (y_d - y_u)^2} = (z_d - z_u)/\sin\gamma$.

Figure 1B is a map of the fault plane in the vicinity of the rupture front. The rupture front travels from $x = -\infty$ to $x = \infty$ at a constant longitudinal rupture velocity c_1, where c_1 must be less than the Rayleigh wave speed. For an observer at $x = 0$, the time $t = 0$ corresponds to the time of passage of the rupture in front of the observation point. As shown in Figure 1B, the rupture front need not be parallel to the dip direction of the fault. Luco and Anderson introduced a "transverse rupture velocity," c_2, which describes the rate at which the rupture front crosses the width of the fault at fixed x. The slip direction on this fault may be arbitrary and it is described by the rake angle ϕ, measured in the fault plane from the horizontal axis. The shape of the time function for slip is the same throughout the fault, and, in this paper, we use a step offset.

The numerical results presented below have been obtained using the analytical solution derived by the authors (Luco and Anderson, 1982) in which the velocity on the surface of the half space is given in terms of a single, finite integral. Accelerations are obtained by numerical differentiation of the synthetic velocity; displacements by numerical integration. Velocities were calculated at a time increment of 0.02 sec and for a total duration of 20 seconds.

EVOLUTION FROM STRIKE-SLIP TO DIP-SLIP DISPLACEMENTS
ON THE FAULT

Anderson and Luco (1982) thoroughly examined the case of a vertical ($\gamma = 90°$) strike-slip ($\phi = 0°$) fault. Some review of the results of Anderson and Luco (1982) would seem to be appropriate. For the vertical strike slip fault, they examined characteristics of the acceleration, velocity, and displacement pulses resulting from this model as a function of distance to the fault, as a function of

horizontal and transverse rupture velocities, and as a function of rise time. The components u_x and u_z are nodal at the fault plane, and achieved peak values at distances y comparable to the depth of the top of the fault. A geometrical factor which controls these peak values is the depth of the top of the fault; the width of the fault is not important (unless it approaches zero). The horizontal rupture velocity c_1 has an important role in controlling peak values, with u_x and u_z being more sensitive than u_y to c_1 when c_1 is near the Rayleigh velocity. The vertical rupture velocity c_2 did not play an important role in modifying peak amplitudes, unless it became much smaller than c_1, but it did significantly modify the pulse shapes. An intriguing aspect of the solution is that for infinite c_2, $\dot{u}_x$ is symmetric about $t = 0$, while $\dot{u}_y$ and $\dot{u}_z$ are anti-symmetric. Finally, the effect of increasing rise time is to reduce the amplitudes of acceleration and velocity to values which are less, and sometimes considerably less, than those seen for the step offset.

This study introduces the effect of changes in two more parameters: the fault dip (γ) and the rake (ϕ). To examine the evolution from vertical strike slip ($\phi = 0°, \gamma = 90°$) to dip slip ($\phi = \pm 90°, \gamma \leq 90°$), we will first look at the effect of the rake for a vertical fault, second look at the effect of dip on waves generated by a strike slip fault, and third look at the effect of the rake on waves generated by a dipping fault. We begin by examining how a change in the rake affects synthetic motions near a vertical fault. Thus Fig. 2 illustrates the change in synthetic displacement, velocity, and acceleration for a site at $y = 5.0\ km$ as the rake changes from $0°$ to $-90°$ on a vertical fault. Other parameters for the synthetics in Fig. 2 are $\alpha = \sqrt{3}\beta = 6.0$ km/sec, $c_1 = 3.0$ km/sec, $c_2 = \infty$, the slip on the fault, $\Delta_o = 100$ cm, $z_u = 2.0\ km$, and $z_d = 10.0\ km$. The parameters α, β, c_1, Δ_o, z_u, and z_d are held at those values for all calculations in this paper. Figure 2 illustrates that the symmetry of $\dot{u}_x$ and the anti-symmetry of $\dot{u}_y$ and $\dot{u}_z$ of strike-slip faulting is absent for arbitrary rake, but a complementary symmetry exists for pure dip-slip faulting. In particular, a component which was symmetric for strike-slip becomes anti-symmetric for dip-slip, and a component with anti-symmetric motions for strike-slip faulting becomes symmetric for dip slip faulting. A second characteristic of the results shown in Fig. 2 is that the peak amplitudes are relatively insensitive to the rake. The components most affected by variation of the rake are $\dot{u}_z$ and u_z, which are increased by a factor of the order of 2 to 3, and $\ddot{u}_y$ which

suffers a reduction also by a factor of the order of 2 to 3 as the rake varies from $0°$ to $-90°$. These observations are further illustrated in Fig. 3, which shows the peak values from Fig. 2 and from additional calculations as a function of the rake.

Next we consider the effect of the dip angle on a fault with pure strike slip motion. The observer is at a point 5 km from the vertical projection of the top of the fault to the free surface ($y - y_u = 5$ km) as shown in Fig. 4. The calculations use a constant offset on the fault, and consequently the moment per unit length increases in these calculations as the dip decreases. In particular, $M_o/L \propto W \alpha \frac{1}{\sin \gamma}$. In shifting the dip from $90°$ to $15°$, this causes an increase of M_o/L by a factor of 3.86. We have not normalized to constant M_o/L because Anderson and Luco (1982) found that close to the fault, the actual slip was a more important factor in determination of peak amplitudes than the width of the fault.

Figure 5 illustrates the synthetic motions generated for three different dip angles. These synthetics give the motions at the site $y - y_u = 5$ km for strike slip on faults with dips of $90°$, $60°$, and $30°$. As in Fig. 2, these synthetics are generated for c_2 infinite. In Figure 5, one sees that while the general features of the pulse shapes are not changed as the dip decreases, the amplitudes increase considerably. Peak amplitudes from Fig. 5 are transferred to Fig. 6, where they are shown as a function of the dip. Peak accelerations $\ddot{u}_x$ and $\ddot{u}_z$ increase by factors of 26 and 37, respectively, as the dip decreases from $90°$ to $15°$. These increases are much larger than the increase in the moment, which as mentioned is only a factor of 3.86. Thus for strike-slip motion on the fault, the dip of the fault plays an important role in the determination of peak amplitudes of ground motion. We note that as the dip decreases, the closest distance from the observer to the fault also decreases.

Next, we investigate the effect of a variable rake on the synthetic pulses generated by a dipping fault. Figure 7 shows the evolution of synthetic acceleration, velocity, and displacement for a site at $y - y_u = 5$ km, and for infinite c_2, caused by a fault with a dip of $30°$ as the rake changes from $0°$ (pure strike-slip faulting) to $-90°$ (pure thrust faulting). Qualitatively the results shown in Figure 7 resemble those on Figure 2 for a vertical fault: arbitrary rake disrupts the symmetry, and the amplitudes of some components are modified by a factor of the order of 2 to 3. The peak acceleration in the y - component experiences a reduction by a factor of the order of 6 as the rake varies from $0°$ to $-90°$. Peak

amplitudes corresponding to this case are shown on Figure 8. It is interesting that strike slip on the dipping fault causes stronger shaking than pure dip-slip motions.

To summarize this section, we have studied the evolution from strike-slip to dip slip faulting. These calculations indicate that the peak amplitudes are quite sensitive to the dip, and less sensitive to the rake.

FURTHER PARAMETRIC STUDIES ON DIP-SLIP FAULTING

The effects of dip angle on the synthetic motions and peak amplitudes for a site near a thrust fault are illustrated in Figures 9-11. We have used the same geometry as in Figure 4 for these calculations. Figure 9 shows synthetic motions generated when $c_2 = \infty$, as it has been in the previous figures. Figure 10 departs from this, and shows the effect of a finite value for the transverse rupture velocity, $c_2 = -2.5$ km/sec. For this case, at any location x along the fault, the rupture occurs first at the bottom of the fault, and propagates across the width of the fault at 2.5 km/sec. The symmetry properties which appear on Figure 9 are absent from Figure 10. The differing delays in the time of occurrence of peak accelerations and velocities is caused because these peaks occur when rupture at the top of the fault passes in front of the observation point; with the successively greater width of faults of smaller dip, it takes longer for rupture to pass from the bottom edge to the top edge of the fault. With the exception of the u_y - component, the peak amplitudes shown in Figures 9 and 10 and summarized in Fig. 11 do not appear to be strongly affected by the dip of the fault. The largest effects occur for peak accelerations which show an increase by a factor of the order of 3 as the dip decreases from 90° to 15°. The peak amplitudes for the transverse component u_y show a strong dependence on the dip angle and exhibit a minimum at a dip = 45°. Figures 9 and 10 indicate that the sense of motion of the u_y - component is reversed between dips of 30° and 60°.

The amplitudes of the acceleration and velocity pulses which are shown in Fig. 10 for finite c_2 are much smaller than those shown in Figure 9 for infinite c_2. Peak amplitudes for the two values of the transverse rupture velocity c_2 are shown on Figure 11. Differences of a factor of 2 to 3 seem to prevail for velocity, and factors of 3 to 10 for acceleration. The exception to this pattern is the u_y - component which for dip angles near 45° and for $c_2 = -2.5$ km/sec exhibits larger peak values for $\ddot{u}_y$ and $\dot{u}_y$ and equal peak values for u_y than the results for $c_2 = \infty$.

In Figure 12, we plot profiles of peak values of acceleration, velocity, and displacement along the free surface for a thrust fault with a dip of 30° and c_2 infinite. The upper edge of the fault lies beneath $y = 3.46$ km. Peak values in the x and z components of motion occur in the vicinity of this point ($y = 3.46$ km), while the peaks of the y-components are shifted slightly toward smaller values of y. Figure 12 shows considerable asymmetry in y, with a less rapid decrease in peak values at $y > 0$, above the fault plane, and illustrates the extreme dependence of peak amplitude on position. We attempted, unsuccessfully, to correlate details of the shapes of the curves in Fig. 12 (such as the minimum of u_y at $y \approx 0$) with the radiation patterns for a point dislocation (Aki and Richards, 1980, p. 80-81) at the top edge of the fault. As pointed out by Archuletta and Hartzell (1981), motion at any one time results from contributions from different parts of the fault, and different wave types. Our failure to isolate a simple radiation pattern effect which correlates with details in Fig. 12 emphasizes that even though the position of the top edge of the fault is among the dominant parameters in determining the peak values, the entire extent of the fault contributes to the motion.

ON MEASURE OF DISTANCE TO FAULTS

The available data with respect to peak accelerations, velocities and displacements are typically organized on the basis of different measures of distance to the fault. In recent correlations, for instance, Campbell (1981) uses as measure of distance the closest distance to the fault while Joyner et al (1981) and Joyner and Boore (1981) use horizontal distance to the closest point on the vertical

540

projection of the fault area on the free surface. For vertical faults which intersect the free surface these two measures of distance coincide. For dipping faults the differences may be significant. This is shown in Fig. 13, where the peak amplitude results presented in Fig. 12 for a dipping thrust fault (dip = 30° are plotted versus three different measures of distance. These measures correspond to : distance from the site to the closest point on the surface area (R-Closest), distance to the top edge of the fault (R-Top), and horizontal distance to closest point on the vertical projection of the rupture area on the free surface (R-Projection). The distance R-Top was motivated by our observation that the depth of the top of the fault is more important than the width of the fault in determining near-field peak amplitudes.

Inspection of Fig. 13 reveals that the definition R-Closest tends to reduce the differences between components and between points at the same value of R-Closest but on different blocks. Even with this definition of distance differences of about one order of magnitude can be observed in the distribution of peak accelerations. The distance R-Projection causes a large scatter at $R \approx 0$ (for the purpose of plotting, the peak amplitudes at R-Projection = 0 are shown to the left of a broken scale since all points on the upper block above the fault are assigned the same distance $R = 0$. We note that our steady-state dislocation model over an infinitely long fault introduces a lower number of characteristic distances than a finite fault for which the use of a single measure of distance may introduce additional scatter.

Joyner and Boore (1981) used the larger of the two horizontal components of acceleration in their regression; Campbell (1981) selected the average of the two horizontal components. For the long period ground motions given by our calculations, Fig. 13 shows that one of the two components is systematically smaller than the other. This would seem to violate Campbell's implicit assumption, in taking average values, that both horizontal components obey the same distribution. As pointed out by Hadjian (1978), in actual accelerograph data, the instrumental axes may be oriented randomly with respect to the fault and, often, with respect to other accelerographs. However, if one vector component in fault based coordinates is systematically larger, such an effect will persist, with scatter, on randomly oriented axes. Incidentally, axes in our synthetic calculation are not necessarily oriented such that the largest peak acceleration will appear on one of the two components. The high frequencies which are

541

present in observations but absent from our calculations might be distributed identically in all vector orientations, but that is not known a-priori.

SUMMARY

Important Parameters in the Model. Within the context of the steady-state, infinite length dislocation model described by Luco and Anderson (1982) we have investigated the importance of several parameters on the pulse shapes and amplitudes of ground motion near a fault. In a separate paper (Anderson and Luco, 1982) we have studied in detail the case of vertical, strike-slip faults. In the present paper we have analyzed the cases of oblique-slip and dip-slip fault models. In this section, we attempt to summarize the results obtained in both studies.

First, we have found that the location of the observation point relative to the fault, and especially the top of the fault, plays an important, and expected role, in determining peak amplitudes of ground motion. Distance from the fault is the most easily recognized effect of location. A radiation pattern effect is also present, but is not always simply related to the radiation pattern from a point source. Near a dipping fault, peak amplitudes are different at equal distances but in opposite blocks.

Static faulting parameters which we studied included the depths of the top and bottom of the fault, the offset and the moment per unit length. Near the fault, the depth of the top of the fault and the offset (for short rise time) have a profound effect on the peak amplitudes; the depth of the bottom of the fault, and thus the moment per unit length, do not appear to play a dominant role at distances less than about twice the depth of the bottom.

For a strike-slip type earthquake, the dip of the fault had an order-of-magnitude effect on the peak amplitudes. On a dip-slip fault, the dip is less important, but still plays a prominent role in determining peak amplitudes. The shallow dipping fault causes larger peak amplitudes than the near-vertical fault. The rake, or slip direction on the fault plane is relatively unimportant (within a factor of 2) in

determining peak amplitudes for a vertical fault, and slightly more important as the fault becomes more shallow-dipping.

The dynamic parameters considered included the rupture velocities c_1 and c_2, and the rise time. The horizontal rupture velocity c_1 was found in Anderson and Luco (1982) to play a crucial role in determining peak accelerations, and a successively lesser role in peak velocities and peak displacements. When the rupture velocity c_1 is close to the Rayleigh wave velocity of the medium, the effect is most impressive. For the strike-slip fault, on which this effect was studied, peak accelerations change by a factor of about 4 for a less than one percent change in c_1 as c_1 approaches the Rayleigh wave velocity. The transverse rupture velocity, c_2, was not very important on the vertical, strike-slip fault, but on the dipping fault it may reduce peak accelerations and velocities considerably. In all cases, it plays an important role in modifying pulse shapes.

The role of the rise time is also important, especially as one extrapolates this model to larger magnitude earthquakes in which the rise time is still unknown. Scholz (1981) has pointed out that if the larger slip in a large magnitude earthquake is accomplished within the same rise time as for a smaller earthquake, the peaks of ground motion would be considerably greater than they would be if the rise time is proportional to the slip.

Extension to Real Earth. Anderson and Luco (1982) were encouraged by the finding that the pulse shapes generated by this model resembled the long-period components of observed ground motion at sites adjacent to the fault associated with the October 15, 1979 Imperial Valley, California earthquake. However, there is a considerable amplitude discrepancy, with the model giving much lower peak values than those in the data. This discrepancy in amplitude was sufficiently great that one possibility for explaining the similarity of shape is that it is a coincidence, with the data pulses caused by some phenomena other than the approach and probable passage of the rupture front by the stations. (e.g. the rupture of a large fraction of the fault as an isolated event). However, the results of Bouchon (1979) suggest that shallow layering might also cause an increase in amplitude sufficient to resolve the

discrepancy. This leads to the conclusion that this model, after extension to a layered medium, will be a useful tool with which one can attempt to examine the strong ground motion in the near-field of a major earthquake.

We may attempt to anticipate the results of this extension by use of the calibration provided by the strike-slip case. With $c_1 = 3$ km/sec, $z_u = 2$ km at $y - y_u = 5$ km, the strike slip case yielded peak accelerations which were too small by a factor of about 15 and peak velocities which were too small by a factor of about 5 compared to correlations of Joyner et al (1981). Compared to low-pass filtered (0.5 Hz) Imperial Valley data, synthetics which had been filtered in the same way underestimated the trend of peak accelerations on the transverse array by a factor of about 6 at a distance of 5 km. These filtered accelerograms are dominated by frequencies comparable to those which dominate the unfiltered velocity records from Imperial Valley.

If we used these "calibration factors" for the strike slip case to anticipate peak values which might be obtained near a thrust fault, we obtain large peak accelerations and velocities. For example, from Fig. 12, which is based on 1 meter offset on a fault which dips at 30°, and for which $c_2 = \infty$, one obtains after application of a factor of 15 a maximum peak acceleration between 3.5g to 4g, and peak accelerations exceeding 1g over a band about 10 km wide parallel to the fault. Applying a factor of 5 increase to peak velocities, the largest peak velocities would exceed 500 cm/sec, and the peak velocities would exceed 100 cm/sec over a band about 15 km wide. As mentioned previously, if one were to extrapolate to larger slips, which are not unusual in significant thrust earthquakes, these values might be scaled upwards depending on how the rise time is handled. Finite values of c_2 may be likely for major thrust mechanism earthquakes, and would tend to cause the peak values to be scaled downwards. In general, our lack of knowledge about what parameters to apply to faulting in major earthquakes tends to limit the confidence of immediate applications of such extrapolations.

ACKNOWLEDGEMENTS

REFERENCES

Aki, K. and P.G. Richards (1980). Quantitative Seismology, Theory and Methods, WH Freeman and Company, San Francisco.

Anderson, J. G. and J. E. Luco (1982). Parametric study of near-field motions for a strike-slip fault model, (submitted for publication).

Archuletta, R.J. and S.H. Hartzell (1981). Effects of fault finiteness on near-source ground motion. Bull. Seism. Soc. Am. 71, 939-957.

Boore, D.M. and M.D. Zoback (1974). Two-dimensional kinematic fault modeling of the Pacoima Dam strong-motion recordings of the February 9, 1971 San Fernando earthquake, Bull. Seism. Soc. Am. 64, 555-570.

Bouchon, M. (1978). A dynamic crack model for the San Fernando earthquake, Bull. Seism. Soc. Am. 68, 1555-1576.

Bouchon, M. and K. Aki (1977). Discrete wave-number representation of seismic-source wave fields. Bull. Seism. Soc. Am. 67, 259-277.

Brock, L.M. (1975). Surface motions due to fault slip in the vertical mode with friction, Bull. Seism. Soc. Am. 65, 1653-1666.

Campbell, K.W. (1981). Near-source attenuation of peak horizontal acceleration, Bull. Seism. Soc. Am., 71, (in press).

Hadjian, A.H. (1978). On the correlation of the components of strong ground motion, Proceedings of the Second International Conference on Microzonation for safer construction - research and application Vol. III, San Francisco, California, 1199-1210.

Joyner, W.B., and D.M. Boore (1981). Peak horizontal acceleration and velocity from strong-motion records including records from the 1979 Imperial Valley, California, earthquake, Bull. Seism. Soc. Am. (in press).

Joyner, W.B., D.M. Boore and R.L. Porcella (1981). Peak horizontal acceleration and velocity from strong-motion records including records from the 1979 Imperial Valley, California, earthquake, Open File Report 81-365, U.S. Department of the Interior Geological Survey, Menlo Park, California.

Litehiser, J.J. (1976). Near-field seismograms from a two-dimensional propagating dislocation, Ph.D. Thesis, University of California, Berkeley.

Luco, J. E. and J. G. Anderson (1982). Steady-state response of an elastic half-space to a moving dislocation of finite width, (submitted for publication).

Madariaga, R. (1980). A finite two-dimensional kinematic fault in a half-space, Publ. Inst. Geophys. Pol.Acad. Sc., A-10 (142), 33-47.

Mal, A.K. (1972). Rayleigh waves from a moving thrust fault, Bull. Seism. Soc. Am. 62, 751-762.

Niazi, A. (1975). An exact solution for a finite, two-dimensional moving dislocation in an elastic half-space with application to the San Fernando earthquake of 1971, Bull. Seism. Soc. Am. 65, 1797-1826.

Schafer, J. (1973). Strong ground motion from dip-slip faulting, M.S. Thesis, Dept. of Mechanics and

Structures, University of California, Los Angeles.

Scholz, C.H. (1981). Scaling laws for large earthquakes consequences for physical models, preprint.
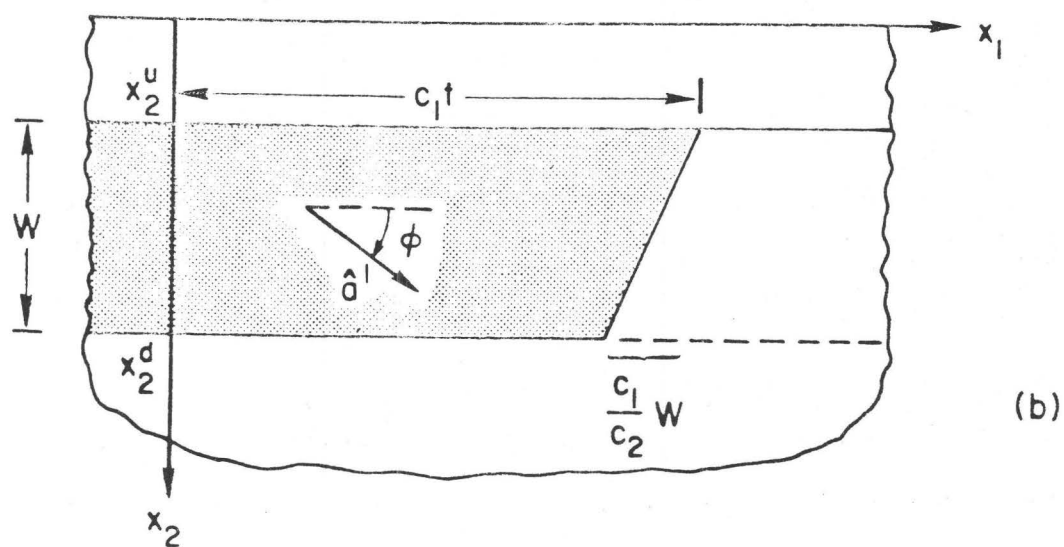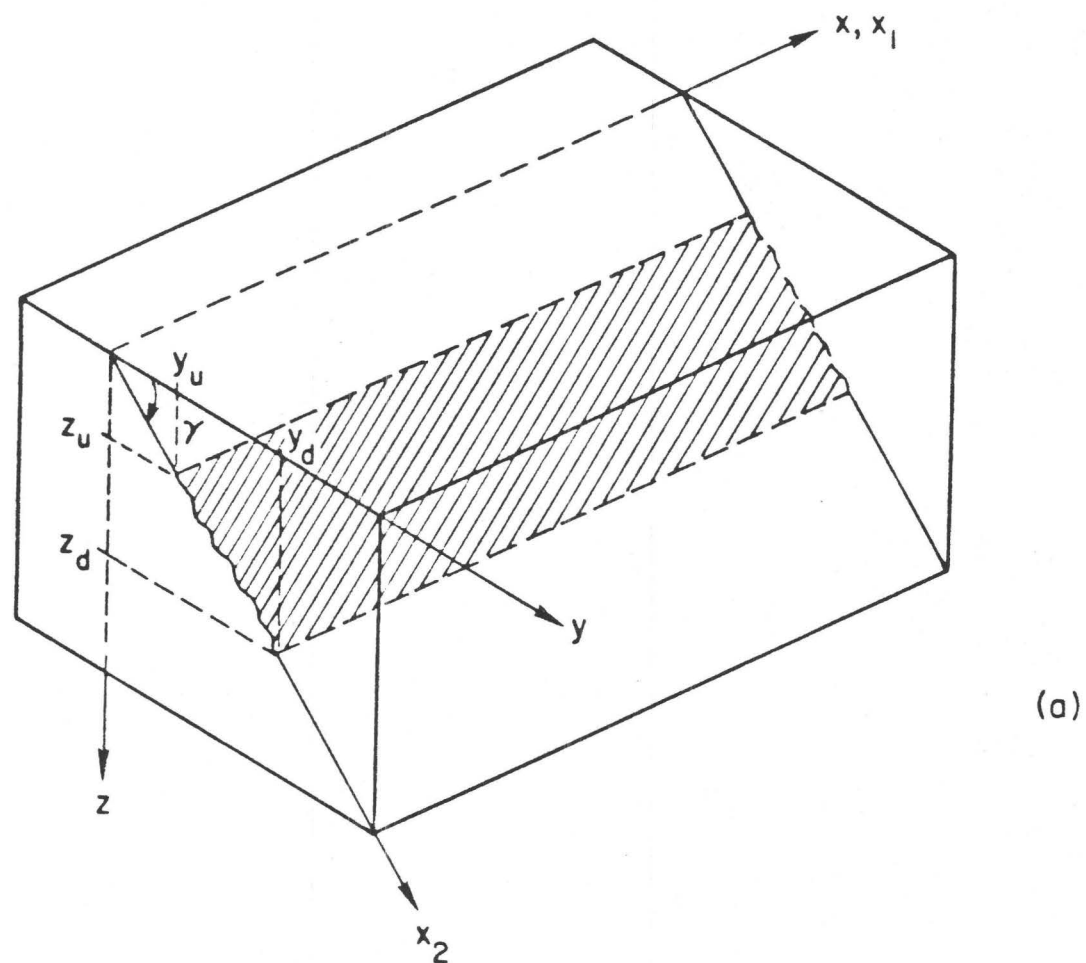
Figure 1. Coordinate system and fault model used in these calculations.
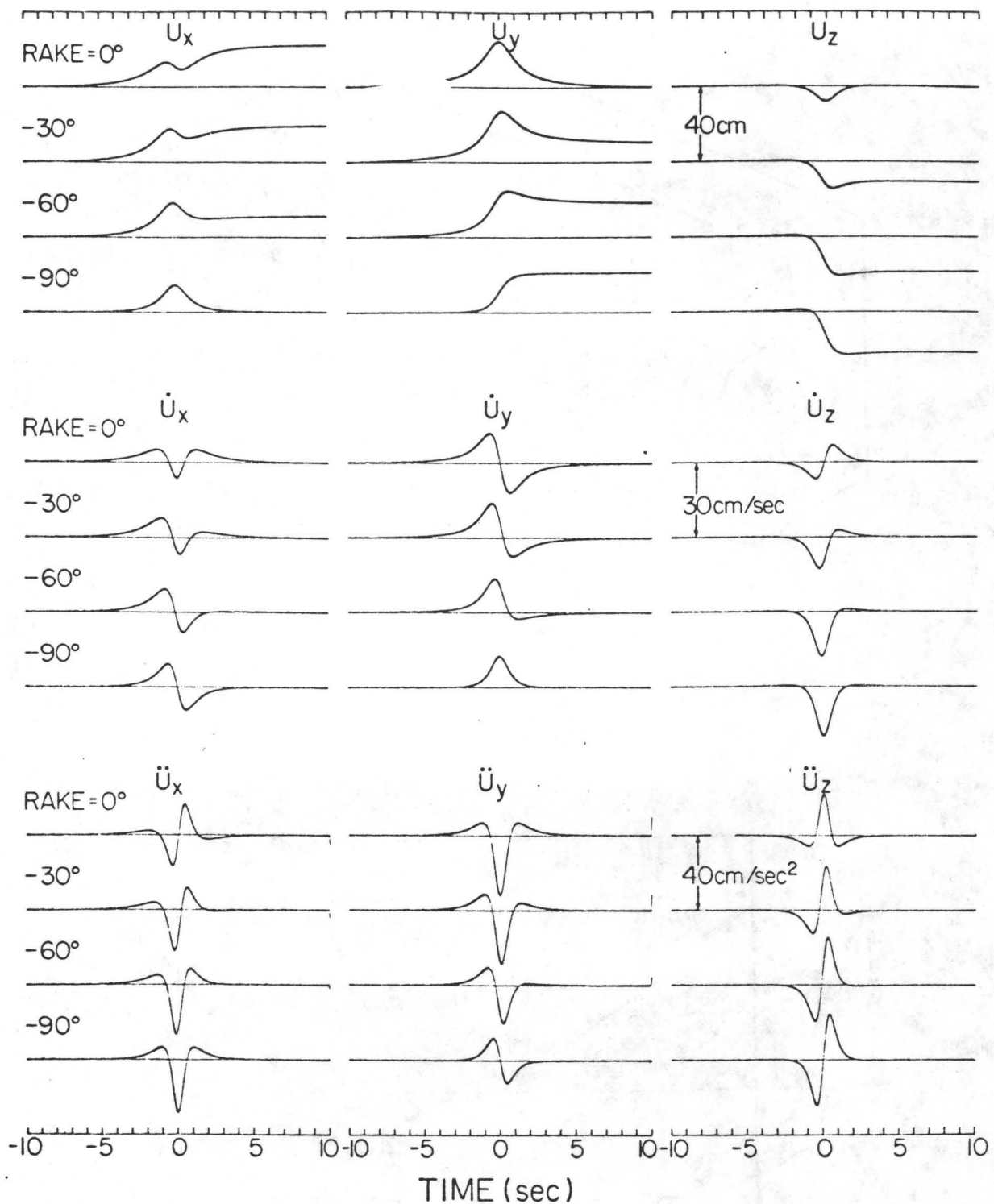
Figure 2. Evolution of synthetic waveforms on a vertical fault as the slip direction (rake) changes from pure strike slip (Rake = 0°) to pure thrust (Rake = −90°). This plot shows synthetic displacement (top), velocity (center) and acceleration (bottom). Other parameters are dip = 90°, $y = 5.0$ km, $y_u = 0.0$ km, $c_1 = 3.0$ km/sec, $c_2 = \infty$, $\Delta_o = 100$ cm, $z_u = 2.0$ km, $z_d = 10.0$ km. Synthetics are calculated at 50 points per second.
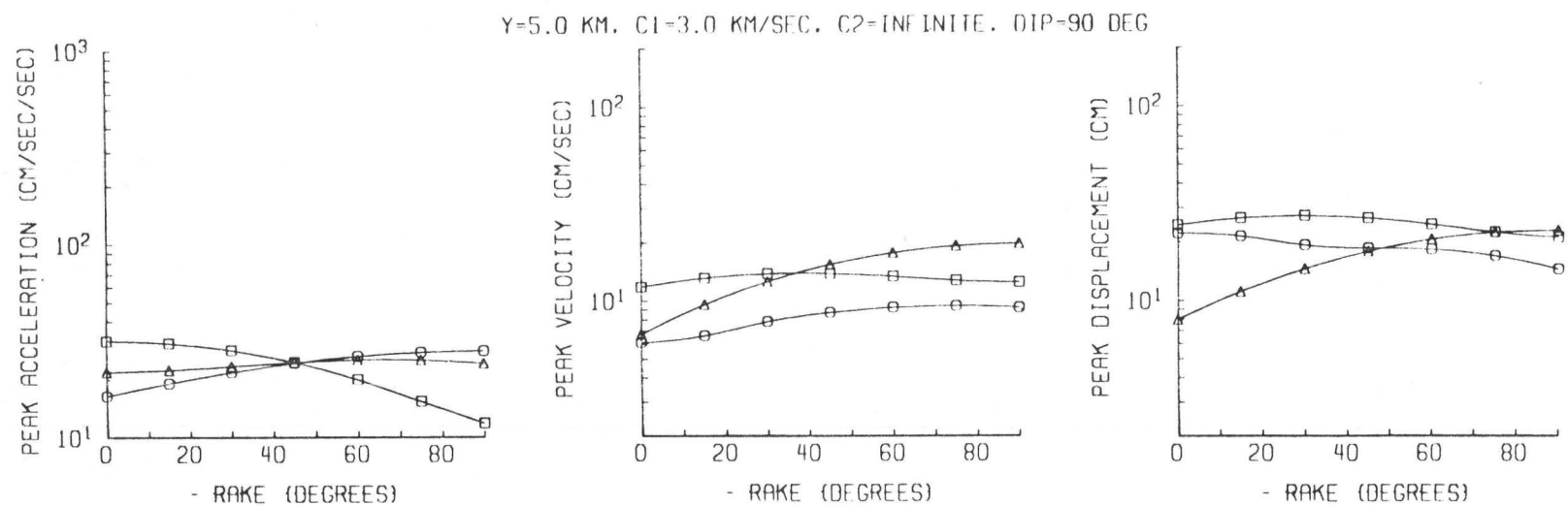
Figure 3. Peak amplitudes as a function of rake near a vertical fault. Faulting parameters are the same as those for Figure 2. Symbols are: circle $- U_x$, square $- U_y$, triangle $- U_z$. Symbols are plotted at all values of the rake where calculations were carried out; curved lines are cubic spline interpolations.
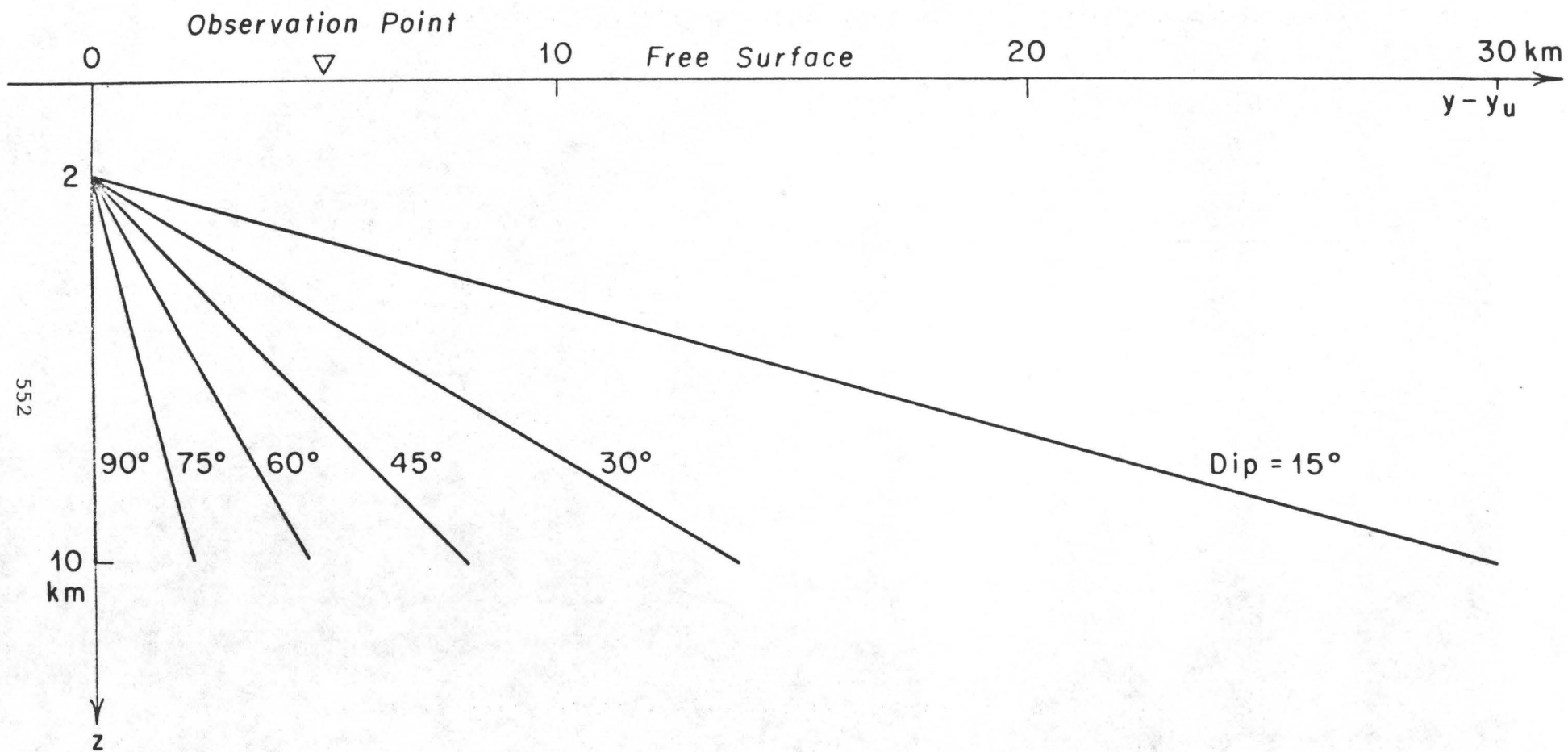
Figure 4. Observer-fault geometry for results shown in Figures 5 and 6.
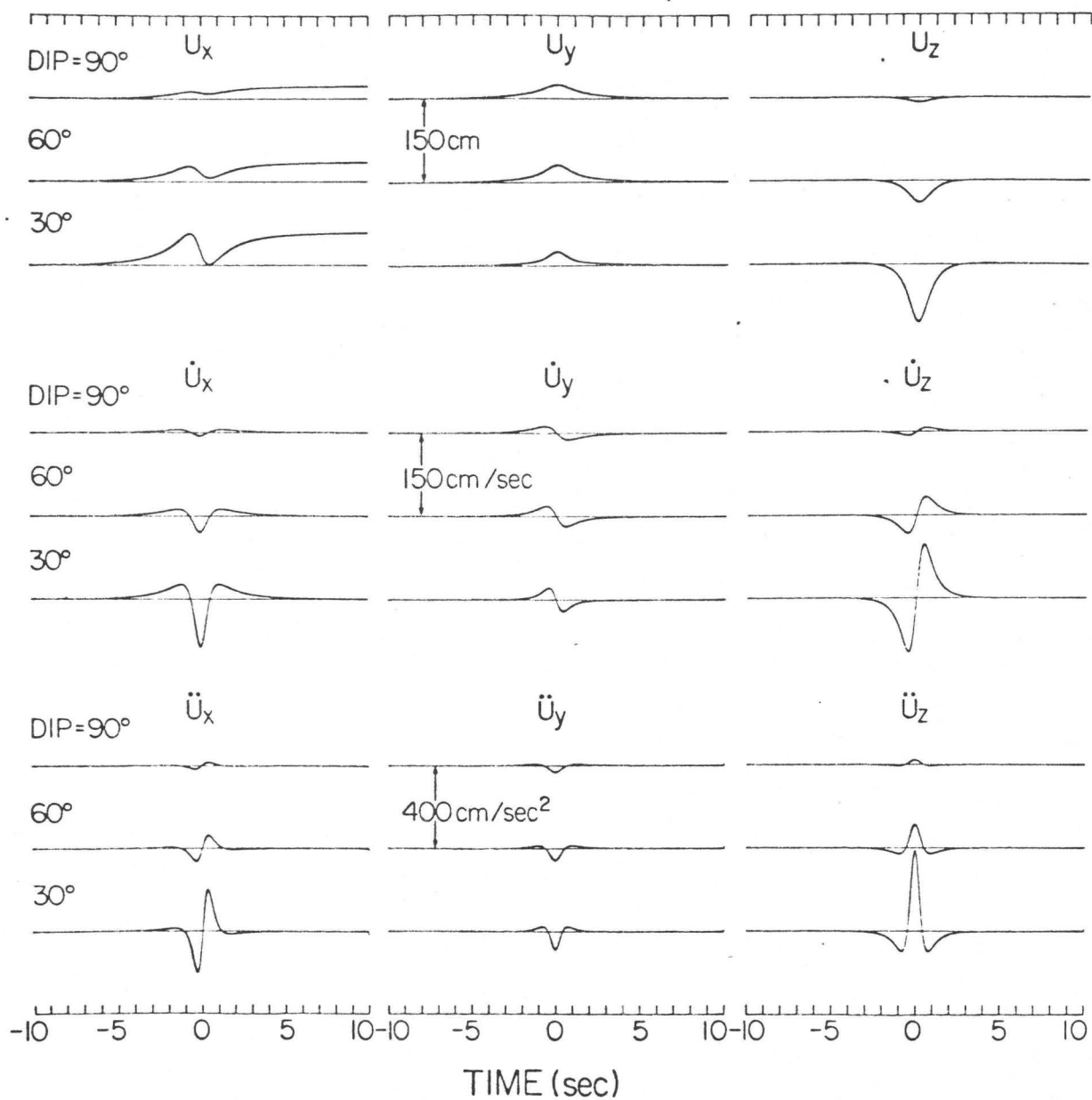
Figure 5. Evolution of synthetic waveforms above a strike slip fault of variable dip. The observation point is on the upper block, 5.0 km from the vertical projection of the top of the fault. Dip of $90°$ corresponds to a vertical fault. Synthetic displacement is at the top, velocity in the center, and acceleration at the bottom. Parameters are rake $= 0°$, $y - y_u = 5.0$ km, $c_1 = 3.0$ km/sec, $c_2 = \infty$, $\Delta_o = 100$ cm, $z_u = 2.0$ km, $z_d = 10.0$ km. Synthetics are calculated at 50 pts/sec.

553
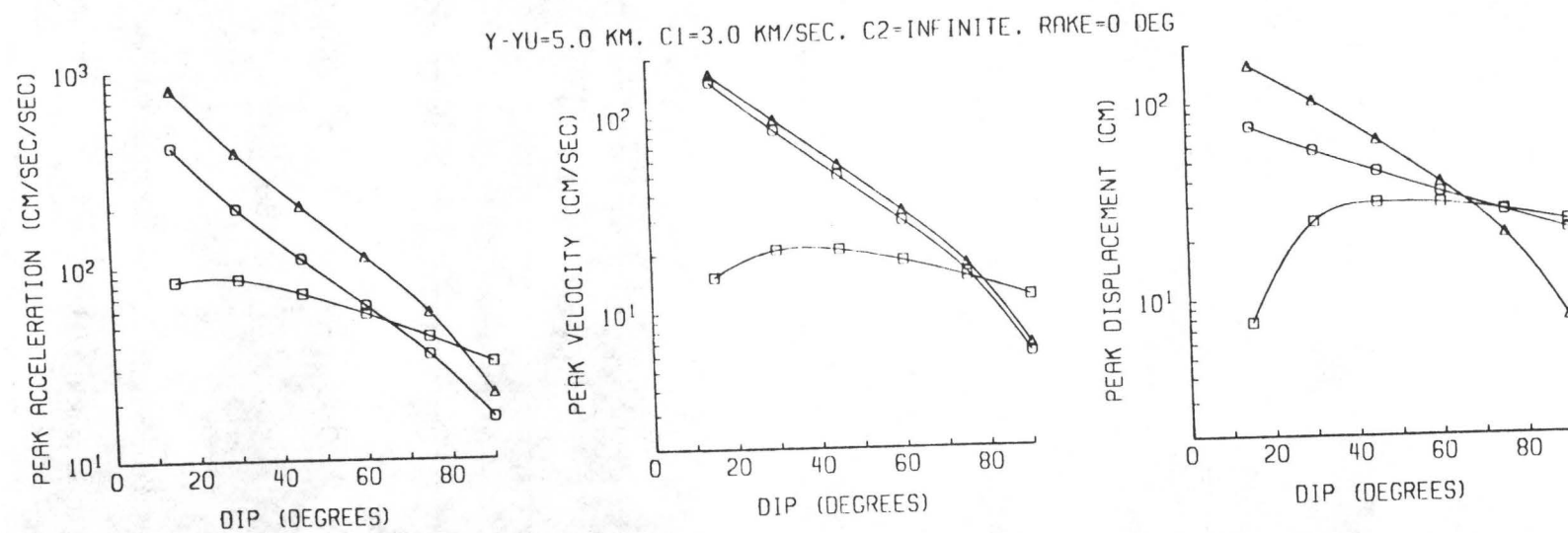
Figure 6. Peak amplitudes above a strike-slip fault of variable dip at a site on the upper fault block, 5.0 km from the vertical projection of the top edge of the fault. Model parameters are the same as in Figure 5. Symbols are circle $- U_x$, square $- U_y$, triangle $- U_z$. Symbols are plotted at each point where calculations are carried out, curves are cubic spline interpolations between these points.
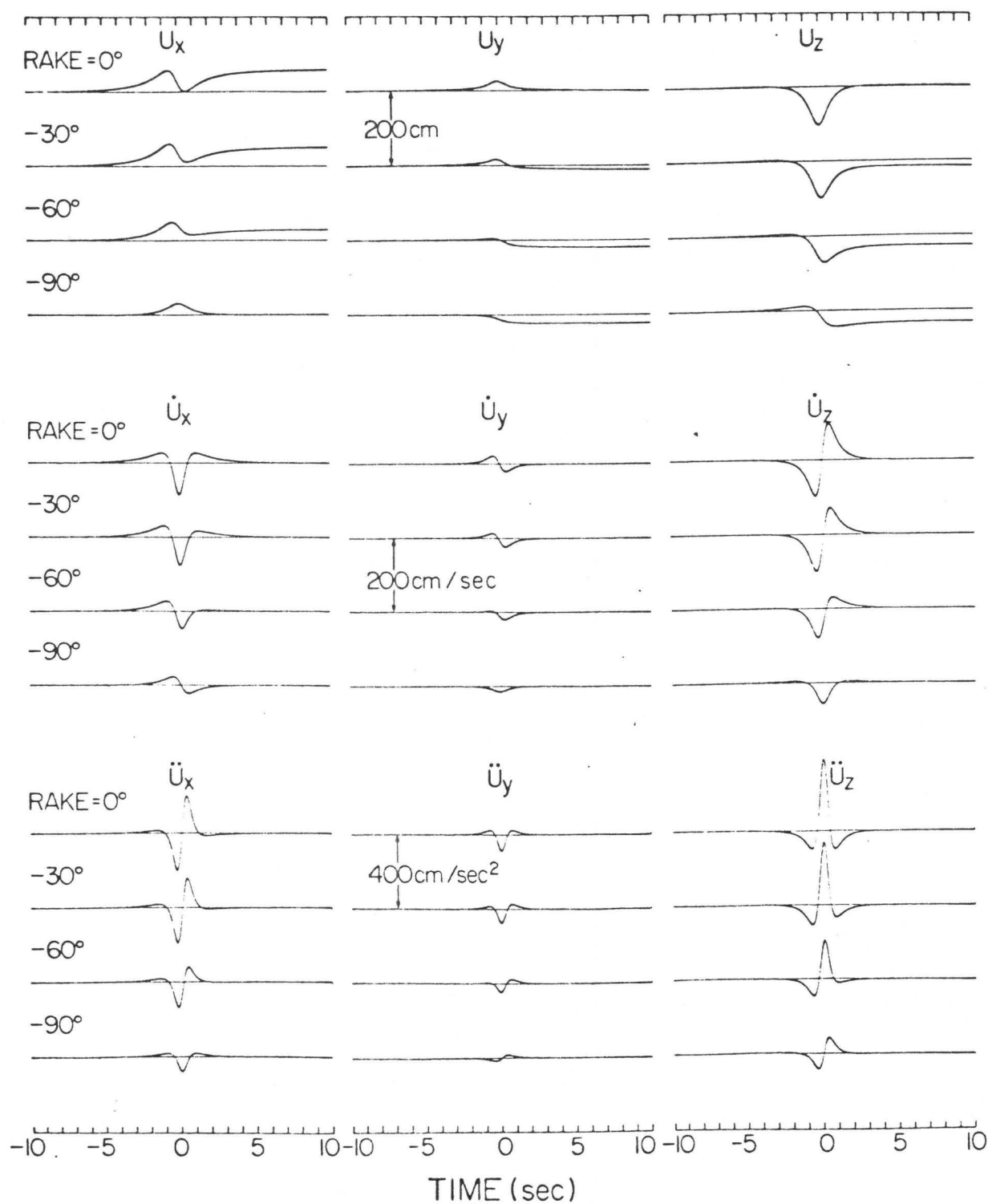
Figure 7. Evolution of synthetic waveforms on a dipping fault (dip $=30°$) as the slip direction changes from pure strike slip (rake $= 0°$) to pure thrust (rake $= -90°$). The observation point ($y-y_u = 5$ km) is above the fault on the upthrust block. Synthetic displacement is at the top, velocity in the center, and acceleration at the bottom. Parameters are dip $= 30°$, $y-y_u = 5.0$ km, $c_1 = 3.0$ km/sec, $c_2 = \infty$, $\Delta_o = 100$ cm, $z_u = 2$ km, $z_d = 10.0$ km. Synthetics are calculated at 50 points/second.

555

Y-YU-5.0 KM. C1-3.0 KM/SEC. C2-INFINITE. DIP=30 DEG
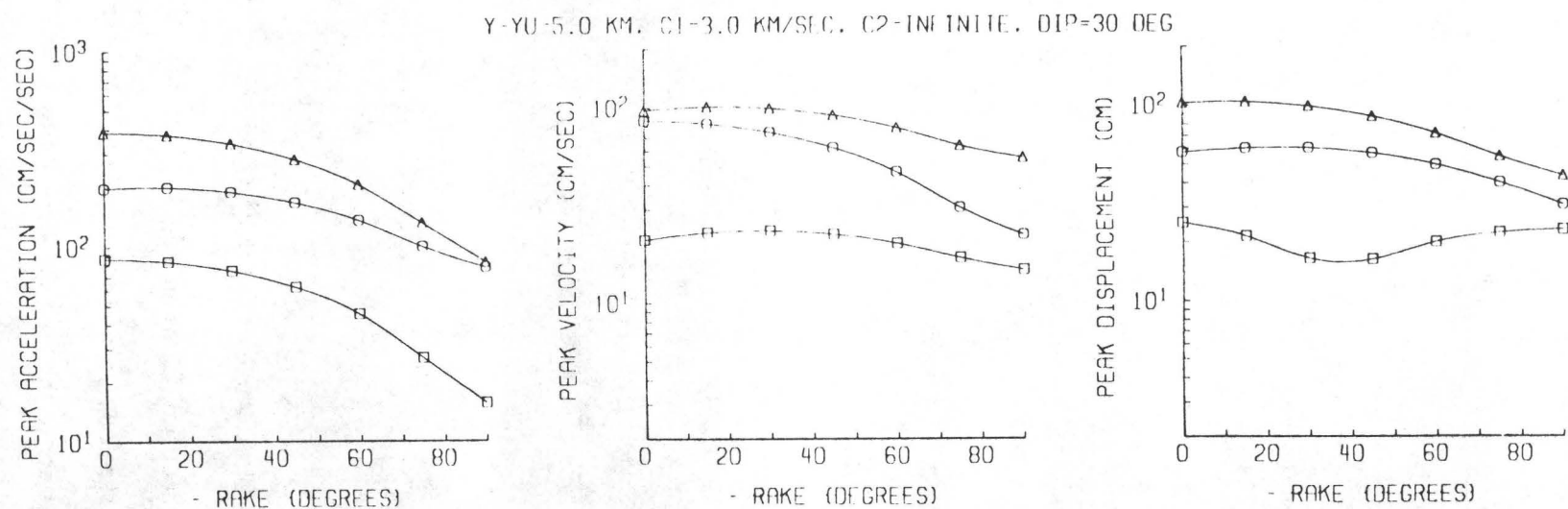
Figure 8. Peak amplitudes as a function of rake on the upthrust block of a thrust fault. Model parameters are the same as those of Figure 7. Symbols are circle $- U_x$, square $- U_y$, triangle $- U_z$. Symbols are plotted at each value of the rake where calculations were carried out; curved lines are cubic spline interpolations.
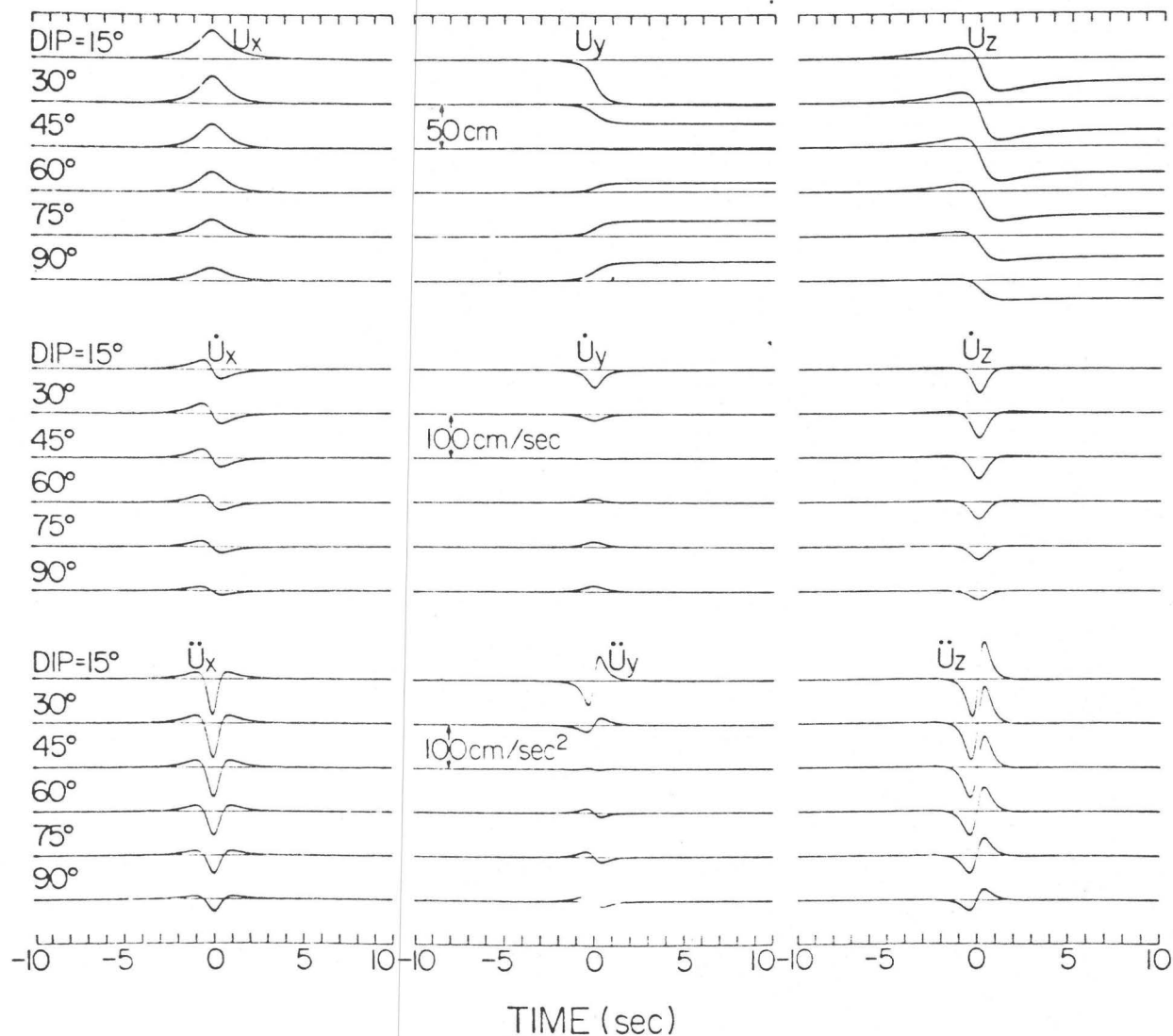
Figure 9. Evolution of synthetic waveforms above a thrust fault of variable dip. The observation point is on the upper block, 5.0 km from the vertical projection of the top of the fault. Dip of $90°$ corresponds to a vertical fault. Synthetic displacement is at the top, velocity at center, acceleration at the bottom. Parameters are rake $= -90°$, $y - y_u = 5.0$ km, $c_1 = 3.0$ km/sec, $c_2 = \infty$, $\Delta_o = 100$ cm, $z_u = 2.0$ km, $z_d = 10.0$ km. Synthetics are calculated at 50 points/sec.
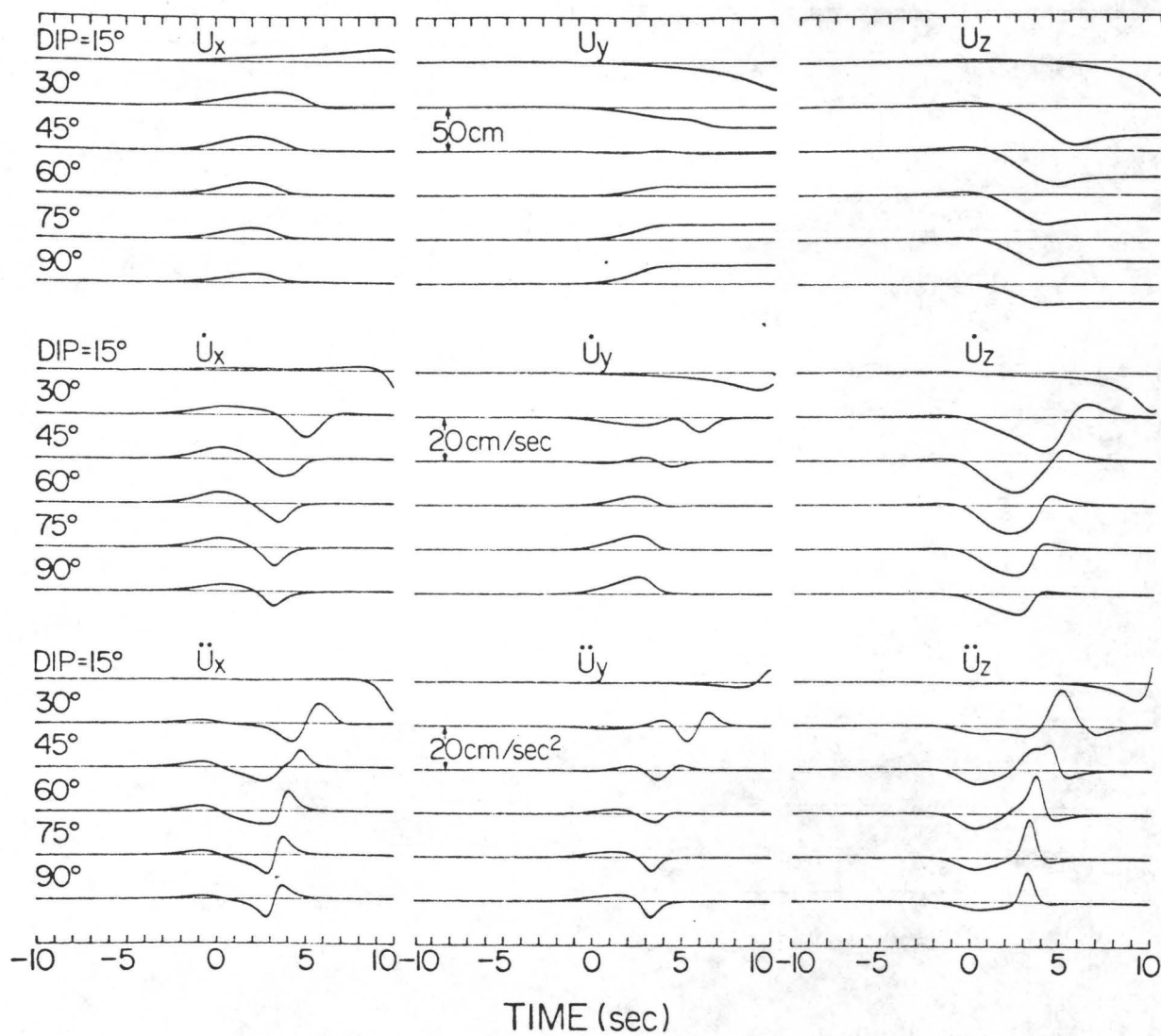
Figure 10. Equivalent of Figure 9, except that $c_2 = -2.5$ km/sec.
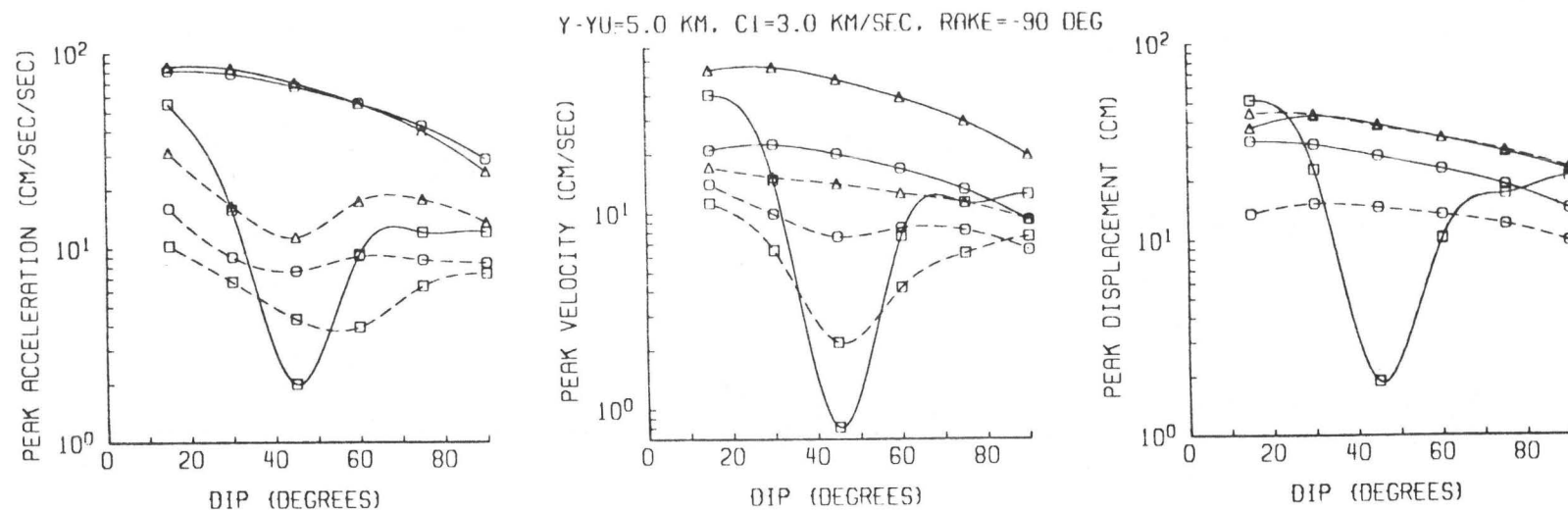
Figure 11. Peak amplitudes above a thrust fault of variable dip at a site on the upper fault block, 5.0 km from the vertical projection of the top edge of the fault. Model parameters are the same as in Fig. 9 and 10. Solid lines correspond to $c_2 = \infty$, dashed lines to $c_2 = 2.5$ km/sec. Symbols are circle $- U_x$, square $- U_y$, triangle $- U_z$. Symbols are plotted at each point where calculations are carried out; curves are cubic spline interpolations between these points.

DIP=30 DEG. C1=3.0 KM/SEC. C2-INFINITE. RAKE=-90 DEG
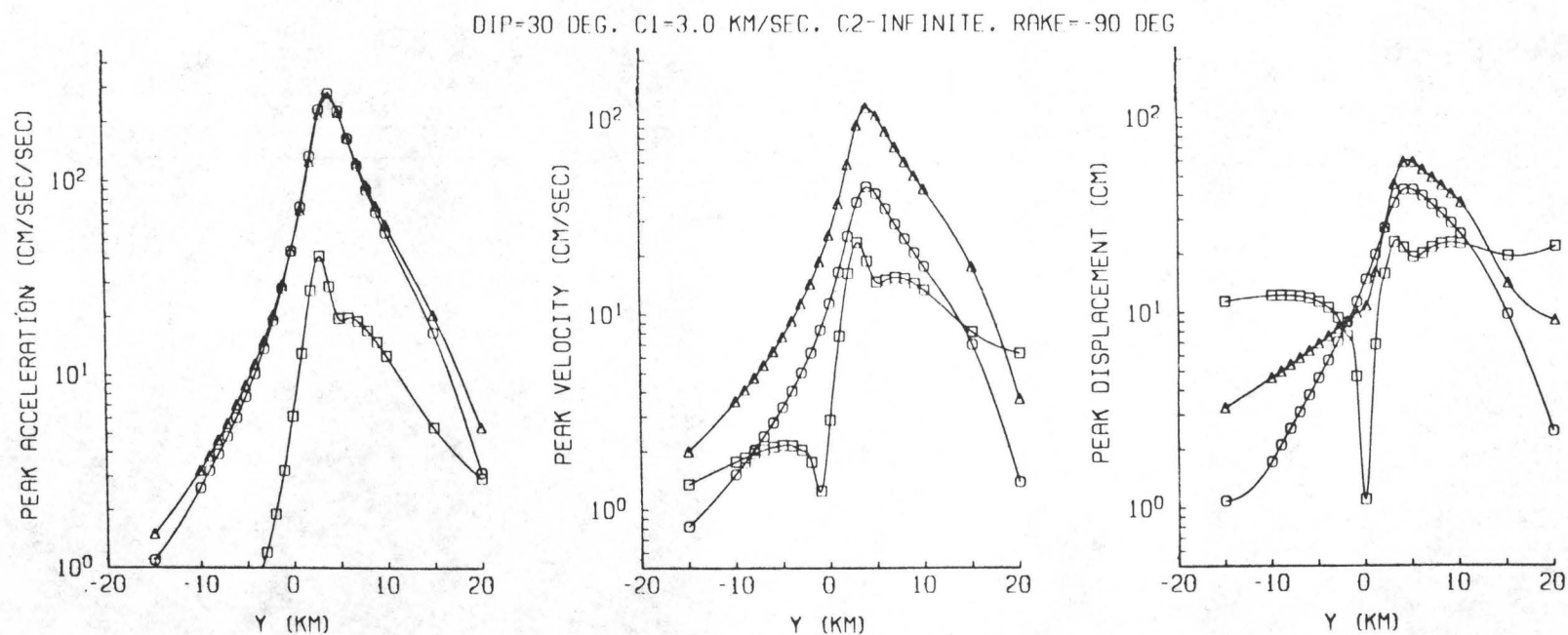
Figure 12. Peaks in acceleration, velocity, and displacement along a profile of sites perpendicular to a thrust fault with dip 30°. The upper edge of the fault occurs at $y_u = 3.464$ km. Model parameters are dip 30°, $c_1 = 3.0$ km/sec, $c_2 = \infty$, $\Delta_o = 100$ cm, $z_u = 2.0$ km, $z_d = 10.0$ km. Symbols are circle $- U_x$, square $- U_y$, triangle $- U_z$. Symbols are plotted at each point where calculations were performed, curves are cubic spline interpolations between these points.
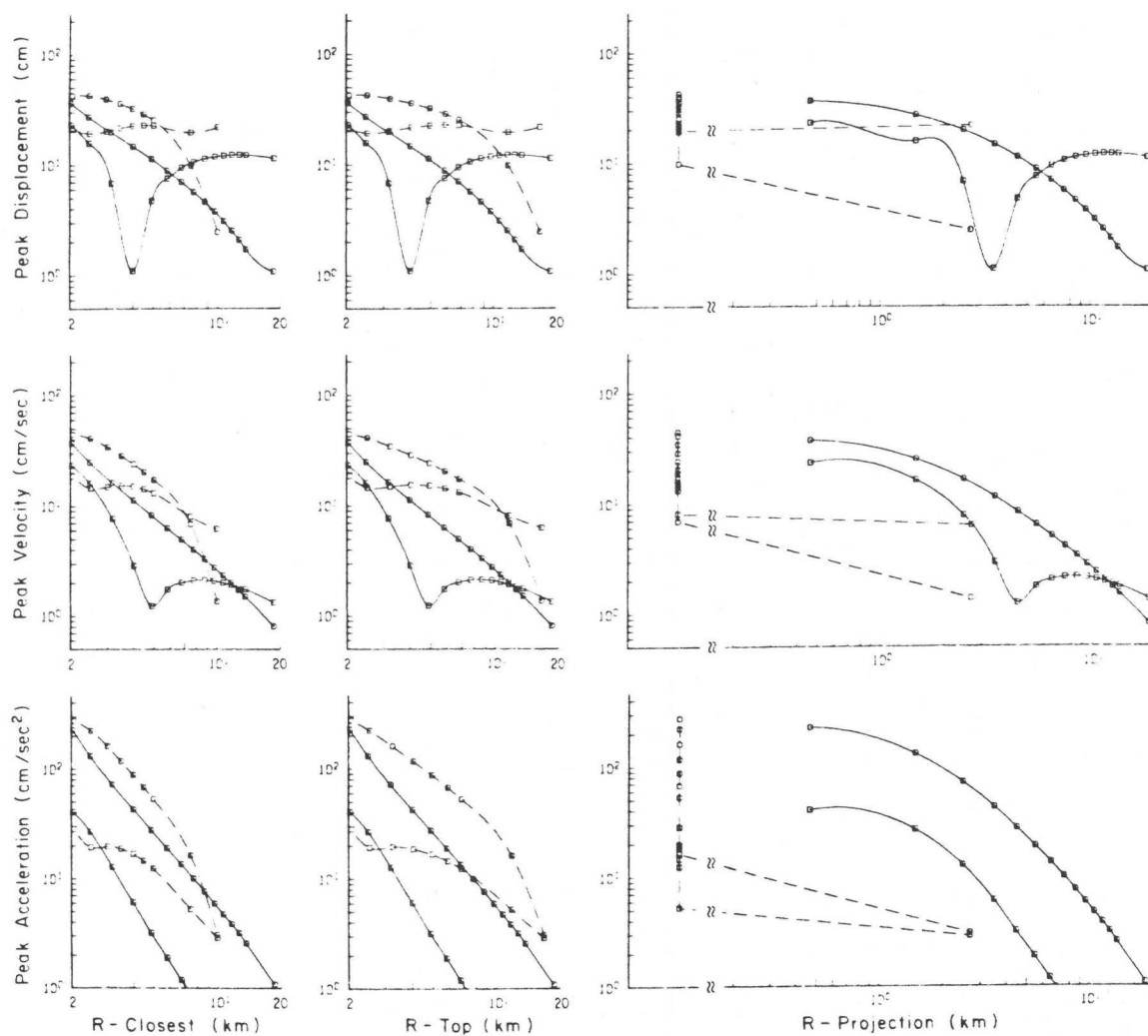
Figure 13. Peak amplitudes from Fig. 12 plotted against three measures of distance to the fault : R-Closest is the distance between the closest point on the fault rupture and the site. R-Top is the distance between the top edge of the fault rupture and the site, and R-Projection is the distance between the site and the nearest surface location of a vertical projection of the fault. Dashed lines connect points with $y - u_u > 0$ (on the upthrust block) and solid lines connect points with $y - y_u < 0$. Circles indicate peak values of the u_x component, and squares indicate peak values of the u_y component; the vertical component is not plotted. The vertical line of points on the attenuation curves plotted against R-Projection are all from sites above the fault plane (R-Projection $= 0$), and have been plotted to the left of a broken scale.

561

UPPER BOUNDS ON NEAR-SOURCE PEAK GROUND MOTION
BASED ON A MODEL OF INHOMOGENEOUS FAULTING
By
A. McGarr

ABSTRACT

Two independent arguments indicate an upper bound of about 10 for the ratio r_o/r_i in the expressions for peak velocity $\underline{v}$ and peak acceleration $\underline{a}$ at close hypocentral distances R: $\underline{v}=(\beta\Delta\tau r_o/\mu R)(0.10r_o/r_i+0.15)$ and $\underline{a}=(\Delta\tau/\rho R)[0.30(r_o/r_i^2+0.45]$, where r_i is the radius of the most heavily loaded asperity that fails within an earthquake source region of radius r_o, $\Delta\tau$ is the stress drop, β is the shear wave velocity, μ is the modulus of rigidity, and ρ is the density; these relationships are for ground motion recorded in a whole-space. First, a recently-reported data set was augmented by observations for six earthquakes in the magnitude range $4 \leq M_L \leq 6.6$, for which ground motion was recorded at a minimum of five sites at hypocentral distances of the order of 10 km; the new events include the 1979 Coyote Lake and 1979 Imperial Valley shocks. The entire data set of 22 events, spanning a range in seismic moment from 5×10^{16} to over 10^{26} dyne-cm, is consistent both with the bound $r_o/r_i < 10$ and with the previous conclusion that this ratio does not depend systematically on earthquake size. Second, a theoretical argument, using the result of Savage and Wood that the apparent stress acting on the earthquake fault plane is less than half of the stress drop, is made to the effect that $r_o/r_i < 10$. In addition, absolute limits, independent of earthquake size, for peak acceleration are related to the state of stress in the crust; for an extensional state of stress $\underline{a} \leq 0.40g$ and for the other two stress states $\underline{a} \leq 1.99g$, where $\underline{a}$ now represents the maximum horizontal acceleration as recorded at the surface directly above the seismic source.

INTRODUCTION

McGarr (1981) described a model of inhomogeneous faulting and used it as a basis for the analysis of peak ground motion for a suite of mine tremors and earthquakes with seismic moments ranging from 5×10^{16} to over 10^{26} dyne-cm. Briefly, the model involves an annular faulted region of outer

radius r_o surrounding an unfaulted "ligament" or "asperity" of radius r_i. The faulting of the annulus is presumably the result either of preceding earthquakes or aseismic creep. An earthquake occurs when the central ligament fails under the influence of loading that depends both on the level of ambient shear stress above the frictional stress resisting fault slip and the ratio of the outer and inner radii of the pre-faulted annulus, r_o and r_i, respectively. The peak velocity $\underline{v}$ and acceleration $\underline{a}$ resulting from such a model are given by

$$\underline{v} = \frac{\beta \Delta \tau r_o}{\mu R}(0.10 r_o/r_i + 0.15) \tag{1}$$

and

$$\underline{a} = \frac{\Delta \tau}{\rho R}[0.30(r_o/r_i)^2 + 0.45] \tag{2}$$

where β is the shear wave velocity, $\Delta \tau$ is the overall stress drop, μ is the modulus of rigidity, R is the hypocentral distance, and ρ is the density. Here $\mu = 3 \times 10"$ dynes/cm^2, $\rho = 2.7$gm/cm^3 and $\beta = 3.5$km/sec unless indicated otherwise and a radiation factor of 0.57 is assumed. Furthermore, it should be noted that (1) and (2) are appropriate for ground motion as recorded in a whole-space rather than on a free surface. In this analysis, the effect of the free surface is assumed to be a doubling of the horizontal components of S-wave motion. The terms in the parentheses of (1) and (2) involving ratios of r_o/r_i correspond to the high-frequency ground motion associated with the failure of the central asperity, and the other terms indicate relatively low-frequency motion due to the broad scale readjustment to a new state of equilibrium over the entire faulted region of radius r_o.

In practice, $\Delta \tau$ and r_o are estimated using standard techniques (e.g., Brune, 1970, 1971; Hanks and Wyss, 1972) and then observations of the peak ground motion can be used to determine the ratio r_o/r_i and, therefore, r_i. In addition, r_i can be estimated from (McGarr, 1981)

$$r_i = 3\beta \underline{v}_i/\underline{a}_i \tag{3}$$

where $\underline{v}_i$ and $\underline{a}_i$ represent the high-frequency contributions to the peak

ground motion due to the failure of the asperity. Thus, we have three independent means of determining the radius of the asperity. Once r_o/r_i is determined, additional variables associated with the inhomogeneous failure can be calculated. Specifically, the stress drop of the small scale asperity failure is given by

$$\Delta\tau_i = \Delta\tau(r_o/r_i)^2 f(r_i/r_o) \tag{4}$$

The small-scale displacement is

$$D_i = \frac{1.52\Delta\tau}{\pi\mu}(r_o^2/r_i)f(r_i/r_o) \tag{5}$$

and the seismic moment of the asperity failure is

$$M_o^i = 1.52\Delta\tau\, r_o^2 r_i f(r_i/r_o) \tag{6}$$

where $f(r_i/r_o)$ is a power series that has a value very close to 1 for $0 \le r_i/r_o \le \frac{1}{2}$; accordingly f is taken as 1 here.

After analyzing 16 seismic events having moments ranging over nearly 10 orders of magnitude, McGarr (1981) concluded from the observations that the ratio r_o/r_i is normally within the range of 1 to 10 and shows no systematic variation with seismic moment Mo. It is important to know whether r_o/r_i is always within this range because, if so, equations (1) and (2) imply that peak velocity and acceleration can be predicted to be within reasonably narrow limits, depending on the seismic source parameters $\Delta\tau$ and r_o. This is especially true for peak velocity because from (1) we see that the dimensionless quantity $R\underline{v}\mu/(\Delta\tau\beta r_o)$ is expected to have a value between 0.15 and 1.

In this study, the question of upper bounds on r_o/r_i has been investigated in two ways. First, the existing set of observations (Table 1 of McGarr, 1981) was augmented by analyzing peak ground motion from six earthquakes in the magnitude range $4 \le M_L \le 6.6$. The six new events are of particular importance because their ground motion was recorded at a minimum of five sites at epicentral distances of roughly 10 km or less. Thus, the ground motion parameters can be determined with considerably more confidence than for

single-site observations, which formed most of the data set of McGarr (1981).
Second, a theoretical argument based on the result of Savage and Wood (1971)
that the apparent stress acting on the earthquake fault plane is less than
half of the stress drop indicates that $r_o/r_i < 10$.

In addition two other analyses are presented that bear on the question of
upper limits to peak ground motion. First, an attempt is made to relate the
results of the inhomogeneous faulting model to those of models involving
homogeneous stress drops, but for which the rupture front propagates
coherently over the fault plane at a given velocity. The results of this
investigation, which involved the analysis of ground motion synthesized for a
theoretical earthquake by Archuleta and Hartzell (1981), suggests an
equivalence between the ratio r_o/r_i and rupture velocity with high rupture
velocities corresponding to high values of r_o/r_i. Second, absolute limits
on the level of peak acceleration at close hypocentral distances are related
to the strength of the crust (e.g. Hanks and Johnson, 1976) which, in turn, is
a function of the state of stress.

ANALYSIS OF PEAK GROUND MOTION

The six earthquakes for which peak ground motion was analyzed are listed
in Table 1 along with parameters relating to the seismic source, ground
motion, and inhomogeneous faulting. These events were chosen for study
primarily on the basis of their ground motion having been recorded at many
sites at hypocentral distances typically of the order of 10 km. The analysis
of these events is now discussed in the order of listing in Table 1.
Imperial Valley earthquake. Occasionally, the greatest difficulty in applying
equations (1) and (2) to the interpretation of peak ground motion involves
uncertainty in the location of the most heavily loaded asperity; that is, the
distance R to the asperity is poorly established. Although in most cases the
source dimension of the earthquake is sufficiently small, relative to the
source-to-site distance, that the asperity can be assumed to coincide with the
located hypocenter with little risk, such an approach was not feasible for the
Imperial Valley earthquake of October 15, 1979. For this event the source
region was of the order of 30 km in extent, and the most significant records
of ground motion were from sites within the zone of aftershocks. Because it
was necessary to know the location of the most significant asperity that

TABLE 1. Source Parameters and Peak Ground Motion Variables

EVENT	M_L	M_0	r_0	D_0	$\Delta\tau$	$R\dot{v}$	ρRa	$(r_0/r_i)_v$	$(r_0/r_i)_a$	r_i	$(r_0/r_i)_{v/a}$	τ_{af}	$\Delta\tau_i$	D_i
		dyne-cm	km	cm	bars	cm^2/sec	bars			km		bars	bars	cm
Imperial Valley, 1979	6.6	7x10^{25}	9.8	77	33	(4.62±0.95)x10^7	762±213	12.2	8.8	1.81±0.47	5.4	119	642	282
Coyote Lake, 1979	5.9	6x10^{24}	4.5	32	29	(1.60±0.57)x10^7	358±208	10.5	8.5	0.77±0.25	5.8	112	650	123
Oroville event B Aug. 3, 0247	4.1	3.6x10^{22}	0.675	8.4	51	(1.52±0.74)x10^6	136±66	3.8	3.0	0.331±0.055	2.0	68	136	11.1
Oroville event T, Sept. 26, 0231	4.0	2.2x10^{22}	0.525	8.6	67	(1.30±0.29)x10^6	171±49	3.2	2.9	0.230±0.024	2.3	103	236	13.0
Oroville event U, Sept. 27, 2234	4.6	8.8x10^{22}	0.545	31.4	238	(3.07±1.48)x10^6	306±103	2.0	2.1	0.263±0.065	2.1	333	700	43.9
Oroville event K, Aug. 8, 0700	4.9	1.8x10^{23}	0.811	29.0	148	(1.80±0.69)x10^6	187±78	1.3	2.0	0.306±0.117	2.6	261	693	51.3
Archuleta-Hartzell, $v_r = 0.75\beta$	6.4	4.5x10^{25}	5.0	190	100	(1.77±0.37)x10^7	487±131	3.6	4.0	1.10±0.08	4.55	303	1380	367
Archuleta-Hartzell, $v_r = 0.90\beta$	6.4	4.5x10^{25}	5.0	190	100	(2.77±1.36)x10^7	834±636	5.6	5.4	1.03±0.16	4.85	323	1568	391

failed during the earthquake, the analysis described here relies heavily on the results of Hartzell and Helmberger (1981) who concluded, on the basis of strong motion modeling, that the region of most concentrated slip was located about 18 km northwest of the hypocenter, at a depth of 6.5 km. S-wave radiation attributed to this localized concentration of slip was analyzed at the eight accelerograph sites within ~ 10 km of the "asperity," and R in equations (1) and (2) was estimated accordingly. Peak velocity $\underline{v}$ and acceleration $\underline{a}$ for the phases having the appropriate timing and polarity to be associated with the asperity were measured from the processed accelerograms of Brady et al. (1980a). The results are listed in Table 1 and illustrated in Figures 1 and 2. The seismic moment Mo was determined by Kanamori and Regan (1981) from very long period Rayleigh waves, and the source radius was chosen to yield a total area of 300 km^2 based approximately on the distribution of significant fault slip deduced by Hartzell and Helmberger (1981). The stress drop of 33 bars was calculated from (Brune, 1970)

$$\Delta\tau = \tfrac{7}{16} M_o / r_o^3 \tag{7}$$

We see in Table 1 that both $R\underline{v}$ and $\rho R\underline{a}$ have reasonably low uncertainties as measured at the eight sites. In fact, the estimates of dimensionless peak velocity $(R\underline{v}\mu)/\Delta\tau\beta r_o)$ and peak acceleration $\rho R\underline{a}/\Delta\tau$ are limited more by the uncertainty in r_o than by the precision of the estimate of the peak ground motion. The ratios r_o/r_i estimated from equations (1) and (2) are each quite high, especially that inferred from the peak velocities. Undoubtedly, the best determination of the asperity dimension is that based on equation (3), which is independent of such effects as radiation pattern and directivity, inasmuch as these sources of uncertainty cancel when taking the ratio $\underline{v}/\underline{a}$. The inferred asperity radius of 1.8 km yields a ratio r_o/r_i of 5.4, which is then used to calculate the remaining entries in Table 1 relating to the inhomogeneous aspect of the failure.

The ambient faulting stress, τ_{af}, is the difference between the regional shear stress applied to the fault plane and the frictional stress that resists sliding across the fault zone surrounding the asperity. A value of 119 bars Table 1 for the Imperial shock is well within the range of estimates listed in Table 1 of McGarr (1981). $\Delta\tau_i$, the localized stress
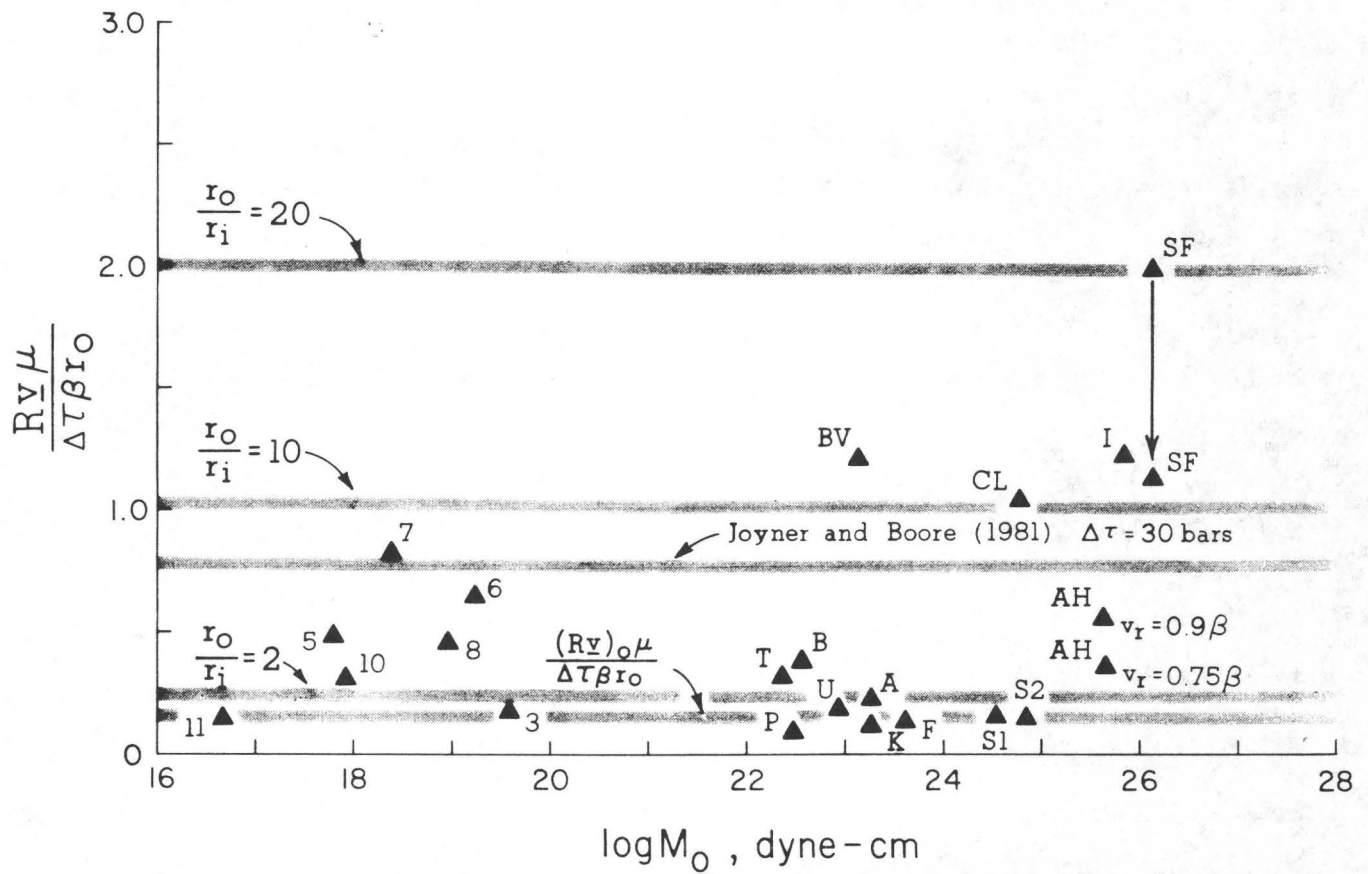
Figure 1. Dimensionless peak velocity parameter as a function of Mo. The numbered data on the left correspond to mine tremors (McGarr et al., 1981). The points denoted P, A, F, K. V, B, and T indicate Oroville aftershocks (Fletcher et al., 1982; Fletcher et al., 1980; Boatwright, 1981). The codes S1, S2, BV, CL, and SF are for the Shumagin Islands 0153, Shumagin Islands 0356 (House and Boatwright, 1980), Stone Canyon (Johnson and McEvilly, 1974; Brady and Perez, 1978), Coyote Lake (Brady et al., 1980b), and San Fernando (Heaton and Helmberger, 1979; Hanks, 1974) earthquakes, respectively. A-H refers to the synthetic event analyzed by Archuleta and Hartzell (1981).
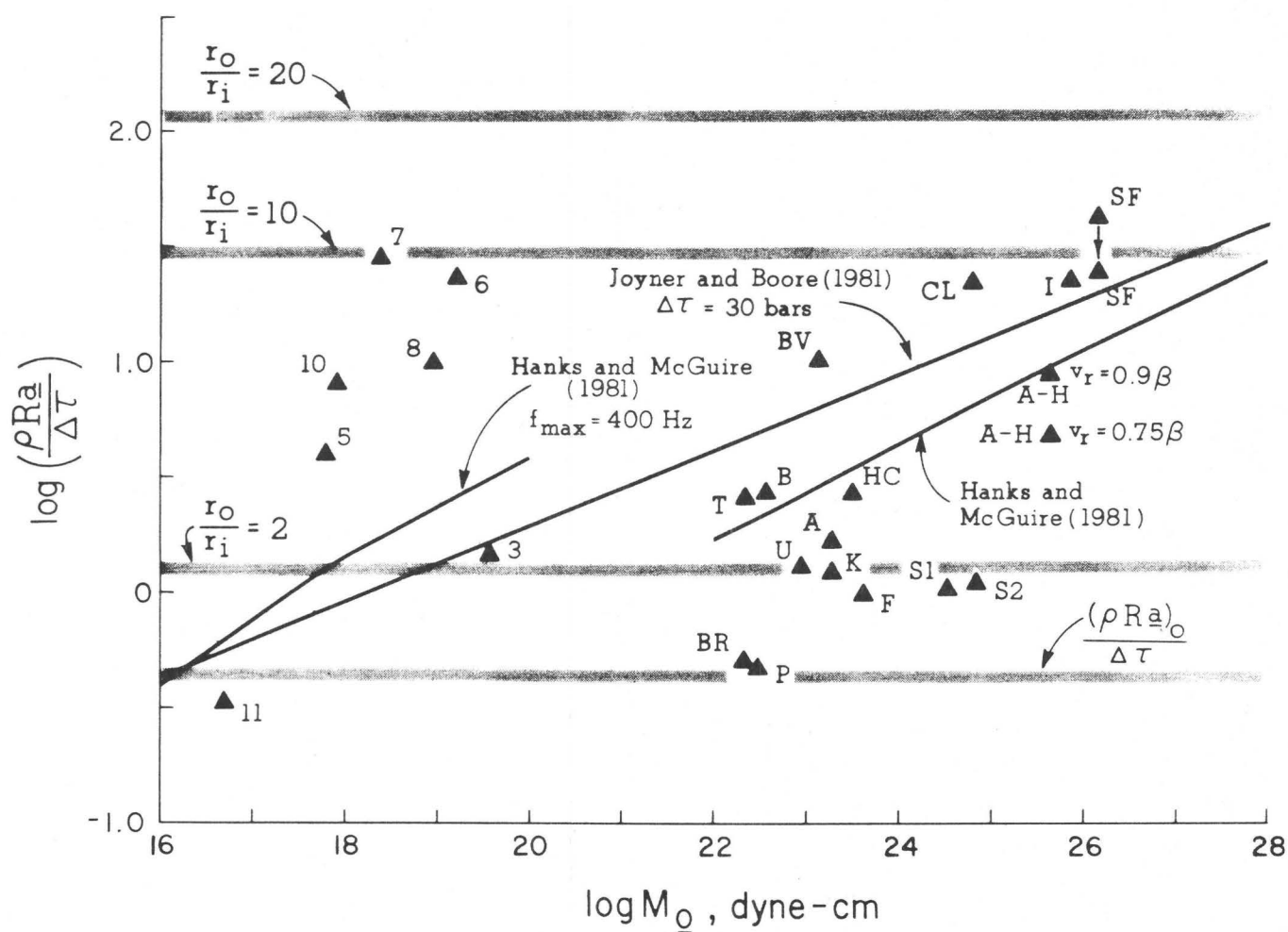
Figure 2   Dimensionless peak acceleration parameter as a function of Mo. The symbol codes are the same as for Figure 1 with the additional codes BR and HC denoting the Brawley (Hartzell and Brune, 1977; Table 1 of McGarr, 1981) and Horse Canyon (Hartzell and Brune, 1979), respectively.

drop associated with the asperity failure, is fairly high at 642 bars but certainly nowhere near the upper limit of the other determinations of this variable (Table 1, McGarr, 1981). The amount of fault slip across the asperity D_i is perhaps the most interesting variable in that the estimate of 282 cm inferred here agrees well with the peak value of about 250 cm at the asperity calculated by Hartzell and Helmberger. In this regard, note that the estimate of r_i of 1.8 km also coincides well with the dimension of the region of concentrated slip seen in Figure 12 (Model 9WM) of Hartzell and Helmberger (1981).

Finally, the seismic moment of the asperity failure, which is given by (McGarr, 1981)

$$M_0 \simeq 1.52 \Delta \tau r_0^2 r_i \qquad (8)$$

is about 8.7×10^{24} dyne-cm, or roughly 12 per cent of the total moment of the earthquake.

Coyote Lake earthquake. The least certain aspect of the Coyote Lake earthquake involves the estimate of the source radios r_0. A source radius of 4.5 km was chosen so as to yield a circular fault plane of approximately the same average dimension as the presumed fault plane of the main shock. As defined by the aftershock distribution,, this fault plane is assumed to extend southeastward of the epicenter to where the Calaveras fault shows a substantial offset to the right (Lee et al., 1979; Reasenberg and Ellsworth, 1982). The value of $M_0 = 6 \times 10^{24}$ dyne-cm (Urhammer, 1980) yielded a stress drop of 29 bars (Table 1).

Although the estimate of r_0 is little more than a guess, the resulting source parameters are in good agreement with those determined by Liu and Helmberger (1981), using a completely independent approach; for example, they concluded that $\Delta \tau = 30$ bars. As will be seen, several inhomogeneous aspects of the Coyote Lake event determined here are also in good agreement with those deduced by Liu and Helmberger.

The peak ground motion parameters Rv and Ra were determined from the processed accelerograms from five sites (Brady et al., 1980b), Coyote Creek, nearly above the hypocenter, and four stations of the Gilroy array approximately 10 km to the southeast. The process of estimating Rv and Ra was

Figure 3   Horizontal velocity and acceleration following the Coyote Lake
earthquake of 6 August 1979. These records are adapted from Brady
et al. (1980b).

GILROY ARRAY NO. 6   SAN MARTIN – COYOTE CREEK

N40W ⟶   S50W ⟶   S20E ⟶   S70W ⟶

571
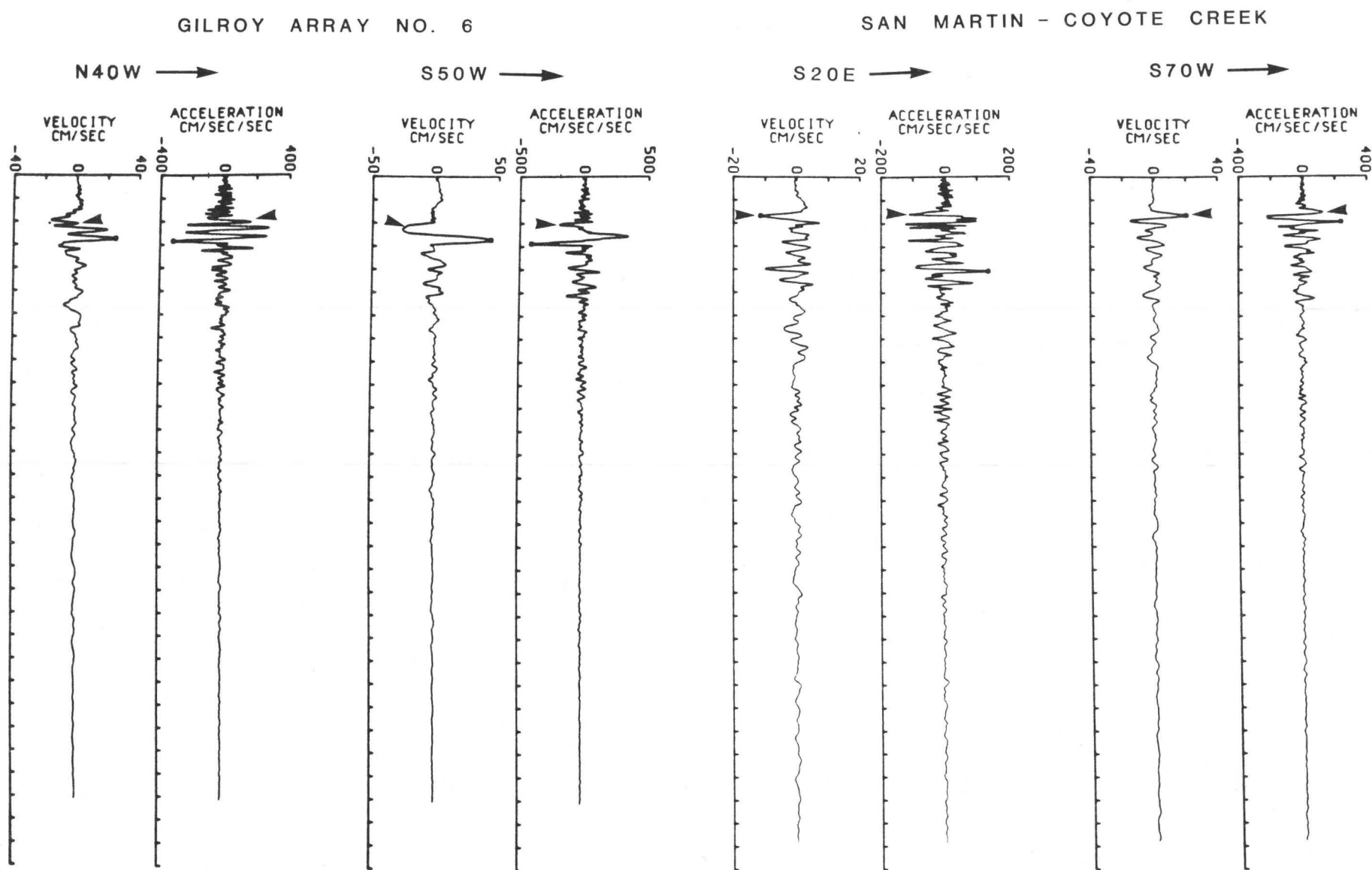
complicated by the recording of S wave radiation from more than one significant asperity. The most energetic of these sources, however, appears to coincide with the hypocenter (e.g. Liu and Helmberger, 1981) and so this hypocentral asperity is analyzed here. The measurement of $\underline{a}$ and $\underline{v}$ from the records of ground motion at the Coyote Creek site was straightforward because of the simplicity of the acceleration and velocity pulses here (Figure 3); presumably, S waves from the hypocentral asperity account for nearly all of the high amplitude ground motion within the first 2 seconds of the S wave arrival. As recorded at Gilroy 6, however, the strong ground motion is more complex and care must be taken to isolate the effect of radiation from the hypocentral asperity. Although the velocity pulse on the S50°W component appears simple, the initial downward motion (Figure 3) seems, in fact, to be the result of two separate pulses. This can be seen most easily on the N40°W component, which shows two upward pulses in velocity coinciding in time with the broader simple-appearing downward pulse on the S50°W component (Figure 3). The other stations of the Gilroy array show similar complexity. In all cases, the first-arriving pulses are associated with the hypocentral asperity as indicated by the arrows in Figure 3 showing where the measurements were made.

As indicated in Figure 3, $\underline{a}$ was, in all cases, measured from the peak in the accelerogram immediately preceding the peak in velocity even though this is not the true peak acceleration for any of the illustrated records. This measurement procedure was followed because of the need to isolate the effect of the hypocentral asperity. The theoretical justification for this procedure is that the source model employed here (McGarr, 1981) yields peak accelerations and velocities associated only with the leading edge of the displacement pulse. Other models (e.g. Madariaga, 1977) often result in peak ground motion corresponding to stopping phases.

As analyzed here (Table 1), the various measures of stress associated with the Coyote Lake event are remarkably similar to those of the Imperial Valley shock, whereas the dimensions and displacements are scaled down by a factor of about 2. The moment M_o^i associated with the hypocentral asperity is, from (8), about 6.9×10^{23}, which is 11 percent of the total moment; again this result is similar to that of the Imperial Valley shock.

Interestingly, the displacement of 123 cm associated with the failure of

the asperity (Table 1) agrees excellently with the corresponding value of 120 cm estimated by Liu and Helmberger (1981). Their peak stress drop for the hypocentral asperity of 137 bars, however, is substantially lower than that inferred using the present analysis.

Oroville aftershocks. The processing of the accelerograms and the determination of the source parameters of the four Oroville aftershocks listed in Table 1 are discussed by Fletcher et al. (1982) and Perez (1979). The peak ground motion parameters were measured at a minimum of seven sites and so the listed standard deviations are well-determined. We see in Table 1 that the three estimates of r_o/r_i for each of the aftershocks are generally in good agreement and that nearly all of these ratios fall in the interval between 2 to 3. These ratios are consistent with those for three other Oroville aftershocks studied by McGarr (1981, Table 1) although for the latter set the ratios tend to be slightly lower. It can easily be demonstrated that for $r_o/r_i \leq 6$ none of the ratios for any of the seven aftershocks is suppressed artificially due to the limited recording bandwidth, which extends to 25 Hz. Thus, for the Oroville aftershock zone r_o/r_i in general is significantly lower than for either the Imperial Valley or the Coyote Lake shocks.

RUPTURE PROPAGATION

Needless to say, there is more than one way to explain the large observed range of peak ground motion parameters for earthquakes with a given set of source parameters Mo, $\Delta\tau$, and r_o. In addition to models involving inhomogeneous stress drops, such as that employed here, faults with homogeneous stress drops but whose failure involves coherent rupture propagation result in ground motion parameters, a, and v, which depend on the rupture velocity, as well as the seismic source parameters.

To acquire some indication of the correspondence between rupture velocity and the ratio r_o/r_i, which plays the key role in the asperity model, the peak ground motion synthesized by Archuleta and Hartzell for a model involving rupture propagation over a circular fault is analyzed using equations (1) and (2). The Archuleta-Hartzell model involves coherent rupture propagation at velocities of either 0.75β or 0.9β over a fault of radius 5 km under the influence of an effective stress of 100 bars; that is, the static stress drop $\Delta\tau = 100$ bars. Ground motion was computed for sites in four different

directions from the fault at a constant hypocentral distance R of 9.22 km, and the numerical computations were over a frequency band extending from 0 to 5 Hz.

The results of applying equations (1) through (6) to the ground motion resulting from the Archuleta-Hartzell model are listed in Table 1 and illustrated in Figures 1 and 2. (Note that for this model $\beta=3.0$ km/sec and $\rho=3.3$ gm/cm^3.) We see that for a rupture velocity $v_r=0.75\beta$ the corresponding ratio r_o/r_i is about 4, whereas for $v_r=0.9\beta$, $r_o/r_i \simeq 5$.

Archuleta and Hartzell (1981) noted that all of their ground motion results scale with the effective stress or $\Delta\tau$. The representation of their results here indicates, in addition, how to scale their results for different M_o or r_o.

Finally, it is perhaps worth mentioning that the analysis of the Archuleta-Hartzell ground motion in terms of the inhomogeneous faulting model provides a convenient means of establishing whether their bandwidth of 0 to 5 Hz was adequate for calculating the accelerations. Consider the corner frequency associated with the asperity failure of the event with a rupture velocity of 0.9β. According to Brune (1970)

$$ f_i = \frac{2.34\beta}{2\pi r_i} $$

and for $r_i=1.03$ km (Table 1) $f_i \simeq 1.3$ Hz. Thus, the band extending to 5 Hz was entirely adequate and the peak accelerations were not suppressed artificially.

The analysis of the Archuleta-Hartzell (1981) model in terms of equations (1) and (2) also serves to emphasize the nonuniqueness of interpreting ground motion data using a specific type of source. It appears, as indicated before by McGarr (1981), that other types of evidence are necessary for determining whether it is more appropriate to interpret the data on the basis of rupture velocity or scale of inhomogeneity. To the examples cited by McGarr (1981) of events involving inhomogeneous stress drops, as well as the Imperial Valley shock (Hartzell and Helmberger, 1981), the case of the 1975 Pocatello Valley earthquake, Idaho, can be added. Bache et al. (1980) interpreted the long

period and short period seismograms at teleseismic distances from this shock and determined, in the present terminology, that $r_o \approx 12$ km from the long period data, and $r_i \approx 2.6$ km on the basis of the short period records. This result can be used to estimate the seismic moment of the asperity failure, and these estimates can then be compared to the corresponding results directly determined by Bache et al. The long period moment for the Pocatello Valley event was estimated to be 2.2×10^{25} dyne-cm. For $r_o/r_i = 4.6$, equation (6) yields $Mo = 3.2 \times 10^{24}$ dyne-cm. Thus, the ratio Mo/M_o^i is about 6.9, which is in the middle of the range of 5 to 10 determined by Bache et al. (1980). In any case, the Pocatello Valley event clearly required an inhomogeneous stress-drop interpretation in spite of the fact that Bache et al. assumed, in their calculation of synthetic seismograms, coherent rupture propagation over each of the fault planes.

UPPER LIMIT TO r_o/r_i

Figures 1 and 2 have been adapted from Figures 3 and 4, respectively, of McGarr (1981) and the data set presented has been augmented by the peak ground motion parameters listed in Table 1. The points plotted in these two figures are nearly all consistent with an upper bound for r_o/r_i of about 10.

The only substantial exceptions are the dimensionless peak velocity and peak acceleration for the San Fernando earthquake. These values were measured at only a single site, Pacoima Dam, which was essentially coplanar with the initial faulting (e.g., Hanks, 1974). As discussed by McGarr (1981) a radiation factor of 1 rather than the factor of 0.57 assumed in equations (1) and (2) is more appropriate for this situation. Accordingly, the effect of this correction is indicated in Figures 1 and 2, and we see that both v and a for this event are then consistent with $r_o/r_i \approx 10$.

It turns out that the upper bound for r_o/r_i of about 10 suggested by the peak ground motion data is consistent with the theoretical upper bound that follows from the relationship developed by Savage and Wood (1971)

$$\sigma_a / \Delta\tau < \tfrac{1}{2} \tag{9}$$

where σ_a is the apparent mean shear stress causing the fault slip during the event.

According to Wyss and Brune (1968)

$$\sigma_a = \frac{\mu E}{M_o} \tag{10}$$

where E is the radiated seismic energy. Perret (1972) has shown that for equidirectional radiation the seismic energy radiated by the S waves is

$$E_s = 4\pi\rho\beta R^2 \int v^2 dt \tag{11}$$

where v is the ground velocity and the integration is performed over a suitable time window to include the entire phase. In the following analysis we assume that the P-wave energy is negligible compared to that of the S waves, an assumption in good accord with observations including those of Boatwright and Fletcher (1982) who found that the energy radiated in the S waves is more than a factor of 20 greater than that in the P waves. Specifically, (11) is used to calculate the total radiated energy E.

Equations (13) and (17) of McGarr (1981) imply

$$Rv(t) = \frac{0.57}{4\pi\rho\beta^3} Mo \frac{\omega^4 t^2}{3} (3-\omega t) e^{-\omega t} \tag{12}$$

where ω is the corner frequency of the S-wave displacement spectrum on the scale of either r_o or r_i. Thus, it is straightforward to integrate R^2v^2 to calculate E_s and therefore σ_a from (10) to obtain

$$\sigma_a(r) = 4.14 \times 10^{-2} Mo/r^3 \tag{13}$$

where r can be either r_o or r_i. It then follows that the apparent stresses that are proportional to the S wave energies radiated from the asperity and overall source radiation are, respectively

$$\sigma_a^i = 4.2 \times 10^{-2} \Delta\tau r_o/r_i$$

and
$$\tag{14}$$

$$\sigma_a^0 = 9.46 \times 10^{-2} \Delta\tau$$

For comparison, incidently, a similar analysis of the Brune (1970) source model yields $\sigma_a = 0.186\Delta\tau$ (Hartzell and Brune, 1977), which means that for a given stress drop $\Delta\tau$, the Brune model radiates about twice as much energy as that due to the large-scale stress relaxation in the present model.

From (9) and (14)

$$\sigma_a/\Delta\tau = \frac{\sigma_a^i + \sigma_a^o}{\Delta\tau} = 4.14 \times 10^{-2}(r_0/r_i + 16/7) < \tfrac{1}{2}$$

and solving for r_0/r_i yields

$$r_0/r_i < 9.8 \tag{15}$$

Inclusion of the P-wave energy in the calculation of σ_a would result in only a slight reduction of the upper bound (e.g. Boatwright and Fletcher, 1982).

ABSOLUTE ACCELERATION BOUNDS

To determine an upper limit for <u>a</u> assume first that the radiation term is 1 in equation (2) rather than 0.57, as has been assumed up to now. Then if equation (4) is used to express equation (2) in terms of $\Delta\tau_i$, the peak acceleration recorded in a whole-space is

$$\underline{a} < 0.79\Delta\tau_i/\rho R \tag{16}$$

assuming that the term in (2) not involving r_0/r_i can be neglected. As noted before (McGarr, 1981), equation (16) is essentially equivalent to equation (3) of Hanks and Johnson (1976) relating the "dynamic shear-stress difference" $\tilde{\sigma}$ to the peak acceleration, assuming that $\Delta\tau_i$, the stress drop of the asperity has the same significance as $\tilde{\sigma}$. Hanks and Johnson suggested that $\tilde{\sigma}$, or $\Delta\tau_i$, might be limited by the strength of the crust in the hypocentral region with corresponding limits on the peak acceleration, according to equation (16), for example. A recent analysis of limits on the state of deviatoric stress imposed by the strength of the lithosphere by Brace and Kohlstedt (1980) provides the means of exploring the implications of the

577

conjecture put forth by Hanks and Johnson (1976) with regard to upper limits on peak ground acceleration.

Before investigating bounds on the depth dependence of $\Delta\tau_i$, equation (16) is converted into a form suited to the situation of acceleration recorded at a station on the surface of a half space directly above the most significant asperity that fails during an earthquake. In this case the ground motion due to the S wave radiated from the asperity at depth z is purely horizontal and the effect of the free surface is to double the amplitude of motion, so that

$$\underline{a} \text{ (upper bound)} < 1.58 \Delta\tau_i / \rho z \tag{17}$$

Now consider limits on $\Delta\tau_i$ as a function of depth. According to Brace and Kohlstedt (1980), if the crust contains fractures of all orientations then Byerlee's (1978) law of friction yields

$$\sigma_1 - P \approx 5(\sigma_3 - P) \tag{18}$$

for $\sigma_3 - P < 110$ MPa
where σ_1 is the maximum principal stress that can be sustained for a given minimum principal stress σ_3 and pore pressure P is taken as hydrostatic here. If either σ_1 or σ_3 is oriented vertically then its value can be taken as ρgz (e.g. McGarr and Gay, 1978) where g is gravity, and (18) can then be used to determine the other principal stress. The upper bound on the stress drop of the asperity is then given by

$$\Delta\tau_i < (\sigma_1 - \sigma_3) / 2 \tag{19}$$

In an extensional state of stress σ_1 is oriented vertically so that from (18) and (19)

$$\Delta\tau_i < 0.4(\rho - 1) gz = 6.7 (\text{MPa/km}) \ z \tag{20}$$

For a compressional state of stress σ_3 is oriented vertically yielding

$$\Delta\tau_i < 2(\rho-1)gz = 33.4(MPa/km)\ z \tag{21}$$

Equations (20) and (21) substituted into (17) yield for upper bounds on peak acceleration

Extensional stress state: $\underline{a}$(upper bound)$\leq$0.40g   (22)

Compressional stress state: $\underline{a}$(upper bound)$\leq$1.99g   (23)

If the state of stress is appropriate for the occurrence of strike-slip faulting it seems most realistic to presume that $\underline{a}$ has the same upper bound as for a compressional stress state (23) because the vertically oriented intermediate principal stress σ_2 can be arbitrarily close in magnitude to the minimum principal stress in such a regime; that is, the stress state for which $\sigma_1 >> \rho gz > \sigma_3$ would be associated with strike slip faulting.

The upper bounds given by (22) and (23) are clearly based on idealized assumptions and so some qualifications are necessary. First, a number of possible propagation and recording site effects have not been taken into account; this analysis is strictly appropriate only for recording on the surface of a homogeneous half space. Second, the pore pressure is assumed to be hydrostatic even though in some regions P=0 is more appropriate (e.g. McGarr et al., 1975); if P=0 then the upper bounds given by (22) and (23) increase by 59 per cent, for an assumed density of 2.7 gm/cm^3. Third, the strength of the crust as a function of depth undoubtedly shows some localized variation not accounted for in equations (20) and (21) due to variations either in the state of stress or in material properties. Of all the qualifications associated with (22) and (23), site effects seem most likely to lead to observed contradictions, especially for earthquakes occurring in extensional states of stress for which the upper bound on $\underline{a}$ of 0.4 g is very low.

Inequalities (22) and (23), even though based on somewhat idealized assumptions, appear to be reasonably realistic for several reasons. First, there are no counterexamples, to my knowledge, for (23), and only a small number for (22), most, or all, of which appear to be due to pronounced site effects (e.g. Seekins and Hanks, 1978; Fletcher et al., 1980). Second,

579

qualitative support for (22) and (23) is provided by the empirical study of Campbell (1981) who found that peak accelerations from reverse faulting events average about 28 percent higher than those from earthquakes on other types of faults; presumably an even greater difference would have been found had his study contrasted reverse and normal faulting shocks.

The most important implications of (22) and (23) are that absolute upper bounds on peak acceleration exist, at least in principle, independent of earthquake size and, all other factors being equal, earthquakes due to normal faulting are associated with much lower bounds on peak acceleration than events resulting from the other two distinct types of faulting.

DISCUSSION

It is of interest to compare the results of the recent studies of ground motion parameters by Joyner and Boore (1981) and Hanks and McGuire (1981) to the conclusions summarized in Figures 1 and 2. Joyner and Boore empirically derived the following expressions. For peak velocity

$\log \underline{v}$ = -5.90+0.326 log Mo-logr-0.00256r+0.17S+0.22P
where $r=(d^2+4.0^2)$,24.0$\leq$log Mo$\leq$27.2 and d is the minimum distance between the surface projection of the fault and the recording site. For peak acceleration

$\log \underline{a}$ = -3.68+0.166 log Mo-log r-0.00255r+0.26P
where $r=(d^2+7.3^2)$,23.5$\leq$log Mo$\leq$27.6

For purposes of plotting the above two relations in Figures 1 and 2 I have taken P=0, which implies a 50 percent probability that the resulting ground motion values would be exceeded, S=0, corresponding to hard rock sites, and r is taken to be R, the distance from the asperity to the recording site. Because the present analysis involves only small hypocentral distances the small linear terms in r above are neglected. For convenience, the coefficient of log M_0 in the expression for $\underline{v}$ has been changed very slightly to 0.333. Lastly, it should be noted that an average stress drop of 30 bars was assumed and the effect of the free surface has been taken into account.

The relationship of Joyner and Boore (1981) for peak velocity (Figure 1)

is equivalent to setting r_o/r_i (equation (1)) equal to 7.7. Their equation is in reasonable overall agreement with the data although it tends to predict somewhat higher velocities than are observed for $Mo < 10^{20}$ dyne-cm.

The Joyner and Boore relationship for peak acceleration, for which $\underline{a}$ scales as $Mo^{0.166}$, is also consistent with the data (Figure 2). The discrepancy between their formula and the peak motion for many of the earthquakes, including those with symbols T, B, U, A, K, F, BR, P, S1, and S2, is actually less than indicated in Figure 2 because an assumed stress drop of 30 bars is not appropriate for these high stress-drop events (Table 1 and Table 1 of McGarr, 1981). For the events with $Mo < 10^{20}$ dyne-cm, an assumed 30-bar stress drop is realistic, and the Joyner and Boore curve tends to be somewhat low although still within the bounds of the data.

According to Hanks and McGuire (1981)

$$\frac{\rho R \underline{a}}{\Delta \tau} = \frac{0.85(2\pi)^2}{106} \sqrt{\frac{f_{max}}{f_0}} \sqrt{2 \ln\left(\frac{2f_{max}}{f_0}\right)}$$

where f_{max} is the maximum recordable frequency and f_0 is the corner frequency of the seismic source spectrum (e.g. Brune 1970, 1971). This relationship is appropriate for the recording of a single horizontal component on the surface of a half space. For purposes of plotting the Hanks and McGuire formula in Figure 2 the factor of 0.85 is changed to 0.74 to simulate the recording of the total vector ground motion in a whole space. Furthermore, following Hanks and McGuire (1981) $\Delta \tau$ is taken as 100 bars for purposes of computing f_0. Since the present analysis is concerned only with ground motion recorded at minimal hypocentral distances, f_{max} is simply the high-frequency limit of the accelerograph. For the earthquakes with $Mo > 10^{22}$ dyne-cm, $f_{max} = 25Hz$ and for the mine tremors with $Mo \leq 10^{20}$ dyne-cm, $f_{max} = 400Hz$ (McGarr et al., 1981). The Hanks and McGuire (1981) curve shows similar scaling to that of Joyner and Boore (1981) and is also in correspondingly good overall agreement with the data (Figure 2).

The most important distinction between the present results and those of Joyner and Boore (1981) and Hanks and McGuire (1981) involves the scaling of peak acceleration with seismic moment. The observations and analysis summarized in Figure 2 indicate that $\underline{a}$ does not vary systematically with Mo whereas the results of the other two investigations indicate a scaling

according to Mo$^{0.166}$ or Mo$^{0.20}$. The results of this study (equations (2), (22), and (23)) are in accord, however, with those of Hanks and Johnson (1976) and Campbell (1981) who concluded that peak acceleration in the near field is independent of magnitude [or moment].

Both Joyner and Boore (1981) and Hanks and McGuire (1981) discussed problems associated with trying to extrapolate their curves to seismic moments in excess of those considered in their studies; in each study the authors concluded that such an extrapolation would be inadvisable. The analysis of this report leading to a theoretical bound on r_0/r_i yields an additional argument against the upward extrapolation of the Joyner–Boore and Hanks–McGuire curves. The Joyner–Boore and Hanks–McGuire relations violate the condition $r_0/r_i < 10$ for Mo in excess of 10^{27} and 10^{28} dyne-cm, respectively (Figure 2).

CONCLUSIONS

In view of the data illustrated in Figure 1 as well as the theoretical upper bound on r_0/r_i of about 10, it is clear that peak velocity at close hypocentral distances is quite predictable. From equation (1) the dimensionless peak velocity $(R\underline{v}\mu)/(\Delta\tau\beta r_0)$ ranges from 0.15 to 1, and so if R, $\Delta\tau$, and r_0 can be specified, then the peak velocity falls within narrow limits. Because the implied scaling of $\underline{v}$ according to Mo$^{1/3}$ holds over nearly 10 orders of magnitude in seismic moment (Figure 1), it seems likely that equation (1) would remain valid beyond the range of the data, in particular, for events with moments in excess of 2×10^{26} dyne-cm.

Peak acceleration $\underline{a}$ is in one sense less predictable and in another sense more predictable than peak velocity. Because $\underline{a}$ is proportional to $(r_0/r_i)^2$ (equation (2)) the dimensionless peak acceleration $\rho R\underline{a}/\Delta\tau$ shows a much broader variation than the dimensionless peak velocity. With an upper limit of 10 for r_0/r_i, $\rho R\underline{a}/\Delta$ can vary from 0.45 to 30.

Peak acceleration is, however, more predictable than peak velocity with regard to absolute upper bounds, independent of earthquake size. Rather than varying systematically with earthquake size the upper bound on peak acceleration is proportional to the strength of the crust, which, in turn, depends on the state of stress. For extensional states of stress the upper bound is quite low at 0.4 g whereas for other stress states peak acceleration

is limited to 1.99 g. Clearly, this factor of five difference in peak acceleration limits means that the state of stress must be taken into account in the prediction of strong ground motion at a given locale.

The analysis of the coherent rupture propagation models of Archuleta and Hartzell (1981) tends to suggest that the primary conclusion of this report, that peak ground motion is limited according to equations (1) and (2) in conjunction with (15), is to some extent independent of the specific model of inhomogeneous faulting considered here and by McGarr (1981). Because rupture velocities exceeding β are implausible and as a rupture velocity as high as 0.9β is equivalent to $r_o/r_i \approx 5$ (Figures 1 and 2, Table 1) it seems likely that upper bounds to ground motion parameters based on models of coherent rupture propagation will correspond to $r_o/r_i \approx 10$, or less.

ACKNOWLEDGMENTS

I thank T. C. Hanks and J. Boatwright for their help in reviewing this manuscript.

REFERENCES

Archuleta, R. J. and S. H. Hartzell (1981). Effects of fault finiteness on near-source ground motion, Bull. Seism. Soc. Am. 71, 939–957.

Bache, T. C., D. G. Lambert, and T. G. Barker (1980). A source model for the March 28, 1975, Pocatello Valley earthquake from time-domain modeling of teleseismic P waves, Bull. Seism. Soc. Am. 70, 405–418.

Boatwright, J. (1981). Quasi-dynamic models of simple earthquakes: A Application to an aftershock of the 1975 Oroville, California, earthquake, Bull. Seism. Soc. Am. 71, 69–94.

Boatwright, J. and J. B. Fletcher (1982). Partition of radiated energy between P waves and S waves, paper in preparation.

Brace, W. F. and D. L. Kohlstedt (1980). Limits on lithospheric stress imposed by laboratory experiments, J. Geophys. Res. 85, 6248–6252.

Brady, A. G. and V. Perez (1978). Seismic engineering data report, 1972 records, strong motion earthquake accelerograms, U.S. Geological Survey Open-File Report 78-941.

Brady, A. G., V. Perez, and P. N. Mork (1980a). Seismic Engineering Data
    Report, The Imperial Valley earthquake, October 15, 1979. Digitization
    and processing of accelerograph records, U.S. Geological Survey Open-File
    Report 80-703.

Brady, A. G., P. N. Mork, and V. Perez (1980b). Processed data from the
    Gilroy array and Coyote Creek records, U.S. Geological Survey Open-File
    Report 81-42.

Brune, J. N. (1970). Tectonic stress and the spectra of seismic shear waves,
    J. Geophys. Res. 75, 4997-5009. (1971. Correction, J. Geophys. Res. 76,
    5002.)

Byerlee, J. D. (1978). Friction of Rocks, Pure Appl. Geophys. 116, 615-626.

Campbell, K. W. (1981). Near-source attenuation of peak horizontal
    acceleration, Bull. Seism. Soc. Am. 71, 2039-2070.

Fletcher, J. B., A. G. Brady, and T. C. Hanks (1980). Strong motion
    accelerograms of the Oroville, California, aftershocks: Data processing
    and the aftershocks of 0350 August 6, 1975, Bull. Seism. Soc. Am. 70,
    243-267.

Fletcher, J. B., J. Boatwright, T. C. Hanks, and A. McGarr (1982). Source
    parameters of the aftershocks of the 1975 Oroville, California,
    earthquake, paper in preparation.

Hanks, T. C. (1974). The faulting mechanism of the San Fernando earthquake,
    J. Geophys. Res. 79, 1215-1229.

Hanks, T. C. and M. Wyss (1972). The use of body-wave spectra in the
    determination of seismic-source parameters, Bull. Seism. Soc. Am. 62,
    561-589.

Hanks, T. C. and D. A. Johnson (1976). Geophysical assessment of peak
    accelerations, Bull. Seism. Soc. Am. 66, 959-968.

Hanks, T. C. and R. K. McGuire (1981). The character of high-frequency strong
    ground motion, Bull. Seism. Soc. Am. 71, 2071-2095.

Hartzell, S. H. and J. N. Brune (1977). Source parameters for the January
    1975 Brawley-Imperial Valley earthquake swarm, Pure Appl. Geophys. 115,
    333-355.

Hartzell, S. H. and J. N. Brune (1979). The Horse Canyon earthquake of
    August 2, 1975--Two stage stress-release process in a strike-slip
    earthquake, Bull. Seism. Soc. Am. 69, 1161-1173.

Hartzell, S. H. and D. V. Helmberger (1981). Strong motion modeling of
    Imperial Valley earthquake of 1979, submitted to the Bull. Seism. Soc. Am.

Heaton, T. H. and D. V. Helmberger (1979). Generalized ray models of the San
    Fernando earthquake, Bull. Seism. Soc. Am. 69, 1311-1341.

House, L. and J. Boatwright (1980). Investigation of two high stress drop
    earthquakes in the Shumagin seismic gap, Alaska, J. Geophys. Res. 85,
    7151-7165.

Johnson, L. R. and T. V. McEvilly (1974). Near-field observations and source
    parameters of central California earthquakes, Bull. Seism. Soc. Am. 64,
    1855-1886.

Joyner, W. B. and D. M. Boore (1981). Peak horizontal acceleration and
    velocity from strong-motion records including records from the 1979
    Imperial Valley, California, earthquake, Bull. Seism. Soc. Am. 71,
    2011-2038.

Kanamori, H. and J. Regan (1981). Long-period surface waves generated by the
    Imperial Valley earthquake of 1979, U.S. Geological Survey Open-File
    Report, Menlo Park, California.

Lee, W. H. K., D. G. Herd, V. Cagnetti, W. H. Bakun, and A. Rapport (1979).
    A preliminary study of the Coyote Lake earthquake of August 6, 1979, and
    its major aftershocks, preprint.

Liu, H.-L. and D. V. Helmberger (1981). Near source ground motion of the
    August 6, 1979, Coyote-Lake, California, earthquake, EOS Trans. AGU 62,
    972-973 (abstract).

Madariaga, R. (1977). High-frequency radiation from crack (stress drop)
    models of earthquake faulting, Geophys. J. R. Astr. Soc. 51, 625-651.

McGarr, A. (1981). Analysis of peak ground motion in terms of a model of
    inhomogeneous faulting, J. Geophys. Res. 86, 3901-3912.

McGarr, A. and N. C. Gay (1978). State of stress in the earth's crust,
    Annu. Rev. Earth Planet. Sci. 6, 405-436.

McGarr, A., S. M. Spottiswoode, and N. C. Gay (1975). Relationship of mine
    tremors to induced stresses and to rock properties in the focal region,
    Bull. Seism. Soc. Am. 65, 981-993.

McGarr, A., R. W. E. Green, and S. M. Spottiswoode (1981). Strong ground
    motion of mine tremors: Some implications for near-source ground motion
    parameters, Bull. Seism. Soc. Am. 71, 295-319.

Perez, V. (1979). <u>U.S. Geological Survey Tapes of Oroville Aftershock Uncorrected and Corrected Data</u>, available from E.D.I.S., NOAA, Boulder, Colorado.

Perret, W. R. (1972). Seismic source energies of underground nuclear explosions, <u>Bull. Seism. Soc. Am.</u> <u>62</u>, 763-774.

Reasenberg, P. and W. L. Ellsworth (1982). Aftershocks of the Coyote Lake, California, earthquake of August 6, 1979: a detailed study, submitted to <u>J. Geophys. Res.</u>

Savage, J. C. and M. D. Wood (1971). The relationship between apparent stress and stress drop, <u>Bull. Seism. Soc. Am.</u> <u>61</u>, 1381-1388.

Seekins, L. C. and T. C. Hanks (1978). Strong motion accelerograms of the Oroville aftershocks and peak acceleration data, <u>Bull. Seism. Soc. Am.</u> <u>68</u>, 677-689.

Urhammer, R. A. (1980). Observations of the Coyote Lake, California, earthquake sequence of August 6, 1979, <u>Bull. Seism. Soc. Am.</u> <u>70</u>, 559-570.

Wyss, M. and J. N. Brune (1968). Seismic moment, stress, and source dimensions for earthquakes in the California-Nevada region, <u>J. Geophys. Res.</u> <u>73</u>, 4681-4694.

U.S. Geological Survey
345 Middlefield Road
Menlo Park, CA 94025

The Rupture Mechanism of the Coyote Lake Earthquake

of August 6, 1979 Inferred From Near-Field Data

by

Michel Bouchon*

Dept. of Earth and Planetary Sciences

Massachusetts Institute of Technology

Cambridge, MA 02139

*Also at: Laboratoire de Geophysique Interne

Universite Scientifique et Medicale de Grenoble

BP 53X, 38041 Grenoble, France

Introduction

The Coyote Lake earthquake of August 6, 1979 was a moderate size event (M_L=5.7) which occurred on the Calaveras fault in Central California. The mechanism of the earthquake obtained from first-motion P waves indicates strike-slip motion along the Calaveras fault (Lee et al., 1979). Aftershocks are spread over an 18 km long segment of the fault and cluster between depths of 4 and 10 km (Figure 1). The ground motion produced by the earthquake was recorded by more than 50 accelerographs, two of them being located within the fault zone itself. Another remarkable set of data are the broadband displacement records obtained at Berkeley, a little more than 100 km away from the source.

The purpose of the present study is to recover from these near-field data information concerning the rupture process. We shall try to infer the velocity of propagation of the rupture, the extent of the fractured area, the rupture front geometry and other characteristics of the fracture mechanism.

Data and Model Parameters

Six of the accelerographs which were triggered during the earthquake were located less than 25 km from the epicenter. Among them, two stations, Coyote Creek and station 6 of the Gilroy array, lie within the fault zone itself (Figure 1a). These two stations are located on hard rock. The four other stations are situated to the west of the fault. Three of them lie in an alluvial valley reaching at its deepest point a

588

sediment thickness of 1.5 km (Mooney and Luetgert, 1981). The
fourth station sits at the edge of the valley opposite the
fault. This complex crustal structure to the west of the fault
is difficult to include in the modeling. Furthermore, the
presence of the alluvial basin is likely to distort
considerably the wave field emitted by the source. For these
reasons, we chose to model only the strong motion displacements
obtained at Gilroy 6 and Coyote Creek. The displacement traces
that we shall use have been obtained by Brady et al. (1980)
after integration and correction of the accelerograph records.
The baseline correction on these data was performed using a
high pass Ormsby filter with a ramp rising from 0.05 to 0.25
Hz. A low pass Ormsby filter with a ramp falling linearly from
23 to 25 Hz was also applied to the data. We shall supplement
these close-in data with the broadband records obtained at
Berkeley, 107 km away from the epicenter. The azimuth from the
epicenter to the Berkeley station being about N37°W, the three
recording sites lie almost along the strike of the fault. At
such locations, we expect the ground motion to be mostly
transverse to the fault strike (e.g. Bouchon, 1980). This is
well verified by the data. At Berkeley, the SW-NE component of
motion is about three times the SE-NW component and four times
the vertical motion (Uhrhammer, 1980). At Coyote Creek and
Gilroy 6, the 250° and 230° displacement components are about
three times the displacements in the other directions. We
therefore further simplify the data set by only retaining, at
the three recording sites, the component of motion transverse
(or almost transverse) to the fault.

589

We model the earthquake as a pure strike-slip propagating fault embedded in a layered medium. The rupture starts at a point - the hypocenter - and spreads radially, as schematically shown in Figure 2. The final fractured area is assumed to be rectangular. The source time dependence is a step-function and the final slip is uniform all over the fault. The calculation is carried out by representing the source as a superposition of numerous shear dislocation points distributed over the fault plane. The ground motion produced by each individual source is computed using the discrete Green's function representation (Bouchon, 1981). The superposition is done in the frequency horizontal-wavenumber domain which insures the stability of the solution.

The coordinates of the hypocenter and the origin time of the earthquake are fairly well known since the shock occurred within the dense seismic network of central California (Lee et al., 1979). We shall take for the hypocentral depth the value of 9.5 km inferred by Lee et al. and we shall assume that the fault plane is purely vertical. Furthermore, as the near-field data are not very sensitive to the lower depth of faulting, we shall assume that the dislocation extends to the depth of 10 km defined by the aftershock distribution.

The crustal structure in the vicinity of the source has been determined by carrying out refraction experiments (Mooney and Luetgert, 1981). The velocity structure in the fault zone, shown in Figure 2, consists of an upper layer, about 1.75 km thick, having a compressional velocity of 4.2 km/s and an underlying crust with a P-wave velocity of 6 km/s.

Rupture Velocity

Records obtained at station 6 of the Gilroy array display the absolute time. At this station, the transverse component exhibits a large displacement pulse (top of Figure 3). By matching the arrival time of this pulse with the synthetics, we can infer the velocity of propagation of the rupture. This is shown in Figure 3. Two fault lengths are considered: in one case the rupture stops before reaching the station, in the other one, rupture propagates beyond the station. The top of the fault is at a depth of 2 km and rupture propagates toward the southeast. The shorter fault length considered (8 km) makes the fault stop at the jump in aftershocks location. The rupture process is simulated by distributing point sources at intervals of 250 m in depth and 500 m along the fault strike. A high pass Ormsby filter similar to the one used to process the data has been applied to the synthetics. Frequencies up to 3.2 Hz are included in the solution. The station is located 10 km away from the epicenter and is assumed, in this calculation, to lie on the fault strike.

Synthetic displacements computed for rupture velocities of 2.2, 2.4, 2.6, and 2.8 km/s are compared to the data in Figure 3. The gradual displacement build up associated with P-wave arrivals, the rapid change of direction of motion produced by the shear wave coming from the hypocentral region, and the large NE displacement pulse are well reproduced by the synthetics. The timing of the S wave arrival is good, which supports the velocity model used for the calculation. Whether

rupture stops at the jump in aftershocks location or propagates beyond it, does not affect the arrival time of the pulse. This pulse can be interpreted either as the stopping phase (L=8km) or as the passage of the rupture front below the station (L=16km). It is interesting to note that the record at Gilroy 6 cannot differentiate between these two eventualities. In both cases, the rupture velocity required to bring the timing of the computed and recorded SH pulses into agreement is about 2.6 km/s. This value corresponds to a ratio of rupture velocity to shear wave velocity equal to 0.75. Changes in the position of the fault top have little effect on the arrival time of the pulse and will not affect these values. As discussed earlier, we have assumed that rupture takes place instantaneously at the rupture front. A rise time longer than the sampling interval considered here (0.15s) would broaden the displacement pulse and deteriorates the fit with the data.

Fault length

The strong motion data are mostly sensitive to the fracture history on the part of the fault closest to the station sites. For this reason, the data obtained at Gilroy 6 and Coyote Creek cannot resolve the total length of rupture. On the other hand, the Berkeley records obtained several fault lengths away from the source should be representative of the whole rupture process. The NE-SW component of motion recorded

by the broadband Berkeley seismograph (Uhrhammer, 1980) is displayed at the top of Figure 4. Also shown on this figure are the synthetic displacements obtained for various source geometries after convolution with the instrument response. The rupture propagation is toward the southeast. Two fault lengths are considered. The shorter one (8 km) makes the fault stop at the jump in aftershocks location while the longer one (16 km) extends to the southeastern end of the aftershock zone. In each case, four different depths to the top of the fault are considered: 100 m, 1 km, 2 km, and 4 km. The crustal model used for the calculation is given in Table 1. The shallow stucture is the same as the one used for the strong motion calculations. The rest of the model is based on Mooney's interpretation (personnal communication) of refraction data obtained northeast of the Calaveras fault. A rupture velocity of 1.8 km/s is assumed in the upper layer. This value is chosen since it keeps the ratio of rupture velocity to shear velocity unchanged (Figure 2). About 400 point sources distributed all over the fault are used to simulate the rupture process. Frequencies above 0.5 Hz are not included in the calculation so the comparison with the data must be restricted to periods longer than 2 s. The ringing which is present in the synthetics is the effect of the sharp frequency cutoff.

The northeast deflection of the recorded displacement associated with the P-wave is well reproduced by the synthetics. The width of the large SH-displacement pulse which characterizes the data and the synthetics is related to the

fault length. As shown on the figure, we measure the pulse width as the time span between the S arrival and the peak of displacement toward the NE. We do so because this peak represents the stopping phase of the rupture. The comparison between the computed and recorded waveforms shows that the SH pulse produced by an 8 km long fault is too narrow while the one resulting from a fault 16 km long is too broad. The extent of the fractured area lies therefore between these two extremes. The best fit is obtained for a fault length of 12 km and is depicted in Figure 5a. This fit can be further improved by letting the rupture propagate a few kilometers toward the northwest. We show this case in Figure 5b. The fault extends 2 km northwest of the epicenter. The total fault length is therefore now 14 km. While the pulse width is unchanged from Figure 5a, the more rapid amplitude build up which follows the arrival of the S-wave from the hypocentral region is in better agreement with the data.

The displacement waveform and amplitude are insensitive to variations of the depth of the fault between 0 and 2 km. The fault slip required to reproduce the peak-to-peak amplitude of the data are respectively 14, 15, and 16 cm for 100 m, 1 km, and 2 km depths. When the fault depth reaches 4 km, the fit with the data deteriorates and the required dislocation increases to 23 cm.

We have now determined independently the rupture velocity and the fault length. We still have to constrain the depth of faulting.

Depth of faulting

As mentioned earlier, the strong motion data obtained at Gilroy 6 and Coyote Creek should be very sensitive to details of the rupture on the part of the fault closest to the station sites. These data therefore should be a good marker of the depth of faulting. We present in Figure 6 the displacement computed at Gilroy 6 for four different fault depths: 100 m, 1 km, 2 km, and 4 km. As the position of the station relative to the earthquake fault is not accurately known (because the fault did not break the surface) two slightly different station sites are considered. The epicentral distance along the fault strike is the same in both cases (10 km), but in case A the station lies on the fault strike while in case B it is located 900 m to the east of the fault. The true site location should be between these two values. The point sources which simulate the rupture process are distributed at 250 m interval in depth and 500 m interval in the horizontal direction, which, in the case of the shallowest fault considered here, amounts to a superposition of about 1200 sources. Frequencies

up to 3.2 Hz are included in the solution. Values of the fault slip required to match the amplitude of the observed motion are indicated in each case. The computed displacement is very weakly dependent on the particular site considered. Consequently, the slight uncertainty in station location will not affect the results.

The displacement waveforms and amplitudes obtained for

fault depths between 100 m and 2 km are very similar. The ground motion produced by a fault as shallow as 100 m is only 10% larger than the one resulting from the same source buried 2 km below the surface. For depths equal to or shallower than 2 km, the relative amplitude of P waves and S waves is well modeled by the synthetics. The major difference between the recorded and computed displacement lies in the width of the SH-pulse. The uniform dislocation model with circular rupture front cannot account for the short duration of the recorded displacement pulse. For a fault depth of 4 km, the fit with the data deteriorates and the required fault slip becomes unrealistically large.

The transverse displacement obtained at Coyote Creek is displayed at the top of Figure 7. The same model parameters are used as in Figure 6. Here again, two slightly different station sites are considered because of the uncertainty in the exact location of the earthquake fault. In both cases the epicentral distance along the fault strike is 1.5 km. In case A, the station directly sits above the fault, while in case B it is located 750 m west of the fault strike. Four different depths of faulting are considered.

The displacement waveform is very weakly dependent on the site considered. The gross features of the first two seconds of observed displacement are reasonably well reproduced by the computed solution corresponding to depths of faulting of 1 or 2 km.

The amount of slip required to match the maximum amplitude of ground motion in the case where the top of the fault is at a depth of 1 km is consistent with the value inferred from the Gilroy 6 record. For a depth of faulting of 2 km the required slip becomes large compared to the value determined from the Berkeley records. The possibility that the fault might be buried by as much as 4 km below the surface is clearly rejected since this would require a fault slip of the order of 1 m, a value about six times the one inferred from the Berkeley records.

From this analysis, it results that the depth of faulting should be close to 1 km and that the amount of slip on the shallow part of the fault should be about 20-25 cm.

Discussion

The geometry of the fractured area that we have inferred from the near-field data sensibly differs from the area defined by the aftershocks location. While only two out of a total of 150 aftershocks located by Lee et al. (1979) are shallower than 3.5 km (Figure 1b), the fault depth that we have obtained is about 1 km. A depth of faulting of 4 km, which corresponds to the extent of the aftershock zone, would require slip of 40 to 100 cm to explain the displacement amplitudes recorded at Gilroy 6 and Coyote Creek. Such large values are incompatible with the Berkeley records and with the geodetic data (King

et al., 1981). The amount of slip inferrred from the close-in stations - 20 to 25 cm - is about 50% larger than the average fault slip obtained from the Berkeley record and suggests the possibility that slip was larger at shallower depths. This could be due to the lack of barriers of high-strength material at these depths, which in turn would provide an explanation for the absence of aftershocks.

The fault length inferred makes the rupture stop about 4 km before the southeastern end of the aftershock zone. Rupture therefore went beyond the offset in aftershocks and its propagation was apparently not affected by the offset. A similar situation occurred in the 1966 Parkfield earthquake where rupture appears to have propagated beyond a well-marked offset in the aftershock zone (Bouchon, 1979; Aki, 1979). In the present case, rupture stopped at the beginning of a large patch of aftershocks which starts about 12 km from the epicenter and extends for about 5 km up to the end of the aftershock zone.

Recent modelizations of teleseismic body waves (Nabelek, 1982) suggest that the fault dips slightly (10°) toward the northeast. Such a dip would have little effect on the transverse motions recorded close to the fault strike.

From the fault geometry inferred and the average slip obtained, one can estimate the seismic moment of the earthquake. We have:

$$Mo = \mu \times \text{average slip} \times \text{fault area} = 6 \times 10^{24} \text{ dyne-cm}$$

598

This value is the same as the one obtained by Uhrhammer (1980) from integration of the Berkeley record and under simplifying assumptions.

We still have to satisfactorily explain the short duration of the displacement pulse associated with the passage of the rupture front below the Gilroy 6 station. Archuleta and Frazier (1978) have shown that the transverse ground motion above a strike-slip fault is very sensitive to the rupture front geometry. We investigate this effect in Figure 8. The fault depth considered is 100 m and the station is assumed to be above the fault. As before, the source time dependence is a step-function. Three cases are considered. The upper trace displayed is obtained for a fault propagating horizontally at 2.2 km/s. The middle trace is the result previously obtained for a circular rupture front. Finally, the lower displacement trace corresponds to the case where rupture nucleates along the complete bottom of the fault and propagates upward at 2.2 km/s. The striking feature of this figure is the very small displacement produced by an upward propagating rupture (about 1/20 the displacement amplitude obtained for a horizontal propagation). The largest displacement amplitude and shortest pulse duration are produced by the horizontally propagating fault. The pulse obtained in this case bears a strong resemblance to the observed one. This suggests that the rupture front below Station 6 was close to the vertical and may represent a local irregularity of the rupture front. We may

also note that a shallower hypocentral depth would make the rupture front more vertical.

In the fault models that we have considered, slip occurs instantaneously along the rupture front. Dynamic crack models, however, predict that slip anywhere on the source takes place in a time span which is roughly equal to the distance to the final location of the crack tip divided by the rupture velocity. For a crack having dimensions of the order of the length or width of the fault, this rise time would be very large and would produce a very broad pulse at Station 6. The impulsive S-wave arrival at Berkeley could not be accounted for either by such a model. If present dynamic models are a realistic representation of crustal earthquakes, the crack size must be very small and a fault like the one of the Coyote Lake earthquake must be made up of a large number of such cracks. At wavelengths larger than the crack dimensions, the radiation from such a composite source will not be distinguishable from the one resulting from a uniform dislocation source.

Conclusion

By combining strong motion records obtained very close to
the fault with broadband seismogram recorded several fault
lengths away from the source, we have been able to infer
independently the rupture velocity, the fault length and the
depth of faulting of the 1979 Coyote Lake earthquake. The
velocity of propagation of the rupture is well constrained by
the arrival time of the large transverse displacement pulse
associated with the passage of the rupture front below the
Gilroy 6 station. The value inferred - 2.6 km/s - corresponds to
a rupture velocity to shear wave velocity ration of 0.75. The
fault geometry obtained sensibly differs from the area defined
by the aftershocks location. The model which gives the best
fit to the data is a 14 km long fault extending between depths
of 1 and 10 km with a fault slip of 15-20 cm and a seismic
moment of 6×10^{24} dyne-cm.

One important result of this study is the finding that
slip at any point on the fault takes place in a very short time
span and that simple dislocation models give a good description
of the rupture process.

REFERENCES

Aki, K., Characterization of barriers on an earthquake fault, J. Geophys. Res., 84, 6140-6148, 1979.

Archuleta, R.J., and G.A. Frazier, Three-dimensional numerical simulations of dynamic faulting in a half-space, Bull. Seismol. Soc. Amer., 68, 541-572, 1978.

Bouchon, M., Predictability of ground displacement and velocity near an earthquake fault. An example: the Parkfield earthquake of 1966, J. Geophys. Res., 84, 6149-6156, 1979.

Bouchon, M., The motion of the ground during an earthquake. 1. The case of a strike slip fault, J. Geophys. Res., 85, 356-366, 1980.

Bouchon, M., A simple method to calculate Green's functions for elastic layered media, Bull. Seismol. Soc. Amer., 71, 959-972, 1981.

Brady, A.G., P.N. Mork, V. Perez, and L.D. Porter, Processed data from the Gilroy array and Coyote Creek records, Coyote Lake, California earthquake of 6 August 1979, U.S. Geological Survey Open-file report 81-42, 1980.

King, N.E., J.C. Savage, M. Lisowski, and W.H. Prescott, Preseismic and seismic deformation associated with the Coyote Lake, California, earthquake, J. Geophys. Res., 86, 892-898, 1981.

Lee, W.H.K., D.G. Herd, V. Cagnetti, W.H. Bakun, and A. Rapport, A preliminary study of the Coyote Lake earthquake of August 6, 1979 and its major aftershocks, U.S. Geol. Surv. Open File Rep., 79-1621, 1979.

Mooney, W.D., and J.H. Luetgert, Seismic-refraction study of
the Santa Clara Valley, west-central California, Trans.
Am. Geophys. Union, 61, 1025 (abstract), 1980.

Nabelek, J., Teleseismic constraints on the faulting mechanism
of the Coyote Lake earthquake of 1979, in preparation, 1982.

Uhrhrammer, R.A., Observations of the Coyote Lake, California
earthquake sequence of August 6, 1979, Bull. Seismol. Soc.
Amer., 70, 559-570, 1980.

Figure Legends

Figure 1a.   Epicenters of the mainshock and of the aftershocks
      of the Coyote Lake earthquake sequence (August 6 to 21,
      1979).   The location of the two accelerograph stations
      Coyote Creek and Gilroy 6 is indicated.

                                                       (modified

      from Lee et al., 1979).

Figure 1b.   Projection of hypocenter locations in a vertical plane
      transverse to the fault strike (from Lee et al., 1979).

Figure 2.   Source-medium-station configuration used in the
      study.   The circles indicate the position of the rupture
      front at successive times.

Figure 3.   Effect of rupture velocity on the displacement
      computed at Gilroy 6.   Two different fault lengths and
      four different rupture velocities are considered.   P and S
      indicate the computed arrival times of the P and S waves.

Figure 4.   Comparison of the Berkeley record with the
      displacement waveforms computed for various fault
      geometries.   P and S indicate the computed arrival times
      of the P and S waves.   Each trace is normalized to its
      maximum value.

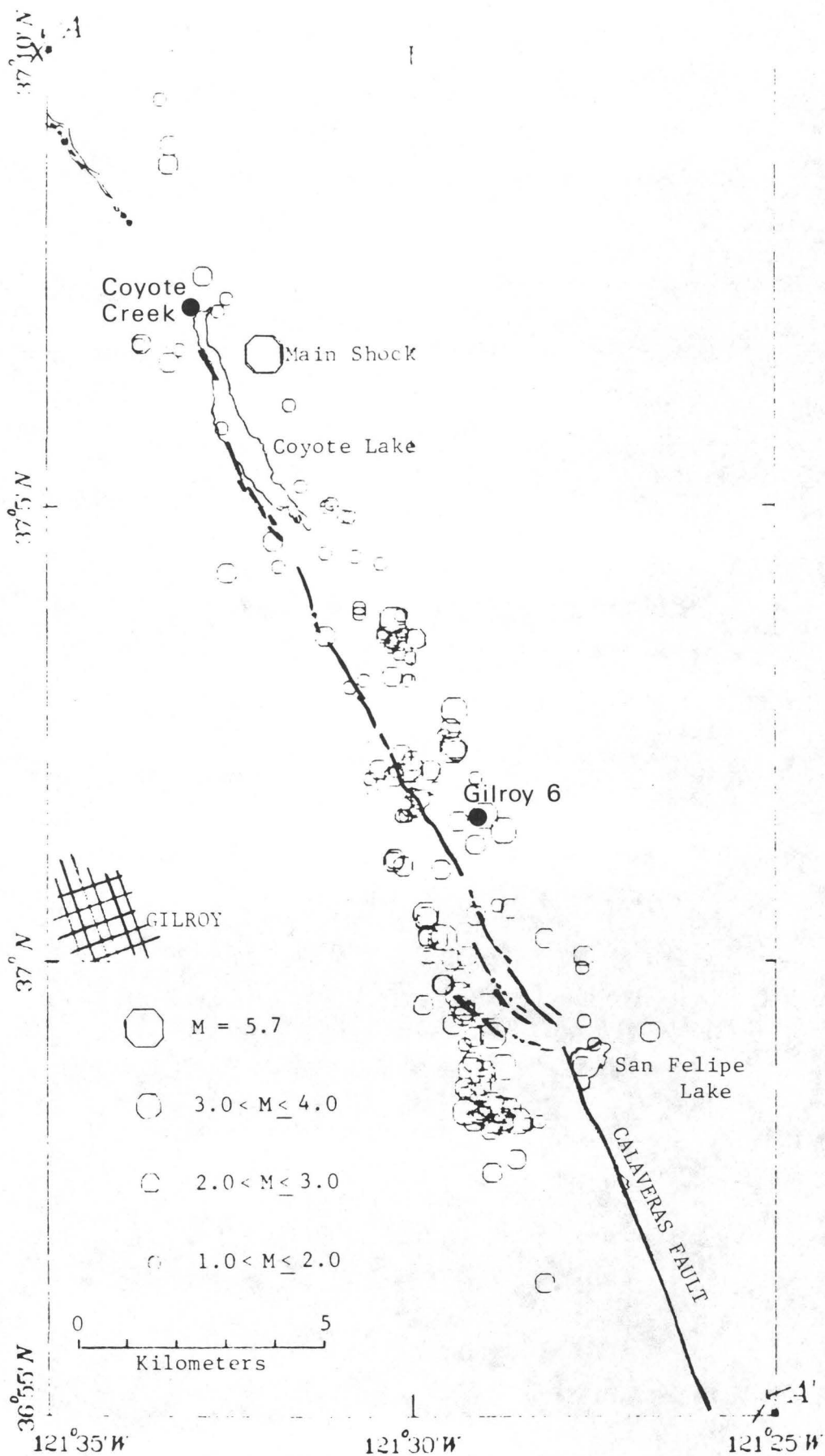Figure 5.   Same as Figure 4 for different fault geometries.

Figure 6.   Comparison of the Gilroy 6 transverse displacement
      record with the displacements computed for different
      depths of faulting.   A and B represent two slightly
      different station locations.   Values of the fault slip
      required in each case to match the observed amplitude are
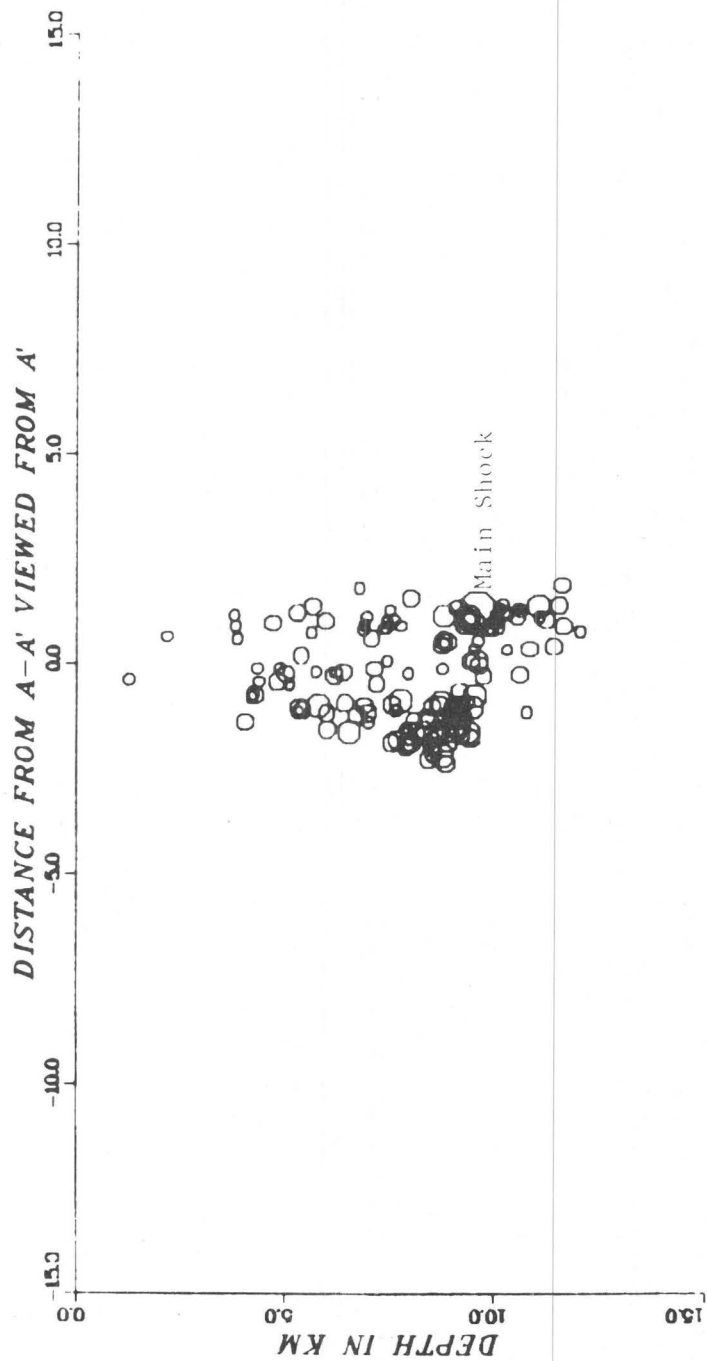   indicated.   605

Figure 7.   Comparison of the transverse displacement recorded
at Coyote Creek with the displacements computed for
different depths of faulting.   A and B represent two
slightly different station locations.   Values of the
fault slip required in each case to match the observed
amplitude are indicated.

Figure 8.   Effect of rupture front geometry on the transverse
displacement computed at the site of the Gilroy 6 station.
Traces A, B, and C illustrate respectively the cases of
vertical, circular, and horizontal rupture fronts.   The
station is assumed to lie above the fault.   U denotes the
amplitude of the fault slip.

Table 1 - Crustal model used in this study

Depth km	compressional velocity (km/s)	shear velocity km/s	density g/cm^3
0			
	4.2	2.4	2.6
1.75			
	6.0	3.5	2.8
18			
	6.6	3.8	2.9
28.5			
	7.9	4.6	3.1

N

A

Coyote
Creek ●

Main Shock

Coyote Lake

GILROY

⬡ M = 5.7

◯ 3.0 < M ≤ 4.0

◌ 2.0 < M ≤ 3.0

○ 1.0 < M ≤ 2.0

Gilroy 6 ●

San Felipe Lake

CALAVERAS FAULT

A'

0 _____ 5
Kilometers

37°10'N

37°5'N

37° N

36°55'N

121°35'W   121°30'W   121°25'W

L = 8 km

L = 12 km

611

S45°W ↑

P   S

100 m

1 km

2 km

4 km

0   15   30   45   60   75
      time (s)

L = 8 km   L = 16 km

612

S45°W ↑

P S

100 m

1 km

2 km

4 km

time (s)

0   15   30   45   60   75

L = 12 km

L = 2 + 12 km

613

S 50°W

9.3 cm

100 m   19 cm

1 km   19 cm

2 km   21 cm

4 km   42 cm

B

100 m   22 cm

1 km   22 cm

2 km   24 cm

4 km   44 cm

0 2 4 6 8 10
time (s)

A
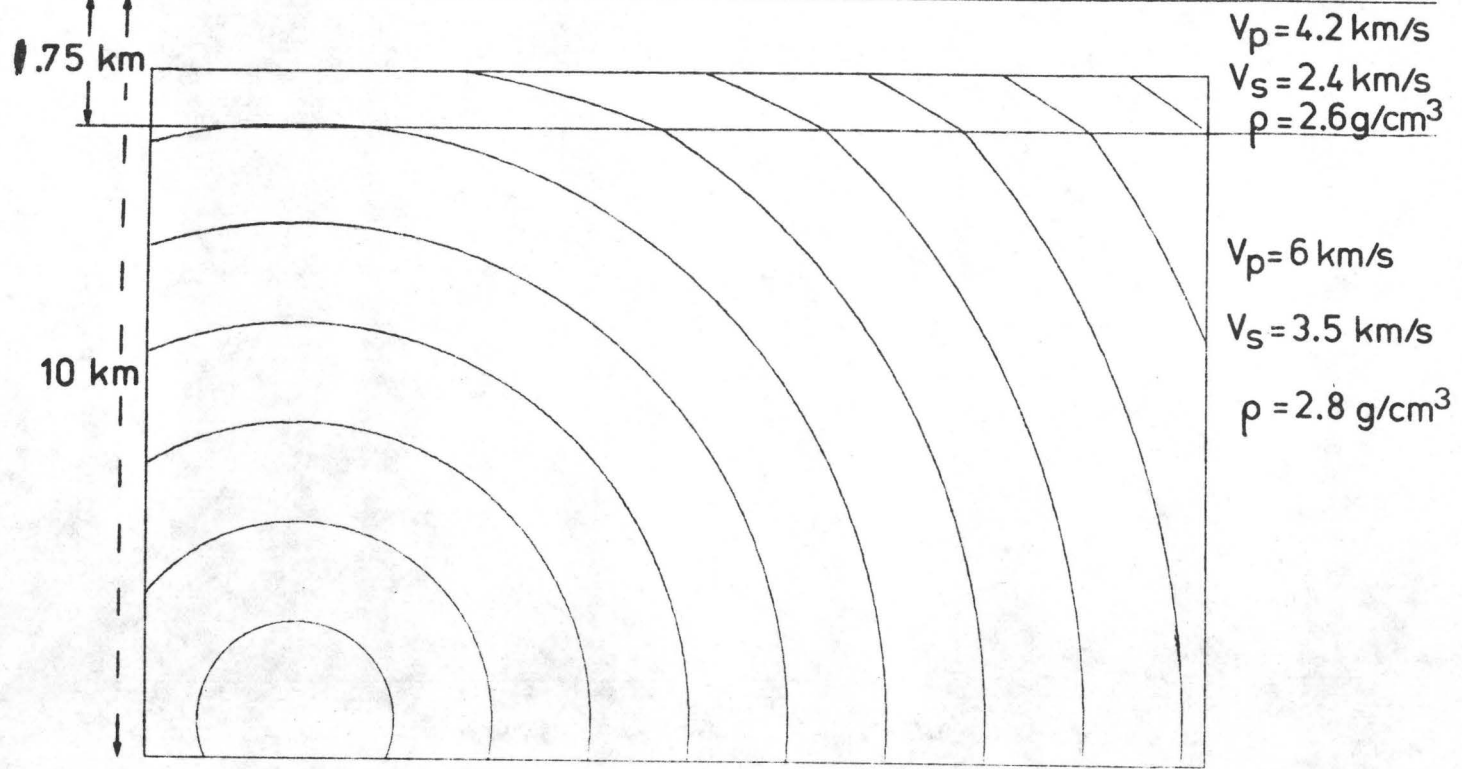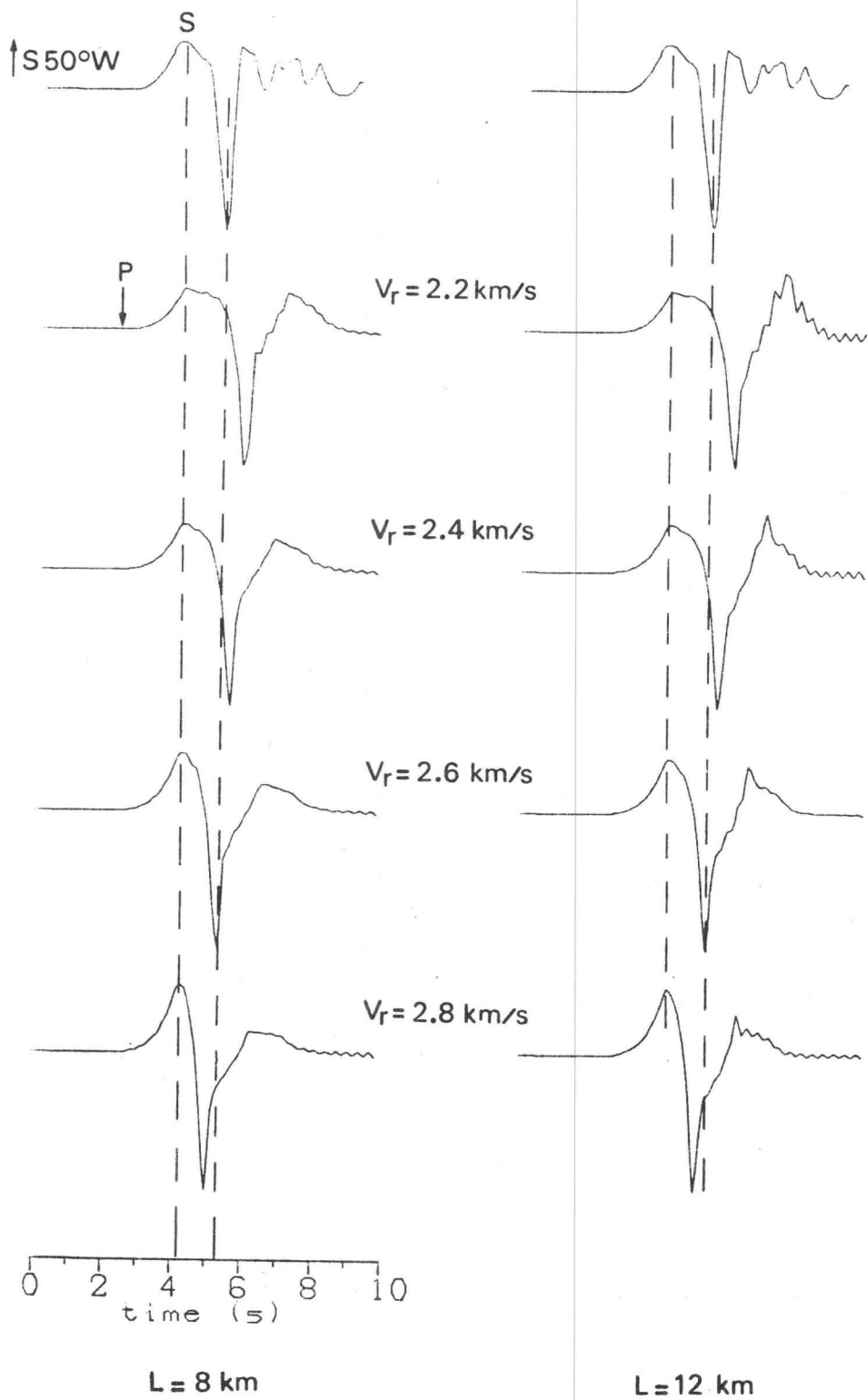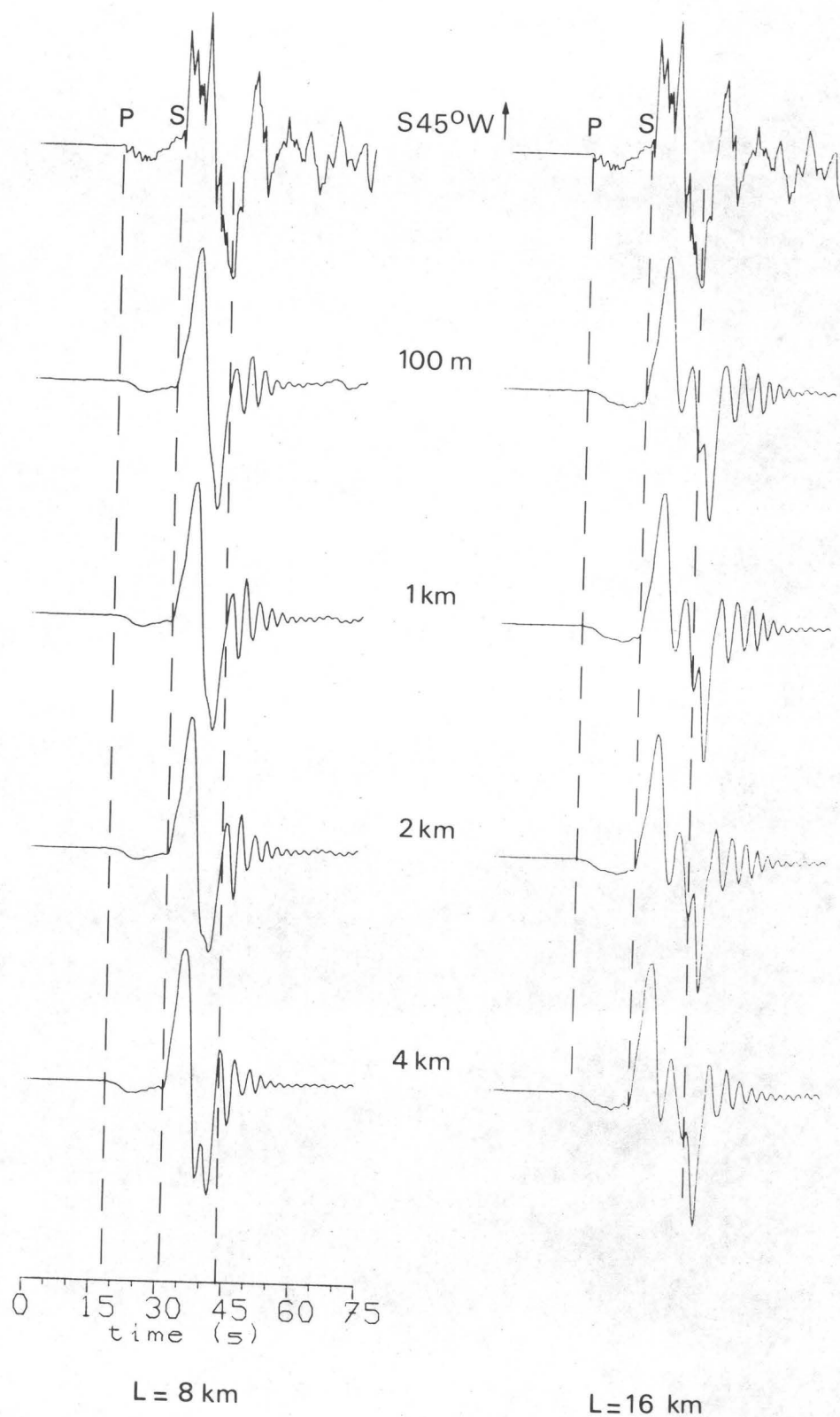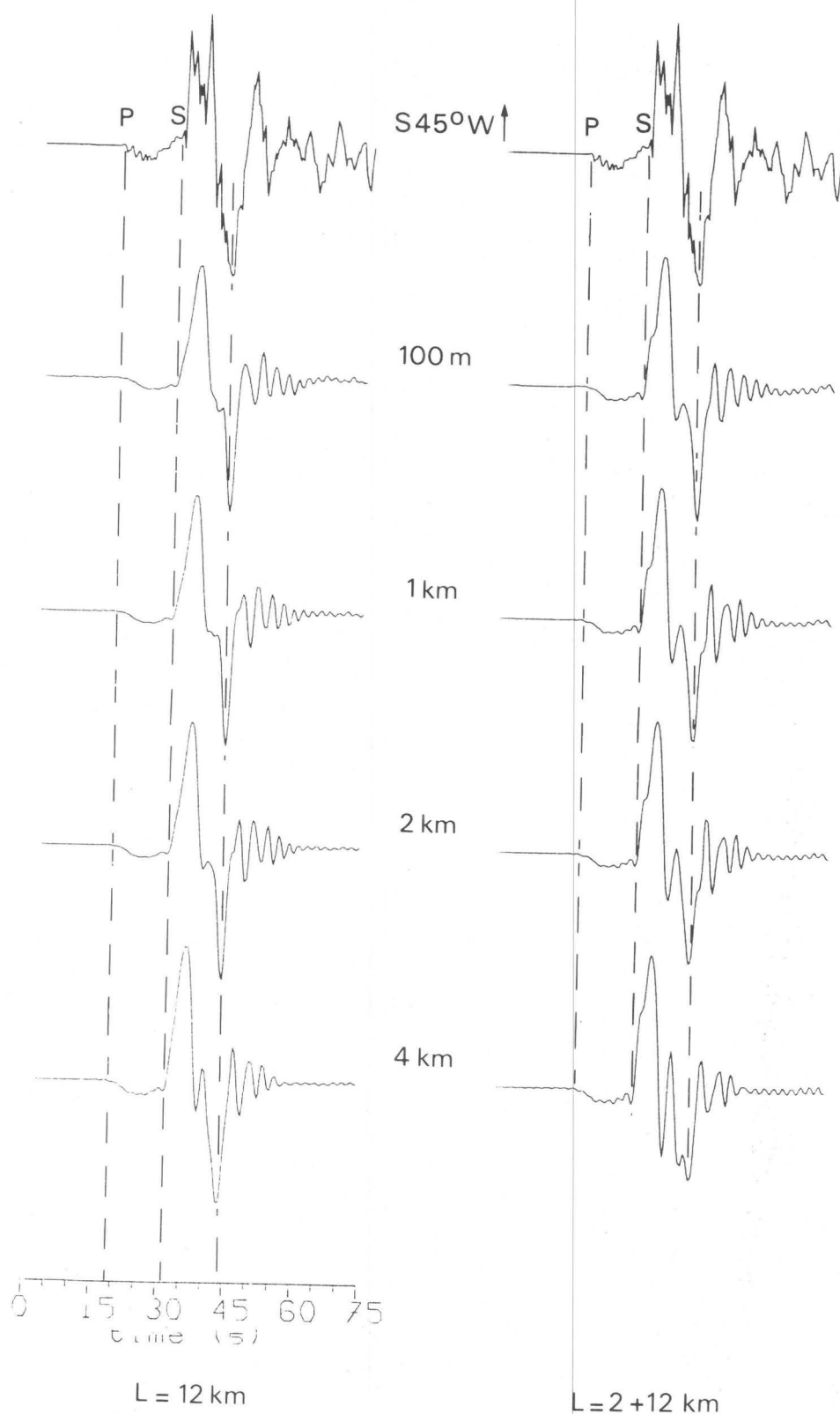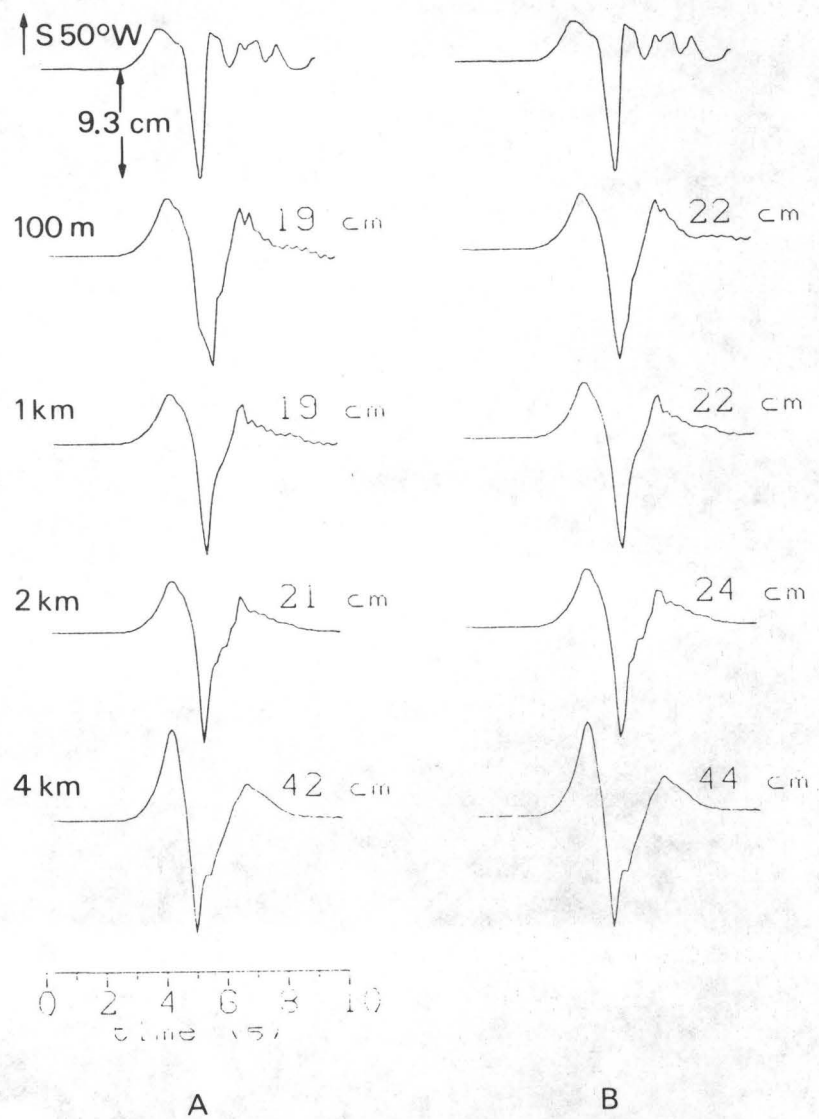
SOURCE MECHANISM AND SURFACE WAVE EXCITATION FOR TWO EARTHQUAKES IN NORTHERN BAJA CALIFORNIA, MEXICO†

F. Alejandro Nava

Instituto de Investigaciones en Matemáticas Aplicadas y en Sistemas,
Universidad Nacional Autónoma de Mexico, Mexico 20, D.F. México.
(905) 550-5570

James N. Brune

Institute of Geophysics and Planetary Physics, Scripps Institution of Oceanography,
University of California, San Diego, La Jolla, California.
(714) 452-2890

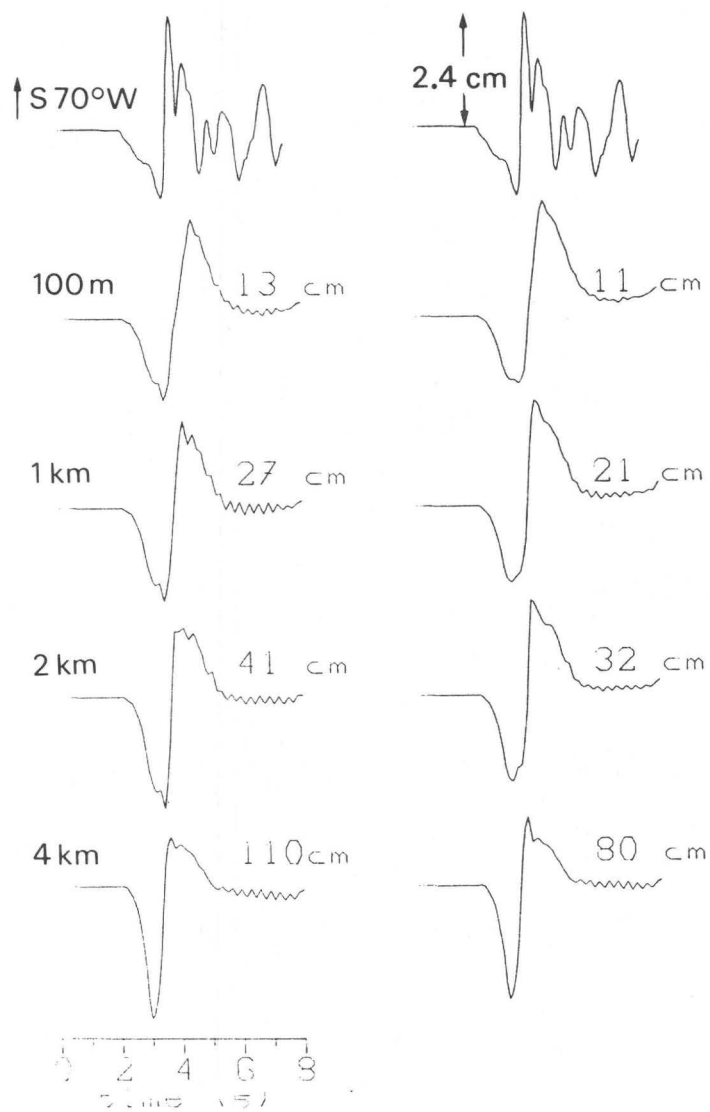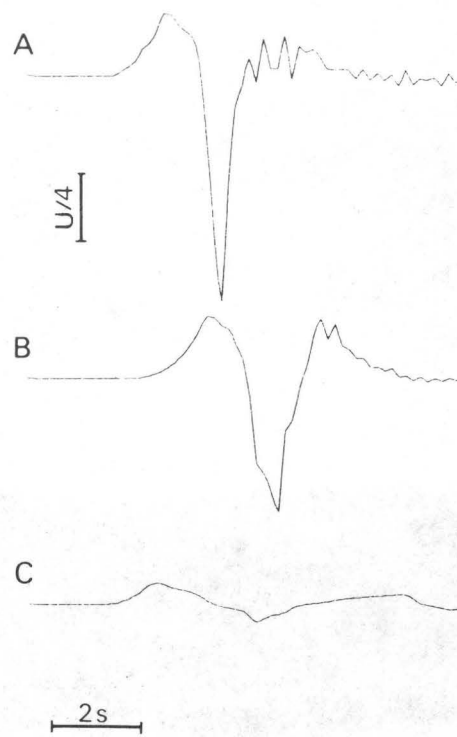Two earthquakes of comparable local magnitude from different regions of Northern Baja California (the July 17, 1975 Pino Solo earthquake, $M_L = 5.1$, from the Peninsular Ranges region, and the Dec 7, 1976 Mesa de Andrade earthquake, $M_L = 5.3$, from the Colorado River Delta region) are studied in detail to determine possible causes for the observed stronger excitation of surface waves by earthquakes from the Delta region relative to earthquakes of comparable local magnitude in the Peninsular Ranges region. Data from distant stations are complemented with data from aftershock studies using local arrays and, for the Mesa de Andrade earthquake, with data from two strong motion stations.

The strong motion records for the Mesa de Andrade earthquake show that it consisted of two events, 45 sec apart, which produced maximum recorded horizontal accelerations of .21g and .24g, respectively, at a distance of 18km from the epicenter. Synthetic seismograms are used to help determine the depth of these events and their source time functions. Both events are relatively simple. The second event is sharp and impulsive and could be thought of as an aftershock, since it has a considerably smaller moment than the first event, even though its recorded acceleration was higher.

Comparison of measured parameters shows that while the local magnitude of the Mesa de Andrade earthquake is only .2 units larger than the Pino Solo earthquake and its source dimension is $\sim$2.2 times larger (source areas $\sim$4.8 times larger), its moment is larger by a factor of 6.2 to 8.5. This is approximately explained by the ω^{-2} scaling law. However, the near source spectra and accelerations recorded on the strong motion accelerograph at Riito, a distance of about 18km, are considerably larger than predicted by the ω^{-2} scaling law. This may be a result of near field focusing (directivity), or high stress drop asperities.

INTRODUCTION

The study reported in this paper has an important bearing on the general problem of understanding earthquake mechanism, and more specifically, the problems of seismic discrimination between earthquakes and explosions and understanding earthquake strong motion. One of the main discrimination criteria used at present is the M_s versus m_b criterion [*Liebermann and Pomeroy*, 1969; *Marshall and Basham*, 1972], which compares the relative excitation of long period surface waves used to determine M_s and the short period body waves used to determine m_b. Points representing earthquakes and explosions lie on different regions of a plot of M_s versus m_b because of the greater relative excitation of surface waves by earthquakes. The earthquake population on M_s/m_b diagrams shows a large scatter, and several authors have noticed a regional dependence in the scatter. They have suggested that the M_s/m_b discriminant be applied regionally. With respect to strong ground motion, it is critically important to know how ground acceleration and velocity scale with both local magnitudes, M_L, and surface wave magnitude M_s, so that better predictions can be made for earthquake resistant design. This study addresses that problem.

---

†This study is based in part on the Ph.D. thesis of Alejandro Nava. The thesis contains additional details supporting the results given in this paper.

Brune et al. [1963] noticed a region of anomalously low surface wave excitation in Northern Baja California while studying events from the California-Nevada area. In contrast, the Gulf of California area was identified as a region of large surface wave excitation by *Wyss and Brune* [1971]. *Thatcher and Brune* [1971] found that earthquakes from a swarm in Wagner Basin in the northern end of the Gulf of California also excited surface waves more than earthquakes in Northern Baja California with similar body wave excitation.

Thatcher [1972] studied the regional variations of spectral parameters in Northern Baja California from observations at Cal Tech stations in Southern California, especially BAR, PLM and PAS. The spectra were interpreted in terms of source parameters such as moment, source dimension and stress drop. Thatcher inferred that Northern Baja sources have dimensions that are typically a factor of four smaller than the dimension of Gulf events of comparable local magnitude. Conversely, moments for the Gulf events were about an order of magnitude larger (for the same M_L) than those for Northern Baja. The average stress drop for the Gulf earthquakes was found to be lower than the average for Northern Baja California.

The above studies of sources in Northern Mexico were based solely on relatively distant (from the epicenter) data, with inherent uncertainties in epicentral distance, source depth, rupture area, attenuation, and high frequency behavior. The present work uses improved data from a sample earthquake from smaller regions; the Pino Solo earthquake of July 17, 1975 from Northern Baja California and the Mesa de Andrade earthquake of Dec 7, 1976 from the Colorado Delta. Both earthquakes have approximately the same local magnitude (determined from the maximum amplitude measured on standard Wood-Anderson seismograms of the type shown in Figure 1). However, the long period excitation is much larger for the Mesa de Andrade earthquake, as is clear from Figure 1, and further illustrated in Figure 2, which shows records of both earthquakes at TUC (long period) and PAS (ultra long period). In this study, the far field data is complemented with local array aftershock studies (to infer fault dimensions) and, for the Mesa de Andrade earthquake, with data from near field strong motion records.

Figure 1 shows that the Pasadena Wood-Anderson seismogram for the Pino Solo earthquake is relatively simple, most of the energy arriving in a burst of only a few seconds duration, while the seismogram from the Mesa de Andrade earthquake is much more complex, with both the high frequency energy (f > 1Hz) and lower frequency energy arriving over a much longer period of time. The bottom trace in Figure 1 shows a tracing of the strong motion displacement record of the Mesa de Andrade earthquake from the station Riito at a distance of about 18km (discussed later), and indicates that the actual energy release occurred in two relatively simple events, the first containing considerably more low frequency energy than the second. Figure 1 indicates that propagation path effects have been important in causing the complexity observed in the Mesa de Andrade seismogram at Pasadena, and less important in the case of the Pino Solo seismogram.

THE PINO SOLO EARTHQUAKE

The Pino Solo earthquake occurred on July 17, 1975, in the Sierra Juarez in Northern Baja California, approximately halfway between Ensenada and the northern end of the Gulf. The epicenter is located just east of the main mapped San Miguel fault that runs along the northeastern edge of the Llano Colorado Valley (see Figure 3).

For aftershock locations, an array of five portable Kinemetrics smoked paper seismographs was installed in the epicentral area in a cooperative project involving the University of California at San Diego (UCSD) and the Centro de Investigacion Cientifica y Ensenada Superior de Ensenada (CICESE) in Ensenada. The array started operating about eight hours after the main shock, and operated for a day and a half before the batteries discharged. Figure 3 shows the location of the portable stations, and the approximate area of the aftershocks. All stations were deployed on granite outcroppings, and all registered sharp P-wave first arrivals and clear but less sharp S-wave arrivals.

Aftershocks were located using velocity model PRCP, a four layer velocity model for the area developed in a separate study [*Nava and Brune*, 1981] and the MICRO location program developed by *Ray Buland* [1976] for small, local arrays (originally for a half-space, and modified by Luis Munguia for

a layered model). Poisson's ratio was estimated for 34 combinations of P- and S-wave observations, and a value of .2492 was obtained, not significantly different from .25, so a value of .25 was used in the location process.

The aftershock area has dimensions roughly 8km (west-northwest) × 2km (north-northeast). Figure 4 shows a plan view of the aftershock epicenters, along with an east-west cross section view of the hypocenters. The hypocentral depths range from 4.4 to 17.9km, the average depth being $<z> = 8.2$km.

A linear regression for the epicenters defines a strike N 7° W. Consideration of the probable errors allows strikes from N 55° W to S 94° W. As described later, the polarities of the first arrivals from the aftershocks, as recorded on the portable stations, are consistent with a fault plane corresponding to a vertical, strike slip fault with a strike of N 57° W. This is not inconsistent with the aftershock location data.

The aftershock region, and hence the earthquake itself, is not associated with any known fault. However, the region is between the intensely fractured Sierra Juarez and San Miguel fault zones (see Figure 3) and hence it is quite reasonable to assume that an active fault exists there. Because of the relatively uniform granitic terrain, the identification of smaller faults is difficult in this region.

Careful relocation of the main event, using data from U.S. stations and Mexican stations at Ensenada and Rio Hardy give a location that within the experimental error lies within the zone of aftershocks (the USGS Earthquake Data Report of July 8, 1976, gives a location some 8.25km northeast of the aftershock zone).

The fault plane solution for the Pino Solo earthquake is shown in Figure 5, a Wulff's net projection through the bottom half of the focal sphere for polarity (i.e., compression or rarefaction) of first motions. Circles represent readings for the main event at permanent stations. Also shown are first motion polarity readings from aftershocks at the portable station network, represented as bands. Under the assumption that aftershocks will tend to have the same mechanism as the main shock, their fault plane solutions should be compatible with that of the main shock.

The observed polarities are compatible with two conjugate vertical nodal planes with orientations of N 33° E and E 33° S. These orientations are relatively well constrained. Based on the aftershock distribution, regional tectonics and observed faulting for surface manifestations of other earthquakes in the region, the plane with the azimuth of 123° was assumed to be the fault plane.

Pino Solo Long Period Seismograms from PAS

For the Pino Solo earthquake, the closest station with calibrated long period instruments was PAS at the California Institute of Technology (distance 337.3km). The path from epicenter to station is almost completely along the Peninsular Ranges, except at the very end where it crosses some sediments before reaching Pasadena at the foot of the San Gabriel Mountains.

The PAS seismograms were digitized, and the two horizontal components combined to provide radial and transverse components. The fundamental Rayleigh and Love modes were extracted from the complete seismograms by means of group-velocity filter, according to the apparent group-velocity obtained from a moving window analysis. For comparison with theory, synthetic seismograms were computed for the Peninsular Ranges PRCP model for various depths using the program of *Harkrider* [1964, 1970]. Although none of the synthetic seismograms fit the observed ones as well as would be desired, the seismograms for a depth of 15km appeared to be fairly close. This depth was also checked by comparing the spectra of the observed and theoretical seismograms, and by comparing the smoothed ratio of the Rayleigh wave spectrum to the Love wave spectrum [*Tsai and Aki*, 1970] with the corresponding theoretical ratio computed for the PRCP model. These comparisons suggest a source depth of about 15 ± 3km, consistent with the source depth estimated from the time domain surface wave shapes and with the arrival time data. The details of the above comparisons may be found in *Nava* [1980]. Study of the source (using the method outlined below) also indicated that its duration was less than about 5.5 sec.

The Pino Solo Earthquake Source Parameters

Directly measurable parameters (e.g., magnitudes and moments) and inferred parameters (e.g., source dimension, stress drop, fault displacement, energy, etc.) were computed for the Pino Solo earthquake (for comparison with the corresponding parameters for the Mesa de Andrade earthquake). Local magnitude M_L was determined from readings of Wood-Anderson standard seismographs at seven stations in Southern California. The average gives $M_L = 5.1$ with a standard deviation $\sigma = .2$ units. This result agrees quite well with the $M_L = 5.0$ given by the USGS Earthquake Data Report.

The body wave magnitude, m_b, was measured for eleven short period stations ranging in distance from $8.7°$ to $45°$, giving an average $m_b = 4.9$ with a standard deviation of $\sigma = .3$. This value agrees perfectly with the value in the USGS Earthquake Data Report, obtained from ten observations at distances ranging from $7.6°$ to $84.4°$.

Surface wave magnitude M_s, was determined using *Marshall and Basham's* [1972] formula for eleven stations at distances ranging from $8°$ to $44.5°$. This gave an average $M_s = 4.0$ with standard deviation $\sigma = .1$.

Moment, M_0, was measured by comparing the long period amplitudes on the observed surface wave records at six stations with those on the synthetic seismograms computed for these stations using *Harkrider's* [1964, 1970] program with a known moment of 10^{25} dyne-cm. The average moment from all measured values is $M_0 = 3.37 \times 10^{23}$ dyne-cm, with a standard deviation of 1.4×10^{23} dyne-cm.

The moment was also estimated at high frequencies ($\sim.9$Hz) by comparison of the observed BAR Wood-Anderson record with a synthetic seismogram computed using the Apsel-Luco wavenumber integration program [*Apsel and Luco*, 1978]. Comparison with the P-phase amplitude yields $M_0 = 1.55 \times 10^{23}$ dyne-cm. The S-phase amplitude is harder to read due to the distortion in the baseline, but the moment is consistent with that determined from the P-wave. This estimation of moment from high frequencies is not very reliable, but will be useful in a later discussion of the spectra.

The main evidence for the dimensions of the source area of the Pino Solo earthquake is the distribution of early aftershocks. As mentioned above, the horizontal length of the aftershock area is ~ 7.5km. Since depth is not very well constrained, a vertical dimension equal to the horizontal is assumed, and a circular rupture area will be used as a first approximation. It is possible that some of the aftershocks may be outside the region of main energy release. Thus the length of the aftershock area might be considered an upper bound to the fault length. If this is the case, exclusion of the events located at the extremes would give a fault length of 5.3km (see Figure 4).

The stress drop for the Pino Solo earthquake was estimated using the *Keilis-Borok* [1960] circular dislocation model which relates the moment and the source dimensions to the stress drop, giving $\Delta\sigma \simeq 7.9$ bars. This value falls within the range found by Thatcher (1972) for Northern Baja earthquakes. The stress drop and fault dimensions correspond to an average displacement of a few cm.

The Mesa de Andrade Earthquake

The Mesa de Andrade earthquake occurred just before 1300 hrs GMT of December 7, 1976, about 50km southeast of Cerro Prieto in the Colorado River Delta area. Although no surface rupture was documented, sand boils were observed in the Mesa de Andrade area (presumably in the region of rupture at depth).

Less than 24 hours after the mainshock, a net of eight portable smoked paper seismographs was operating in the aftershock area, installed by UCSD in cooperation with CICESE in Ensenada. All the locations were done by Javier Gonzalez at CICESE (see Figure 6). Positive identification of the S-phase was uncertain, and no S readings were used for these locations, hence depth determinations are not very reliable.

As part of a joint project between Scripps Institution of Oceanography (SIO, UCSD), and Instituto de Ingenieria (UNAM), several strong motion instruments (triaxial, analog, film recording, SMA-1s) had been previously installed in Northern Baja California [*Prince et al.*, 1976]. The Mesa de Andrade earthquake triggered three of these instruments, at Riito, Delta and Cerro Prieto. Figure 6 shows the location of these instruments and the locations of the aftershocks.

The strong motion records show that the Mesa de Andrade earthquake consists of two large events with origin times about 45 sec apart, close enough so that the instruments were still recording (triggered by the first event) when the second event occurred, and separated enough so that the energy from the first event was negligible at the time of the arrival of waves from the second event. The maximum horizontal accelerations recorded for the first event were .21g, .17g and .04g at Riito, Delta and Cerro Prieto respectively. For the second event, the corresponding accelerations were .24g, .13g and .04g.

Consideration of the relative arrival times of the various phases on the strong motion records indicates that within the uncertainties the two events had the same epicenter, among the aftershocks (whose epicenters are well determined), approximately 18km from Riito.

Accelerogram Analysis

Henceforth, records will be identified by the name of the station, followed by a digit that identifies the event (i.e. 1 or 2).

The original accelerograph 70mm films were amplified 3X and digitized on a "Calma" digitizer. The equispaced series were corrected for instrument response and integrated to give ground displacement, using the process described by *Trifunac and Lee* [1970]. The processing required judicious choice of a high pass filter to remove the long period part of the spectrum introduced by the process of double integration. We found that a high pass filter with a corner frequency of .6Hz was a good compromise between leaving in too much unreasonable long period energy on the one hand and filtering out reliable signal and distorting the pulse shape on the other hand.

Figure 7 shows the resulting Riito horizontal displacement seismograms for the first event. The wave forms have been resolved into longitudinal and transverse components in the bottom part of the figure. Figure 8 shows corresponding seismograms for the second event at Riito, and Figures 9 and 10 corresponding seismograms for both events at Delta. In each figure, the amplitude and time scales are the same.

Figures 7 and 8 show that the pulse of energy at Riito is primarily SH motion, and is a much sharper pulse for the second event than for the first. The Delta seismograms (Figures 9 and 10) show a second pulse arriving about 6 seconds after the S-wave. This pulse is believed to be a reflection multiple and will be discussed later.

Green's Function Synthetics and Source Depth

Depth is difficult to establish for this earthquake, since depths are uncertain even for the aftershocks. Thus, we estimated the depth by matching the observed strong motion records with synthetic seismograms obtained using the PROSE program developed by *Apsel and Luco* [1978]. This program calculates Green's functions for a flat layered model. The model used was the KHC2-IV model for the Imperial Valley [*Hartzell and Brune*, 1977] with a crustal thickness of 32.4km. Synthetics for source depths between 5 and 15km were obtained for Riito and Delta. The alignment of the aftershock epicenters suggests that the Mesa de Andrade earthquake was associated with transcurrent motion along the Cerro Prieto Fault. Hence, right lateral strike slip motion along the Cerro Prieto Fault was assumed for calculating initial synthetic seismograms for comparison with the observed displacement time series. A step source time function was assumed.

Figure 11 shows the synthetic seismograms for radial and transverse components, for different depths, at Riito. Figure 12 shows the corresponding synthetics computed for Delta. The synthetics computed for a depth of 5km are dominated by short period energy trapped in the sediments. This energy is not seen in the observed records (Figures 7 and 8). The synthetics for 7km source depth also show too much surface wave energy, especially for the Delta records (compare Figure 12 with Figures 9 and 10). The synthetics for 10km source depth (center) agree well with the Riito 2 records, and the first large pulse of the Delta 2 records. Synthetics for Riito for a source deeper than 10km, exhibit a larger radial pulse than observed.

The main differences between synthetic and observed seismograms for Delta relate to the pulse (B) arriving some five seconds after S on the transverse synthetic (Figure 12) and the intermediate period pulse arriving some seven seconds after S on the observed radial record (Figures 9 and 10). For 13 and 15km source depth, the second pulse on the Delta synthetic diminishes, but a prominent S arrival, not seen as obviously on the observed records, appears on the Riito synthetics for the radial component. The second pulse (B) on the 10km source depth synthetic for the Delta record was identified as a multiple reflection traveling from the source to the surface, thence to the bottom of the sediments and up to the surface again. The conspicuous feature marked (C) on the synthetic seismogram is another multiple, this time from the surface and twice reflected at the interface between layers four and five.

Attempts to obtain a synthetic pulse resembling the observed multiple by assuming different fault orientations and slip direction proved fruitless. It is possible that this problem results from the limitations of a flat layered model. The basement structure in the epicentral region is probably highly distorted. It is known that the basement of the Colorado Delta is heavily fractured, with blocks ascending toward the edges of the valley [Kovach et al., 1962; Alonso, 1966]. The Cerro Prieto Fault, a major transform fault, strikes from the epicenter toward Delta. Thus, it is possible that the predominantly tangential energy was coupled into radial energy by reflection at some inclined feature. This suggests that we attempt to match only the direct wave at Delta. In this case, a source depth of 10km produces the synthetic seismogram that best fits the observations.

The depth determination for the first event is less certain, mainly because its shape does not resemble the synthetic shapes as closely as was the case for the second event. However, the time between the S pulse and the multiple reflection phases appear to be the same for both events (see Figures 9 and 10). Hence, it is not unreasonable to assign a source depth for the first event similar to that for the second event.

A search for different fault orientations and/or slip directions indicated that any large deviation from the initial choice decreased the overall fit. Hence, the simple case of pure strike slip on a vertical plane along the Cerro Prieto Fault is our favored model for the mechanism of the Mesa de Andrade earthquake.

Green's Function Synthetics and Source Finiteness

An interpretation of the differences between the observed and synthetic records in terms of the behavior of a finite source was made using only the records at Riito, since it is obvious from comparison of Riito and Delta records for both events that a large part of the high frequency information present in the Riito records has been lost by the time the signals reached Delta. A related reason is that since Q values are uncertain, it is better to work with the Riito records for which, due to the proximity to the source, errors in the estimation of Q will have a smaller effect. Since the transverse component is the one having more energy and hence the highest signal/noise ratio, it will be emphasized in the following analyses.

As an approximation, the effect of a point source traveling horizontally, with step function time behavior, was computed by convolution with a boxcar function with width determined from the known fault plane-station angle, and a phase velocity corresponding to that for the first S-wave arrival from a source at 10km depth. Figure 13(a) shows the observed seismograms and Green's function (center) at Riito. As a rough approximation we may say that the first event is a pulse of duration about 1 second and the second event is a pulse of duration about 1/5 second. Unidirectional and bidirectional rupturing with several combinations of fault lengths and rupture velocities were tried as models. Figure 13(b) shows a sample result which approximately resembles the second event. Figure 13(c) shows two sample results which resemble the first event.

There is a wide range of source dimensions and rupture velocities which can explain a given pulse width. The pulse width T for a simple unidirectional propagating rupture is: $T = b(c/v - \cos\theta)/c$ where b is the rupture length, c is the wave velocity, v is the rupture velocity and θ is the angle between the direction of rupture and the station, $\sim 29°$. If we take c to be the wave velocity at the source 3.8km/sec, and v to be 3km/sec, then a pulse width of 1 sec for the first event can be explained

by a rupture toward the northwest of length about 10km, approximately in agreement with the observed length of the aftershock zone. If the rupture were to the southeast, the corresponding fault length would only be about 1.8km, much smaller than the length of the aftershock zone. For the second event, with pulse length about 0.2 sec, if we assume the rupture is to the southeast, the length is .4km, and if we assume that rupture is to the northwest, the rupture length is about 2km.

Because of the large uncertainty in rupture velocity, rupture length, and direction of rupture, we can conclude little beyond suggesting that the pulse widths are consistent with both events being ruptures to the northwest, the first with length about equal to the length of the aftershock zone, and the second with a smaller length.

Equivalent Source Time Function

In order to see if we could obtain an alternate indication of the dimensions and time duration of the source, we have used a technique of deconvolution of the observed seismogram by the theoretical point source response. The step function convolution factor $C(t)$ is defined as the factor that, when convolved with a step function (i.e., integrated), yields the "source time function" $S(t)$ which represents the combined effects of the spatial and temporal behavior of the source. It may be obtained as the inverse Fourier transform of

$$C(\omega) = \frac{A(\omega)}{A_0(\omega)}$$

where $A(\omega)$ is the spectrum of the observed seismogram, and $A_0(\omega)$ is the spectrum of the synthetic seismogram (obtained using a step source time function), both suitably filtered [*Nava*, 1980]. Interpretations here will be based mainly on $C(t)$. The second event will be considered first since it is simpler. For the second event (Figure 14), $C(t)$ appears to have a shape not incompatible with a band limited (Dt = .08 sec) version of the boxcar function that would be expected from the results of the simple directivity calculations earlier. The only complication appears to be at the point marked as "B," which could be interpreted as a second minor energy pulse.

The result for the first event at Riito (transverse component) is shown in Figure 15. The same filtering was applied. In this case, $C(t)$ is more complicated although roughly consistent with a source duration of about 1 sec. The event may be composed of perhaps six smaller pulses indicated as A, B, C, D, E, F, although this is speculative.

Moment Estimated from Strong-Motion Records

The long period portion of the displacement spectra for the strong motion records is not very reliable due to the presence of noise and the effects of low frequency filtering in the base line correction. Thus, the method for the determination of the seismic moment from the flat long period portion of the far field displacement spectrum has to be applied very cautiously.

The long period level associated with the second event at Riito, after being corrected for the effects of the sedimentary amplification, free surface amplification and radiation pattern yields the moment $M_0^{R2} = 6.39 \times 10^{23}$ dyne-cm. The corresponding values for the first event at Riito is $M_0^{R1} = 1.74 \times 10^{24}$ dyne-cm. The sum of these two values yields a total moment $M_0^{R1+R2} = 2.38 \times 10^{24}$ dyne-cm. The seismic moment can also be estimated from the area under the step-function convolution factor $C(t)$, obtained above, times the known synthetic moment, and nearly the same results are obtained ($M_0^{R2} = 5.98 \times 10^{24}$ dyne-cm, and $M_0^{R1} = 1.54 \times 10^{24}$ dyne-cm, and the sum $M_0^{R1+R2} = 2.14 \times 10^{24}$ dyne-cm). The fact that both sums are somewhat smaller than the total moment determined from surface waves at distant stations (see below) indicates some contribution to the total moments from periods longer than those reliably recorded on the strong motion records.

Overall Moment Estimated from Distant Stations

The seismic moment for the Mesa de Andrade earthquake was also estimated by comparison of observed surface waves at seven stations with synthetic surface wave seismograms computed using

Harkrider's [1964, 1970] method. The synthetic seismograms were computed for the Great Basin velocity structure [*Priestly and Brune*, 1978] and a source depth of 10km. A composite synthetic seismogram for directivity and summing the modified seismograms for the two strong motion events, appropriately scaled and shifted in time [*Nava*, 1980]. This composite seismogram showed that the second event was sufficiently delayed so that it does not appreciably influence the value of M_0 as measured from the long periods at the beginning of the record. The average moment obtained was 2.14×10^{24} dyne-cm $\pm$ .57 $\times 10^{24}$ dyne-cm. The true overall moment is probably slightly larger because of the long period waves from the second event arriving too late to be taken into account. Since the moments estimated from the strong motion instruments indicate that the moment for the second event is .35 times that of the first event, an estimate for the Mesa de Andrade moment as would have been determined using waves with periods long compared with the 45 seconds between the two events is about $M_0 \simeq 2.89 \times 10^{24}$ dyne-cm.

Overall Source Dimensions and Stress Drop

For distant stations, the two events appear as one complex event, and the contribution of the second event to the magnitude (especially M_s) is relatively small. Also, as seen above, its contribution to the value of the moment which would have been obtained by fitting the early long-period part of the distant records (without realizing that there were two events involved) will be very small. The aftershock area probably gives the most reliable estimation of the overall source dimension; it would be the only estimation possible for an observer not having the strong motion information. Hence, the results obtained from this assumption will be representative of the usual determination when only aftershock data is available. The aftershock distribution with a length of ~11.5km and a depth range of ~4.5km, suggests the use of a rectangular fault model, although as mentioned before, the aftershock depth determination is somewhat uncertain so the estimation of the depth range may not be accurate. Thus, the possibility of a circular source with radius $r = L/2 = 5.75$km may be considered as an upper bound for the source area. Use of these two fault geometries, plus the overall moment $M_0 = 2.89 \times 10^{24}$ dyne-cm, yields $\Delta\sigma = 15.53$ bars for the rectangular fault, and $\Delta\sigma = 5.81$ bars for the circular one. The average displacement across the fault, $\bar{u}$, was approximately 5 to 10cm.

COMPARISON AND INTERPRETATION OF THE PARAMETERS FOR BOTH EARTHQUAKES

The parameter values determined above will now be discussed, together with other published values for other earthquakes in the region. Table I is a compilation of the estimated seismic parameters for both earthquakes, including ratios of values. Values determined from short periods, $T < 5$ sec, are denoted by an asterisk. For the two Mesa de Andrade events separately the equivalent local magnitude, M_L, was determined from the deconvolution-convolution technique suggested by *Kanamori and Jennings* [1979] to produce equivalent Wood-Anderson records from strong motion records. For logarithmic quantities like the magnitudes, the logarithm of the ratio (logratio) shown is the difference between the values being compared. The energies (E_s) were computed from the local magnitudes using the revised *Gutenberg-Richter* [1956] relation ($\log E = 9.9 + 1.9\ M_L - 0.024\ M_L^2$), and the apparent stresses $\eta\bar{\sigma}$ [*Aki*, 1966] were calculated using these energy values.

A comparison of M_s and M_L for the Pino Solo and Mesa de Andrade earthquakes shows that M_s/M_L is much larger for Mesa Andrade than for Pino Solo, as discussed earlier. This raises the question: is M_s unusually large (for the given M_L) for Mesa de Andrade, or unusually small for Pino Solo, or partly both? If we choose as references the M_s versus M_L relationships found by *Wyss and Brune* [1968] for the Western United States and for the Parkfield region we obtain estimated M_s values of 4.6 and 4.9 for the Pino Solo earthquake and 4.9 and 5.2 for the Mesa de Andrade earthquake. Thus, it is the Pino Solo earthquake which has an anomalously low M_s (4.0). This next raises the question as to whether the Pino Solo earthquake, having such a low M_s, could be discriminated from explosions on an M_s/M_b diagram. Figure 16 is an M_s/m_b plot modified from *Hartzell* [1978], after *Marshall and Basham* [1972], showing the Pino Solo and Mesa de Andrade earthquakes. Both events discriminate from explosions, but Pino Solo is a borderline case while Mesa de Andrade lies well within the earthquake population.

A comparison of M_0 and M_L values for the Pino Solo and Mesa de Andrade earthquakes with a plot of M_0 versus M_L from *Thatcher* [1972] shows that the M_0 data for the Pino Solo earthquake plots near the border between the "Northern Baja" population and the "Gulf" population. The Mesa de Andrade values lie within the Gulf population.

Comparison of the M_L and source dimension data in Table I with the plot of M_L versus source dimension shown in *Thatcher* [1972] also indicates that the Pino Solo earthquake and the Mesa de Andrade earthquake have characteristics similar to earthquakes from Thatcher's "Northern Baja" and "Gulf" group, respectively, however the Pino Solo earthquake lies near the border between the two populations.

Figure 17, modified from *Thatcher and Hanks* [1973], is a graph showing source dimension, moment and stress drop for earthquakes from various California locations. The Mesa de Andrade earthquake is close to the "Gulf" population and the Pino Solo earthquake lies between the "Gulf" population and the "Northern Baja" population.

The following is a summary of the comparisons just made:

(a) The Pino Solo and Mesa de Andrade earthquakes, as measured at distant stations, appear to be approximately representative of their respective regions.

(b) Using the parameter values for Pino Solo as a reference, some characteristics common to the corresponding values for the Mesa de Andrade earthquake measured at distant stations are: (i) relative to M_s, m_b is smaller; (ii) relative to M_0, M_L is smaller; (iii) relative to the source dimension, M_L is smaller.

(c) The second Mesa de Andrade event probably had a smaller source dimension (and higher stress drop) than either the Pino Solo earthquake and the first Mesa de Andrade event.

(d) The overall average stress drop is approximately the same for the Pino Solo and Mesa de Andrade events.

Interpretation

In order to interpret the similarities and differences between the parameters of the Pino Solo and Mesa de Andrade earthquakes presented above, it is important to consider the frequency associated with each measurement. A good example of this is indicated in the Wood-Anderson records shown in Figure 1, where it can be seen that the maximum amplitude (and hence the M_L value) is associated with a frequency $\simeq 1.81$ Hz (period $\sim.55$ sec) for the Pino Solo record, and with a frequency of $\sim.33$ Hz (period ~ 3 sec) for the Mesa de Andrade record. Values of parameters and the frequencies at which they were measured have been converted into spectral values and plotted in Figure 18, together with values from actual measured spectra, to illustrate the relation of the measured parameters to the spectra.

All observed values were converted into spectral values corresponding to a distance R = 10km and an "average" azimuth (such that the radiation pattern $R_{\theta\phi} = .6$) in a homogeneous full-space characterized by a density $\rho = 2.7$g/cc, and a shear wave velocity $\beta = 3.7$km/sec (values appropriate for the crust under the Imperial Valley). Thus, the spectral density associated with a particular value of the moment is obtained from the relation [*Keilis-Borok*, 1960]

$$M_0 = \frac{4\pi\rho\beta^3}{R_{\theta\phi}} R\Omega_0$$

which for our case gives

$$\Omega_0 = 3.4912 \times 10^{-25} M_0$$

(Ω_0 in cm-sec, M_0 in dyne-cm).

The observed spectral values were transformed into equivalent full-space values by correcting for distance by a factor of 10km divided by epicentral distance; for amplification at the free surface by a factor of .5, for radiation by a factor of .6 divided by the observed $R_{\theta\phi}$ value and for the amplification of the Imperial Valley sediments, by multiplying by a factor of .4 [*Hartzell and Brune*, 1971]. Since the

BAR record for the Pino Solo earthquake was not suitable for digitization, the short period spectral value was estimated from the synthetic spectrum scaled so that the synthetic seismogram would have the same maximum amplitude as the observed one.

Relative magnitude values were used to estimate relative spectral values in the following way: the value of the magnitude measured for Pino Solo was associated with the Pino Solo spectrum at the frequency at which the magnitude measurement was made, and used as the reference from which the relative position of the corresponding spectral value for the Mesa de Andrade earthquake was placed (after correcting for the effects of different frequencies and/or instrument response). The reference points on the curve for Pino Solo are: $M_L = 5.1$ at a frequency of 1.81 Hz, $m_b = 4.9$ at $\sim$.82 Hz, and $M_s = 4.0$ at $\sim$.073 Hz (see Figure 18). The relative spectral values thus determined for the Mesa de Andrade events are represented on Figure 18 as triangles, identified by their magnitude value and the type of magnitude they represent (connected to the corresponding value for the Pino Solo earthquake by a dotted line).

Error bars associated with magnitude are .1 magnitude unit in each direction, representing the standard error found for the distant station determination of local magnitude for both earthquakes (the Pino Solo M_L value at BAR, shown as a circle with a B in it, is not very reliable, since it was measured from a single component). The other symbols used in Figure 18 are the same as for previous figures.

The solid lines in Figure 18 represent approximate fits to the equivalent spectral values (dashed where only approximately established). As a rough check on these results we also calculated the spectra from the Pasadena Wood-Anderson records of each earthquake. The results approximately confirmed the relative positions of the overall spectra shown in Figure 18 at frequencies below .5Hz. They also approximately confirmed the absolute positions of the curves, under the assumption that the waves recorded on the Wood-Anderson records were body waves, with corrections made approximately as done by *Thatcher and Hanks* [1973]. The curve with large dash marks labeled $\Omega_M(\gamma=2)$ is the estimated overall spectrum for the Mesa de Andrade earthquake with a high frequency falloff beyond the corner frequency assumed to be proportional to f^{-2}.

We are now in a position to attempt to answer some of the questions that prompted the present work.

As noted earlier, the Pasadena Wood-Anderson seismogram for the Pino Solo earthquake (Figure 1) is relatively simple, most of the energy arriving in a burst of only a few seconds duration, while the seismograms for the Mesa de Andrade earthquake is more complex, with both the high frequency energy $(F > 1$ Hz) and lower frequency energy arriving over a much longer period of time $(\sim 1$ minute). However the Riito integrated strong motion displacement seismogram for the Mesa de Andrade earthquake at a distance of $\sim$18km (bottom, Figure 1), indicates that the actual energy release occurred in two relatively simple events, the first containing considerably more low frequency energy than the first (see spectra in Figure 18), while the second was a sharper event with somewhat higher accelerations (see also Figure 8). Figure 1 indicates that most of the complexity observed on the Mesa de Andrade seismogram must have come from scattering and multipathing as a result of the complex geologic path between the Mesa de Andrade earthquake and Pasadena. For the Pino Solo record, the geologic path to Pasadena is much simpler, and this results in a relatively simple pulse of energy. Thus the comparison in Figure 1 shows that the high frequency energy from the Mesa de Andrade earthquake has been spread out in time and this may have reduced the M_L magnitude for Mesa de Andrade relative to the Pino Solo. The spreading out of energy by scattering will have a much less pronounced effect on spectra than on M_L. It is also possible that differential attenuation due to lower Q values for the part of the propagation path in the Salton trough has selectively reduced the high frequencies for the Mesa de Andrade earthquake.

The moments and corner frequencies shown in Figure 18 are in approximate agreement with ω^{-2} for the spectra of earthquakes [*Aki*, 1967; *Brune*, 1970,1971; *Hanks*, 1979]. The corner frequency of the Mesa de Andrade earthquake (ignoring Ω_{M2}) is about a factor of two lower than for the Pino Solo earthquake, whereas the corresponding low frequency amplitudes are approximately eight times higher. Thus the corner frequencies and moments for the Mesa de Andrade and Pino Solo earthquakes are in agreement with the $\gamma = 2$ model for two earthquakes of approximately the same stress drop, but with source dimensions a factor of two different [*Hanks*, 1979].

However, the Riito strong motion spectra are not consistent with the $\gamma = 2$ model (Figure 18). For the first event the spectra are about three times higher between .8Hz and 2Hz, and for the second event the spectra are about four times higher at 1Hz and seven times higher at 2Hz to 5Hz, estimated relative to the heavy dashed line labeled $\Omega_M(\gamma=2)$ in Figure 18. This is probably a result of both rupture propagation toward Riito and a higher stress drop for the second event. This causes M_L^* (Table I) determined from the nearby Riito strong motion record (using the technique of *Kanamori and Jennings* [1979]), to be higher for the second event (5.5) than for the first event (5.2). At other azimuths and larger distances (where the high frequencies have been attenuated and scattered) and focusing is not effective, M_L calculated for the second event, if it could be seen, would probably be smaller for the second event than for the first event (because the moment and low frequency spectrum are lower). Actually, the energy from the second event cannot be clearly identified at distant stations because of the presence of energy from the first event (see Figure 1).

The M_L^* values computed for station Delta are even higher, about 6.1 for both the first and second events. This could be in large part due to directively focusing since Delta is directly in the direction of rupture. However there may be other factors contributing, e.g. local amplification, or perhaps the Richter attenuation curve assumed in the calculation of M_L^* is not appropriate for the region. The station Delta also recorded anomalously high ground motion from the 1979 Imperial Valley earthquake [*Brune et al.*, 1981].

The relatively high ground motion at Riito and Delta clearly demonstrate the difficulty in predicting peak motion in the near field from parameters measured at distant stations. The acceleration value of .21 and .24g at Riito exceed the 84 percentile correlation curves of *Joyner et al.*, [1982]. The Delta peak acceleration values exceed these curves by more than a factor of 2.

CONCLUSION

The overall stress drops for the Mesa de Andrade and Pino Solo earthquakes were found to be nearly the same, but the source dimension of the Mesa de Andrade earthquake is approximately two times that of the Pino Solo earthquake. In terms of the $\gamma = 2$ seismic source model, this explains most of the greater moment and greater excitation of surface waves for the Mesa de Andrade earthquake. The difference in local magnitude (0.2) is also, within the uncertainty in measurement, consistent with the $\gamma = 2$ model. However greater complexity in the Wood-Anderson records from the Mesa de Andrade earthquakes, when compared with the simple displacement strong motion records, indicates that scattering due to complexities in geologic path effects the magnitude determinations from earthquakes in the Salton trough and could be in part responsible for the apparent higher excitation of surface waves from earthquakes in that area. However, final determination of the reason for the differences in surface wave excitation must await more studies of the type presented here, especially for larger earthquakes.

The high accelerations and spectra recorded at the strong motion stations Riito and Delta are not expected from the $\gamma = 2$ model, and may have resulted from near field focusing (directivity). Another possibility is that they represent two relatively high stress drop events (possibly asperities breaking) on an otherwise relatively low stress-drop rupture surface.

REFERENCES

Allen, C., 1968. The tectonic environment of seismically active and inactive areas along the San Andreas fault. *Stanford Univ. Publ. Geol. Sci.* **11**, 70−82.

Alonso, H., 1966. La zona geotermica de Cerro Prieto, Baja California. *Bol. Soc. Geol. Mex.* **29**-1, 17−47.

Apsel, R. and Luco, E., 1978. Dynamic Green functions for a layered half-space. University of California, San Diego Report: Dept. of Appl. Mech. and Eng. Sci., UCSD, La Jolla.

Brune, J., Espinosa, A. and Oliver, J., 1963. Relative excitation of surface waves by earthquakes and underground explosions in the California-Nevada region. *J. Geophys. Res.* **68**, 11, 3501−3513.

Brune, J., 1970. Tectonic stress and the spectra of seismic shear waves from earthquakes. *J. Geophys. Res.* **75**, 26, 4997−5009.

Brune, J., 1971. Correction. *J. Geophys. Res.* **76**, 20, 5002.

Brune, J., Archuleta, R. and Hartzell, S., 1979a. Far-field S-wave spectra, corner frequencies, and pulse shapes. *J. Geophys. Res.* **84**, B5, 2262−2272.

Buland, R., 1976. The mechanics of locating earthquakes. *Bull. Seism. Soc. Am.* **66**, 1, 173−187.

Gaulty, N., Burford, R., Allen, C., Gilman, R., Johnson, C. and Keller, R., 1978. Large creep events on the Imperial fault, California. *Bull. Seism. Soc. Am.* **68**, 2, 517−521.

Gutenberg, B. and Richter, C., 1956. Magnitude and energy of earthquakes. *Ann. Geofis (Roma)* **9**, 1−15.

Harkrider, D., 1964. Surface waves in multilayered elastic media. Part I. Rayleigh and Love waves from buried sources in a multilayered elastic halfspace. *Bull. Seism. Soc. Am.* **54**, 627−679.

Harkrider, D., 1970. Surface waves in multilayered elastic media. Part II. Higher mode spectra and spectral ratios from point sources in plane layered earth models. *Bull. Seism. Soc. Am.* **60**, 1937−1987.

Hartzell, S. and Brune, J., 1977. Source parameters for the January 1975 Brawley-Imperial Valley earthquake swarm. *Pageoph* **115**, 333−355. (*In*: Stress in the Earth, Ed., Max Wyss, 458pp, Birkhauser)

Hartzell, S., 1978. Interpretation of earthquake strong-motion and implications for earthquake mechanism. Ph.D. Thesis, University of California, San Diego, 269pp.

Henyey, T. and Bischoff, J., 1973. Tectonic elements of the northern part of the Gulf of California. *Geol. Soc. Am. Bull.* **84**, 1, 315−330.

Kanamori, H. and Jennings, P., 1978. Determination of local magnitude, M_L, from strong motion records. *Bull. Seism. Soc. Am.* **65**, 471−485.

Keilis-Borok, V., 1960. Investigation of the mechanism of earthquakes. *Sov. Res. Geophys.* **4** (Transl. *Tr. Geofiz. Inst.* **40**, 1957) AGU, Consultants Bureau, NY, 201pp.

Kovach, R., Allen, C. and Press. F., 1962. Geophysical investigations in the Colorado Delta region. *J. Geophys. Res.* **67**, 2845−2872.

Liebermann, R. and Pomeroy, P., 1969. Relative excitation of surface waves by earthquakes and underground explosions. *J. Geophys. Res.* **74**, 6, 15775−1590.

Madariaga, R., 1977. Implications of stress-drop models of earthquakes for the inversion of stress-drop from seismic observations. *Pageoph* **115**, 301−316. (*In*: Stress in the Earth; Ed. Max Wyss, Birkhauser)

Marshall, P. and Basham, P., 1972. Discrimination between earthquakes and underground explosions employing an improved M_s scale. *Geophys. J. R. Astro. Soc.* **28**, 431−458.

Munguia, L, J.N. Brune, R. Adair, J. Gonzalez, R. Simons and F. Vernon, 1978. Digital seismograph and strong motion recordings of earthquakes in the Victoria, B.C., Mexico swarm of March, 1978. Abstract in *EOS* **59**, 12, 113l.

Nava, A., 1980. Study of seismic wave excitation for two earthquakes in Northern Baja California. Ph.D. Thesis, University of California, San Diego, 268pp.

Nava, A. and Brune, J., 1981. An earthquake-explosion reversed refraction line in the Peninsular Ranges of Southern California and Baja California Norte. *Bull. Seism. Soc. Am.* (submitted).

Prian, R., 1978. Correlaciones litológicas de los pozos del campo de Cerro Prieto con base en la interpretación de los registros eléctricos. *In*: Proceedings of the First Symposium on the Cerro Prieto Geothermal Field, Baja California, Mexico (456pp), 49−56.

Priestley, K. and Brune, J., 1978. Surface waves and the structure of the Great Basin of Nevada and Western Utah. *J. Geophys. Res.* **83**, 2265—2272.

Prince, J., Brune, J. and Nava, A., 1977. Strong motion instrumentation of Northern Baja California. *Geol. Soc. Am. Abstracts with Programs* **9**, 4, 484. Meeting of the Seismological Society of America, April 5—7, 1977, Sacramento, California.

Smith, D., 1974. Heat flow, radioactive heat generation and theoretical tectonics for Northwestern Mexico. *Earth Planet. Sci. Lett.* **23**, 43—52.

Smith, D., Nuckels, C., Jones, R. and Cook, G., 1979. Distribution of heat flow and radioactive heat generation in Northern Mexico. *J. Geophys. Res.* **84**, B5, 2371—2379.

Thatcher, W. and Brune, J., 1971. Seismic study of an oceanic ridge earthquake swarm in the Gulf of California. *Geophys. J. R. Astr. Soc.* **22**, 473—489.

Thatcher, W., 1972. Regional variation of seismic source parameters in the Northern Baja California area. *J. Geophys. Res.* **77**, 8, 1549—1565.

Thatcher, W. and Hanks, T., 1973. Source parameters of Southern California earthquakes. *J. Geophys. Res.* **78**, 35, 8547—8576.

Thatcher, W., 1979. Horizontal crustal deformation from historic geodetic measurements in Southern California. *J. Geophys. Res.* **84**, B5, 2351—2370.

Trifunac, M. and Brune, J., 1970. Complexity of energy release from the Imperial Valley, California, earthquake of 1940. *Bull. Seism. Soc. Am.* **60**, 1, 137—160.

Trifunac, M. and Lee, V., 1973. Routine computer processing of strong-motion accelerograms. Earthquake Eng. Res. Dept., California Institute of Technology, Pasadena, CA.

Tsai, Y. and Aki, K., 1970. Precise focal determination from amplitude spectra of surface waves. *J. Geophys. Res.* **75**, 5729—5743.

Wyss, M. and Brune, J., 1968. Seismic moment, stress, and source dimensions for earthquakes in the California-Nevada region. *J. Geophys. Res.* **73**, 14, 4681—4694.

Wyss, M. and Brune, J., 1971. Regional variations of source properties in Southern California estimated from the ratio of short to long-period amplitudes. *Bull. Seism. Soc. Am.* **61**, 1153—1167.

TABLE I

PARAMETER	PINO SOLO VALUE		MESA DE ANDRADE VALUE	PINO SOLO/ MESA DE ANDRADE	
				Ratio	Logratio
M_0 (dyne-cm)	3.4×10^{23}		2.9×10^{24}	.12	$-$ .93
M_0^* (dyne-cm)	1.6×10^{23}	(1)	1.7×10^{24}	.09	-1.03
		(2)	6.4×10^{23}	.25	$-$ .60
M_L	5.1		5.3	.63	$-$ .20
M_L^*		(1)	5.2	.40	$-$ .40
		(2)	5.5	.20	$-$ .70
m_b	4.9		5.3	.40	$-$ .40
M_s	4.0		5.1	.08	-1.10
D (km)	5.3		11.5	.46	$-$ .34
D^* (km)	5.3		~ 11.5	.46	$-$ .34
$\Delta\sigma$ (bars)	7.9		5.8	1.36	.13
$\Delta\sigma^*$ (bars)	3.8		3.5	1.09	.04
$\bar{u}$ (cm)	3.9		7.4	.53	$-$ .28
$\bar{u}^*$ (cm)	1.8	(1)	3.9	.46	$-$ .34
E_s (ergs)	9.2×10^{18}		2.0×10^{19}	.46	$-$ .34
E_s^* (ergs)	2.9×10^{18}	(1)	1.4×10^{19}	.21	$-$ .68
$\eta\bar{\sigma}$ (bars)	10.9		3.5	3.11	.49
$\eta\bar{\sigma}^*$ (bars)	7.3	(1)	3.1	2.35	.37

PAS
TORSION NS (31)

PINO SOLO EQ. $\Delta = 337.3$ km
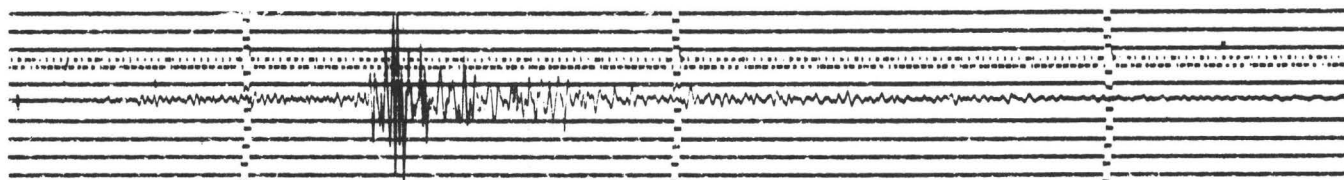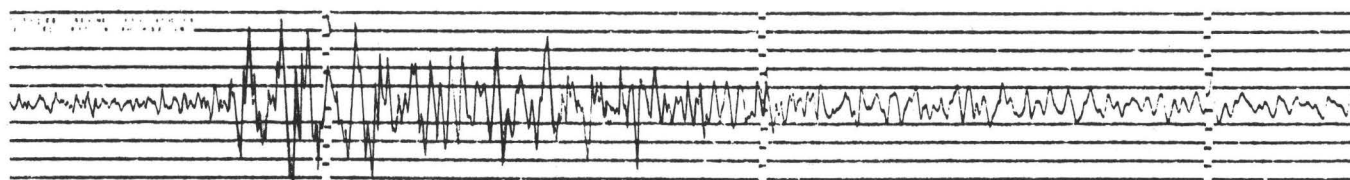

├─── 45 sec ───┤

MESA DE ANDRADE EQ. $\Delta = 387.5$ km
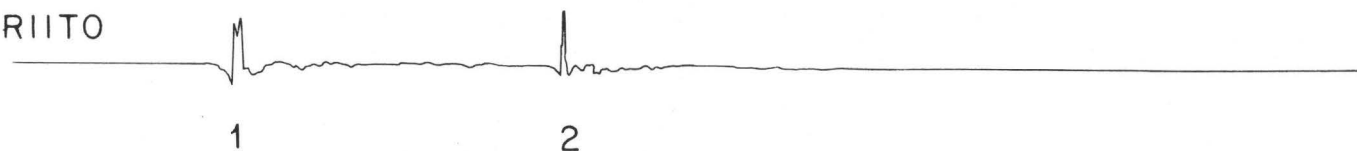

RIITO

1   2

Figure 1. Pasadena North-South component Wood-Anderson torsion seismometer records ($T_0 = .8$ sec) for the July 17, 1975 Pino Solo and Dec 7, 1976 Mesa de Andrade earthquakes. The bottom trace is the displacement strong motion seismogram for the Mesa de Andrade earthquake at Riito.

TUC LP. Z

PAS
U.L.P.Z. (35c)

PINO SOLO EQ.
Δ = 337.3 km
18 / 25

PINO SOLO EQ.
Δ = 481.4 km

MESA DE ANDRADE EQ.
Δ = 390.08 km

MESA DE ANDRADE EQ.
Δ = 387.5 km

632

Figure 2. Pino Solo and Mesa de Andrade seismograms: vertical component long-period ($T_0 = 15$ sec, $T_G = 100$ sec) from Tucson (left), and ultra long-period ($T_0 = 100$, $T_G = 480$ sec) from Pasadena (right).

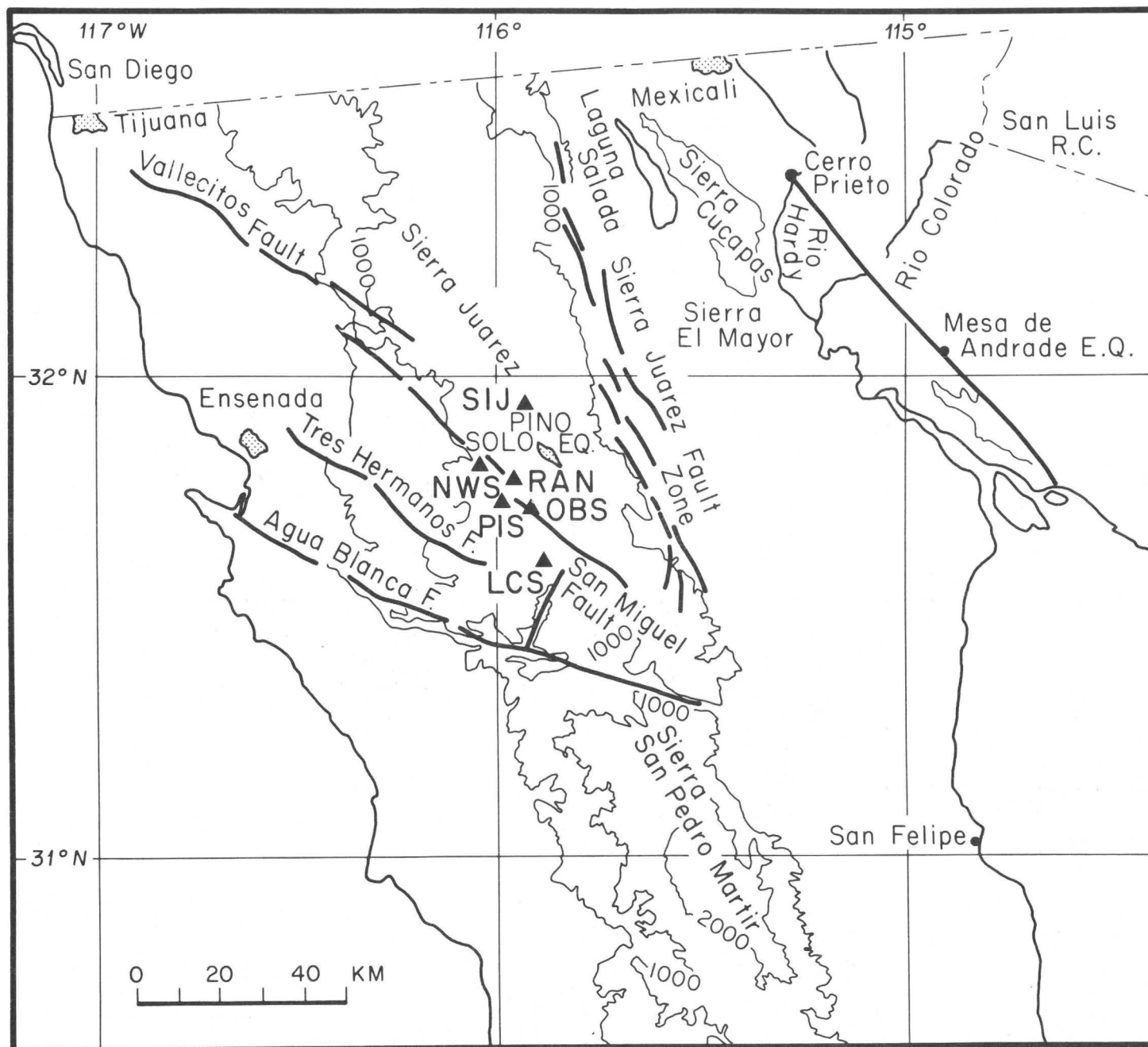Figure 3. Fault map showing locations of portable seismograph stations, permanent stations, and the aftershock zone and epicenter (hatched region) of the Pino Solo earthquake.
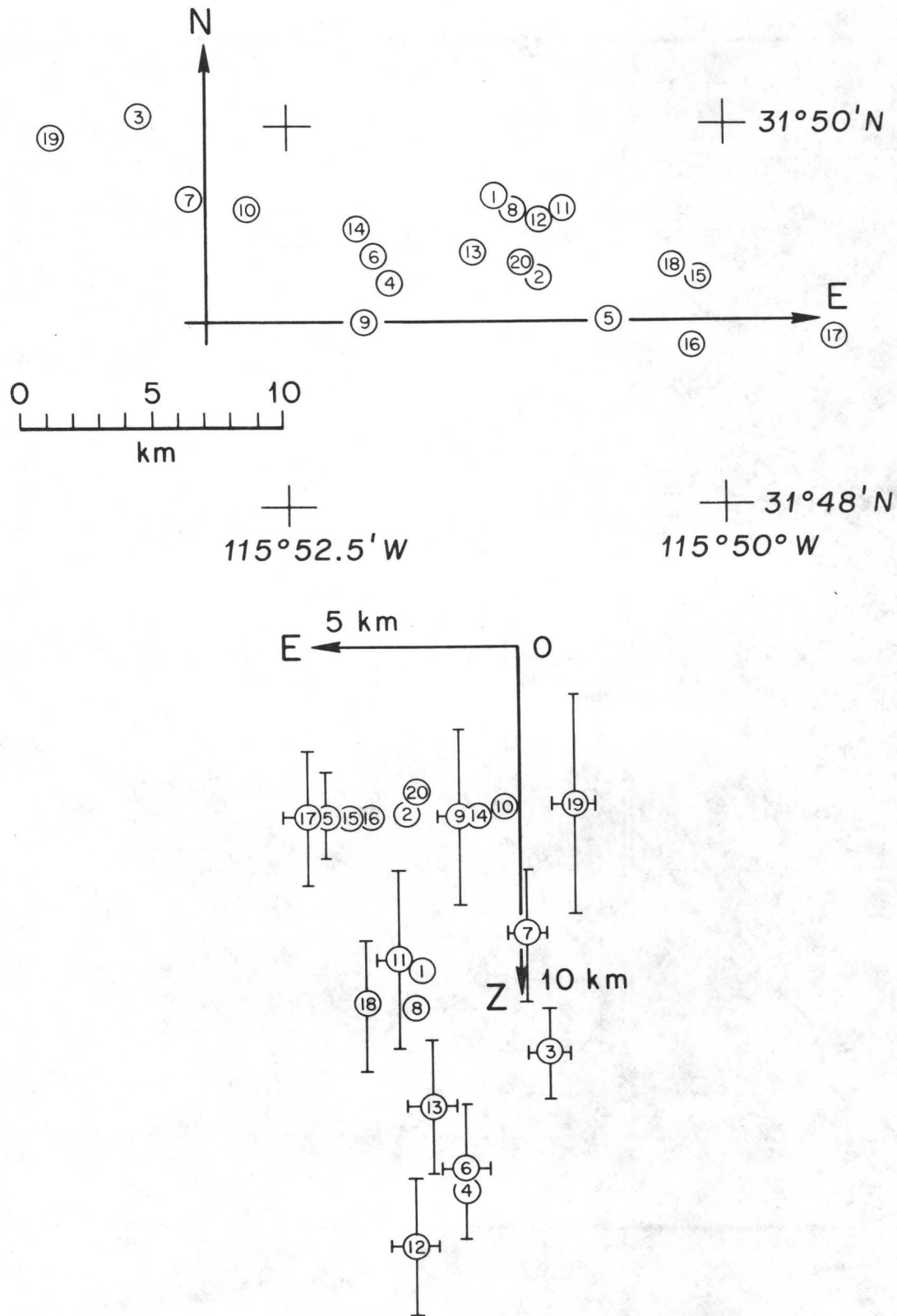
Figure 4. Detailed map of epicenters (top), and East-West cross section of hypocenters showing representative error bars, of aftershocks of the Pino Solo earthquake.
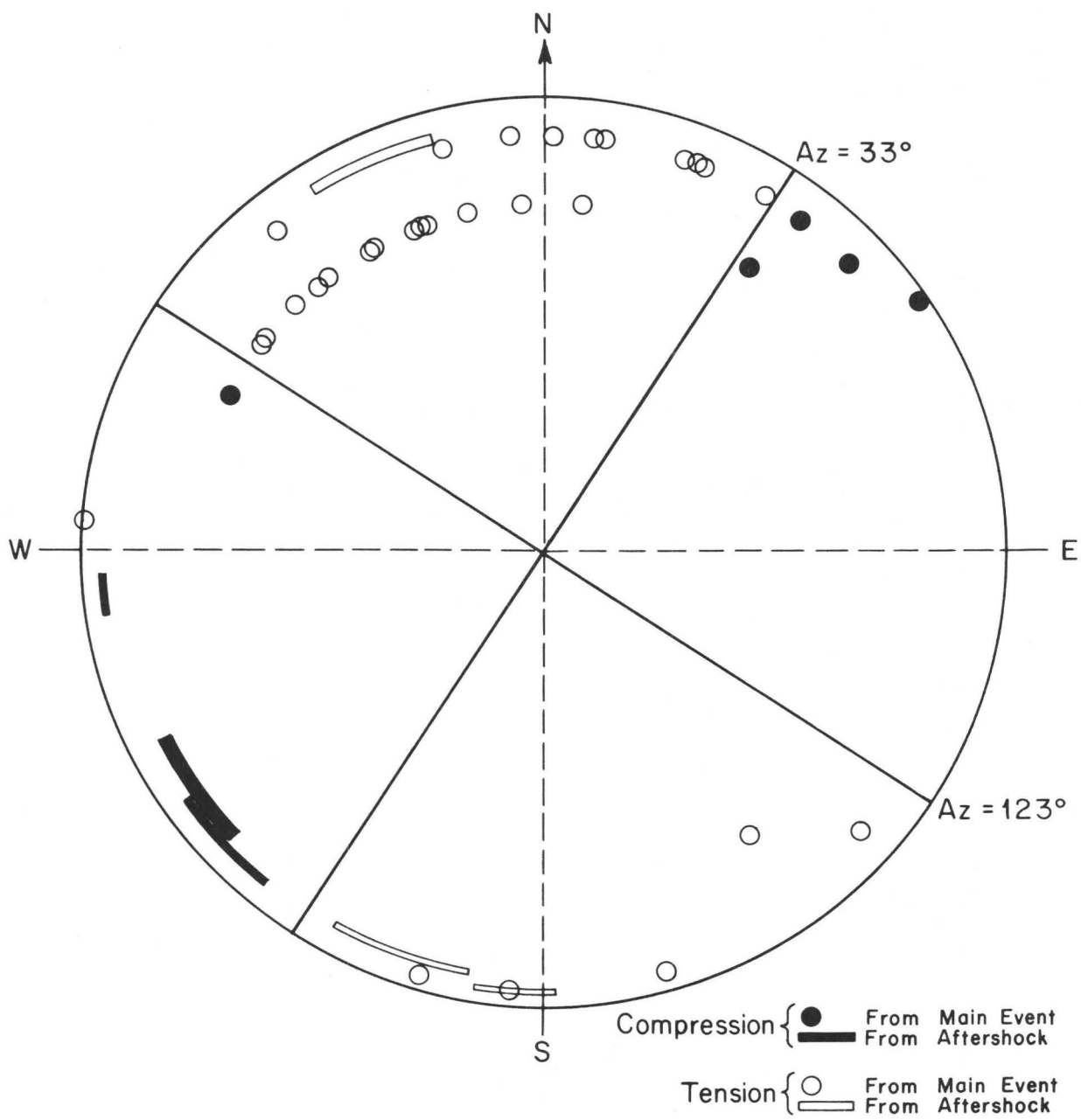
Figure 5. Wulff's net, composite fault plane solution for the Pino Solo earthquake.
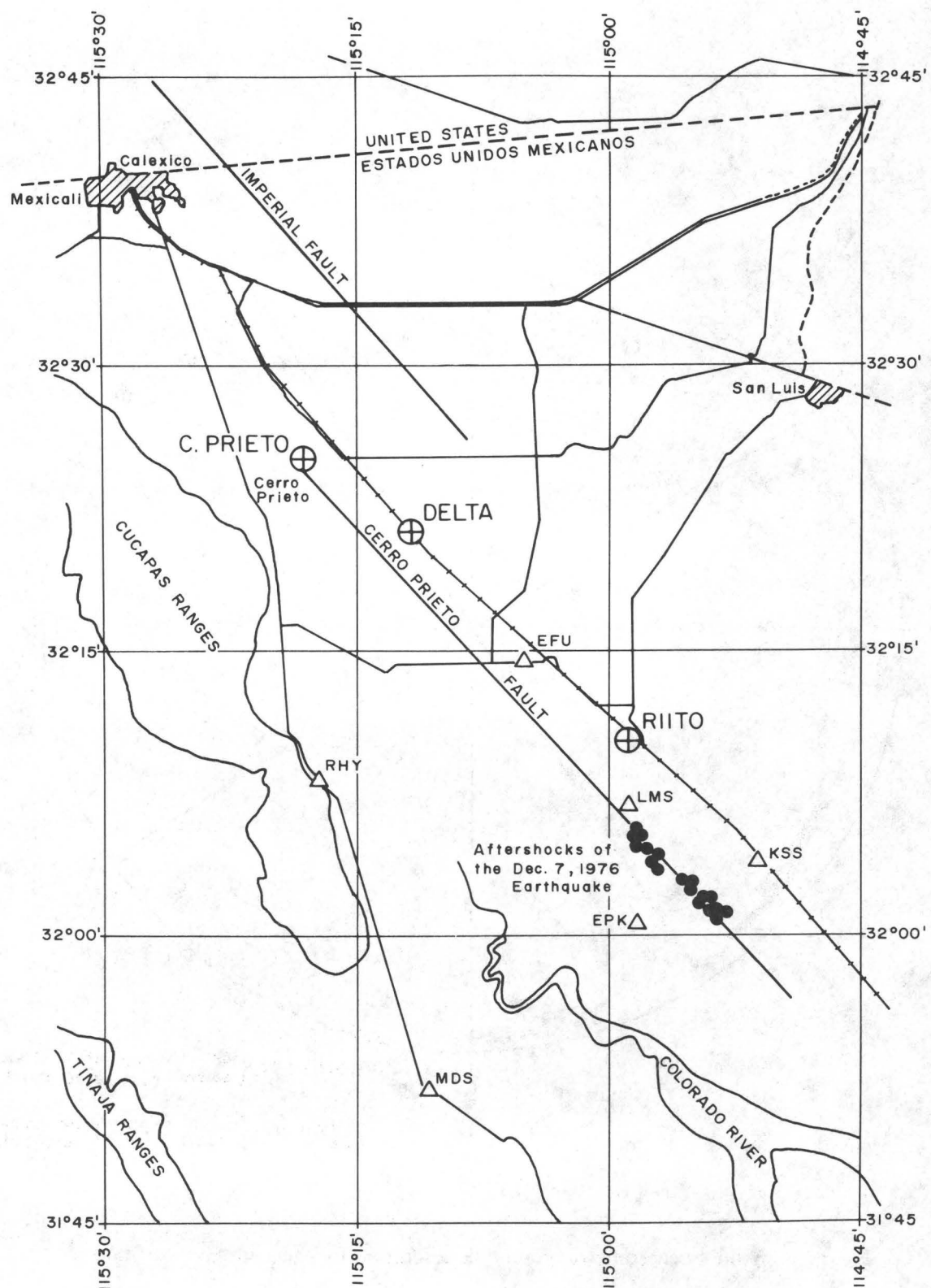
Figure 6. Map of Mexicali Valley showing locations of aftershocks (solid dots), seismograph stations (triangles), and strong motion stations (circles with crosses).
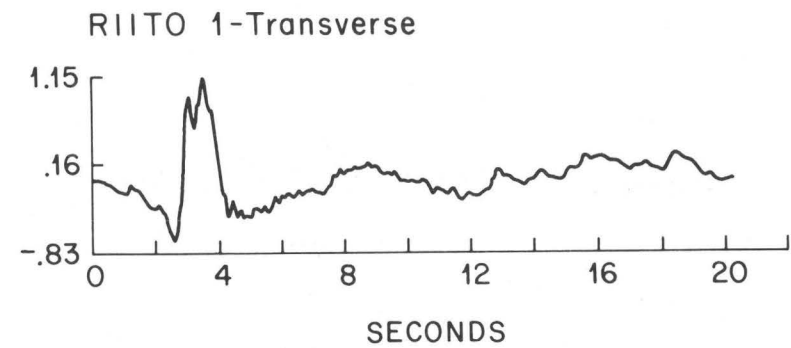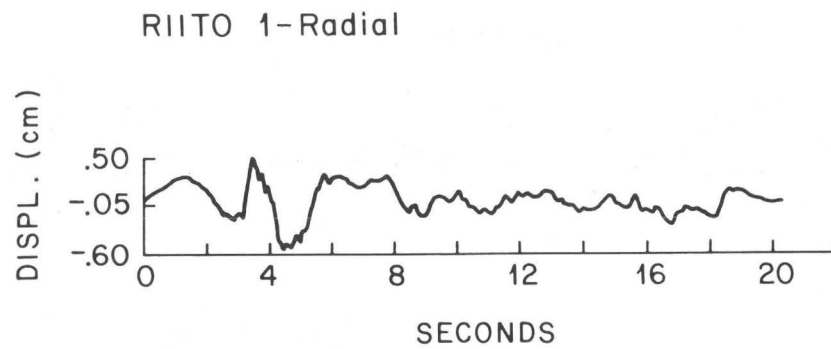
Figure 7. Riito strong-motion resolved radial and transverse displacement seismograms for first Mesa de Andrade event.
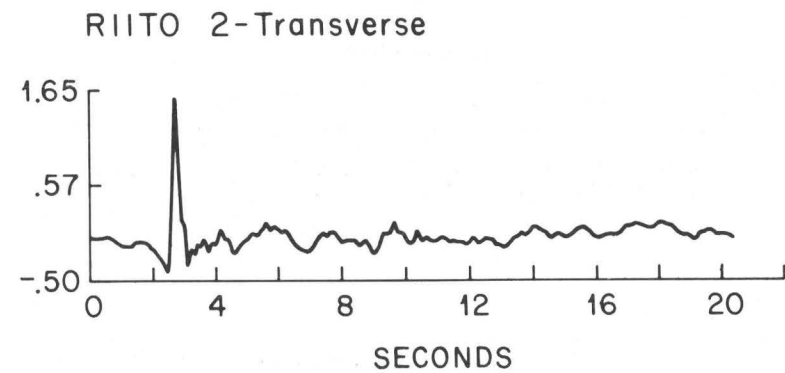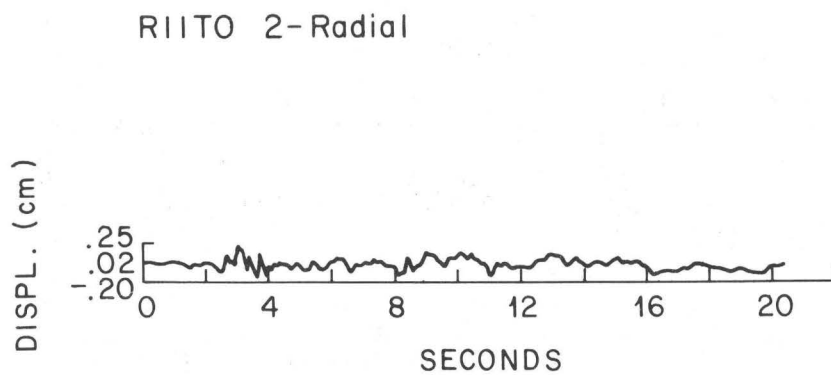

Figure 8. Riito strong-motion resolved radial and transverse displacement seismograms for second Mesa de Andrade event.

DELTA 1-Radial
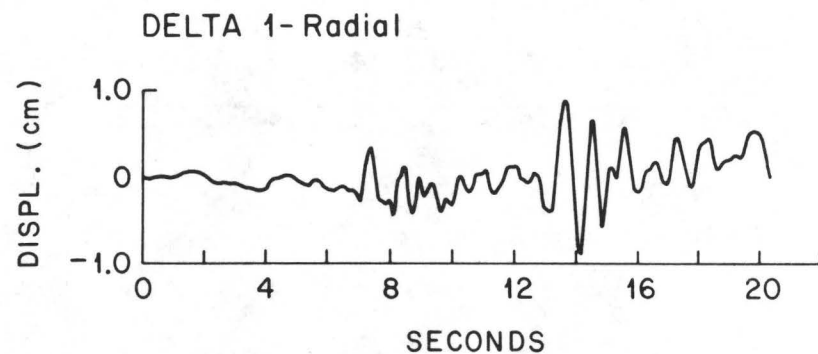
DELTA 1-Transverse

Figure 9. Delta strong-motion resolved radial and transverse displacement seismograms for first Mesa de Andrade event.
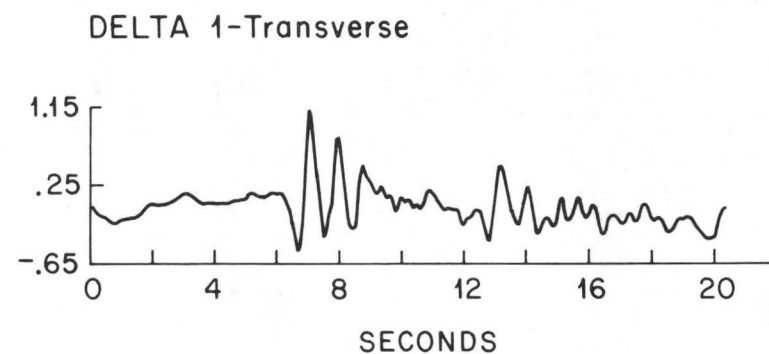
DELTA 2-Radial
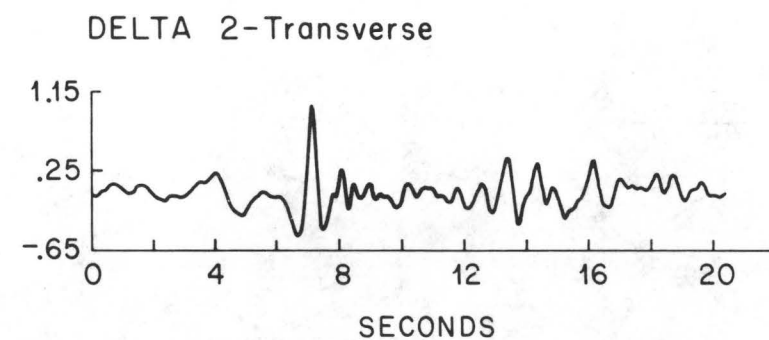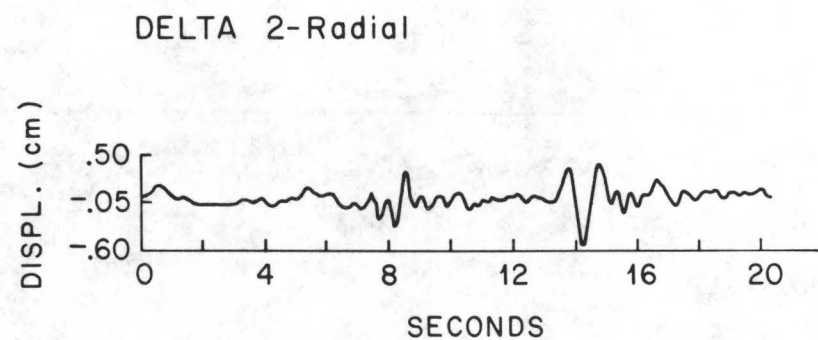
DELTA 2-Transverse

Figure 10. Delta strong-motion resolved radial and transverse displacement seismograms for second Mesa de Andrade event.

RIITO SYNTHETIC SEISMOGRAMS

Source Depth 5.0

R

AZ

Source Depth 7.0

R

AZ

Source Depth 10.0

R

AZ

Source Depth 13.0

R

AZ

Source Depth 15.0

R

AZ
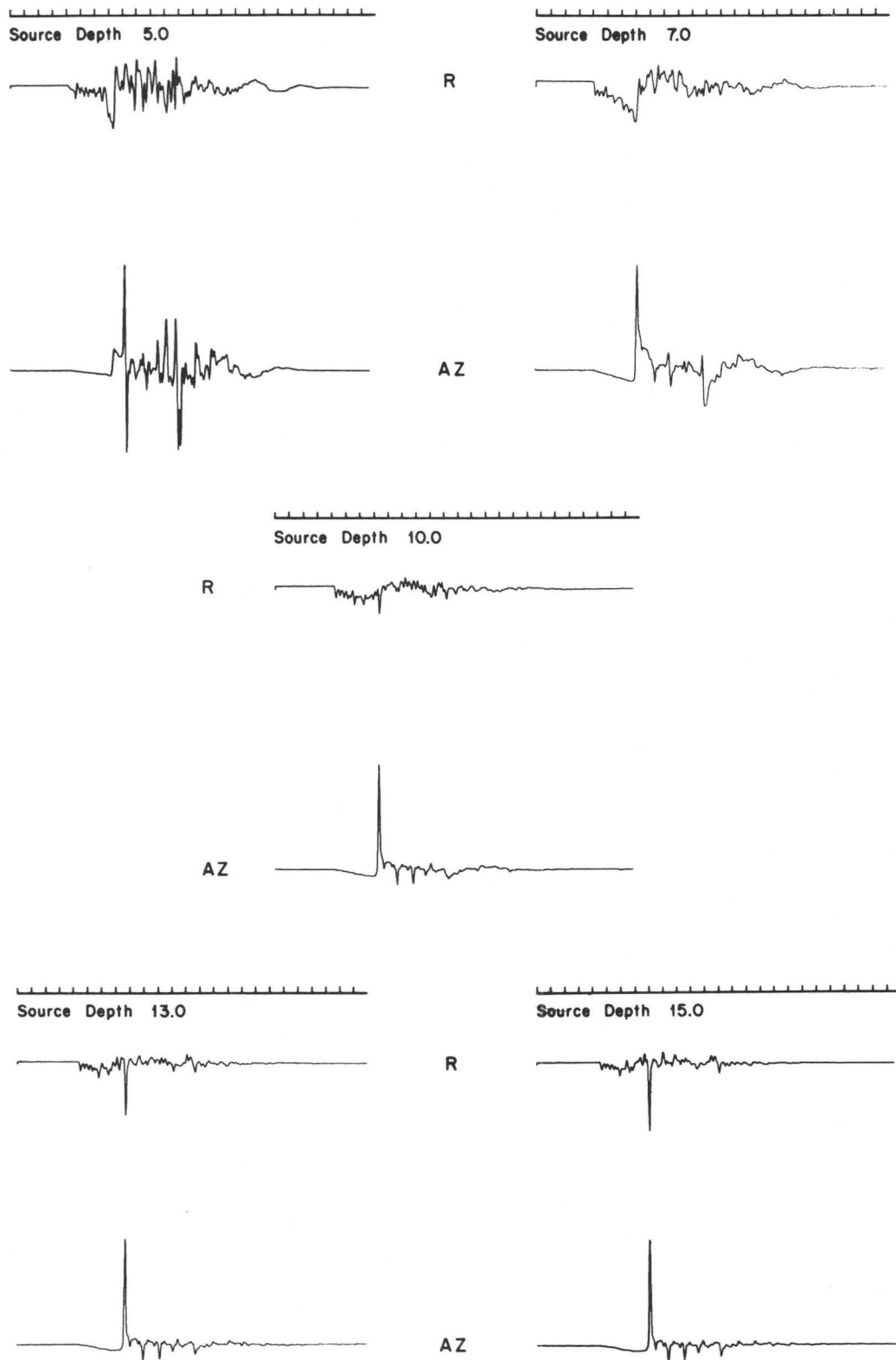
Figure 11. Riito synthetic seismograms for selected hypocentral depths.

DELTA SYNTHETIC SEISMOGRAMS

Source Depth 7.0

Source Depth 10.0

R

R

AZ

AZ

Source Depth 13.0

Source Depth 15.0

R

R

AZ
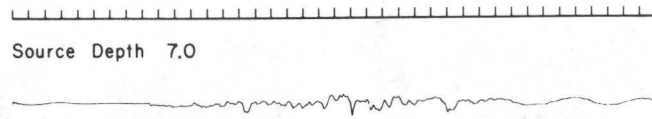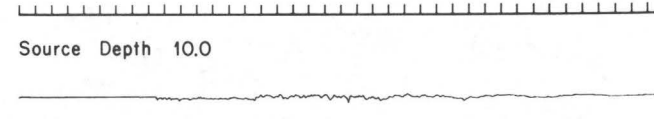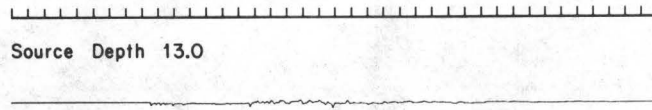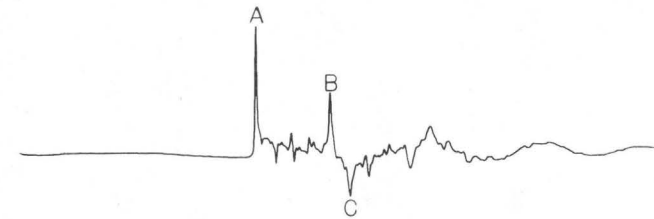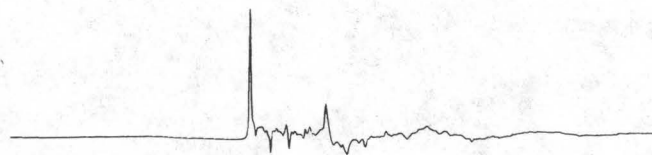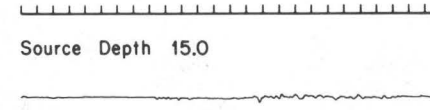
AZ

Figure 12. Delta synthetic seismograms for selected hypocentral depths.
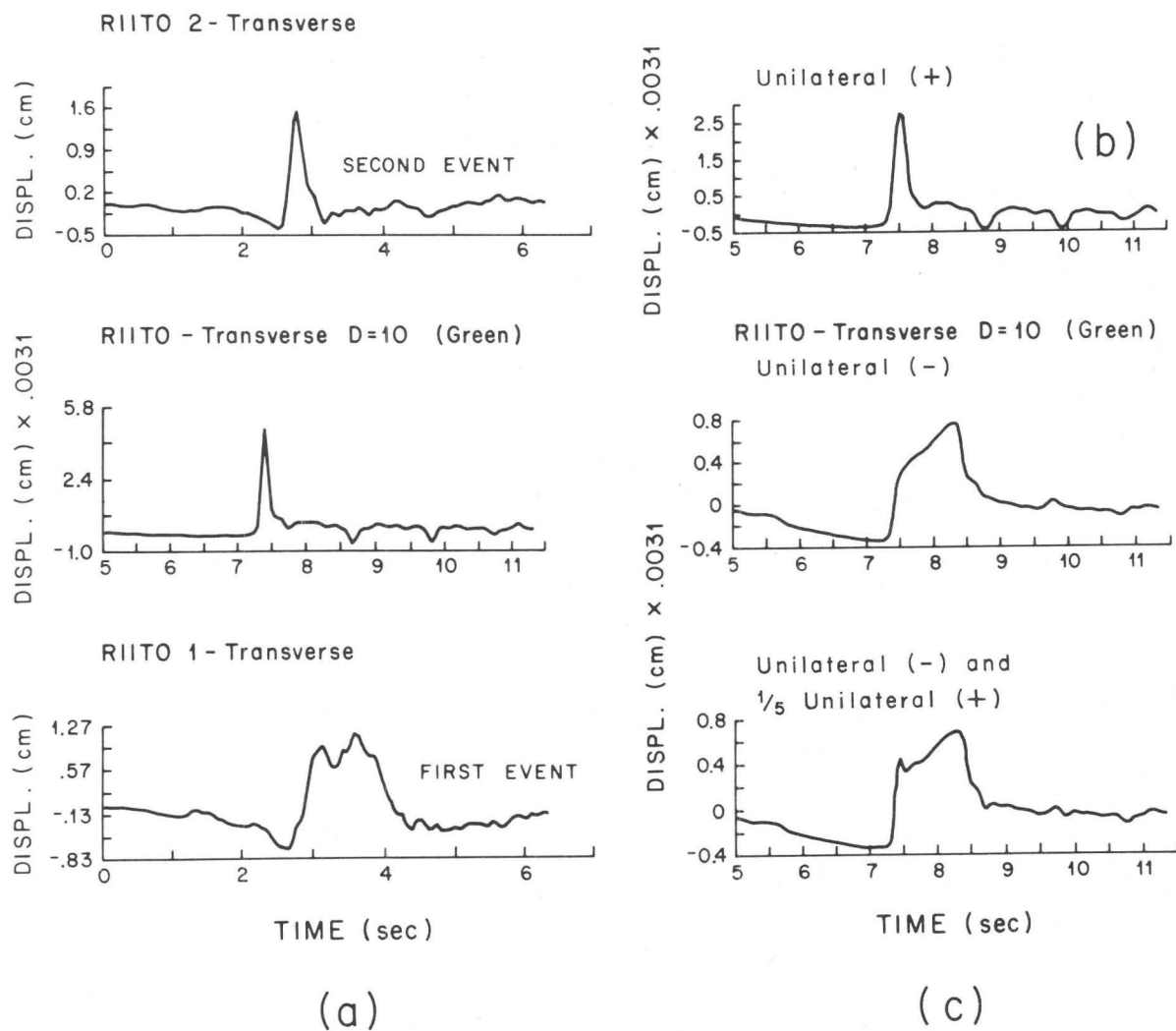
Figure 13. Comparison of Riito strong-motion displacement seismograms [(a) top and bottom] with point source Green's function seismogram [(a) middle], and Green's function seismograms modified for the effect of a propagating source. (b) approximates the second event and (c) approximates the first.
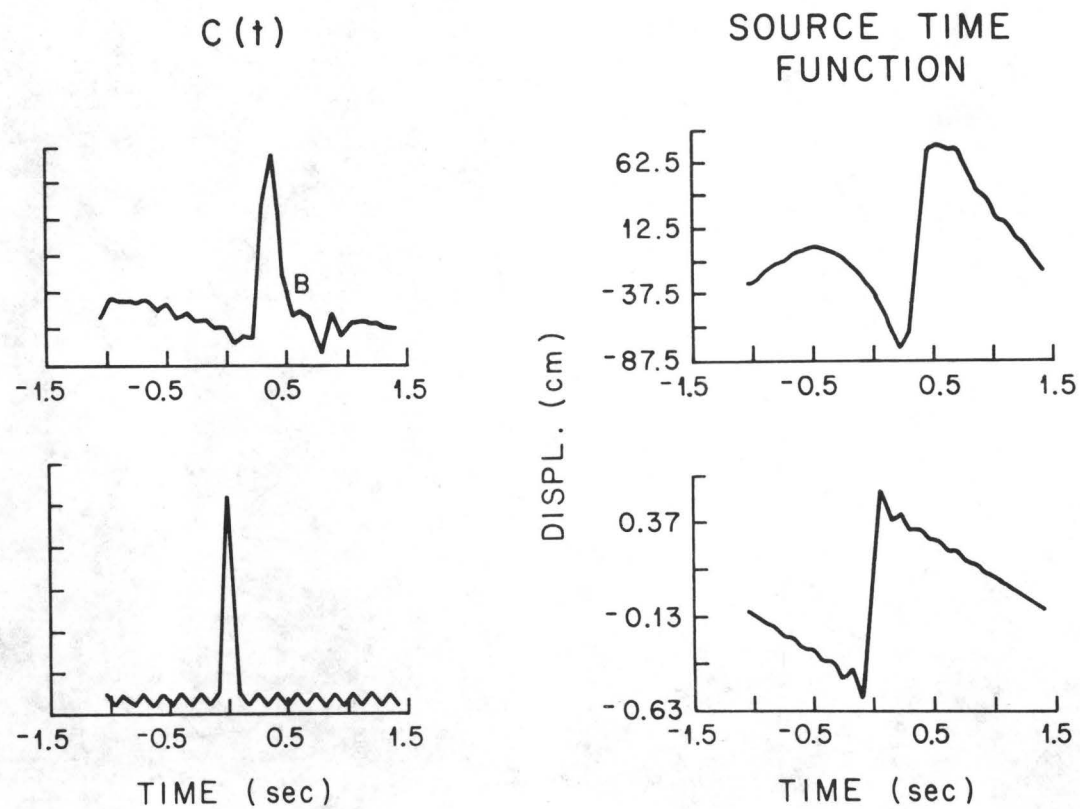
Figure 14. Comparison of convolution factor and source time function for the second Mesa de Andrade event with the same for an idealized point source.
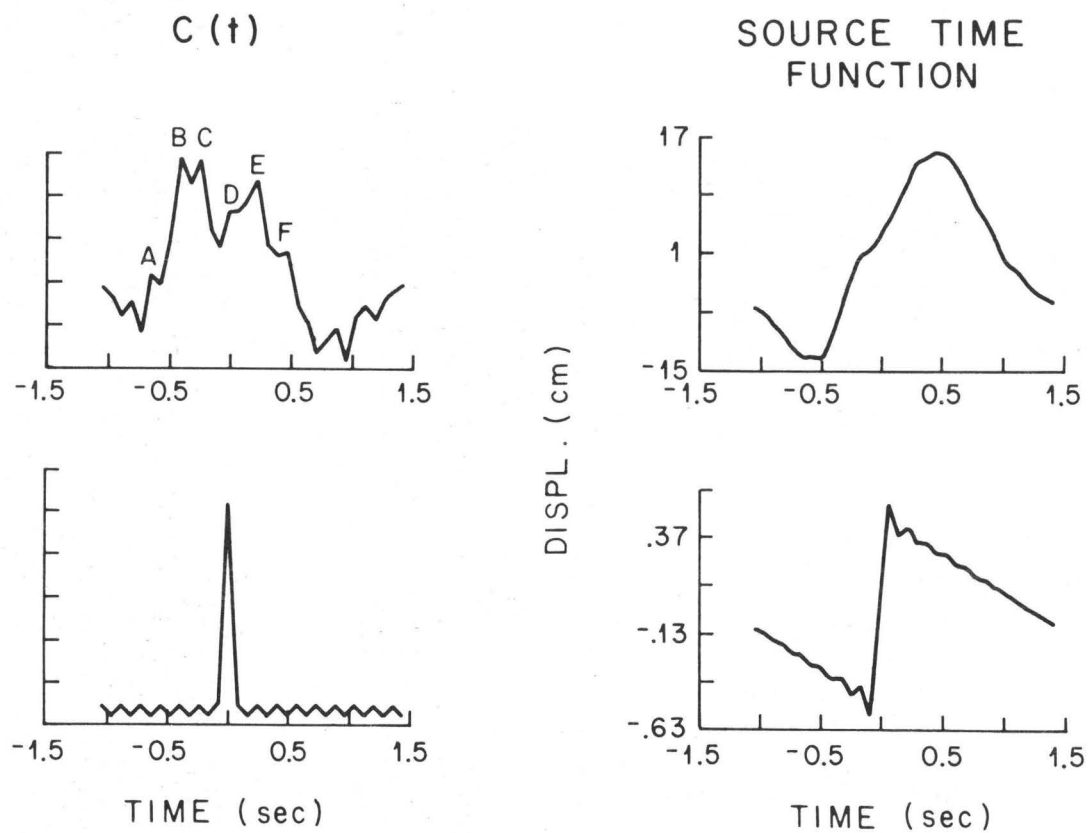
Figure 15. Comparison of convolution factor and source time function for the first event with the same for an idealized point source.
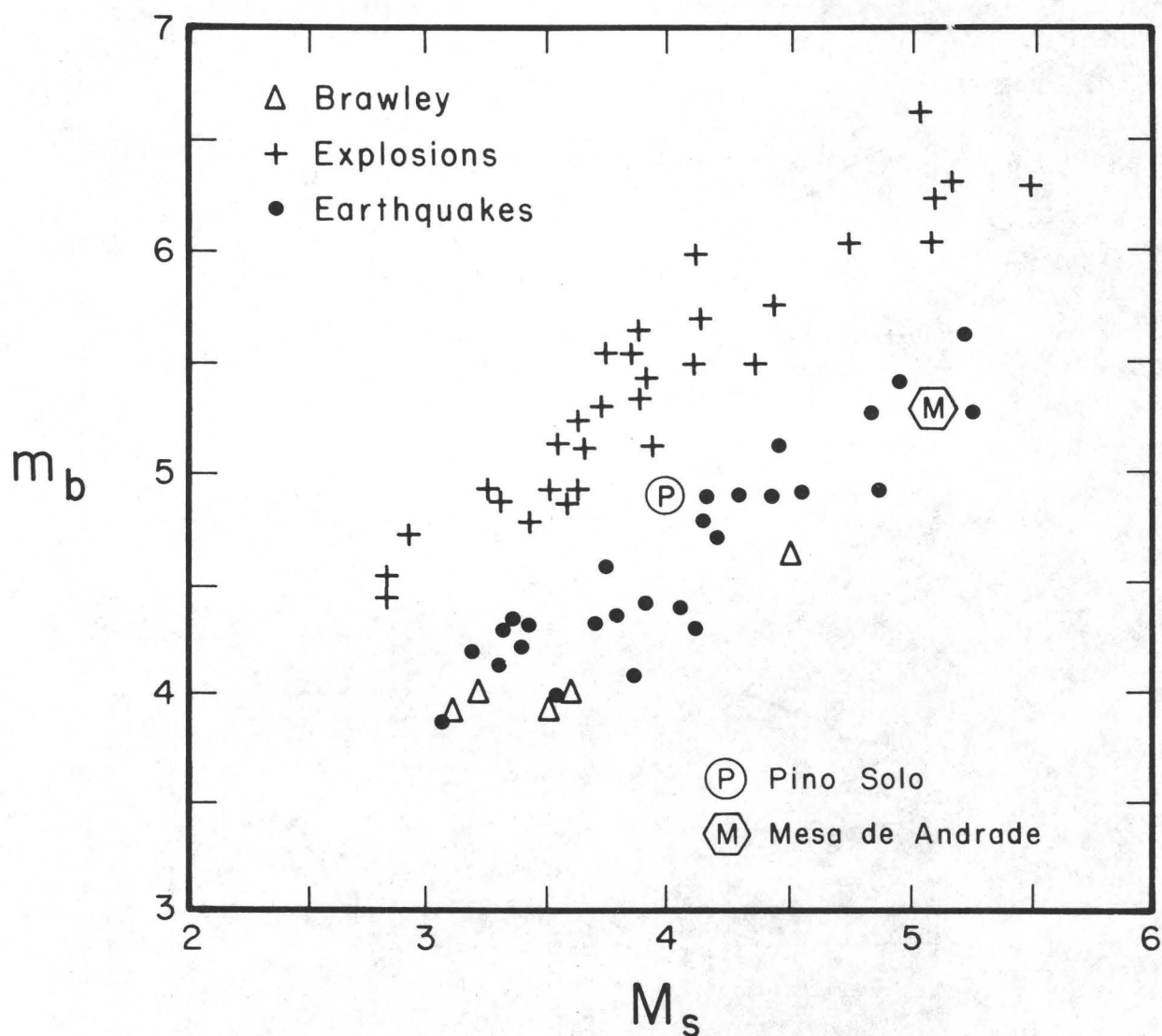
Figure 16. m_b versus M_s diagram modified from Hartzell and Brune (1977), after Marshall and Basham (1972), showing points for the Brawley earthquake swarm (1975) and for the Pino Solo and Mesa de Andrade earthquakes. In this and the following figures, parameters for the Pino Solo earthquake are represented by a circle with an inscribed "P" when measured at distant stations, and with an inscribed "B" when measured at BAR. The parameters for the Mesa de Andrade earthquake are represented by hexagons with an inscribed "M" when determined at distant stations, and with an inscribed "1" or "2" when they refer to the first or second events, respectively, in the double Mesa de Andrade earthquake.
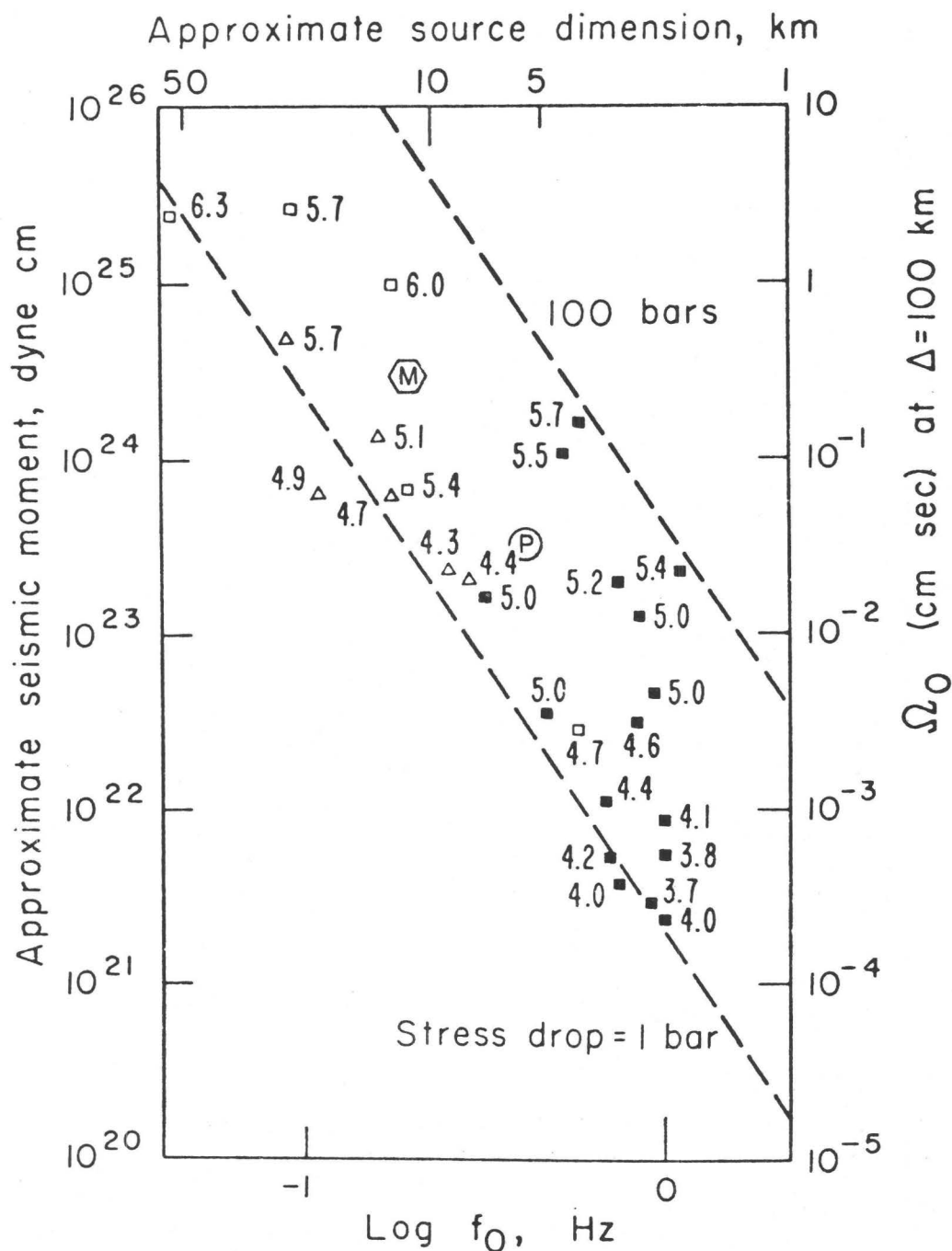
Figure 17. $\Omega_0 - f_0$ representation of seismic sources in the northern Gulf of California—Baja California region: northern Gulf sources ($\triangle$), northern Baja sources (■), and 1954 Baja sequence sources (□). The number represents the local magnitude of the earthquake represented by the $\Omega_0 - f_0$ point. Dashed lines are lines of constant stress drop, with the indicated value. After *Thatcher* [1972]. Mesa de Andrade and Pino Solo earthquakes represented by Ⓜ and Ⓟ respectively.
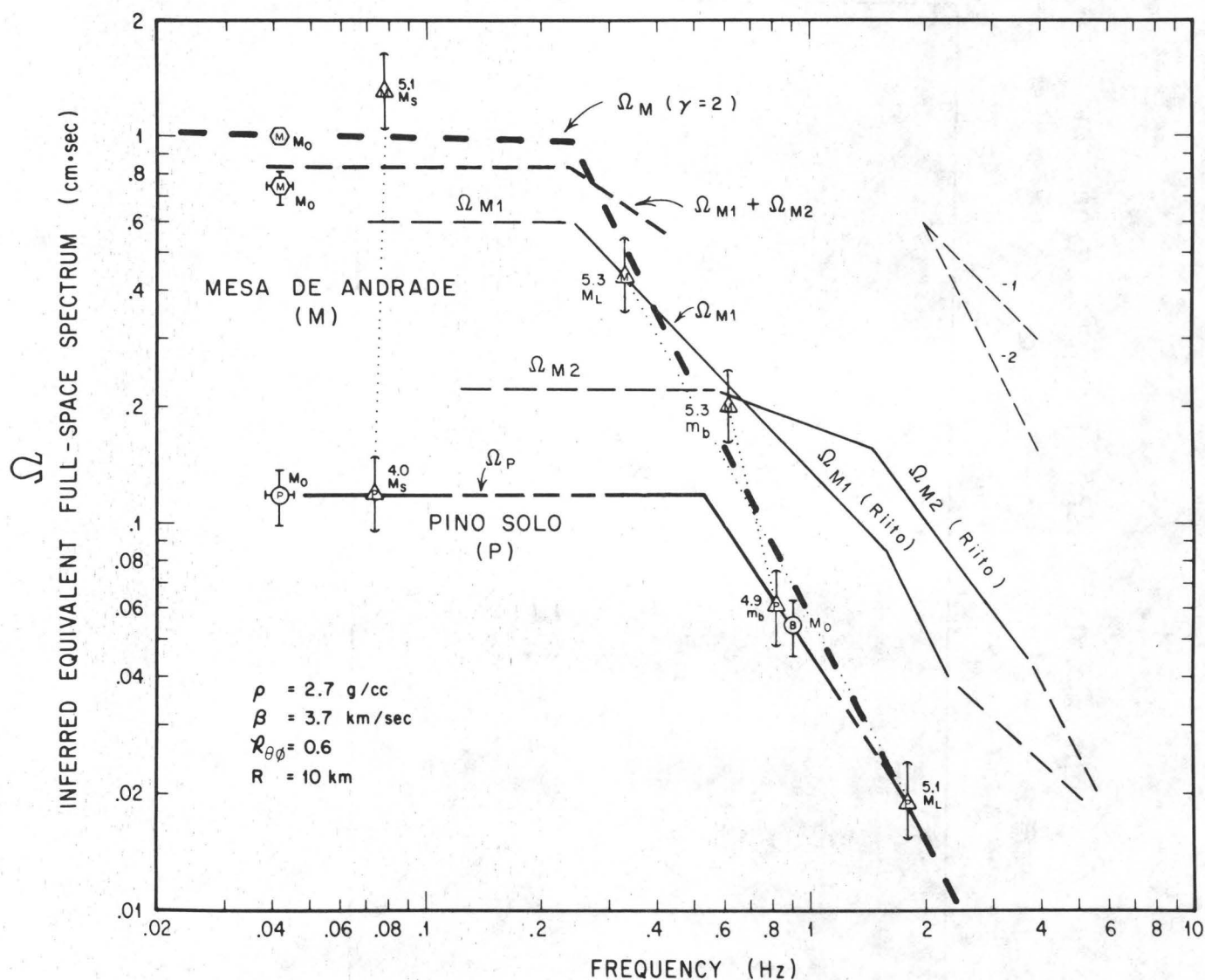
Figure 18. Inferred equivalent full-space spectral values for the Pino Solo and Mesa de Andrade earthquakes. Triangles represent (relative) spectral values calculated from magnitudes. The hexagons and circles represent estimations of moment. The solid parts of the curves labeled Ω_{M_1} and Ω_{M_2} are derived directly from the spectra of the two strong motion events of the Mesa de Andrade earthquake recorded at Riito. The error bars assigned to each spectral value represent the estimated standard error. Two spectral points represent M_0 for the Mesa de Andrade earthquake as determined at distant stations. The lower one corresponds to M_0 as measured in the time domain, using surface waves. The higher one represents M_0 when the second event's contribution is added (see above). It is an estimate of the moment that would have been determined at distant stations from very long period spectra (periods greater than the interval between the two events).

INVERSION OF COMPLEX BODY WAVES

Masayuki Kikuchi* and Hiroo Kanamori
Seismological Laboratory
California Institute of Technology
Pasadena, California 91125

*Permanent address: Physics Department, Yokohama City University Yokohama
236, Japan

(213) 356-6914

Abstract
     A numerical method to deconvolve complex body waves into a multiple
shock sequence is developed. With the assumption that all the constituent
events of a multiple shock have identical fault geometry and depth, the
far-field source time function is obtained as a superposition of ramp
functions. The height and the onset time of the ramp functions are
determined by matching the synthetic waveforms with the observed ones in the
least square sense.

     The individual events are then identified by pairs of ramp functions or
discrete trapezoidal pulses in the source time sequence. The method can be
used for the analysis of both single-station data and multi-station data.
Teleseismic long-period P-waves from the 1976 Guatemala earthquake is
analyzed as a test of our method. The present method provides a useful tool
for a systematic analysis of multiple event sequences.

1. Introduction
     The spectra and waveforms of seismic body waves provide important
information on the details of the source rupture process. In frequency
domain analysis, the low-frequency asymptote and the corner frequency of the
displacement spectrum are used to estimate the seismic moment and the source
dimension (Brune, 1970). In time domain analysis of body waves, the
observed waveforms are modelled by a source time function, and the time
constants associated with it are interpreted in terms of the source
dimension and the particle velocity of the fault motion (Aki, 1968;
Haskell, 1969; Kanamori, 1972; Abe, 1974).

     When the observed body-waveforms are relatively simple, the modelling
can be done by using either forward or inverse methods. Langston (1976) and
Burdick and Mellman (1976) used a time-domain inversion method to determine
some of the complexities of the source time function. For a very large
earthquake, however, the body-waveform is extremely complex and no standard
method is available for the inversion. Several attempts have been made to
explain the complexity of body waves from large earthquakes by using a
multiple event model. Earlier attempts consisted of identifying distinct
phases in the body-wave signal as the beginning of distinct events and of
locating them with respect to the first one (Imamura, 1937, p 267; Miyamura
et al. 1964; Wyss and Brune, 1967). In more recent studies, synthetic

647

seismograms were used to make a more quantitative interpretation (Fukao, 1972; Chung and Kanamori, 1976). Kanamori and Stewart (1978) modelled the waveforms of P-waves from the 1976 Guatemala earthquake by matching them, in the least square sense, with a series of trapezoidal source time functions. Rial (1978) modelled the Caracas earthquake by using three distinct events. Boatwright (1980) employed a direct inversion of the body waves from the 1979 St. Elias, Alaska earthquake to resolve a few subevents.

The complexity of the source time function reflects the heterogeneity in the mechanical properties in the fault zone, which is often characterized by asperities or barriers. Many recent studies have suggested the importance of asperities in various seismological problems such as the nature of strong ground motion (Das and Aki, 1977; Ebel and Helmberger, 1981), foreshocks (Jones and Molnar, 1979), seismicity patterns (Wesson and Ellsworth, 1973; Kanamori, 1981) and the regional variation of rupture mode (Lay and Kanamori, 1981).

In view of this importance, it is desirable to develop a systematic method for inversion of complex body waves consisting of contributions from several sources. This is obviously a difficult problem. For example, the 1976 Guatemala earthquake was modelled by about 10 pulses each representing a distinct seismic source. Even in the simplest source model, about 6 parameters (the seismic moment, 3 fault parameters, 2 time constants (e.g., rise time and pulse width)) are necessary to describe each source. Thus, if we are to model a multiple shock with 10 distinct events, about 100 parameters including the origin time and the coordinates of the individual events would have to be determined. In view of the amount, the quality and the limited bandwidth of the data usually available for this type of modelling, it would be very difficult to determine all of these parameters. Furthermore, in view of the complexity of the structure near the source, along the path, and near the receiver, it would not be easy to prove that all the complexities in the body-waveform are due to the source.

Because of these difficulties, we will be mainly concerned with the gross complexities of multiple events rather than the minute details of the source function, and a number of simplifications will be made. Inevitably a certain amount of non-uniqueness and subjectivity exists. The validity of the model should eventually be judged in the light of other data such as local strong-motion data, distribution and geometry of surface breaks and macro-seismic data. As we will show in the later sections, the method we present here can invert complex observed seismograms into a source time function in a systematic and reasonably objective way, thereby providing a means for interpreting complex observed records in terms of asperities and barriers in the fault zone.

2. Method

In an infinite homogeneous space, the far-field body wave form due to a shear dislocation source is given by (eg., (10) in Haskell, 1964)

$$U_c(\vec{x},t) = \frac{R_c \mu}{4\pi\rho c^3 r_o} \iint_A \dot{D}(\vec{\xi}, t-r/c) \, dA \qquad (1)$$

where A = dislocation surface; $\vec{\xi}$ = a variable point on A; $\vec{x}$ = an observation point; t = time; r = $|\vec{x} - \vec{\xi}|$; r_o = the average of r; $D(\vec{\xi}, t)$ = relative slip velocity; R_c = radiation pattern; ρ = density; μ = rigidity; c = body wave velocity.

When the source region is small, the travel time r/c in (1) can be approximated by its average, r_o/c. The wave form is then given by :

$$U_c(\vec{x},t) = \frac{R_c}{4\pi\rho\,c^3 r_o}\,S(t-r_o/c) \tag{2}$$

where S(t) is the far-field source time function defined by

$$S(t) = \mu \iint\limits_A \dot{D}(\vec{\xi},t)\,dA \tag{3}$$

Here we assume that the time history of dislocation at a point is given by a function of the time measured from the arrival of a rupture front. Let $t'(\xi)$ be the arrival time at a point $\vec{\xi}$, then the dislocation function is expressed as

$$D(\vec{\xi}) = D(t-t'(\vec{\xi})) \tag{4}$$

Noting that $dA = (dA/dt')dt'$ is the area swept by the rupture front during the time interval dt', we can write equation (3) as:

$$S(t) = \mu \int_o^\infty \dot{D}(t-t')\,\dot{A}(t')dt' \tag{5}$$

where dot denotes the time derivative. Thus the far-field source time function is expressed by a convolution of the dislocation velocity and the fault area expansion rate.

We assume that the dislocation time history is given by a ramp function with rise time τ as

$$D(t) = D_o\,s(t)$$

where D_o is the final dislocation and s(t) is the unit ramp function:

$$s(t) = \begin{cases} 0 & t < 0 \\ t/\tau & 0 \le t \le \tau \\ 1 & t > \tau \end{cases}$$

If rupture propagation is characterized by abrupt changes of the fault area expansion rate, then

$$\dot{A}(t) = \sum_i \Delta\dot{A}_i \, H(t-t_i) \qquad (6)$$

where $\Delta\dot{A}_i$ is the increment of the fault area expansion rate at time t_i, and $H(t)$ is the Heaviside step function. The source time function $S(t)$ is then given by superposition of ramp functions:

$$S(t) = m_i \, s(t-t_i) \qquad (7)$$

where

$$m_i = \mu D_0 \, \Delta\dot{A}_i.$$

For example, in case of unilateral rupture propagation,

$$A = W \, v \, t \quad (0 \leqslant t \leqslant T)$$

$$(W = \text{fault width}, \ v = \text{rupture velocity})$$

and the far-field source time function can be described by a pair of pulses as follows:

$$m_1 = \mu W v D_0, \quad t_1 = 0; \quad m_2 = -\mu W v D_0, \quad t_2 = T.$$

When these pulses are convolved with $s(t)$ a trapezoidal far-field source time function is produced. In case of asymmetric bilateral rupture,

$$A = 2 \, w \, v \, t \quad \text{for} \quad 0 \leqslant t \leqslant T_1$$

$$w \, v \, t \quad \text{for} \quad T_1 \leqslant t \leqslant T_2$$

and

$$m_1 = 2 \, \mu W \, v \, D_0, \quad t_1 = 0; \quad m_2 = -\mu W \, v \, D_0, \quad t_2 = T_1;$$

$$m_3 = -\mu W \, v \, D_0, \quad t_3 = T_2$$

In this representation, a positive and negative m_i indicate the beginning and the end of a discrete rupture respectively. When an earthquake source consists of multiple events with identical fault orientation and depth, the far-field source time function is given by a superposition of trapezoidal pulses. Then the area under each trapezoid gives the seismic moment of the individual event. The source time function in this case is also described

in the form of equation (7), and is used for the analysis of teleseismic body waves from a complex multiple shock. We assume that an earthquake source is expressed as a superposition of point dislocations with identical fault orientation and depth. The fault geometry is assumed to be known from the radiation pattern of body waves and/or surface waves. The only unknown is the source time function which is sought in the form of a ramp function series.

In the following we shall restrict ourselves only to P-wave analysis. First we shall treat a record from a single station and then extend the analysis to simultaneous deconvolution of multi-station data.

Single-station data analysis

Let $x(t)$ denote an observed P-wave form (vertical component) at a station and $w(t)$ denote a synthetic wavelet corresponding to a unit source ramp function : $s(t)$. In the synthesis of the wavelet, a double couple point source is placed at a depth in a homogeneous half space. Then the far-field P-wave seismogram is given as follows (Langston and Helmberger, 1975; Kanamori and Stewart, 1976):

$$w(t) = \frac{R_{pz}}{4\pi\rho\alpha^3} (\frac{1}{r_o}) [s(t) + R_{pP} \, s(t - \Delta t_{pP})$$

$$+ \frac{\eta_\alpha}{\eta_\beta} R_{sP} \, s(t - \Delta t_{sP})] *Q(t)*I(t) \tag{8}$$

where the time is measured from the initial arrival of P-wave, $(1/r_o)$ denotes the effective geometrical spreading, and the notation for other parameters is the same as in Langston and Helmberger (1975). As a first approximation, the rise time τ is estimated by comparing the synthetic wavelet to the initial portion of the observed wave form.

First we take a single wavelet and determine m_1 and t_1 by minimizing the error defined by:

$$\Delta_1 = \int_0^\infty [x(t) - m_1 \, w \, (t-t_1)]^2 \, dt \tag{9}$$

Equation (9) can be written in terms of correlation functions as follows:

$$\Delta_1 = r_x(0) - 2r_{wx}(t_1)m_1 + r_w(0)m_1^2 \tag{10}$$

where

$$r_x (t') = \int_0^\infty x(t) \, x(t + t') \, dt$$

$$r_{wx}(t') = \int_0^\infty w(t) \, x(t + t') \, dt$$

$$r_w(t') = \int_0^\infty w(t)\, w(t + t')\, dt \tag{11}$$

The right-hand side of equation (10) has a quadratic form with respect to m_1. Since $r_w(0)$ is positive Δ_1 is minimized if

$$\partial \Delta_1 / \partial m_1 = 0 \text{ or } m_1 = r_{wx}(t_1)/r_w(0) \tag{12}$$

For this value of m_1,

$$\Delta_1 = r_x(0) - r_w(0)m_1^2 \tag{13}$$

From equation (13) we find that Δ_1 is minimized if the onset time t_1 is chosen so that

$$[r_{wx}(t_1)]^2 = \text{maximum} \tag{14}$$

Next we apply the above procedure to the residual wave form:

$$x'(t) = x(t) - m_1 w(t-t_1) \tag{15}$$

Then the values of t_2 and m_2 for the second wavelet are determined by minimizing $(r_{wx}(t_2))^2$ and by

$$m_2 = r_{wx}(t_2)/r_w(0).$$

The above procedure is iterated until no more significant decrease in the error occurs. After N iterations, the N largest m_i's and the corresponding t_i's are obtained, and the source time function $S(t)$ can be calculated by equation (7). Also the synthetic wave form $y(t)$ and the approximation error are obtained by:

$$y(t) = \sum_{i=1}^{N} m_i\, w(t-t_i) \tag{16}$$

$$\Delta_n = \int_0^\infty [x(t) - y(t)]^2 dt$$

$$= r_x(0) - r_w(0)\left[\sum_{i=1}^{N} m_i^2\right] \tag{17}$$

It should be noted here that, if the number of iterations N is fixed, the approximation error ΔN can be regarded as a function of the rise time τ used in the synthesis of the wavelet. Hence, after some trial and error, we adjust the value of τ so that it minimizes ΔN.

Multi-station data analysis

A similar method can be used for the analysis of multi-station data. However, if the source location differs from event to event in a multiple shock sequence, the relative arrival times of these events with respect to the first event are different from station to station. It is therefore necessary to introduce the source location as an additional parameter. This requires a slight modification of the single-station method described above.

Here we shall consider a multiple shock where rupture occurs along a relatively narrow fault plane. Let W be the fault width and ℓ be the distance along the fault strike measured from a reference point. Considering the dependence of the travel time on the location of a shear dislocation source, we write equation (1) as follows:

$$u_\alpha(\vec{x}, t) = \frac{R_\alpha}{4\pi\rho\alpha^3 r_o} S_\alpha(t - r_o/\alpha; \; \Phi) \qquad (18)$$

where

$$S_\alpha(t; \; \Phi) = \mu W \int_0^\infty \dot{\overline{D}}(\ell, \; t + \ell \cos\Phi/\alpha)\,d\ell \qquad (19)$$

$\dot{\overline{D}}$ being the slip velocity averaged over the fault width, Φ, the angle between the ray path and the rupture direction. The function $S_\alpha(t; \Phi)$ becomes equivalent to the far-field source time function $S(t)$ defined by (3) if $\Phi = 90^\circ$ or the entire fault length is small enough for $\ell \cos \Phi/\alpha$ to be neglected.

Using a ramp function for the dislocation time history, we find

$$S_\alpha(t; \Phi) = \mu \; W \; D_o \int_0^\infty \frac{s(t - t' + \ell \cos\Phi/\alpha)}{1 - v \cos\Phi/\alpha} \; \dot{v} \; dt' \qquad (20)$$

where ℓ is the coordinate of the rupture front at time t', $v = \dot{\ell}$ is the rupture velocity. Under a condition similar to relation (6), we find an expression for $S_\alpha(t; \; \Phi)$ as follows:

$$S_\alpha(t; \Phi) = \sum_i m_i \; s(t - t_i + \ell_i \cos \Phi/\alpha) \qquad (21)$$

where

$$m_i = \mu D_0 W \Delta v_i / (1 - v_i \cos \Phi / \alpha) \qquad (22)$$

For a shallow earthquake with which we are concerned here,

$$\cos \Phi = \sin i_0 \cos \Delta \phi$$

where i_0 is the take-off angle and $\Delta \phi$ is the angle between the station azimuth and the fault strike. Since we use only stations with the distance $\Delta \geqslant 40^{\circ}$ and the rupture velocity v is expected to be less than the shear wave velocity, the azimuth-dependent factor of m_i, $(1 - v \cos \Phi / \alpha)$ can be replaced by 1 as a first order approximation. Thus the i-th source pulse is specified by a set of three parameters : (m_i, t_i, ℓ_i).

Let $x_j(t)$ denote the P-wave form observed at j-th station and $w_j(t, \ell)$ denote a synthetic wavelet which is generated by a unit source at a distance ℓ from the reference point and recorded at j-th station. Taking the azimuth-dependent time shift ($\ell \cos \Phi_j / \alpha$) into account, we write

$$w_j(t; \ell) = w_j(t + \ell \cos \Phi_j / \alpha) \qquad (23)$$

where $w_j(t) \equiv w_j(t;0)$ is the function given by (8). Then the first source pulse (m_1, t_1, ℓ_1) can be determined by minimizing the error:

$$\Delta_1 = \sum_{j=1}^{M} \int_0^{\infty} [x_j(t) - m_1 w_j(t-t_1; \ell_1)]^2 dt \qquad (24)$$

where M is the number of stations. By using the same procedure as the one used for single-station data, we can determine t_1 and ℓ_1 from

$$[r_{wx}(t_1, \ell_1)]^2 = \text{maximum} \qquad (25)$$

and

$$m_1 = r_{wx}(t_1; \ell_1)/r_w(0) \qquad (26)$$

where r_{wx} and r_w are the sums of correlation functions defined by :

$$r_{wx}(t'; \ell) = \sum_{j=1}^{M} \int_0^{\infty} [w_j(t; \ell) \, x_j(t + t')] \, dt$$

$$= \sum_{j=1}^{M} r_{w_j x_j}(t' - \ell \cos \Phi_j / \alpha) \qquad (27)$$

$$r_w(0) = \sum_{j=1}^{M} \int_o^\infty [w_j(t; \ell)]^2 \, dt = \sum_{j=1}^{M} r_{w_j}(0) \qquad (28)$$

The residual wave forms are then defined by

$$x'j(t) = x_j(t) - m_1 \, w_j \, (t-t_1; \ell_1) \qquad (29)$$

and the same procedure is repeated for $x_j'(t)$ to obtain the second source pulse (m_2, t_2, ℓ_2).

The above procedure is iterated until no significant decrease in the error occurs. After N iterations, the source time function $S(t; 90^o)$ can be calculated by equation (7); the synthetic P-wave form $y_j(t)$ and the approximation error Δ_N are obtained by

$$y_j(t) = \sum_{i=1}^{N} m_i \, w_j(t-t_i + \ell_i \cos \Phi_j/\alpha) \qquad (30)$$

$$\Delta_N = \sum_{j=1}^{M} \int_o^\infty [x_j(t) - y_j(t)]^2 \, dt$$

$$= r_x(0) - r_w(0) \sum_{i=1}^{N} m_i^2 \qquad (31)$$

where

$$r_x(0) = \sum_{j=1}^{M} r_{x_j}(0)$$

$$r_w(0) = \sum_{j=1}^{M} r_{w_j}(0)$$

In the iterations we need to calculate only the cross-correlation $r_{wx}(t;\ell)$. For the sake of computation the coordinate ℓ along the fault strike is descretized. The cross-correlation r_{wx} is then computed at discrete points on the two-dimensional $(t-\ell)$ plane. In this case we can use a recursive formula for r_{wx} to facilitate the computation (see Appendix).

3. Analysis

As a test of our method, we analyze teleseismic long-period P-waves from the Guatemala earthquake, February 4, 1976. The WWSSN records for this event has been already studied in detail by Kanamori and Stewart (1978).

The extent of the surface breaks and the aftershock area indicate that the source of this earthquake is characterised by a long shallow strike-slip fault (Plafker, 1976; Langer et al. 1976). Kanamori and Stewart (1978) analyzed the teleseismic long-period P-waves and showed that the earthquake consisted of about ten distinct events with a total duration of about two minutes. They assumed that the mechanisms of the individual events are the same as the mechanism of the main shock determined by body-wave first motions and long-period surface waves. The same source parameters as those used by Kanamori and Stewart (1978) are used here to synthesize the basic wavelet (i.e., fault strike = N75^{O}E, dip angle = 90°, slip angle = 185°, depth = 5 km).

We first use the record at NUR and examine the convergence of the synthetic wave form to the observed P-wave. A double couple point source is placed at a depth of 5 km in a homogeneous half space and the deconvolution was made by using the single-station method.

Fig. 1 shows the error Δ_n normalized to $\Delta_o = r_x(0)$ as a function of N, where the rise time τ is fixed at 4 sec. It can be seen that the error does not decrease significantly after about 20 iterations. Then we vary the rise time τ with N fixed at 20, and seek the value of τ which minimizes the error Δ_{20}. As shown by Fig. 2, Δ_{20} is minimized at τ = 3 sec. This value is therefore considered to be the most appropriate for the rise time of the overall source time function.

The sequence of deconvolution iterations is shown in Fig. 3. The source time function S(t) thus obtained and the resulting synthetic wave form are shown in Figs. 4-a,b. The source time function consists of about five distinct trapezoids.

In the analysis of other records, the same values of N and τ are used. Fig. 5 shows the far-field source time functions thus derived from the individual stations, where a modification is made to remove a linear trend from each source time function.

The linear trend is probably caused by the inadequate response of the recording instrument (WWSSN LP) at long period, and is not meaningful. In fact, we can remove the linear trend from the source time function without changing the synthetic wave form significantly. In Fig. 6 the synthetic wave forms corresponding to the modified source time functions are shown. The agreement between the synthetic and the observed waveforms is satisfactory. The sequence of the source pulses is very similar from station to station. We can identify five major events as marked in Fig. 5. Each of these major events may be divided into sub-events. It can be seen that the onset time of the later events (4 and 5) vary in a systematic way as the azimuth of the station changes. This suggests that the later events occurred at some distance from the first event. This point will be made clear in the multi-station data analysis as described later.

The seismic moment of the individual events are estimated from the area under the source time function. The results are shown in Table 1. The

standard deviation of the seismic moments estimated from different stations is about 30 percent. The result shown in Table 1 is in good agreement with that obtained by Kanamori and Stewart (1978).

Next we apply the multi-station method to the same records as used above. We take 11 points, each 30 km apart, along the fault strike as the discrete source locations. The far-field source time function $S(t; 90^{\circ})$ thus obtained and the resulting synthetic wave forms are shown in Figs. 7 and 8 respectively. The approximation error $\Delta_2 0/\Delta_0$ is about 20%. This value is quite satisfactory since it includes the amplitude variation from station to station as well as noise in the records.

Five major events are now clearly identified in the time sequence. The individual process times and seismic moments are shown in Table 2. In Fig. 9 the locations of the larger sources are plotted on the space-time plane, where positive and negative pulses are indicated by solid and open circles, respectively. In event 1 the rupture initiated near the eastern end of the fault and first propagated eastward. Then the rupture propagated primarily westward with a few pauses. Through the sequence from event 1 to event 4, almost 180 km of the fault length is ruptured. The total process time is about 50 sec and the mean rupture velocity is about 3.5 km/s. However almost 30 sec of the total rupture time is spent during the transition from event to event; accordingly the apparent rupture velocity was about 2 km/s.

Finally, the largest event occurred near the western end of the fault (event 5). The location obtained suggests that this event occurred along the same fault segment as that of the previous events 3 and 4. Kanamori and Stewart (1978) suggested that the large events in the later stage, which correspond to events 4 and 5 in this paper, are related to the large surface breaks observed near the western end of the fault. This feature is more clearly seen in the present results.

4. Discussion

In the present study, we assumed that a multiple shock is represented by a series of point dislocations with an identical fault geometry. Once the fault geometry is known, we can calculate the impulse response, namely a wavelet caused by an impulsive point dislocation. The far-field source time function is then obtained by deconvolution of the observed record with the impulse response.

An alternative approach to this problem is to design a linear inverse filter of the impulse response as devised by Levinson (1947). The source time function can be obtained by convolution of this filter with the observed record. The inversion is straightforward since no assumption is needed for the source time function. However, a certain criterion is necessary to identify the individual events. This approach has been used by Strelitz (1980) and Boatwright (1980).

Another method is to parameterize the unknown source time function using a certain number of parameters which characterize the individual events. These parameters are determined by matching the resulting synthetic records with the observed ones (Burdick and Mellman, 1976). In this

approach the identification of the individual events is straightforward, but some assumption about the shape of the source time function (e.g., a triangular source pulse or a trapezoidal pulse) is needed to start the analysis.

It should be noted that, in any method, the far-field source time function $S(t)$ can in principle be determined uniquely for a given source geometry while the identification of the event is somewhat arbitrary. In other words the same $S(t)$ can be decomposed into a different series of discrete events.

Our approach is a hybrid of the two approaches described above. The far-field source time function is expressed as a superposition of ramp functions with an identical rise time. In this sense the source time function is parameterized. On the other hand we do not specify the shape of the individual events during the analysis. In this sense our method is similar to the direct inversion method.

In the single-station data analysis, the far-field source time functions are derived from the individual stations. Multiple events are then identified as discrete pulses which should be identical for all the stations if the events have the same fault mechanism as used for the analysis. The validity of the model can therefore be tested by the similarity of all the source time sequences. In the multi-station data analysis, on the other hand, a single source time function is derived from the multi-station records. In this case, the quality of the model can be measured by how well the synthetic seismograms match the data.

In the present paper, the fault mechanism is assumed to be the same for all the events of a multiple shock. This is probably a reasonable assumption for most events, but there may be cases where substantial changes in the mechanism occur during the sequence. If the change is very drastic, it is possible to detect it by examining the result obtained by the single-station method. If the mechanism of an event is different from the one assumed, the polarity and the amplitude of the source-time function corresponding to it varies substantially from station to station. If the azimuthal coverage of the station is relatively complete, a more appropriate mechanism for that event may be obtained from the polarity and the amplitude variations.

As demonstrated in the earlier section, even a complex event such as the 1976 Guatemala earthquake can be analyzed in a systematic way. Since the Guatemala earthquake is probably one of the most complex strike-slip events, the method presented here provides a useful tool for the analysis of other complex events.

Acknowledgements

Planetary Sciences, California Institute of Technology, Pasadena, California 91125.

Appendix. Recursive formula for R_{wx}

Since a single-station record can be regarded as a limit of multi-station records, we here consider only the multi-station data. After the first source pulse (m_1, t_1, ℓ_1) is determined, the residual wave forms are given by :

$$x_j^1(t) = x_j(t) - m_1 w_j(t-t_1; \rho_1) \qquad (A-1)$$

Taking the cross-correlation of $w_j(t;\ell)$ with $x_j^1(t)$, we have

$$r_{w_j x_j'}(t';\ell) \equiv \int_0^\infty [w_j(t;\ell)x_j'(t + t')\ dt$$

$$= \int_0^\infty [w_j(t;\ell)x_j(t + t^1)]\ dt$$

$$- m_1 \int_0^\infty [w_j(t;\ell)w_j(t + t' - t_1; \ell_1)]\ dt$$

$$w_j(t + t'n - t' + \ell_1 \cos \Phi_j/\alpha)]\ dt$$

$$= r_{wjx} \equiv (t';\ell) - mr_{w_j}(t'-\tau_1 - (\ell-\ell_1)\cos_j/\alpha) \qquad (A-2)$$

where $r_{wj}(t)$ is the auto-correlation of $w_i(t)$. Taking the sum with respect to j, we have

$$r_{wx}'(t';\ell) = r_{wx}(t';\ell) - m_1 r_w(t'-t_1; \ell-\ell_1) \qquad (A-3)$$

where

$$r_{wx} = (t';\ell) \sum r_{w_j x_j}(t';\ell)$$

$$r_w(t;\ell) = \sum r_{wj}(t-\ell \cos \Phi/\alpha) \qquad (A-3)$$

References

Abe, K., 1974. Seismic displacement and ground motion near a fault: The Saitama Earthquake of September 21, 1931, J. Geophys. Res., 79, 4393-4399.

Aki, K., 1968. Seismic displacement near a fault, J. Geophys. Res., 73, 5359-5376.

Boatwright, J., 1980. Preliminary body-wave analysis of the St. Elias Alaska earthquake of February 28, 1979, Bull. Seism. Soc. Am., 70, 419-436.

Brune, J. N., 1970. Tectonic stress and spectra of seismic shear waves, J. Geophys. Res., 75, 4997-5002.

Burdick, L. J. and Mellman, G. R., 1976. Inversion of the body waves from the Borrego Mountain Earthquake to the source mechanism, Bull. Seis. Soc. Am., 66, 1485-1499.

Chung, W-Y. and Kanamori, H., 1976. Source process and tectonic implications of the Spanish deep-focus earthquake of March 29, 1954, Phys. Earth Planet. Inter., 13, 85-96.

Das, S. and Aki, K., 1977. Fault plane with barriers : A versatile earthquake model, J. Geophs. Res., 82, 5658-5670.

Ebel, J. E. and Helmberger, D. V., 1981. P-wave complexity and fault asperities : the Borrego Mountain, California, Earthquakes of 1968.

Fukao, Y., 1972. Source process of a large deep-focus earthquake and its tectonic implications - the Western Brazil earthquake of 1963. Phys. Earth Planet. Inter., 5 61-76.

Haskell, N. A., 1964. Total energy and energy spectral density of elastic wave radiation from propagating faults, Bull. Seism. soc. Am., 54, 1811-1841.

Haskell, N. A., 1969. Elastic displacemens in the near-field of a propagating fault, Bull. Seism. Soc. Am., 59, 865-908.

Imanura, A., Theoretical and Applied Seismology, 358 pp. Maruzen, Tokyo, 1937.

Jones, L. M. and Molnar, P., 1979. Some characteristics of foreshocks and their possible relationship to earthquake prediction and premonitory slip on faults, J. Geophys. Res., 84, 3596-3608.

Kanamori, H., 1972. Determination of effective tectonic stress associated with earthquake faulting. The Tottori earthquake of 1943, Phys. Earth Planet. Inter., 5, 426-434.

Kanamori, H. and Stewart, G. S., 1976. Mode of the strain release along the Gibbs fracture zone, Mid-Atlantic ridge. Phys. Earth Planet. Inter., 11, 312-332.

Kanamori, H. and Stewart, G. S., 1978. Seismological Aspects of the Guatemala earthquake of February 4, 1976, J. Geophys. Res., 83, 3427-3434.

Kanamori, H., 1981. The nature of seismicity patterns before large earthquakes, Ewing Series, 1981.

Langer, C. J., Whitcomb, J. P. and Aburto, A. Q., Aftershocks from local data, the Guatemalan earthquake of February 4, 1976, A preliminary Report, U. S. Geol. Surv. Prof. Pap., 1002, 30-38.

Langston, C. A. and Helmberger, D. V., 1975. A procedure for modelling shallow dislocation sources, Geophys. J. R. astr. Soc., 42, 117-130.

Langston, C. A., 1976. A body wave inversion of the Koyna, India, Earthquake of December 10, 1967, and some implications for body wave focal mechanisms, J. Geophys. Res., 81, 2517-2529.

Lay, T. and Kanamori, H., 1981. An asperity model of great earthquake sequences, Ewing Series, 1981. Levinson, H., The Wiener RMS (root-mean-square) error criterion in filter design and prediction, J. Math. Phys., 1947, 261-278.

Miyamura, S., Omote, S., Teisseyre, R. and Vesanen, E., 1964. Multiple shocks and earthquake series pattern. Int. Inst. Seismol. Earthquake Eng. Bull., 2, 71-92.

Plafker, G., 1976. Tectonic aspects of the Guatemala earthquake of 4 February 1976, Science, 93, 1201-1208.

Rial, J. A., 1978. The Caracas, Venezuela, Earthquake of July 1967 : A multiple-source event, J. Geophys. Res., 83 5405-5414.

Strelitz, R. A., 1980. The fate of the downgoing slab : A study of the moment tensors from body waves of complex deep-focus earthquakes, Phys. Earth Planet. Inter., 21, 83-96.

Wesson, R. L. and Ellsworth, W. L., 1973. Seismicity preceding moderate earthquakes in California, J. Geophys. Res., 78, 8527-8546.

Wyss, M. and Brune, J. N., 1967. The Alaska earthquake of 28 March 1964: A complex multiple rupture, Bull. Seism. Soc. Am., 57, 1017-1023.

(This paper has been published in the Bulletin of the Seismological Society of America)
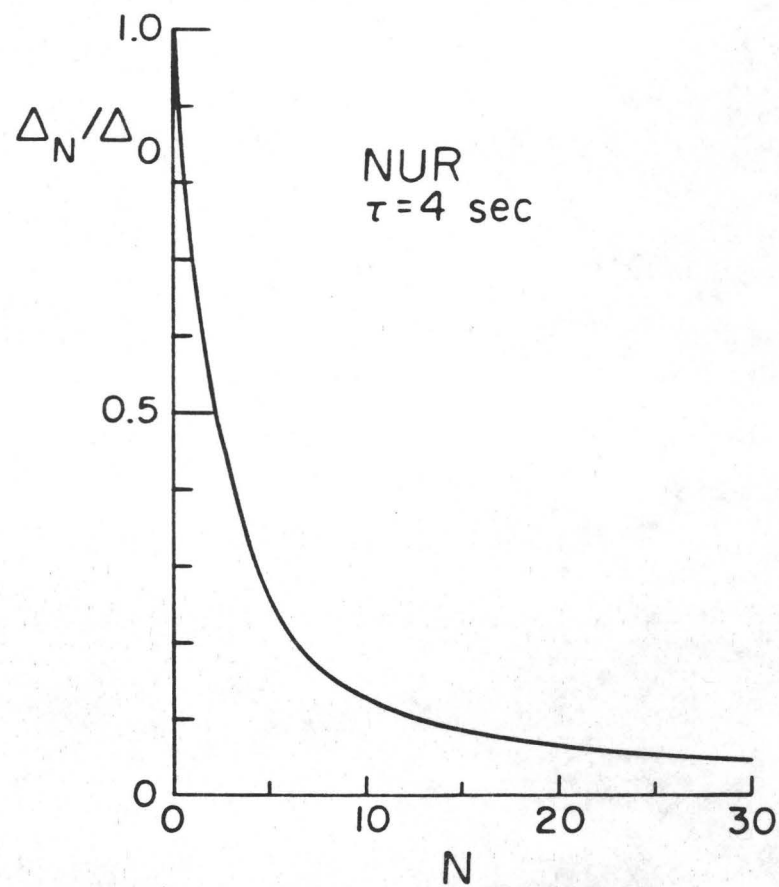
Fig. 1. Normalized approximation error, Δ_{20}/Δ_0 versus iteration N (NUR, the Guatemala earthquake). The rise time τ of ramp functions used for constructing the source time function is fixed at $\tau = 4$ sec.
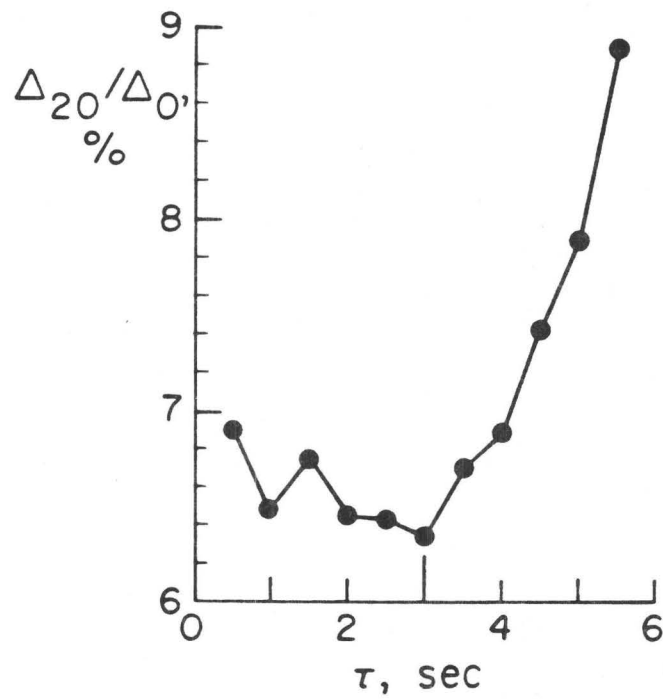
Fig. 2. Normalized approximation error, Δ_{20}/Δ_0 versus the rise time τ (NUR, the Guatemala earthquake). The number of iterations is fixed at N = 20.
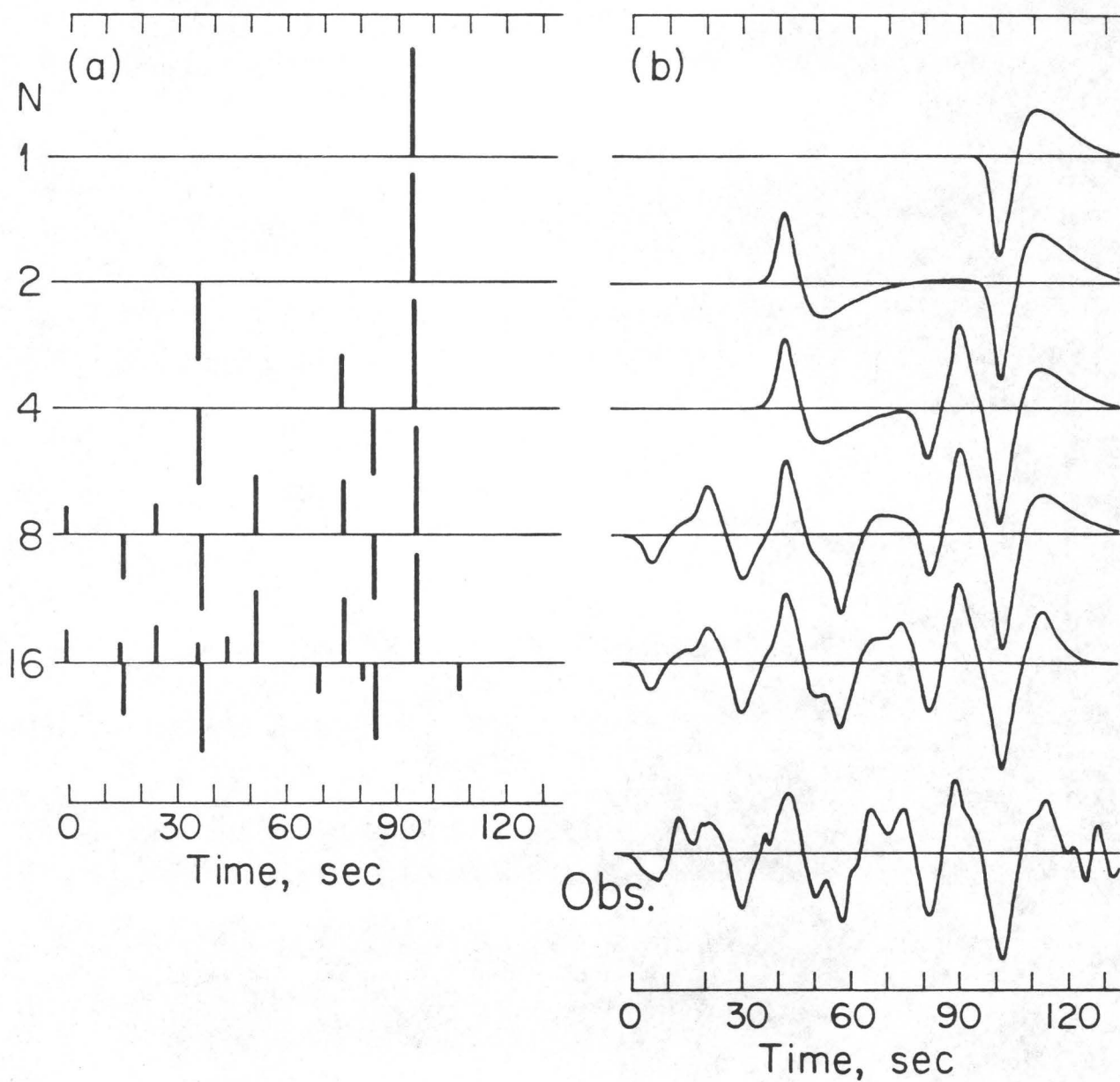
Fig. 3. Sequence of deconvolution procedure in single-station data analysis (NUR, the Guatemala earthquake). (a): source pulses (height of ramp functions); (b): corresponding synthetic wave form. Note that larger pulses are obtained at the earlier steps in the iterations.
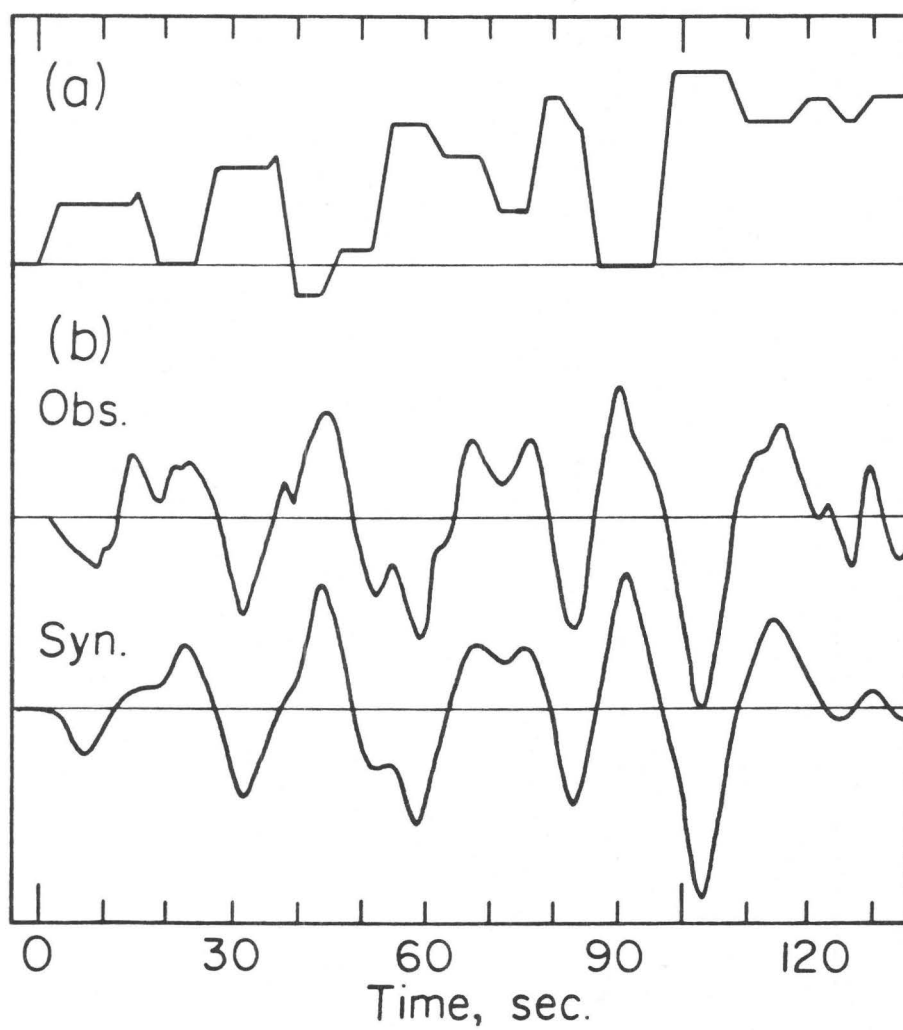
Fig. 4. (a): far-field source time function obtained after
        20 iterations; (b) the resulting synthetic wave form
        and the observation (NUR, the Guatemala earthquake).
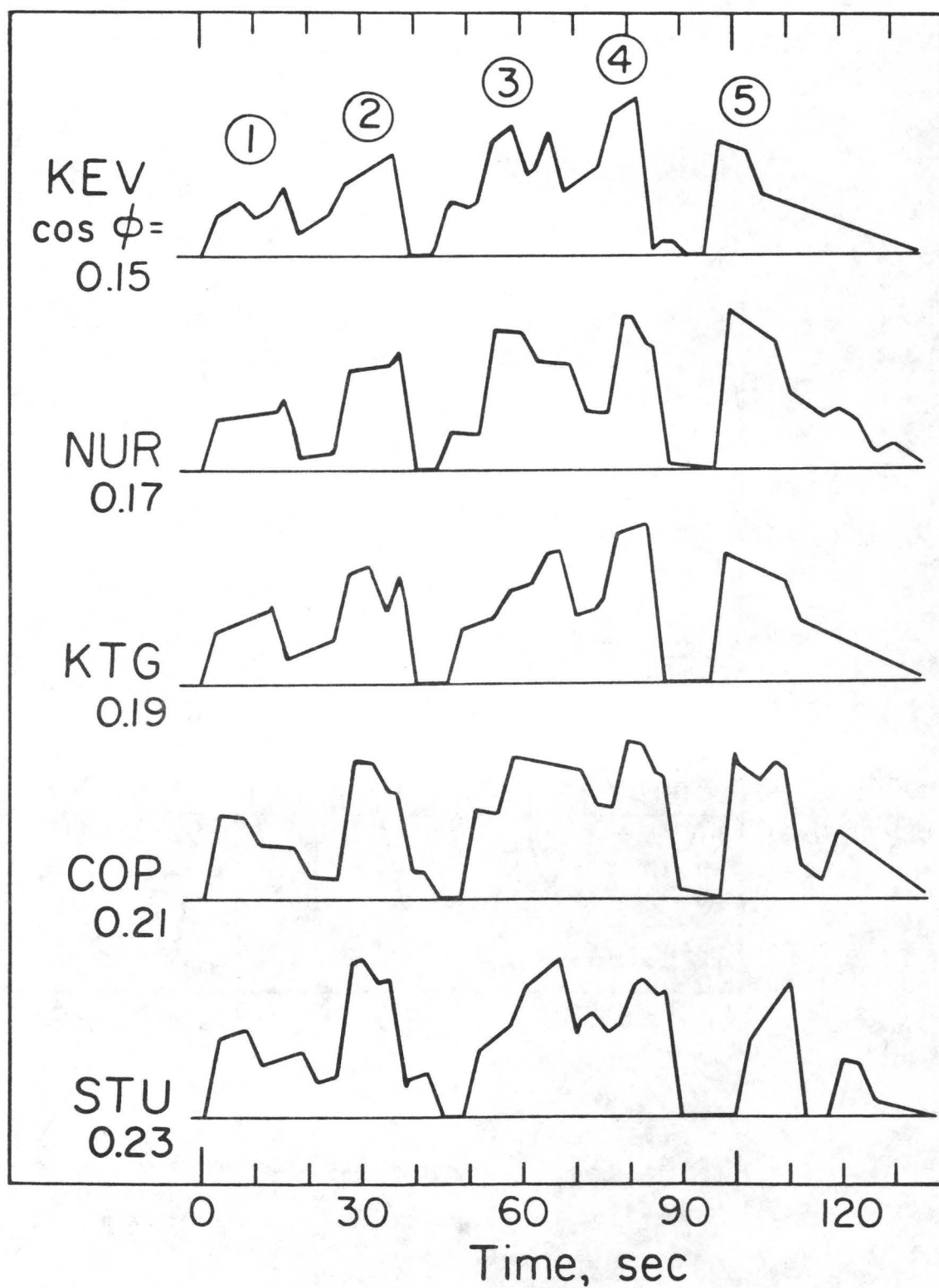
Fig. 5. Far-field source time functions obtained from five stations. Five major events are identified as marked 1,....,5 by the distinct onset in the time sequences.
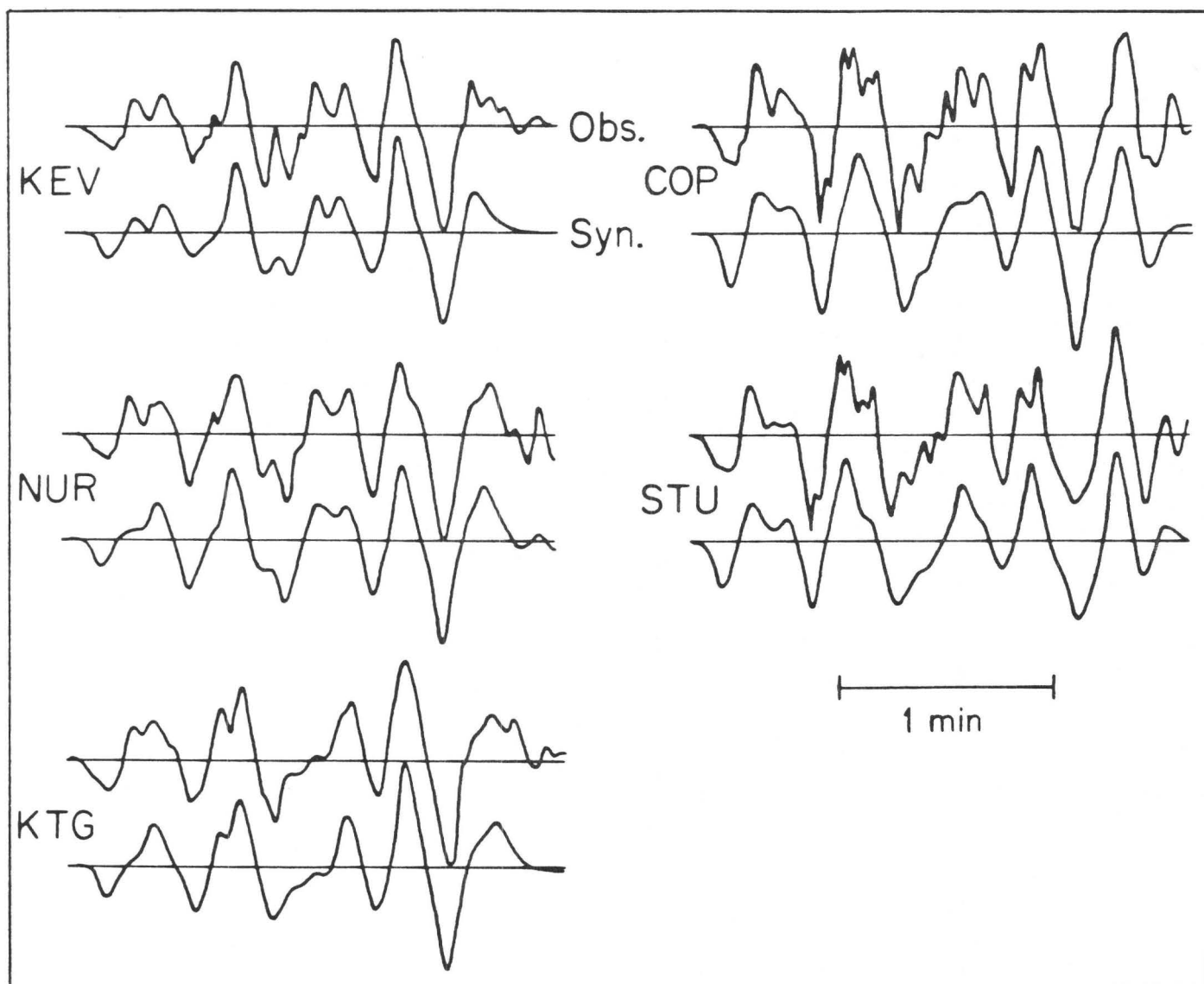
Fig. 6. The synthetic wave forms corresponding to the source time functions of Fig. 5 are shown in comparison with the observed wave forms.
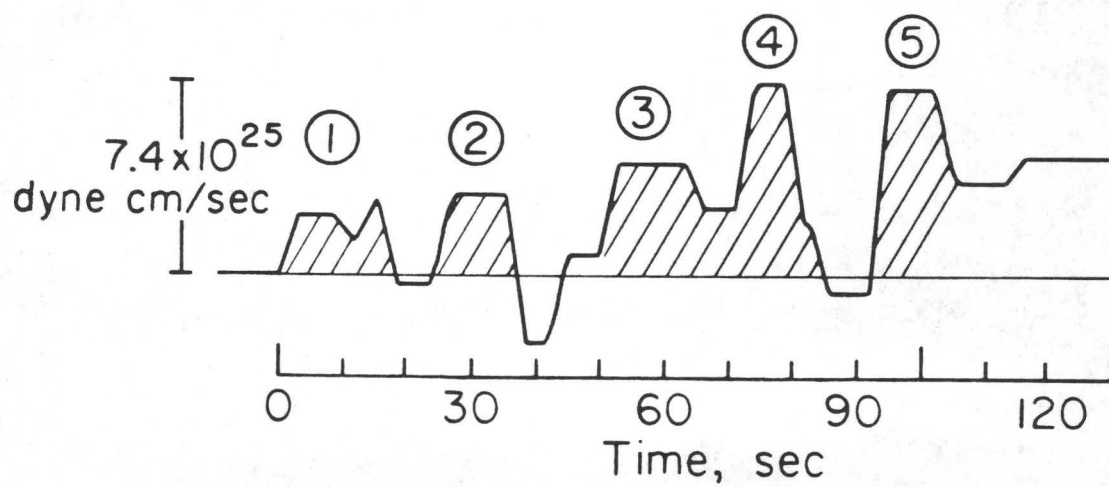
Fig. 7.   Far-field source time function, S(t; 90°) obtained by
multi-station data analysis (the Guatemala earthquake).
Five major events are clearly identified.
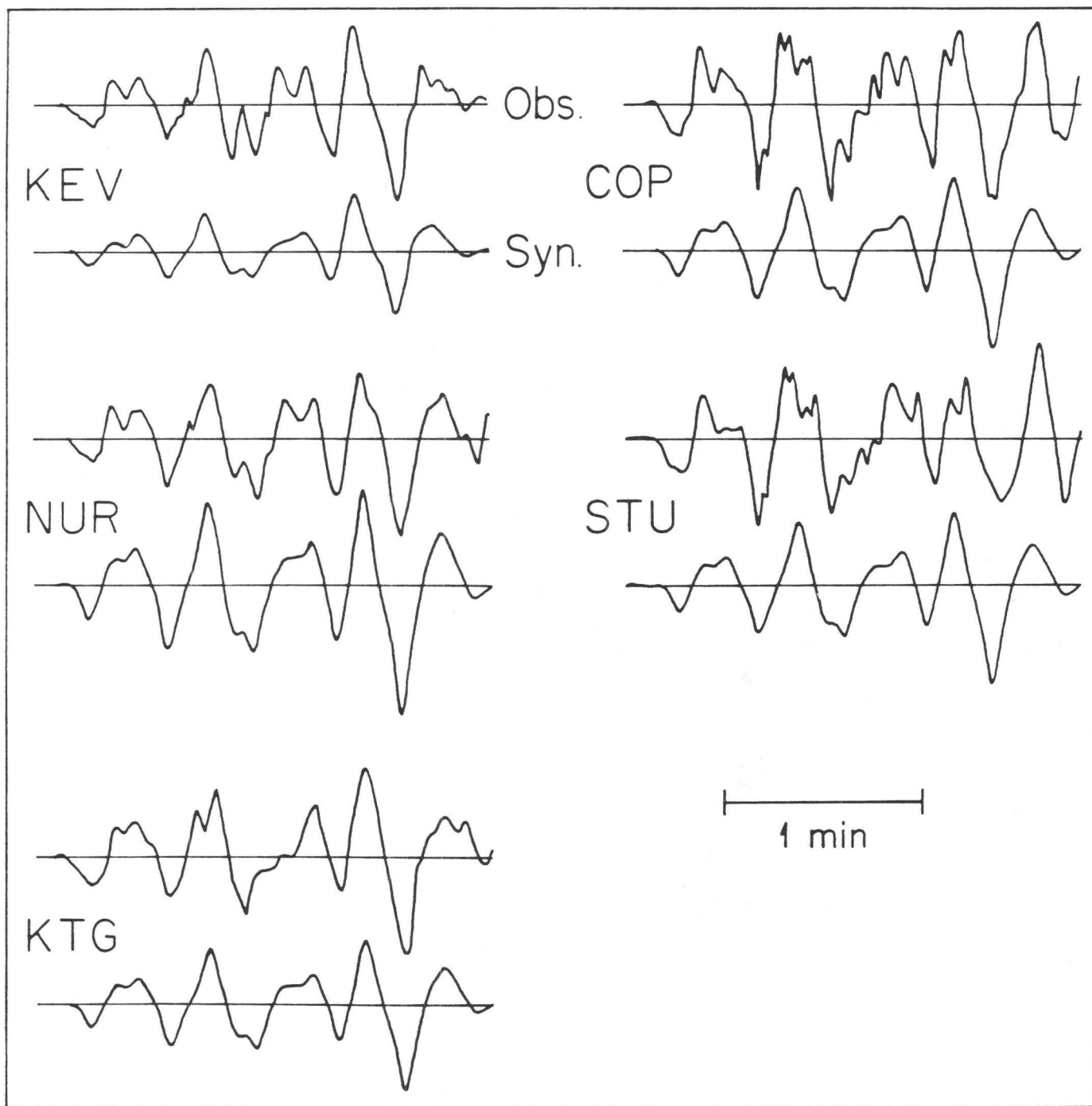
Fig. 8. Synthetic P-wave forms correspsonding to the source time function of Fig. 7.
The amplitude scale is the same as that of the observed wave forms at the
the individual stations.
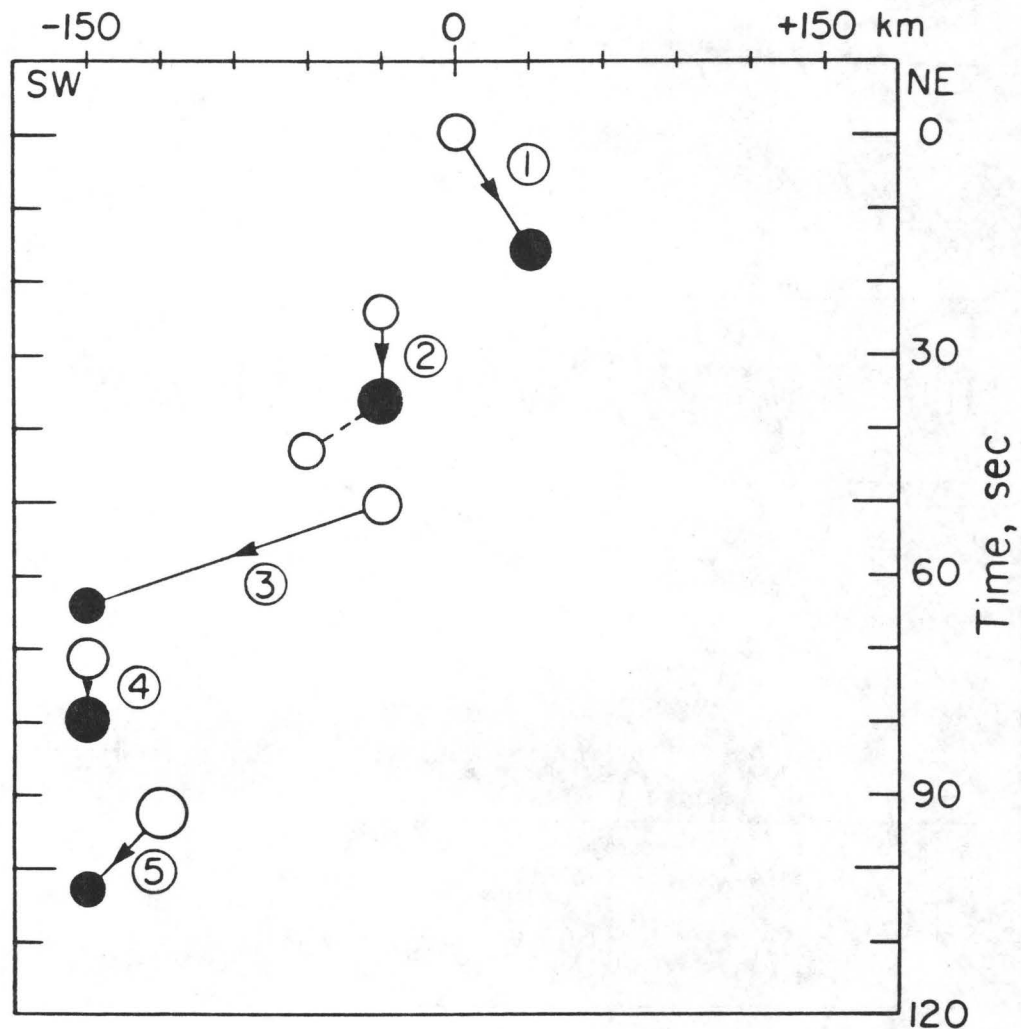
Fig. 9. Location and onset time of 11 largest source
pulses obtained by multi-station data analysis
(the Guatemala earthquake). Open and closed
circles show positive and negative pulses,
respectively. Number marked in the figure
corresponds to that in Fig. 7.

Broadband Analysis of the Extended Foreshock Sequence of the Miyagi-Oki
Earthquake of June 12, 1978

by

George L. Choy
U. S. Geological Survey
Box 25046 MS 967
Denver Federal Center
Denver, CO 80225

John Boatwright
U. S. Geological Survey
345 Middlefield Road MS 77
Menlo Park, CA 94025

ABSTRACT

The Miyagi-Oki earthquake of June 12, 1978, a large (M_S 7.8) interplate thrust
event, occurred in a region which had not experienced earthquakes of
magnitude greater than 7 since 1938. A sequence of four moderate-sized
($5.4 < m_b < 6.1$) earthquakes encircled the rupture zone of the Miyagi-Oki
earthquake of June 12, 1978 over a period of two years before the mainshock.
Broadband displacement and velocity records of body waves recorded digitally
by stations of the GDSN are analysed to determine the static and dynamic
characteristics of the sequence. These characteristics include moment,
radiated energy, dynamic and static stress drop, and apparent stress.
Inversions of duration measurements made on the velocity waveforms permit
quantifying the complexity of an event as well as constraining its rupture
geometry.

Intervals of 7-8 months separated the first three events; the mainshock
occurred 4 months after the third event. The rupture process of the third event
was unusually complex and had a substantially higher dynamic stress drop (175
bars) than the stress drops of the first two events (9 and 10 bars, respectively).
The inferred rupture direction of this third event pointed toward the focus of the
mainshock. These observations suggest that the third event was an
intermediate-term precursor to the mainshock. The fourth event, a short-term
precursor to the mainshock, occurred about eight minutes before the
mainshock. Its dynamic stress drop (20 bars) was lower than that of the third
event but higher than that of the first two events.

INTRODUCTION

In many time-domain studies of the earthquake source, the greatest weight is given to the analysis of long-period data such as the photographic records provided by the WWSSN stations. This is chiefly because the analysis of body-wave seismograms is greatly simplified if the wavelengths involved are larger than the spatial extent of the source so that directivity effects can be neglected. Restricting the frequency band in this fashion, however, implies that only the static properties of the source (such as depth, focal mechanism, and moment) can be determined confidently. By exploiting an extended frequency band, it is possible now to obtain a dynamic description of the rupture process as well as to obtain conventional static source parameters. In order to consider the dynamics of the earthquake source, however, the body wave recordings must contain spectral information including and above the corner frequency of the earthquake. For most earthquakes that are recorded at teleseismic distances (i.e., those with $m_b > 5.0$) the frequency band of interest ranges from 0.1 to 5 Hz. This frequency band does not coincide with the peaks of the instrument response of commonly used seismographs (e.g., the WWSSN long- and short-period instruments). Frequency dependent effects that arise from source finiteness or from the propagation of body waves through the earth are obscured by the narrow bandwidth of the response of these instruments. These difficulties can be avoided through the analysis of broadband pulse shapes. By modelling broadband pulse shapes, Choy and Boatwright (1981) analysed the dynamic characteristics of the rupture processes of two moderate-sized earthquakes (m_b's of 5.5 and 5.9). One purpose of this paper is to demonstrate that a dynamic analysis can be obtained without the extensive waveform modelling employed by Choy and Boatwright (1981). Furthermore, the analysis can be done routinely because of the availability of data from the recently deployed global network of digitally recording seismographs, the GDSN (Global Digital Seismograph Network). The digital data from the GDSN have excellent broadband content and, when the network is completed, the global distribution of stations will provide good coverage of the focal sphere for most earthquakes.

A second purpose of this paper is to investigate the utility of determining the dynamic characteristics of the events of a foreshock sequence. The analysis of such a foreshock sequence is of critical importance for predicting large offshore earthquakes. By examining the moderate-sized events preceding a main shock, it might be possible to detect intermediate- and short-term variations in the regional stress field. We have chosen to analyse the characteristics of an earthquake sequence that encircled the eventual rupture zone of the large (M_S 7.8) Miyagi-Oki earthquake of June 12, 1978. The sequence occurred over a period of two years prior to the mainshock, a time-span during which a significant number of GDSN stations became operational. This dynamic information is then used to complement the tectonic interpretation from seismicity patterns and focal mechanisms that has been obtained for the Miyagi-Oki region by Yoshii (1979) and Seno (1982).

THE EXTENDED FORESHOCK SEQUENCE

The Miyagi-Oki earthquake that occurred off the northeastern coast of Honshu on June 12, 1978 was a large interplate earthquake (m_b 6.8; M_S 7.8) that caused loss of life and extensive damage in the Miyagi prefecture of Japan. An analysis of this earthquake by Seno et al (1979) found that the rupture was complex, consisting of at least two subevents which ruptured two distinct zones. The pattern of seismicity that developed from a few hours to a few months after the mainshock (Fig. 1) showed that one of the aftershock zones continued to grow beyond the primary rupture area (Engdahl et al., 1978; Engdhahl et al.,
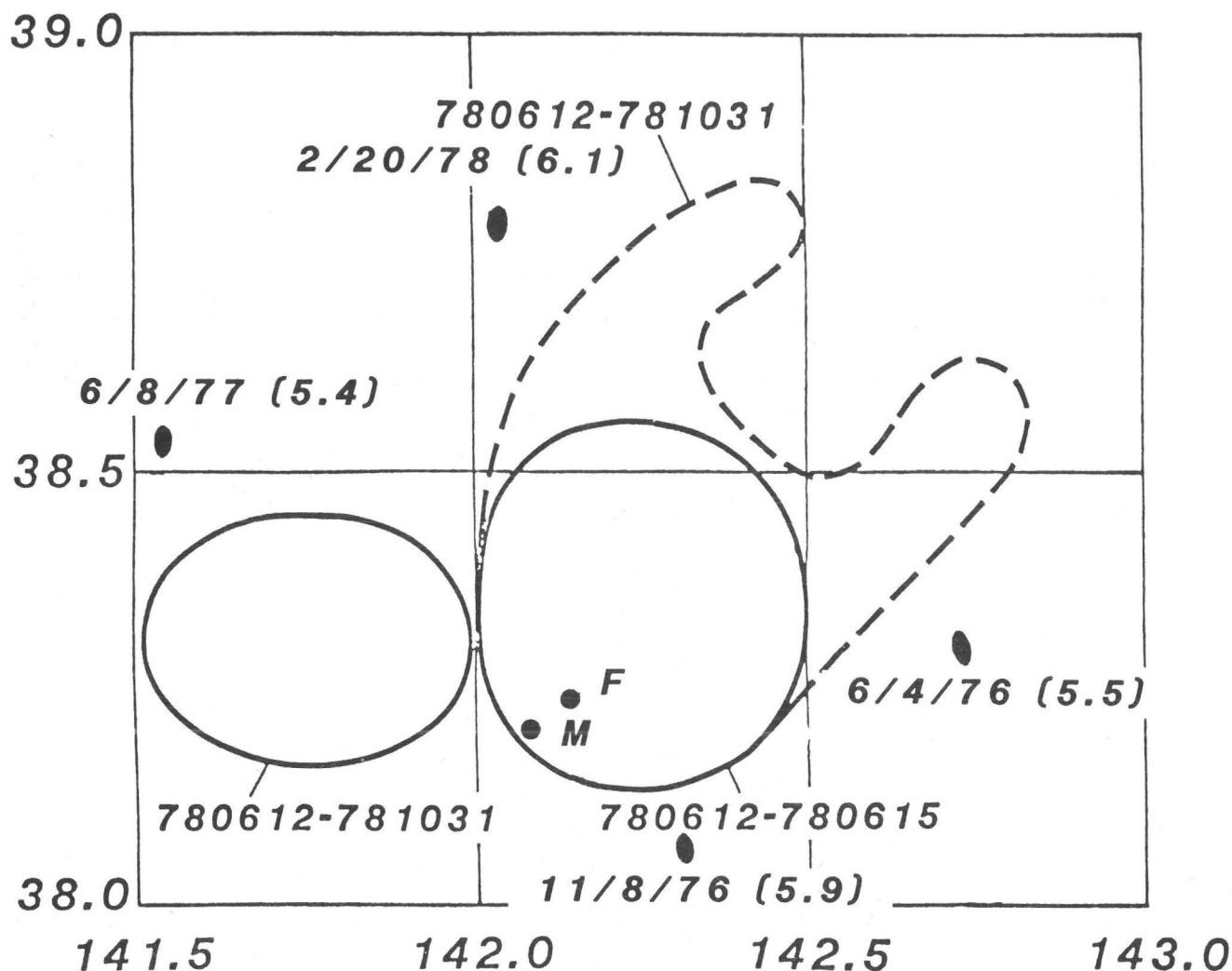
Figure 1. The rupture zones of the Miyagi-Oki earthquake as determined by aftershocks occurring a few days after the rupture (solid lines) and the growth of the aftershock zone (dashed lines) between June 12, 1978 until October 31, 1978 as determined by Engdahl et al. (1979). The solid lines also correspond to the rupture zones determined by Seno et al. (1980). Epicenters of the foreshock (F), mainshock (M) and earthquakes with $m_b > 5.4$ that occurred in the two years prior to the mainshock are indicated along with their date and magnitude. Note that the event of June 4, 1976 was not analyzed as no GDSN stations were operating at the time. (Figure modified from Engdahl et al. (1979)).
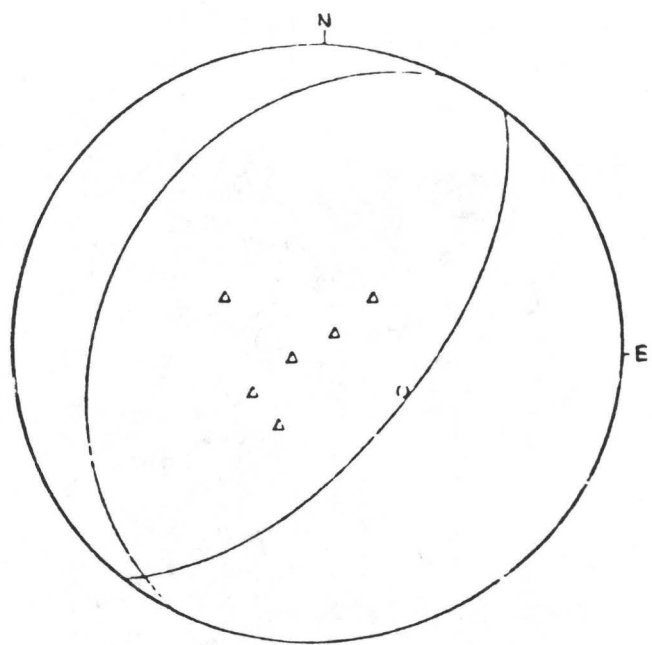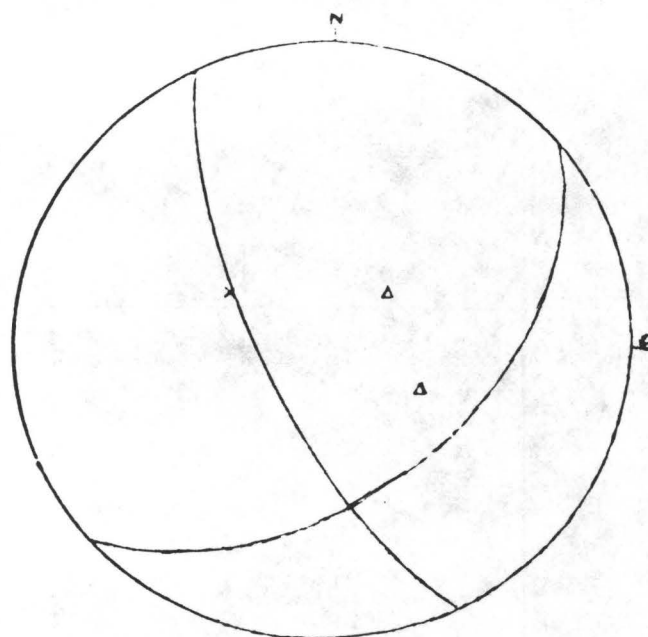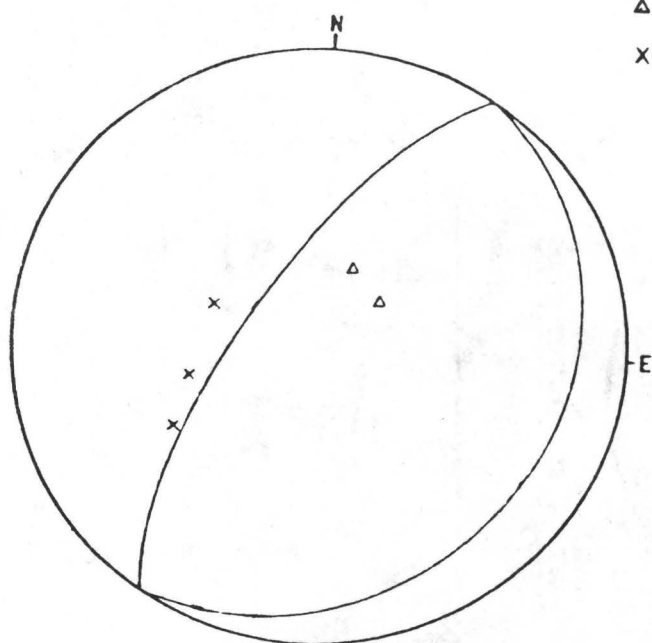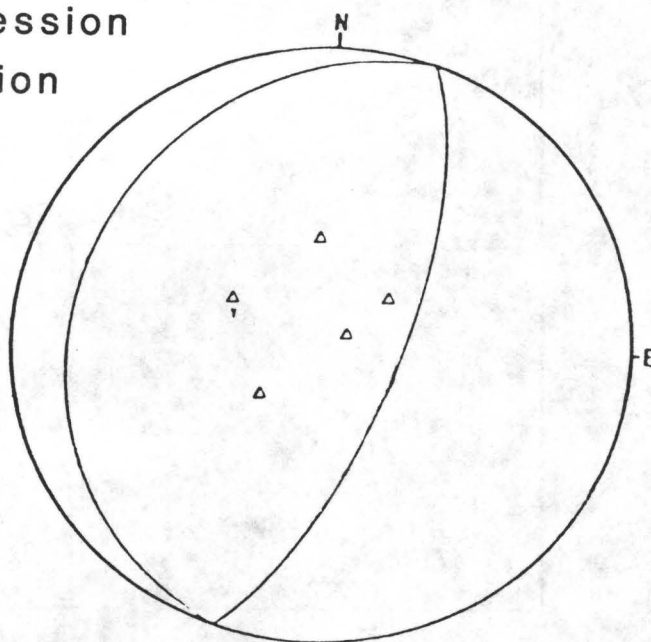
Figure 2. Lower hemisphere focal mechanisms of the four events listed in Table 1. The fault planes were constrained by P-wave motions from stations reporting to the NEIS. Takeoff directions and polarities of P and pP waves that were available from GDSN stations are shown. Triangular symbols are compressions; crosses indicate dilatations; and circles are sP takeoff angles.

Table 1. Hypocentral parameters of the extended foreshock sequence and the mainshock from Engdahl et al. (1979).

Event	Origin time			lat °N	lon °E	depth km	m_b	strike	dip	rake
1. November 8, 1976	08h	19m	28.8s	34.115	142.311	38	5.9	205°	30°	80°
2. June 8, 1977	14	25	47.7	38.517	141.545	72	5.5	152	78	45
3. February 20, 1978	04	36	59.41	38.793	142.030	53	6.1	212	70	90
4. June 12, 1978 (Foreshock)	08	06	12.13	38.237	142.104	35	5.7	198	20	90
5. June 12, 1978 (Mainshock)	08	14	27.83	38.206	142.079	37	6.8 (M_s7.8)	198	24	90

1979). This paper is concerned, however, only with the source characteristics of the moderate-sized earthquakes that preceded the main shock. Engdahl et al. (1978; 1979) found that prior to the mainshock, the region between 36°-39°N off the coast of northeast Honshu had been seismically quiet for earthquakes of magnitude greater than 7 since 1938 and for events greater than 6.5 since 1962. In the 11 years between 1964-1975, the NEIS has reported only 5 earthquakes for the region defined by Fig. 1 with m_b between 5.4-6.1, with no events larger than 6.1. We use a lower limit of 5.4 because that apparently is the threshold below which spectral information recorded at GDSN stations can not be used to analyse source mechanics. The detection threshold, of course, is much lower. In the two years preceding the mainshock (from 1976 until June 1978), there were five moderate-sized events including a foreshock. As shown in Fig. 1, these events encircled the eventual rupture zone of the mainshock. Only one of these events (that of June 12, 1978) is an obvious foreshock because it occurred about 8 minutes before the mainshock and was well within the final rupture zone. The spatial and temporal proximity of the other events to the mainshock suggests that they are causally related to the 1978 mainshock. Thus, the sequence is referred to as an extended foreshock sequence.

Of the five events in the extended foreshock sequence, four occurred after a significant number of GDSN stations had become operational. The conventional hypocentral parameters for these four events are given in Table 1. Their focal mechanisms (E. R. Engdahl, personal communication) are shown in Fig. 2. Note that all these parameters were derived from ray theoretical techniques which make minimal use of waveform data. For example, epicentral locations are the result of processing travel times, while the magnitudes are a measure of the maximum amplitude of a waveform. By themselves, these hypocentral parameters reveal little about the stress-state of the region prior to the main shock, although clusters of seismicity can be used to indicate regions of either high stress or low strength. A more complete understanding of each event and its relation to the faulting environment can be obtained if the phase and amplitude information in the waveforms is also exploited. In the next section we describe how the dynamic characteristics of rupture can be routinely determined from teleseismic recordings using as examples the waveforms generated by the Miyagi-Oki sequence.

DERIVATION OF SOURCE PARAMETERS FROM WAVEFORMS

Data processing

As the response functions of most conventional seismograph systems are shaped to match the inverse spectrum of earth noise, information in the frequency band between 0.1 to 1 Hz is heavily filtered. This makes detailed source studies of moderate-sized earthquakes difficult, as their corner frequencies are within the filtered passband. Fortunately, the high dynamic range of the GDSN instruments and the digital format of the recorded data permit spectral information in this frequency band to be retrieved. Broadband records of displacement and velocity are obtained using the method detailed in Choy and Boatwright (1981) and Harvey and Choy (1982), whereby a simultaneous deconvolution of the instrument response is applied to the long- and short-period channels of the GDSN data.

An example of the data processing is presented in Fig. 3. It shows a portion of the MAIO record for the earthquake of November 8, 1976 (depth 38 km; m_b 5.9) that contains direct P and sP. The absence of pP on the record is the result of the proximity of its takeoff angle to a nodal plane. The first two seismograms are the original long- and short-period channels, which were recorded digitally. Because of the instrumental filtering, these records each emphasize only a

676

Long period SRO

Short period SRO

Broad-band
displacement

P   s*P*

Velocity

v^2

10 sec
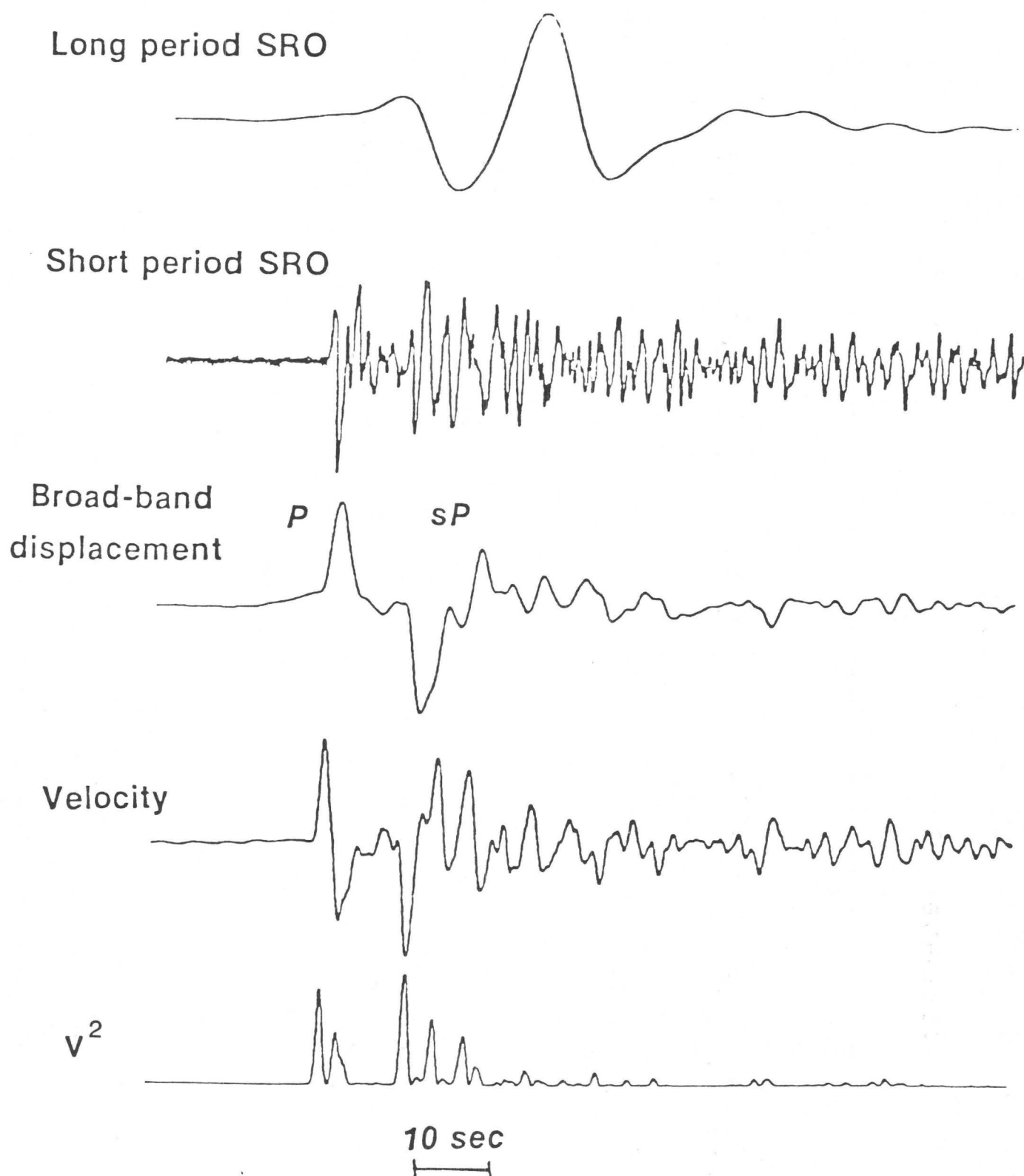
Figure 3. (Top two records) Digitally recorded long- and short-period vertical component seismograms at station MAIO (Δ 63.7°) containing P and sP arrivals from the event of November 8, 1976. Start time of the record section is 08h 29m 52.05s. The long-period channel is sampled at 1 Hz while the short-period channel is sampled at 20 Hz. (Third record from top) The broad-band record of ground displacement constructed by the simultaneous deconvolution of the instrument response from the original long- and short-period records. (Fourth record from top) Corresponding record of velocity. (Bottom) Corresponding record of velocity-squared.

677

November 1976

June 1977

1.3
1.0

1.1
.77

displacement

678

1.1
.87

1.2
.85
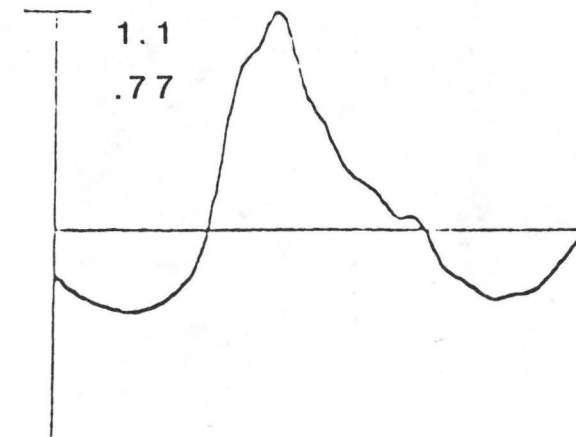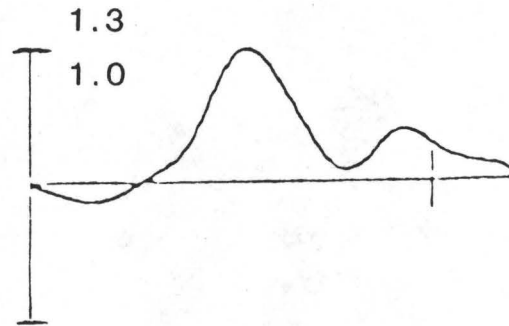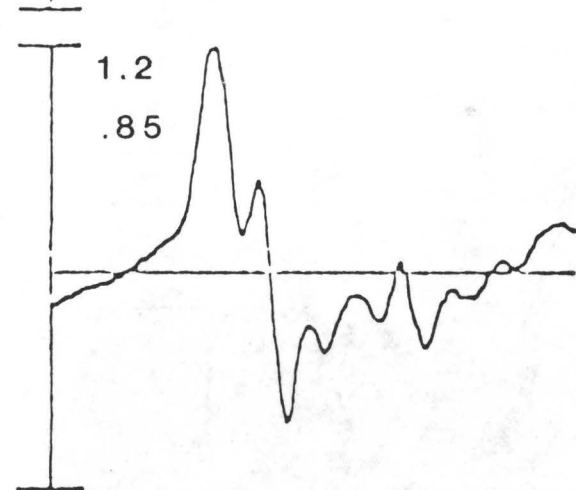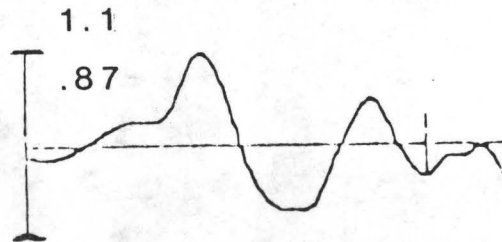
velocity

4 sec

Figure 4a. The P-waves at station ANMO (Δ~83.4°) for the events of November 8, 1976 and June 8, 1977 are shown. Top record is displacement and bottom record is velocity. Next to each trace is the maximum absolute amplitude in microns for displacement and in microns/sec for velocity before (upper number) and after (bottom number) multiplication with a radiation pattern coefficient given by the corresponding focal mechanism of Fig. 2 and Table 1.

February 1978

June 1978   (foreshock)

displacement

7.2
5.3

.62
1.3

velocity

5.4
4.0

.75
1.6

679

4 sec
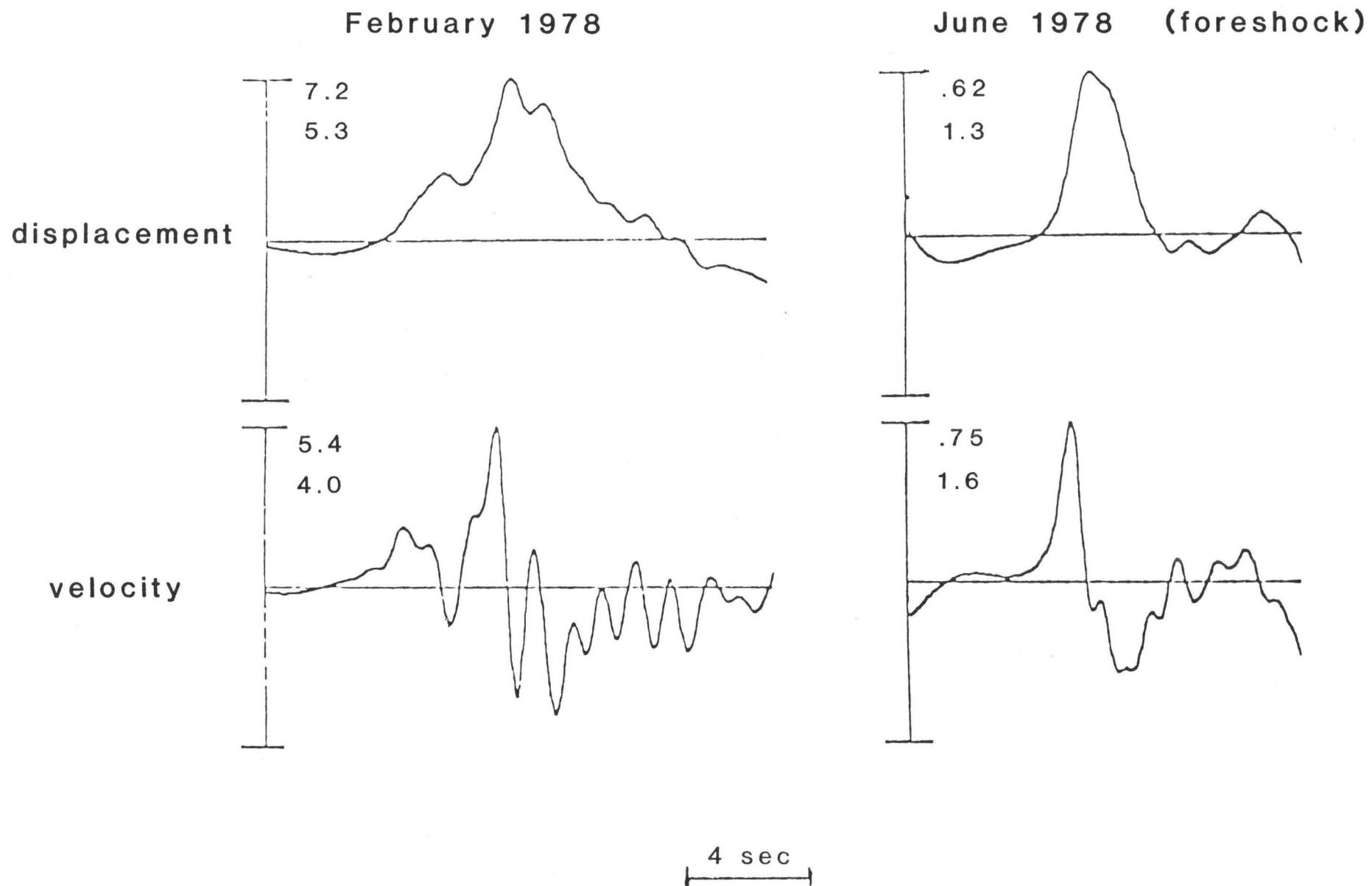
Figure 4b. Same as Figure 4a for the P-waves at station ANMO for the event of
February 20, 1978 and the foreshock of June 12, 1978.

narrow band of information. Consequently, they are not particularly useful except for determining an arrival time and a maximum amplitude. The ground displacement obtained by simultaneous deconvolution is shown in the next record. In contrast to the raw records, a rise time and signal duration can generally be associated with body-wave displacements. The next trace shows velocity. As described in a subsequent section of this paper on inversion of pulse duration measurements, the pulse shapes often exhibit substantial complexity which is easiest to analyse using the velocity records. The rise time of the ground displacement, for example, becomes a single pulse in velocity. The final trace shows the velocity-squared record, which may be considered to be a record of the energy flux rate (Boatwright, 1980). In addition, depth phases are much easier to distinguish using the broadband records.

Fig. 4 compares the P-waveforms at one station, ANMO, for each of the four earthquakes in the sequence. For each event both the broadband displacement (top) and the corresponding velocity (bottom) at ANMO are shown. The top number alongside each trace is the absolute amplitude at ANMO. The lower number is obtained by correcting the top one for the radiation pattern, using the appropriate focal mechanism in Fig. 3. For purposes of comparing the waveforms, it is not necessary to correct for variations in geometrical spreading, as all the events have essentially the same correction. The body wave radiated by the event of February 20, 1978, which preceded the main shock by a little more than three months, differs significantly from the other waveforms. Its duration on both the displacement and velocity records is longer, and the waveform more complicated, than the waveforms of the other events. As described later, the complexity in the waveform can be decomposed into at least two subevents. The slope of the velocity pulse of the second subevent (dashed line) for this P-wave is substantially steeper than than in any of the other waveforms.

Figs. 5-8 show the data from the GDSN stations that were used in the analysis of each earthquake. In each figure, the broadband velocity pulse shapes have been plotted about the focal sphere. The fault plane and takeoff directions of the body waves have been rotated so that the fault plane coincides with the plane of the stereonet. The downdip direction is indicated by the arrow in the center.

Moment, radiated energy, dynamic and apparent stress drops

By removing the distortion of the instrument response from the data, properties of the displacement and velocity waveforms can be directly measured and used to estimate a number of source parameters. Assuming that the pulse shapes are not distorted by propagation effects other than causal attenuation, the moment can be determined from the area under the pulse shape of individual body phases; the dynamic stress drop can be estimated from the initial slope of the velocity pulse; and the radiated energy can be obtained from the integral of the velocity-squared pulse shape. However, in order to make proper use of these measurements it is equally important to apply corrections for the focal mechanism and the effects incurred by body waves propagating through the earth.

For P-waves between approximately $30° < \Delta < 90°$, the propagation operator for a point source consists primarily of the effects of geometrical spreading and attenuation. While attenuation does not affect the area under a displacement pulse, it can significantly reduce the the initial slope of the velocity pulse as well as reduce the area under the integral of velocity squared. The distortion in the waveform can be corrected by deconvolving the propagation operator with the data. If a Futterman operator (say, t^*) which describes attenuation is known a

Table 2. Extended set of source parameters derived from broadband telese-
ismic waveforms. Rupture geometry and direction are the quantities derived
from the inversions of the signal durations, τ. Rupture length is measured from
the hypocenter to the fault perimeter along the direction of greatest unilateral
propagation. Rupture half-width is measured from the hypocenter to the fault
perimeter along a direction normal to the rupture length. The rupture direction
is measured clockwise from the downdip direction. The apparent rupture velo-
city is normalized to the P-wave velocity at the source.

Event	Moment (10^{24}dyne·cm)	Radiated Energy (10^{20}dyne·cm)	Dynamic Stress Drop(bars)	Apparent Stress Drop(bars)
1. November 8, 1976	4.6 ± 1.8	0.5	9 ± 3	5
2. June 8, 1977	2.5 ± 0.8	0.1	10 ± 5	3
3. February 20, 1978	56.0 ± 19.0	30.0	35 ± 12 175 ± 75	30
4. June 12, 1978 (Foreshock)	4.0 ± 1.8	0.4	20 ± 9	9
5. June 12, 1978 (Mainshock)	3100.0 †		33 ± 11 85 ± 20††	

Event	Static Stress Drop(bars)	Complexity	Average Rupture Velocity	Rupture Geometry Length (km)	Half-width (km)	Rupture Direction
1. November 8, 1976	15	1.1	0.40	9.2 ± 3.8	5.7 ± 2.5	$90°\pm60°$
2. June 8, 1977	16	1.2	0.37	13.3 ± 12.0	3.4 ± 3.4	$90°\pm20°$
3. February 20, 1978	102	1.7	0.31	11.6 ± 3.2	6.1 ± 2.0	$255°\pm20°$
4. June 12, 1978 (Foreshock)	69	1.2	0.38	9.6 ± 8.0	2.4 ± 2.4	$60°\pm40°$
5. June 12, 1978 (Mainshock)	95 145 †††					

† From Seno et al (1979).

†† Dynamic stress drop of first 2 of 3 subevents using waveforms.

††† Static stress drop of last 2 of 3 subevents from the two-segment model of
Seno, et al (1979).

priori, then the propagation operator can be approximated by convolving t* with R($\underline{x}, \underline{\xi}_0$), the ray-theory coefficient describing the geometrical spreading between $\underline{x}$ and $\underline{\xi}_0$, the receiver and source coordinates, respectively. The operator for surface-reflected arrivals such as pP and sP should be multiplied by the free-surface reflection coefficient. Expressions for R can be found in Aki and Richards (1979, ch. 4). As a t* is generally not known a priori, we prefer to obtain the propagation operator explicitly through seismogram synthesis. We use the full wave theory (as described by Richards, 1973; Choy, 1977; and Cormier and Richards, 1977). In addition to using analytic expressions to describe dispersive attenuation (Cormier and Richards, 1976), the method remains valid for rays at near-grazing incidence to a discontinuity. Thus, it correctly describes the effects of diffraction, and the system of rays that arise from a cusp or a caustic. This is an important aspect, because body phases which have strong frequency-dependent interactions with earth structure (e.g., PKP, P(diff)) are recorded very often. Because of the coarse station distribution of the GDSN, it is necessary to include as many pulse shapes as possible in the source analysis.

The crustal model of Yoshii and Asano (1972) was used to describe the structure near the source region. For the mantle, a Q-model which is appropriate to the frequency band of the data was used, the AFL model (Archambeau, et al., 1969; Lundquist and Cormier, 1980; Choy and Boatwright, 1981). For the earth's core, the model PEMS' of Choy and Cormier (1982) was used.

The moment may be estimated from body-wave pulse shapes using the relation

$$M_0 = 4\pi \left[\rho(\underline{\xi}_0)\, \rho(\underline{x})\, c(\underline{x}) \right]^{\frac{1}{2}} c(\underline{\xi}_0)^{\frac{5}{2}} \frac{R(\underline{x}, \underline{\xi}_0)}{F(\vartheta, \varphi)}\, u(\underline{x}, \omega \to 0) \tag{1}$$

where $\rho(\underline{\xi}_0)$ and $c(\underline{\xi}_0)$ are the average density and wave velocity at the hypocentral region, $\rho(\underline{x})$ and $c(\underline{x})$ are the density and wave velocity at the receiver, $F(\vartheta, \varphi)$ is the radiation pattern coefficient for the body wave with takeoff angle ϑ relative to the fault normal and azimuth φ relative to the slip direction. Here, $u(\underline{x}, \omega \to 0)$ is the low-frequency asymptote of the displacement spectrum or, equivalently, the area under the displacement pulse.

Assuming the event grows as a self-similar crack, then the dynamic stress drop can be measured from the initial slope of the velocity waveforms using the relation given by Boatwright (1980)

$$\tau_e = \frac{\left[\rho(\underline{\xi}_0)\, \rho(\underline{x})\, c(\underline{x}) \right]^{\frac{1}{2}} c(\underline{\xi}_0)^{\frac{5}{2}}}{C\left(\frac{v}{\beta}\right) v^2 \beta(\underline{\xi}_0)} \left| \frac{R(\underline{\xi}_0, \underline{x})}{F(\vartheta, \varphi)} \right| (1 - \zeta^2)^2 \left| \frac{\dot{u}(\underline{x}, t)}{t} \right| \tag{2}$$

where $C(v/\beta)$ is the Kostrov function, v is the rupture velocity, β is the shear-wave velocity, and $\zeta = v \sin\vartheta / c(\underline{\xi}_0)$ where ϑ is the takeoff angle relative to the fault normal. The last term in brackets is the average initial slope after correcting for attenuation. There are two assumptions implicit in our use of equation 2. First, we assumed that the rupture velocity of the subevents in each earthquake was constant throughout the sequence with a value of $.75\beta$. Although small perturbations from this value (such as $.7\beta$ or $.8\beta$) affect the absolute value of the stress drop, the ratio of the values over the foreshock sequence will be preserved. A second assumption is that the subevents that comprise a multiple rupture nucleate as point sources. Provided the rupture phases are sufficiently
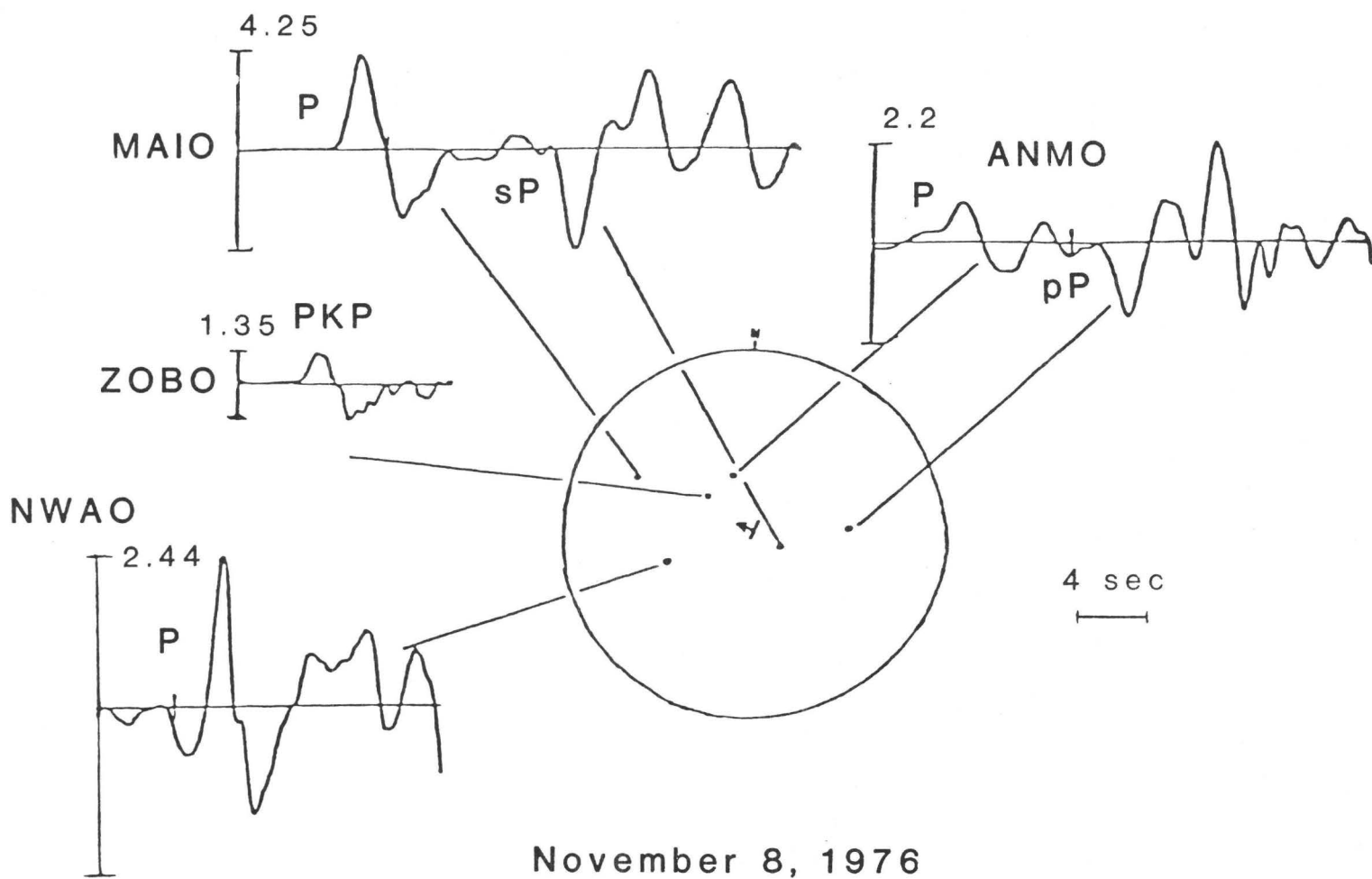
Figure 5. Plotted about the focal sphere are the deconvolved velocity pulse shapes for the suite of body waves recorded by the GDSN stations for the event of November 11, 1976. Note that the fault plane and the takeoff directions of the body waves have been rotated so that the fault plane coincides with the plane of the stereonet. The downdip direction is indicated by the symbol in the center. The maximum ground velocity in microns/sec is given next to each body phase.
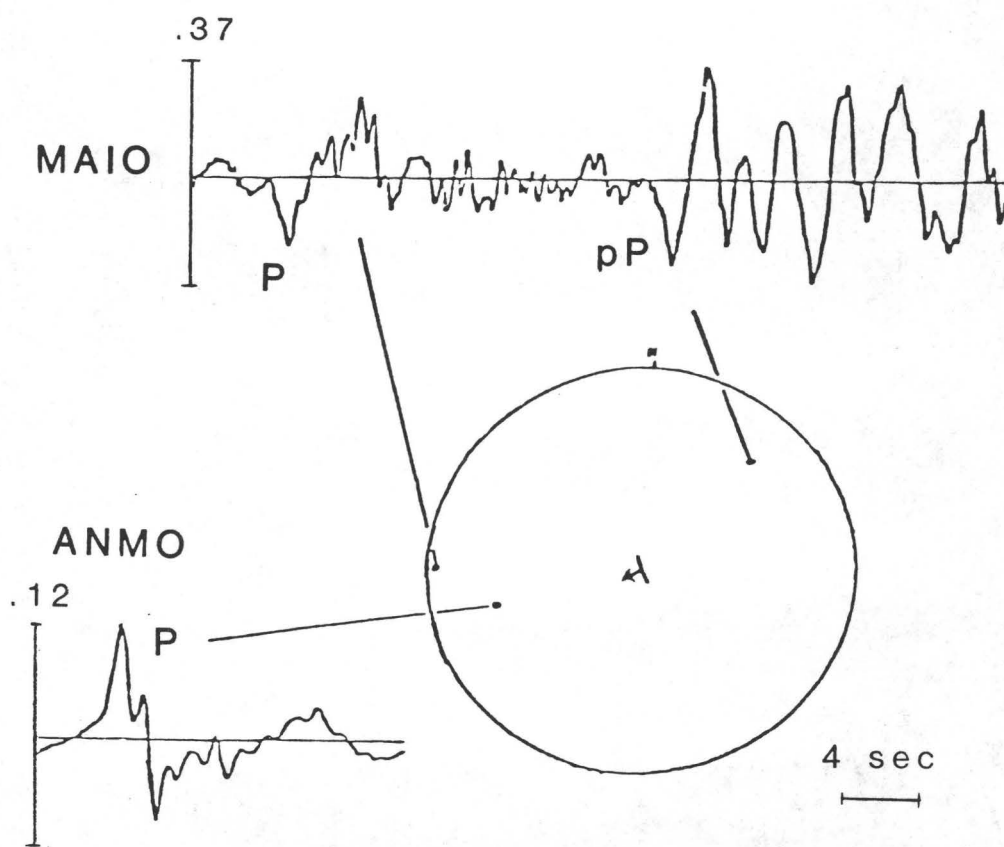
June 8, 1977

Figure 6. Same as Fig. 5 for the event of June 8, 1977.
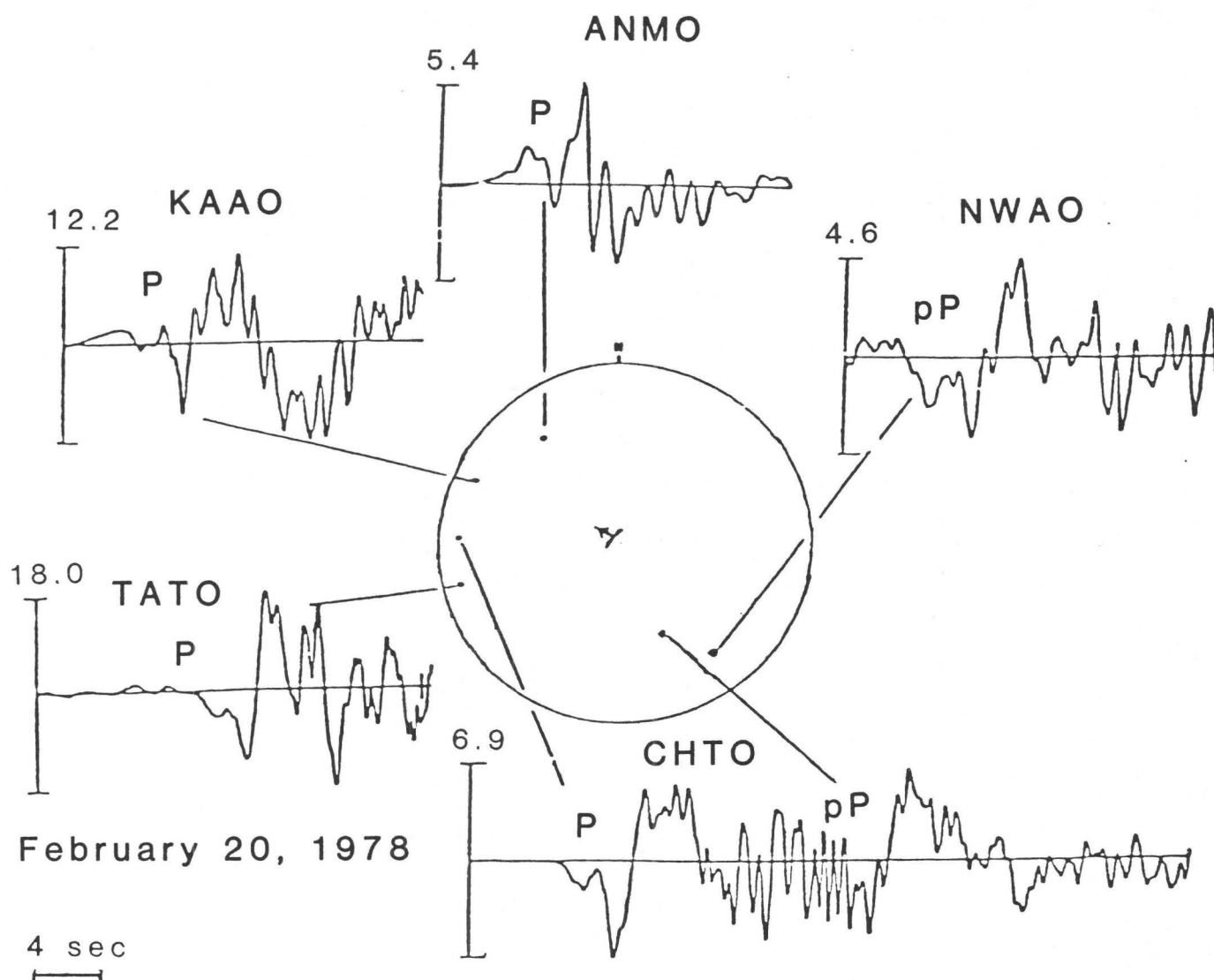
Figure 7. Same as Fig. 5 for the event of February 20, 1978. Note that parameters derived from the TATO waveform were given less weight than other station values because of the uncertainty in the model of the upper mantle used in computing a propagation operator for its epicentral distance, 22.0°.
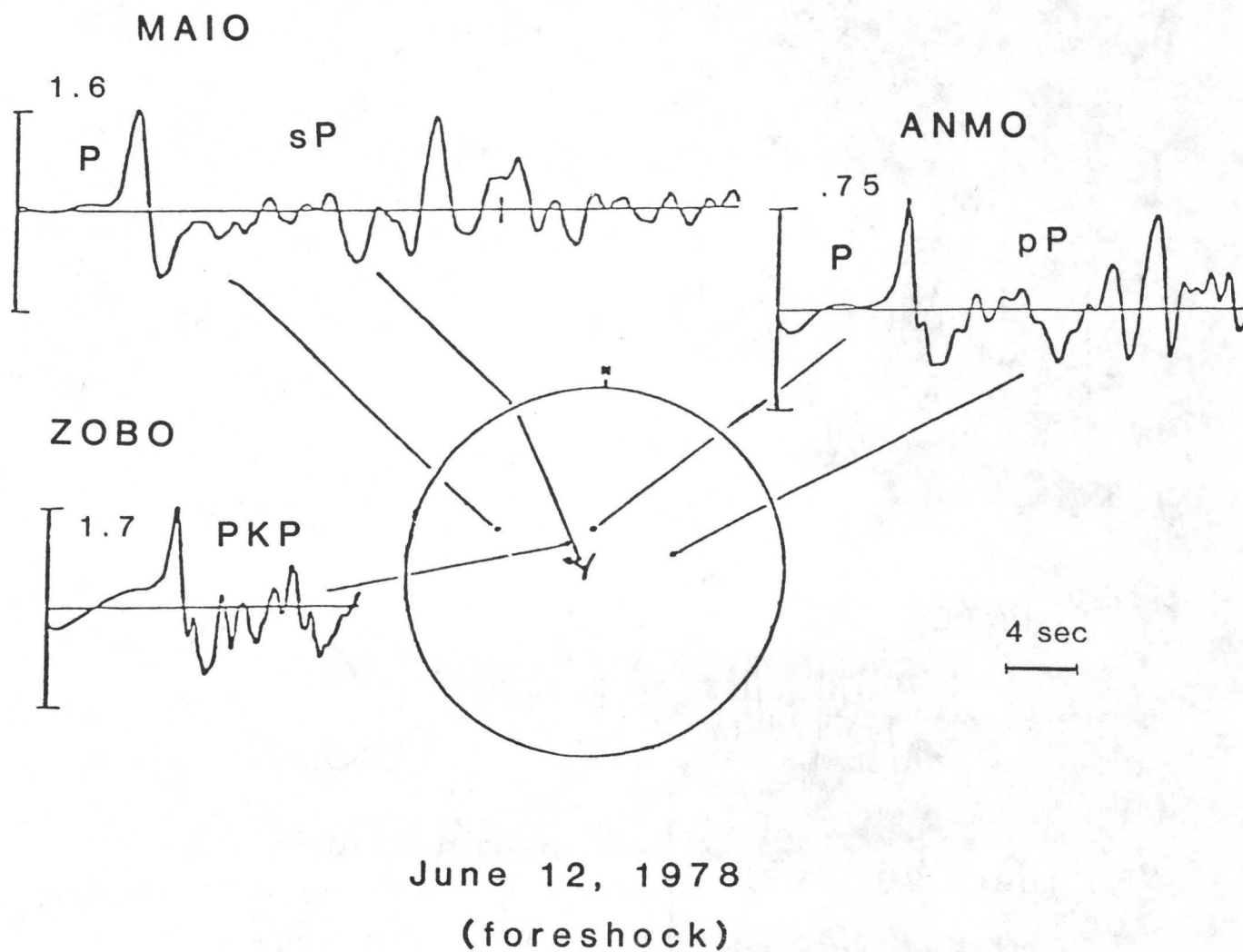
Figure 8. Same as Fig. 5 for the foreshock of June 12, 1978.

distinct in the overall pulse shape, this permits a dynamic stress drop to be computed for each subevent. However, it is important to recognize the limit of this approximation. As a dynamic release of stress affects the stress state of areas outside of the immediate rupture, the secondary events may represent a complex failure of a finite area. As an example, consider the waveforms of the event which occurred on February 20, 1978 (Figs. 7 and 9). The slope of the first subevent can be clearly measured. Because this subevent is significantly more energetic than the first subevent, the approximation that it nucleates from a point does not bias the estimate of the stress drop.

In addition to these foreshocks, dynamic stress drops could be obtained for the first two of the three subevents that comprise the main shock. However, the complexity of the later parts of the waveforms generated by the mainshock precluded estimating a stress drop for the third subevent. On the basis of aftershock data, Seno et al. (1979) were able to compute static stress drops for the the last two large subevents, but not the initial tiny one. Our dynamic stress drop for the second subevent (τ_e=85 bars) compares well with Seno's static stress drop (σ=95 bars). These values are also given in Table 2.

The radiated energy is related to the energy flux (integral of the velocity-squared) by the relation given by Boatwright (1980),

$$E_s = \left[\frac{R(x,\xi_0)}{F(\vartheta,\varphi)} \right]^2 \frac{\rho(x)c(x)}{e_c(\vartheta,\varphi)} I(x) \tag{3}$$

where $I(x)$ is the integral of the square of the ground velocity. The factor e_c is the fractional energy flux which relates the energy flux radiated by a wave type in a particular direction to the total radiated energy. As can be seen in Fig. 2, there is little difficulty in choosing the correct time window for computing $I(x)$ for each body phase. The largest uncertainty occurs in making the correction for attenuation. We make no estimate of this uncertainty, leaving understood that it is related to the appropriateness of our Q model. Nevertheless, by using a consistent Q model for all the events, the ratios of the radiated energy among the events is approximately constant.

The apparent stress is determined from the moment and radiated energy using the relation of Wyss and Brune (1968),

$$\tau_A = \mu \frac{E_s}{M_0} \tag{4}$$

where μ is the average rigidity at the hypocenter. The values of moment, radiated energy, dynamic stress drop, and apparent stress are compiled in Table 2. The most striking feature of this table of parameters is that the February 20, 1978 event, while having a somewhat lackluster m_b of 6.1, has stress drops and moment several times that of the other events.

Inversion of duration measurements for complexity and rupture geometry

Because moderate-sized earthquakes are not usually followed by aftershocks that are sufficiently large to locate teleseismically, the rupture geometry must be determined directly from body-wave observations. Choy and Boatwright (1981) have demonstrated that the broadband pulse shapes obtained by processing GDSN data can vary significantly over the focal sphere for deep earthquakes as small as m_b 5.5. They determined the rupture geometry for two deep events by adding together the synthetic pulse shapes from an assumed set of coherent subevents to model the broadband pulse shapes. This technique,

however, becomes time-consuming for strongly complex ruptures. In this section, we briefly describe a technique wherein the rupture geometry may be directly determined from a set of duration measurements made on the broadband velocity pulse shapes. The method is a simplification of Boatwright's (1982) analysis of eight aftershocks of the 1975 Oroville, California, earthquake.

Boatwright (1982) assumes that a complex rupture can be modelled as a sequence of coherent subevents, each of which has the same rupture velocity, separated by a set of rupture delays. From observational experience, we can usually correlate a specific positive half-cycle in the ground velocity across a suite of pulse shapes from the same event. To quantify the complexity of the rupture process, then, we consider the the ratio of the signal duration of the whole complex waveform, τ, to the pulse duration of this specific pulse, $\tau'_{1/2}$. Assuming that the complex rupture process is made up of c subevents of duration $2\tau'_{1/2}$, separated by c-1 delays of duration $2g\tau'_{1/2}$, the ratio of the signal duration to the pulse duration may be written as

$$\frac{\tau}{2\tau'_{1/2}} = c + g(c-1) \tag{5}$$

where c is the complexity, or multiplicity, of the rupture process. The parameter g depends on the relative compactness of the waveforms. In this analysis, g is assumed to 1.0. The measurements of $\tau'_{1/2}$ and τ for the pulse shapes radiated by the February 20, 1978 event are shown in Fig. 9. The estimate of the complexity computed from eq. (5) for this event is c=1.7.

The principal effect of this rupture complexity is to decrease the average rupture velocity of the complex rupture process. The sum of the rupture lengths of the c subevents is approximately $2cv'\tau'_{1/2}$, where v' is the rupture velocity of the subevents; setting this length equal to $v\tau$, where v is the average rupture velocity, gives

$$\frac{v}{v'} \approx \frac{2c\tau'_{1/2}}{\tau} \tag{6}$$

By assuming the rupture velocity of the subevents and quantifying the complexity of the waveforms as discussed above, the average rupture velocity of a complex rupture can be determined from eq. (6). While the preceding analysis is rather simplistic, it represents an important new consideration in interpreting complex waveforms.

The rupture geometries of the subevent and the complex event may be estimated from the $\tau'_{1/2}$ and τ duration measurements, respectively, by minimizing the error,

$$\chi^2 = \sum_{i=1}^{N} \frac{[\tau_i - (1-e)\tau_c(\frac{a}{v}) - e\tau_u(\frac{a}{v},\varphi_r)]^2}{\sigma_i^2} \tag{7}$$

where τ_i and σ_i are the pulse durations and standard deviations measured from N body-wave arrivals, e is the percent unilateral rupture (bounded as $0 \leq e \leq 1$), $\tau_c(\frac{a}{v})$ is the pulse duration expected from a circular rupture of radius a and body wave velocity c and $\tau_u(\frac{a}{v},\varphi_r)$ is the duration expected from a unilateral rupture of length a in the direction φ_r. The formulae for $\tau_c(\frac{a}{v})$ and $\tau_u(\frac{a}{v},\varphi_r)$
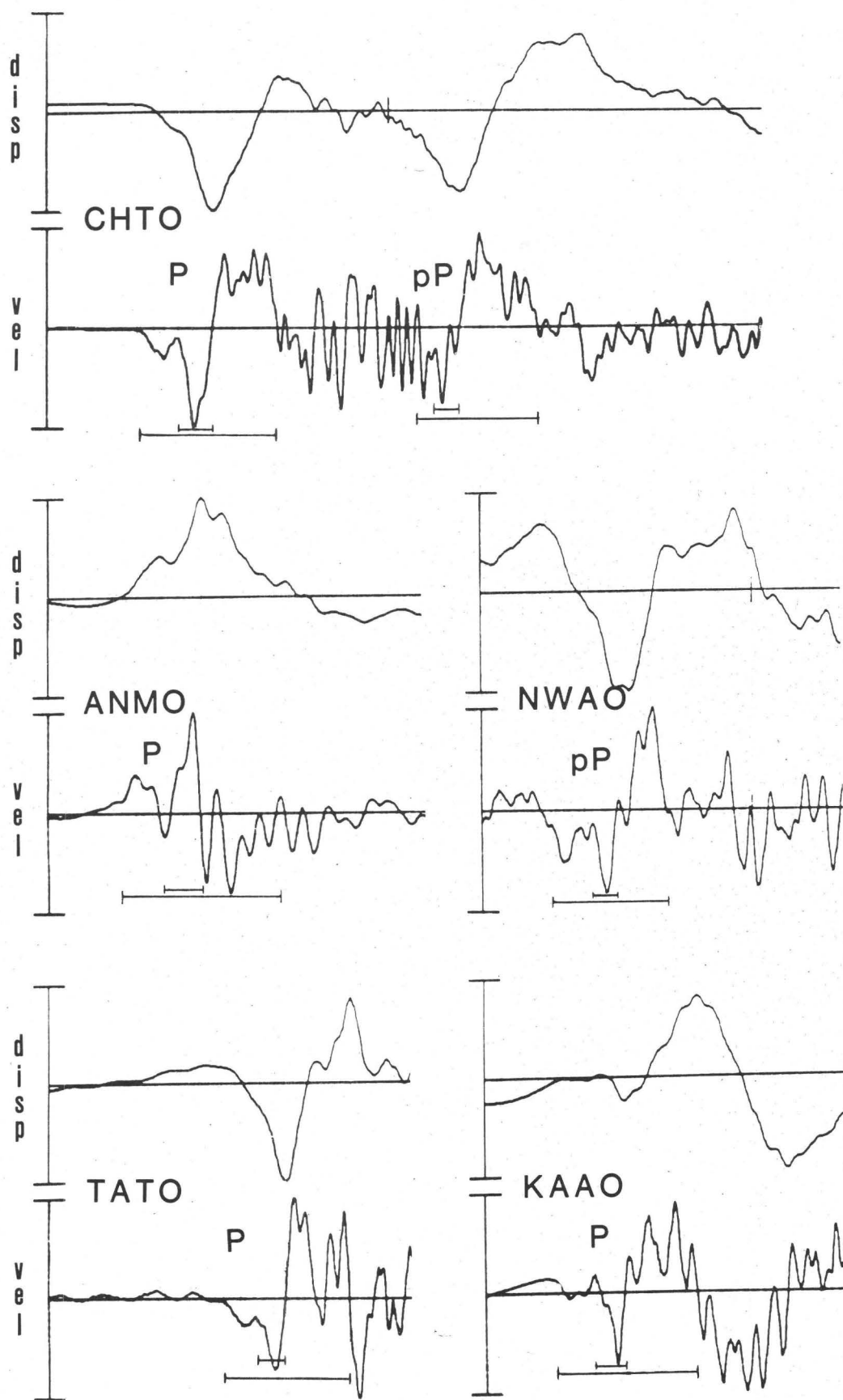
Figure 9. The choice of the total pulse duration (τ) and the half-duration ($\tau'_{1/2}$) of a dominant subevent for the P-waves from the February 20, 1978 event are indicated by the long and short horizontal brackets, respectively.

appropriate for the inversion of the pulse-duration and the signal-duration measurements, respectively, are derived in the Appendix of Boatwright (1982). These formulae are linear in the geometrical parameters e and a/v, so that a best fitting rupture geometry can be determined for any direction of rupture. The direction of rupture is then searched in 15° increments for the minimum χ^2. The rupture velocity used for the inversion of the pulse durations, $\tau'_{1/2}$, is the assumed subevent rupture velocity $(.75\beta)$, while the velocity used for the inversion of the signal durations, τ, is the average rupture velocity obtained from eq. (6) and listed in Table 2.

To obtain the rupture geometry of the complex event, the rupture width is estimated from the rupture length and the percent unilateral rupture as

$$w = \frac{a\left[1 + (1-e^2)^{\frac{1}{2}}\right]}{2(1+e)} \tag{8}$$

The static stress drop is then estimated as

$$\Delta\sigma = \frac{(1+e)}{2aw^2} M_0 \tag{9}$$

A measure of the accuracy of this technique can be obtained by comparing our results with those of Seno (1982). Because the largest and most complex event of the sequence, the February 20, 1978 event, was followed by significant seismic activity, Seno was able to map a rupture zone from the aftershock distribution and obtain a static stress drop. The aftershock distribution indicated that the event ruptured almost unilaterally to the southwest and has a total extent of ~20 kms and a width of ~10 kms. The results from our inversion of the signal durations indicate that the rupture length was ~12 kms towards the southwest, in a direction slightly updip or along strike, with a half-width of ~6 kms. One reason the source areas are somewhat different is that body waves are shaped by the source region in which there was a sudden stress release. On the other hand, aftershocks are recorded over a comparatively long time interval and may represent an adjustment of stress over an area greater than the primary rupture zone itself. Our static stress drop using eq. (9) was 102±52 bars, which would appear to be in excellent agreement with Seno's value of 100 bars, obtained from the aftershock area and a moment of 0.8×10^{26} dyne-cm, derived from surface-wave analysis.

The rupture geometry (i.e., rupture length, per-cent unilateral rupture and rupture direction) determined from the signal durations, and the static stress drop for each event in the sequence are listed in Table 2. The rupture geometries and rupture directions are also plotted in Fig. 10, as projected on the earth's surface. The projected rupture areas of the June 8, 1977 and February 20, 1978 events are distorted because these ruptures occurred on steeply dipping fault planes. The inversions for the rupture geometries of the June 8, 1977 and the June 12, 1978 foreshocks are poorly constrained because of the lack of data (3 and 5 pulse shapes, respectively), while the rupture direction of the November 8, 1978 event cannot be determined because of the distribution of takeoff angles. The large static stress drop (69 bars) for the June 12, 1978 foreshock is the result of the unilateral geometry, also weakly constrained, returned by the inversion of the signal-duration estimates. The lack of constraints on the rupture geometry of these events, a result of poor sampling of pulse shapes, corresponds to a realistic physical uncertainty about rupture geometries. Methods of estimating source size which assume a specific

geometry (e.g., the circular geometry assumed in Brune's (1970) method) return unreliable estimates of source size (Boatwright, 1982).

DISCUSSION

The only source parameters analysed in most studies of foreshock sequences are patterns in hypocentral locations (which can delineate seismically active zones as well as seismic gaps), magnitudes (which can be used to monitor b-values), and patterns of stress axes from focal mechanisms (which permit the inference of regional stress directions). These parameters can help to provide a qualitative interpretation of the tectonic activity in a region. If spatial and temporal patterns in an extended set of dynamic parameters, derived from teleseismic broadband waveforms, are also examined, the tectonic environment in the short and intermediate time scale (i.e., from a few years up to the time of the mainshock) might be inferred. In this section, we complement the tectonic interpretation of the Miyagi-Oki region that has been obtained by using seismicity patterns and focal mechanisms with the pattern of source parameters that developed in the extended foreshock sequence.

Using well-located hypocenters and focal mechanisms, Yoshii (1979) obtained a general kinematic description of the seismic behavior of the region off the coast of northeastern Honshu. His model is illustrated schematically in Fig. 11. Tectonic features of a typical cross-section include the trench axis, the volcanic front (VF) and the aseismic front (AF). The aseismic front is Yoshii's term for the the wedge of material with low Q and low velocity that is bounded by the lithosphere and the descending slab. On the seaward side of the aseismic front, the seismicity in the descending slab is characterized by low-angle thrust-faulting, which is characteristic of the interaction between a down-going oceanic slab and the continental lithosphere. In the descending slab that is landward of the aseismic front, a double seismic zone develops. The zones are each about 10-15 km thick and are separated by about 35 km. The seismicity in the upper zone is characterized by focal mechanisms with down-dip compression axes. In contrast, the focal mechanisms of the lower zone are characterized by down-dip tensional axes. The double-zone pattern could be the result of an unbending of stresses in the slab (Engdahl and Scholz, 1977; Isacks and Barazangi, 1977), of a sagging of the slab (Smith and Toksoz, 1972), or of thermal effects on the descending slab (House and Jacob, 1982).

This extended foreshock sequence was chosen for investigation for several reasons. It represented an unusual increase in moderate-sized seismic activity in the two years prior to the mainshock; the sequence encircled the aftershock zone clockwise in map view (Fig. 1) and counterclockwise in plane view (Fig. 12). Another unusual aspect is that when Yoshii's data base (from 1964-1973) was supplemented by high quality focal mechanisms for events up to 1978, Seno and Pongsawat (1982) and Seno (1982) found that the region where the Miyagi-Oki earthquake occurred deviated from Yoshii's model significantly prior to the main shock. An examination of the pattern of focal mechanisms in the vicinity of the eventual mainshock (Seno and Pongsawat, 1982) showed that the upper layer of the double seismic zone in the descending slab seemed to have extended at least 50 km seaward of the aseismic front to form a triple zoned pattern: a zone of low-angle thrust faulting near the slab interface (typified by the November 8, 1976 event and the June 12, 1978 foreshock and mainshock); a zone of down-dip compression beneath it (evidenced by the June 8, 1977 and the February 20, 1978 events); and lastly a zone of down-dip tensional mechanisms. The focal mechanism of the February 20, 1978 event had a down-dip compressional axis. Such a mechanism on the seaward side of the aseismic front (Fig. 12) with magnitude ≥ 5.4 had not been observed at least between
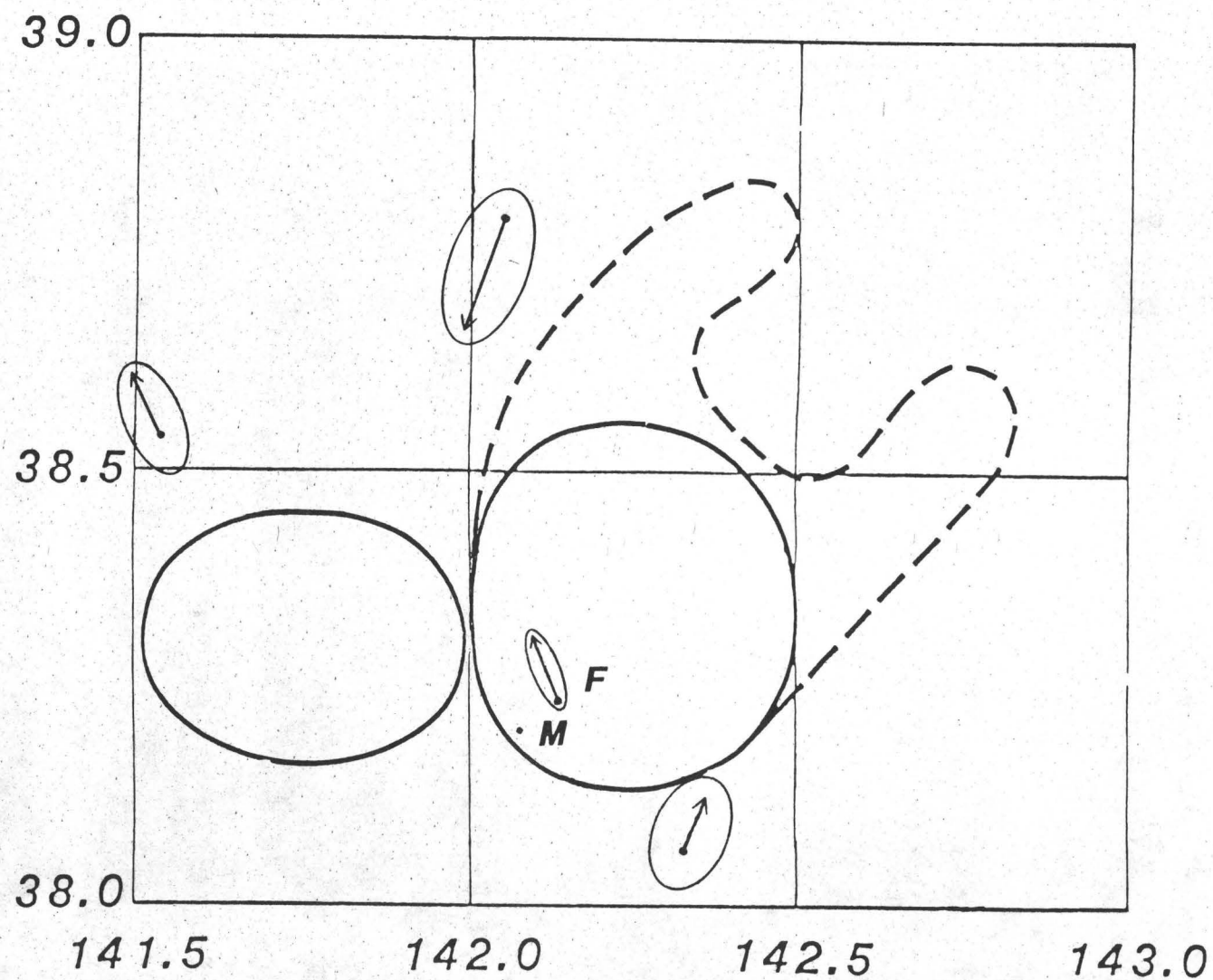
Figure 10. The rupture geometries from the inversion of the signal duration for each event of the extended sequence are shown. The arrows indicate the rupture direction obtained by this inversion.
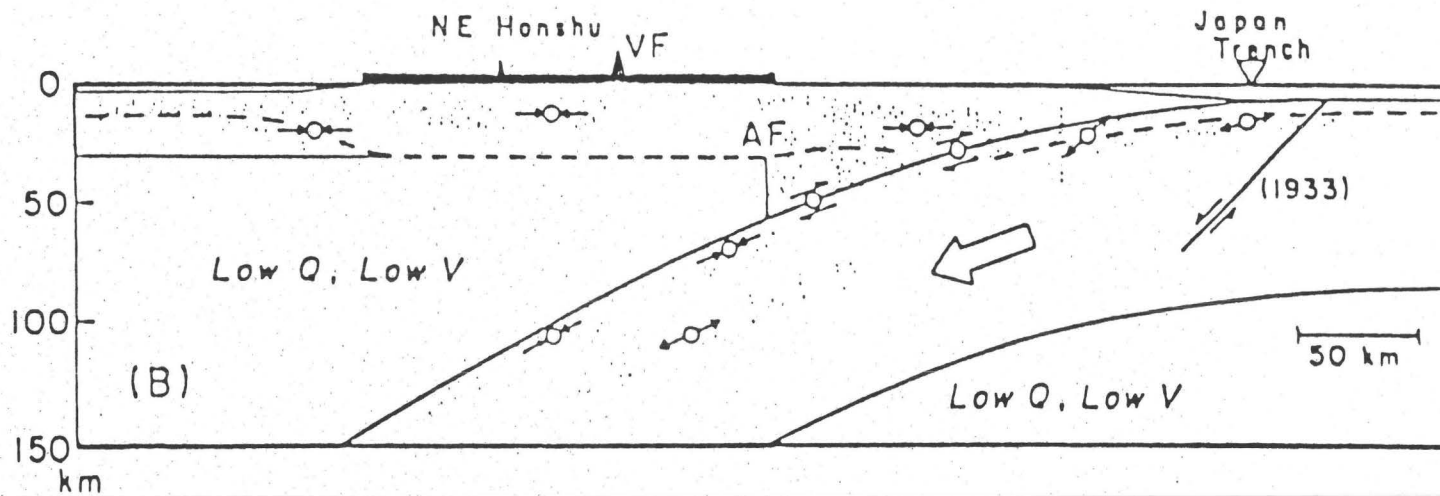
Figure 11. A schematic of   the seismic behavior of the region off the coast of northeastern Honshu. Tectonic features include the volcanic front (VF), the Japanese trench and the aseismic front (AF) which is the seaward boundary of the wedge of low Q and low velocity material. (Figure modified from Yoshii, 1979.)

Figure 12. A plane view of the region of the Miyagi-Oki earthquake. Hatched areas indicate the zones of the eventual rupture. The first three events of the extended foreshock sequence encircled the rupture zone in a clockwise fashion. (Figure modified from Seno, 1982.)

1964-1978.

Several other observations indicate that the February 20, 1978 event was anomalous. The estimates of stress drop (apparent, dynamic and static) jumped dramatically for the February 20, 1978 event relative to the previous two events. Even the stress drops associated with the foreshock and the first two subevents of the mainshock were lower than those of the February event. The increase in stress drop cannot be entirely attributed to the change in focal mechanism as the June 8, 1977 event had a similar (high-angle reverse) mechanism. In addition, the February event was a significantly more complex rupture than the preceding events. Its rupture complexity and the ensuing high aftershock activity indicate that the strength of the fault plane was markedly heterogeneous. This event, which had a focus located immediately beneath the area of the mainshock in the upper part of the double zone, also has a well-constrained direction of rupture which points toward the focus of the mainshock. It should also be noted that the focal mechanisms of this and the June 1977 event are very different from that of the mainshock. Thus, this is an example where the focal mechanisms of possible precursory events with moderate-sized magnitudes are dissimilar to the mechanism of the mainshock.

While the stress drops of the events in the extended foreshock sequence generally increased in time (except for the June 12, 1978 foreshock, which had a smaller stress drop than the preceding February 20, 1978 event), it is difficult to esimate the time of occurrence of the mainshock from such a variation. The immediate foreshock (June 12, 1978) appears to be a valid short-term precursor in that it represents a return of activity within the seismic gap. The decrease in stress drop relative to the last of the encircling events might well be another premonitory characteristic. Its utility as a precursor for the Miyagi-Oki earthquake is moot, however, because it occurred only minutes before the mainshock.

No systematic variation with time could be usefully inferred from the rupture geometries and rupture directions of the events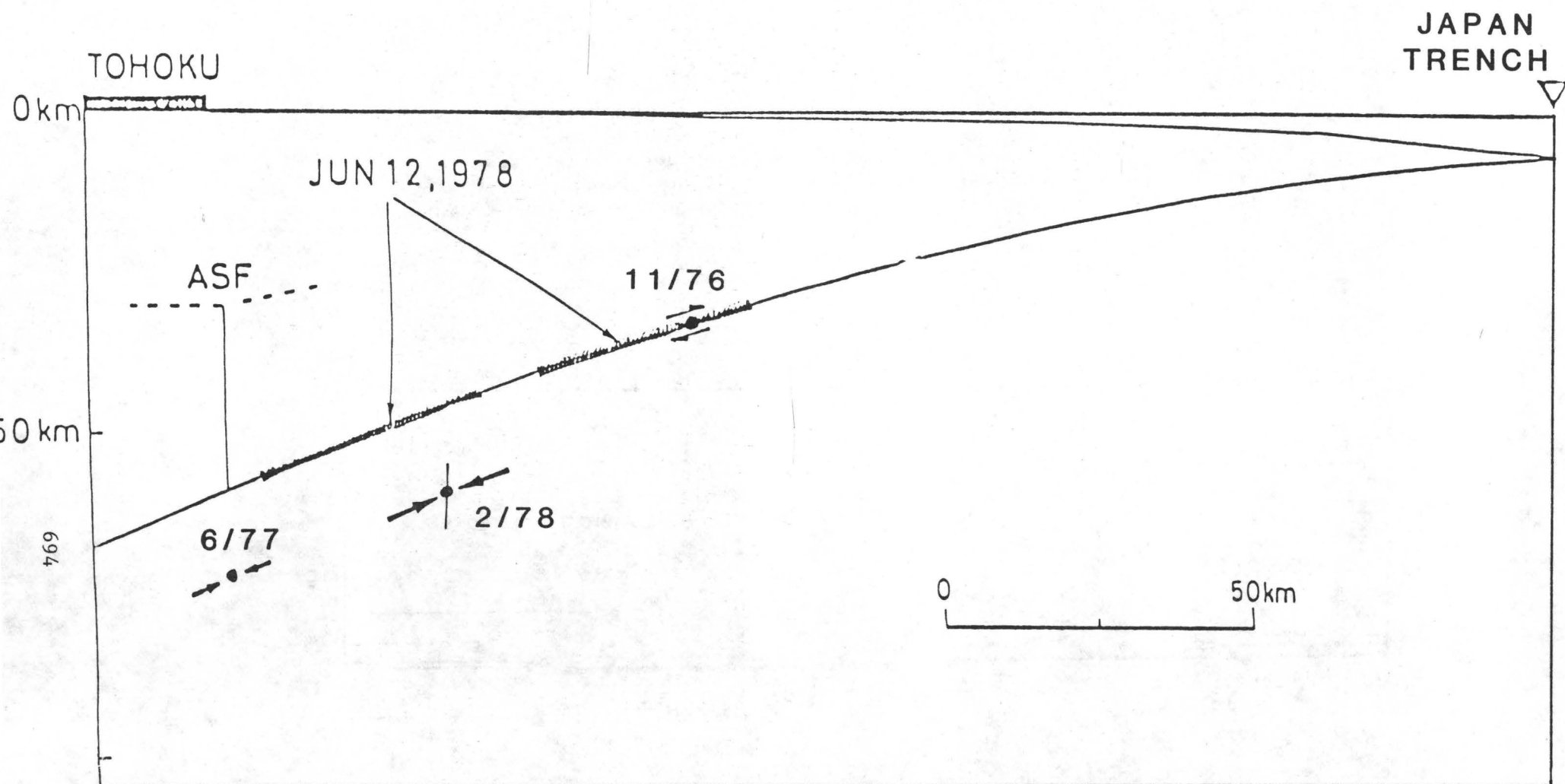 in the extended foreshock sequence because of their generally large uncertainties. While this does not rule out the possible utility of rupture direction/geometry as a premonitory parameter, it does indicate the difficulty in constraining rupture geometry without good station coverage. When these earthquakes occurred, few GDSN stations were operating. At this time, there are about 19 operative stations.

CONCLUSIONS

In many instances, the seismic potential within a region that has been surrounded by seismic events remains ambiguous until after the region has ruptured. This study suggests that additional criteria derived from waveforms can be combined with conventional parameters (e.g., earthquake locations and mechanisms) to infer the long- and short-term tectonic processes that existed prior to the occurrence of a major earthquake. Given sufficient broadband spectral content, waveforms can be used to infer significant information about the rupture geometry and the dynamic stress drop of moderate-sized earthquakes. For the Miyagi-Oki foreshock sequence, substantial changes in dynamic stress drop and the rupture complexity preceded the occurrence of the magnitude 7.8 mainshock. However, there is insufficient information to have permitted any prediction of the time of main shock. All that can be said is that the zone was seismically quiescent for earthquakes larger than magnitude 7.8 for 50 years and for earthquakes larger than m_b 6.5 for at least 15 years. The sudden appearance of moderate-sized earthquakes delineated the eventual rupture zone of the mainshock. The first three events occurred at intervals of

7-8 months. Four months following of the February 1978 event which had an anomalously high stress drop and complex waveforms, the encircled zone ruptured.

ACKNOWLEDGMENTS

REFERENCES

Aki, K. and P. G. Richards (1980). Quantitative Seismology: Theory and methods, W. H. Freeman, San Francisco.

Archambeau, C. B., E. A. Flinn and D. G. Lambert (1969). Fine structure of the upper mantle, *J. Geophys. Res.*, **74,** 5825-5866.

Boatwright, J. (1982). The effect of rupture complexity on estimates of source size, *Bull. Seism. Soc. Am,* submitted.

Boatwright, J. (1980). A spectral theory for circular seismic sources: simple estimate of source dimension, dynamic stress drop, and radiated seismic energy, *Bull. Seism. Soc. Am.,* **70,** 1-27.

Brune, J. N. (1970). Tectonic stress and the spectra of seismic shear waves from earthquakes, *J. Geophys. Res.,* **75,** 4997-5009.

Choy, G. L. (1977). Theoretical seismograms of core phases generated by a frequency dependent full wave theory, and their interpretation. *Geophys. J.,* **51,** 275-312.

Choy, G. L. and J. Boatwright (1981). The rupture characteristics of two deep earthquakes inferred from broadband GDSN data, *Bull. Seism. Soc. Am.,* **71,** 691-711.

Choy, G. L. and V. F. Cormier (1982). The structure of the inner core inferred from short-period and broadband GDSN data, *Geophys. J. R. astr. Soc.,* in press.

Cormier, V. F. and P. G. Richards (1976). Comments on the damping of core waves by Anthony Qamar and Alfredo Eisenberg, *J. Geophys. Res.,* **81,** 3066-3068.

Cormier, V. F. and P. G. Richards (1977). Full wave theory applied to a discontinuous velocity increase: the inner core boundary, *J. Geophys.,* **43,** 3-31.

Engdahl, E. R. and C. Scholz (1977). A double Benioff zone beneath the central Aleutians: an unbending of the lithosphere, *Geophys. Res. Letters,* **4,** 473-476.

Engdahl, E. R., N Umino and A. Takagi (1978). The 1978 Miyagi-Ken-Oki earthquake, *Earthquake notes,* **49,** 67.

Engdahl, E. R., N. Umino and A. Takagi (1979). Seismicity patterns related to the occurrence of interplate earthquakes off the coast of northeastern Japan, *EOS, Trans. Am. Geophys. Union,* **60,** 312.

Harvey, D. and G. L. Choy (1982). Broadband deconvolution of GDSN data, *Geophys. J. R. astr. Soc.,* in press.

House, L. S. and K. H. Jacob (1982). Thermal stresses in subducting lithosphere can explain double seismic zones, *Nature,* **295,** 587-589.

Isacks, B. L. and M. Barazangi (1977). Geometry of Benioff zones: Lateral segmentation and downwards bending of the subducted lithosphere, Maurice Ewing Series I, Am. Geophys. Union, Washington, D.C.

Lundquist, G. M. and V F. Cormier (1980). Constraints on the absorption band model of Q, *J. Geophys. Res.,* **85,** 5244-5256.

Richards, P. G. (1973). Calculation of body waves for caustics and tunnelling in core phase, *Geophys. J.,* **35,** 1575-1588.

Seno, T. (1982). Seismicity and earthquake mechanisms preceding the 1978 Miyagi-Oki, Japan, earthquake of June 12, 1978, in preparation.

Seno, T. and B. Pongsawat (1982). A triple-planed structure of seismicity and earthquake mechanisms at the subduction zone off Miyagi prefecture, Northern Honshu, Japan, in preparation.

Seno, T., K. Shimazaki, P. Somerville, K. Sudo, and T. Eguchi (1980). Rupture process of the Miyagi-Oki, Japan, earthquake of June 12, 1978, *Phys. Earth*

    Planet. Inter., **23,** 39-61.

Smith, A. T. and M. N. Toksoz (1972). Stress distribution beneath island arcs, *Geophys. J. R. astr. Soc.*, **29,** 289-318.

Wyss, M. and J. Brune (1968). Seismic moment, stress, and source dimensions for earthquakes in the California-Nevada Region, *J. Geophys. Res.*, **73,** 4681-4694.

Yoshii, T. (1979). A detailed cross-section of the deep seismic zone beneath northeastern Honshu, Japan, *Tectonophysics*, **55,** 349-360.

Yoshii, T. and S. Asano (1972). Time-term analysis of explosion seismic data, *J. Phys. Earth*, **20,** 47-57.

INHOMOGENEOUS STRESS RELEASE IN THE FEBRUARY 4, 1965
RAT ISLAND EARTHQUAKE

Jim Mori

Lamont-Doherty Geological Observatory and Department of
Geological Sciences of Columbia University
Palisades, New York 10964
(914) 359-2900

Abstract

Short and long period records of the P-wave of the 1965 Rat
Islands earthquake were analyzed to locate subevents within the main
rupture. Four short period subevents were identified in the first 100
seconds and two long period subevents in the first 30 seconds. The
short and long period subevents do not coincide. The short period
subevents cluster in an area 100 km south of the initial epicenter, an
area in which two larger aftershocks have relatively high stress
drops. The long period subevents are located 90 km west of the
initial epicenter. The times and locations of the first short and
long period subevents indicate they were triggered by a front moving
near the P-wave velocity.

Introduction

Large earthquake ruptures in the Earth have been observed to be
complex processes consisting of various subevents, which are
identified by sudden increases in the radiated energy, as seen on the
seismogram. Subevents occur on all time scales and their
identification depends on the frequency response of the recording
instruments. Long period records were used to observe subevents on
the scale of 10 to 20 seconds in the 1976 Guatemala earthquake
(Kanamori and Stewart, 1978) and the 1979 St. Elias earthquake
(Boatwright, 1980), short period records were used to observe
subevents on the scale of 1 to 2 seconds by Cipar (1981) for the 1976
Friuli earthquakes, and strong motion accelerograph records were used
to recognize stopping phases on the scale of 0.1 to 0.5 seconds among
the Oroville aftershocks (Boatwright, 1981). Understanding the nature
of these subevents is important to strong ground motion studies since
it is the complexity of the earthquake which controls the high
frequency content of the radiated energy. The purpose of this study
is to identify in time and space both high and low frequency subevents
within the rupture of the Rat Islands earthquake of February 4, 1965.
This is one of the larger earthquakes which has occurred in the last
20 years and has a moment of 1.25×10^{28} dyne-cm (Kanamori and
Anderson, 1976).

Figure 1 shows the P-wave from this event as recorded on a low
gain broadband instrument (1 sec. seismometer, 75 sec. galvonometer)
located at Palisades, New York. The top trace is the digitized
record. The following traces are band-passed velocity plots.

Depending on the frequency window one can see various arrivals at different time scales. For example, in the 0.5 to 2.5 second range there are numerous bursts of high frequency, and in the 20-50 second range there is a large increase of energy tens of seconds after the initial arrival. Since broadband instruments are not so numerous, WWSSN records were used for this study. The instrumentation of a WWSSN station limits the frequency band that can be studied; using short period records we can look at a range of periods around 1.0 to 5.0 seconds, and using long period records we can look at a range of 10-40 seconds. However, these two period ranges are actually very useful, since the 1.0-5.0 second range gives high frequency information which is important for strong motion studies, and using the 10-40 second range, one may be able to see the large scale behavior of the rupture.

Short Period

Eleven clearly recorded short period WWSSN records were digitized, interpolated to 0.3 seconds and band-pass filtered from 0.5 to 10 seconds. The filtering was done using 3rd order Butterworth filters run forward and backwards over the data. The effect of the instrument was deconvolved from the signal using standard frequency domain expressions. Since we are not looking at frequencies much above one hertz, the effects of the high self-inductance of the Benioff seismometer were ignored. The displacement seismogram was then differentiated to velocity. To further enhance the arrivals of high frequency radiation, energy flux was looked at by using velocity squared plots. These steps in processing are shown in Figure 2.

The velocity-squared plots for four stations spread over 180° in azimuth are shown in Figure 3, lined up from the initial P arrival. Although there is some ambiguity in identifying arrivals, we believe there are prominent arrivals which correlate from station to station across this wide range in azimuth. In these records one can see a very small arrival around 10-20 seconds, a medium arrival around 20-30 seconds and two large arrivals at 40-50 seconds and 75-85 seconds. These arrivals are numbered 1 through 4 as shown in Figure 3.

The relative location of these subevents was determined as described in Wyss and Brune (1967) and Wu and Kanamori (1973). By plotting the arrival time of the subevent relative to the initial P-arrival, versus azimuth as in Figure 4, one can immediately see the general direction of the location of the subevent from the initial epicenter by the distribution of arrival times. For take-off angles to stations directed toward the subevent, the relative arrival times will be earlier than for directions away from the location of the subevent. So, for example, in Figure 4 the location of the subevent is generally to the south. The exact arrival times are given by

$$\wedge t = T_0 - D \cos (\phi_0 - \phi) P$$

assuming no change in depths between the events. $\wedge t$ is the arrival time relative to the initial P arrival, T_0 is the time between the events, D is the distance between events, ϕ is the azimuth to the station, ϕ_0 is the azimuth of a line segment connecting the original epicenter and the location of the subevent, and P is the ray

parameter. If one plots Δt versus $\cos(\phi_O - \phi)$ P, one should then obtain a straight line. ϕ_O is found by stepping through various values of ϕ_O trying to find the value which best fits a linear relationship between Δt and $\cos(\phi_O - \phi)$P. Figure 5 shows the RMS error of the fit to a straight line as a function of ϕ_O, for subevent 1. The arrow shows a clear minimum in the error and indicates the azimuth chosen to be the direction to the subevent. Once the azimuth ϕ_O is determined the slope of the line gives the distance and the time the line crosses $\cos(\phi - \phi_O) = 0$, gives the time separation. Figure 6 show the determined best fit lines to the data for these four short period subevents. Error bars represent a one second uncertainty in picking the arrival. The standard deviation from the least squares fit line are 1.3, 0.80, 0.87, and 0.83 seconds for subevents 1, 2, 3, and 4, respectively. There are a few bad points such as on event 2 which shows a very late arrival at $\cos(\phi_O - \phi)$ P = -6.7 for station RAB. This point was not used for the fit to a straight line, especially since there was another station, ADE, at nearly the same azimuth which does fit the line. Such a late arrival may be attributed to local station structure. The resolution on the azimuth for these locations is $\pm 10°$. The resolution on the distance ranges from about ± 5 percent to ± 15 percent. Figure 13 shows the location of the short period subevents relative to the rupture zone as mapped out by the aftershocks. They range from 40 to 135 km generally south of the epicenter. The initial P wave arrivals on short period records were generally within a second of the predicted time calculated from the ISC hypocenter, indicating that the initial location of the mainshock is fairly good. The location results are tabulated in Table 1.

Long Period

In order to look at the low frequency content of the P-waves, long period WWSSN records were examined. This was done previously by Wu and Kanamori (1973) whose results appear to be consistent with the above short period results. They show 3 subevents occurring 30 to 140 km in a generally southerly direction from the epicenter. However, an examination of the long period records seems to show directivity effects which indicate propagation toward the west. Figure 7 shows long period records from varying azimuth. The time scale of each record was scaled according to the ray parameter, so that one can see the azimuthally dependent directivity effects with no dependence on the distance. The line segment underneath each seismogram is 50 sec. Notice how the energy is gradually pushed toward the beginning of the record as one sweeps counter-clockwise through azimuths of 59° to 270°. At 270° SEO appears to be approximately in the direction of the rupture since at this azimuth the energy is shifted the most toward the early part of the signal. As one continues in azimuth the energy again spreads out. This directivity indicates a rupture toward SEO or in a westward direction. Stations in the azimuthal range of 265° to 8° have very similar pulse shapes (see Figure 7), so it becomes unambiguous to correlate the subevents from station to station. At azimuths outside this range the arrival of depth phases makes picking subevents more uncertain. Using only the stations with similar pulse shapes relative locations were determined using the method described

above for 2 subevents (I and II). The plots of relative arrival time versus cos $(\phi - \phi_0)$ • P are shown in Figure 8. Error bars represent 1 second uncertainties in picking arrivals on the 3 cm/minute records and 2 second uncertainties on the 1.5 cm/minute records. After the first 25 seconds the signal becomes more complicated and so no further picks were attempted.

For these 2 subevents there is a question of whether we are just picking depth phases and identifying them as subevents. Assuming focal mechanism similar to the surface wave solution given by Wu and Kanamori and the aftershock solutions done by Stauder (1968) the relative amplitudes of P, pP and sP are calculated and listed in Table 2. At these azimuths pP has the opposite polarity as P so pP cannot be mistaken for a subevent. Also the amplitudes of sP are generally equal or less than the amplitude of P, so the fact that successive arrivals grow in size, precludes these later arrivals from being sP. The location of these 2 long period subevents are both about 90 km west-northwest of the epicenter as shown in Figure 13 and listed in Table 1. There is a standard deviation of 0.42 and 0.67 seconds in the fit to a straight line for subevents I and II, respectively.

Possible Sources of Error

Since we moved the long period locations of Wu and Kanamori (1973) from the south to the west one may wonder if we can do the same with the short period subevents which we located to the south. In order to do so one has to either increase the relative arrival time for stations in the south or decrease the times for stations to the north. The most likely way to do this is to assume that the arrivals at northern stations are depth phases and thus the direct P comes earlier. But Table 2 shows that amplitude of the direct P is generally larger than the pP and sP, again assuming a thrust solution. However, there is a good chance that the small subevents as seen on the short period records have different focal mechanisms than that given by the surface waves and long period P waves. Furthermore, given the location of these subevents there is a chance that these are normal faulting events. The amplitudes for P, pP, and sP are given in Table 2 for a normal faulting solution given by Stauder (1968) for a nearby aftershock. In this case sP is often equal to or a little larger than P, which could be introducing errors into our location. However, looking at the velocity-squared plots one notices that in most cases the arrivals are clusters of spikes and not just a single spike. In identifying subevents the beginning of the cluster was picked as the arrival time, so hopefully one is picking the arrival of the direct P. But there still remains a problem in picking the arrival of a subevent because of the non-linear enhancement due to the velocity-squared plots. The energy flux emphasizes the high frequency so the beginning of any kind of emergent arrival would be totally lost.

A second source of error might be in differences in path from the initial hypocenter compared to the path from the subevents. If the initial hypocenter is at 40 km depth, take-off angles toward the north could travel down the subducting slab arriving early at European stations, while shallow subevents located further out toward the trench would not travel down the slab. This would result in early

arrival times of the initial rupture for European stations which would locate the initial epicenter too far north. 3-D ray tracing done by Jacob (1972) indicates the arrival time anomaly could be as large as 2 seconds. This could decrease the distance between the initial epicenter and the subevent by about 10 percent.

A third source of error comes from the fact that we assumed there was no dip on the line segment connecting the initial hypocenter with the epicenter. We assumed no dip because we cannot resolve significantly better fits by changing the dip small amounts. A change in dip does not affect the azimuth significantly but it does change the time and distance to the event. For example, assuming a maximum dip from the initial hypocenter at 40 km to subevent 1 at 0 km one obtains a distance of 173 km instead of 140 km and a time of 24 seconds instead of 16 seconds.

Discussion and Relation to Aftershocks

If the errors mentioned above do not contribute significantly to the location of the subevents, we can make some interesting conclusions from their spatial and time distribution. The location of the subevents are shown in Figure 13 along with the epicenter, and aftershocks with magnitudes greater than 5.5. The most apparent result is that the long and short period subevents do not correlate at all in space. They do not correlate in time, either. Short period subevents occur at 15, 33, and 44 seconds after the initiation. Long period subevents occur at 12 and 22 seconds after the initiation. The observation that the short period subevents are not prominent on the long period record and vice versa indicates that the subevents are of different nature. The short period subevents are small high frequencies events while the long period subevents seem to have much more moment without generating as much high frequency.

It is interesting that the short period subevents are located close to one another in space, but occur over a time span of 70 seconds. This means that for this earthquake the high frequency (1-5 seconds) radiation is not dominated by the propagation of the rupture front. Instead the high frequency is being generated from one local area. For the short period records approximately 100 seconds of P-wave was examined. Assuming a rupture velocity of 4 km/sec (Wu and Kanamori, 1970), this means that the rupture has extended 400 km, yet in all that time all the identified high frequency bursts come from one small region about 100 km south of the epicenter. This area seems to be a region of stress concentrations which rupture with large amounts of high frequency. This idea is supported by looking at some of the larger aftershocks.

Dynamic stress drops (Boatwright, 1980) were calculated for the nine aftershocks shown in Figure 12 and listed in Table 3. Focal mechanisms for eight of these events were done by Stauder (1968). Aftershocks 3, 5, 7, and 9 are normal-faulting events located near the trench. Aftershocks 1, 2, 3, 6, and 8 are shallow-angle thrusts. Aftershock 4 was also assumed to be a shallow-angle thrust. Figure 10 shows some of the waveforms as recorded on the Palisades broadband instrument. The data was instrument corrected to velocity and an inverse Q operator (Mori, 1982) applied to the data. For the inverse Q operator a value of T* = 0.6 was used. Although the value of T*

703

will change the absolute value of the stress drops, since we are only looking at relative stress drops among the aftershocks, the exact value of T* is not important. The dotted lines show the slope of the velocity pulse used in calculating dynamic stress drop. For aftershock 5 there are three estimates of stress drop since the initial pulse is quite complicated. But note that all three values are quite high compared to the other aftershocks. This is an aftershock located close to the short period subevents (see Figure 12). Aftershock 7 which is also located in the same region has the second highest stress drop among the aftershocks, although it is not significantly higher than aftershocks 1 and 6.

As a check on the dynamic stress drops which were determined from only one record, stress drops were also calculated using the m_b-Ms curves of Archambeau (1978). Since m_b and Ms values from 1965 do not seem reliable, the magnitudes were recalculated from WWSSN film chips. The same ten stations spread over 230° in azimuth were used in calculating the magnitude for each earthquake. The highest and lowest values were ignored and the remaining eight values averaged together. The stress drops calculated from the m_b-Ms ratio and the dynamic stress drops are shown in Figure 11 and Table 3. Note that although there is quite a difference between the dynamic stress drop and the m_b-Ms estimate, the relative differences between aftershocks track fairly consistently. Again aftershocks 5 and 7 which are located among the short period subevents have the highest values. The m_b-Ms stress drop of aftershock 5 seems anomalously low. But this is reasonable when considering it has an m_b of 6.9 which is near the level body wave magnitudes saturate. Also Archambeau's curves are based on simple scaling laws which break down for the larger and more complex events.

So the area about 100 km south of the initial epicenter seems to be an area that generated relatively high frequencies both during the mainshock and aftershock sequence. This is similar to the observation made in the 1964 Alaskan earthquake where a high frequency aftershock was identified near the location of a high frequency subevent (Mori, 1982).

The two long period subevents also locate close together. They are separated by 10 seconds in time but very little in space. The location of the subevents do indicate rupture in a west-northwest direction as one might expect the long period information to show. If one assumes that those subevents are associated with a rupture front, then this is consistent with a barrier type model (Das and Aki, 1977a). A rupture encounters a barrier and temporarily slows down, but a slowing down of the rupture velocity allows more energy to be concentrated in the crack tip, so the rupture then breaks through the barrier. The distribution of larger aftershocks also is consistent with this idea, since the location of the long period subevents is near the area where the concentration of large aftershocks begins (see Figure 13).

Using the location and time of the first short period subevent and the first long period subevent one can calculate the velocity at which a rupture front reaches these points. For the first short period subevent one obtains a velocity of 8.3 km/sec and for the first long period subevent one obtains 7.0 km/sec. These values are surprisingly high. Even if one puts the maximum dip on the line

segment connecting the initial hypocenter with the subevent location, one obtains a rupture velocities of 7.1 km/sec and 6.6 km/sec. Both these velocities are close to the P wave velocities, the velocity at the Moho in the oceanic lithosphere through which a ray must travel to reach a location near the trench, 8.2 km/sec and the P velocity in the subduction zone at 40 km is 7.6 km/sec. Although analytic expressions restrict the rupture velocity to the Rayleigh wave velocity (Richards, 1976), numerical solutions indicate that the rupture velocity is not bounded by such limits (Das and Aki, 1977b). Another possibility is that the subevents were not triggered by the rupture front but by the first passing P wave.

Conclusions

Long and short period subevents were located within the rupture zone of a great earthquake. The long and short period subevents do not occur at the same location. High frequency subevents are clustered on the trenchward edge of the aftershock zone and two aftershocks in this area also produce relatively large amounts of high frequency (high stress drop). This has significance in trying to predict strong ground motion of large thrust earthquakes, since the sources of the high frequency radiation may be concentrated in very local areas on the trenchward edge of the rupture zone.

Long period subevents show a rupture toward the west-northwest and the location of these large scale subevents may indicate the presence of a barrier, especially since this is an area where the large aftershocks begin to concentrate. The timing of both the long and short period subevents indicates that the front which triggered the subevents travels at close to the P wave velocity.

References

Archambeau, C., Estimation of non-hydrostatic in the earth by seismic methods: Lithospheric stress levels along Pacific and Nazca plate subduction zones, Proceedings of Conference VI: Methodology of Identifying Seismic Gaps and Soon-To-Break Gaps, U.S. Geol. Surv. Open-File Report 78-943, 1978.

Boatwright, J., A spectral theory for circular seismic sources; simple estimates of source dimension, dynamic stress drop and radiated energy, Bull. Seismol. Soc. Amer., 70, 1-27, 1980a.

Boatwright, J., Preliminary body wave analysis of the St. Elias, Alaska, earthquake of February 28, 1979, Bull. Seismol. Soc. Amer., 70, 419-436, 1980b.

Boatwright, J., Quasi-dynamic models of simple earthquakes: Application to an aftershock of the 1975 Oroville, California, earthquake, Bull. Seismol. Soc. Amer., 70, 60-94, 1981.

Cipar, J., Broadband time domain modeling of earthquakes from Friuli, Italy, Bull. Seismol. Soc. Amer., 71, 1215-1232, 1981.

Das, S., and K. Aki, Fault plane with barriers: A versatile earthquake model, J. Geophys. Res., 82, 5658-5670, 1977a.

Das, S., and K. Aki, A numerical study of spontaneous rupture propagation, Geophys. J. Roy. astr. Soc., 50, 643-668, 1977b.

Jacob, K. H., Global tectonic implications of anomalous seismic P travel times from the nuclear explosion Longshot, J. Geophys. Res., 77, 2556-2573, 1972.

Kanamori, H., and D. L. Anderson, Theoretical basis of some empirical relations in seismology, Bull. Seismol. Soc. Amer., 65, 1073-1095, 1975.

Kanamori, H., and G. S. Stewart, Seismological aspects of the Guatemala earthquake of February 4, 1976, J. Geophys. Res., 83, 3427-3434, 1978.

Mori, J., Dynamic stress drops of moderate earthquakes in the eastern Aleutians, in preparation, 1982.

Stauder, W., Mechanism of the Rat Island earthquake sequence of February 4, 1965, with relation to island arcs and sea floor spreading, J. Geophys. Res., 73, 3847-3858, 1968.

Wu, F. T., and H. Kanamori, Source mechanism of February 4, 1965, Rat Island earthquake, J. Geophys. Res., 78, 6082-6096, 1973.

Wyss, M., and J. N. Brune, The Alaska earthquake of 28 March 1964: A complex multiple rupture, Bull. Seismol. Soc. Amer., 57, 1017-1023, 1967.

Table 1

	Azimuth	Distance	Time Delay	Standard Deviation
Short Period				
1	170°	124 km	15 sec	1.3 sec
2	225°	110 km	33 sec	0.80 sec
3	190°	109 km	44 sec	0.87 sec
4	170°	90 km	80 sec	0.83 sec
Long Period				
I	285°	90 km	12 sec	0.42 sec
II	280°	89 km	22 sec	0.67 sec

Table 2. P, pP, and sP Amplitudes For

Thrust Mechanism strike = 70°, dip = 18°, rake = 138°
Normal Mechanism strike = 142°, dip = 50°, rake = 100°

Station	Azimuth	Distance	Normal			Thrust		
			P	pP	sP	P	pP	sP
AKU	7.68°	62.67°	1.38	-1.12	0.22	-1.15	0.78	1.84
KTO	8.04°	57.69°	1.34	-0.96	0.26	-1.17	0.82	1.84
CAR	64.26°	96.63°	0.55	-0.48	-0.55	-1.31	1.41	1.93
BHP	75.19°	90.41°	0.37	-0.33	-0.87	-1.32	1.15	1.83
HKC	264.88°	56.97°	1.21	-0.84	0.45	-1.55	1.08	1.32
SEO	269.72°	38.50°	1.28	-0.94	0.22	-1.21	0.39	1.18
POO	292.80°	84.57°	1.50	-1.31	1.33	-1.87	1.63	0.47
QUE	304.93°	79.10°	1.65	-1.34	1.26	-1.79	1.45	0.61
NUR	346.28°	66.59°	1.60	-1.23	0.78	-1.50	1.15	1.22
COP	351.82°	72.78°	1.56	-1.19	0.71	-1.45	1.10	1.35

Table 3

	Date	Time	Dynamic Stress Drop	M_b	Ms	M_b-Ms Stress Drop
1	Feb 4, 1965	1206	56 bars	6.0	6.3	80 bars
2	Feb 6, 1965	0402	20 bars	6.1	5.6	200 bars
3	Feb 7, 1965	0217	14 bars	5.9	5.7	80 bars
4	Feb 25, 1965	0522	9 bars	5.8	6.1	45 bars
5	Mar 30, 1965	0227	160 bars	6.9	7.3	250 bars
6	May 23, 1965	2346	50 bars	6.1	5.9	200 bars
7	Oct 1, 1965	0852	60 bars	6.5	6.1	560 bars
8	Nov 22, 1965	2025	49 bars	6.1	5.8	200 bars
9	Jun 2, 1966	0327	26 bars	5.8	5.3	200 bars
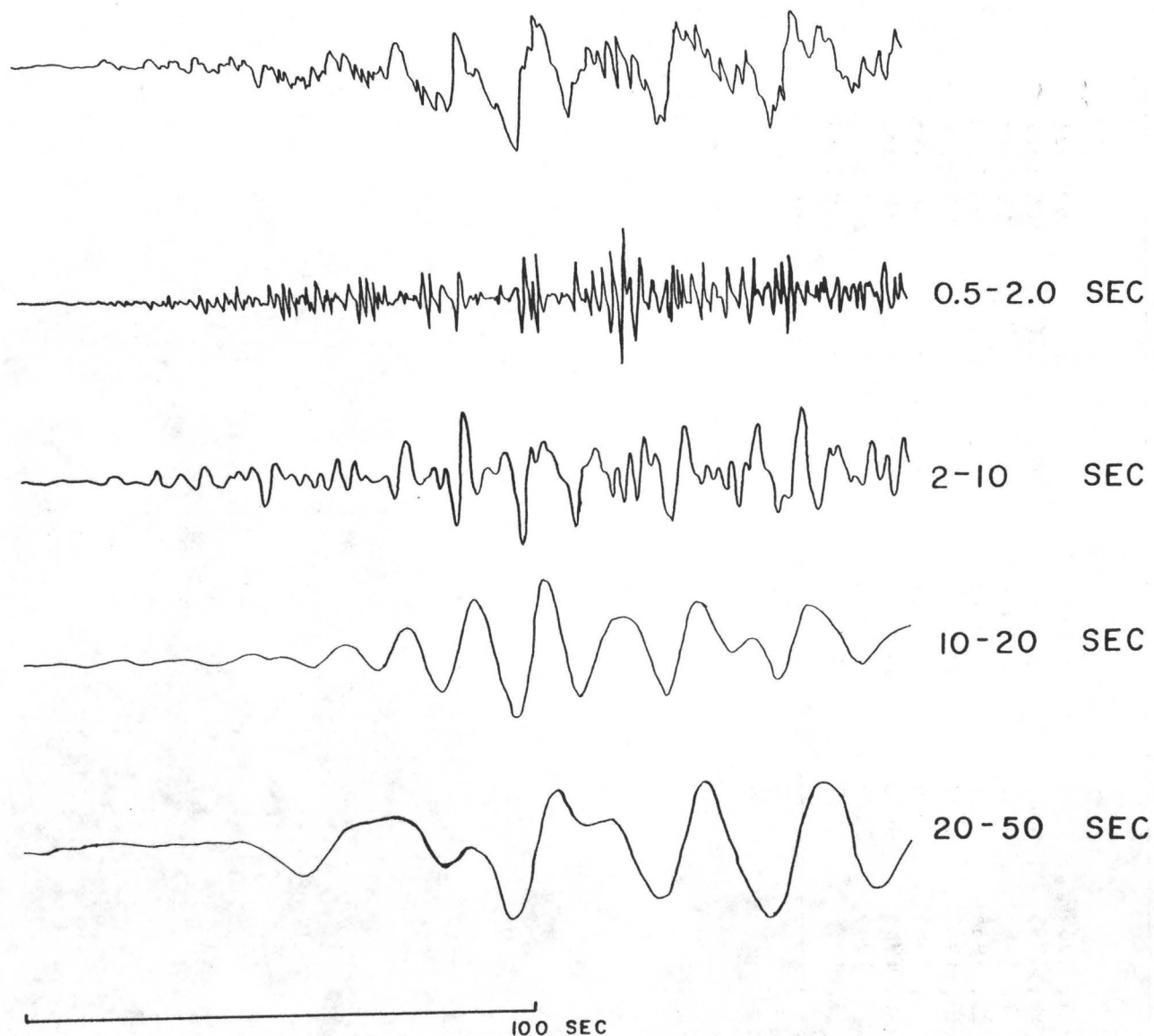
Figure 1. Palisades broadband record of February 4, 1965 Rat Islands earthquake. Top trace is digitized record. Four successive traces are band-passed velocity plots. Note that different arrivals can be seen in each frequency window.

DIGITIZATION

BAND PASS
0.5 - 10 sec

DISPLACEMENT

VELOCITY

VELOCITY SQUARED

10 sec
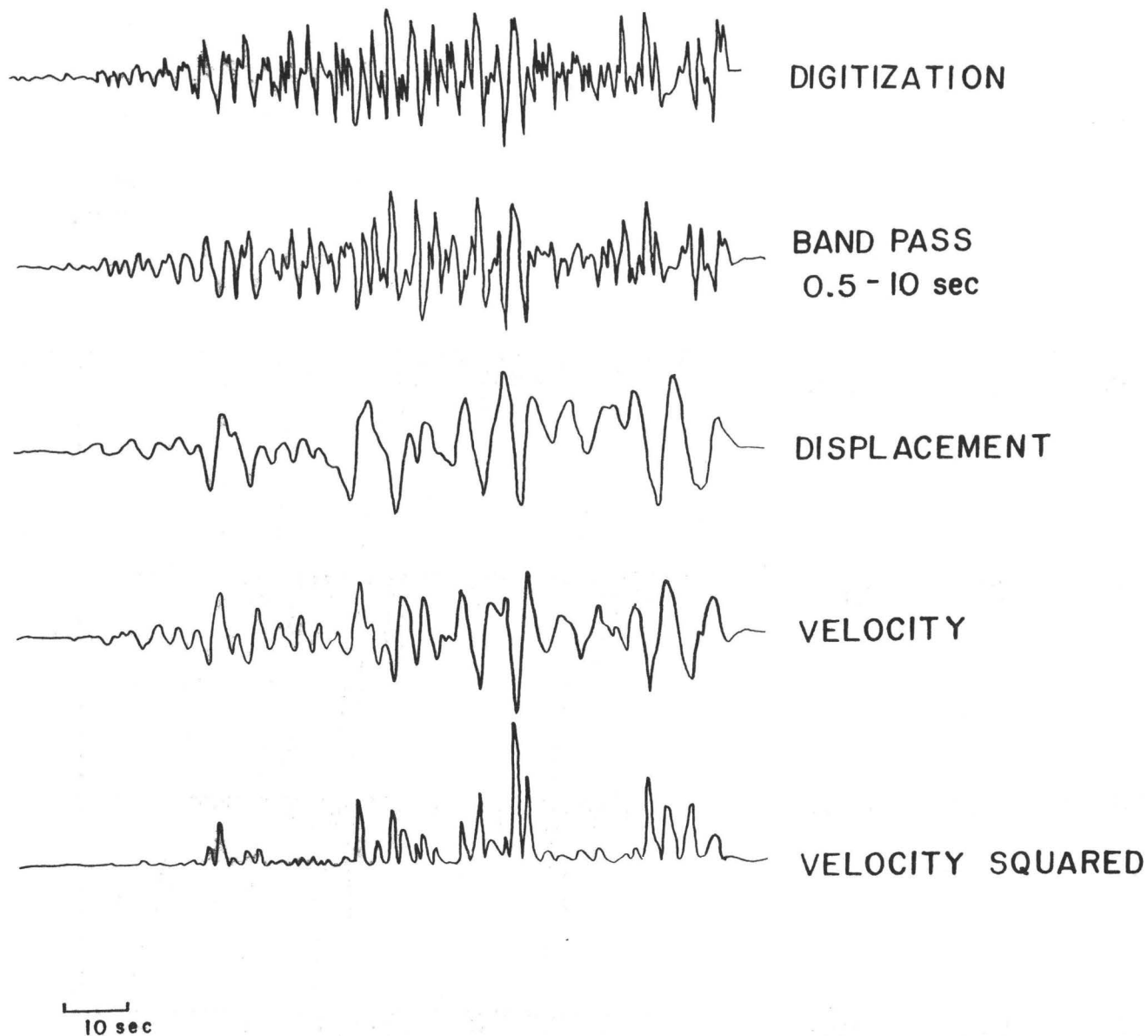
Figure 2.   Processing of short period records. Top trace is digitized record.
Second is band-passed filtered 0.5-10.0 sec. Third is deconvolved
displacement.   Fourth is velocity. Fifth is velocity squared.

	ϕ	$\triangle$
DAV	244	62
POO	293	85
NUR	346	67
KTG	8	58

1 2 3 4

10 sec
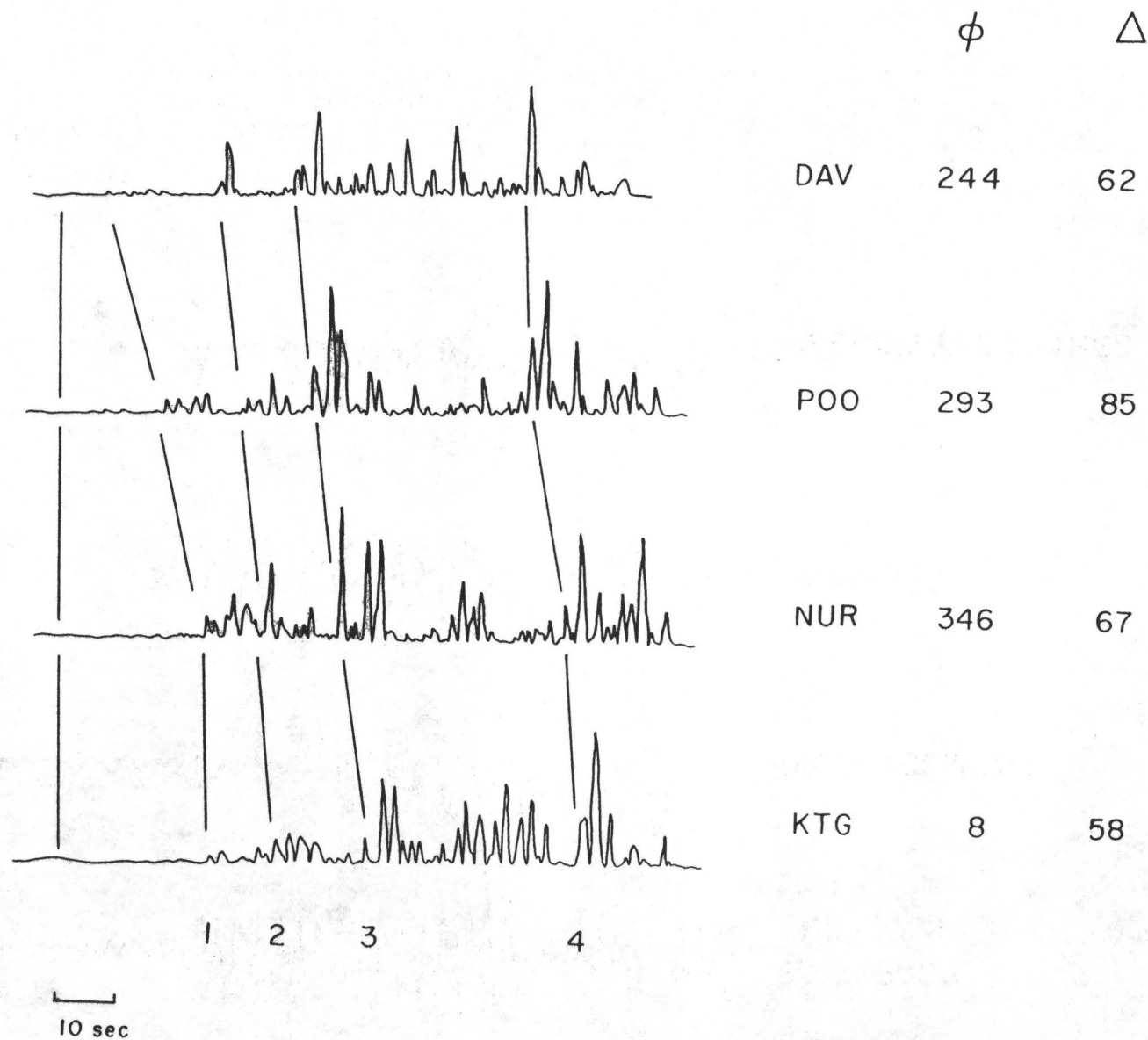
Figure 3. Four velocity-squared plots for stations at varying azimuth. Note that four distinct arrivals can be seen on each. These four arrivals are identified as subevents 1-4.
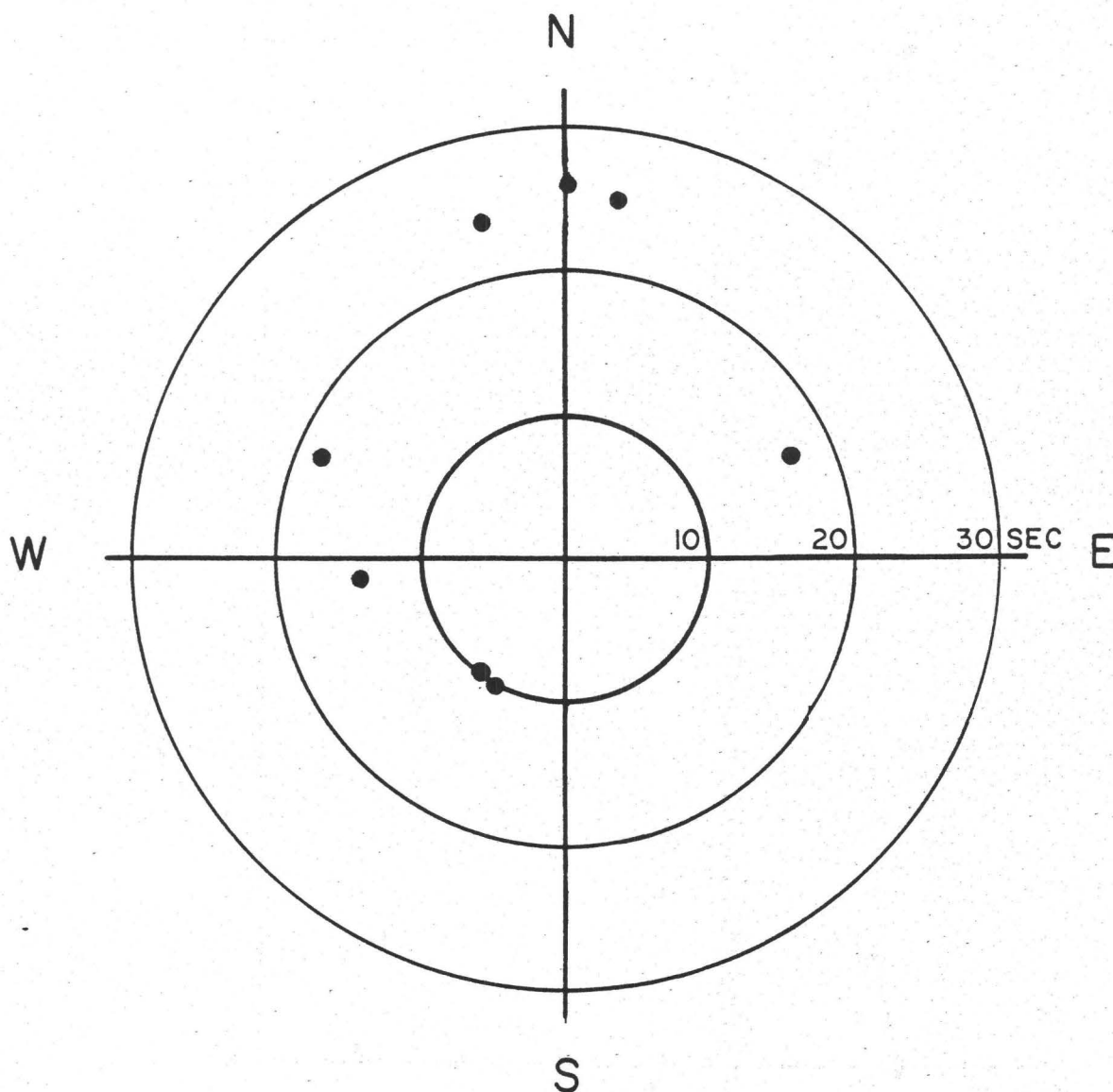
Figure 4. Arrival times of subevent 1 relative to the initial P.
Arrivals are plotted with respect to azimuth. Note
that southern stations have early arrival times relative
to northern stations, indicating that the subevent is
located south of the initial epicenter.
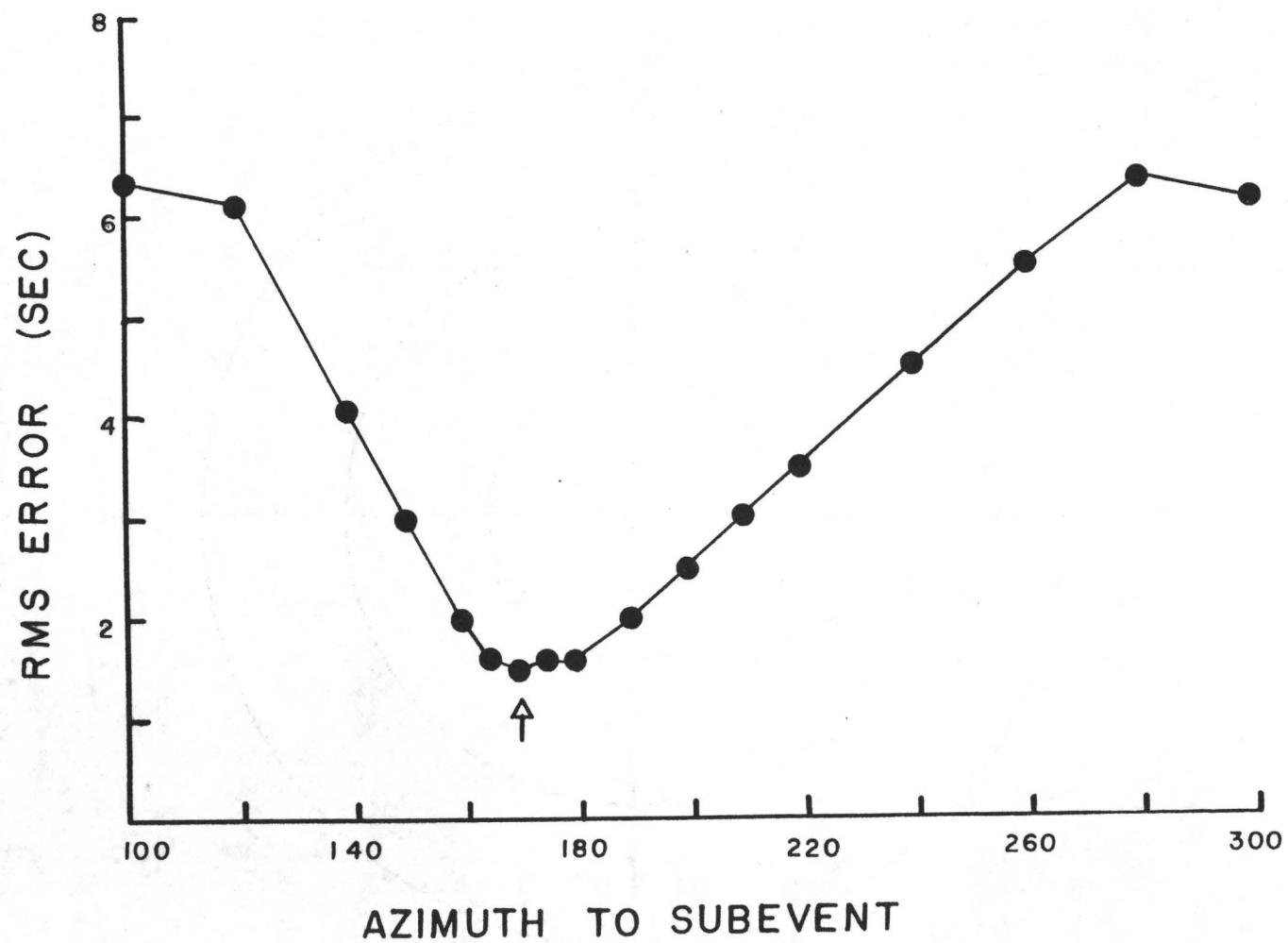
Figure 5. RMS error of fit to a straight line plotted as a function of azimuth to subevent 1. Arrow indicates azimth chosen as direction to subevent.
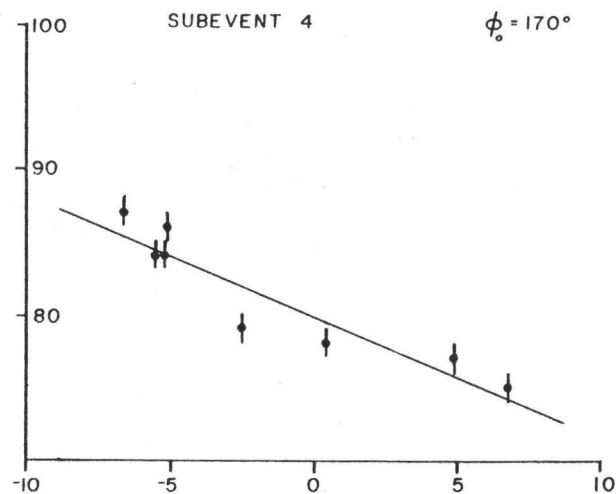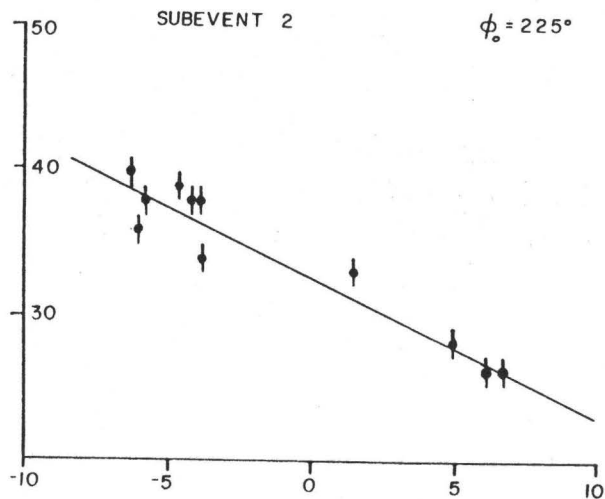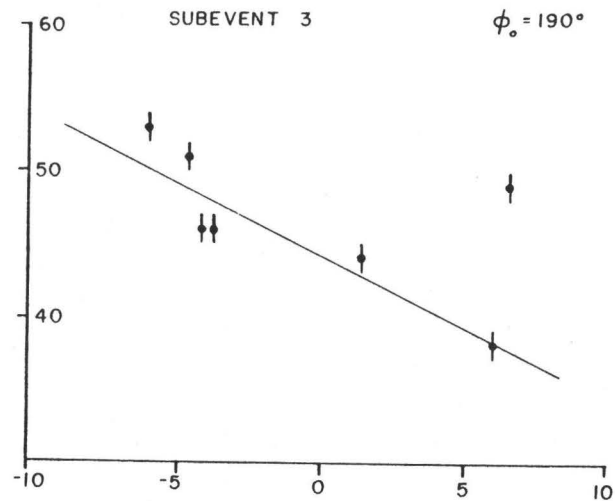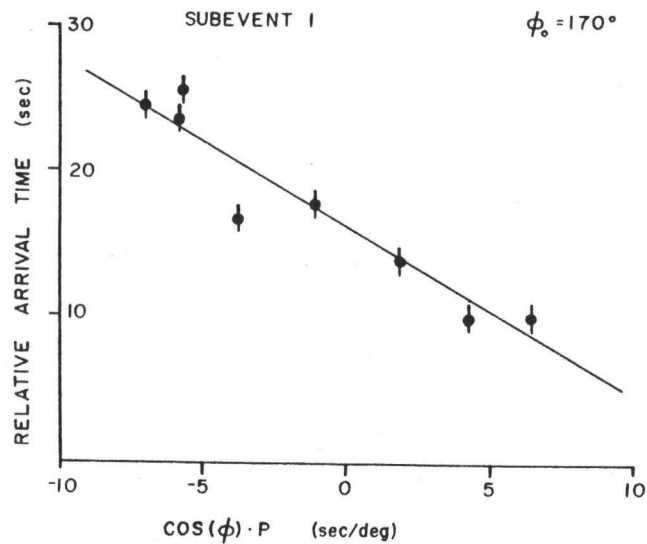
Figure 6. Best fit lines for relative arrival times plotted against cosine of azimuth times ray parameter are shown for the four short period subevents. ϕ_o is the direction of the subevent from the initial epicenter. The time difference between the initial rupture and the subevent is given by the time corresponding to $\cos(\phi)=0$.

	φ	Δ
BEC	50	78
AKU	63	63
ESK	1	74
IST	337	84
SEO	270	39
HKC	265	57
ADE	212	93
RIV	203	88
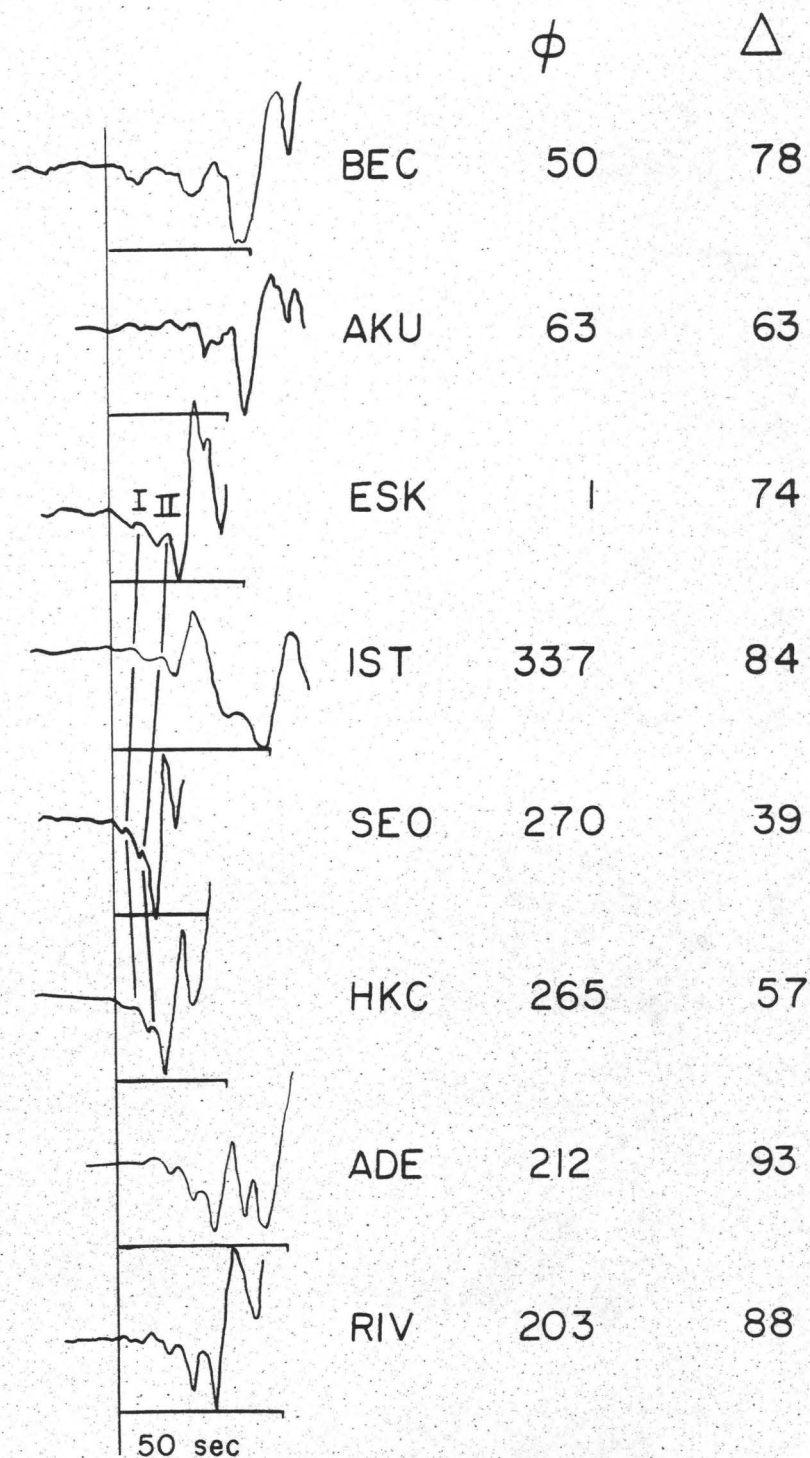
50 sec

Figure 7.   Long period P-waves from stations of varying azimuth.
Note the focusing of energy in the direction of SEO.
Time scales have been scaled to the ray paramenter
so that the line under each seismogram represents 50
seconds. I and II indicate the long period subevents.
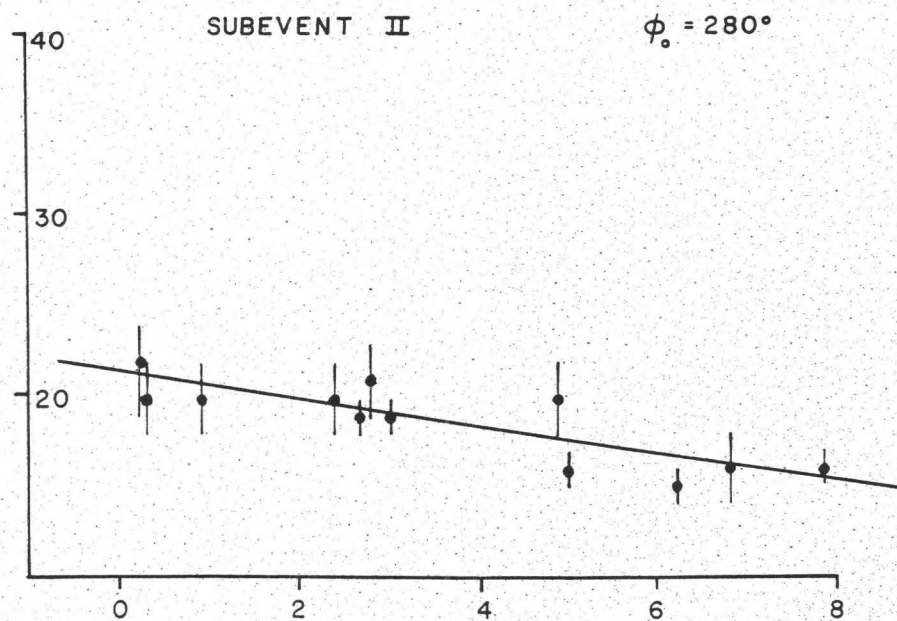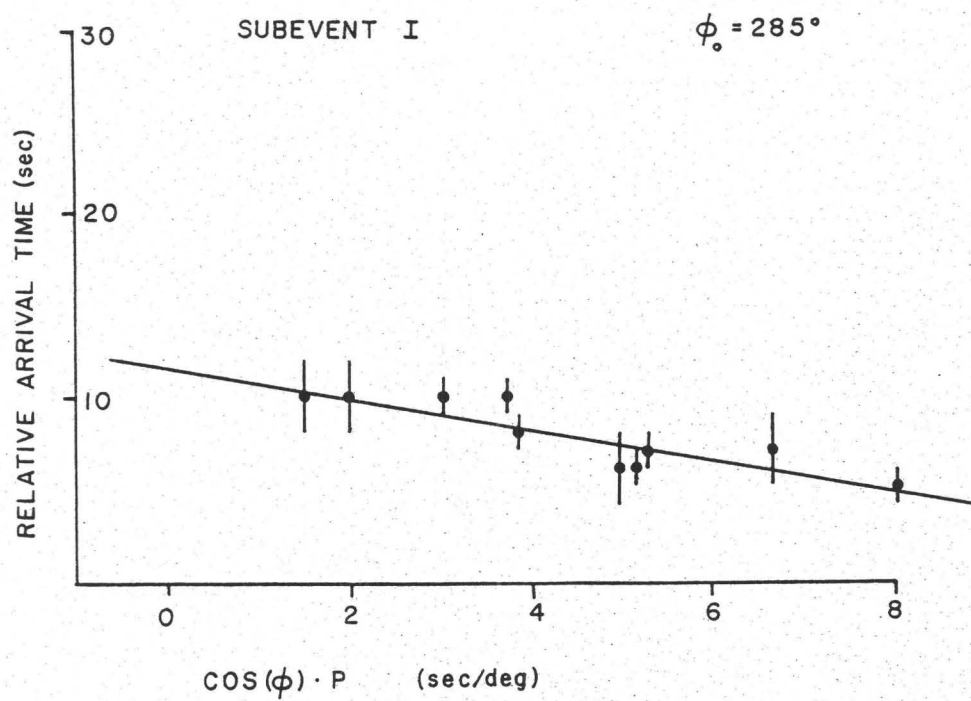
Figure 8. Same as Figure 6 except for the long period subevents.
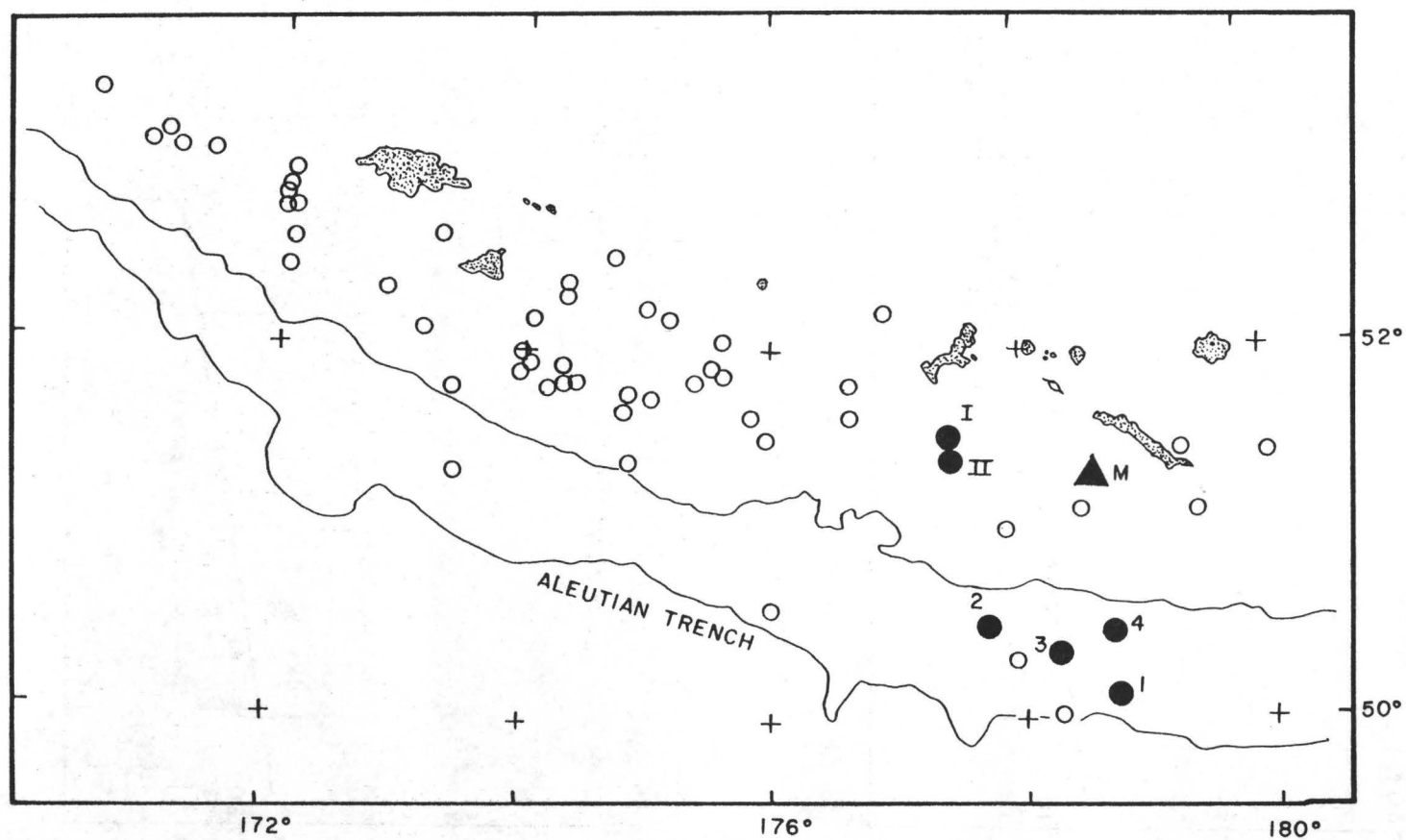
Figure 9. Map showing rupture zone of 1965 Rat Islands earthquake. Open circles are after-shocks with $m_b > 5.5$. M indicates the initial epicenter of the mainshock. Filled circles 1-4 are the short period subevents. Filled circles I and II are the long period subevents.

718
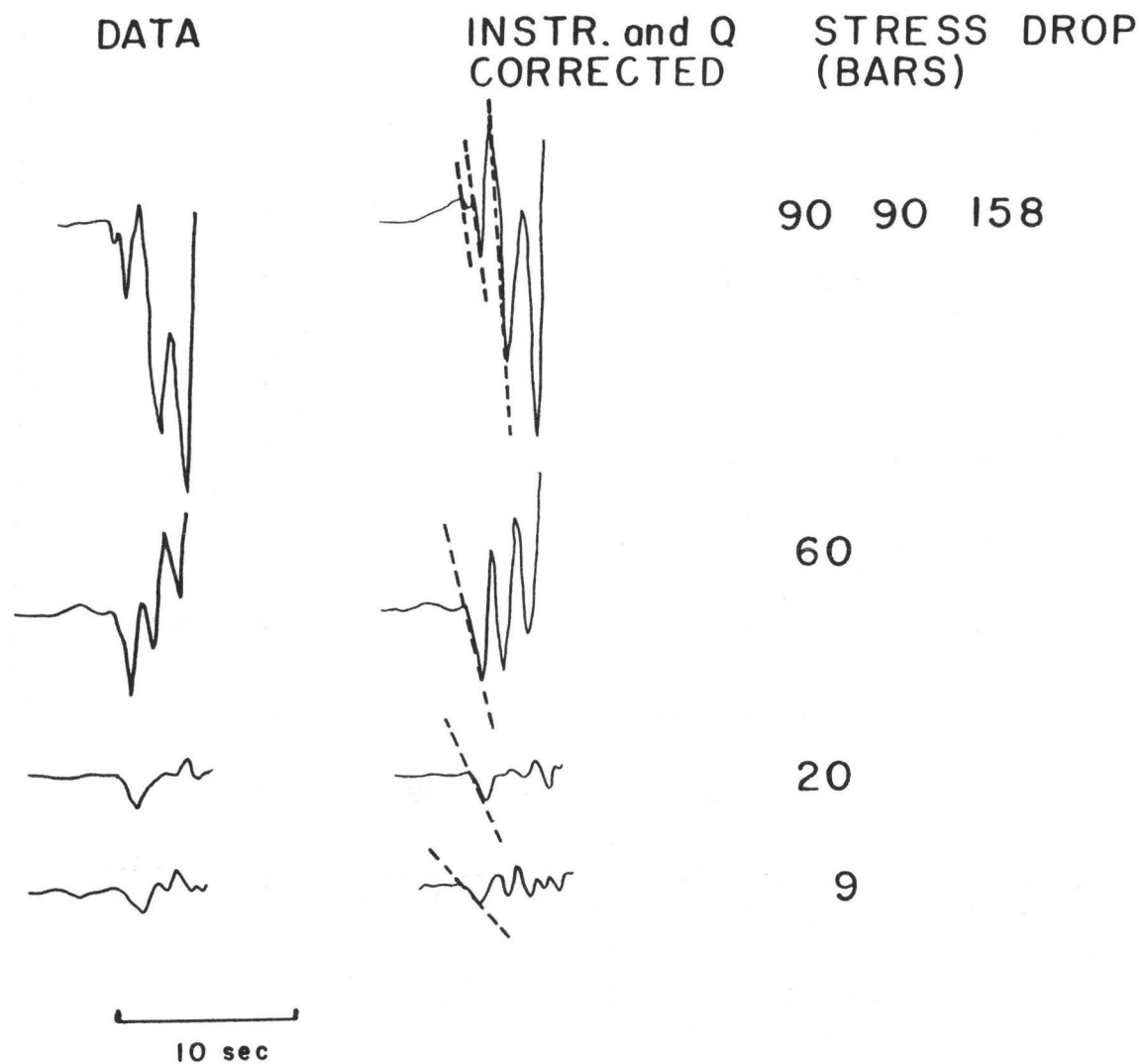
Figure 10. Waveforms of several aftershocks used in calculating dynamic stress drop. Dotted lines show slope of velocity pulse used for the estimate.
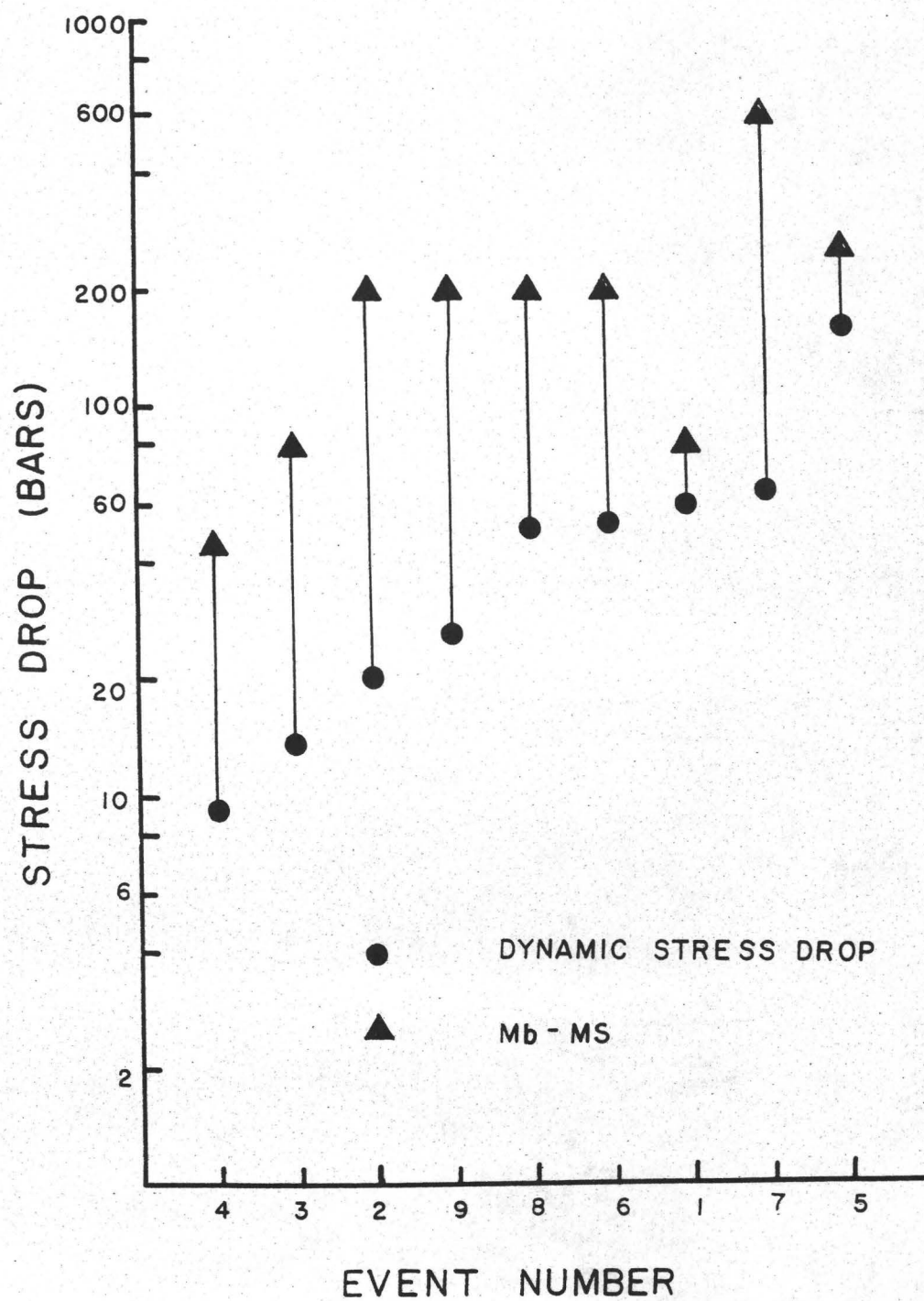
Figure 11. Plot of dynamic stress drop and m_b-Ms stress drop for the nine aftershocks.
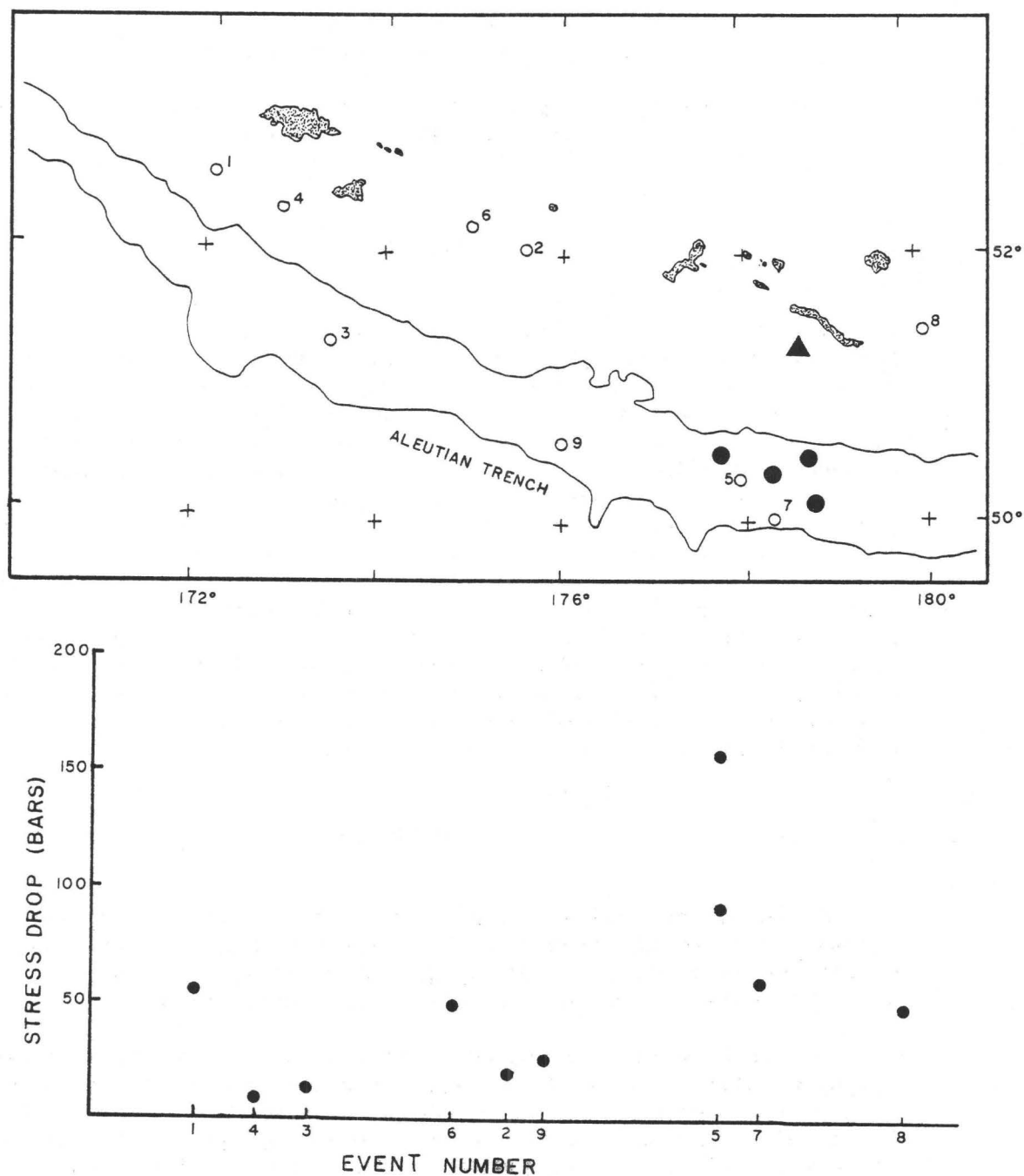
Figure 12. Map showing location and plot of dynamic stress drop for nine
aftershocks. Note high stress drop aftershocks 5 and 7 are near
the short period subevents (filled circles).

SCALING RELATIONS FOR STRONG GROUND MOTION IN LARGE EARTHQUAKES

C. H. Scholz
Department of Geological Science
and
Lamont-Doherty Geological Observatory of Columbia University
Palisades, New York   10964
(914) 359-2900

ABSTRACT

The problem we address is how to predict strong ground motions for very large earthquakes from observations made of such motions produced by events of moderate size. The discussion is in terms of two basic rupture models; a W model in which slip is controlled by fault width and an L model in which slip is controlled by fault length. Because mean slip is observed to increase linearly with fault length, a long earthquake cannot be modeled as a series of shorter events placed end to end. Rather, to explain the correlation of slip with length a W model will predict that stress drop increases with length, whereas an L model will predict that stress drop is constant but rise time (slipping duration) increases with length. Thus a W model predicts that peak and RMS accelerations and peak and asymptotic particle velocities increase linearly with fault length. An L model predicts that RMS acceleration and asymptotic velocities are independent of length but that the velocities increase with the square root of length and peak acceleration with $\ln\sqrt{L}$.

INTRODUCTION

An important need for analysing seismic hazard is to be able to estimate the strong ground motion expected for a future very large earthquake from observed strong ground motions, which are at present available only for small to moderate size earthquakes.

The problem is illustrated in Figure 1, where we show in map view two hypothetical cases of earthquakes which rupture from the surface to the same depth, but one of which is much longer than the other. The problem that we address is the following: given that we have an observation of the strong ground motions that would be experienced by resulting from the earthquake depicted in Figure 1A, what can be said about the expected strong ground motions that would be experienced by an observer the same distance from the fault at point B in the case of the earthquake with much longer rupture length shown in Figure 1B?

One might first reason that, aside from focusing effects due to rupture propagation, the strong ground motion at B is largely governed

by the motion on the fault just adjacent to B, say in segment CD. Since CD is about the length of the entire length of faulting in case A, we might then guess that B will experience about the same strong ground motions as did point A in the smaller earthquake. In other words, we can model the long earthquake as a series of shorter earthquakes placed end to end.

This, however, is incorrect because the mean slip in large earthquakes increases linearly with fault length (Scholz, 1982). Thus if the length of faulting in case B is 10 times longer than in case A, we would expect that the slip also to be 10 times greater. There are two alternative ways in which this greater slip may be achieved in case B. Either the particle velocity is much higher in case B than case A and the rise time (duration of slip at any point on the fault) the same, or, quite simply, vice versa. These are the predictions of W models and L models, respectively.

The difference between these two basic classes of rupture models has been discussed previously (Scholz, 1982). A W model is one in which slip is constrained at the base of the fault so that slip is determined by the width of the fault and scales with $\Delta\sigma$, the dynamic stress drop. With this type of model one must interpret the correlation between slip and length as meaning that $\Delta\sigma$ also increases linearly with length. An L model, on the other hand, is one in which the fault is mechanically unconstrained (or loosely constrained) at the base so that slip is determined by the length of faulting. With an L model the correlation between slip and length is explained if $\Delta\sigma$ is constant.

The contrasting way in which these two models work is illustrated in Figure 2. On the left is shown schematically a short earthquake, similar to case A, above. What is shown is a snapshot of slip on the fault at some typical time. We show only the part that is slipping at any one time. We also show the time history of slip at some representative point. For simplicity that is shown to be simply a ramp of duration t_R, the rise time.

On the right is shown the predictions of the W and L models for a longer earthquake. In a bilateral case as shown, a W model predicts that the slipping patch separates into two patches of length $\approx$ W, the fault width, that propagate away from each other at twice the rupture velocity (see Day, 1979; Archuleta and Day, 1980; Das, 1981, for descriptions of models of this type). The rise time $t_R \approx W/2\beta$ remains the same as in the shorter earthquake so that the average particle velocity must be much higher to produce the greater slip. In the L model, slip spreads out as an expanding patch within which slip continues until the final dimensions are reached. In that case particle velocities are the same as in the case of the shorter earthquake but the rise time, $t_R \approx L/2\beta$ is much greater (Scholz, 1982).

These two models represent the extreme classes of models of large earthquakes within which any specific model, whether it be kinematic or dynamic, simple or heterogeneous, must belong. They predict very different scaling of strong ground motion in large earthquakes.

SCALING OF HIGH FREQUENCY GROUND ACCELERATIONS

The width of large shallow earthquakes is restricted in any tectonic environment to be W_O, the distance measured along dip between the free surface and the base of the seismogenic layer. It is useful to take as a 'unit' large earthquake a square rupture in which its length, $L* = W_O$, because for those dimensions the predictions of the L and W models are the same. In the following discussion all starred parameters, $\Delta\sigma*$, t_R*, etc. are the parameters of the unit event. Thus,

$$t_R* = \frac{L*}{2\beta} \tag{1}$$

and the prediction of the two models are,

$$t_R = t_R*$$

$$\Delta\sigma = \Delta\sigma* \frac{L}{L*}$$ W model (2

and,

$$t_R = t_R* \frac{L}{L*}$$

$$\Delta\sigma = \Delta\sigma*$$ L model (3

One can argue on dimensional grounds that the rms value of high frequency acceleration and the dynamic stress drop are related by,

$$a_{rms} = \frac{D\Delta\sigma}{\rho R} \tag{4}$$

where ρ is density, R is distance and D is a model dependent parameter (Hanks, 1979; McGuire and Hanks 1980; Hanks and McGuire, 1981; Boatwright, 1981).

Since high frequency acceleration appears to be close to gaussian white noise (Hanks and McGuire, 1981), the peak acceleration, a_{max}, is given by

$$a_{max} = \sqrt{\ln \frac{t_R}{t_o}} \; a_{rms} \tag{5}$$

where t_o is the period of the highest frequency observed.

Combining 2 and 3 with equations 4 and 5 we have the following predictions of the two models,

$$\left. \begin{array}{l} a_{rms} = a^*_{rms} \dfrac{L}{L*} \\[2em] a_{max} = a^*_{max} \dfrac{L}{L*} \end{array} \right\} \qquad \text{W model} \tag{6}$$

and

$$\left. \begin{array}{l} a_{rms} = a^*_{rms} \\[2em] a_{max} = \sqrt{\ln \dfrac{L}{L*}} \; a^*_{max} \end{array} \right\} \qquad \text{L model} \tag{7}$$

PARTICLE VELOCITIES

In order to discuss particle velocities we adopt a slip function shown schematically in Figure 3. It is the solution of Kostrov (1964) of a dynamically expanding crack propagating at a uniform rupture velocity V_R. The peak velocity $v_{max} \approx c \frac{\Delta\sigma}{\rho\beta}\left(\frac{2fL*}{v_R}\right)1/2$ is obtained by averaging the singularity in the solution over a 'cutoff' period $1/f$ (Day, 1979). The asymptotic value of velocity, $v_o = \frac{\Delta\sigma}{\rho\beta}$ is the value obtained when the crack tip is a large distance from the point in question. The constant c depends on rupture velocity and r is the distance between the point illustrated and the rupture initiation point.

With this slip function, the peak particle velocity in our 'unit' earthquake would be (Day, 1979),

$$v^*_{max} = c \frac{\Delta\sigma}{\rho\beta}\left(\frac{2fL*}{v_R}\right)^{\frac{1}{2}} \tag{8}$$

and the asymptotic value,

$$v_0^* = c \frac{\Delta\sigma^*}{\rho\beta} \qquad (9$$

The dependency on r in the expression for v_{max} results from the increase of the stress intensity factor $K = \Delta\sigma\sqrt{r}$ as the crack grows. Therefore r refers to the dimension of the crack which is slipping at any one time. Thus r reaches a maximum of W in a W model (Day, 1979) but will grow to L in an L model. Taking this into account, and combining equations 2 and 3 with 8 and 9, we obtain the scaling relations,

$$\left.\begin{aligned} v_{max} &= v_{max}^* \frac{L}{L^*} \\[2ex] v_0 &= v_0^* \frac{L}{L^*} \end{aligned}\right\} \qquad \text{W model (10}$$

and

$$\left.\begin{aligned} v_{max} &= v_{max}^* \sqrt{\frac{L}{L^*}} \\[2ex] v_0 &= v_0^* \end{aligned}\right\} \qquad \text{L model (11}$$

Those scaling relations for the velocities are quite similar to those obtained for the accelerations. That value of v_{max} in (11) would be realized only near the ends of the fault, but the a_{max} value from (7) is relevant to any point along the fault.

DISCUSSION

Most three dimensional models of large earthquakes that have previously been described in the seismological literature are W models. We previously have pointed out the difficulties encountered with reconciling that type of model with the observation that mean slip correlates with fault length (Scholz, 1982). The L model was proposed as a hypothetical alternative. In terms of the scaling relations discussed here, a specific example is useful to illustrate the differences in the two types of models.

Suppose we wish to estimate the strong ground motions experienced in the 1906 San Francisco earthquake from those observed in the 1966 Parkfield or 1968 Borrego Mountain earthquakes, say. We take as

reasonable measures of near fault a_{rms} and a_{max} from the accelerographs written by the Parkfield earthquakes values of 0.15 g and 0.4 g, respectively (T.C. Hanks, personal communication, 1981). Scaling this to the 1906 earthquake, which had 15 times the length and slip of Parkfield would yield the following estimates: a_{rms} = 2.2 g, a_{max} = 6 g, and t_R = 2-3 sec. for a W model; a_{rms}= 0.15 g, a_{max} = 0.65 g and t_R = 30-45 sec for an L model. The 1906 earthquake originated somewhere off the Golden Gate and propagated in both directions away from the San Francisco Bay area (Boore, 1977). Contemporary accounts were that the period of most violent shaking felt in the Bay area lasted 45 to 60 seconds (Reid, 1910, pp.1-4), which seems more consistent with the L model prediction. The accelerations predicted by the W model seem unrealistically high. In any case, the discrepancy is large; clearly we must resolve the question of which of these types of models is a better representation of a large earthquake before we will be able to estimate, in the absence of direct observations, strong ground motions for great earthquakes.

The L model was introduced as a hypothesis. The most serious drawback to it is that one did not know if it could physically operate. Recently, however, a dynamic, spontaneous model has been developed (Das, this meeting) with some of the characteristics of an L model and some characteristics of a W model. Thus the possibility remains that some intermediate model may be appropriate, in which case the scaling of strong ground motions will be intermediate to the extremes discussed here.

It should be emphasized that we have only discussed problems in predicting the average ground motions. Near field strong ground motions will largely be controlled by local, rather than average, properties of the fault, which, because of the heterogeniety of fault zone properties, may vary widely from the mean.

ACKNOWLEDGEMENTS

REFERENCES

Archuleta, R.J., and S.M. Day (1980), Dynamic rupture in a layered medium: the 1966 Parkfield earthquake, Bull. Seismol. Soc. Am., 20, 671-689.

Boatwright, J. (1981), The dependence of ground acceleration on the dynamics characteristics of faulting, Bull. Seismol. Soc. Am., submitted.

Boore, D.M. (1977), Strong motion recordings of the California earthquake of April 18, 1906, Bull. Seismol. Soc. Am., 67, 561-578.

Das, S. (1981), Three-dimensional spontaneous rupture propagation and implications for the earthquake source mechanism, Geophys. J. R. Astron. Soc., 67, 375-393.

Day, S. (1979), Three-dimensional finite difference simulation of fault dynamics. Final Rept., SSS-R-80-4295, 71pp., Systems, Science and Software, La Jolla, California.

Hanks, T.C. (1979), b-values and $w^{-\gamma}$ seismic source models: implications for tectonic stress variations along active crustal fault zones and the estimation of high-frequency strong ground motion, J. Geophys. Res., 84, 2235-2242.

Hanks, T.C., and R.K. McGuire (1981), The character of high-frequency strong ground motion, Bull. Seismol. Soc. Amer., 71, in press.

Kostrov, B.V. (1964), Selfsimilar problems of propagation of shear cracks, J. Appl. Math. Mech., 28, 1077-1087.

Reid, H.F. (1910), The California Earthquake of April 18, 1906, Rept. State Earthquake Invest. Comm., v. II, Carnegie Inst. of Wash., Wash, D.C., pp 192.

Scholz, C.H. (1982), Scaling laws for large earthquakes: consequences for physical models, Bull. Seismol. Soc. Amer., 72, 1-14.
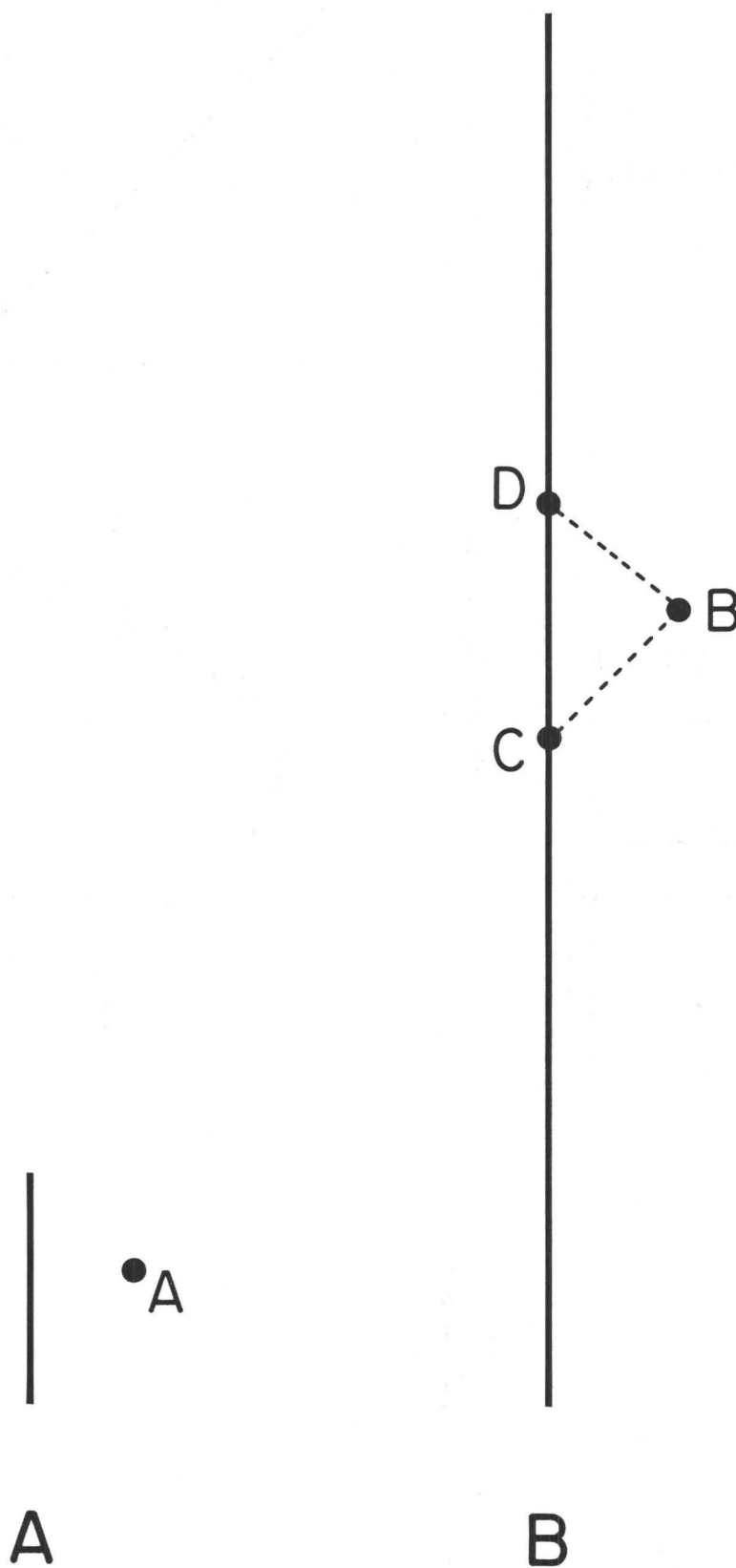
Figure 1: Schematic representation of two earthquakes, the one in B
having a much longer rupture length than in A. The problem ad-
dressed is if we have an observation of strong ground motion at
point A for event A, what can be said about the expected ground
motions at point B for the larger event?

730
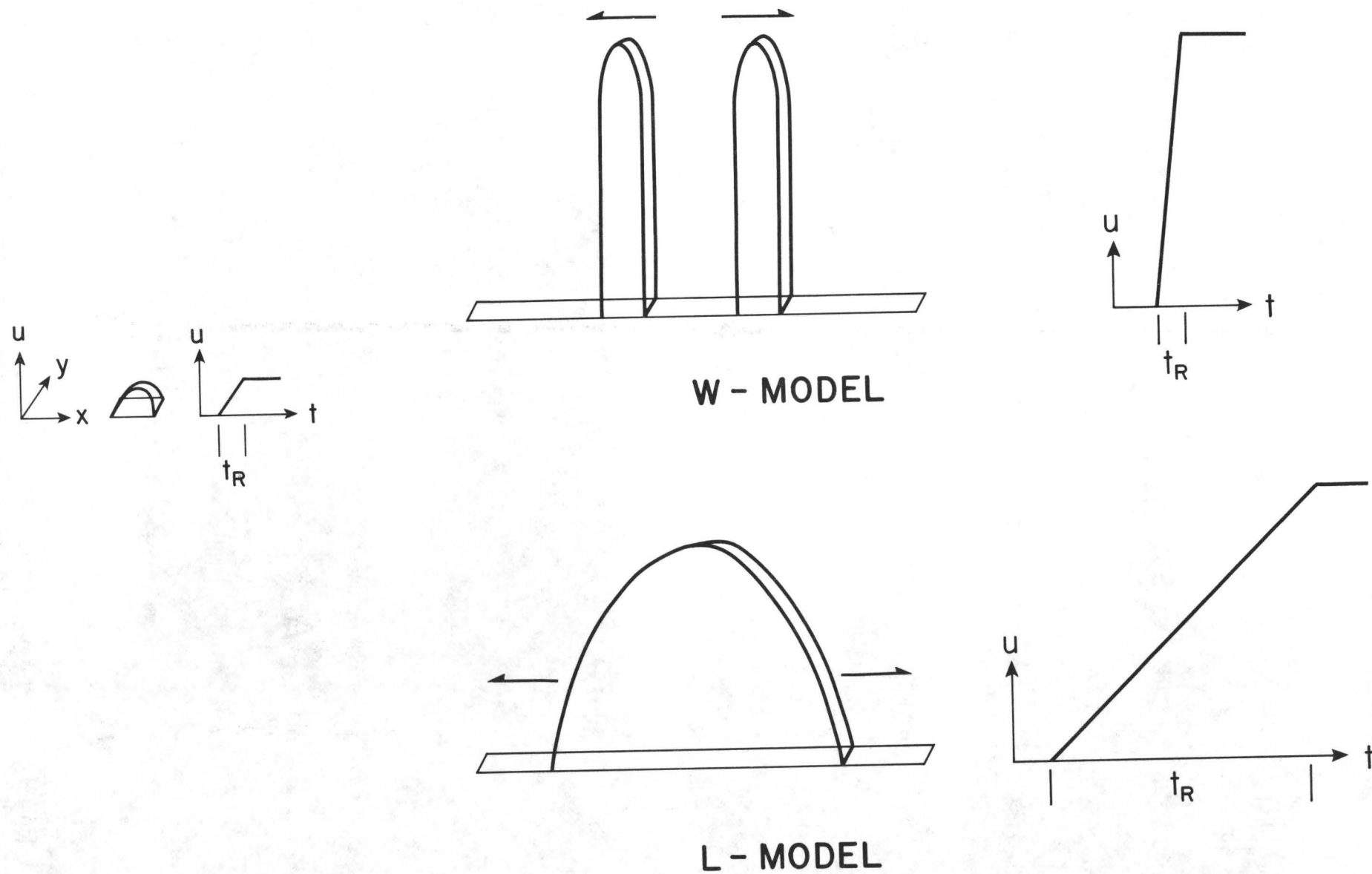
W – MODEL

L – MODEL

Figure 2: A schematic diagram to illustrate the contrasting way in
the W and L models scale.

$$V_{MAX} \approx C \frac{\Delta\sigma}{\rho\beta} \left(\frac{2fr}{V_R} \right)^{1/2}$$

$$V_0 = C \frac{\Delta\sigma}{\rho\beta}$$

PARTICLE VELOCITY

TIME

Figure 3: The slip time function assumed for particle velocity. It is the solution of Kostrov (1964).

NUMERICAL EXPERIMENTS TO INVESTIGATE APPROPRIATE BOUNDARY CONDITIONS FOR MODELLING VERY LONG EARTHQUAKES

Shamita Das
Lamont-Doherty Geological Observatory of Columbia University
Palisades, New York 10964
(914) 359-2900

ABSTRACT

We have studied two sets of models to find appropriate boundary conditions for the theoretical modelling of very long earthquakes (i.e., those for which the length L is larger than the width W of the rectangular aftershock area). In the first set, we study the conventional rectangular crack model (for L/W = 2 and 4), i.e., the stress-drop is confined to a rectangular region and the slip is constrained to be zero at all four crack edges, the stress-drop and slip being zero everywhere outside this region. In the second set of models -- which is suggested by geologic and geodetic data -- we constrain the stress-drop to a rectangular zone ("seismogenic layer") but we do not have any constraint on the slip above and below this layer. The applied stress in this region above and below the seismogenic layer is taken to be exactly equal to the yield stress of the material. This is equivalent to assuming that the material on either side of the seismogenic layer is shearing aseismically just before the earthquake occurs. We find that for the second set of models, the rupture propagates for some distance into the stress-drop free zone above and below the seismogenic layer, and the slip in large parts of this zone without stress-drop is found to be non-negligible. The slip is still confined to a finite width but this width is larger than the width of the seismogenic (brittle) later. For the second set of models, the aftershock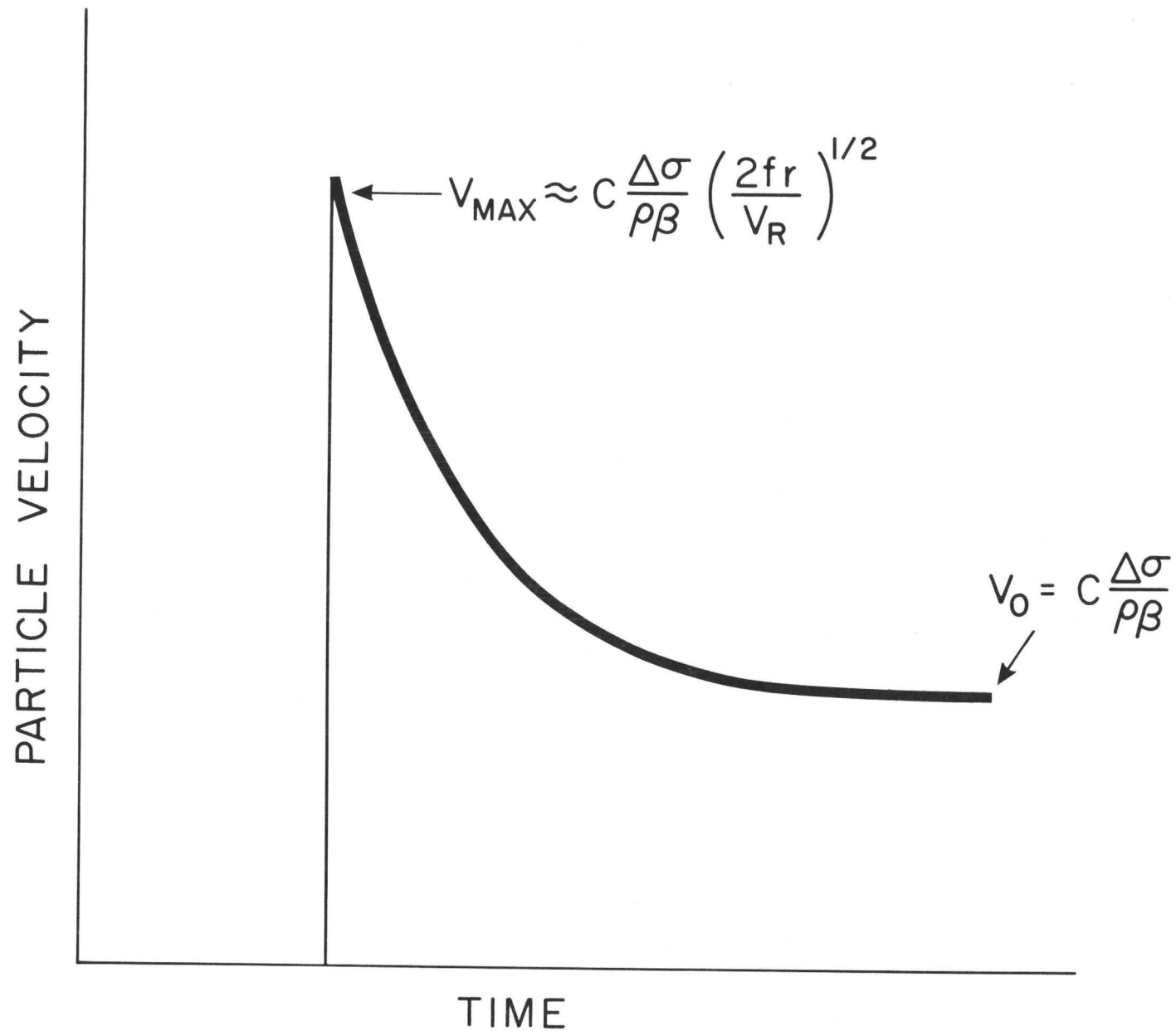 area would underestimate the actual rupture area. The moment and the slip at the center for the second set of models are larger than for the first set for the same L/W ratio of the stress-drop region. In fact, the moment estimated from seismograms for the first set of models can be regarded as the lower bound of the real seismic moment. For L/W = 2, the duration of slip at interior points on the fault for the two models are the same but for L/W = 4, the duration of slip at a given interior point is much larger for the second set of models. However, the particle velocity during this added time of slip for the second class of models is small and almost constant, so that (at least for L/W up to 4) this difference may not be significant for strong ground motion near such a fault. The rise-times and slips at any interior point of the fault is mainly width controlled for the first set of models and length-controlled for the latter set. Since longer faults are observed to have have larger slips than shorter ones of the same width, the first set of models would predict that stress-drops increase with rupture length (for the same fault width). However, this observation can be explained by the second set of models

even for constant stress-drops. For the latter set of models we find that a fault twice the size of another, has much less than double the slip for the same average stress-drop.

INTRODUCTION

In the last few years it has become very productive to model earthquake faults as propagating plane shear ruptures with various geometries. These studies have been carried out both for the two and three dimensional problems for ruptures with known constant velocities, as well as for spontaneously propagating ruptures in which the rupture velocity is determined by using some fracture criterion, and have provided insight into what the slip on a fault may be. In particular, one finds that the final slip, the rise-time and the static stress drop on the fault may vary with position on the fault, even for smooth faults, i.e., in which no variation is assumed in the physical properties on the fault. A common feature of all these models is that the slip and stress-drop are constrained to be zero at the edges of the fault. With such a boundary condition, it is found that the rise-time and final slip at a point on the fault are controlled by the smallest dimensions of the fault. For rectangular faults, this is the fault width. Observations of slip on faults of different lengths but same width show, however, that the longer fault has the larger slip (Bonilla and Buchanan, 1970; Sykes and Quittmeyer, 1981; Scholz, 1981, 1982). The only way this can be explained by the existing models is if the stress drop is also larger for the larger earthquakes (Das, 1981). Scholz (1981) has put forward some arguments against this and has suggested that for very long earthquakes viz. ones that rupture completely through the seismogenic zone, the boundary condition that the slip at the bottom of the fault is zero may not be valid. Analysis of rock deformation textures in exhumed fault zones (Sibson, 1979, 1982) as well as the fact that in major fault zones the after-shock activity is confined to some finite zone (called the" seismogenic zone") indicate that within this zone the material is brittle and rupture occurs dynamically but 'at greater depths shearing is.... accomodated by some form of aseismic slip or ductile flow' (Figure 1). This property has been incorporated into models of slow deformation (Nur and Mavko, 1974) and strain accummulation (Turcotte and Spence, 1974; Budiansky and Amazigo, 1976) at plate boundaries. Such models are in agreement with Scholz's (1981) point of view that there is no physical basis for assuming that the slip at the bottom of the fault during the dynamic rupture of the seismogenic layer is zero. Thus for very long earthquakes, e.g., the 1906 San Francisco earthquake, it does not seem justified to so constrain the slip. For smaller earthquakes which do not completely rupture through the seismogenic zone, however, the existing models may be adequate. The reason it is important to investigate this problem is because a major problem of strong motion seismology is to predict the expected strong ground motion for a large earthquake by measuring that from a smaller one. But if the two problems are controlled by different boundary

733

conditions, it would be more complex to do this than if the boundary conditions for both the small and large earthquakes were similar. The purpose of this paper is to use a numerical boundary integral equation technique to study the consequences if the condition of slip being zero at the bottom of the fault is relaxed. In the next two sections we describe the two classes of models -- when the slip is zero at the bottom and when the bottom of the fault is allowed to slip freely and calculate the rupture process, slip, particle velocities, rise-times, moments, etc. for these cases. Finally, we discuss the implications of the models for the earthquake source mechanism and strong ground motion predictions.

DESCRIPTION OF MODELS

The numerical method used in this study was discussed in detail by Das (1980, 1981) and will not be described here. The notation used here is in conformity with that of the earlier papers. The results in the earlier papers were obtained by using a numerical grid spacing given by $\alpha \Delta t/\Delta x = .5$, where α is the compressional wave velocity and Δx and Δt are respectively, the spatial and temporal grid lengths. We have since implemented the method for $\alpha \Delta t/\Delta x = .25$ and all results in this paper are for the finer mesh size. We shall study the four cases illustrated in Figure 2 and described below -- mathematically as well as in words. For all the cases, we consider the uniform applied shear stress $\sigma_{13}{}^{\circ} = 5\tau e$, where τe is the dynamic stress drop in the seismogenic layer and is taken as a constant independent of applied stress. The stippled circles indicate the initial crack shape and size. The small line segments shown within the rectangular regions in Figure 2 indicate the kind of line that will be used to plot the displacements for each case in Figures 3-6.

Case I

In $\begin{vmatrix} x_1 \\ x_2 \end{vmatrix} \begin{array}{l} < 7.5 \ \Delta x, \\ < 3.5 \ \Delta x \end{array}$ slip $\neq 0$,
                                         $\tau e \neq 0$,
                                         uniform yield stress or static limiting frictional stress $\sigma u = 5.6 \ \tau e$

In $\begin{vmatrix} x_1 \\ x_2 \end{vmatrix} \begin{array}{l} > 7.5 \ \Delta x, \\ > 3.5 \ \Delta x \end{array}$ σu is too high relative to the applied stress for rupture to occur
                                         slip $= 0$
                                         $\tau e = 0$

Thus, slip is allowed inside a rectangular region 7 Δx by 15 Δx and prevented from occurring outside this region by placing unbreakable barriers there.

Case II. This is similar to Case I but the longer dimension of the rectangular region of slip is now about double that in the previous case. Thus,

in $\begin{vmatrix} x_1 \end{vmatrix} < 15.5 \, \Delta x,$ slip $\neq 0$, $\tau e \neq 0$, $\sigma u = 5.6 \, \tau e$
$\begin{vmatrix} x_2 \end{vmatrix} < 3.5 \, \Delta x$

and outside this region, slip $= 0$, $\tau e = 0$, σu is very high relative to the applied stress.

Case III

In $\begin{vmatrix} x_1 \end{vmatrix} < 7.5 \, \Delta x,$ $\tau e \neq 0$
     $\begin{vmatrix} x_2 \end{vmatrix} < 3.5 \, \Delta x$ slip $\neq 0$
                     $\sigma u = 5.6 \, \tau e$

In $\begin{vmatrix} x_2 \end{vmatrix} > 3.5 \, \Delta x$ for all x_1, $\tau e = o$
                               $\sigma u = \sigma_{13}°$ (i.e., stress-drop
                                         is zero)
                         slip $\neq 0$

In $\begin{vmatrix} x_2 \end{vmatrix} < 3.5 \, \Delta x,$ slip $= 0$, $\tau e = 0$, σu is very high relative to
     $\begin{vmatrix} x_1 \end{vmatrix} > 7.5 \, \Delta x,$ the applied stress

In other words, the <u>stress-drop</u> is confined to the rectangular region 7 Δx by 15 Δx (the seismogenic layer) and slip is prevented on the two sides of this region ($\begin{vmatrix} x_1 \end{vmatrix} > 7.5 \, \Delta x$, $\begin{vmatrix} x_2 \end{vmatrix} < 3.5 \, \Delta x$) by making the yield strength very high relative to the tectonic stress but slip is not constrained to be zero above and below this region ($\begin{vmatrix} x_2 \end{vmatrix} > 3.5 \, \Delta x$ for all x_1). So, the top and bottom of the fault are allowed to slip freely. The applied stress in the region above and below the seismogenic layer is exactly at the yield stress and there is also no stress drop there. This assumption that $\sigma u = \sigma_{13}°$ is equivalent to assuming that the material is shearing aseismically just before the earthquake (Savage and Burford, 1973). We point out here that we do not consider the process that creates the initial stress state but only study the changes in the stress state due to the dynamic rupture process.

Case IV. This is similar to Case II but the longer dimension of the rectangular region where stress-drop occurs is about double that in the previous case, so that the region of stress-drop is now given by $\begin{vmatrix} x_1 \end{vmatrix} < 15.5 \, \Delta x$, $\begin{vmatrix} x_2 \end{vmatrix} < 3.5 \, \Delta x$.

Before we discuss our results in the next section, we point out some of the limitations of our analysis. Our method of solution is only applicable, at least at present, to the case of faulting in an infinite, elastic medium. We therefore do not claim that these models correspond to actual faulting on a physically realistic fault plane. We only study a very simplified mechanical model of faulting which has some of the characteristics of the real physical system to simulate the effects of these characteristics on the real system. For example, in this paper we are particularly interested in studying the effect on the slip distribution, particle velocities and rise-time, over the fault, of relaxing the condition of vanishing slip at the lower edge of the fault. Even though we are not able to introduce ductile behavior below the lower edge of the fault and the free surface effect at the upper edge, the results will be useful in general, in furthering our understanding of the processes occurring at the earthquake source, and in particular in suggesting the actual boundary conditions that control fault processes for very long earthquakes. Clearly there

may be implications from the simple models which may be unrealistic and may have to be ignored. If such implications arise, we will discuss them in the section of the implications of our results for the earthquake faulting process.

RESULTS

Figures 3, 4, 5 and 6 show the comparison between the normalized half-slips as a function of normalized time at points A, B, C and D (marked in Figure 2) for the four cases studied. The particle velocity at the point A is shown at the top of each figure for all four cases. Figure 7 shows the final slip at the center 0 of the fault (i.e., after all motion has ceased) as a function of x_2 and Figure 9 shows three-dimensional plots of the final slip for the four cases. The normalization factors for slips and particle velocities are the same as in Das (1980, 1981). The crack is started as a small circular region and allowed to propagate spontaneously. The "critical stress level" fracture criterion (Das, 1981) is used to determine the rupture velocity. No healing criterion is used to stop the slip. (In fact, to prove that the healing criterion of Das (1981) is a very weak criterion, one case was studied both with and without the healing criterion and no perceptible difference was found in the results.) The solid dots indicate the approximate arrival times of diffracted shear waves from the nearest point at top and bottom of the fault, the crosses and stars respectively indicate the P and S "stopping phase" from the closest point at nearer crack end in the x_1-direction, for Case I and II. These are illustrated in Figure 2b.

Comparison of Case I and II

We compare the slip and particle velocity due to two faults, one of length twice the width and the other of length four times the width, and having the same average dynamic stress-drop. These are conventional models where the slip is zero at all the fault edges and has been studied in detail by Day (1979, 1982) and Das (1981). Our results are in general agreement with the comparisons made by Day of different fault length to width ratio but we include a brief discussion here for the sake of completeness.

The slip for the different cases is labelled by a roman numeral indicating the case and a letter in parentheses indicating the point on the fault (marked in Figure 2) at which the slip is plotted. The point A represents the slip at points near the center of the fault. We see that for these two cases the slip at the center is almost the same implying that the slip is mainly width-controlled. The fact that the longer fault has slightly larger slip near the center (also found by Day, 1982) may indicate that some small amount of slip still occurs even after the information of finiteness of fault width has reached A. Unfortunately, probably due to the extremely long computer time required, faults that are say ten, twenty or thirty times longer than

wide have not yet been studied though they do exist in nature. The sum of the slip over the fault is proportional to the moment M_O. Table I shows this sum as well as the maximum slip at the center 0 of the fault for all four cases. The moment is Case II is slightly more than double that in Case I.

Even though we have only considered values of L/W up to 4, we may suggest how the slip and moment on longer rectangular faults will behave by considering the static solution for an elliptic crack (Eshelby, 1957), having a constant static stress drop τ_e. For elliptic cracks having semi-major axis a and semi-minor axis b, Table II shows the factor η of Eshelby, for various values of a/b, for an elastic solid having a Poisson's ratio of 1/4 (as we have in the numerical models). The normalized half slip at the center is $6b/\eta$ and the average half-slip $\bar{u}$ is $4b/\eta$ and are shown in Table II for b = 3.5 Δx (i.e., for the same crack half-width as used in the rectangular cracks of Case I and II). We see that η is virtually constant for all a/b, which implies that the maximum slip at the center and the average slip over the fault are essentially constant even for large values of L, for a given value of W. [It is very instructive to note the details of the behavior of η, and hence the maximum and average slip, as a function of a/b. As we go from a circular crack (a/b = 1) to more and more eccentric elliptic cracks, η at first decreases, then increases and levels off at a constant value. Thus as a/b increases, the maximum and average slip at first increases, and then decreases to a constant value for very long faults!] The quantity $(M_O/4\mu)$ is also shown in Table II. We cannot compare this value for the rectangular and elliptic faults as the areas are different for the same length to width ratio. We may note, however, that the ratios of this quantity for L/W = 2 and 4 is almost the same as that for a/b = 2 and 4.

The point C is exactly at one corner of the fault for the shorter fault but not for the longer one and hence the difference in the displacements at C. The point B is intermediate between A and C and the difference between the final slips between Case I and II is also intermediate. The particle velocity at A is shown at the top of Figure 3. The particle velocity goes to zero at almost the same time for Case I and II, again implying that the slip is mainly width-controlled. The regions on the fault where the major amount of slip is occurring at any time are two regions whose x_1 dimension is controlled by fault width, (for a unilateral fault, Archuleta and Day (1980) found that there is only one such region), which move away from the point of rupture nucleation, leaving behind regions where the slip is small. For a fault that is say ten times longer than wide, it seems likely that the particle velocity may be non-zero for a longer time but our results indicate that it will probably be small and the difference may not be detectable from observations.

Comparison of Case I and III

The rectangular region of stress-drop is the same for both cases but the slip in Case III is not constrained to be zero at the upper and lower edge. The rupture can expand into the regions above and

below with associated slip, though there is no stress-drop here. Figures 8 and 9 show the final area of where slip is non-zero. It is found that only in the zone adjacent to the region of stress-drop is the slip significant. The rupture front passes through the rest of the zone at a speed very close to the P-wave speed of the medium since the yield strength is equal to the applied stress in the material below the seismogenic layer, but the slip there is found to be negligible. The slip is still confined to a finite width in Case III but it is a larger width than in Case I. There is a strong stress concentration at the upper and lower edges of the fault in Case I but no such stress concentration in Case III.

The actual shape of the rupture area we find may be slightly unrealistic as we have artificially placed very strong barriers in the seismogenic layer to limit the region of slip in this layer in the x_1 direction. Very long earthquakes (e.g., those that fill in "seismic gaps") often stop by running into the rupture zones of previous great earthquakes, i.e., by running out of strain energy. In other words, the stress-drops at the ends decrease and the rupture stops. If we used such a model, the shape of the rupture are would be more even and will not have the rather unrealistic shape it has now.

Figure 4 shows that the slip in Case III continues for a slightly but not significantly longer time than in Case I. The final slip at the points A, B, C are larger but may not be significantly larger for us to be able to distinguish between these models from observations. What is larger is the rupture area and hence the moment (Table I).

Comparison of Case II and IV

The difference between Case I and III was not significant except for moment. The difference between Case II and IV, however, is major. The slip for Case IV which is unconstrained at the bottom is much larger for the same region of stress-drop as in Case II, all over the fault except for the point D which is very close to one end of the fault. The rupture penetrates very far into the region above and below the brittle layer (Figures 7 and 9) and the shape is found to be similar (but larger) than in Figure 8. The duration of slip at A is much longer now than in all the previous cases and the level of the particle velocity is low. So the slip in Case IV continues slowly for a long time and the final slip and hence moment is larger than in all the other cases. Thus the slip in these models is length-controlled unlike the Case I and II. The stress concentrations at the crack ends are stronger for Case IV than for Case II and there is no stress concentration at the upper and lower edges in Case IV as there is in Case II.

Comparison of Case III and IV

In this case, dots, crosses and stars indicate the arrival times of waves for a width-controlled model (like Case I or II) of the same width as the width of the stress-drop zone in these two cases. Clearly, when the information of the finiteness of the stress-drop region comes to a interior point on the fault the point slows down

perceptibly, but unlike Case I and II does not stop abruptly. Instead is slows down very gradually and has a very low particle velocity but very long slip duration. The slip for the longer fault is now much larger than the shorter fault. Note, however, that though the fault length for the longer fault is double that of the shorter fault, the slip at the center is not doubled. The average slip (and therefore moment) is, on the other hand, more than doubled due to the area of rupture being much larger for the longer fault.

IMPLICATIONS FOR EARTHQUAKE SOURCE MODELS

We have studied two classes of models -- the conventional rectangular fault models for which the slip is zero at the base of the seismogenic layer and a class of models suggested by geologic and geodetic data, where slip is not so constrained. By the latter class of models we have tried to simulate very long faults that completely rupture through the seismogenic layer and have shown that such faults may propagate for some distance into the zone of ductile flow. Since the Green functions we have used in our solution are for an elastic medium, the actual amount of slip in the region below the seismogenic layer and the actual rupture area are not simulated correctly by this model. In fact, we expect the slip for a region of ductile flow to be lower than that for the elastic layer with no stress-drop. How much lower the slip will be will depend on the properties of this layer, which are probably not known well enough at present to warrant detailed numerical calculations for such models. We also find that for the former set of models for L/W ratios of 2 and 4 (Case I and II), the rise-times and slip are mainly controlled by fault width. The implications of this result has been discussed by Das (1981) and Scholz (1981) viz. that since longer faults are observed to have larger slip, the stress-drop for the longer fault must be larger than that for the shorter fault. By considering the static solution for elliptic cracks, we suggest that for L/W = 10, 20 or 30, the final slip will not be significantly larger for these cases. For most thrust earthquakes, L/W is usually less than about 3 or 4 (the 1960 Chilean earthquake may be an exception) but large strike slip earth- 20 or 30. For L/W = 2, it is not possible to distinguish easily between the two classes of models (Case I and III), but for L/W = 4 significant differences are predicted from our models. The seismic moment for the model where slip is allowed below the seismogenic zone is significantly larger. Determinations of seismic moment from very long period seismic waves or from geodetic data may correctly account for the total moment. An error would arise if one tried to determine average slip for the latter set of models by dividing the moment by the aftershock area (since that presumably only measures the portion of the rupture zone within the seismogenic layer). However, if the slip velocity in the zone below the seismogenic zone is very low, then it may not be detected from seismograms, so that in that case, the seismic moment determined from the seismogram is the lower bound for the real seismic moment. A possible example of Case III and IV may be

the earthquakes along the Colombia-Ecuador subduction zone studied by Kanamori and McNally (1982), in which the portion of the plate boundary that broke in a very large earthquake in 1906, later again broke in three smaller segments. These authors found that the sum of the moments of the three smaller earthquakes is a fraction of (about 1/5) that of the larger one, as would be expected for Case III and Case IV.

We also show that the duration of slip for the Case IV (L/W = 4) is theoretically predicted to be much longer than for the corresponding conventional model (Case II) but the particle velocity during the entire period of slip is almost constant so the acceleration is almost zero and thus the difference may not be significant from the point of view of strong ground motion. Also, the particle velocity level during this time may be too low to be significant, i.e., this slow increase of slip may not affect strong ground motion. For larger L/W we cannot again predict the result definitively but it is not unlikely that the particle velocity level may be higher. Finally, since the slip (and rise-times) are controlled by length in the latter models and we find that the longer fault has the larger slip, the stress-drop is not necessarily larger for the longer fault for this latter class of models. The data in Scholz (1982) suggests that the fault slip increases with length but it is not clear at all from the data if this increase is linear or non-linear. Hence it is not yet clear if the models and data are compatible with constant stress-drops. The implications of this for strong ground motion is discussed by Scholz (1981). The interesting fact we have found by comparing Case III and IV is that a fault of twice the length as another does not have twice the slip (for the same average stress-drop), for such models. Many cases of L/W need to be studied to predict theoretically how L/W controls slip for the length-controlled models.

We may point out here that whereas in Cases I and II we have artificially simulated the effect of finite seismogenic depth by constraining slip to be zero outside this region, it arises quite naturally for Cases III and IV from assumptions of some reasonable properties of the material outside this region. It is hoped these models will stimulate future work on dynamic models of more realistic behavior beneath the seismogenic zone, e.g., incorporating the effects of strain hardening or strain rate effects of ductile materials (negative stress-drop) and encourage reviewing of existing seismic and geodetic data from a different point of view than that traditionally used.

REFERENCES

Archuleta, R. J. and S. M. Day (1980). Dynamic rupture in a layered medium: The 1966 Parkfield earthquake, Bull. Seismol. Soc. Am., 70(3), 671-689.

Bonilla, M. G. and J. M. Buchanan (1970). Interim report on world wide historic surface faulting, U.S. Geol.Surv. Open File Rept., Washington, D.C.

Budiansky, B. A., and J. C. Amazigo (1976). Interaction of fault slip and lithology creep, J. Geophys. Res., 81, 4897-4900.

Das, S. (1980). A numerical method for determination of source time functions for general three-dimensional rupture propagation, Geophys. J. R. astr. Soc., 62, 591-604.

Das, S. (1981). Three-dimensional rupture propagation and implications for the earthquake source mechanism, Geophys. J. R. astr. Soc., 67, 375-393.

Day, S. M. (1979). Three dimensional finite difference simulation of fault dynamics, Final Report SSS-R-80-4295, Systems, Sciences and Software, La Jolla, California.

Day, S. M. (1982). Three dimensional finite difference simulation of fault dynamics: Rectangular faults with fixed rupture velocity, Bull. Seismol. Soc. Am., submitted for publication.

Eshelby, J. D. (1957). The determination of the elastic field of an ellipsoidal inclusion, and related problems. Proc. Roy. Soc. Lond., A241, 376-396.

Kanamori, H., and K. McNally (1982). Variable rupture mode of the subduction zone along the Ecuador-Colombia coast, Bull. Seismol. Soc. Am., in press.

Nur, A., and G. Mavko (1974). Postseismic viscoelastic rebound, Science, 183, 204-206.

Savage, J. C., and R. O. Burford (1973). Geodetic determination of relative plate motion in Central California, J. Geophys. Res., 78(5), 832-845.

Scholz, C. H. (1981). Scaling relations for strong ground motion in large earthquakes, this issue.

Scholz, C. H. (1982). Scaling laws for large earthquakes: Consequences for physical models, Bull. Seismol. Soc. Am., 72, 1.

Sibson, R. H. (1979). Fault rocks and structure as indicators of shallow earthquake source processes, Proc. Conf. VIII on "Analysis of Actual Fault Zone in Bedrock, Open File Rept. 79-1239, 276-304.

Sibson, R. H. (1982). Fault zones, models, heat flow and the depth distribution of earthquakes in the continental crust of the United States, submitted to Bull. Seismol. Soc. Am.

Sykes, L. R., and R. C. Quittmeyer (1981). Repeat times of great earthquakes along simple plate boundaries, in Earthquake Prediction: an International Review, vol. 4, Third Maurice Ewing Symposium, D. W. Simpson and P. G. Richards, eds., Am. Geophys. Un., Washington, D.C.

Turcotte, D. L., and D. A. Spence (1974). An analysis of strain accumulation on a strike slip fault, J. Geophys. Res., 79, 4407-4412.

TABLE I

Model type	(Maximum) normalized half-slip at center of fault	$\sum 1/4(\text{Mo}/\mu)$NORMALIZED over total ruptured area
Case I (L/W = 2)	≈ 12.7	$\approx 260.$
Case II (L/W = 4)	≈ 12.85	$\approx 555.$
Case III	≈ 14.0	$\approx 640.$
Case IV	≈ 18.4	$\approx 1875.$

TABLE II

Elliptic fault (static solution of Eshelby)

a/b	1.	1.5	2.	3.	4.	5.	10.	20.	30.
η	1.83	1.75	1.71	1.72	1.78	1.83	1.9	1.9	1.9
(Maximum) normalized half space at center for $b = 3.5\,\Delta x$	11.5	12.0	12.3	12.2	11.8	11.5	11.0	11.0	11.0
Average slip u over fault for $b = 3.5\,\Delta x$	7.7	8.0	8.2	8.2	7.9	7.7	7.4	7.4	7.4
$1/4\ M_0/\mu$ (normalized) for $b = 3.5\,\Delta x$	21.0	33.0	45.0	67.1	86.5	105.1	202.5	405.0	607.6

FREE SURFACE

Discontinuous
faulting
(brittle)
"Seismogenic layer"

CATACLASITE

(Zone of microearthquake
and aftershock activity)

CRITICAL ISOTHERM

Continuous
faulting
(ductile)

MYLONITE
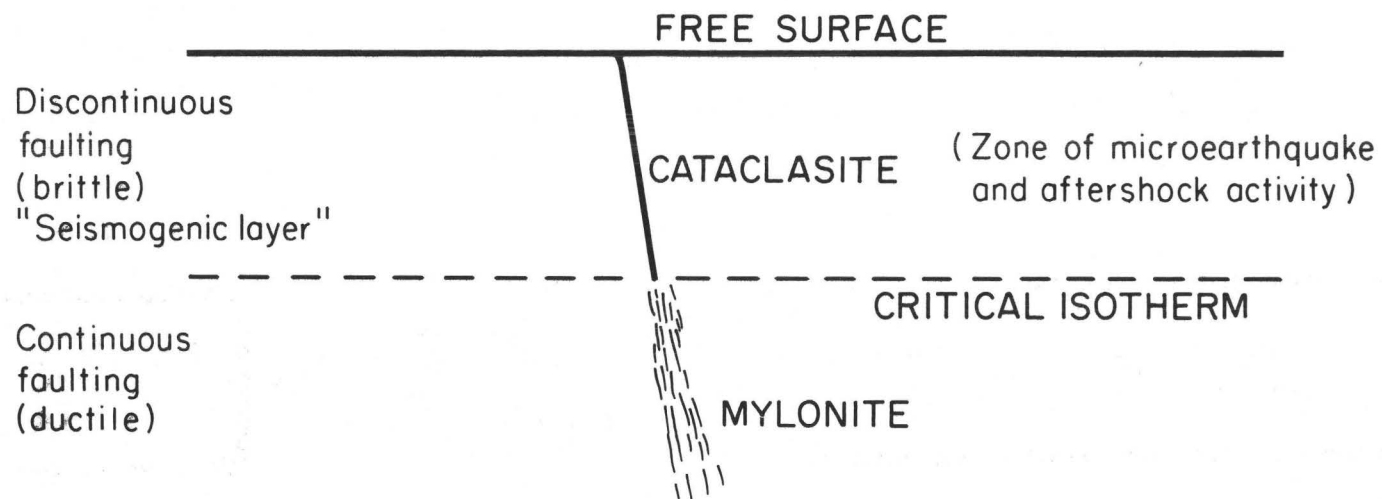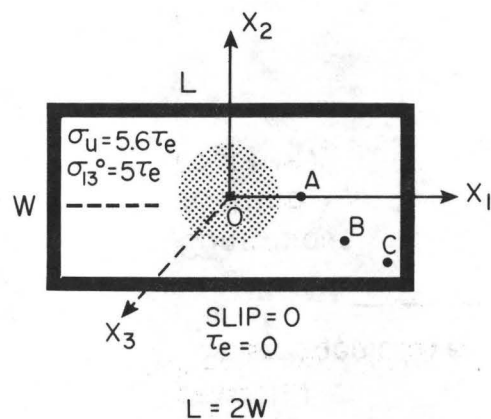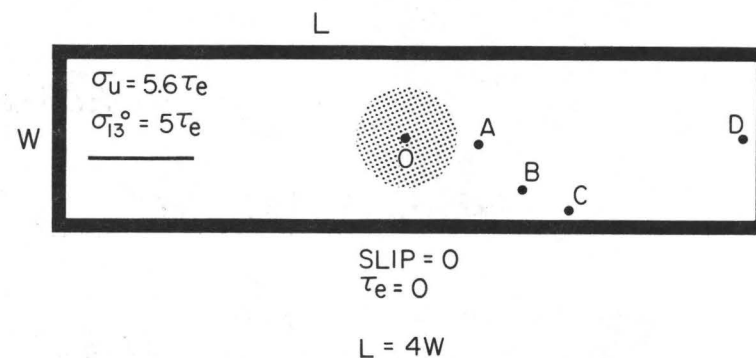
Figure 1. Schematic representation (based on Sibson, 1979) of cross-section of a typical fault zone.
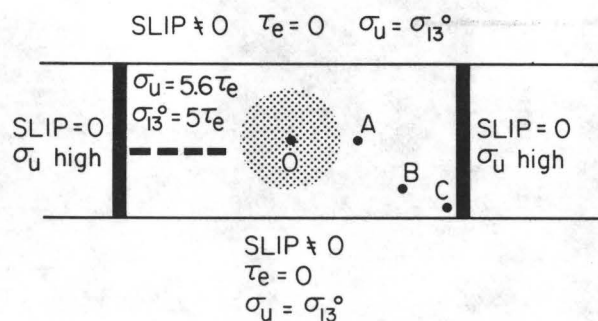
CASE I

$\sigma_u = 5.6\tau_e$
$\sigma_{13}^\circ = 5\tau_e$

X_2
X_1
X_3
L
W

A
B
C
O

SLIP = 0
$\tau_e = 0$

L = 2W

Models in which slip is constrained to vanish at top and bottom of fault as well as at other two sides.

CASE II

L
W

$\sigma_u = 5.6\tau_e$
$\sigma_{13}^\circ = 5\tau_e$

O
A
B
C
D

SLIP = 0
$\tau_e = 0$

L = 4W

CASE III

SLIP ≠ 0 $\tau_e = 0$ $\sigma_u = \sigma_{13}^\circ$

$\sigma_u = 5.6\tau_e$
$\sigma_{13}^\circ = 5\tau_e$

SLIP = 0
σ_u high

SLIP = 0
σ_u high

A
B
C
O

SLIP ≠ 0
$\tau_e = 0$
$\sigma_u = \sigma_{13}^\circ$

Models in which stress-drop is confined to a finite width but slip is not constrained to vanish at top and bottom

CASE IV

SLIP ≠ 0 $\tau_e = 0$ $\sigma_u = \sigma_{13}^\circ$

SLIP = 0
σ_u high

$\sigma_u = 5.6\tau_e$
$\sigma_{13}^\circ = 5\tau_e$

O
A
B
C
D

SLIP = 0
σ_u high
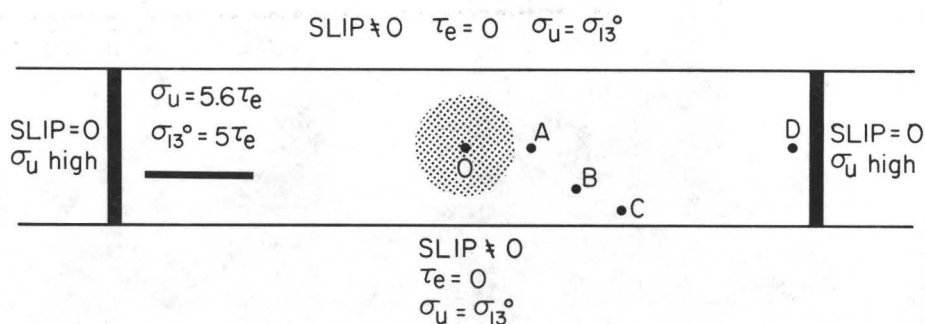
SLIP ≠ 0
$\tau_e = 0$
$\sigma_u = \sigma_{13}^\circ$

Figure 2. (a) Geometry of the four models studied. The two top figures are models with slip contrained to be zero at all edges, as shown by the heavy lines. The two lower figures are models where the slip is constrained to be zero at the ends (heavy lines) in the seismogenic zone but there is no such constraint at the upper and lower edges. The stippled regions is the initial crack and the axes of coordinates are shown. The small line segments within the rectangular area in each case shows the kind of line that will be used to denote slips and particle velocities for that case. The points A, B, C and D are the points at which the slips will be plotted.
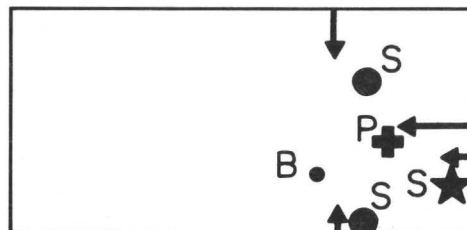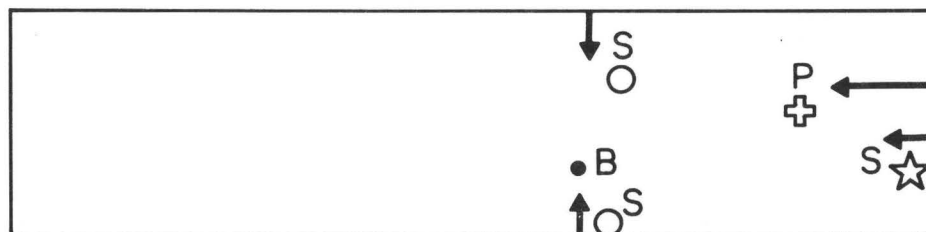
Figure 2. (b) Schematic explanation of the dots, crosses and stars used to denote arrival of various waves at any given point (illustrated for point B) on the fault for Case I and II. Note that for points A and D the shear waves from the top and bottom arrive at the fault at the same time since these points lie on the x_1-axis.
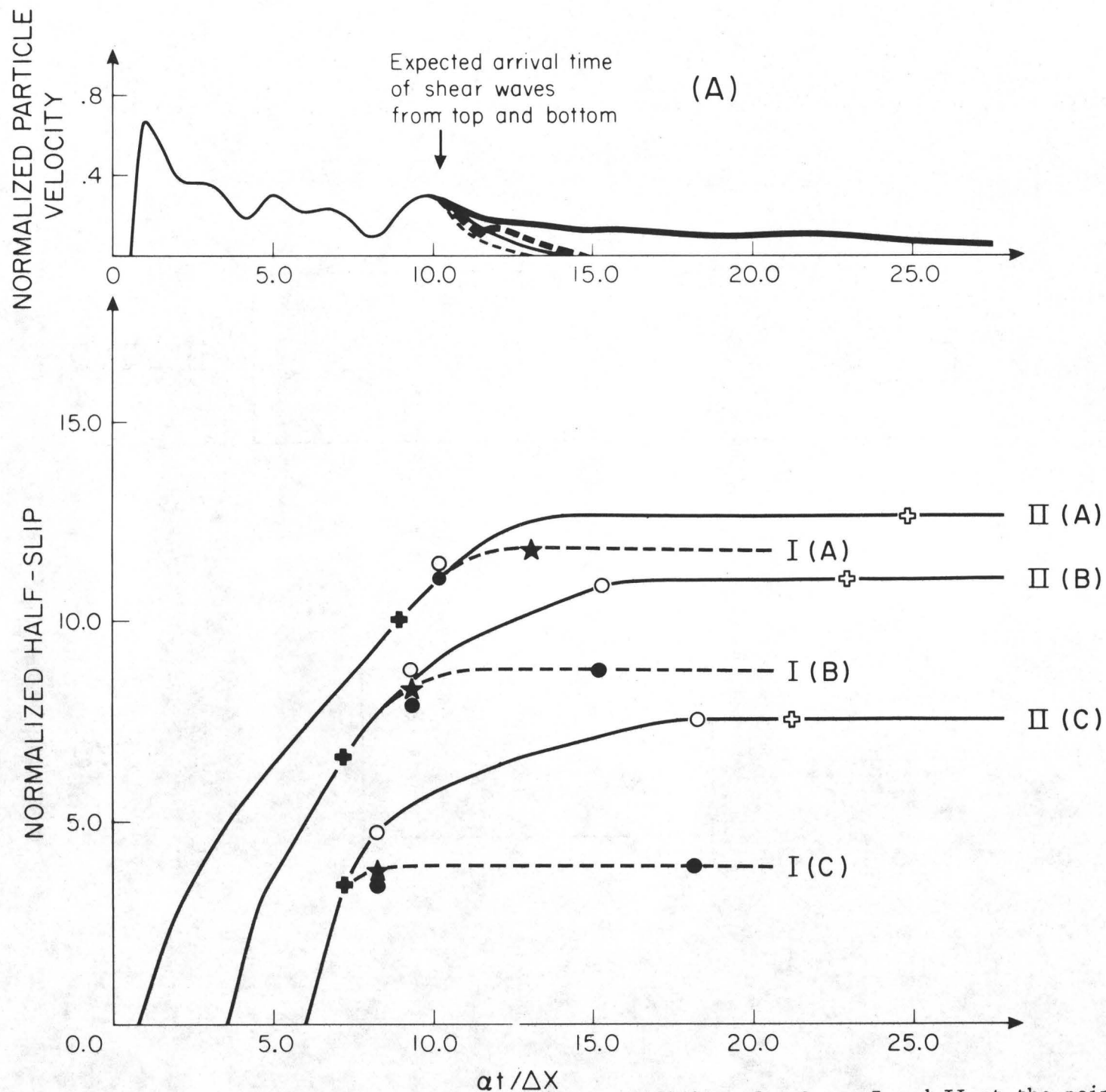
Figure 3. Half-slip normalized by $\tau e \, \Delta x / 3\mu$, μ being the coefficient rigidity, for Cases I and II at the points A, B and C. The normalized particle velocity at the point A only, is shown at the top of the figure for all four cases. The dots, ~~~~~~~~~~~~~~~~~~~~~~~~~~~~~~ are explained in Figure 2b.
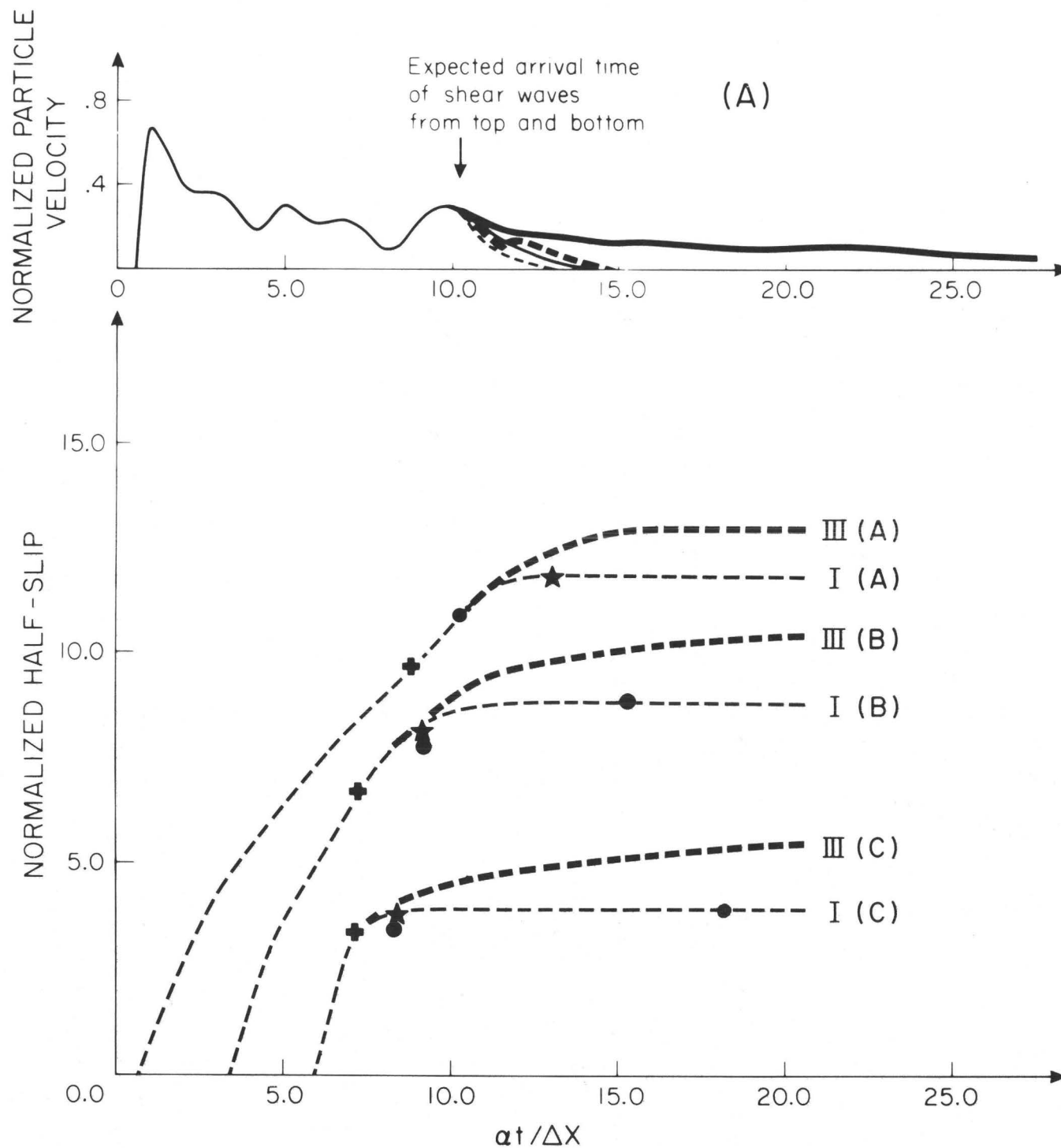
Figure 4. Same as Figure 3 but for Cases I and III.
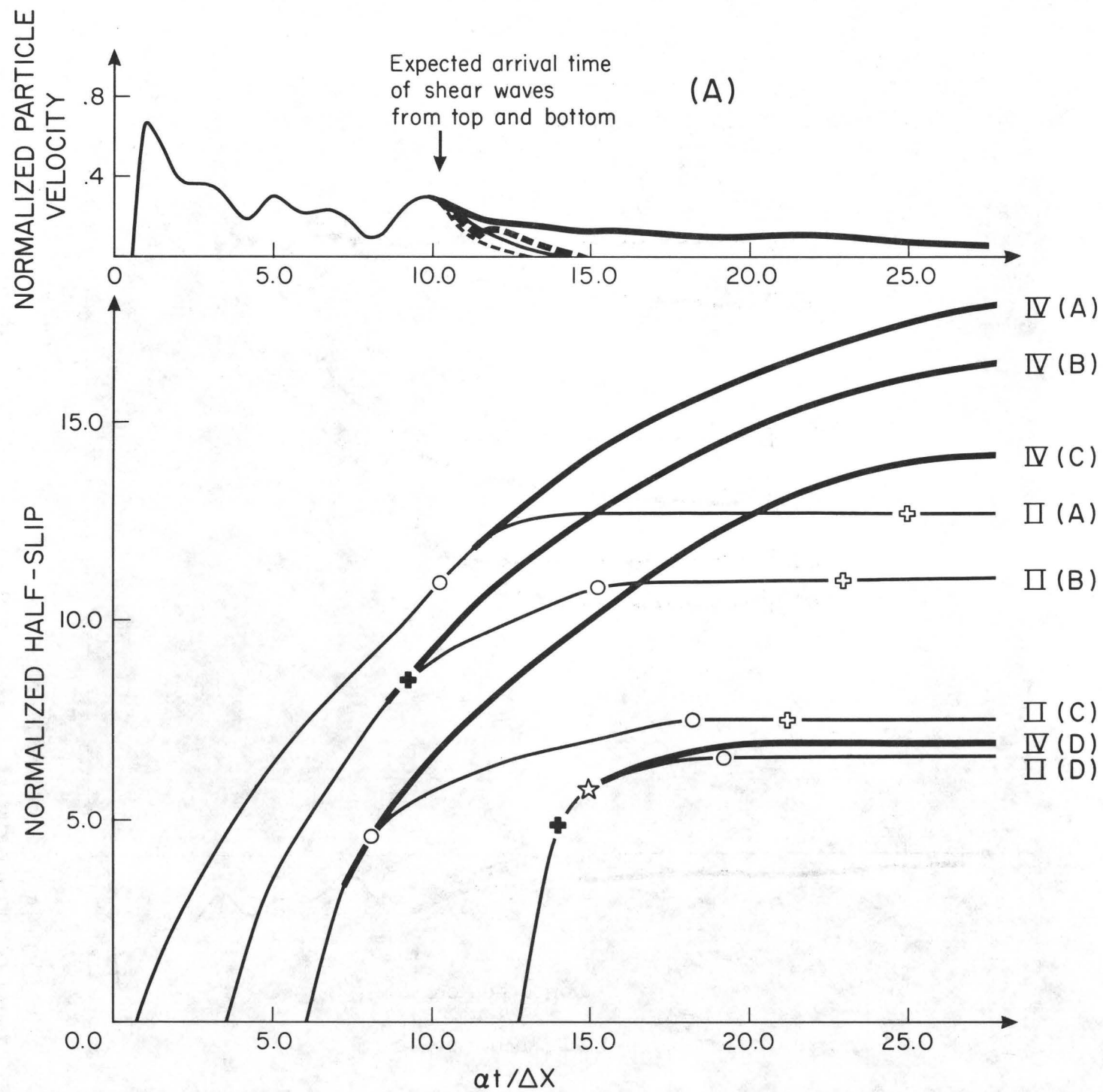
Figure 5. Same as Figure 3 but for Cases II and IV.
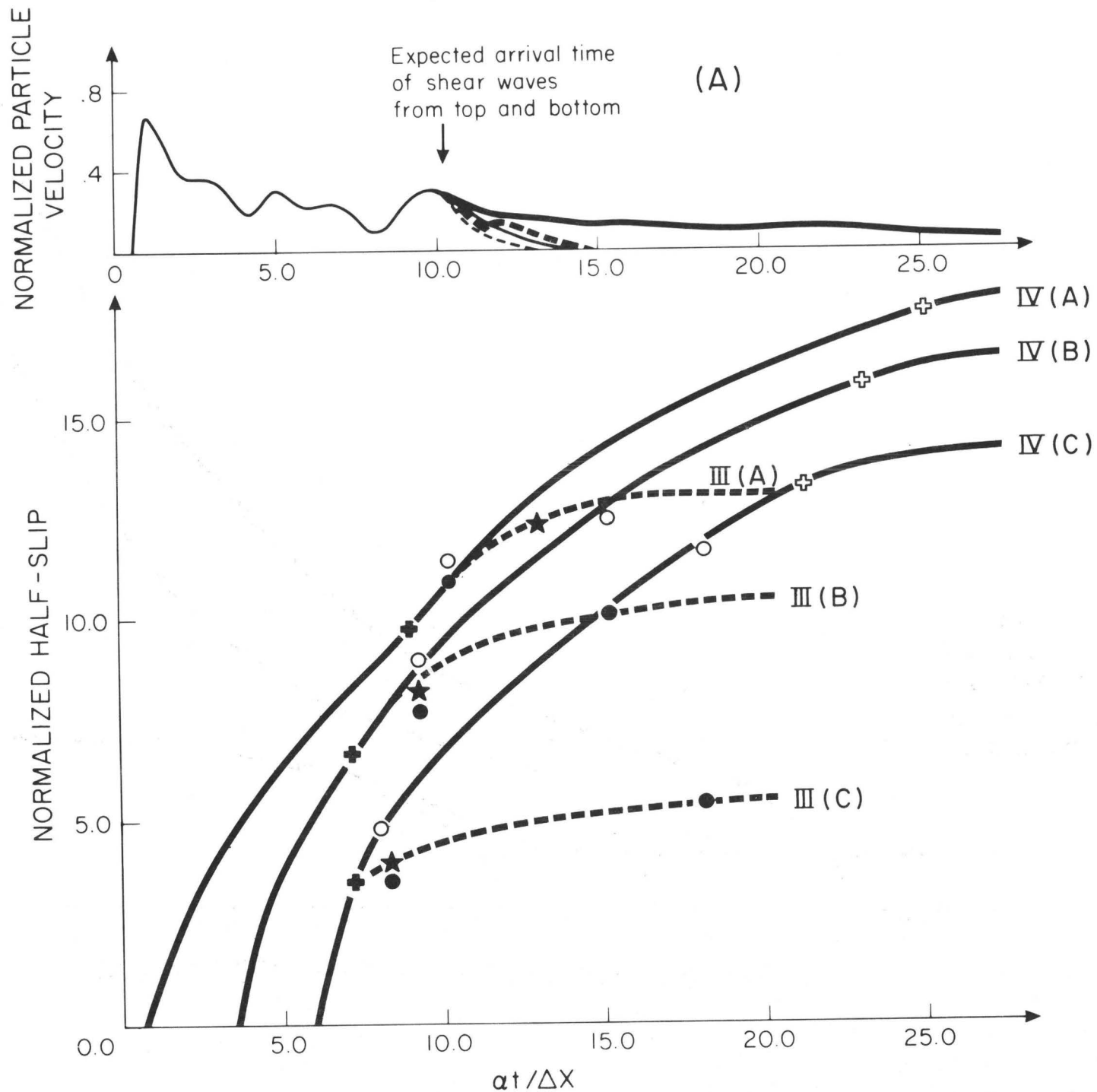
Figure 6. Same as Figure 3 but for Cases III and IV. The dots, crosses and stars now represent the arrival time of waves for the corresponding width controlled models.

NORMALIZED HALF-SLIP AT CENTRE OF FAULT

I(0)   II(0)   III(0)   IV(0)

Level below which
stress drop is zero
for Case III & IV, but
slip is not constrained
to vanish

$\frac{\Delta X}{X_2}$ (DEPTH)

752

Figure 7.   Final slip at the center 0 of the crak for all four cases studied.

753

Figure 8. Final rupture are for Case III. Only one quadrant is shown, the other three being mirror reflections of this about the x_1 and x_2 axes.

CASE I

CASE II

CASE III

CASE IV

Figure 9. Three-dimensional plots of the final slip on crack for the four cases studied.

SEGMENT RUPTURE MODELS OF NEAR FAULT
HIGH FREQUENCY GROUND MOTION

by

Robin K. McGuire*

and

Gabriel R. Toro**

INTRODUCTION

The construction of important engineering facilities in high seismic zones has generated an interest in predicting ground motion characteristics close to the source of large (M $\simeq$ 7-1/2) earthquakes. Indeed, this interest has led to extensive research in near-field ground motion estimation, 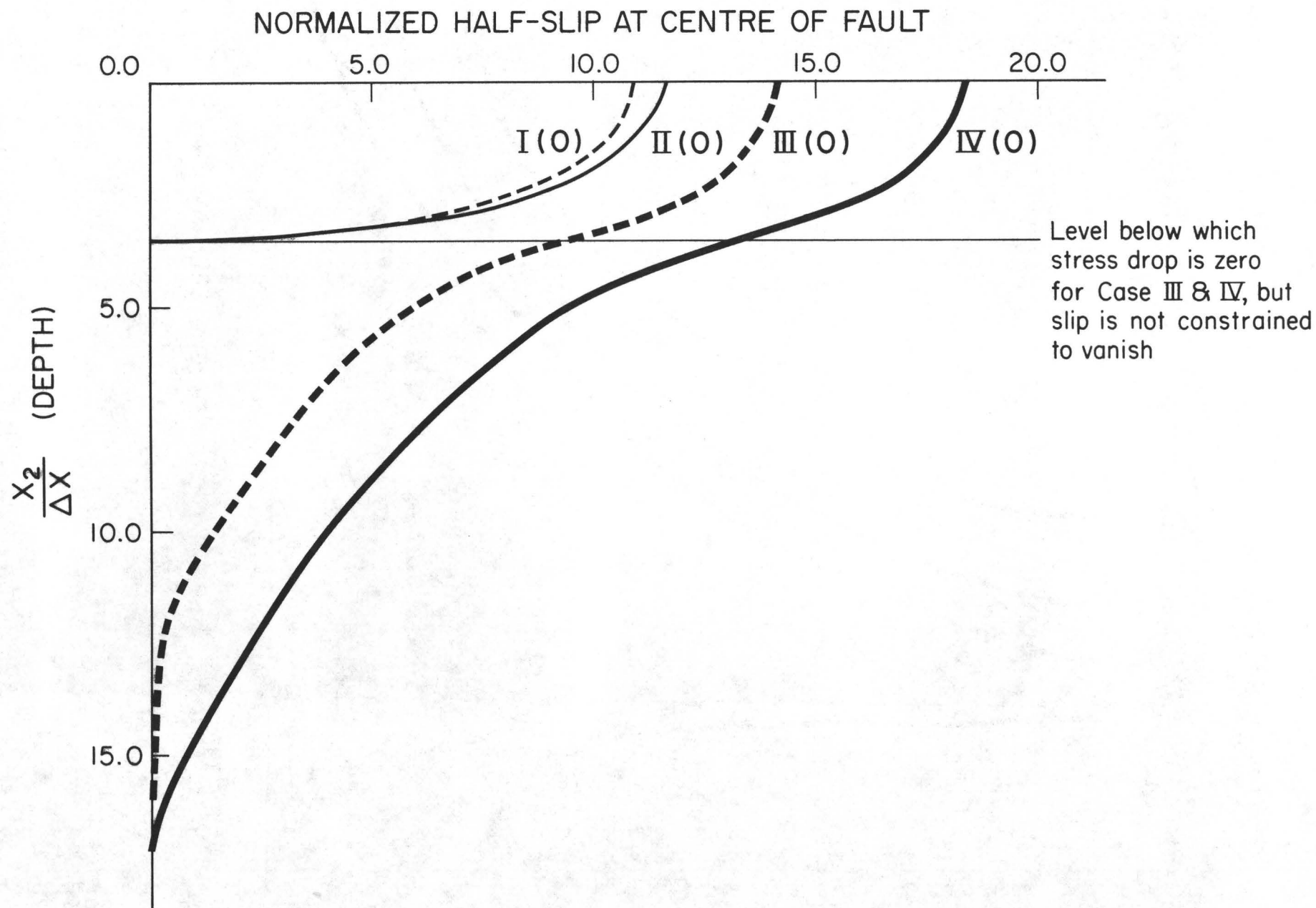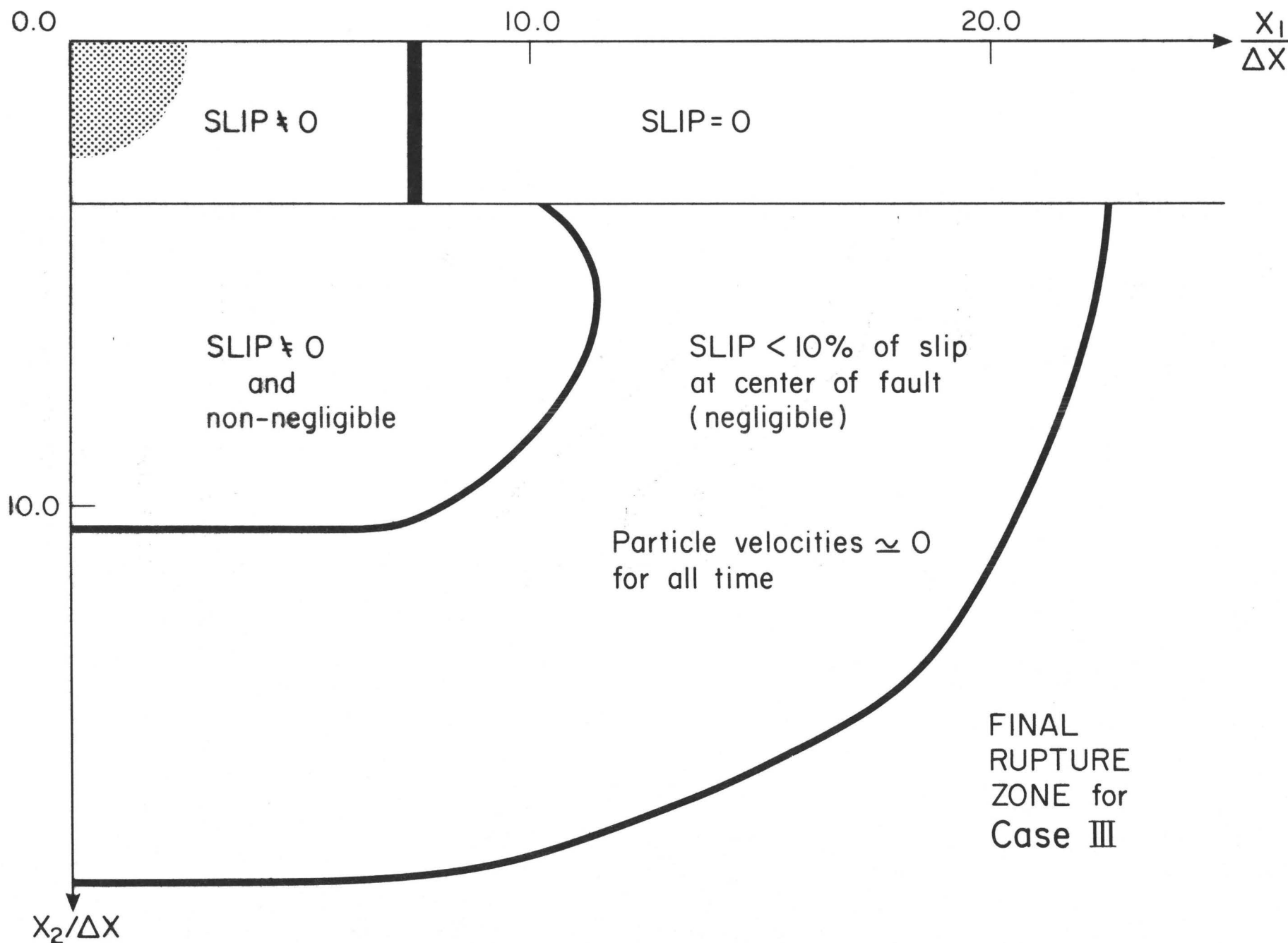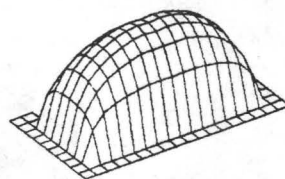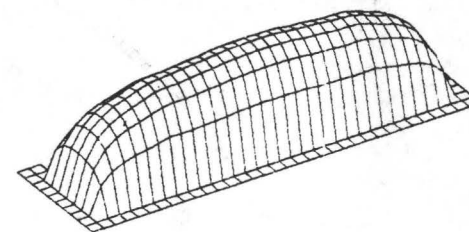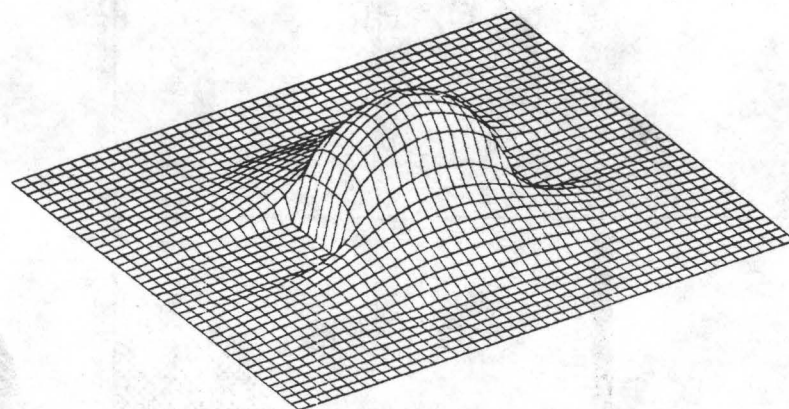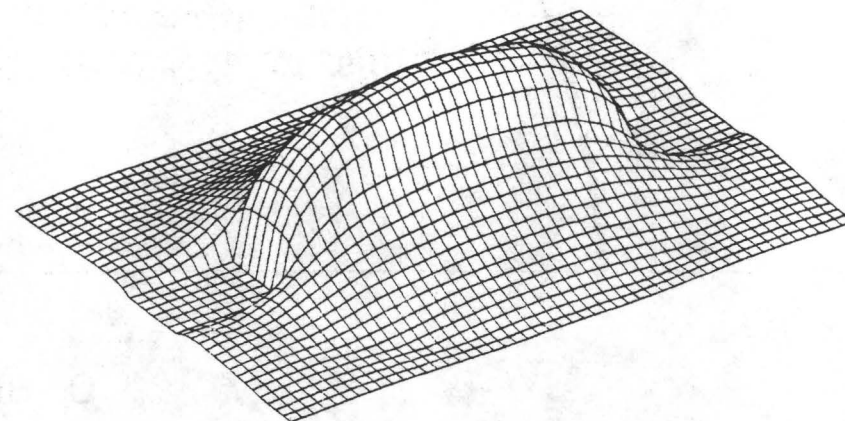and has resulted in intense debate (e.g., Joyner et al., 1981; Campbell, 1981) in the literature and elsewhere on the results of that research. These debates will not be entirely resolved until the empirical data base for near-field strong ground motion during large earthquakes is extensive. Nevertheless, the prediction of near-fault strong ground motion must be made with the most sophisticated technology available if we are to make rational seismic design decisions for critical facilities.

For both engineering and historical reasons, the primary focus of interest has been on the high frequency characteristics of ground motion in general, and on peak accelerations in particular. Methods that have been used fall into one of two categories. First are equations with parameters determined using empirical data; these equations are extrapolated to large magnitudes and close distances (e.g., Joyner et al. 1981; Campbell, 1981). The second category of methods models the energy source as a finite length, dynamic rupture, and calculates high frequency ground motion characteristics at sites, often using synthetic time histories of acceleration.

The purpose of the present study is to estimate high frequency near-field ground motion characteristics during $M_L \simeq$ 7-1/2 earthquakes using the work of McGuire and Hanks (1980) and Hanks and McGuire (1981). The basis is the Brune (1970, 1971) model representation of the seismic source. The method accurately estimates both root-mean-square (rms) and peak accelerations for California earthquakes in the range $4.0 \leq M_L \leq 6.5$, when the energy source can be treated as a point. The model is a logical method to investigate in an attempt to model a line source to ground motion at a site can be predicted. This extension of the model can also provide a probabilistic, rather than a merely determinist, representation of ground motion characteristics.

---

* Director of Decision Analysis, Ertec Rocky Mountain, Inc., 1658 Cole Blvd., Golden, Colorado 80401

** Graduate Student, Dept. of Civil Eng., Massachusetts Inst. of Tech., Cambridge, Massachusetts 02139

The present study treats a long line source as a series of segments, in the manner of Rascon and Cornell (1969). The characteristics of the ground motion time series at sites are derived, accounting for the distance from each segment to the site, the duration of rupture for each segment, and any change in power of the motion due to rupture propagation effects. This provides a stochastic representation of the earthquake ground motion (time intervals and rms accelerations). The distribution of peak acceleration for the entire strong motion duration is easily derived from this representation.

The major advantage of this endeavor over extrapolation of empirical formulas is that our extrapolation is physically logical. It accounts for the extended length of the source of energy in logical fashion by determining the contributions of segments of that length to ground motion, rather than by merely extrapolating point-source models to represent large magnitude earthquakes. The model has been verified for smaller events ($M_L \leq 6\text{-}1/2$); the treatment of an $M_L \simeq 7\text{-}1/2$ shock as a series of sequential smaller events for the purpose of estimating high frequency ground motion characteristcs, provides an intuitively reasonable representation of unilateral rupture on a long fault.

GROUND MOTION MODEL

The method used here to represent ground motion is based on the spectral representation of seismic shear waves in the far-field (Brune, 1970, 1971). Applying Parseval's theorem allows estimation of the rms acceleration (Hanks, 1979; McGuire and Hanks, 1980):

$$a_{rms} = (0.85) \frac{(2\pi)^2}{106} \frac{\Delta\sigma}{\rho R^{3/2}} \sqrt{\frac{Q\beta}{\pi f_o}} \qquad (1)$$

where $\Delta\sigma$ is stress drop, ρ is crustal density, R is source-to-site distance, Q is specific attenuation, β is shear wave velocity, and f_o is spectral corner frequency. Accelerations are approximately band-limited, white Gaussian noise between frequencies f_o and $f_{max} = Q\beta/\pi R$ (Hanks and McGuire, 1981). They are assumed to apply for a duration equal to the faulting duration $T_d = f_o^{-1}$ in the point-source representation; this duration is modified as described below to account for rupture velocity and direction.

Peak acceleration a_p is estimated using a simple result from random process theory, which is consistent with the band-limited, white, Gaussian character of accelerations (Vanmarcke and Lai, 1980):

$$a_p = a_{rms} \sqrt{2 \ln (2 s_o f_1)} \qquad (2)$$

where s_o is the duration of accelerations, f_1 is the characteristic frequency, and the value in the radical must be ≥ 2. Duration s_o and frequency f_1 are discussed in more detail below.

Equations (1) and (2) are assumed to estimate the median a_p; individual peak accelerations are taken to be lognormally-distributed, with a coefficient of variation of 0.66. This is a typical representation of scatter observed for California data on peak acceleration. In fact one could estimate theoretically the distribution of peak accelerations using a variation of equation (2), but observed peak acclerations exhibit more dispersion than would be predicted theoretically. This results in part because real earthquake ground motions are not exactly white and Gaussian. Hence, it is more appropriate to make the assumption described above on the distribution of a_p; this is consistent with empirical scatter observed in a_{rms} and with the strong observed correlation between a_p and a_{rms} (Hanks and McGuire, 1981).

REPRESENTATION OF FINITE FAULTS

We seek to develop a probabilistic representation of high frequency ground motion close to an earthquake caused by rupture on a fault with significant length. For this application, the use of equations given in the previous section is inappropriate because these are for far-field motions. Moreover, these equations implicitly assume that all seismic energy originates at a distance R from the site. It would be an unacceptable approximation to assume that <u>all</u> seismic energy from a long rupture originates at any fixed distance from a site located close to the rupture. As an example, using these far-field models to represent ground motion during a $M_L \approx 7\text{-}1/2$ event at 5 km distance would be very conservative upper-bound on the ground motion, as will be demonstrated below.

The representation we develop here follows ideas first proposed by Rascon and Cornell (1969). The source of energy release is idealized as a straight horizontal line of length l_r, located at a depth d representing the predominant source of energy (Figure 1). We divide the fault into n segments, each of which has length l_s. To calculate segment-to-site distance, the energy from each segment is assumed to emanate from the center of that segment. The duration of motion at the site from segment i can be computed as:

$$s_i = \frac{r_{i+1}}{\beta} + \frac{l_s}{v_r} - \frac{r_i}{\beta} \qquad (3)$$

where v_r is the velocity of rupture.

The rms acceleration (equation 1) must be modified to account for propagation effects, i.e., s_i in equation (3) is, in general, different from the time the rupture takes to pass through segment i, which is l_s/v_r. We accomplish this by assuming that the total energy in the motion (which is proportional to a_{rms}^2) is unchanged by propagation effects. Thus the rms acceleration from segment i is given by:

$$a_{rmsi} = \sqrt{\frac{l_s}{v_r s_i}} \ (0.85) \ \frac{(2\pi)^2}{106} \ \frac{\Delta\sigma}{\rho R^{3/2}} \sqrt{\frac{Q\beta}{\pi f_{oi}}} \qquad (4)$$

where f_{oi} is the corner frequency of segment i (more about this below). The peak acceleration is estimated using a form similar to equation (2):

$$a_{pi} = a_{rmsi} \sqrt{2 \ln(21_s f_1/v_r)} \tag{5}$$

A stochastic representation of a_{pi} is used with a lognormal distribution and c.o.v of 0.66. In equation (5), no modification is necessary to account for propagation effects because any change in the duration of ground motion during energy from segment i would affect the characteristic frequency f_1 similarly.

This representation of the fault results in a stochastic representation of ground motion at the site, both in terms of a band-limited Gaussian process with rms accelerations a_{rmsi} over durations s_i, with i from 1 to n, and in terms of a sequence of peak accelerations a_{pi} represented as lognormal distributions. If we assume that dynamic stress differences along each fault segment are independent, it is logical to assume that peak accelerations caused by rupture on each segment are mutually independent. The cumulative distribution of peak acceleration at a site j for the entire earthquake a_{pj} is given as:

$$F_{a_{pj}} = \prod_{i=1}^{n} F_{a_{pi}} \tag{6}$$

Finally, to produce general results, we wish to consider all sites located the same distance R_c from the fault (see Figure 2). The entire rupture will propagate toward some of these sites and away from others. The distribution for a typical site located R_c from the fault is:

$$F_{a_{pe}} = \lim_{m \to \infty} \sum_{j=1}^{m} F_{a_{pj}} \frac{1}{m} \tag{7}$$

where m is the number of sites. In practice we limit m to a reasonable number to minimize computer time.

In representing a long rupture as a series of shorter ruptures, there are several ways in which to estimate source parameters of the smaller events from the main earthquake. The most critical parameter for high frequency characteristics, stress drop, we choose to keep constant and equal to 100 bars; this value has been shown to be appropriate for California earthquakes over a range $4.0 \leq M_L \leq 6.5$ (Hanks and McGuire, 1981). Of the other source parameters, only one of the pair M_o, f need be specified; under the assumption of equation (1), specification of one of these and $\Delta\sigma$ implies specification of the other.

We examine three methods of determining M_{oi} (seismic moments of segment events) and present these through specification of M_{Li}, the magnitudes of events representing rupture on the fault segments. It should be understood that we can, and do, transform between M_{oi} and M_{Li} using (Hanks and Kanamori, 1979).

$$\log M_{oi} = 1.5 M_{Li} + 16 \qquad (8)$$

The starting point for estimating ground motion near a moderate to large earthquake is to estimate its length of rupture l_r:

$$M_L = 4.65 + 1.351 \log l_r \qquad (9)$$

(Slemmons, 1977). We invert this, ignoring for this investigation any potential problems induced by inverting equations with coefficients determined by regression analyses (which is justified by results presented below),

$$l_r = 10^{(M_L - 4.65)/1.351} \qquad (10)$$

to calculate the total length of rupture for event M_L.

One method of estimating the moment M_{oi} and magnitude M_{Li} of n segment events representing one major event M_L is to use the segment rupture lengths l_s and equation (9). This leads to

$$M_{Li} = M_L - 1.351 \log n \qquad (11)$$

A second method is to assume that the seismic moments M_{oi} equal M_o/n. From equation (8), we obtain

$$M_{Li} = M_L - 0.667 \log n \qquad (12)$$

A third possible method assumes that the total energy E of the large shock is equally divided into the segment events. Using the relation (e.g., Richter, 1958):

$$\log E = \text{const.} + 1.5 M_S \qquad (13)$$

and the Nuttli (1979) relation

$$M_L = .625 M_S + 2.28 \qquad (14)$$

we can divide E by n to obtain

$$M_{Li} = M_L - 0.417 \log n \qquad (15)$$

All of these possible segmentations of a large magnitude earthquake into smaller magnitudes result in the same form:

$$M_{Li} = M_L - c_n \log n \qquad (16)$$

and we report and compare results below for values of c_n equal to 1.351, 0.667, and 0.417.

The alternative choices of M_{Li} and M_{oi} result in alternative values of f_{oi} for the segment events. It is not clear which is the most appropriate choice for corner frequency. The option of specifying

f_{oi} as a function of the segment size is not viable under the assumptions of the Brune model, which assumes a rupture dimension that is more or less circular. For long faults, this requirement would restrict the model to large values of n (many segments). We are violating this implicit assumption in using equation (1) to estimate a_{rms} for long faults, but this is a second-order violation; we ignore it for the moment in order to see how this methodology works.

COMPARATIVE DATA BASE

The proliferation of strong motion instruments in California has resulted in a bevy of near-source strong motion data in recent years, albeit for small to moderate earthquakes. These data serve two purposes in the present study: they illustrate the applicability of equation (1) for $M_L \simeq 5.5$ events, and they show how the proposed methodology works in the near-source region of $M_L \simeq 6.5$ earthquakes.

Figure 3 shows the available peak horizontal acceleration data for $5 \leq M_L < 6$, and Figure 4 shows comparable data for $M_L \simeq 6\text{-}1/2$. The abscissa is distance from the recording site to the nearest trace of the fault, where this is known, or to the surface projection of the fault, or in a few cases to the epicenter. These plots form the data base with which we will evaluate the results obtained by the segment rupture model.

RESULTS AND DISCUSSION

Distributions of peak horizontal accelerations have been generated for $M_L = 5.5$, 6.5, and 7.5 earthquakes using the methodology described above. In all cases the location of the sites examined is shown schematically in Figure 2; only sites on one side of the rupture need be analyzed because of symmetry. The depth of energy release was assumed to be 5 km, and values of constants used were as follows: β = 3.2 km/sec, v_r = 2.2 km/sec, ρ = 2.8 g/cm^3, Q = 300, and $\Delta\sigma$ = 100 bars. In equation (2), f_1 was taken to be 3.3 hz, the mean value found by Vanmarcke and Lai (1980), rather than f_{max} = Qβ/πR as discussed in Hanks and McGuire (1981). The value of f_{max} becomes very high at the close distances of interest here even if limited by the instrumental frequency of 25 hz. In any case, the dependence of a_p on f_1 is small: changing f_1 from 3.3 to 25 hz increases the peak factor (a_p/a_{rms}) by only 20 to 25 percent for typical values of duration of interest here (5 to 10 seconds).

Expected (mean value) peak horizontal accelerations for a randomly-selected typical site located 1 km from the trace of a fault generating an M_L = 5.5 earthquake are presented in Figure 5a. The abscissa is n, the number of segments into which the rupture is divided, and results are given for all three values of coefficient c_n discussed above. These expected values are obtained from the distribution a_{pe}, equation (7). The "point source" calculation obtained from the site located perpendicular to the midpoint of the fault, i.e., at a 1 km distance from

the surface projection of the energy center is also shown. This is somewhat greater than the value of a_p obtained from equations (1) and (2) using R = 5.1 km (the hypocentral distance) because those equations give <u>median</u> values of a_p, and <u>mean</u> values are plotted on Figure 5a.

Several points are evident from Figure 5a. First, c_n = 0.417 and 0.667 give consistent results for n = 1, 2, and 4 (the mean values of a_p are about the same for these values of n) but c_n = 1.351 does not. This implies that smaller values of c_n are more appropriate. The larger value of 1.351 does not allow enough energy in the segment ruptures to represent a larger earthquake accurately. Secondly, for n = 8 or larger values, the expected values of a_p decrease. This means that we cannot represent a single rupture as a larger number of very small earthquakes. In particular, the assumption of stationary Gaussian motion inherent in equation (2) is not correct.

Figures 5b, 5c, and 5d present similar results for distances of 5, 10, and 20 km from the M_L = 5.5 rupture. These illustrate the same points that are evident from Figure 5a. In general, for representing an $M_L \simeq 5.5$ earthquake as several segment ruptures, two segments are appropriate and c_n = 0.4 to 0.7 looks best.

Figure 5e shows <u>median</u> values of a_p plotted versus distance for n = 2 and c_n = 0.417 and 0.667, along with the near-field data discussed earlier. The median value estimates are appropriate to compare with acceleration data plotted logarithmically. These estimates match observations to an acceptable degree, and this is not surprising: the model has previously been demonstrated and calibrated (via $\Delta\sigma$) for $4.0 \leq M_L \leq 6.5$ in the far-field (Hanks and McGuire, 1981). For M_L = 5.5, this includes $R \simeq 5$ km. At R = 1 the results presented here should be viewed with some caution: even for n = 2 the far-field assumption implicit in equation (2) is not met, so the results may be conservative by an unquantifiable amount.

Figures 6a through 6d present mean values of a_p versus n for M_L = 6.5. The same general trends observed for M_L = 5.5 apply except that there is a larger difference between the "point source" result and the n = 1 result. The reason is the long rupture length: for n = 1, most sites are farther away from the single energy center than the distance listed on the figures, but the site located perpendicular to the midpoint of the fault (from which the point source results are obtained) is not. The values of a_p increase with n up to n = 4, then level off and decrease for n = 16. The increase results from more sites being closer to segments (energy centers). The decrease for large n results, as before, because from the scaling relations the small magnitude events do not have enough energy to represent an M_L = 6.5 earthquake for 16 segments.

We interpret the horizontal portions of the curves in Figures 6a through 6d to indicate the best estimate of peak accelerations at the distances listed. For smaller values of n, values of a_p are too small because most sites are farther away from the centers of segment rupture

than they are from fault trace. For larger n, the values of a_p are too small because the large number of small earthquakes cannot represent the original event in terms of ground motion effects.

A further result shown on Figure 6d is that a_p estimated for n = 4 and 8, and n_c = 0.417, is equal to the point source result, which we know is conservative. At farther distances, the results for n = 8 and c_n = 0.417 would exceed the point source results. This implies that c_n = 0.417 is too low: it allows too much energy for the segment earthquakes. Of the values investigated, c_n = 0.667 apparently gives the most consistent scaling of segment magnitude and moment (it corresponds to calculating segment moments M_{oi} by dividing the entire earthquake moment by n).

Figure 6e shows median values of a_p plotted versus distance, along with the available near-field data, for n = 8 and n_c = 0.667. Again, the result for R = 1 km is rather tenuous and should be viewed as such. The estimates agree rather well with the observations and this is encouraging, since the calculated rupture length for M_L = 6.5 is 23.4 km. Thus estimates at 5 km certainly constitute the "geometric" near-field, where simple extrapolations from far-field data can be expected to be poor, and we find the segment rupture model is appropriate for estimating peak accelerations at this distance.

The last set of results, shown in Figures 7a through 7d, are for M_L = 7.5. In this case there is an even wider discrepancy between the point source results and the n = 1 results. The results do not increase uniformly for small values of n simply because we limited the number of sites over which equation (7) was calculated to nine to reduce computer time; with more sites these curves would smooth out. For larger values of n this is not a problem.

Adopting from M_L = 5.5 and 6.5 results, the coefficient c_n = 0.667, we see that n = 32 gives what we consider to be best estimates of a_p. This allows us to make first-order estimates of peak acceleration during M_L = 7.5 earthquakes. These are shown in Figure 7e as a function of distance. It is appropriate to emphasize the tenuousness of these estimates, since they are based on extrapolation from data of at least one magnitude unit. It is also appropriate to emphasize that this extrapolation was done in a physically logical manner, not by simply extrapolating equations determined from data obtained at lower magnitudes.

Several points of discussion are worth making. First, a segment length of about 4 km seems to be appropriate for characterizing ruptures in the manner investigated here. This is independent of the earthquake size and of the choice of coefficient c_n. Second, it is apparent that ruptures other than unilateral could be accommodated by this methodology. We have just started with the simplest representation of fault rupture. Finally, results for a single site can easily be generated in terms of a_{rms}, i.e., a series of durations and associated values of a_{rms}. It would be difficult, however, to generate a single meaningful

762

distribution of a_{arms} for the entire strong motion duration, or to present combined a_{rms} results for all sites. Therefore, we have concentrated here on presentation of peak acceleration results.

CONCLUSIONS

The segment rupture model provides a logical means of calculating characteristics of high frequency strong ground motion for higher magnitudes and closer source-to-site distances than have yet been well documented with strong motion records. Although a simple unilateral rupture has been studied here, a bilateral or multi-lateral rupture of arbitrary complexity could as easily be modeled.

Several critical parameters affect the estimates of peak acceleration developed here. Most obvious of these is coefficient c_n, which determines how the magnitude or seismic moment of segment events is determined from the total seismic moment. The most promising coefficient corresponds simply to dividing the total seismic moment by the number of segments to obtain the segment seismic moment; but this conclusion is tentative. Further, the depth of energy release is not well determined, and this has a major effect on near-source peak acceleration estimates.

This study has concentrated on peak acceleration because that parameter is a topic of current interest and research. The segment rupture model provides not only distributions of peak acceleration, but allows acceleration time series to be generated using wide-band Gaussian processes with a specified series of rms accelerations over a series of durations. Artificial time histories could be generated, and response spectra could be calculated either from the artificial motions or through random vibrations methods. Thus this concept of representing a large earthquake rupture as a series of segments, with a demonstrated ability to predict high frequency ground motion characteristics accurately for the segments, has a broad range of potential products for solving earthquake engineering problems.

ACKNOWLEDGEMENTS

REFERENCES

Brune, J.N. (1970), "Tectonic Stress and the Spectra of Seismic Shear Waves from Earthquakes," Journal of Geophysical Research, vol. 75, no. 26, Sept. 10, pp. 4997-5009.

_____, (1971), "Correction," Journal of Geophysical Research, vol. 76, no. 20, July 10, p. 5002.

Campbell, K.W. (1981), "Near-Source Attenuation of Peak Horizontal Acceleration," submitted to Bull. Seis. Soc. Am., May.

Hanks, T.C. (1979), "b Values and w- Seismic Source Models: Implications for Tectonic Stress Variations Along Active Crustal Fault Zones and the Estimation of High Frequency Strong Ground Motion," Journal of Geophysical Research, vol. 84, no. B5, May 10, pp. 2235-2242.

Hanks, T.C., and Hiroo Kanamori (1979), "A Moment Magnitude Scale," Journal of Geophysical Research, vol. 84, no. B5, May 10, pp. 2348-2349.

Hanks, T.C., and R.K. McGuire (1981), "The Character of High Frequency Strong Ground Motion," Bull. Seis. Soc. Am., vol. 71, no. 6, Dec.

Joyner, W.B., D.M. Boore, and R.L. Porcella (1981), "Peak Horizontal Acceleration and Velocity from Strong-Motion Records Including Records from the 1979 Imperial Valley, California, Earthquake," U.S.G.S. Open-File Report 81-365, March, 46 pp.

McGuire, R.K., and T.C. Hanks (1980), "RMS Accelerations and Spectral Amplitudes of Strong Ground Motion During the San Fernando Earthquake," Bull. Seis. Soc. Am., vol. 70, pp. 1907-1919.

Nuttli, O.W. (1979), "The Relation of Sustained Maximum Ground Acceleration and Velocity to Earthquake Intensity and Magnitude," State-of-the-Art for Assessing Earthquake Hazards in the United States, Misc. Paper 5-73-1, Rept. 16, U.S. Army Corps of Engineers, Vicksburg, Miss., Nov., 74 pp.

Richter, C.F. (1958), Elementary Seismology, W.H. Freeman and Co., Inc., San Francisco, Ca., 768 pp.

Rascon, O.A., and C.A. Cornell (1969), "A Physically Based Model to Simulate Strong Earthquake Records on Firm Ground," Proceedings, 4th World Conference on Earthquake Engineering, Santiago, Chile.

Slemmons, D.B. (1977), "Faults and Earthquake Magnitude," State-of-the-Art for Assessing Earthquake Hazards in the United States, Misc. Paper 5-73-1, Rept. 6, U.S. Army Corps of Engineers, Vicksburg, Miss., May, 129 pp.

Vanmarcke, E.H., and S.S.P. Lai (1980), "Strong Motion Duration and RMS Amplitude of Earthquake Records," Bull. Seis. Soc. Am., vol. 70, pp. 1293-1307.

DIRECTION OF RUPTURE PROPOGATION →

Segment 1   Segment 2

1_s 1_s

Segment n

r_1 R_1 r_2 R_2 r_3

R_c
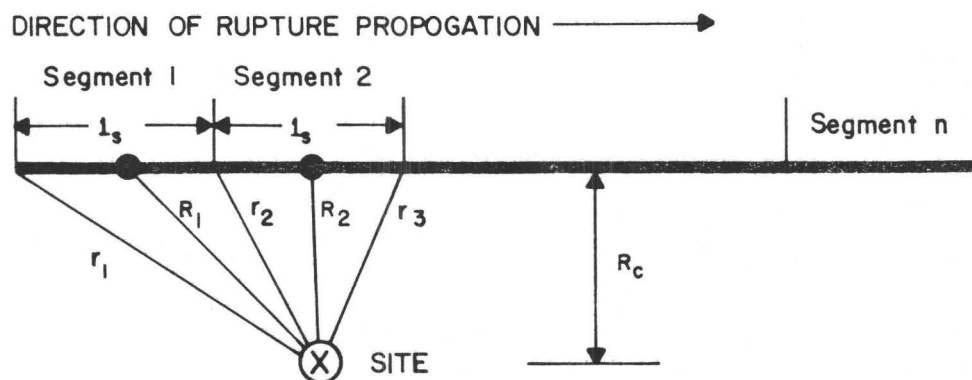
SITE

FIGURE I

GEOMETRY OF FAULT REPRESENTATION AS RUPTURE SEGMENTS
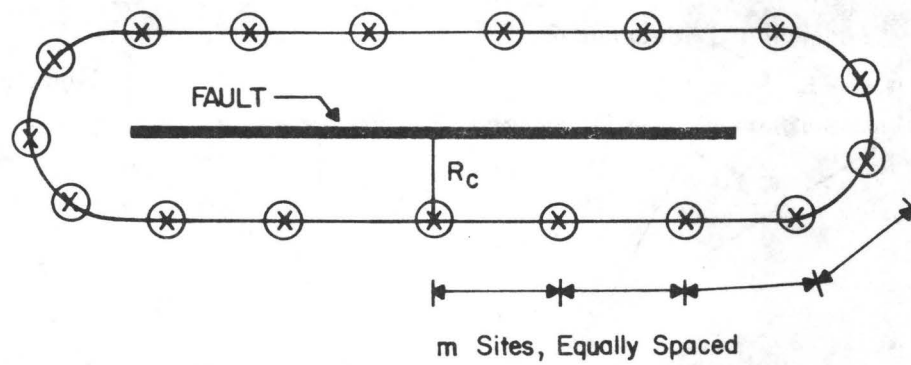
FIGURE 2

LOCATION OF SITES AT DISTANCE R_c FROM THE FAULT

FIGURE 3

Peak Acceleration data for M ≃ 5.5
                            L
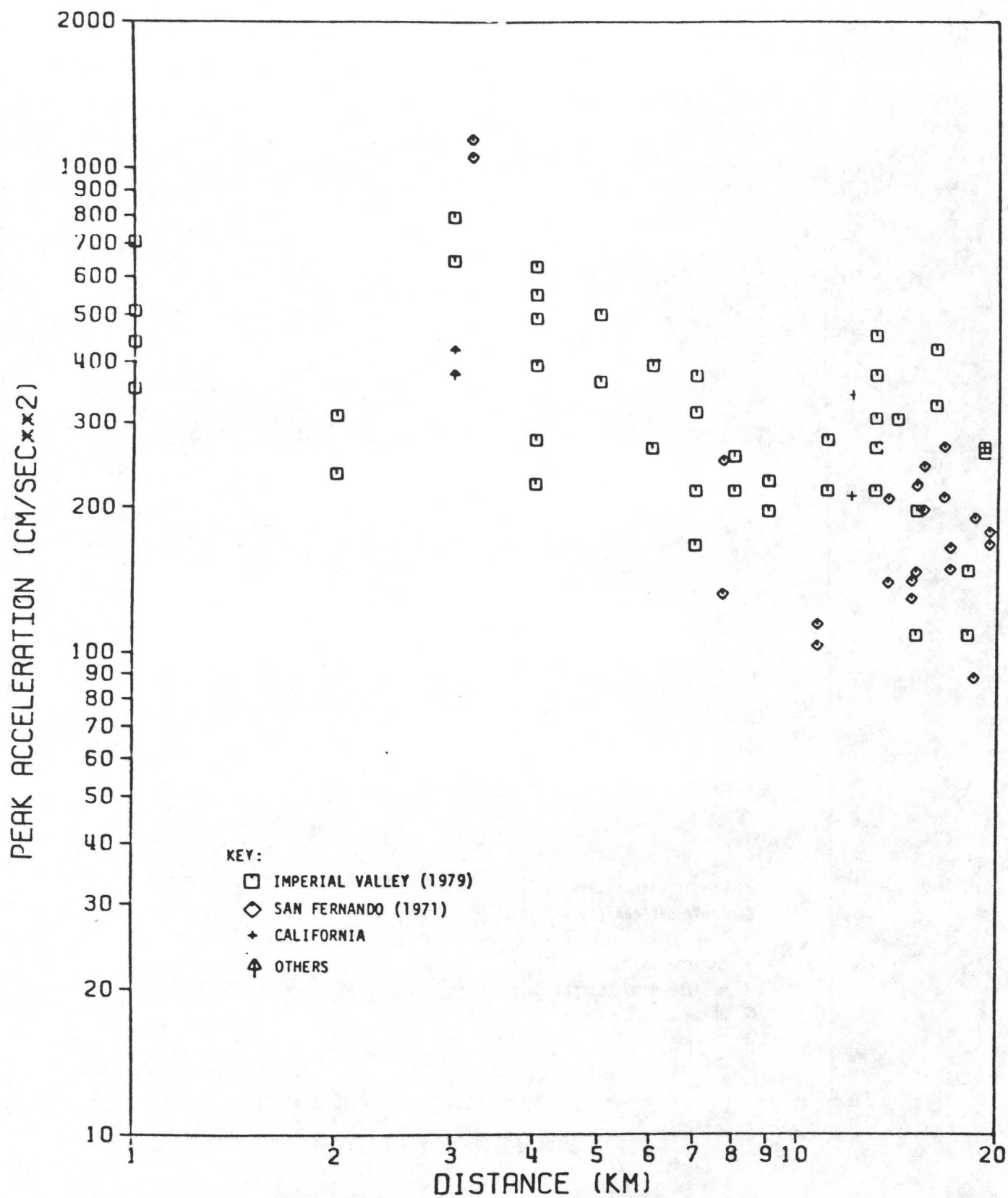
FIGURE 4

Peak Acceleration data for $M_L \simeq 6.5$

768

FIGURE 5A

MEAN PEAK ACCELERATION VERSUS N FOR M_L = 5.5 AND R_c = 1 km

FIGURE 5B

MEAN PEAK ACCELERATION VERSUS N FOR $M_L = 5.5$ AND $R_c = 5$ km

FIGURE 5C

MEAN PEAK ACCELERATION VERSUS N FOR M_L = 5.5 AND R_c = 10 km

771

FIGURE 5D

MEAN PEAK ACCELERATION VERSUS N FOR M_L = 5.5 AND R_c = 20 km

FIGURE 5E

MEDIAN PEAK ACCELERATION VERSUS DISTANCE FOR $M_L = 5.5$

FIGURE 6A

MEAN PEAK ACCELERATION VERSUS N FOR $M_L = 6.5$ AND $R_c = 1$ km

FIGURE 6B

MEAN PEAK ACCELERATION VERSUS N FOR M_L = 6.5 AND R_c = 5 km

775
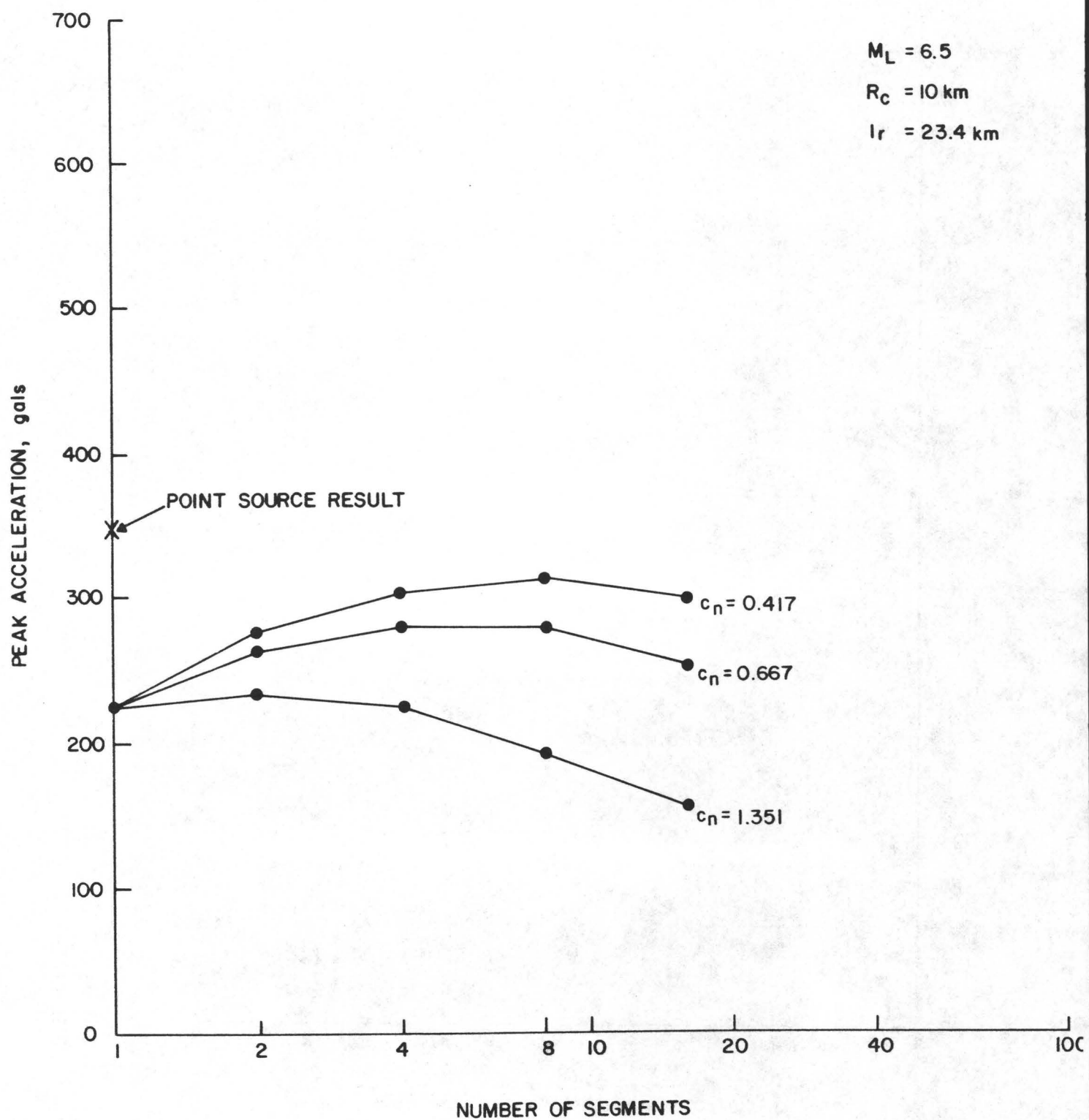
FIGURE 6C

MEAN PEAK ACCELERATION VERSUS N FOR M_L = 6.5 AND R_c = 10 km
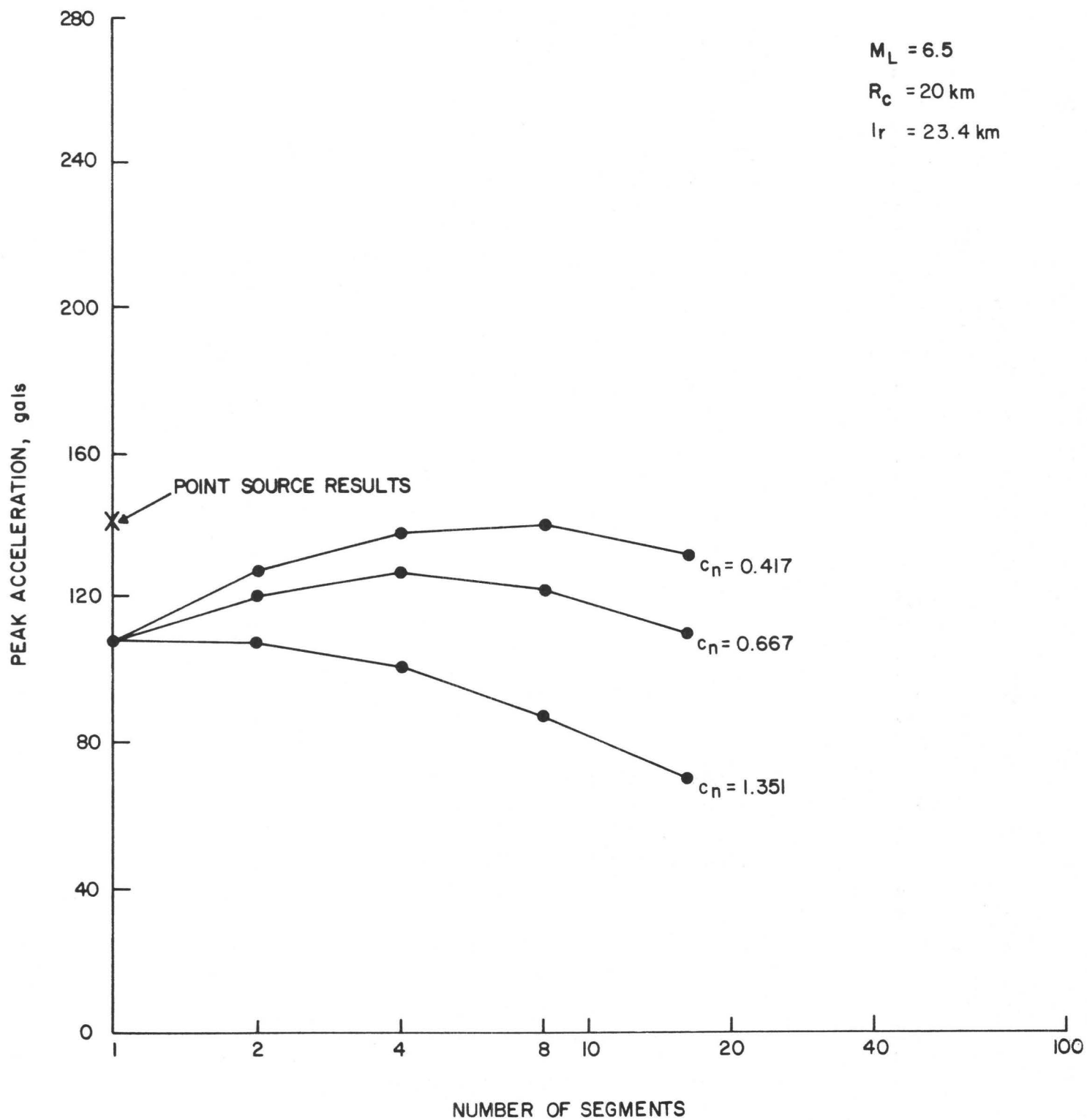
FIGURE 6D

MEAN PEAK ACCELERATION VERSUS N FOR $M_L = 6.5$ AND $R_c = 20$ km
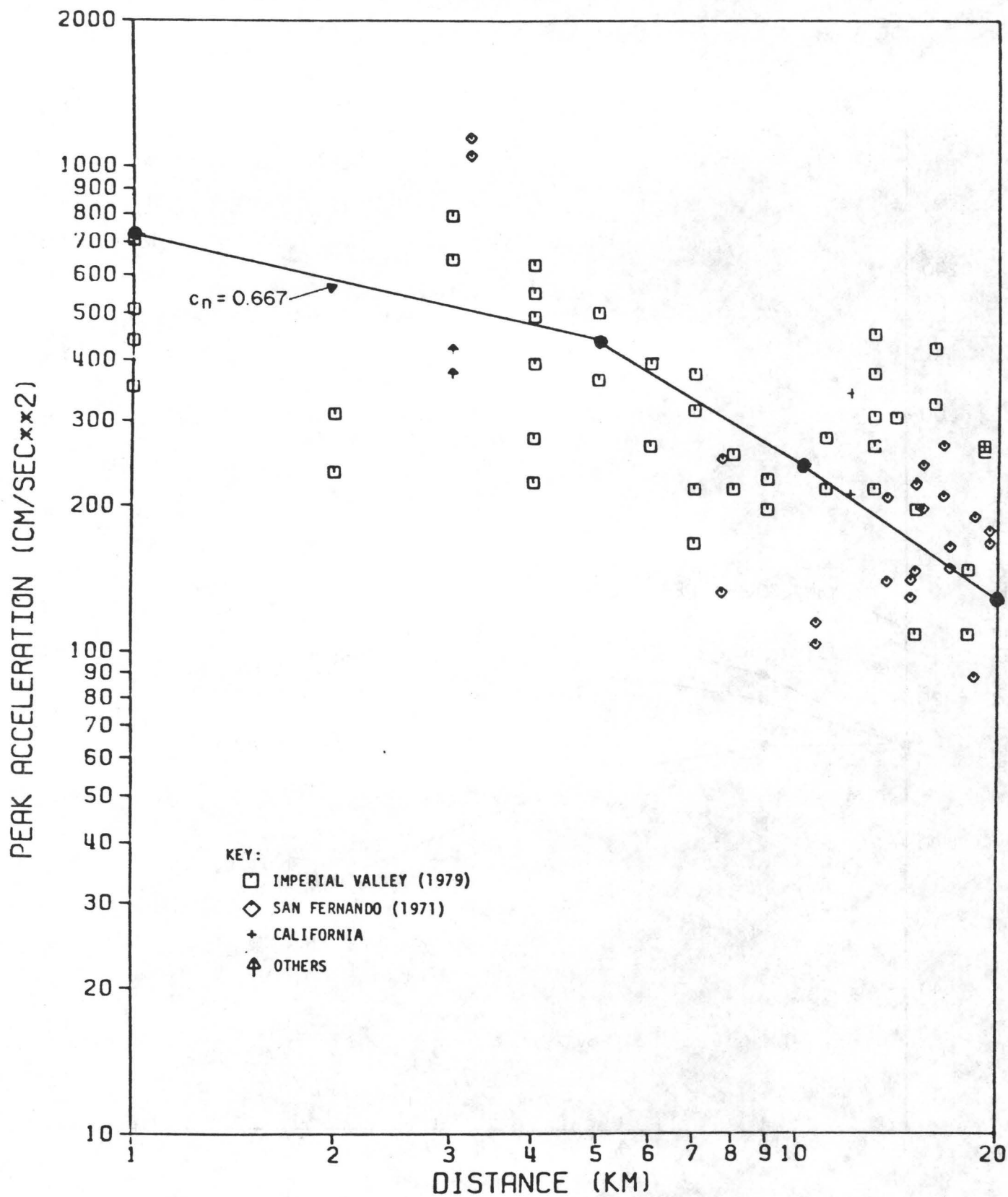
FIGURE 6E

MEDIAN PEAK ACCELERATION VERSUS DISTANCE FOR $M_L = 6.5$
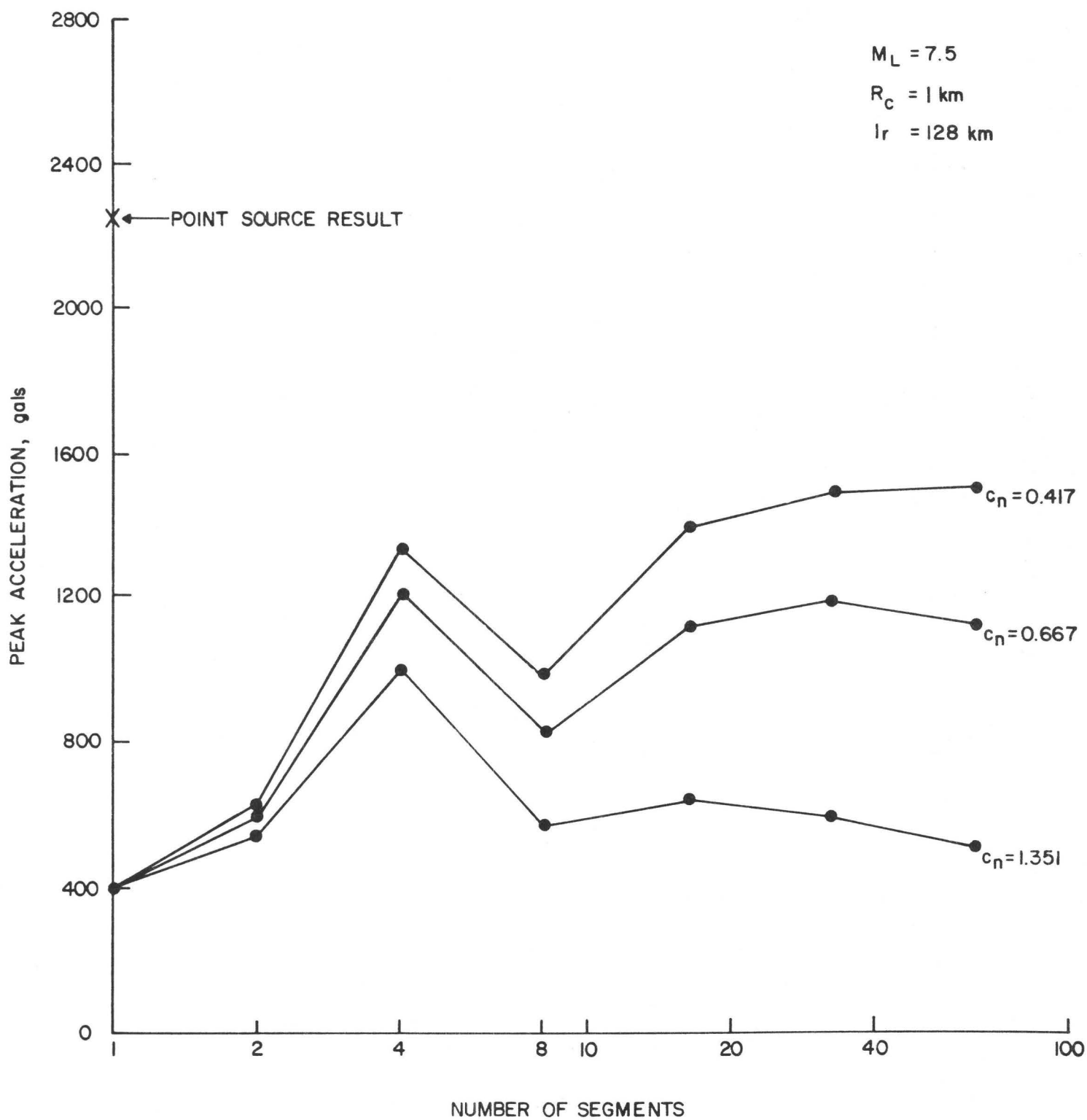
FIGURE 7A

MEAN PEAK ACCELERATION VERSUS N FOR $M_L = 7.5$ AND $R_c = 1$ km
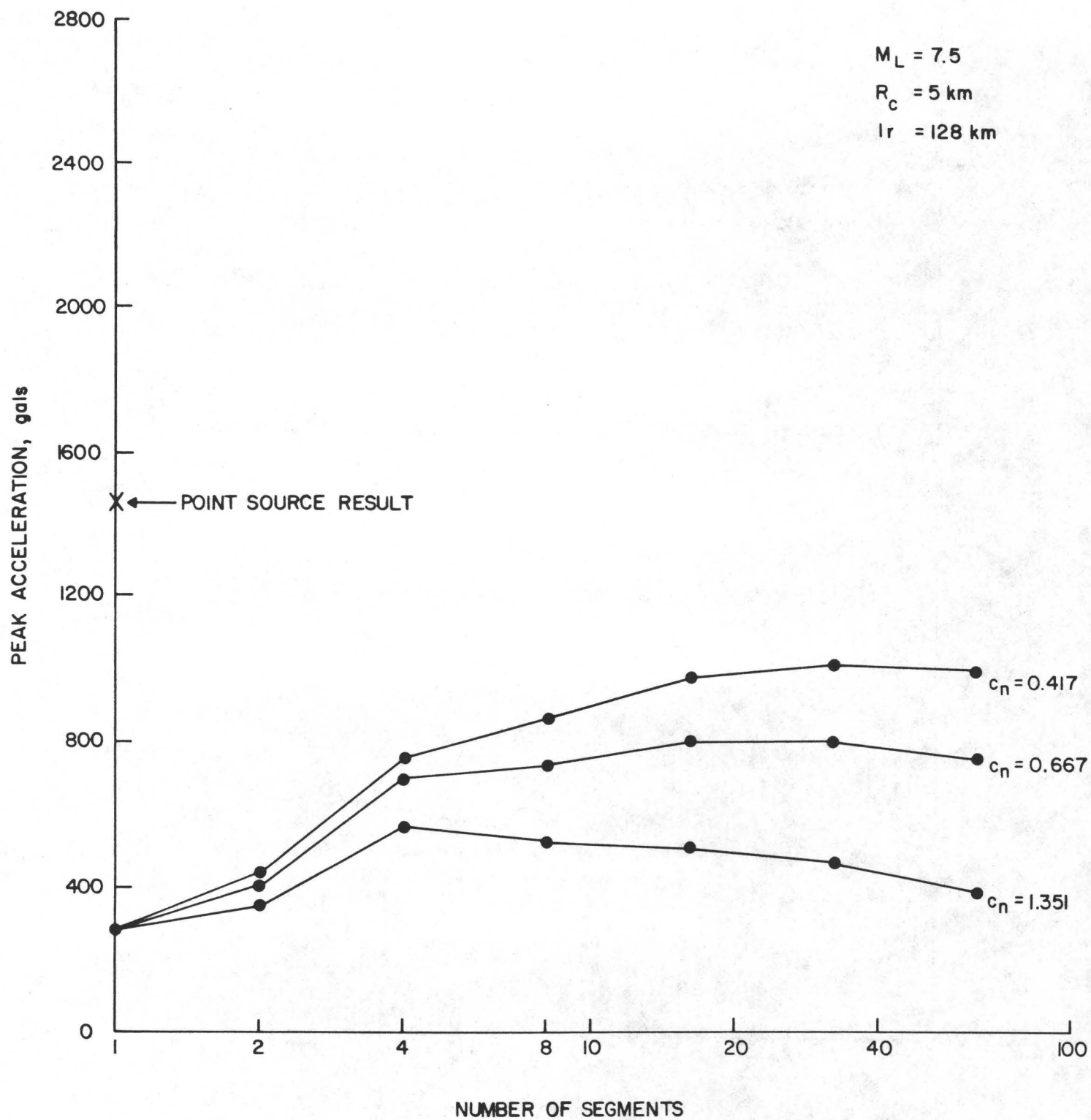
FIGURE 7B

MEAN PEAK ACCELERATION VERSUS N FOR M_L = 7.5 AND R_c = 5 km
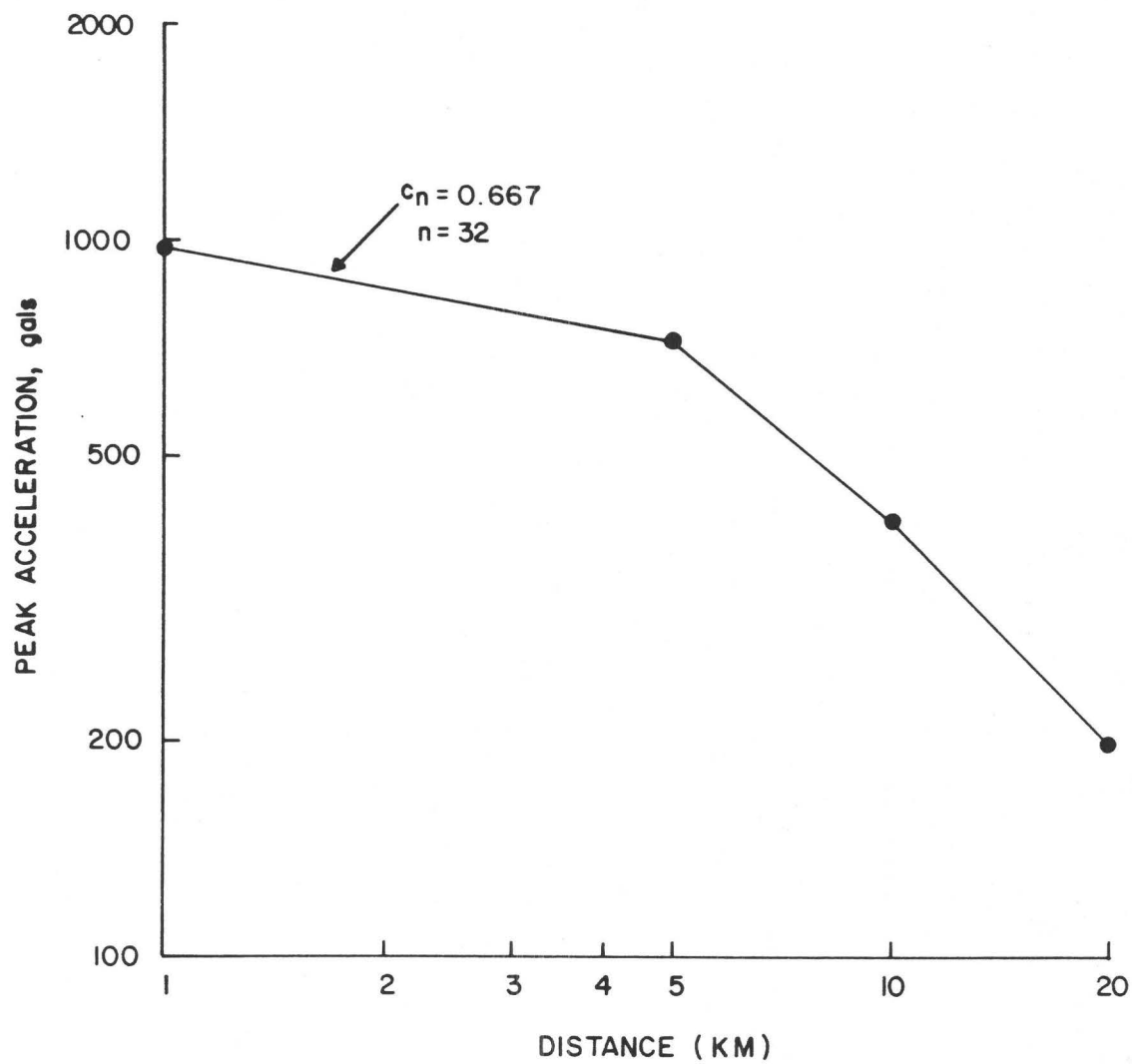
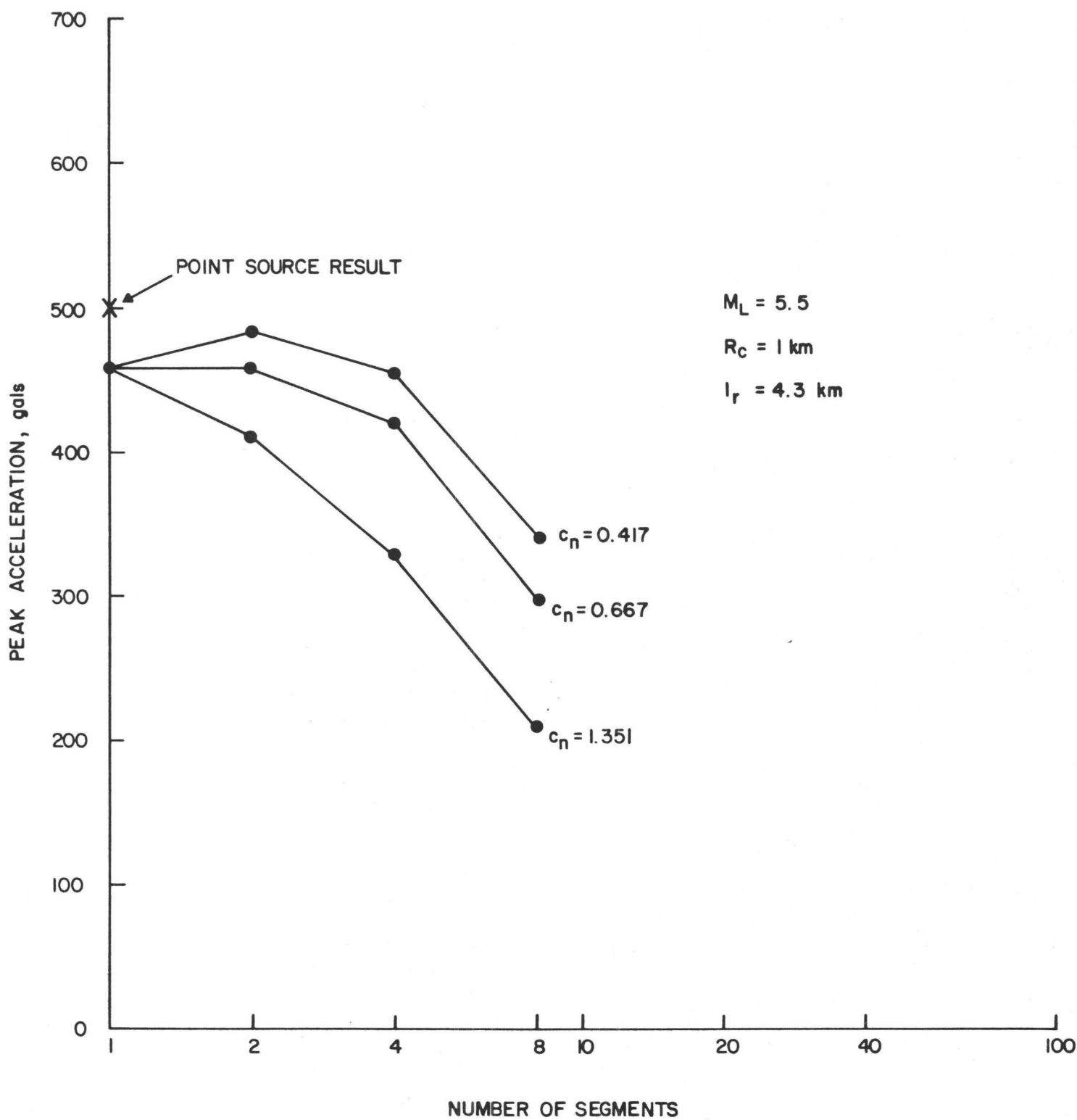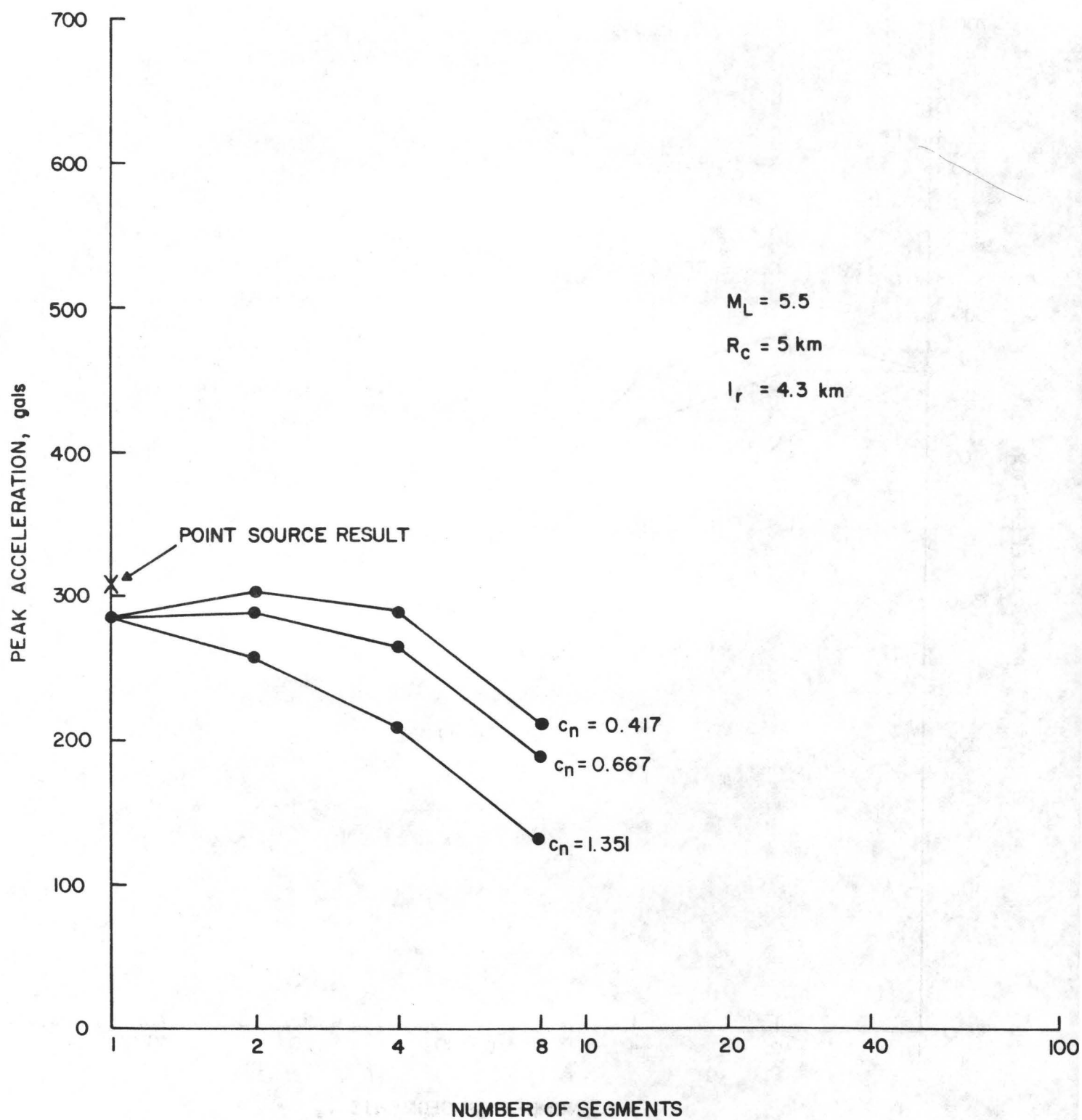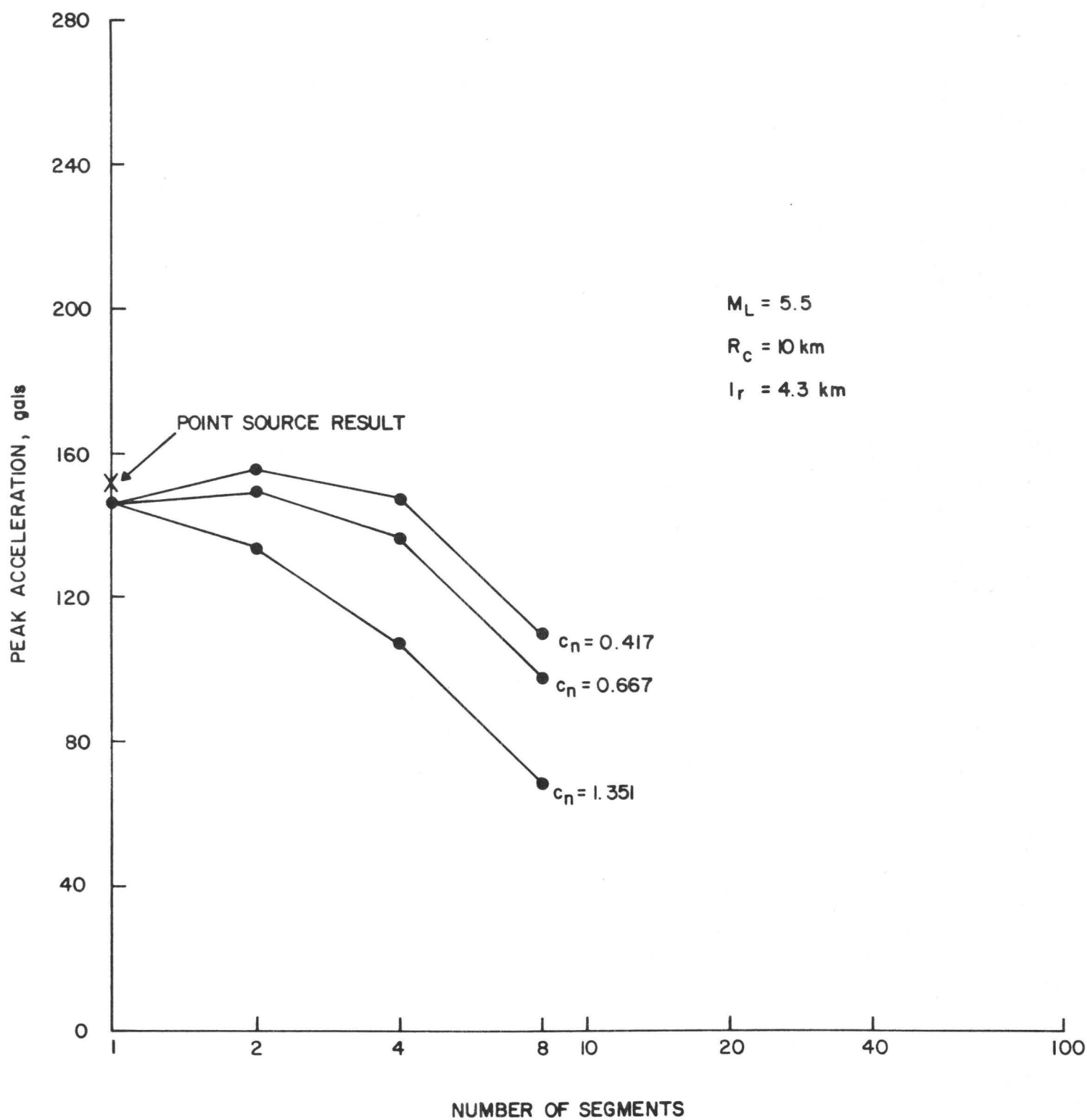FIGURE 7E

MEAN PEAK ACCELERATION VERSUS DISTANCE FOR $M_L = 7.5$
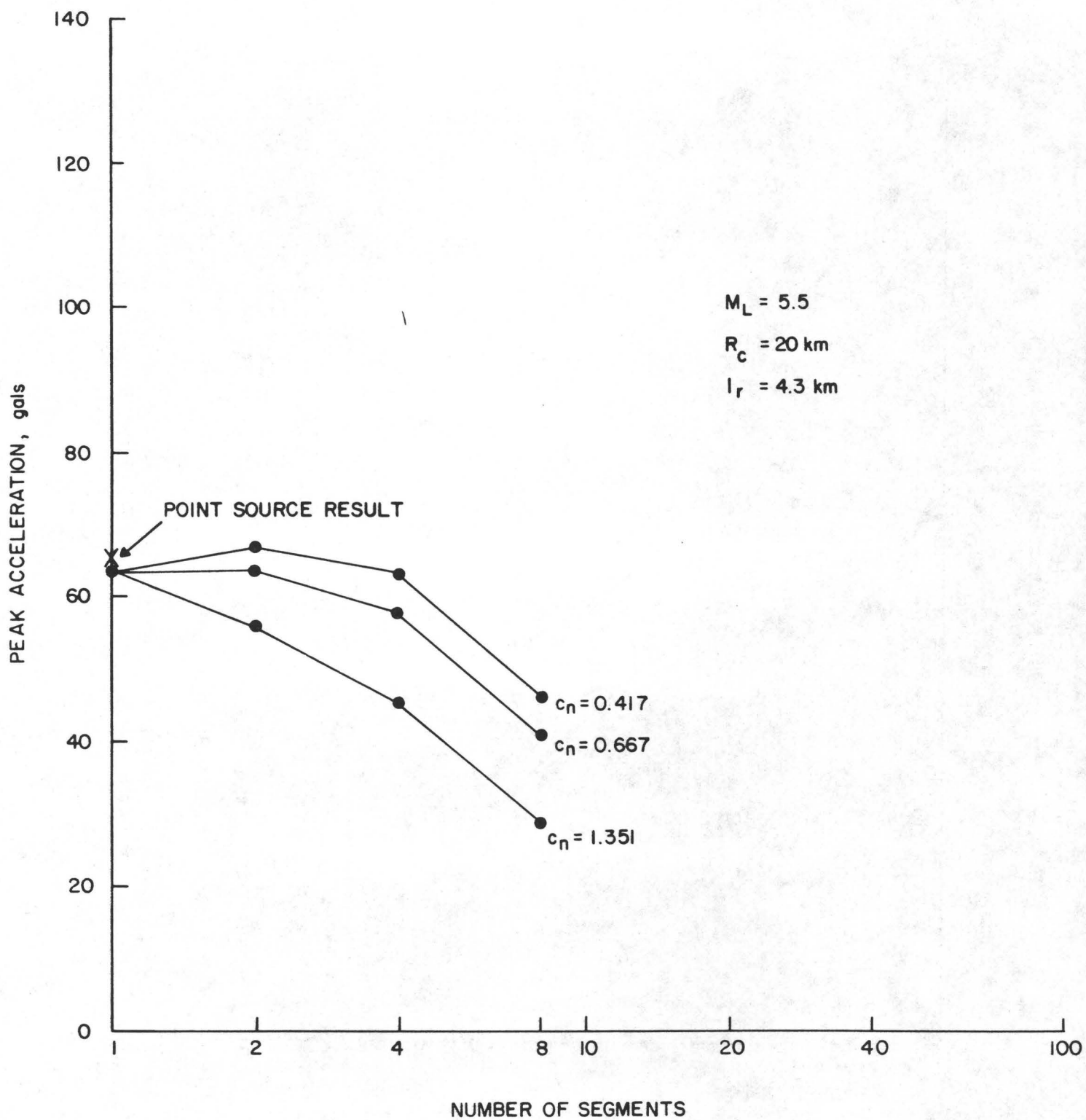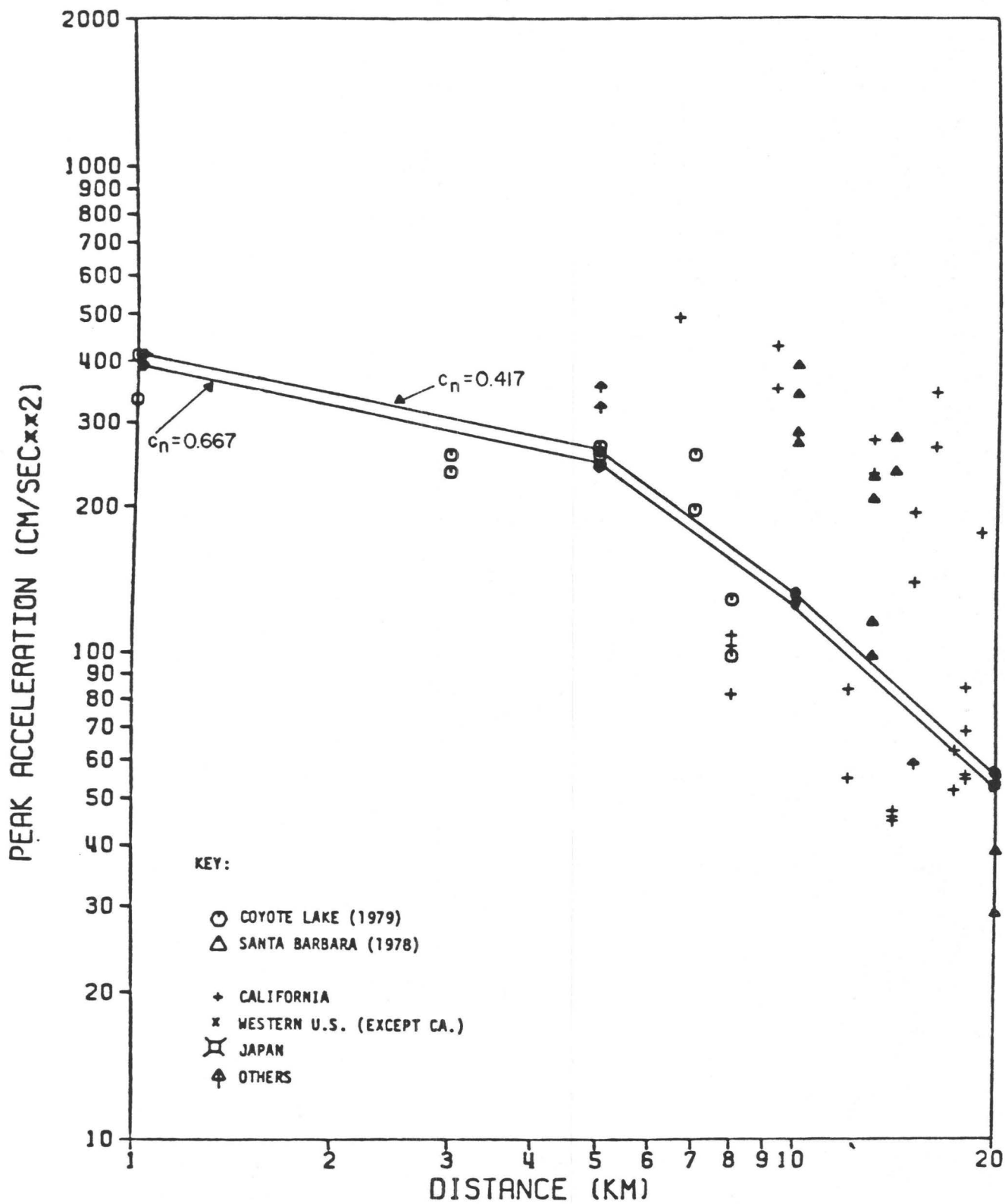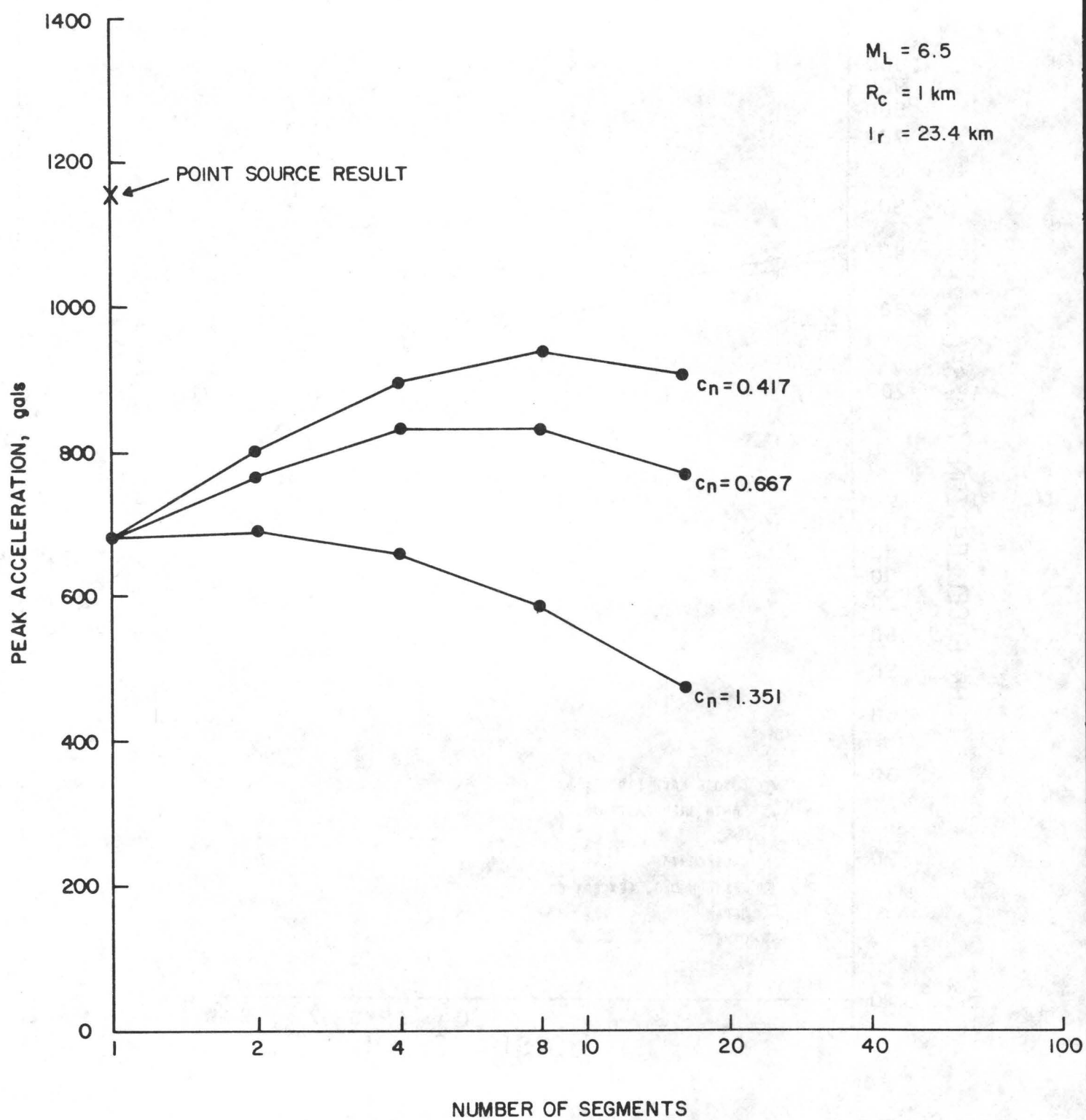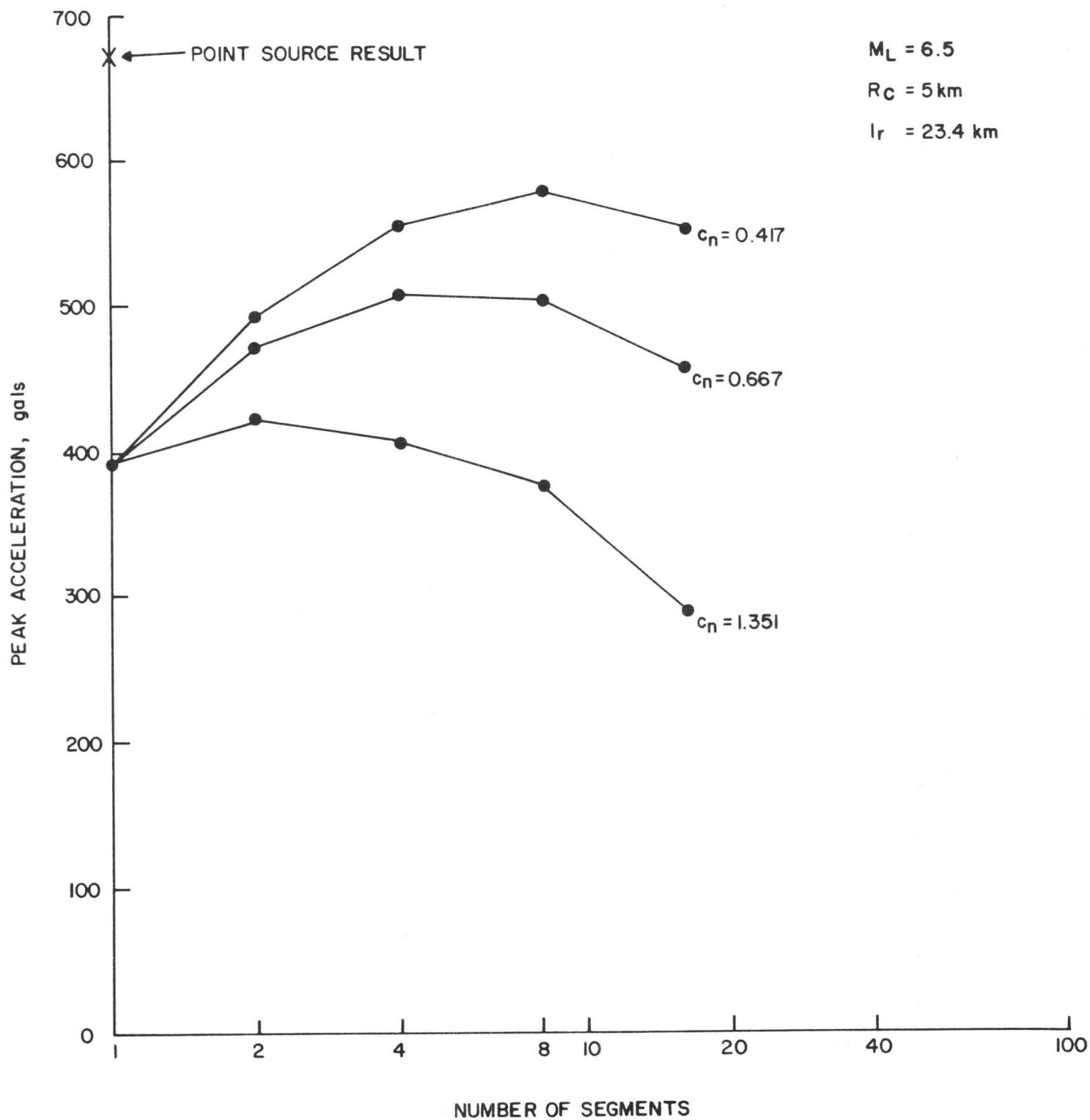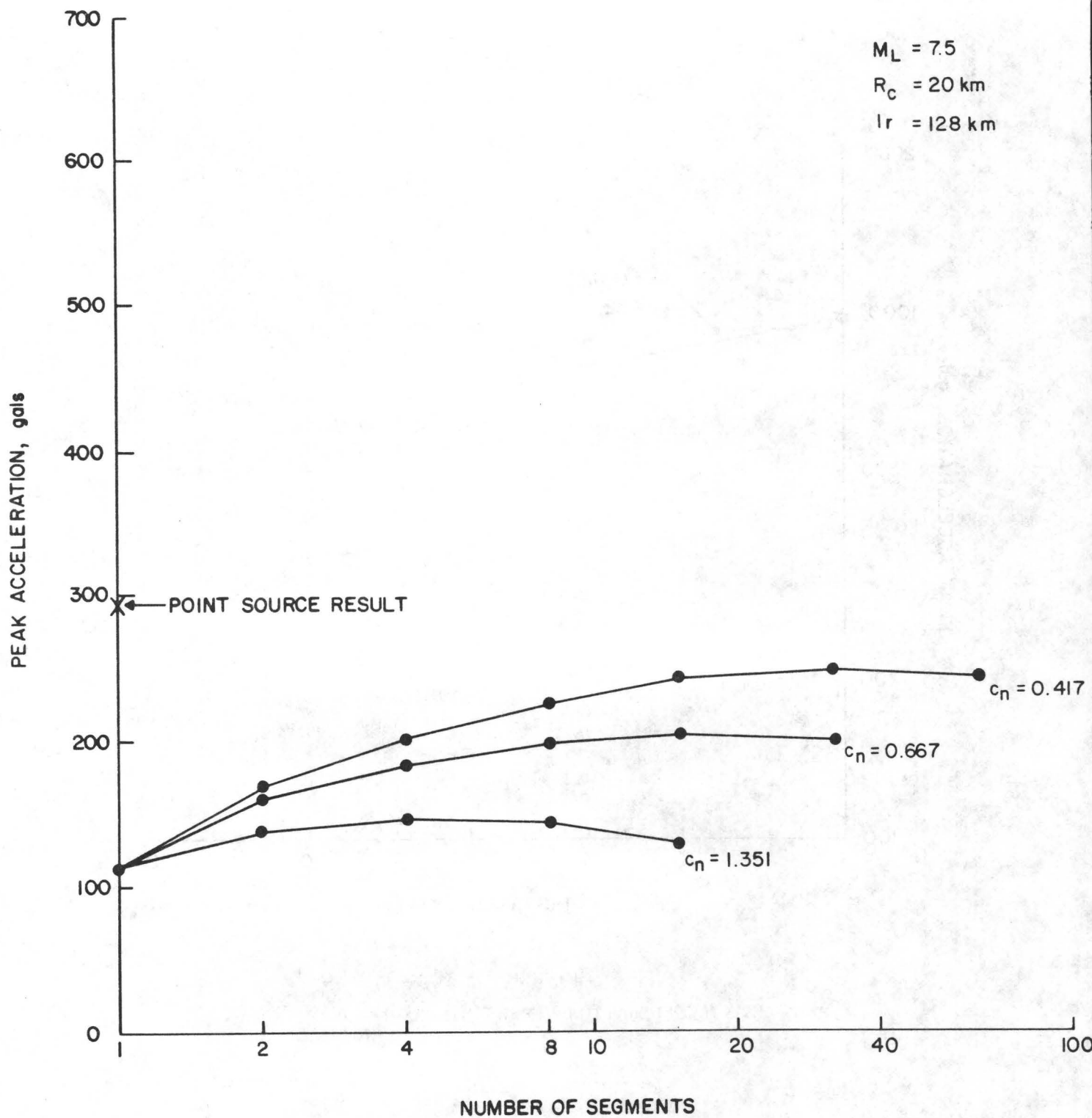
FIGURE 7D

MEAN PEAK ACCELERATION VERSUS N FOR $M_L = 7.5$ AND $R_c = 20$ km
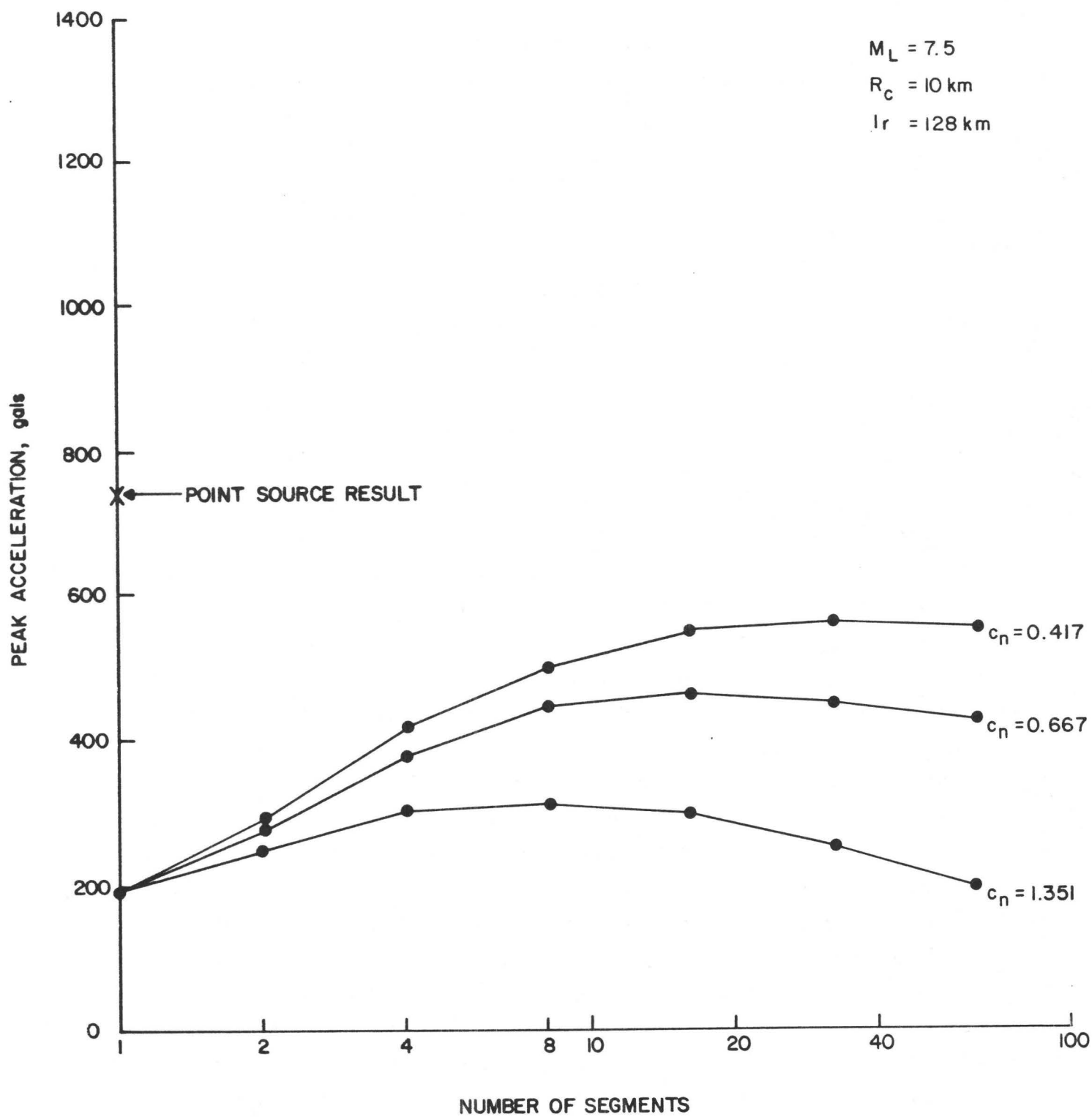
FIGURE 7C

MEAN PEAK ACCELERATION VERSUS N FOR $M_L = 7.5$ AND $R_c = 10$ km

Analysis of Near-Source Static and Dynamic
Measurements from the 1979 Imperial Valley Earthquake

Ralph J. Archuleta
Paul Spudich

(Both at the U.S. Geological Survey, 345 Middlefield Road,
Menlo Park, CA   94025)

ABSTRACT

The 1979 Imperial Valley M_L 6.6 earthquake has provided an extraordinary set of near-source data. More than 40 strong motion instruments within 35 km of the fault trace recorded the mainshock. Horizontal and vertical offsets delineate the surface rupture. The dynamic and static measurements are used to infer gross features of the earthquake mechanism.

Using an average value of 40.5 cm of the right-lateral surficial slip we estimated a lower bound for the seismic moment of 2.5×10^{25} dyne-cm. To be consistent with farfield estimates of the seismic moment the average slip should be about 100 cm. Using an average slip of 100 cm and a faulting depth of 10 km we deduced a static stress drop of 12 bars. However, if one uses an average slip of 40.5 cm on the upper 5 km of the fault's width and 120 cm on the lower 5 km of the fault, the seismic moment is consistent with farfield estimates of the seismic moment, but the static stress drop is 51 bars. From the lower estimate of 12 bars we inferred an average strain drop of 32 μ strain. This strain drop is four times greater than the strain that could have been accumulated since the 1940 El Centro earthquake based on measured strain rates for the region. Hence, we inferred that a major portion of the strain released in the 1979 mainshock had been accumulated prior to 1940.

One of the most interesting features of the acceleration recordings is the presence of large amplitude (500-600 cm/sec/sec) vertical accelerations at stations E05, E06, E07, E08, EDA of the El Centro array and the 5 stations of the differential array near EDA. Although the peak acceleration of 1705 cm/sec/sec at E06 is probably amplified by a factor of 3 due to local site conditions, these large amplitude vertical accelerations are unusual in that they are evident on only a few stations all of which are near the fault trace and at about the same epicentral range. Two possible explanations were considered. First they are due to a direct P-wave generated from a region about 17 km north of the hypocenter, or second they are due to a PP phase that is unusually strong in the Imperial Valley due to the large P-wave velocity gradient in the upper 5 km of the Imperial Valley.

Based on the distribution of both the horizontal and vertical offsets we concluded that the rupture went beyond stations E06 and E07. Although the surface rupture passed directly between stations E06 and E07, there is no obvious manifestation in the particle motion of the passage of the rupture front. By exploiting the antisymmetry of the parallel components of particle velocity between E06 and E07 and by examining polarization diagrams of the particle velocity at E06 and E07 we determined an average rupture velocity of 2.5-2.6 km/sec between the hypocenter and station E06.

INTRODUCTION

The October 15, 1979, Imperial Valley earthquake has provided the most complete set of near- and far-field data for a damaging earthquake to date. More than 40 strong motion instruments in the United States (Brady et al., 1980) and in Mexico (Brune et al., 1982) recorded the near-source ground acceleration at distances less than 35 km from the Imperial fault. The right-lateral horizontal offsets and the vertical offsets were measured within days of the mainshock (Sharp et al., 1982). A coseismic strain offset was recorded by three laser strainmeters at Pinon observatory about 130 km from the epicenter (Wyatt, 1980). Throughout the world the M_L =6.6 (Chavez et al., 1982) mainshock was well recorded on long period seismometers (Julian et al., 1982). Since the mainshock was well recorded both near and far and over the entire seismic frequency band, the Imperial Valley earthquake provides an extraordinary opportunity for studying the earthquake mechanism from many different viewpoints. Our approach in this paper will be to examine the near-field static measurements and the strong motion particle acceleration and velocity. It is not our intention to conclude with a detailed description of the faulting process, but rather to provide a framework from which future investigations can be initiated.

At first glance the quality and quantity of near-source data for this moderate sized strike-slip earthquake provide an optimistic basis for analysis of the earthquake mechanism. However as one attempts to reconcile the many different pieces of data, the overall picture of the earthquake mechanism becomes less clear. Even the gross features of the 1979 earthquake do not fit into a neatly bound package. For example, while surface ground breakage extended along a 35-km long segment of the Imperial fault (Sharp et al., 1982), no ground breakage was found within 7.5 km of the epicenter. Using the mean surface displacement, 40.5 cm (Sharp et al., 1982), one can estimate the earthquake's seismic moment, but this moment is still a factor of two to three times smaller than the seismic moment determined from farfield measurements. The ground motions caused by this earthquake have some unusual characteristics if one thinks of the earthquake mechanism as being a uniform stress drop on a vertical strike-slip fault. The peak particle velocities, which reach 115

cm/sec at EMO and 108 cm/sec at E06 and E07 on the perpendicular component of motion, are asymmetric about the strike of the fault; contrary to normal expectations the peak vertical accelerations, as high as 1.7 g (g being the acceleration due to gravity), often exceeded or matched the peak horizontal accelerations of 0.6 to 0.8 g on many instruments.

The purpose of this paper is to try to extract as much information about the nature of the 1979 Imperial Valley earthquake mechanism from a straightforward analysis of the data. The complications that can arise in the near-source particle motion just from the finiteness of the faulting process can be overwhelming (Archuleta and Hartzell, 1981), and those complications coupled with the velocity structure are certain to lead to many ambiguities in the interpretation of the data. Nevertheless the P-wave velocity structure for the Imperial Valley has been well determined (Fuis et al., 1982; McMechan and Mooney, 1980); the static offsets have been carefully documented and the dynamic motion was well recorded on many instruments, some of which have absolute time. It seems to us that an analysis of this information is sufficient to give a general outline to the earthquake mechanism of the 1979 earthquake.

HYPOCENTER

To take full advantage of the absolute timing on many of the strong motion accelerograms, an accurate hypocentral location and origin time are needed. By taking into account lateral variations in the depth of sediments, the depth of the 6.6 km/sec refractor (Fuis et al., 1982), and vertical variations in V_p/V_s, Archuleta (1982) determined a hypocenter using the short-period vertical seismometer readings of Chavez et al. (1982). The hypocenter determined by Archuleta (1982) is 32° 39.50' N 118° 19.80' W, 8.0 km depth and 23:16:54.4 GMT origin time (Figure 1). Compared to the hypocenter of Chavez et al., (1982) this hypocenter is more consistent with the S-wave arrival times at nearby strong motion accelerographs. This hypocenter is 2.0 km shallower and 2.5 km farther north along the Imperial fault than the hypocenter of Chavez et al. (1982). The hypocenter determined by Archuleta (1982) will be used for subsequent analysis. This hypocenter gives an dip of 82° NE to the Imperial fault.
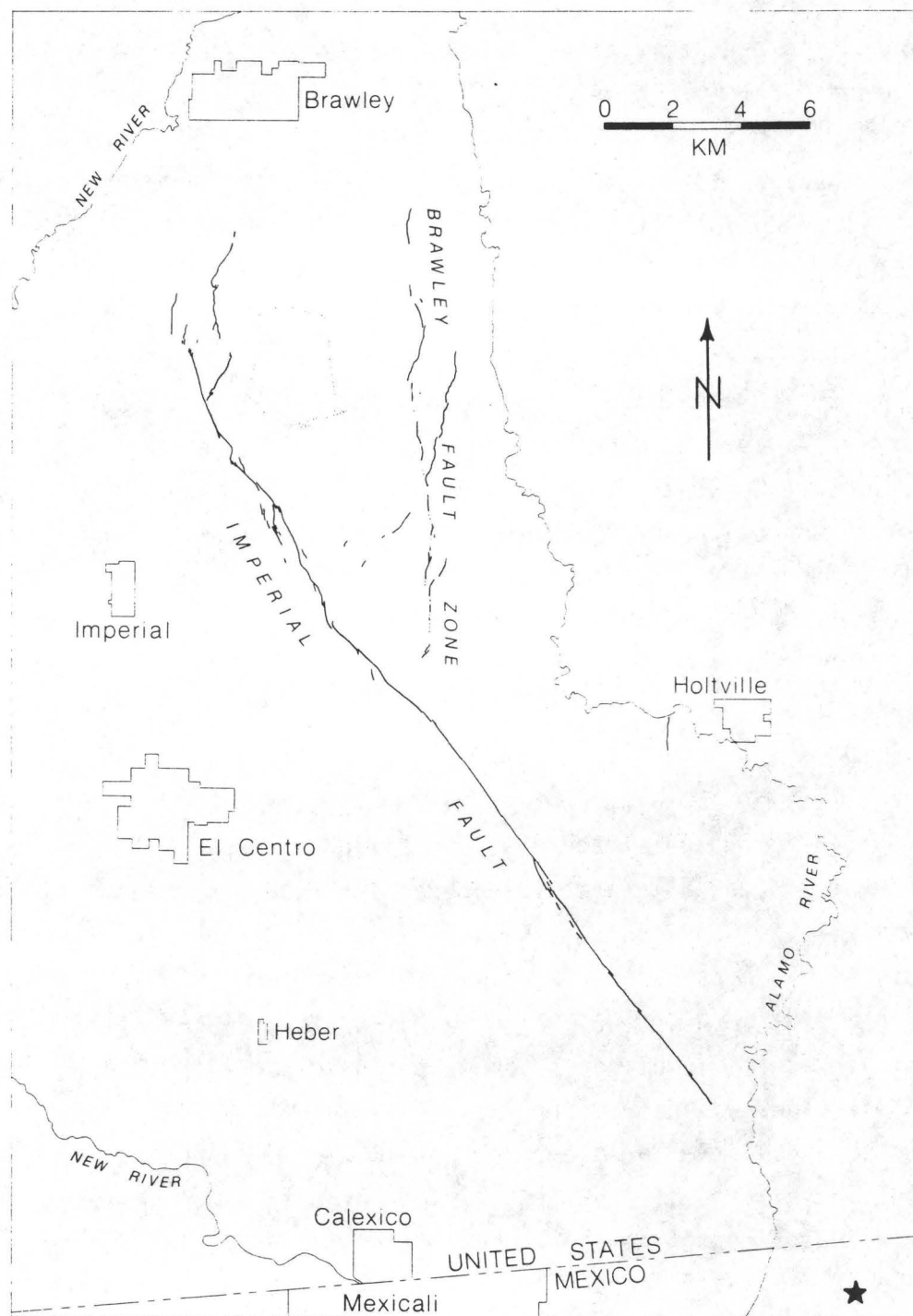
Figure 1: A map of the region of California directly affected by the mainshock. Surface traces of the Imperial fault, striking NNW, and the Brawley fault, striking N, on which slip was measured are also shown. The star marks the epicenter.

Several other lines of evidence support the likelihood of a dip on the Imperial fault. From refraction profiles in the Imperial Valley Fuis et al. (1982) estimated a dip of 70° NE on the southeast end and 78° NE on the northwest end of the Imperial fault. Earthquakes with $M_L \geq 3.0$ generally have epicenters that are 2 to 3 kms east of the Imperial fault (Johnson, 1979). Using 2.5 km as a representative value for the distance east of the fault and assuming representative depths of 6 km and 10 km, we find dips of 67° NE and 76° NE, respectively. An arithmetic average of all of these values or almost any combination of them yields an average dip of 75° NE. The presence of a dip on the Imperial fault is an important effect in examining the near-source dynamic ground motion.

PARTICLE ACCELERATIONS

The first 10 seconds, after triggering, of the vertical, 230° and 140° components of particle acceleration, are superimposed on a map view of the Imperial Valley in Figures 2, 3, and 4, respectively. The 230° component is the positive horizontal ground acceleration directed along an azimuth 230° clockwise from North; similarly the 140° component is positive ground acceleration at a 140° azimuth. With the exception of station EMO which was operated by the California Division of Mines and Geology, all of the free-field accelerographs shown were maintained by the U.S. Geological Survey (Brady et al., 1980). The three-letter station codes are taken from the list of strong motion accelerographs (Switzer et al., 1981). The Imperial fault, trending northwest, and part of the Brawley fault, trending north, are shown for reference. The crosshairs mark the epicenter. Table 1 gives station coordinates, trigger times, azimuth between station and epicenter, and epicentral distances.

The preeminent aspect of Figure 2 is the 1705 cm/sec^2 peak ground acceleration (pga) at station E06. The true pga may be even larger than this once the instrument response is accounted for (Raugh, 1981). Although the large amplitude at E06 dominates, stations E05, E07, E08, and EDA also show peak vertical accelerations on the order of 500-600 cm/sec^2. At E06, the amplitude is amplified by a factor of about 3 (Mueller and Boore, 1981) due to
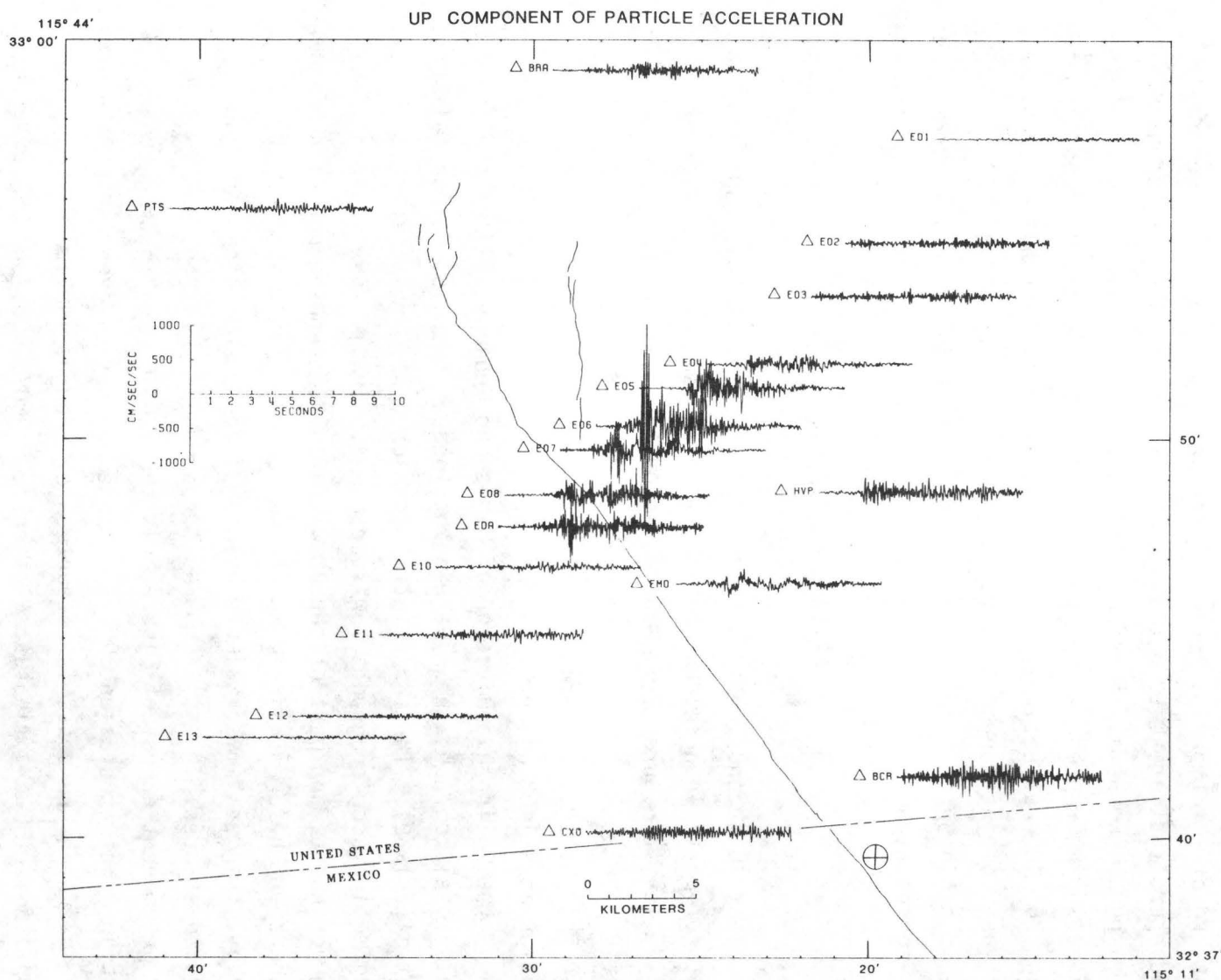
Figure 2: Mainshock vertical particle accelerations, recorded by strong motion accelerographs in the United States, superimposed on a map view of the Imperial Valley. The triangles mark the locations of the accelerographs. The lines trending NNW and N, are the Imperial and Brawley faults, respectively. The crosshairs mark the epicenter. Only the first 10 seconds, after triggering, of the particle accelerations are shown.
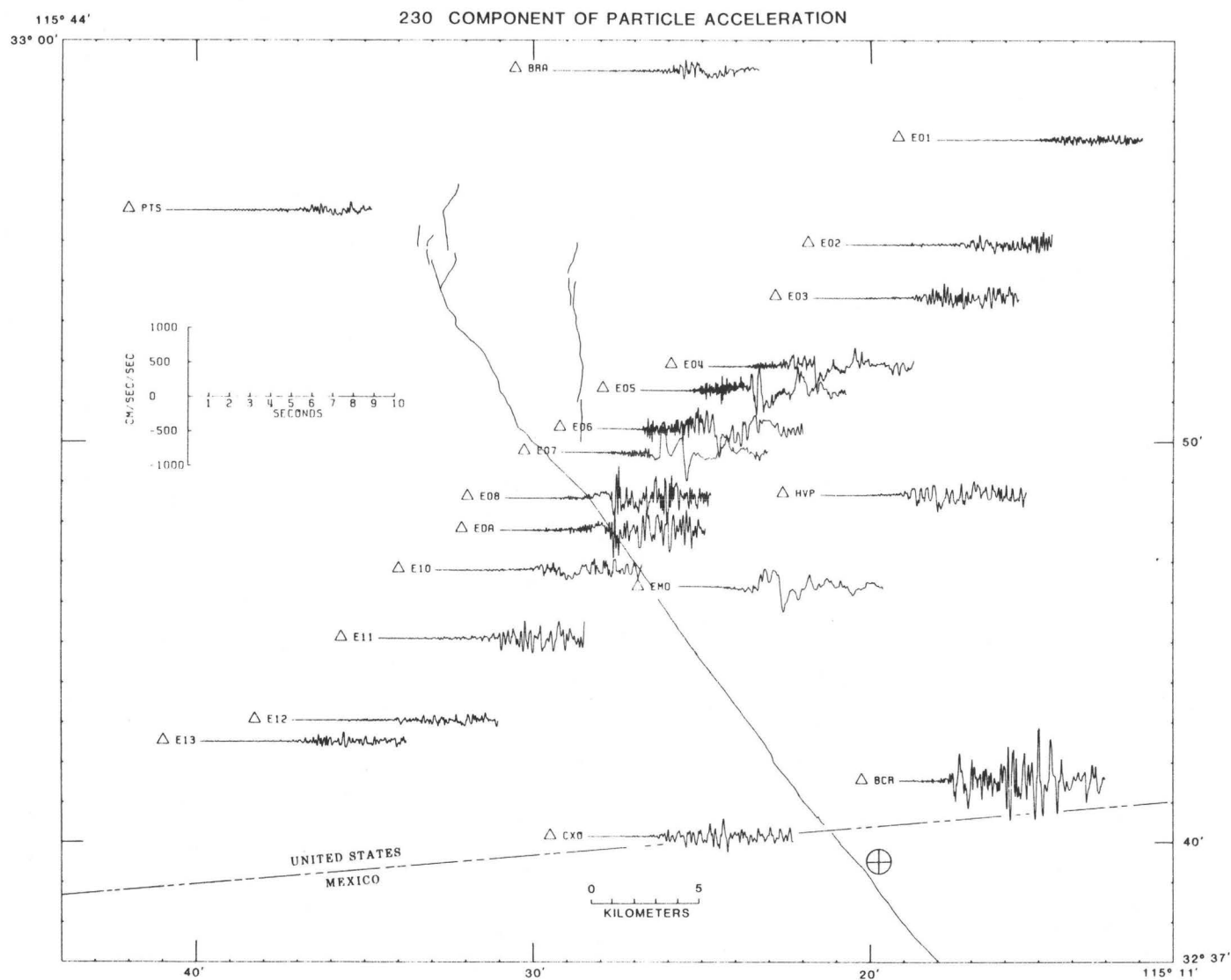
Figure 3: The mainshock 230° horizontal component of particle acceleration superimposed on a map view of the Imperial Valley. Positive motion is along the 230° azimuth measured clockwise from North. This component is basically perpendicular to the strike of the Imperial fault. See caption of Figure 2.

791
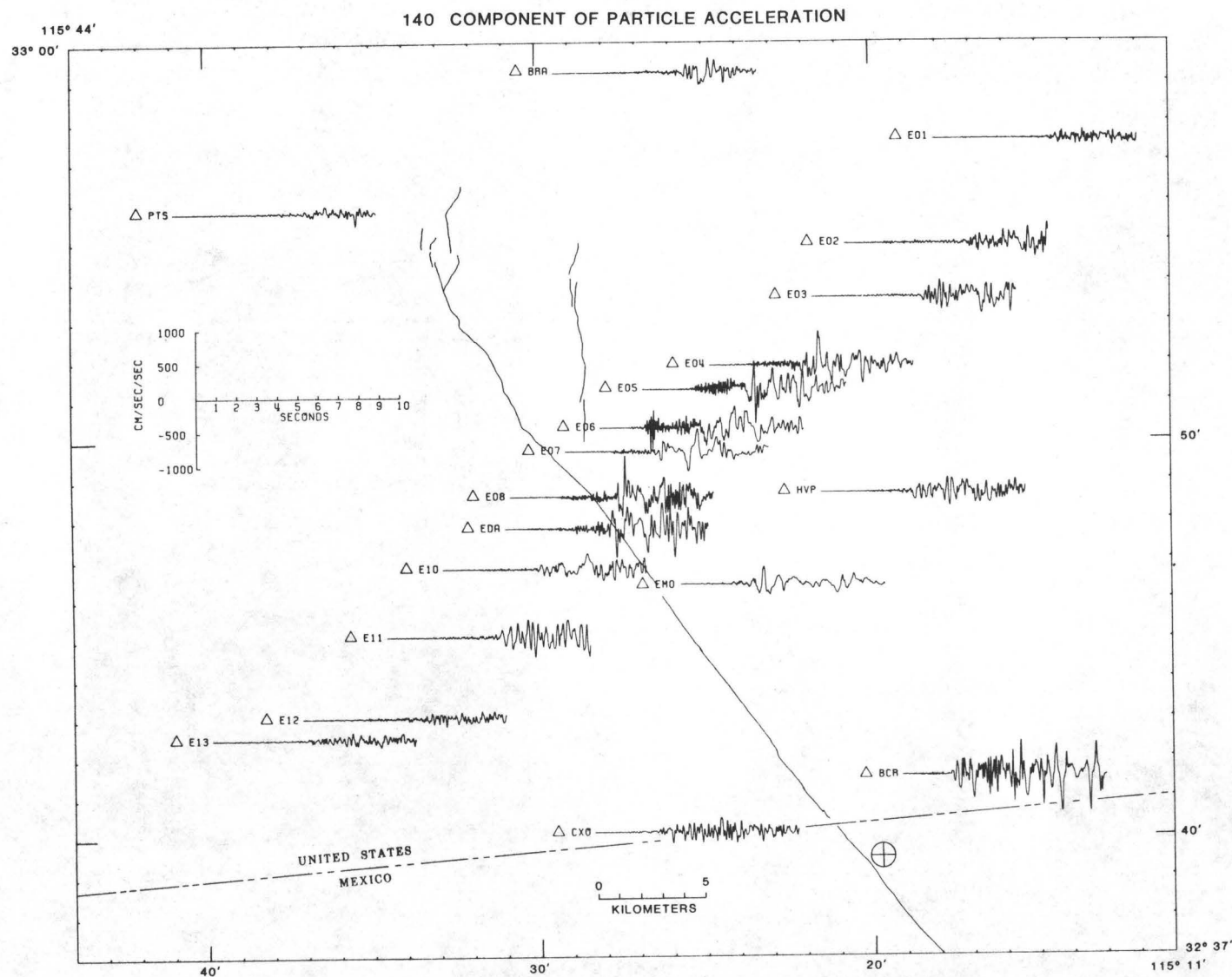
Figure 4: The mainshock 140° horizontal component of particle acceleration superimposed on a map view of the Imperial Valley. Positive motion is along the 140° azimuth measured clockwise from North. This component is basically parallel to the strike of the Imperial fault. See caption of Figure 2 for details.

local site conditions; if one corrects for the site amplification, the pga at E06 is approximately the same as those at E05, 07, 08, and EDA. These large accelerations are anomalous in that they appear on vertical rather than horizontal components; they are found on only stations which are at approximately the same epicentral range and close to the fault; they are near a node for P-wave radiation from a vertical fault, and precede the arrival of the direct S-waves from the hypocenter. Later we examine possible causes for these vertical accelerations.

The horizontal components of acceleration are characterized by their long periods that signal the arrival of the first S-waves from the hypocenter, such as at stations E07 and EMO in Figures 3 and 4. The maximum horizontal acceleration, 794 cm/sec^2, occurs on the 230° component at Bonds Corner (BCR) almost 7 seconds after triggering.

PARTICLE VELOCITIES

The particle velocity time histories obtained by integrating (Brady et al., 1980) the vertical, 230° and 140° components of acceleration are shown in Figures 5, 6, and 7, respectively. The map view of the Imperial Valley in Figures 5, 6, and 7 is identical to that shown in Figures 2, 3, and 4. However, in Figures 5, 6, and 7 the first 30 seconds, after triggering, of the velocity time histories are shown as compared to the first 10 seconds of the acceleration time histories. Although there is some evidence of the large vertical accelerations, the striking aspect of the vertical particle velocity (Figure 5) is the presence of surface waves with periods around 4 seconds. The maximum values of the vertical particle velocities are significantly smaller than the maximum horizontal particle velocities.

In terms of amplitude alone, the 230° component of particle velocity (Figure 6) dominates with values of 115 cm/sec at EMO and 108 cm/sec at E06 and E07. Although these values are among the highest particle velocities ever recorded, the feature that stands out in Figure 6 is the remarkable similarity and simplicity of the waveforms. If the faulting were pure strike-slip on a vertical plane in a laterally homogeneous medium, the 230° component would be perfectly symmetrical about the fault plane. It is obvious from Figure 6 that
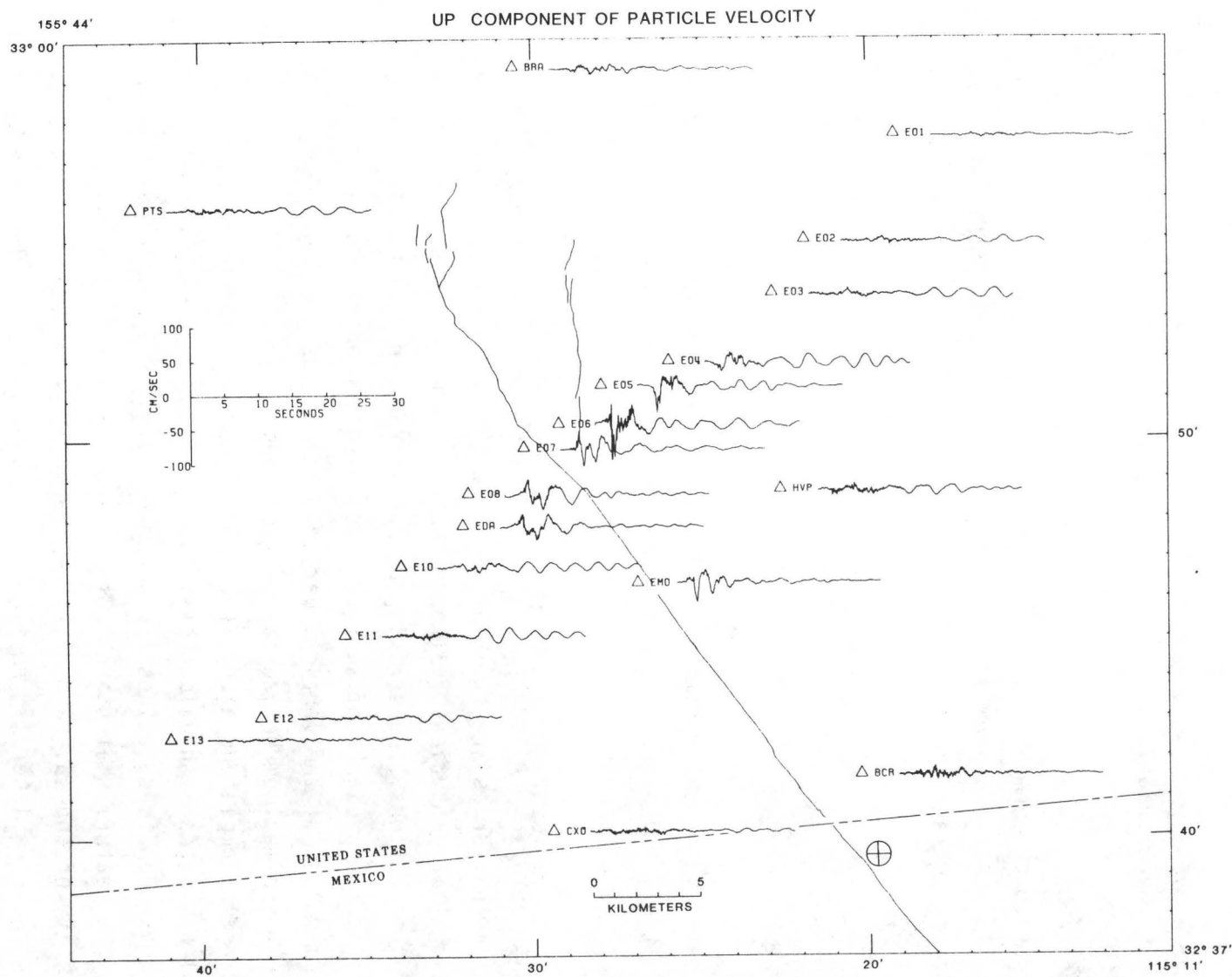
Figure 5: Mainshock vertical particle velocities obtained by integrating the particle accelerations. The first 30 seconds after triggering is plotted. See caption of Figure 2.
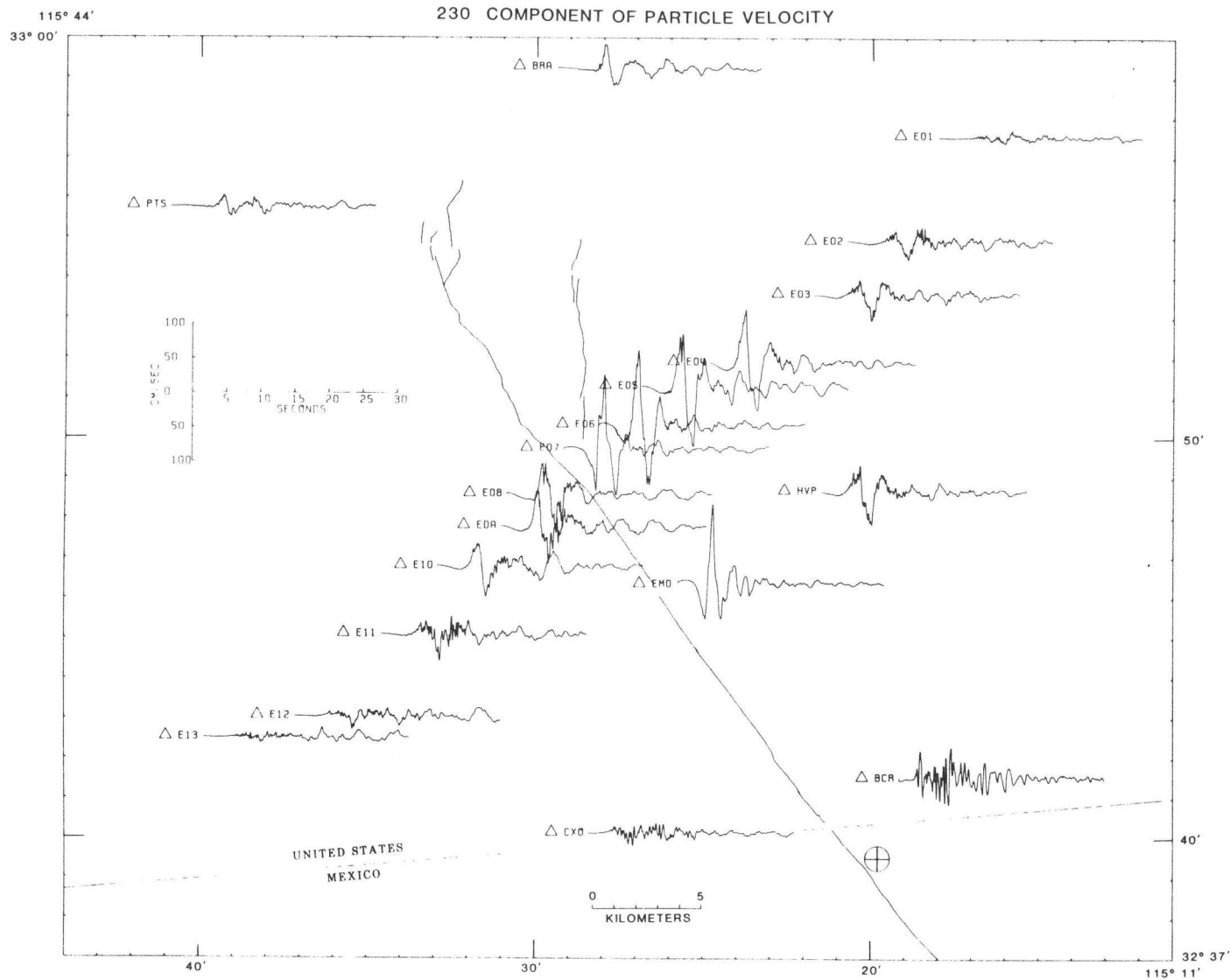
Figure 6: Mainshock 230° component of particle velocity obtained by integrating the 230° component of the particle acceleration. The first 30 seconds after triggering is plotted. See caption of Figure 2.
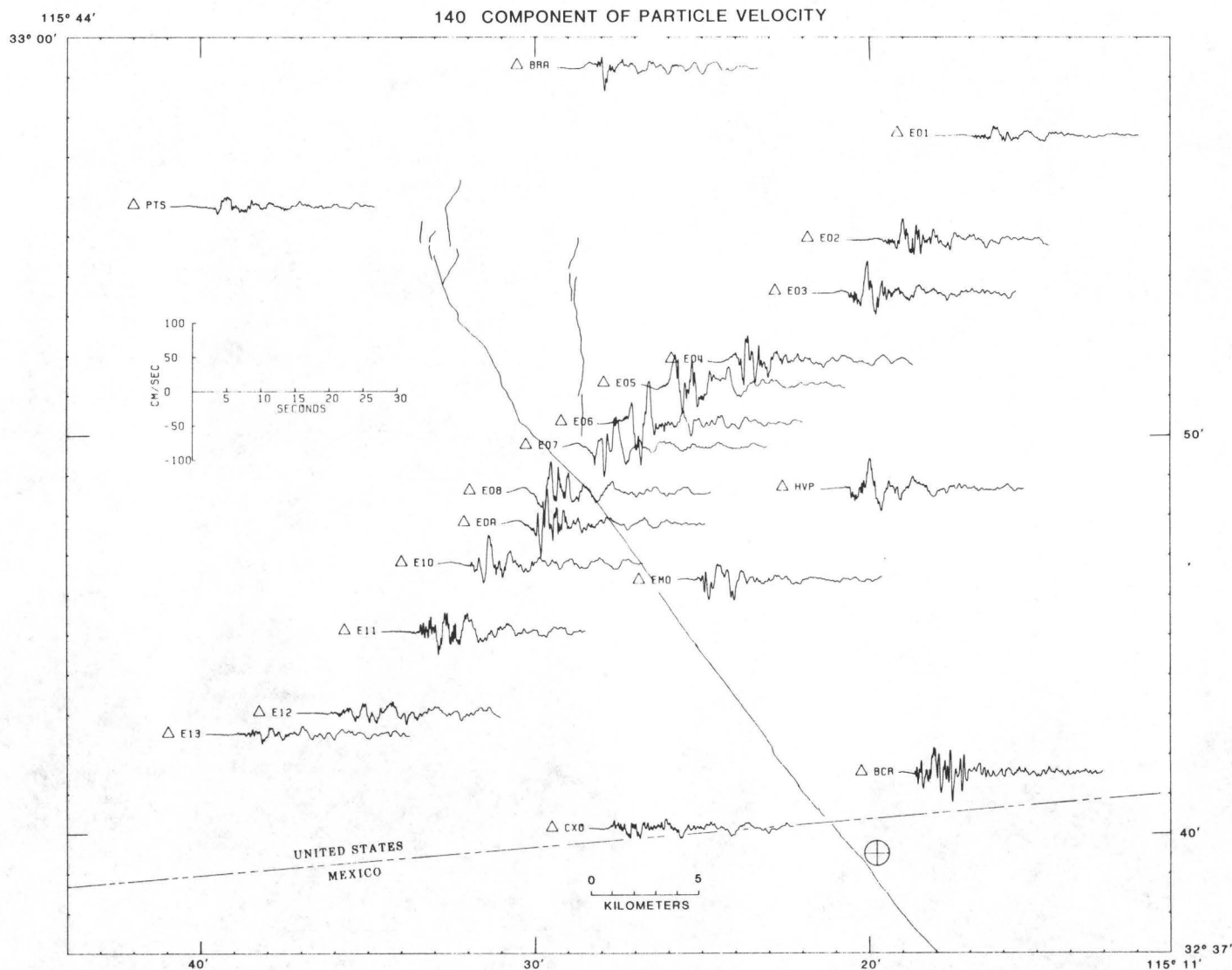
Figure 7: Mainshock 140° component of particle velocity obtained by integrating the 140° component of particle acceleration. The first 30 seconds after triggering is plotted. See caption of Figure 2.

the east side of the fault has larger amplitudes when comparing E05 with E08 and E04 with EDA. For perpendicular distances greater than about 12 km, between a station and the fault, the amplitudes are roughly equal on both sides of the fault. Although there are lateral variations in the velocity structure, a more probable cause for the lack of symmetry is a northeastward dip on the Imperial fault.

Two other aspects of the particle velocities in Figure 6 are due to the nature of a propagating rupture. First, the amplitudes are larger and more pulse-like at the northern stations than the stations near the epicenter. Second, stations such as HVP, E02, E03, and E11 have similar shapes to one another but different from the pulse shape at E06, for example. The observation that the amplitudes are larger and more pulse-like in the direction of propagation is the effect of focussing from a propagating rupture. Near-source studies of a propagating stress drop in a halfspace (Archuleta and Frazier, 1978) and in a vertically varying medium (Archuleta and Day, 1980) show that the near-source particle velocities are amplified in the direction of rupture propagation. This amplification is due not only to directivity (Ben-Menahem, 1962) but also to a feedback mechanism when the rupture velocity is less than the local shear wave velocity (Archuleta and Frazier, 1978). However, if we assume that there is a uniform stress drop moving at a constant rupture velocity, focussing cannot explain the amplitude difference on the 230° component of Meloland compared to E06 or E07. Meloland (EMO) is closer to the epicenter than E07. If focussing due to a uniform stress drop moving at a constant velocity were the only cause of larger amplitudes, EMO should have a smaller amplitude than E07 (Archuleta and Frazier, 1978; Archuleta and Day, 1980), but the converse is true. This suggests that either the stress drop or the rupture velocity is not uniform over the fault.

The shape of the pulses at stations such as HVP and E03 is due in part to the changing radiation pattern as the rupture propagates from south to north (Archuleta and Hartzell, 1981). If one imagines the rupture as a single double-couple moving at a constant velocity, then the radiation pattern will also be equivalent to the radiation pattern of a double-couple moving with a constant velocity. In the forward and backward directions, the radiation

pattern coefficient remains constant with time. However, for points that lie well off the fault plane, the radiation pattern is continuously changing. In fact, as the rupture propagates, the radiation pattern coefficient of any component of motion for stations such as HVP can theoretically pass through zero (Archuleta and Hartzell, 1981), although other factors such as the depth of faulting and lateral variations do not allow for actual zeroes. Basically the particle motions at stations such as EMO and E07 are caused by to the force couple perpendicular to the fault whereas particle motion at stations like HVP and E11 are due to the force couple parallel the fault.

The horizontal particle velocity oriented parallel to the strike of the fault is shown in Figure 7. Note that it has considerably smaller peak amplitudes than the corresponding perpendicular component. The parallel component of motion would be expected to show antisymmetry with respect to a vertical fault in a laterally homogeneous medium. As a consequence, stations near the fault would be nodal. Clearly the 140° component of motion at stations EMO, E06, and E07 is not nodal just as the vertical motion was not nodal. Since a vertically heterogeneous medium cannot, by itself, influence the postion of a nodal plane relative to a vertical fault, we presume that the motion on the 140° and vertical components is further evidence of some dip on the Imperial fault.

VELOCITY STRUCTURE

One of the most fortunate aspects in analyzing the Imperial Valley earthquake is the availability of detailed P-wave velocities throughout the entire region north of the United States-Mexico border. Fortuitously, an extensive refraction survey of the Imperial Valley was done in February 1979 (Fuis et al., 1982). As a result of this refraction survey, the P-wave velocity (V_p) structure is well determined to depths of 15 km (Fuis et al., 1982; McMechan and Mooney, 1980). The basic character of the vertical profile for the P-wave velocity for the refraction line analyzed by McMechan and Mooney (1980), a line east of the Imperial fault, is shown in Figure 8. In the upper 5.0 to 6.0 km (the "sediments" using the terminology of Fuis et al., 1982) a strong gradient (0.64 km/sec/km) raises the velocity from 1.8 km/sec
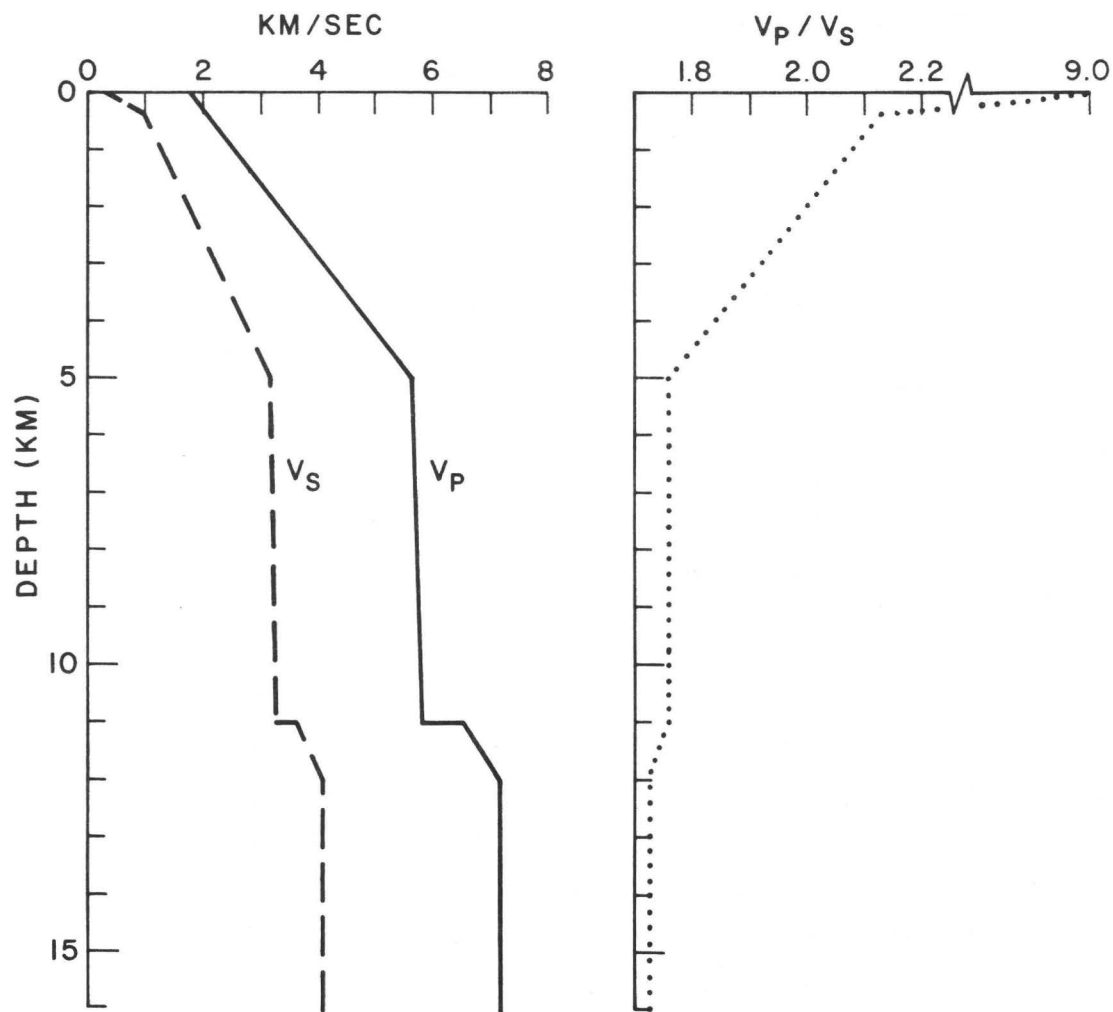
Figure 8: Vertical profiles of the S-wave (V_S) and P-wave (V_P) velocity
structure in the Imperial Valley. Shown at the right is the ratio of P-wave
to S-wave velocity as a function of depth.

at the surface to 5.65 km/sec at a depth around 6.0 km. Between 6 km and 11 km (the "basement") the velocity is nearly constant, reaching 5.85 km/sec at 11 km. In the "subbasement" at 11 km there is a jump to 6.6 km/sec from which the velocity rapidly changes to 7.2 km/sec at a depth around 12 km. The depth of the sediments and the depth to the 6.6 km/sec refractor vary laterally throughout the Imperial Valley (Fuis et al., 1982; McMechan and Mooney, 1980). Other refraction lines analyzed by Fuis et al. (1982), in particular the line between shotpoints 6 and 1 which cuts across the Imperial fault, shows that the west side of the Imperial fault is faster than the east side.

An S-wave velocity (V_s) structure (Figure 8) was derived from the study of aftershocks of the Imperial Valley mainshock (Archuleta et al., 1979) and drill logs in the Imperial Valley (Shannon et al., 1976). The V_p/V_s ratio monotonically decreases from 9.0 at the surface to 2.13 at 0.35 km. From 0.35 km to 5 kms, the ratio decreases from 2.13 to 1.78. From 5 km to 11 km, the ratio is held constant at 1.78, a value appropriate for oceanic crustal material. Below 11 km the poisson solid value of 1.73 is used.

To illustrate some of the principal phases that are discussed later we show in Figures 9A and 9B travel time curves for point sources located at 4.0 and 8.0 km, respectively. The labelled branches of the travel time curves in Figures 9A and 9B are shown schematically in the insets to Figures 9A and 9B. We follow a nomenclature system similar to that used for teleseismic phases with p and s denoting P- and S-waves which are travelling upward from the source, and P and S denoting waves travelling downward from the source. Of particular note are the families of free-surface reflected phases. Because of the strong velocity gradient in the top 5 km of the Imperial Valley (McMechan and Mooney, 1980; Fuis et al., 1982), these phases can be observed at much smaller epicentral distances than usual. The phases PP and PPP were quite large in the refraction profiles of McMechan and Mooney (1980) and Fuis et al. (1982). For buried sources these phases have large amplitudes at the cusps of their travel-time curves, i.e., at the epicentral distances where pP and PP, or sS and SS, merge. Because the time separation between the pP and PP arrivals is so small, we will use the term "PP" to refer to the combined arrival.
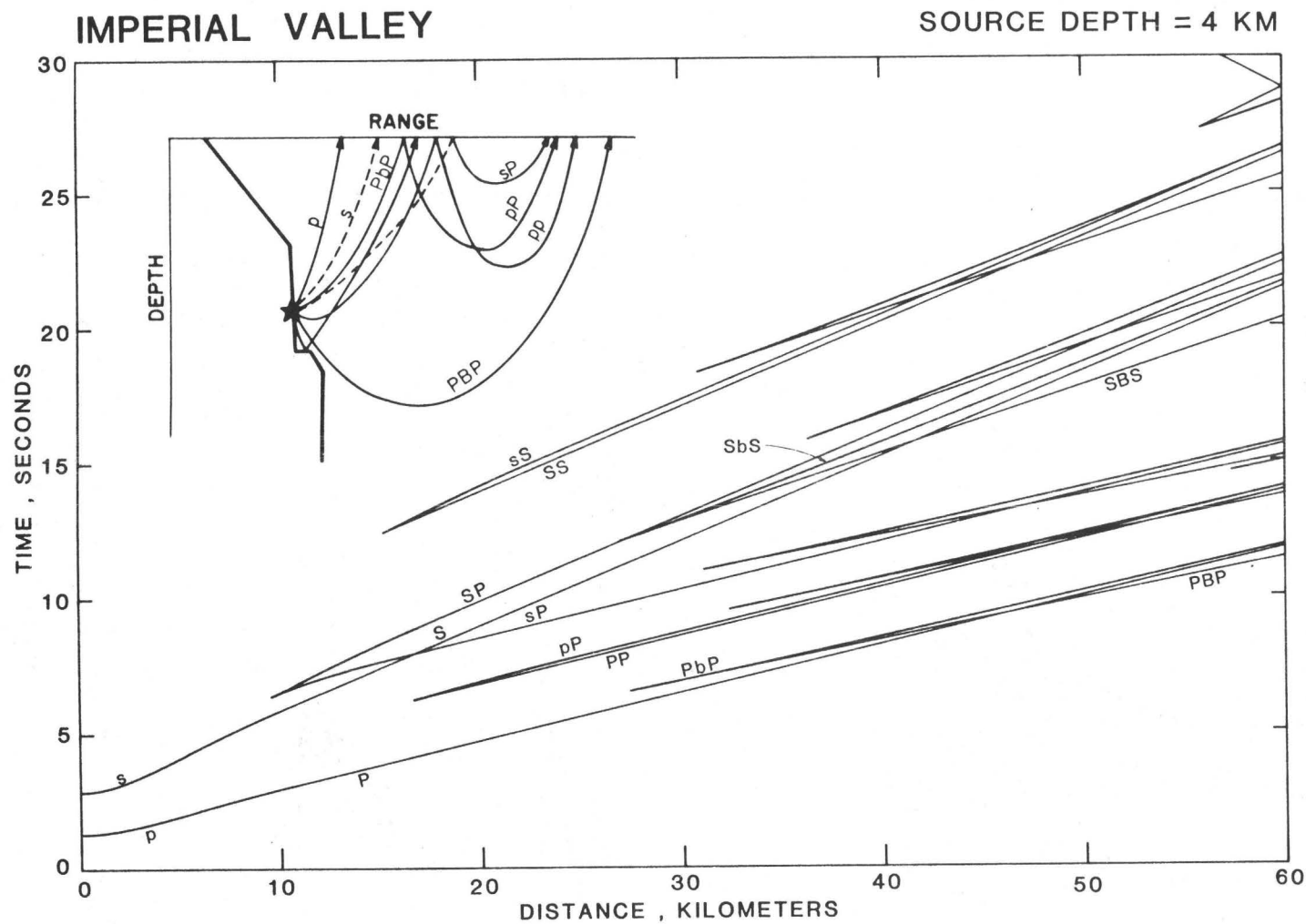
Figure 9A: Travel time curves for the Imperial Valley assuming a flat-layered
velocity structure based on Figure 8. The source is at 4.0 km depth. Phases
shown are P, PP, PPP, S, SS, SSS, the reflections from the 6.6 km/sec
discontinuity and S to P conversions. The inset is a schematic representation
of the geometrical ray paths.
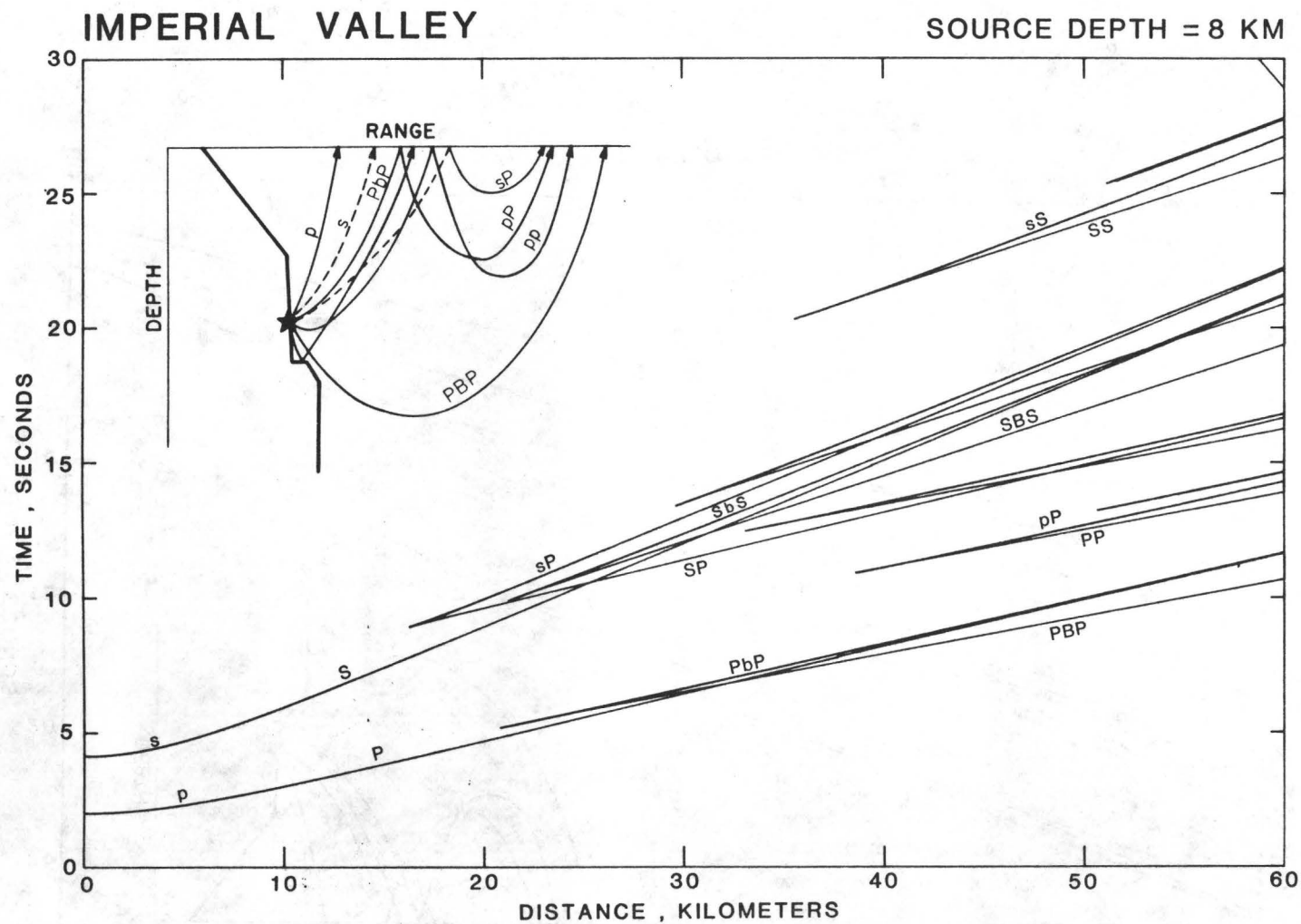
Figure 9B: Travel time curves for the Imperial Valley assuming a flat-layered velocity structure based on Figure 8. The source is at 8.0 km depth. Phases shown are P, PP, PPP, S, SS, SSS, the reflections from the 6.6 km/sec discontinuity and S to P conversions. The inset is a schematic representation of the geometrical ray paths.

RUPTURE VELOCITY

As discussed in a later section, the measurements of the static horizontal and vertical slip strongly suuport the idea that the rupture passed between stations E06 and E07. Assuming that the dynamic rupture did indeed pass between E06 and E07, we might expect to see some irrefutable evidence that indicated the time of the passing of the rupture. In particular we might have expected that the motion parallel to the strike of the fault (the 140° component) would become strongly antisymmetric between E06 and E07 at the time of the passing of the rupture (Archuleta and Frazier, 1978). As discussed below such is not the case. Apparently the complexities due to the velocity structure, depth of faulting, and the dip of the fault have obscured any direct measurement of the time of the passing of the rupture. Thus we have to deduce the probable rupture velocity from physical arguments. Before we do this, let us explain what the phrase, "passing of the rupture front," means in a vertically varying medium.

Of course, we can only observe waves emitted by the rupture front, not the rupture front itself. In the case of the 140° component for stations E06 and E07 close to the fault, but on opposite sides, we would like to determine the point at which there is clear antisymmetry in the particle acceleration or the slope of the particle velocity between the two stations due to their being at maxima in opposing polarity lobes of the rupture's SH radiation pattern. In the case of the 230° component, which is nearly symmetric for stations E06 and E07, we first wish to determine the time when the waves we observe change from originating from the leading lobe of the moving double-couple's radiation pattern to originating from the following lobe. Since the shear-wave velocity in the basement (between depths of 5 and 10 km) of the Imperial Valley is so much greater than that at the surface (Figure 8), it is likely that the rupture at depth will pass by station E06 and E07 much earlier than the surficial rupture. If most of the seismic energy is liberated in the basement, then the polarity changes we observe will most likely be related to the passage of the rupture at depth.

The most direct measurement of the arrival of the rupture front might have come from examination of the 140° component of particle velocity or acceleration at stations E06 and E07. Once the rupture had started to pass between the two stations, which are on opposite sides of the fault, the particle motion would clearly be 180° out of phase. Unfortunately station E07 does not have absolute time, so it is not clear where we should look for this 180° phase difference in the particle motion. We have attempted to assign relative timing to E07 by cross-correlating its 230° particle velocity with the 230° particle velocity at station E06. We can use the 230° component because this motion is continuous across the fault, and both E06 and E07 are in almost the same place relative to the radiation coefficient for this component of motion. Even if absolute time were available on E07, this would be the appropriate procedure to follow since it removes the effects of near-surface delays. Based on cross-correlation we determined that the time series from station E07 should be shifted 0.3 seconds earlier to align with E06. However there is evidence from an aftershock study (Boore and Fletcher, 1982) that S-waves arrive about 0.5 sec later at E06 than at E07 for earthquakes south of those two stations. If we were to combine these two results to assign absolute time to E07, we would infer that E07 triggered 0.8 seconds before E06.

In Figure 10 we show the first 20 seconds of the three components of particle velocity for stations E06 and E07 with the time series for E07 shifted by 0.3 seconds relative to E06 based on the cross-correlation only. In Figure 10 the positive motion for the particle velocity is in the up, 230° and 140° directions, e.g., a -80.0 cm/sec on the 230° component would be directed along the 50° azimuth. A primary consideration in examining the 140° components is that the acceleration should be in the 320° direction at E07 and in the 140° direction at E06 for a right-lateral vertical fault rupture that passes between them. After the arrival of the first S-waves from the hypocenter, there are two places where the 140° component of velocity on E06 and E07 have opposite slopes. These two places are indicated by the vertical dashed lines in Figure 10. The earlier time is 5.8 seconds after trigger time on station E06 and the later time is 6.3 seconds after trigger time. If we add the 6.3 seconds to the E06 trigger time, we find that the S-waves from the rupture arrived 13.3 seconds after origin; the earlier time gives 12.8 seconds after origin.

STATION 7 LAGGED -0.3 SECONDS TO FIT STATION 6
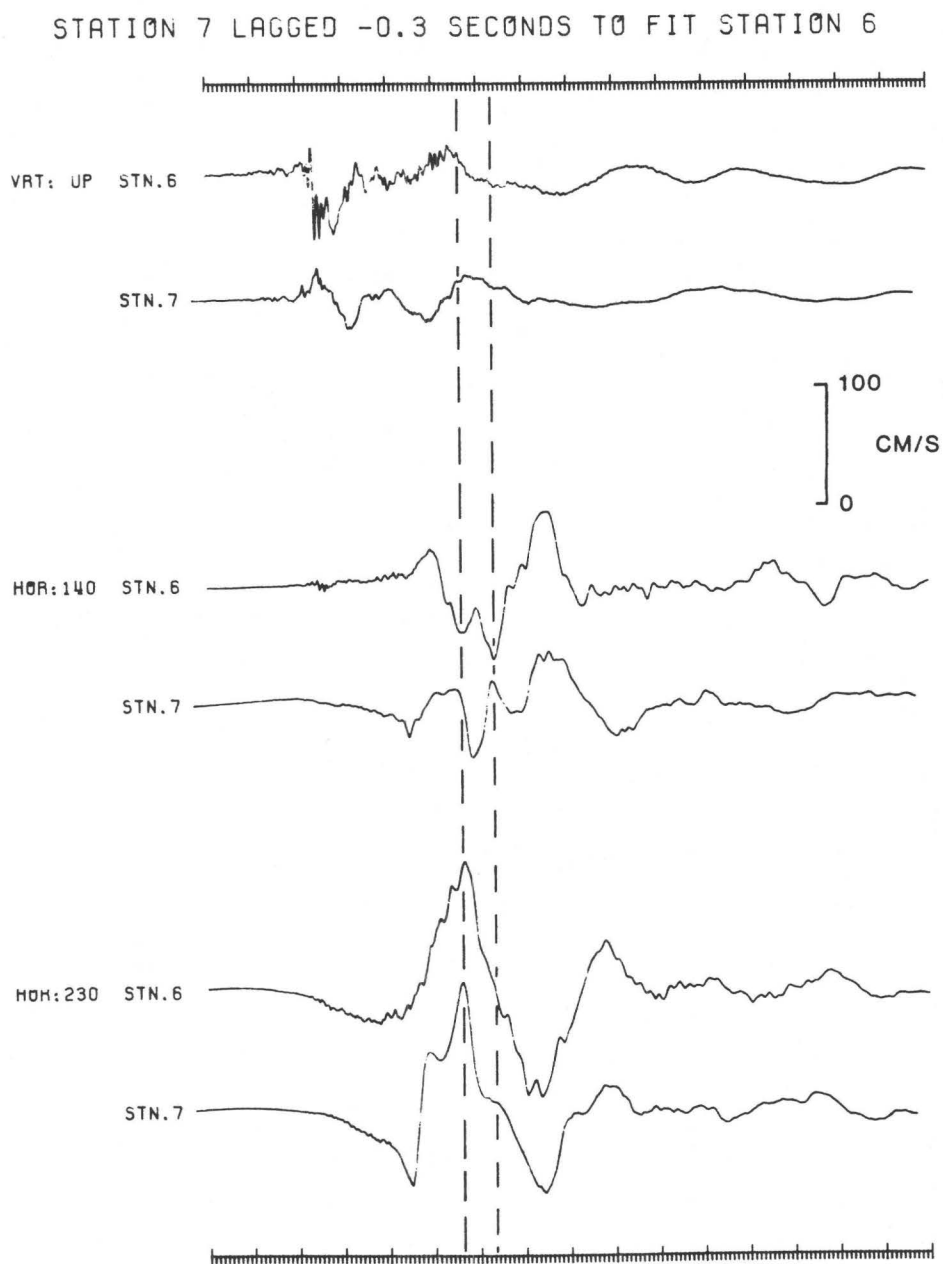
Figure 10: A comparison of the first 16 seconds the three components of particle velocity at stations E06 and E07. Station E07 has been shifted 0.3 seconds relative to E06 based on a cross correlation of E06 and E07. Two choices for the time of the rupture front passing at depth between the two stations are shown as the vertical dashed lines.

The second method of inferring the time of arrival of S-waves from the rupture front is by studying the polarization of the particle velocity for stations near the fault. The initial direction of polarization due to the near-field terms should be opposite to that of the S-wave field; hence the initial particle velocity will be in the 50° direction. When the S-waves from the hypocenter arrives the particle velocity will move in the 230° direction. Once the rupture passes the observation point, the particle velocity will start to move in the 50° direction because the sign of the lobe of the S-wave radiation changes sign. To illustrate these main points we show in Figure 11 a polarization diagram for the motion at station E06.

The 140° component of particle velocity is shown along the abscissa; the 230° component is shown along the ordinate. On the 45° line the polarization is plotted as a function of time. The time axis on the 45° line is stretched by the factor $\sqrt{2}$ relative to the orthogonal axes. For each tenth of a second we have computed the magnitude of the polarization $P = \sqrt{\dot{u}(140)^2 + \dot{u}(230)^2}$ and the angle of polarization $\theta = \arctan(\dot{u}(230)/\dot{u}(140))$. The length of each ray on the 45° axis is P; the angle is θ. We have drawn a circle of radius 100 cm/sec and labeled the primary angles for interpretation of the magnitude and direction of the polarization.

Initially the particle motion is almost entirely polarized in the 50° azimuth, consistent with the near-field term for this station and a right-lateral strike-slip fault. With the arrival of the S-waves, the polarization reverses direction to the 230° azimuth. About 6.0 seconds after trigger the polarization starts to rotate toward the 320° direction; at 6.3 seconds it is parallel the 320° direction, and shortly thereafter reverses to the 50° azimuth. A similar polarization diagram can be constructed for station E07 although the reversal from 230° to 50° occurs about three tenths of a second later than it does at station E06. The polarization results corroborate the earlier result that the change observed on the 140° components is due to S-waves from the rupture front passing these two stations. However the polarization diagram does not necessarily indicate which of the two points in time is preferable.
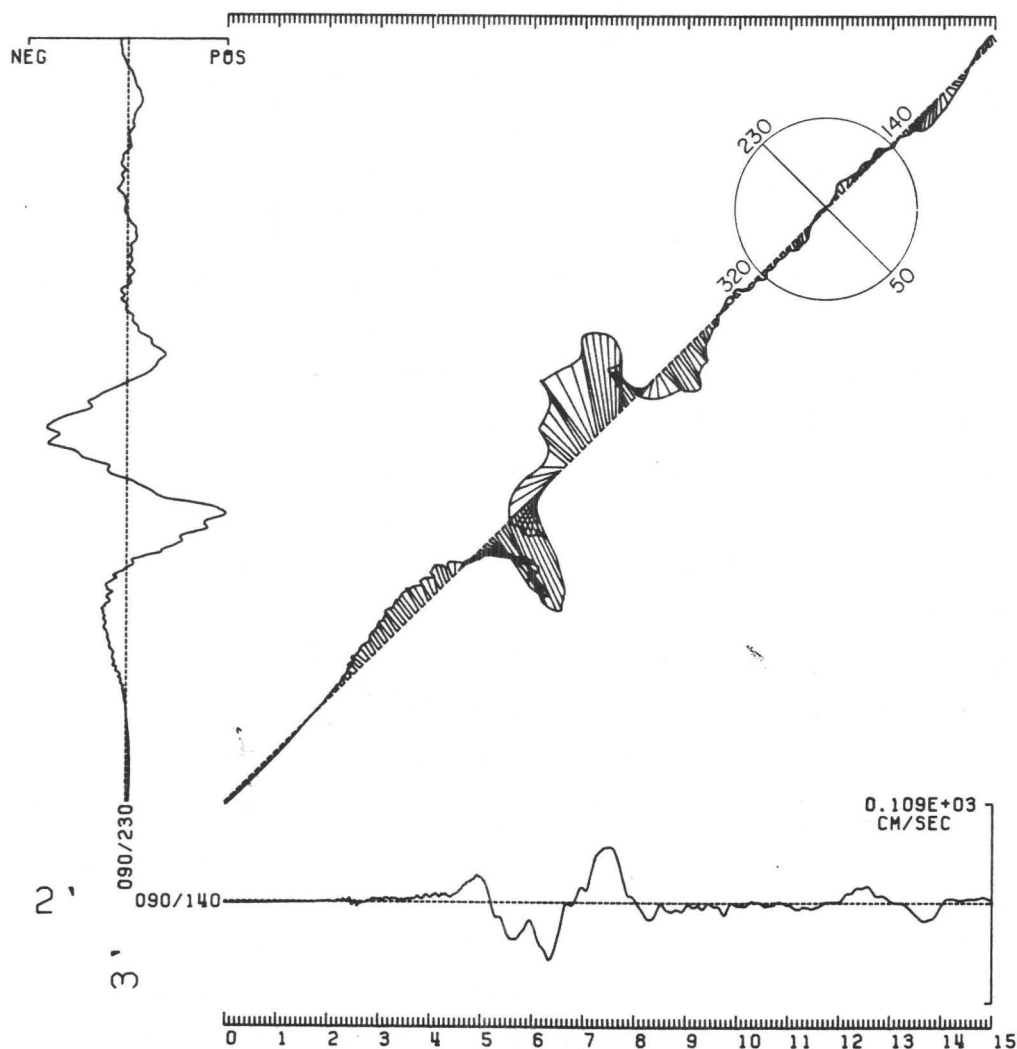
Figure 11: A polarization plot constructed from the two horizontal components of particle veloctiy at station E06. The ordinate is the 230° component; the abcissa is the 140° component. Along the 45° line the polarization magnitude and direction are plotted as a function of time. See text for the definition of polarization magnitude and angle. A circle with amplitude 100 cm/sec and the four principal angles is shown near the end of the 45° ray in order to interpret the direction and scale of the polarization.

Because of the tradeoff between the source time function and the rupture velocity (Anderson and Richards, 1975), one might suspect that a very short source time function is responsible for the reversal in the polarization diagram, i.e., the change in the particle velocity from the 230° direction to the 50° direction. However, we have calculated synthetic seismograms that indicate that varying rise times do not significantly affect our rupture velocity determination. To illustrate this point we show in Figure 12 synthetic particle velocities for the 230° component computed from a fault 35 kms long and 10 kms deep dipping at 75° in a laterally homogeneous medium with a vertical velocity profile given by Figure 8, except that we used a surficial shear velocity of 0.8 km/sec to reduce computational costs. The synthetic seismograms were calculated using the method of Spudich (1981) and the discrete-wavenumber finite-element method of Olson (1982). The receiver is in the same location relative to the fault and hypocenter as E06 is to the Imperial fault. Since we are only interested, at this time, in demonstrating how the particle velocity is affected by either the rupture velocity or the duration of the slip function, we assume that the slip velocity is a boxcar with an amplitude variation that remains the same for each computation. The duration of the boxcar is constant for each computation as indicated on Figure 12. Since the duration was allowed to vary for the different computations but the amplitude stayed constant, the seismic moment will also vary. It is this variation that leads to the different amplitudes which are irrelevant in this discussion. In four of the synthetics the duration is fixed at the same value, but the rupture velocity is a different constant fraction of the local shear wave velocity. In three of the synthetics, the rupture velocity is a constant fraction of the local shear wave velocity but the duration of the slip velocity is different. The time at which S-waves from the rupture at depth reach the station is indicated by a solid circle on each synthetic. It is clear in these examples that the time at which the rupture passes the station at depth is at or after the peak in the particle velocity on the 230° component.
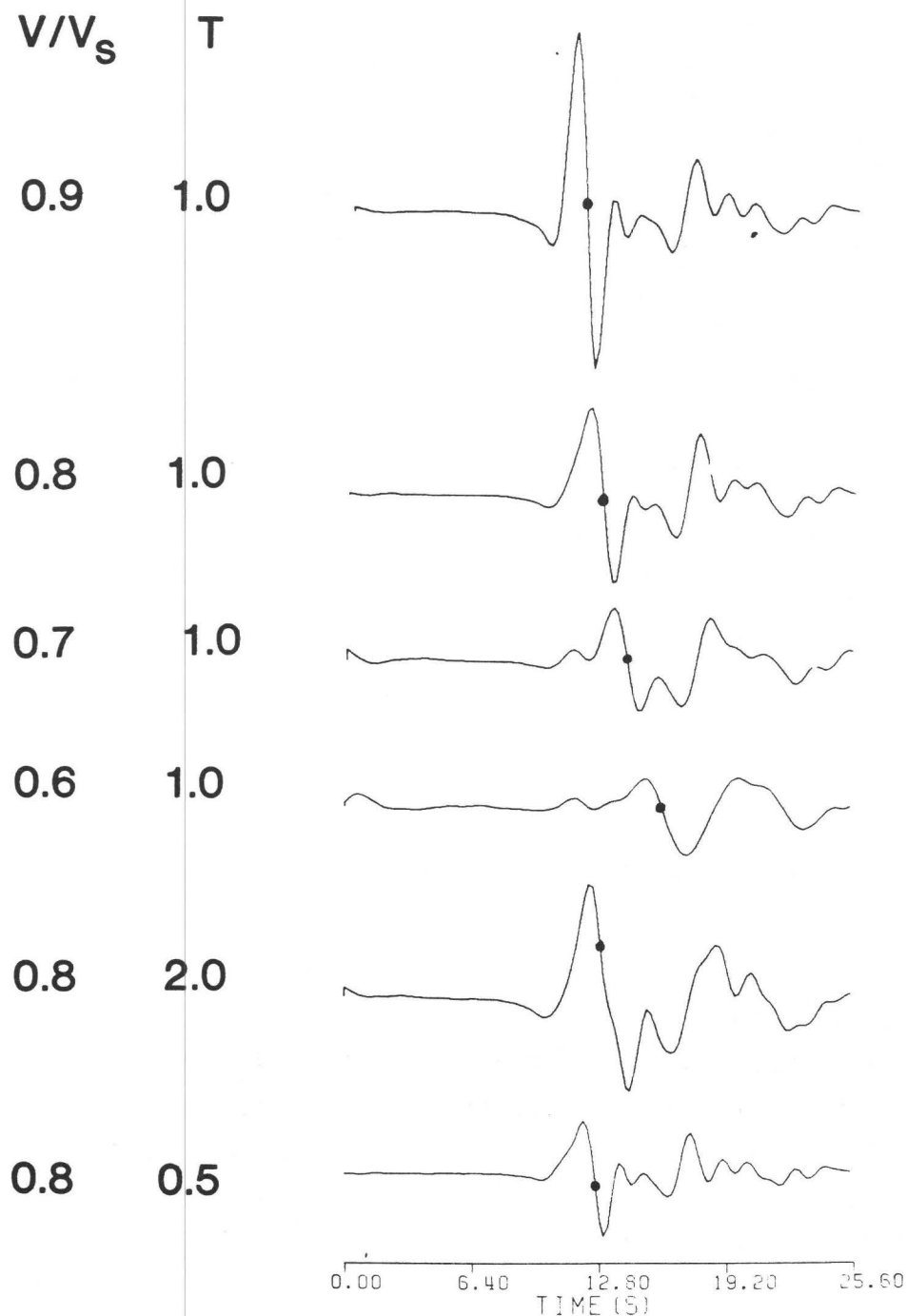
Figure 12: Synthetic particle velocities from extended sources. Either the ratio of rupture velocity to local shear velocity (V/V_s) or the duration (T) of a boxcar time function for the slip velocity was allowed to vary on the fault. The component of motion is equivalent to the 230° component for station E06 relative to the Imperial fault. The solid dot shows the theoretical time at which the rupture at depth is passing the station.

The time of 13.3 seconds leads to an estimate of rupture velocity at depth of about 2.5 km/sec, which is about 0.78 times the local shear wave velocity on the east side of the fault (Figure 8). We deduced the value of 0.78 by considering the S-wave velocity structure. Basically the S-wave velocity is almost constant for depths between 5 and 10 kilometers. The hypocenter lies in this region. Thus a rupture front moving at a constant fraction of the shear-wave velocity will look almost like a plane wave propagating along the strike. Using an average value of 3.2 km/sec (the S-wave velocity) and a distance of 24.9 km between the epicenter and E06, the time for a rupture propagating at the S-wave velocity would be 7.8 seconds. We must also allow for at least 3.2 seconds for an S-wave generated at 5.0 km depth to reach the station using the S-wave profile shown in Figure 8. Adding the 3.2 seconds to the 7.8 seconds leaves us 2.3 seconds short of the 13.3 seconds. This suggests that the rupture is traveling at a velocity less than the shear wave speed. Using a value of 2.5 km/sec gives a travel time of 10.0 seconds for the 24.9 km epicentral distance to station 6. Adding the time of 3.2 seconds to estimate the S-wave arrival from a depth of 5 km gives a total time of 13.2 seconds. The value of 13.2 seconds is quite close to the 13.3 seconds inferred from the polarity of station 6 relative to station 7. The same reasoning yields a velocity of 2.6 km/sec if we use 12.8 seconds after origin.

If the rupture velocity is a known fixed fraction of the shear velocity at all points along the rupture, then it is easy to estimate the rupture evolution since the paths of "rupture rays," i.e., points on the rupture front moving normally to it, are governed by Snell's law and follow exactly the same paths S-waves would follow. Using our estimate of $0.78 \, V_s$ and a two-dimensional ray tracing program (Cerveny, 1977), we show the evolution of faulting north of the hypocenter (Figure 13). A cross-section of the Imperial Valley in the plane of the fault is shown at the bottom. On the fault the position of the rupture front is indicated at 2, 4, 6--14 seconds after origin time. The dashed lines are arbitrary; the exact depth of faulting is unknown and the rupture did not break the surface for 7.5 km north of the hypocenter. The time at which the rupture breaks the surface is plotted against distance along the fault. This time is slightly earlier than the true value because we
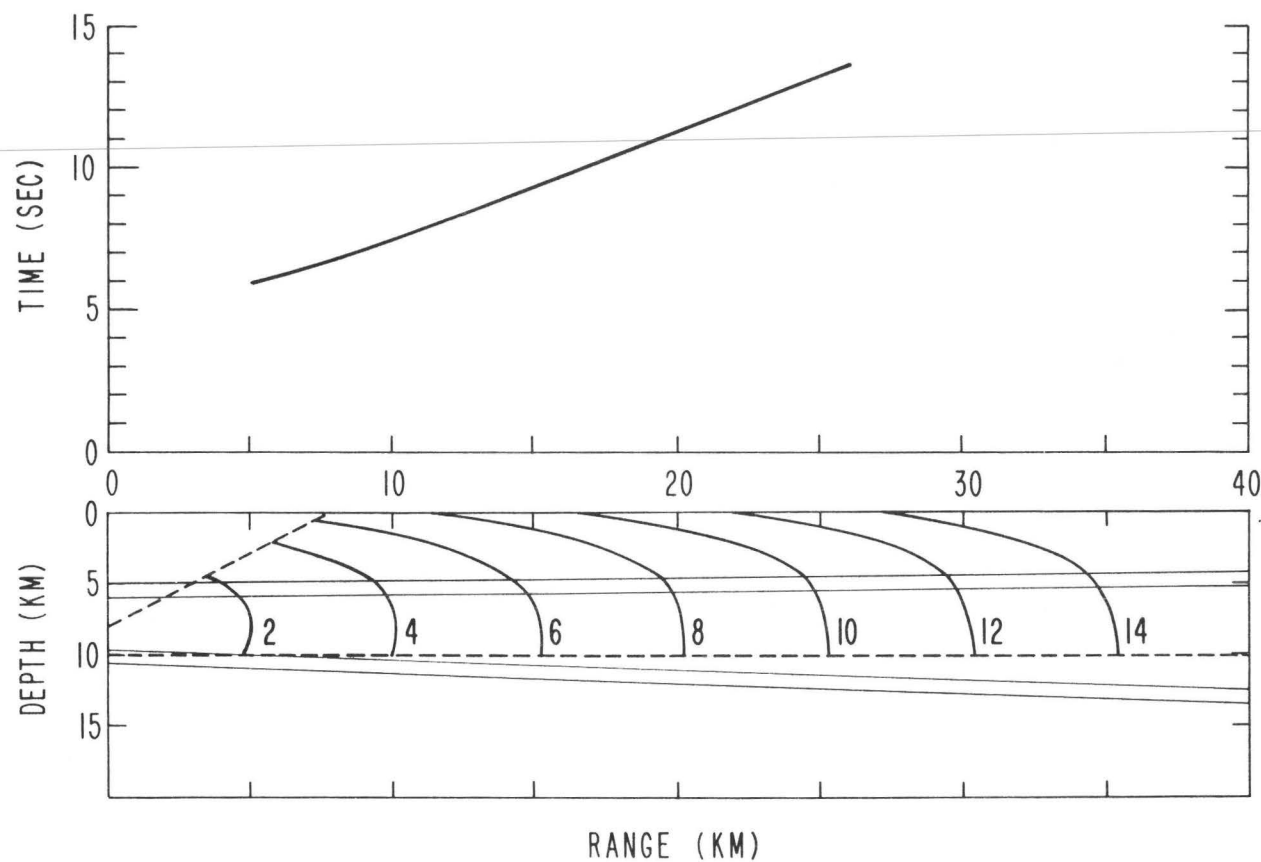
Figure 13: Propagating with a velocity of 0.78 times the local shear wave velocity the position of the rupture front on a cross section of the Imperial fault is shown at 2 second intervals after initiation. The travel time curve gives the time at which the rupture front would be breaking the earth's surface.

could not incorporate the large gradient in the upper 0.35 km into our ray tracing program. We simply extrapolated the S-wave velocity profile below 0.35 km to the surface. So we are overestimating the surfcial S-wave velocity thereby giving a faster velocity to our rupture front in the upper 0.35 km..

LARGE AMPLITUDE VERTICAL ACCELERATIONS

One of the most interesting features of the near-source ground motion is the presence of the large amplitude vertical accelerations (LAVA's) at some, but not all, of the recording sites. As discussed earlier, the maximum acceleration of 1705 cm/sec^2 at station E06 is due, in part, to a local amplification of a factor of three (Mueller and Boore, 1981). Nevertheless stations E05, E06, E07, E08, and EDA (Figure 2) and five digital strong motion stations, the differential array (Bycroft, 1980), within 225 m of EDA, all show peak vertical acceleration larger than or comparable to either component of horizontal acceleration. The same type of phase, reduced in amplitude, is observed at E04 and HVP. LAVA's have four important characteristics: (1) they were recorded on stations all at about the same epicentral distance; (2) at each of these stations the LAVA arrived before the S-wave from the hypocenter; (3) LAVA's are all clearly observed within 11 km either side of the fault trace; and (4) relative to the fault strike, they are near the P-wave node in the radiation pattern.

What caused this phase? Is it primarily due to the earthquake rupture or is it due to a propagation effect? Since this phase arrives before the S-wave from the hypocenter, it must travel part of its path as a P-wave, presuming sub-shear rupture velocity. This conclusion is supported by the fact that the amplitude is much larger on the vertical component than on either horizontal. If we use the result of the preceding section, i.e., the average rupture velocity is less than the local shear wave velocity, then travel-time considerations eliminate the possibility that this phase is a P-wave which was converted from a S-wave at the free surface. Such a phase will always arrive after the LAVA's for the following reason. Since in Figure 9B it can be seen that sP always arrives earlier than SP at equal epicentral range, we need consider only sP. Assume momentarily that the rupture velocity equals the

local shear velocity. Then rupture ray paths and travel times are identical to S ray paths and travel times. By Fermat's principle, the path of sP from the hypocenter to the observer is a minimum time path, and consequently its arrival time is also the earliest possible for an sP generated anywhere on the fault. Since the stations observing the LAVA are at about 25 km epicentral range, Figure 9B shows that the earliest possible sP arrival time is 10.4 sec after origin, which is about 1 sec after the LAVA's are actually observed. This time discrepancy becomes even greater if the rupture travels at less than the local shear velocity.

While we can rule out S to P conversion at the free surface by timing arguments, we cannot exclude the possibility of an S to P conversion at an internal boundary using timing. However, fairly substantial velocity discontinuities are necessary to generate such converted phases and no such discontinuity has yet been detected in the central Imperial Valley (Fuis et al., 1982). Since any S to P conversion is unlikely, we are limited to phases that travel their whole path as compressional waves, direct P or PP. Any other P phase will have travel times that are too late to match the observed times of arrival.

Since the LAVA's are probably P or PP, it is curious that they are so large near the fault trace which is a node for P-wave radiation from a vertical strike-slip or dip-slip fault in a laterally homogeneous medium. Two effects occur in the Imperial Valley which may partially diminish the nodal character of the fault trace. First, the refraction work of Fuis et al. (1982), particularly the 6NW-1SE profile, shows a change in the velocity structure across the Imperial fault with the west side of the fault having P velocities at most 0.5 km/sec faster than the east side. While this leads to the possibility of lateral refraction of P waves back onto the fault trace, it would be surprising if this rather small lateral change were sufficient to generate the LAVA's near the fault trace. A second factor that would diminish the nodality of the fault trace is the likelihood that the Imperial fault dips about 75° NE. A dip would diminish the nodal character of the fault trace since a P-wave initially emitted travelling parallel to the fault surface, i.e., a nodal P-wave, would be refracted upward and out of the fault plane, emerging at the earth's surface shifted off the surface fault trace. The

813

amount of shift would vary depending on the source depth and epicentral range of the P-wave. For example, if we use the P-wave velocity profile for the Imperial Valley for a strike-slip point source buried 4 km deep on a fault that dips 77°, the nodal P observed at 18 km epicentral range will be shifted 4 km off the fault trace onto the hanging side of the fault; for the same source nodal PP will emerge about 0.25 km of the trace in the same direction.

While these two factors may operate to smear out the P-wave node near the fault trace, unfortunately a glance at Figure 2 shows the LAVA's to be distinctly antinodal in character near the fault trace. Hence we must conclude that theoretical radiation patterns are not very useful in explaining propagation of 10-20 Hz seismic waves in this region.

Ironically, while we find that the LAVA's are dominant near the fault trace where we expect a nodal character, we find that they become very small off the fault where we would expect amplitude maxima. In particular we note in Figure 2 that they are large at EDA and nonexistent at E10, only 3 km farther west, and at all other stations west of E10. Similarly, on the east side of the fault the LAVA's are diminishing at E04 and nonexistent for stations to the east of E04. This observation places a strong constraint on their source and propagation paths. Having already deduced that the LAVA's are either a direct P or PP type phase, let us consider the consequences of these two possibilities.

First let us assume that the LAVA's are direct P-waves. Except for the influence of theoretical radiation pattern nodes, there is no factor which would prevent P-waves emitted from any point on the Imperial fault from being observed throughout the Imperial Valley. This is particularly true if they are emitted from a point in the basement (This last qualification is made because a P-wave generated and bottoming in the sediments will be considerably stronger than one generated in the sediments and bottoming in the basement.). Although we have discounted the usefulness of radiation pattern nodes for explaining the existence of LAVA's near the fault, we must invoke radiation pattern nodes to explain the nonexistence of LAVA's at E10 and west and east of E04. The high frequency content and the duration of one to one and a half seconds imply that the LAVA's were generated on a small part of the fault.

The simplest possibility is that they were generated when a small region of the fault broke with a large stress drop and sub-shear rupture velocity. In this case the P-wave radiation pattern would be nearly the usual four-lobed double couple radiation pattern with a very slight modification for P-wave directivity. Depending on the precise nature of this source it is unlikely that a small source region can have radiation pattern nodes at all stations east of E04, at E10 and all stations to the west and at BCR and CXO, though we have not done a feasibility study of such a source. Another consequence of this source is that at regional distances P-waves from the hypocenter would travel nearly identical paths to regional observers as P-waves from the high stress drop region. Hence we would expect that a large stress change occurring after the rupture began would cause a sudden amplitude change in the P-wave train of seismograms recorded at regional distances. With this in mind we examined the records of 14 U.S. Geological Survey low-gain, three-component seismometers in central and northern California (epicentral distances on the order of 600-1200 kms), but other than changes associated with P-wave crustal and Moho phases, we found no amplitude changes larger than a factor of two.

Hartzell and Helmberger (1982) have identified the LAVA's with direct P-waves from a region of large (200 bars) stress drop. To satisfy timing requirements they place this region at 8 km depth under station EMO. A difficulty with this hypothesis, which they recognize, is that stations E10 and E04 lie almost exactly on a P-wave radiation pattern maxima for a strike-slip source beneath EMO. To explain the absence of LAVA's at these and more distant local stations under the direct P hypothesis, it becomes necessary to invoke a source having appropriately placed radiation pattern nodes.

The theoretical P-wave radiation pattern can be altered from the usual double-couple radiation pattern by a sudden change in the rupture velocity, or by a rupture propagating near the P-wave velocity. The least likely of these two possibilities is that the LAVA's are produced by a rupture deceleration from near the shear velocity to zero, or acceleration from zero to near shear velocity. Both Madariaga (1977) and Boatwright (1982) have shown that in these situations P-wave radiation is slightly enhanced in the backward direction, which completely contradicts the observations (We are presuming

here that if the LAVA's are direct P waves, their source is southeast of E06 and E07, consistent with the timing arguments of Hartzell and Helmberger, 1982.). The second possibility is that at some point south of E06 the rupture accelerated from sub-shear to nearly P-wave velocity. Very little theoretical work has been done on acceleration pulses radiated in this situation, but it is likely that P waves would be focussed in the forward direction. Theoretically, once accelerated to near P velocities, the normal directivity (Ben-Menahem, 1962) for P-waves would continue to focus energy in the forward direction.

It is difficult to say whether the available data supports the possibility of super-shear rupture velocity occuring for more than a second or so. By inverting observed accelerations in the period range of 3-10 seconds, Olson and Apsel (this volume) have obtained results which could be interpreted as supporting a 4.5 km/sec rupture velocity over a 20 km long portion of the Imperial fault beneath 5 km depth. They caution that this velocity is a horizontal phase velocity and the true velocity may be lower depending on the vertical component of the rupture velocity. Hartzell and Helmberger (1982) have used a 2.5-2.7 km/sec rupture velocity to model the observed displacements, although they speculated that the LAVA's resulted from the super-shear rupture of their region of large slip beneath EMO. Niazi (this volume) has obtained 2.7 km/sec rupture velocity estimate by examining P-wave particle motions; preliminary results of Spudich and Cranswick (1982) also indicate a 2.5 km/sec rupture velocity up to and possibly during the time of generation of the LAVA's. While not supporting a super-shear rupture velocity, their preliminary work does offer some support for the proposal that the LAVA's are direct P-waves. By cross-correlating the vertical components at the five stations of the differential array (Bycroft, 1981), Cranswick and Spudich (1981) determined a phase velocity of 20-30 km/sec for the peak acceleration across the array. By mapping this apparent phase velocity onto the fault Cranswick and Spudich (1981) concluded that the large vertical accelerations could be a direct P-wave from an area about 17 km north of the hypocenter. This region of the fault is about 3 km south of the area that has the maximum displacement in the model of Hartzell and Helmberger (1982).

Thus, some evidence supports the hypothesis that the LAVA's are direct P waves, although to explain their spatially limited range of observation one must invoke a mechanism that uses radiation pattern nodes to account for their small amplitude at HVP, and their nonexistence at stations west of EDA, east of EO4, and at EMO, the station closest to their presumed origin. In view of the lack of any observable P-wave node near the fault trace, the fortuitous combination of a node and a significant site effect would probably be required to explain the abrupt disappearance of the LAVA between EDA and E10. Any mechanism requiring sustained rupture propagation at super-shear velocities is not unambigously supported by the strong motion data.

An alternative possibility that explains the limited range of occurrence of the LAVA without recourse to radiation patterns is that the large accelerations result from a phase of the PP type. A built-in feature of such phases is that their amplitude-distance curves have sharp maxima, which provides a mechanism for focussing energy without invoking source complexity. The PP and PPP families were prominent arrivals on the vertical seismograms recorded during the refraction survey in the Imperial Valley (McMechan and Mooney, 1980; Fuis et al., 1982). In Figure 14 we show a record section of self-scaled vertical accelerograms that have absolute time. The time scale and range are relative to the origin time and epicenter, respectively. The P-wave travel time from the hypocenter is shown as the dashed line. The PP travel time curve is the line connecting X's. The travel time curve of the PP phase has taken into account the time necessary for the rupture to propagate from the hypocenter into the sediments using the evolution depicted in Figure 13. The density of the X's is a good indicator of the amplitude. In the lower part of Figure 14 the paths of the geometrical rays that form the PP travel time curve are shown. Note that the source of the PP phase is at a depth of 4 km and 5.5 km north of the hypocenter. A subset of the P waves generated by a stress drop in the sediments reflects off the earth's surface. Because of the large gradient, these waves turn in the sediments, forming a caustic that manifests itself as large amplitude compressional motion over a very limited horizontal range. The strength of the PP phase and the short epicentral range at which it is observed directly result from the high gradient of the P-wave velocity in the sediments. The large amplitude, compared to direct P-waves, is due to structure and not a large stress drop.

IMP VALLEY P-WAVES,Z=4.,V=10000 PP

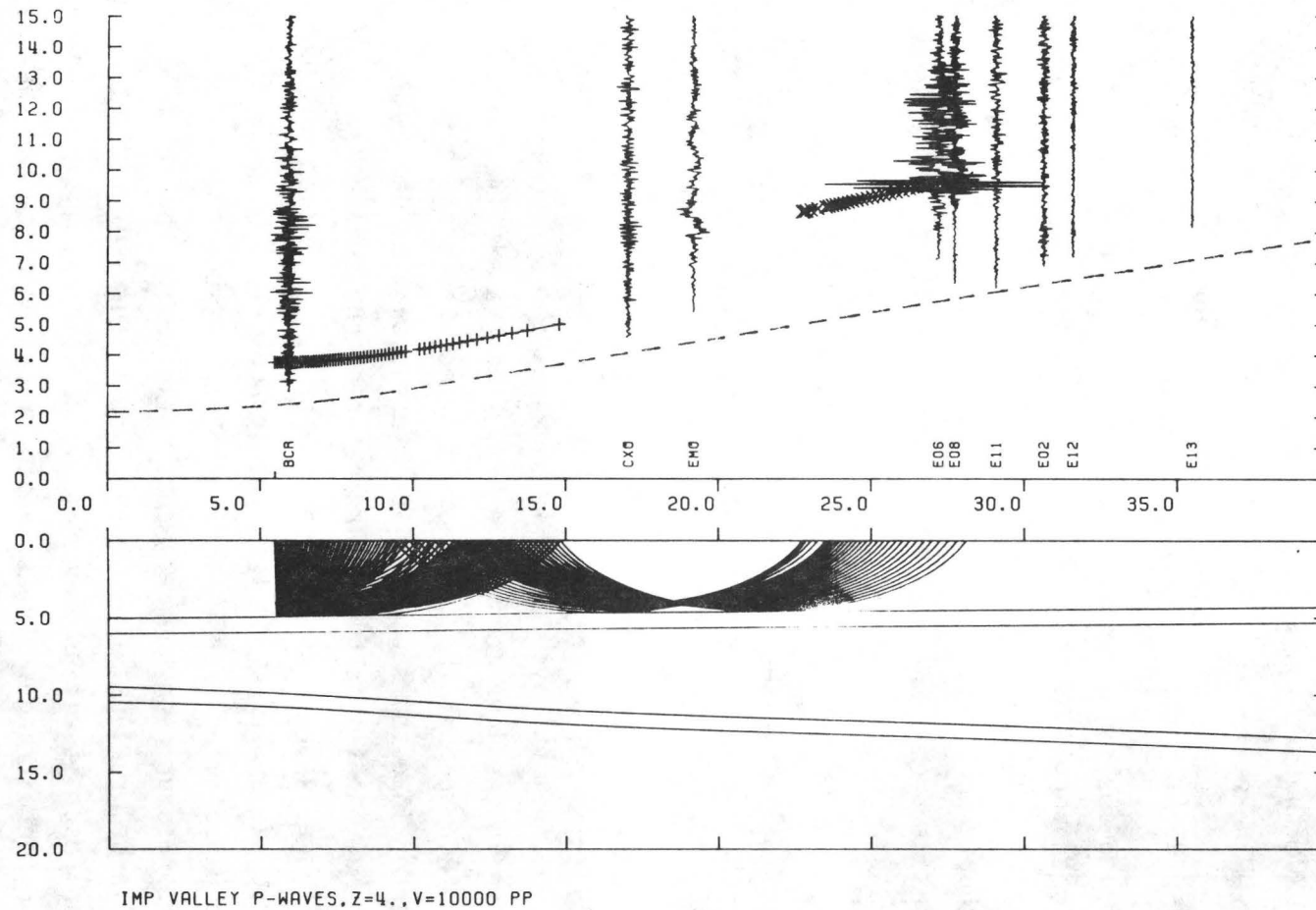Figure 14: A record section using vertical accelerations with absolute time
shows the travel time curve for a PP phase from a source 4 km deep and 5.5 km
north of the hypocenter. For reference the travel time curve of direct P from
the hypocenter is shown as the dashed line. The lower half of the figure is a
cross section of the Imperial Valley showing the geometrical ray paths
travelled by the PP phase.

Although the travel time is consistent with the data and our faulting scenario, and the flux of geometrical rays indicate large amplitudes, we have also used the method of Kind (1978) to construct synthetic vertical accelerograms from a point double-couple source with 75° dip located at 4 km depth in a velocity structure approximating the Imperial Valley structure (Figure 15). In this velocity structure we allowed the P-wave Q to rise linearly from 206 at the surface to 400 at and below 5 km depth. The S-wave Q was derived from the assumption that all attenuation arose from shear, leading to a S-wave Q which rose from 34 at the surface to 170 at and below 5 km depth. The ranges are all at an azimuth 13° counterclockwise off strike. Although there are many large amplitude phases present, mostly due to SP phases, the phase of interest is clearly seen at the ranges of 16 to 22 km. About 2 seconds after the direct P-wave is a large, simple, clean pulse that arrives before the direct S wave. This pulse is PP. Note its sudden growth in amplitude at 16 km epicentral range and its limited range of occurrence. It is these attributes which cause it to be a candidate for the LAVA's.

To see how PP fits naturally into the radiation, consider the following. The large vertical accelerations show up on only a few stations, but all with nearly the same hypocentral distance. The phase arrives after the first P waves but before the direct hypocentral S wave. Its amplitude is an order of magnitude greater than the first P phase, depending on azimuth. Now consider our scenario for faulting. The rupture nucleates at a depth of 8 km, a depth below the sediments. Since the rupture breaks the surface about 7.5 km north of the epicenter, it obviously propagates into the sediments some time after initiation. After the rupture penetrates the sediments about 5.5 km north of the hypocenter, PP phases are generated. As the rupture propagates toward the surface, PP phases from all depths are possible, but the caustic is more diffuse for sources at shallower depths. Once the rupture in the sediments is closer than about 16 km to any station, the PP phase will cease being observed.

Although the hypothesis that the PP phase is responsible for the large vertical accelerations reconciles most of the observations with theory, there are some conflicts for which we can offer only ad hoc explanations. Namely, once the rupture continues to propagate northward, stations such as E02 or E12 might be expected to fall into the critical range. Why then is there no obvious PP phase?

IV STR-SL DC, DIP=75, ZS=4 KM, AZ=-13.
VERTICAL COMPONENT

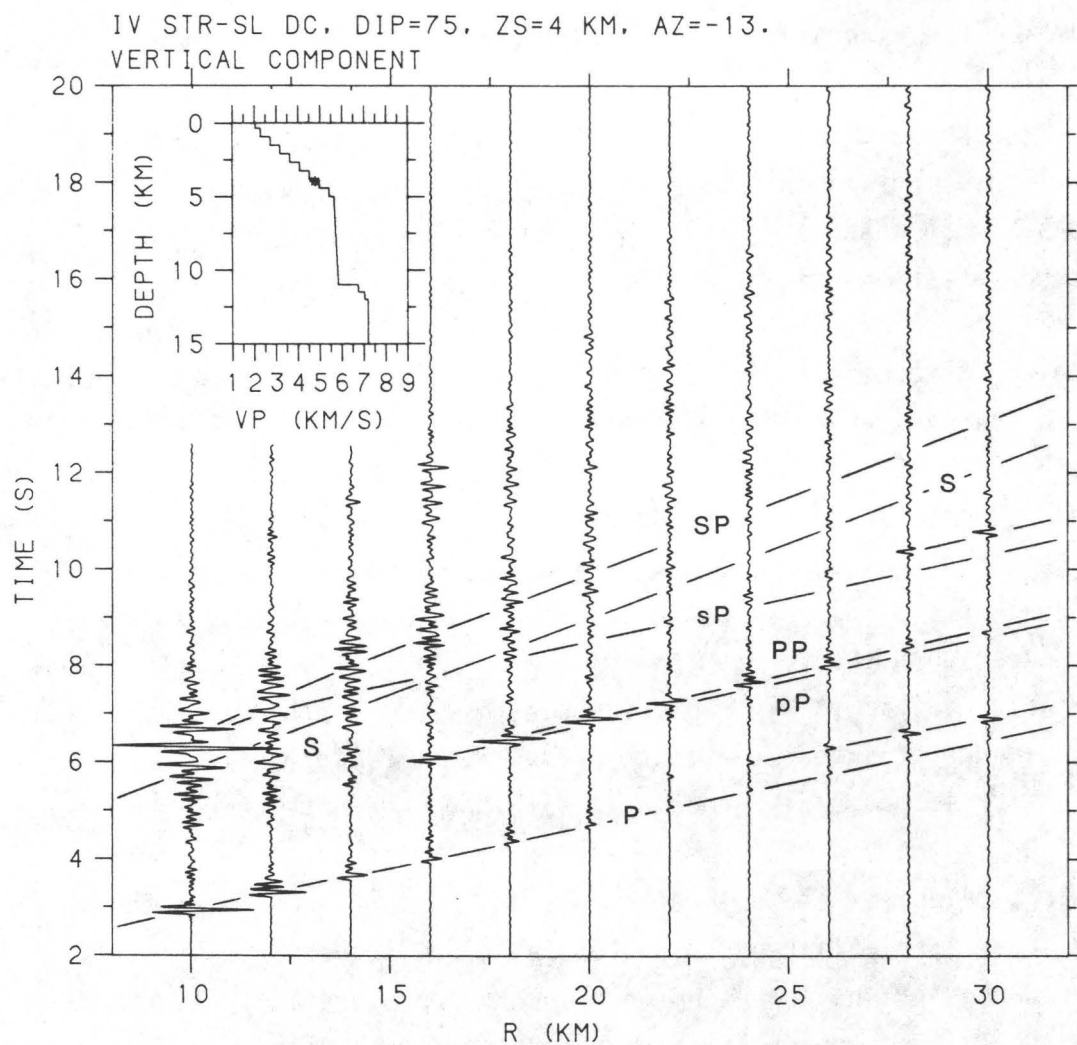Figure 15: A record section of synthetic vertical accelerations is made for a double-couple source with 75° dip at a 4 km depth. All ranges are at an azimuth 13° counterclockwise off strike of the double-couple. The synthetic accelerograms are computed for the frequency range 0-12 Hz. The P-wave velocity structure meant to approximate the velocity structure of the Imperial Valley is shown in the inset.

One possibility arises from the observation that the strength of the PP phase depends critically on the velocity structure not only at the source but also at its turning points. Since the sediments in the Imperial Valley are thinning as one moves either east or west of the fault (Fuis et al., 1982), it is possible that the P-waves reflected from the surface do not turn in the sediments for the stations more than 10 km off the fault. In short, if the velocity gradient is about the same everywhere but the sediment thickness thins as one moves away from the fault, then the turning points, which are necessarily at depths greater than or equal to the source, will not lie in the high gradient zone, and the PP phase will be very weak.

We have examined this possibility. Using a velocity structure in which the sediments thin from 5 km to 2 km over a distance of 40 km, a thinning consistent with the results of Fuis et al. (1982), we have used the ray tracing program to look at the dependence of the PP phase on such a velocity structure. First we found that in this structure the source, i.e., the location where the slip takes place, must be shallower than 4 km to produce a PP phase with turning points in the sediments. We also found that the presence of a dipping sedimentary layer reduced the range over which the PP phase exists from the 16-20 km range to a 14-16 km range with the most intense PP amplitudes at the closer distance. Using the median range of 15 km, stations E01, E02, E12 and E13 are entirely eliminated from recording PP. Stations E03, E11, BCR and CXO would be candidates only after the rupture was farther north than Meloland (EMO). EMO is always at a distance less than the range where PP can be observed. The vertical accelerogram at HVP does show an abrupt amplitude change that precedes the arrival of the S-wave from the hypocenter. HVP is at an epicentral distance where the geometric rays for PP will arrive but only for a short time because as the rupture moves north HVP will move out of the critical range. Because HVP is within the critical range for only a short period of time, the amplitude change on HVP might be expected to be less than that observed on other stations. The only two stations that might be expected to record a strong PP, but do not, are E04 and E10. The vertical accelerogram at E04 does show some high amplitudes preceding the arrival time of the S-wave although the amplitudes are not as pronounced as at E05. The accelerogram at E10, though, is totally devoid of any amplitudes

comparable to those recorded at EDA. The sediments are thinning as one moves in the direction of E04 and E10 but probably not enough to eliminate totally the expected PP phase. We are left with speculating that there is some path effect, unknown to us, that has eliminated the PP phase. This path effect could be subtle and local since the region on the fault that can generate an observable PP phase at E10 and E04 is only about 2 km in length. Once the rupture has passed through that region, stations E10 and E04 will be too close to the fault to record PP. Another factor that may be contributing to the non-observance of the PP phase is the amount of slip that is occuring in the sediments. If the distribution of surface slip mirrors the amount of slip occuring within the sediments, then the sourthern part of the fault will be the biggest contributor to the PP phase (Figure 16A). The combination of the thinning of the sediments east and west of the Imperial fault and the distribution of slip along the strike of the fault provides a reasonable explanation for why the PP phase might or might not be recorded.

STATIC MEASUREMENTS

Within 24 hours of the mainshock, measurements of right-lateral horizontal offsets and vertical offsets on the Imperial fault were started (Sharp et al., 1982). A secondary fault, the Brawley fault, showed primarily vertical offset of much smaller amplitude than the offsets on the Imperial fault (Sharp et al., 1982). The fault traces on which measurable offsets were recorded are shown in Figure 1. The Imperial fault continues along the strike shown (Figure 1) into Mexico. The epicenter is about 2.0 km south of the United States-Mexico international border (Archuleta, 1982), but the southernmost observed surface offsets (Figure 16A,B) were recorded about 5.0 km north of the international border. From the location of the epicenter and the places where surface slip was measured it is likely that the rupture propagated primarily northward from the epicenter, although Apsel et al. (1981), Olson and Brune (1981), and Olson and Apsel (this volume) give evidence for some southward propagation of the rupture at depth. Shown in Figure 16A the right-lateral offset on the Imperial fault about 160 days after
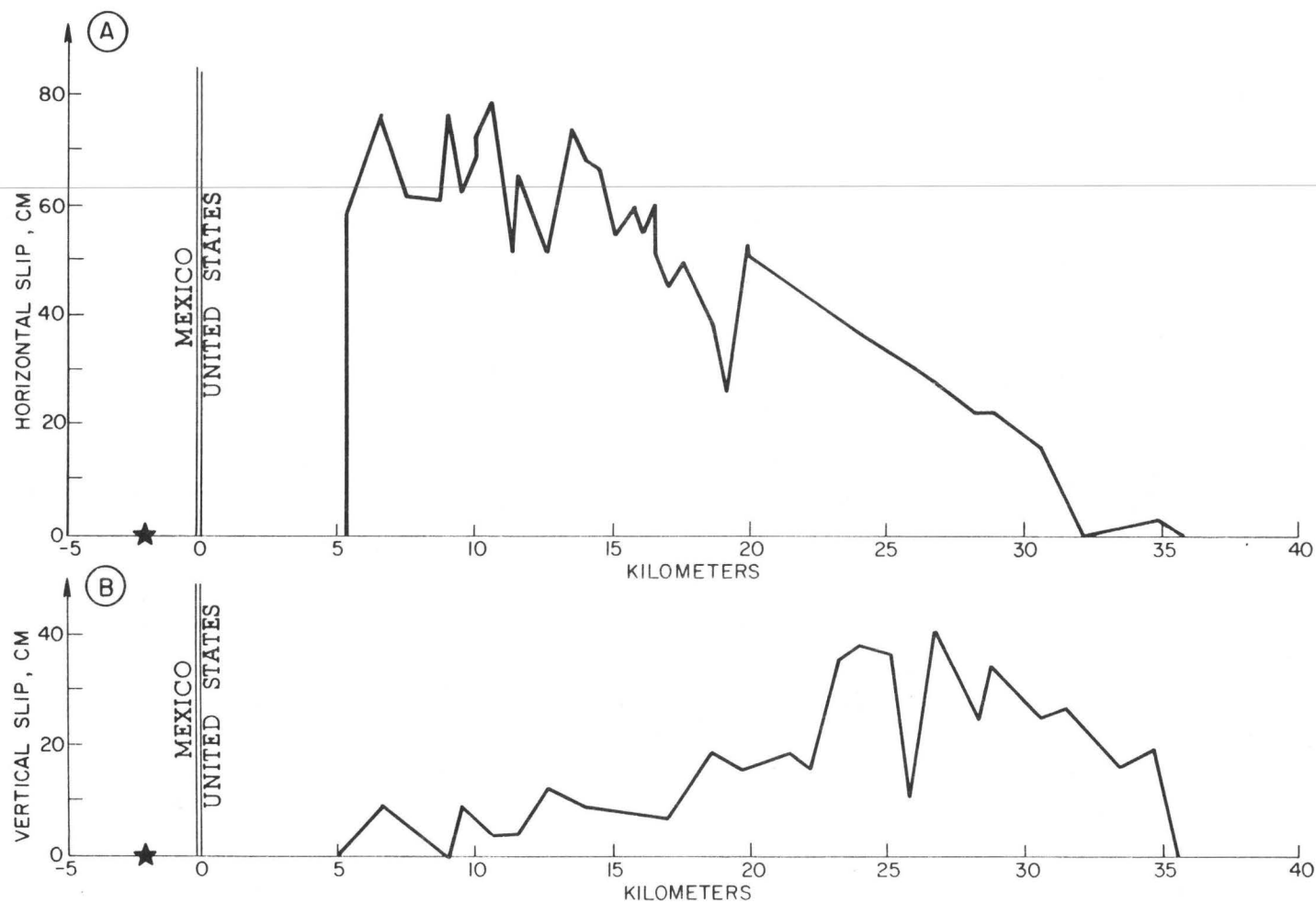
Figure 16: A. The amount of right-lateral horizontal slip measured about 160 days after the mainshock is plotted against distance along the Imperial fault. The epicenter is shown as the star south of the international border. B. The total vertical slip measured about 160 days after the mainshock.

the earthquake. Their was an almost logarithmic increase in the total offset following the coseismic offset (Sharp et al.,1982) similar to measurements after the 1966 Parkfield earthquake (Smith and Wyss, 1968). This post-seismic slip after the mainshock could be due to the release of near-surface strain concentrated by larger slip at greater depth (Archuleta and Day, 1980).

Vertical offsets were found along the entire surface break with the largest offsets near the northern terminus of the Imperial fault (Sharp et al., 1982) (Figure 16B). The existence of vertical offsets at the northern end of the Imperial fault from past earthquakes is obvious from a prominent scarp with the west side up by about 8 m relative to the east side (Sharp and Lienkaemper, 1982). Even though the Imperial fault is almost exclusively strike-slip, the vertical offsets are expected when one considers that the fault plane terminates at the northern end and it intersects the free surface (Chinnery, 1961).

The strong motion accelerograph array crosses the Imperial fault about 25 km north of the epicenter. This would place stations E06 and E07 about 18 km north of the international border (Figures 16A,BA). At the point on the Imperial fault closest to E06 and E07, the horizontal slip was 21 cm from measurements made about 3 days after the mainshock; at the same time the maximum horizontal slip was about 62 cm at 6 km north of the international border (Sharp et al.,1982). Although the amplitude of the horizontal slip increased with time, the distribution of slip measured within several days after the earthquake is very similar to the slip distribution shown in Figure 16A. An important feature of this slip distribution is that the continuous break extends at least 9 kms north of the stations E06 and E07. In addition to the horizontal offsets, the vertical offsets measured about 10 days after the mainshock show a distribution along strike almost identical to that shown in Figure 16B. The maximum vertical offset was 36 cm about 4 km north of E06 and E07. Based on the observed distribution of vertical offsets we would infer that the end of the faulting was also 4 km north of the strong motion stations (Chinnery, 1961). Regardless of the exact end of the faulting we think that the distibution of static measurements definitely support the idea that the rupture passed by E06 and E07.

Knowing that the Imperial Valley is not a uniform halfspace there is an open-ended question as to how much information about the seismic moment, static stress drop and strain drop can be deduced from the static offsets. As we progress in our discussion of these source parameters it will become clear that the uncertainty in the estimates of these parameters depends upon one's knowledge of the slip distribution at depth. The determination of a detailed slip distribution such as that given by Hartzell and Helmberger (1982) is beyond the scope of this paper. Although we may not have precise estimates of the source parameters, we can determine lower bounds which are useful in discussing some of the gross features of the faulting.

First we consider estimating the seismic moment M_0 from the horizontal slip. The seismic moment can be written as (Aki, 1966)

$$M_0 = \int \mu \, s \, dA \tag{1}$$

where μ is the shear modulus, s is the slip, dA is the incremental area and A is the total area of the fault. In order to approximate this integral a number of approximations must be made. Our first assumption is that the depth of faulting extends only to 10 kms. Historically seismicity on the Imperial fault has been located to depths of 9 to 11 kms (Fuis et al., 1978). Two aftershocks within minutes of the mainshock were located on the Imperial fault south of stations E06 and E07.; the M_L 3.8 aftershock has a depth around 5 km and the M_L 5.2 has a depth around 10 km (C. Mueller, personal communication). Furthermore the mainshock hypocenter is at 8 kms (Archuleta, 1982). Although we have no direct evidence that places a limit on the depth of faulting, we think 10 kms is a reasonable value. As alluded to above the length of faulting is also ill-determined. Based on the distance from the epicenter to the point of last measurable horizontal slip we find a length of 37.5 kms. If we select the point on the Imperial fault where both the horizontal slip and vertical slip are zero, we find a length of 34 kms. If we use the distribution of vertical offsets following models by Chinnery (1961), we would infer a length of 29 kms. All of these estimates ignore any faulting at depth south of the epicenter. However since the surface slip is entirely

north of the border, we will assume that the length of faulting at depth is 34 kms. For the shallow part of the fault we will assume a length of 27 kms based on the length of the continous break. Looking at the velocity profile (Figure 8) we divided the fault into two parts: (1) The first part extends from the surface to 5 kms depth. It has a length of 27 kms. Using the S-wave velocity profile we determined an average V_s^2 of 3.3 km^2/sec^2 which we multiplied by an assumed constant density of 2.7 gm/cm^3 to produce an average shear modulus of 0.9 X 10^{11} $dynes/cm^2$. (2) The second part of the fault extends from 5 kms to 10 kms depth with a length of 34 kms. In this region the S-wave velocity is almost constant (3.2 km/sec). Assuming a density of 2.9 gm/cm^3 we found an average shear modulus of 3.0 X 10^{11} $dynes/cm^2$. Since we have no direct means of inferring what the distribution of slip is with depth, we will first assume that the average surface slip of 40.5 cm (Sharp et al., 1982) is constant over the entire fault. The combined effect of all of these assumptions is to produce a lower bound for the seismic moment. Using these assumptions we approximate Equation 1 by

$$M_o = \mu_1 s_1 L_1 W_1 + \mu_2 s_2 L_2 W_2 \qquad (2)$$

where the subscript 1 applies to the shallow part of the fault and subscript 2 applies to the deep part of the fault with L the length and W the width. Using the values given above for each of the variables in Equation (2) we find

$$M_o = (0.5 + 2.0) X 10^{25} \text{ dyne-cm} \qquad (3)$$

$$M_o = 2.5 X 10^{25} \text{ dyne-cm} \qquad (4)$$

Even though this may be a crude estimate of the true seismic moment, this analysis indicates that the deeper part of the fault may have a significanly greater contribution to the near-source ground motion than the shallow part of the fault due to its larger area and shear modulus.

Comparing our lower bound estimate of seismic moment with that determined by other investigators we find that it is 2.4 times smaller than the estimate made by Kanamori and Regan (1982) using surface waves and 3.6 times smaller than the estimate made by Wyatt (1980) using strain steps at Pinon Observatory about 130 kms from the Imperial fault. Although our estimates of the length and depth of faulting may be imprecise, it is unlikely that we could realistically change these variables to account for a factor of 2 or 3. Although the shear modulii depend on the S-wave velocity structure, the major contribution to the seismic moment comes from the nearly homogeneous layer at depth where the assumed S-wave velocity is a rather typical value for crustal material. Some error in the average modulus for the shallow part of the fault may exist, however, it is unlikely to account for a factor of 2 or 3. The most likely source of the discrepany between the estimate of seismic moment determined from the static slip and the farfield estimates is the assumption that the average slip of 40.5 cm at the surface is valid at all depths. Let us consider two hypothetical slip distributions that are consistent with the farfield estimates of seismic moment. The first model has an average slip at all depths of 100 cm; the second model has a constant value of 40.5 cm in the upper 5 km of the fault and a constant value of 120 cm on the lower 5 kms of the fault. The first model has a seismic moment of 6.2×10^{25} dyne-cm; the second model has a seismic moment of 6.4×10^{25} dyne-cm. Of course, there is an infinite number of slip distributions that are consistent with the farfield estimate of seismic moment. The important point is that the average surface slip produces a lower bound that is only 2 to 3 times smaller than the estimates of seismic moment made by other means. In addition, it is clear that to the degree that the surface slip reflects slip in the shallow part of the fault, the deeper part of the fault is likely to play a significant role in the near-source dynamic ground motion.

Although the average surface slip measurements provide an estimate of the seismic moment which is an average property of the faulting, there is greater uncertainty about the usefulness of a static stress drop inferred from the average surface slip. As demonstrated in a theoretical study by Mavko (1982), different faults with the same average moment and the same average stress drop can have stress variations that differ by an order of magnitude from one fault

to the next. These stress variations arise from the fact that it is the derivative of the slip with respect to the depth coordinate that determines the local value of stress (Bilby and Eshelby, 1969; Mavko, 1982). Bearing in mind that large stress variations may exist and the effect of such variations can be important in determining the near-source particle motions (Boatwright, this volume; McGarr, this volume; Hartzell and Helmberger, 1982), the average static stress drop has its primary utility for comparison purposes with other large earthquakes whose stress drops are based on a similar analysis. The average static stress drop for a long strike-slip earthquake in a uniform halfspace is related to the average slip by (Kanamori and Anderson, 1975)

$$\sigma = 2 \mu s / \pi W \qquad (5)$$

where σ is the average static stress drop, μ is the shear modulus, s is the average slip and W is the width of faulting for the given average slip. Rather than use the average surface slip to estimate the static stress drop, we will use the average value of 100 cm which is consistent with the farfield seismic moment of Kanamori and Regan (1982). Since the 100 cm applies to the entire fault, the appropriate width is 10 kms. To determine an average shear modulus we first determined an average V_s^2 by integrating the V_s profile squared from 0 to 10 kms and dividing by 10 kms. Multiplying V_s^2 by 2.8 gm/cm^3 we estimate an average shear modulus of 1.9 X 10^{11} dynes/cm^2. Substituting these values into Equation 5 we find an average static stress drop of 12 bars. This estimate is consistent with the static stress drops of 5 to 10 bars determined by Hartzell and Helmberger (1982) and Archuleta and Sharp (1980) [A typographical error in the abstract of Archuleta and Sharp shows 54 bars when it should have been 5.4 bars.] However we can estimate the static stress drop in another way. Suppose we consider the hypothetical example in which the upper 5 km has a average displacement of 40.5 cm and the lower 5 kms has an average displacement of 120 cm. If we rewrite Equation 5

$$\sigma = 2 \mu_1 s_1 / \pi W_1 + 2 \mu_2 s_2 / \pi W_2 \qquad (6)$$

where the subscript 1 refers to variables in the upper 5 kms of the fault and

the subscript 2 refers to variables in the lower 5 kms of the fault, then we find that

$$\sigma = 5 \text{ bars} + 46 \text{ bars} \tag{7}$$

$$\sigma = 51 \text{ bars} \tag{8}$$

This estimate is considerably higher than the previous estimate. Although the different shear modulus used for each part of the fault has an influence, the primary reason that this estimate is much higher is due to the assumed width over which the slip is constant. Considering that the maximum particle velocities were on the order of 100 cm/sec and the maximum horizontal accelerations were on the order of 0.5 to 0.8 g, this estimate of 50 bars for the static stress drop may seem more likely than the estimate of 12 bars if we consider Brune's (1970) source model as an indicator of the amplitude of the near-source ground motion for a given stress drop. A better estimate of the average stress drop must be deferred to a later paper in which modelling of the near-source particle velocities can better define the slip distribution with depth.

Although the static stress drop estimate of 12 bars may be a lower bound on the actual average stress drop, this lower bound has important implications about the strain released during the mainshock. Using Hooke's law the strain drop is

$$\epsilon = \sigma / 2\mu \tag{9}$$

where ϵ is the strain drop, σ the average static stress drop and μ the average shear modulus. Using 1.9×10^{11} dynes/cm^2 for the average shear modulus and 12 bars for the average static stress drop, we find a lower bound for the strain drop of 32 μstrain. If one assumes that the 1940 El Centro earthquake ($M_s = 7.1$) relieved all of the tectonic strain when it ruptured this segment of the fault and a uniform shear strain buildup at a rate of 0.2 μstrain (Savage and Burford, 1970; Savage et al., 1981) for 39 years, the accumulated shear strain would be only 8 μstrain, four times smaller than a

lower bound estimate for the strain drop of the 1979 mainshock. Considering
that the average shear strain rate was 0.2 μstrain for the period 1941-1967
(Savage and Burford, 1970) and 0.25 μstrain for the period 1972-1978.9
(Savage et al., 1981), the assumption of uniform strain accumulation seems
reasonable. There is the possibility that something unusual occurred in the
period 1967-1971. The probable explanation for this discrepancy is that the
1940 earthquake did not relieve all the tectonic strain on the northern part
of the Imperial fault. Clear evidence of this possibility is the distribution
of slip following the 1940 earthquake (Figure 16 of Hartzell and Helmberger
(1981)) which shows over 250 cm of slip from the international border south
but only about 80 cm of slip on the same part of the Imperial fault that
ruptured in the 1979 earthquake. Even if the 1979 surface slip were added to
the 1940 slip, the slip deficit on the northern part of the Imperial fault
would still be about 2.5 times smaller than the slip that occurred for 20 km
south of the United States-Mexico border during the 1940 earthquake. It is
possible that south of the United States-Mexico border the slip that occurred
during the 1940 event better reflects the slip at depth, whereas based on the
earlier calculations of the seismic moment the surface slip in 1979 could be a
factor of two or three smaller than the slip at depth. Another possibility is
that there is still enough residual strain on the northern part of the
Imperial fault for another earthquake equal to or larger than the 1979 event
at any time.

SUMMARY

The 1979 Imperial Valley earthquake produced near-source data that is
unsurpassed in quality and quantity. The static offsets are well documented
(Sharp et al., 1982); the dynamic ground motion was well recorded (Brady et
al., 1980; Brune et al., 1982). This information together with the results of
a detailed refraction survey (Fuis et al., 1982; McMechan and Mooney, 1980)
have formed the basis for an interpretation of the gross features of the
mainshock mechanism.

Based on the hypocentral location (Archuleta, 1982) and surface offsets, we have presumed an entirely unilateral rupture. Although a unilateral rupture is consistent with the near-source strong motion records in the United States that we have analyzed, the strong motion records in Mexico (Brune et al., 1982) may require some faulting south of the hypocenter (Olson and Apsel, this volume; Apsel et al., 1981). By analyzing the particle velocities at stations E06 and E07 and by taking into account the shear wave velocity structure we deduced an average rupture velocity in the range 0.78-0.81 times the local shear wave velocity. Using a rupture velocity of 0.78 times the local shear wave velocity we depicted an evolution of faulting in Figure 13. This faulting scenario is consistent with one of the most interesting features of the 1979 Imperial Valley earthquake--the presence of large amplitude vertical accelerations.

Several stations recorded peak vertical accelerations on the order of 500-600 cm/sec^2 with station E06 recording a 1705 cm/sec^2 peak. The stations at which the large amplitude vertical accelerations were recorded are all at about the same hypocentral distance. The arrival time for this acceleration comes after direct hypocentral P-waves but before the direct hypocentral S-waves. From our examination of the near-source records and far-field seismograms, we found little evidence to support the proposal that the large amplitude vertical accelerations were caused by a concentrated stress drop (Hartzell and Helmberger, 1982). Instead most of the evidence supports the hypothesis that the local P-wave velocity structure is responsible for these accelerations. Once the rupture penetrated the sediments, those compressional waves that reflected off the free surface were turned by the P-wave gradient with the sediments thereby forming a ray caustic. This caustic provides the amplification to produce the large vertical accelerations.

Using the S-wave velocity profile, the hypocentral location of the mainshock, depths from seismicity, and the distribution of the static slip measurements we divided the fault into two parts: (1) between 0 and 5 km depth the length is 27 km with an average shear modulus of 0.9 X 10^{11} dynes/cm^2, (2) between the depth of 5 and 10 km the length is 34 km with an average shear modulus of 3.0 X 10^{11} dynes/cm^2. Using an average static offset of 40.5 cm, we determined a lower bound of 2.5 x 10^{25} dyne-cm for the seismic

moment. This estimate is 2.4 times smaller than the estimate based on surface waves (Kanamori and Regan, 1982) and 3.6 times smaller than the estimate based on observed strain steps (Wyatt, 1980). For the fault we have assumed the average slip would have to be about 100 cm to be consistent with the farfield estimates of seismic moment. Using 100 cm for an average slip we determined a lower bound on the static stress drop of 12 bars. We considered a second possibility in which the upper part of the fault had an average slip of 40.5 cm and the deeper part of the fault had an average slip of 120 cm. This model is also consistent with the farfield estimate of seismic moment, but the static stress drop for this model is 51 bars. Considering peak particle velocities of 115 cm/sec at EMO and 109 cm/sec at E06, the static stress drop of 50 bars may be a more reasonable estimate than 12 bars. As shown in Figure 16 the overall spatial distribution is more trapezoidal than elliptical. This distribution plus the fact that EMO has a larger peak particle velocity on the 230° component than E06 suggests that the stress drop was not uniform.

A lower bound estimate of the strain released by the 1979 mainshock is 32 µstrain. This strain drop is four times greater than the amount of strain that could have accumulated since the 1940 El Centro earthquake assuming a uniform strain accumulation of 0.2 µstrain per year (Savage and Burford, 1970; Savage et al., 1981). This estimate of 32 µstrain plus the distribution of slip following the 1940 earthquake (Hartzell and Helmberger, 1982) implies that the El Centro earthquake (M_S 7.1) did not relieve all of the tectonic strain on the northern part of the Imperial fault in 1940. The strain released by the 1979 earthquake was, in part, due to tectonic strain accumulated prior to 1940. The fact that the strain drop was at least four times greater than the strain that could have been accumulated, assuming a uniform strain rate, implies that while "time predictable" models (Shimazaki and Nakata, 1980) may apply to great earthquakes, such models may not apply to moderate sized, though damaging earthquakes.

Acknowledgments

REFERENCES

Aki, K. and P. G. Richards, 1980, Quantitative Seismology, Theory and Methods, W. H. Freeman and Co., San Francisco.

Aki, K., 1966, Generation and propagation of G waves from the Niigata earthquake of June 16, 1964. 2. Estimation of earthquake movement, released energy and stress-strain drop from G wave spectrum, Bull. of the Earthquake Res. Inst. 44, 23-88.

Anderson, J. G. and P. G. Richards, 1975, Comparison of strong ground motion from several dislocation models, Geophys. J. 42, 347-373.

Apsel, R. J., A. H. Olson, and G. A. Frazier, 1981, Numerical inversion for localized zones of energy release, Earthquake Notes 52, 79.

Archuleta, R. J., 1982, Hypocenter for the 1979 Imperial Valley, California, earthquake, accepted for publication in Geophys. Res. Letters.

Archuleta, R. J. and S. H. Hartzell, 1981, Effects of fault finiteness on near-source ground motion, Bulletin of the Seismological Society of America, 71, 939-957,.

Archuleta R. J. and R. V. Sharp, 1980, Source parameters of the Oct. 15, 1979 Imperial Valley earthquake from nearfield observations, EOS, 61, 297.

Archuleta, R. J. and S. M. Day, 1980, Dynamic rupture in a layered medium: the 1966 Parkfield earthquake, Bull. Seism. Soc. Am., 70, 671-689.

Archuleta, R. J., P. A. Spudich, and A. Olson, 1979, Synthetic seismogram studies of an aftershock of the 1979 Imperial Valley, California, earthquake, Earthquake Notes 50, 50.

Archuleta, R. J. and G. A. Frazier, 1978, Three-dimensional numerical simulations of dynamic faulting in a half-space, Bull. Seism. Soc. Am., 70, 541-572.

Ben-Menahem, A., 1962, Radiation of seismic body waves from a finite moving source in the earth, J. Geophys. Res. 67, 345-350.

Bilby, B. A. and J. D. Eshelby, 1969, Dislocations and the theory of fracture, in Fracture, Volume 1, Academic Press Inc., New York.

Boore, D. M. and J. B. Fletcher, 1982, A preliminary study of selected aftershocks of the 1979 Imperial Valley earthquake from digital acceleration and velocity recordings, U.S. Geological Survey Professional Paper No. 1254, The Imperial Valley earthquake of October 15, 1979, in press.

Brady, A. G., V. Perez, and P. N. Mork, 1980, The Imperial Valley earthquake, October 15, 1979. Digitization and processing of accelerograph records, U.S. Geological Survey Open-File Report 80-703, 1-309.

Brune, J. N., J. Prince, F. L. Vernon III, E. Mena, and R. S. Simons, 1982, Strong motion data recorded in Mexico during the October 15 mainshock, U.S. Geological Survey Professional Paper No. 1254, The Imperial Valley earthquake of October 15, 1979, in press.

Bycroft, G. N., 1980, El Centro California differential ground motion array, U. S. Geological Survey Open-File Report 80-919.

Cerveny, V., I. A. Molotkov, and I. Psencik, 1977, Ray method in seismology, Univerzita Karlova, Praha, 214 pp.

Chavez, D., J. Gonzalez, A. Reyes, M. Medina, C. Duarte, J. N. Brune, F. Vernon III, R. Simons, L. K. Hutton, P. T. German, and C. E. Johnson, 1982, Main-shock location and magnitude determination using combined United States and Mexican data, U.S. Geological Survey Professional Paper No. 1254, The Imperial Valley earthquake of October 15, 1979, in press.

Chinnery, M. A., 1961, The deformation of the ground around surface faults, Bull. Seism. Soc. Am., 51, 355-372.

Cranswick, E. and P. Spudich, 1981, What caused the large vertical arrivals observed in the 1979 Imperial Valley, California earthquake, EOS 62, 972.

Fuis, G. S., W. D. Mooney, J. H. Healy, G. A. McMechan, and W. J. Lutter, 1982, Crustal structure of the Imperial Valley region, U.S. Geological Survey Professional Paper No. 1254, the Imperial Valley earthquake of October 15, 1979, in press.

Fuis, G. S., C. E. Johnson and D. J. Jenkins, 1978, Preliminary catalog of earthquakes in the northern Imperial Valley October 1977-December 1977, U. S. Geological Survey Open-File Report 78-673.

Hartzell, S. and D. Helmberger, 1982, Strong motion modeling of the Imperial Valley earthquake of 1979, submitted to Bulletin of the Seismological Society of America.

Johnson, C. E., 1979, CEDAR--an approach to the computer automation of short-period local seismic networks; seimotectonics of the Imperial Valey of southern California, Ph.D. dissertation, California Institute of Technology, Pasadena, California, 1-343.

Julian, B. R., M. Zirbes, and R. Needham, 1982, The focal mechanism from the global digital seismograph network, U.S. Geological Survey Professional Paper No. 1254, the Imperial Valley earthquake of October 15, 1979, in press.

Kanamori, H. and J. Regan, 1982, Long-period surface waves generated by the 1979 Imperial Valley earthquake, U.S. Geological Survey Professional Paper No. 1254, the Imperial Valley earthquake of October 15, 1979, in press.

Kanamori, H. and D. L. Anderson, 1975, Theoretical basis of some empirical relations in seismology, Bull. Seism. Soc. Am. 65, 1073-1095.

Kind, R., 1978, The reflectivity method for a buried source, J. Geophys. 44, 603-612.

Madariaga, R., 1982, A string model for the high frequency radiation from earthquake faulting, U. S. Geological Survey Open-File Report , this volume.

Madariaga, R., 1977, High-frequency radiation from crack (stress-drop) models of earthquake faulting, Geophys. J. Roy. Astron. Soc. 51, 625-651.

Mavko, G. M., 1982, Easy computation of static stress drop, slip, and moment on 2-D heterogeneous faults, submitted to Bull. Seism. Soc. Am.

McMechan, G. A. and W. D. Mooney, 1980, Asymptotic ray theory and synthetic seismograms for laterally varying structures: theory and application to the Imperial Valley, California, Bulletin of the Seismological Society of America 70, 2021-2035.

Mueller, C. S. and D. M. Boore, 1981, Site amplification at El Centro strong motion array station No. 6, Earthquake Notes 52, 84.

Olson, A. H., 1982, Forward simulations and linear inversions of earthquake ground motions, Ph.D. dissertation, University of California, San Diego.

Olson, A. H. and R. J. Apsel, 1982, Finite faults and inverse theory with applications to the 1979 Imperial Valley earthquake, submitted to Bull. Seism. Soc. Am., this volume.

Olson, A. H., and J. N. Brune, 1981, Non-uniqueness in strong-motion modelling, Earthquake Notes 52, 78.

Raugh, M. R., 1981, Procedures for analysis of strong-motion records, Earthquake Notes 52, 17.

Sharp, R. V., J. J. Lienkaemper, M. G. Bonilla, D. B. Burke, B. F. Cox, D. G. Herd, D. M. Tiller, D. M. Morton, D. J. Ponti, M. J. Rymer, J. C. Tinsley, J. C. Yount, J. E. Kahle, E. W. Hart, and K. E. Sieh, 1982, Surface faulting in the central Imperial Valley, U.S. Geological Survey Professional Paper No. 1254, The Imperial Valley earthquake of October 15, 1979, in press.

Savage, J. C., 1966, Radiation from a realistic model of faulting, Bull. Seism. Soc. Am. 56, 577-592.

Savage, J. C., W. H. Prescott, M. Lisowski, and N. E. King, 1981, Strain accumulation in southern California, 1973-1980, Journal of Geophysical Research 86, 6991-7001.

Savage, J. C. and R. O. Burford, 1970, Accumulation of tectonic strain in California, Bulletin of the Seismological Society of America 60, 1877-1896.

Shannon and Wilson, Inc. and Agbabian Associates, 1976, Geotechnical and strong motion earthquake data from U. S. accelerograph stations, 1, report NUREG-0029, prepared for the N. R. C..

Shimazaki, K. and T. Nakata, 1980, Time-predicatable recurrence model for large earthquakes, Geophys. Res. Lett., 7, 279-282.

Spudich, P. and E. Cranswick, 1982, Use of near-source seismic-array data to reveal details of the earthquake rupture process, Earthquake Notes   , .

Spudich, P., 1981, Frequency domain calculation of extended source seismograms, EOS, 62, 960.

Smith, S. W. and M. Wyss, 1968, Displacement on the San Andreas fault subsequent to the 1966 Parkfield earthquake, Bulletin of the Seismological Society of America 58, 1955-1973.

Switzer, J., D. Johnson, R. Maley, and R. Matthiesen, 1981, Western hemisphere strong motion accelerograph station list-1980, U. S. Geological Survey Open-File Report 81-664.

Wyatt, F., 1980, Theoretical and observed surface deformations due to a distant earthquake, EOS 61, 211.

Table 1

Selected Strong Motion Stations in the United States and Mexico

Station	Code	Latitude(N) (Deg. Min.)	Longitude(W) (Deg. Min.)	Trigger[+] Time (Min:Sec)	Epicentral Distance (Km)	Azimuth[++] (degree)
*Aeropuerto	APO	32 39.00	115 19.80	NAT	0.93	140.0
Bonds Corner	BCR	32 41.56	115 20.25	16:57.11	3.88	- 29.6
*Islas Agrarias	AGR	32 37.25	115 18.07	16:56.88	4.96	173.0
*Mexicali	MEX	32 37.20	115 25.20	NAT	9.45	76.8
Calexico	CXO	32 40.16	115 29.49	16:58.87	15.18	45.4
**Meloland	EMO	32 46.38	115 26.88	16:59.70	16.86	1.0
Holtville	HVP	32 48.71	115 22.59	NAT	17.59	- 25.6
*Chihuahua	CHI	32 29.00	115 14.20	16:59.32	21.31	164.2
*Compuertas	COM	32 34.80	115 5.40	NAT	24.11	-151.2
Differential Array	EDA	32 47.83	115 32.11	NAT	24.63	11.3
EC Array 6	E06	32 50.36	115 29.20	17:01.40	24.90	- 3.9
EC Array 4	E04	32 51.93	115 25.91	17:01.78	24.91	- 17.5
EC Array 7	E07	32 49.77	115 30.26	NAT	25.06	0.7
EC Array 5	E05	32 51.33	115 27.93	17:01.39	25.31	- 9.9
EC Array 8	E08	32 48.63	115 31.94	17:00.62	25.39	8.3
EC Array 9	E09	32 47.75	115 32.92	NAT	25.54	13.3
EC Array 10	E10	32 46.82	115 33.98	NAT	25.96	18.5
*Cerro Prieto	CPO	32 25.52	115 18.34	16:58.84	25.97	-145.0
**Imp'l County Center	ICC	32 47.57	115 33.81	NAT	26.49	15.7
EC Array 3	E03	32 53.63	115 22.82	NAT	26.58	- 29.8
EC Array 11	E11	32 45.12	115 35.68	17:00.48	26.89	27.2
EC Array 2	E02	32 54.96	115 21.85	17:01.18	28.79	- 33.6
EC Array 12	E12	32 43.07	115 38.24	17:01.48	29.54	37.1
EC Array 1	E01	32 57.59	115 19.17	17:02.24	33.49	- 41.7
EC Array 13	E13	32 42.54	115 40.96	17:02.45	33.51	40.4
*Delta	DEL	32 21.37	115 11.70	17:01.39	35.86	160.7
*Cucapah	CUC	32 18.30	115 19.92	NAT	39.23	139.7
Brawley	BRA	32 59.30	115 30.54	17:03.54	40.29	- 15.40
*Victoria	VIC	32 17.40	115 6.00	NAT	46.23	167.8

[+] All times are for 23 hour October 15, 1979 GMT. NAT - No Absolute Time.

[++] The angles are degrees measured from the strike of the fault N40°W. Positive angles are counterclockwise; negative angles are clockwise.

* Strong motion stations operated jointly by the Instituto de Ingeneria, Universidad Nacional Automa de Mexico and the institute of Geophysics and Planetary Physics, Scripps Instituion of Oceanography, University of California, San Diego.

** Strong motion stations operated by the California Division of Mines and Geology.

STRONG MOTION MODELING OF THE
IMPERIAL VALLEY EARTHQUAKE OF 1979

Stephen Hartzell*

Donald Helmberger

Seismological Laboratory, 252-21
California Institute of Technology
Pasadena, California 91125

Revised October 22, 1981

Present address: U.S. Geological Survey, MS-77, 345 Middlefield Road,
Menlo Park, California 94025

Abstract

Twelve three-component strong-motion displacement records are modeled for the 1979 Imperial Valley earthquake to recover the distribution of slip on the Imperial fault plane. The final model, for which point source responses are calculated by a discrete wavenumber/finite element technique, uses a structure with gradients in material properties rather than layers. The effects of a velocity gradient are investigated by comparing synthetics with a layer-over-a-half-space model using generalized rays. It is shown that a uniform fault rupture model on a rectangular fault plane does not explain the data. The preferred fault model has slip concentrated below 5 km (in the basement material) and between the epicenter (5 km south of the international border) and Highway 80. Within this region there appears to be two localized areas of larger dislocations; one just north of the border near Bonds Corner and a second under Interstate 8 at Meloland Overpass. A major arrival associated with large amplitude vertical accelerations (up to 1.7 g) is identified in the El Centro array records. This arrival has an S-P time of approximately 2.3 sec at many of the array stations and is modeled as originating from a localized source 8 km to the south of the array. The moment is estimated to be 5.0×10^{25} dyne-cm from the strong-motion records, which is consistent with teleseismic body-wave estimates. The preferred fault model is strike-slip with a 90° dip. The average strike is 143°. However, to explain vertical waveforms near the fault trace a corrugated or wiggly fault plane is introduced. The average rupture velocity is in the range 2.5 to 2.7km/sec (0.8 to 0.9 times the basement shear wave velocity). The preferred model has unilateral rupture propagation to the north, although the data would allow a small amount of propagation to the south. The estimated stress drop for the entire fault plane is only 5 to 10 bars; however, the stress drop over the more localized sources is about 200 bars. The fault model is consistent with the pattern of seismicity and observations of aseismic creep in the Imperial Valley and suggests that the southern half of the Imperial fault acts as a locked section which breaks periodically.

Introduction

This paper presents results on the modeling of strong ground-motion displacement records for 12 of the near-source stations for the October 15, 1979 Imperial Valley earthquake (M_L=6.6). The main objective of the work reported on here is to determine the general distribution of slip which occurred on the Imperial fault during the October 15 earthquake. Generalized ray theory with the Cagniard-de Hoop technique is used to calculate displacements for point shear dislocations for a layer-over-a-half-space model. These results are compared with displacements calculated using a discrete wavenumber/finite element approach for a vertical velocity gradient model. With both techniques the point shear dislocation responses are summed to form a finite fault. We are primarily concerned with modeling the near-source displacement. However, our analysis also offers some constraints on the possible origin of the unusually high-amplitude accelerations recorded near the Imperial fault. The measured surface offsets and the distribution of aftershocks are also considered and discussed in terms of the preferred fault model.

The origin time of the 1979 Imperial Valley earthquake is 23hr16min 54.5 sec with an epicenter of 32.63°N, 115.33°W, or approximately 5km south of the international border (Brady et al. 1980). The estimated focal depth is 12 km. However, the above values are sensitive to the choice of velocity structure and the distribution of stations. Archuleta and Spudich (1981) have obtained the following estimates: origin time 23hr16min54.4sec, epicenter 32.66°N 115.33°W, depth 8.0km. The surface-wave moment is estimated to be 6.0 x 10^{25} dyne-cm from long-period Love and Rayleigh waves at Berkeley and Pasadena, and 7.0 x 10^{25} dyne-cm from an average of seven IDA station Rayleigh waves at 200-250 sec (Kanamori and Regan, 1982). The 1979 Imperial Valley earthquake is not particularly large compared to other recent Southern California events: the 1968 Borrego Mountain earthquake, M_0 = 11.2 x 10^{25} dyne-cm (Burdick and Mellman, 1976), and the 1971 San Fernando earthquake, M_0 = 8.6 x 10^{25} dyne-cm (Langston, 1978). However, it is a very significant event because of the rich set of strong-motion accelerograms recorded at close distances, and the largest peak accelerations recorded to date of 1.7 g.

The remainder of this paper is divided into four sections. The first section contains a qualitative investigation of the amplitude distribution and relative patterns of the strong-motion data, as a prelude to quantitative calculations. The second section discusses the finite-fault modeling technique. The third section presents and discusses several models of faulting. Here we make use of the qualitative observations made in the first section. In the final section the preferred fault model is discussed in terms of the faulting patterns and the apparent mode of strain release in the Imperial Valley.

Qualitative Investigation of the Strong-Motion Data

Before becoming involved in the specifics of deterministic finite-fault models, we first look at the strong-motion data set in an overall, qualitative manner. When using involved, finite-fault computer codes, it is possible to convince oneself incorrectly that certain fault parameters are well-constrained, simply because a match is made between synthetic ground motion

and the observations. This pitfall exists because of the non-uniqueness of the solution and is also true if one relies on a poorly constrained inversion. Therefore, we wish to first gather as much insight from the data as possible before attempting to model it.

Figure 1 is a map of the southern Imperial Valley showing the surface traces of the Imperial and Brawley faults and the locations of strong-motion instruments of interest here. Additional records obtained at stations further to the north and south (not in Figure 1) are much lower in amplitude. Stations numbered 1 through 13 comprise the El Centro strong-motion array and will be referred to as the array stations. Epicenters for both the 1979 and 1940 Imperial Valley earthquakes are indicated by stars. Similarities and differences between these two events will be discussed in the final section.

During the 1979 earthquake, ground breakage occurred on both the Imperial and Brawley faults. Surface faulting on the Imperial fault is primarily right lateral with maximum offsets of 60 to 70 cm on the section of the fault extending 5 to 10 km north of the border (Sharp et al., 1982). As one moves further north, the magnitude of the surface offsets decreases. Near the northern end of the Imperial fault at Harris Road on the periphery of Mesquite Lake, surface faulting is primarily normal with the east side down. There are no surface offsets in the epicentral region or within 5 km of the international border. Offsets on the Brawley fault are mainly normal with the west side down, and secondary in amplitude to those on the Imperial fault.

Figure 2 compares horizontal velocities from the 230° components of the array stations. Five pairs of records are shown, each comparing stations laying on opposite sides of the Imperial fault, and at approximately the same distance from the fault (Figure 1). The 230° component is approximately transverse to the Imperial fault. For strike-slip motion on the Imperial fault, the 230° component is dominated by SH motion. There is a high degree of correlation between waveforms in Figure 2 and thus symmetry in the SH radiation across the Imperial fault. Two inferences can be made from this observation. First, slip on the Brawley fault cannot be an important factor in the observed strong-ground motion. If the contribution from the Brawley fault were significant, the above symmetry would not exist. We do not consider further here motion on the Brawley fault, other than to speculate in the final section that it might be sympathetic or induced slip. Secondly, since a maximum in the SH radiation pattern lies along the fault strike for a strike-slip mechanism, the 230° component "sees" the entire fault plane of the Imperial fault. Unlike the vertical and radial components, the 230° component is not strongly sensitive, except for a distance effect, to any particular segment of the fault plane. Then, given the simplicity and uniformity of the SH waveforms, their general shape can be explained by a simple Haskell fault model. However, the good symmetry in the SH waveform on the 230° component is not carried over to the P-SV waveforms on the 140° and vertical components. Thus, there are added complexities not explained by a Haskell model.

Further insight into the faulting complexities can be obtained by considering the peak amplitudes. Peak SH velocities are plotted in Figure 3 for the array stations as a function of distance from the Imperial fault. There is asymmetry in the SH amplitude pattern. Amplitudes on the NE side of the fault are significantly higher than those on the SW side. For a strike-slip fault with a strike equal to the average trend of the surface trace of

the Imperial fault (N143°E); the pattern in Figure 3 should be symmetric about zero. (We assume here that the fault dip is not significantly different from 90°. Analysis of teleseismic records indicates that a dip less than 75° is unlikely (Gordon Stewart, personal communication, 1981)). It is possible to explain the asymmetric SH pattern by a different strike on part or parts of the Imperial fault at depth. Of course, there are alternative explanations. Local amplification due to lateral heterogeneity may be a factor. However, P-wave amplitudes offer some supportive evidence for the varying strike hypothesis. P-wave radiation should be nearly nodal along the strike of the Imperial fault (array stations 6 and 7) for a predominantly strike-slip mechanism. But, P-wave amplitudes on the vertical component are maximum near the strike of the fault (see Figure 4). A simple fault plane with a constant strike and a strike-slip mechanism cannot explain these data.

An indication of the depth of faulting is possible from a cursory investigation of the vertical strong motion. In Figure 4 vertical velocity records are plotted as a function of distance from the closest section of the trace of the Imperial fault. The first ten seconds of each record is dominated by body waves (P and SV). The waveforms spread out in time by only a small amount in moving from the trace of the Imperial fault out to a distance of 9 km. The limited dispersion indicates that the major portion of faulting occurred deep, perhaps below 5 km. Although variable in thickness, the top 5 km of the Imperial Valley appears to be sediments, possessing a strong velocity gradient. The basement below 5 km has a relatively constant velocity down to about 12 km (Fuis et al., 1982). The change in seismic velocities at 5 km is undoubtedly correlated with a change in structure and/or composition but may also be correlated with a change in the way accumulated strain is released. This point will be discussed in a later section in the context of the preferred fault model.

Figure 5 takes a closer look at the strong motion from one particular array station, #7. Station 7 is about 1 km from the trace of the Imperial fault and is representative of the other array stations. The first trace in Figure 5 is the acceleration, corrected for the response of the instrument. The second trace is the ground motion viewed through an alternate instrument. The alternate instrument record is obtained by first deconvolving the response of the recording instrument from the acceleration and then convolving with the response of another single-degree-of-freedom, simple, damped, harmonic oscillator. The free period of 5 sec and faction of critical damping of 0.7 of the new instrument are chosen to yield records at displacement periods. The advantage of this form of processing over the standard parabolic baseline, Ormsby filtering, is that noncausal first motions are eliminated. Figure 6 compares three forms of processing; standard Ormsby, alternate instrument, and direct trapezoidal rule integration of the acceleration. Note the noncausal first motions with the standard processing. It should also be noted that direct integration works well for this record, but is not useful for records with a greater amount of long-period drift. In such cases a baseline correction is necessary.

Station 7 clearly triggered on low amplitude accelerations that have very little corresponding longer period energy (Figure 5). These low amplitudes last for about 2 sec, at which point there is a major arrival on the vertical component. This arrival is characterized by a pulse-like vertical displacement and near-field P type long-period displacements on the horizontal

the Imperial fault (N143°E); the pattern in Figure 3 should be symmetric about zero. (We assume here that the fault dip is not significantly different from 90°. Analysis of teleseismic records indicates that a dip less than 75° is unlikely (Gordon Stewart, personal communication, 1981)). It is possible to explain the asymmetric SH pattern by a different strike on part or parts of the Imperial fault at depth. Of course, there are alternative explanations. Local amplification due to lateral heterogeneity may be a factor. However, P-wave amplitudes offer some supportive evidence for the varying strike hypothesis. P-wave radiation should be nearly nodal along the strike of the Imperial fault (array stations 6 and 7) for a predominantly strike-slip mechanism. But, P-wave amplitudes on the vertical component are maximum near the strike of the fault (see Figure 4). A simple fault plane with a constant strike and a strike-slip mechanism cannot explain these data.

An indication of the depth of faulting is possible from a cursory investigation of the vertical strong motion. In Figure 4 vertical velocity records are plotted as a function of distance from the closest section of the trace of the Imperial fault. The first ten seconds of each record is dominated by body waves (P and SV). The waveforms spread out in time by only a small amount in moving from the trace of the Imperial fault out to a distance of 9 km. The limited dispersion indicates that the major portion of faulting occurred deep, perhaps below 5 km. Although variable in thickness, the top 5 km of the Imperial Valley appears to be sediments, possessing a strong velocity gradient. The basement below 5 km has a relatively constant velocity down to about 12 km (Fuis et al., 1982). The change in seismic velocities at 5 km is undoubtedly correlated with a change in structure and/or composition but may also be correlated with a change in the way accumulated strain is released. This point will be discussed in a later section in the context of the preferred fault model.

Figure 5 takes a closer look at the strong motion from one particular array station, #7. Station 7 is about 1 km from the trace of the Imperial fault and is representative of the other array stations. The first trace in Figure 5 is the acceleration, corrected for the response of the instrument. The second trace is the ground motion viewed through an alternate instrument. The alternate instrument record is obtained by first deconvolving the response of the recording instrument from the acceleration and then convolving with the response of another single-degree-of-freedom, simple, damped, harmonic oscillator. The free period of 5 sec and faction of critical damping of 0.7 of the new instrument are chosen to yield records at displacement periods. The advantage of this form of processing over the standard parabolic baseline, Ormsby filtering, is that noncausal first motions are eliminated. Figure 6 compares three forms of processing; standard Ormsby, alternate instrument, and direct trapezoidal rule integration of the acceleration. Note the noncausal first motions with the standard processing. It should also be noted that direct integration works well for this record, but is not useful for records with a greater amount of long-period drift. In such cases a baseline correction is necessary.

Station 7 clearly triggered on low amplitude accelerations that have very little corresponding longer period energy (Figure 5). These low amplitudes last for about 2 sec, at which point there is a major arrival on the vertical component. This arrival is characterized by a pulse-like vertical displacement and near-field P type long-period displacements on the horizontal

components. The waveforms in Figure 5 suggest that this arrival is a P-wave from a later and larger break. The location of this break may not be near the hypocenter, although at this point in the analysis the location is indeterminate. However, it is possible to measure S-P times from the array station records as is done in Figure 5 for Station 7. The results are given in Table I. The times in Table I are relative to the trigger time of each instrument and have been taken from records processed similarly to those in Figure 5. The average S-P time is about 2.3 sec with no systematic increase for stations further from the fault. These results suggest a source significantly to the south of the array stations.

The salient features which have been deduced from a qualitative investigation of the strong motion data are summarized below.

(1) The overall SH waveform pattern at the array stations suggests that the rupture occurred to first order as a simple Haskell fault.

(2) Asymmetry with respect to the Imperial fault of SH amplitudes and the large P-wave amplitudes along the strike of the Imperial fault imply complexities in faulting not explained by a simple planar Haskell model.

(3) Coherence of vertical velocities and apparent lack of strong surface waves implies that most of the faulting occurred deep (possibly below 5 km).

(4) The array stations triggered on low amplitude accelerations followed about 2 sec later by a much larger amplitude impulsive arrival, possibly originating from a region of great slip north of the hypocenter, but south of the array stations.

Description of Finite Fault Modeling Technique

In this section we digress briefly from our analysis of the strong-motion records to explain the modeling technique employed in the following section. The method is the same as that used by Heaton and Helmberger (1979) in their study of the 1971 San Fernando earthquake. A finite fault is modeled by summing the contributions of a regular gridwork of point shear dislocation,

$$\underline{U}(t) = \sum_{j=1}^{n} \sum_{k=1}^{n} m_{jk} \underline{Y}_{jk}(t) * \dot{D}(t).$$

Here $\underline{U}(t)$ is the displacement at a station, j is the jth source along the fault strike, k is the kth source down the fault dip, m_{jk} is the moment, $\underline{Y}_{jk}(t)$ is the step function response of the j,k^{th} source, and $\dot{D}(t)$ is the derivative of the time history of slip on the fault.

The point shear dislocation responses, $\underline{Y}_{jk}(t)$, were first computed using a single layer-over-a-half-space structure, the solid curves in Figure 7. The top layer is intended to represent 5 km of sediments. This structure was chosen since the required Green's functions could be computed simply and inexpensively using generalized ray theory (Helmberger and Harkrider, 1978; Heaton, 1978). However, after computing several finite-fault synthetics, it became clear that this simple structure was inadequate to explain the

observations. The refraction work reported by Fuis et al. (1982) shows that the upper 5 km of the Imperial Valley has a pronounced velocity gradient. This gradient is probably due to the lithification of sediments and has the effect of greatly steepening the angle of incidence at the free surface. Although a velocity gradient may be approximated using many layers, the computation of Green's functions using generalized ray theory becomes quite tedious and expensive. The second velocity structure considered includes this velocity gradient and is shown in Figure 7 by the dashed curves. The P-wave velocities are based closely on the refraction results of Fuis et al., (1982). The S-wave velocities are obtained by assuming a Poisson solid ($b = a/\sqrt{3}$) below a depth of 5 km and varying smoothly to $b = a/2.37$ at the surface (R. Archuleta and P. Spudich, personal communication, 1981). Green's functions for this gradient structure are computed using the Discrete Wavenumber/Finite Element program (DWFE) of Olson (1978) which is similar to the finite difference method of Alekseev and Mikhailenko (1979, 1980). In the next section we compare finite-fault synthetics for the layer over a half-space structure with the Fuis et al. velocity gradient structure.

Examples of the functions $\int \underline{Y}_{ik}(t)dt$ are shown in Figures 8 and 9 for the layer-over-a-half-space structure using generalized rays. The 230° component is shown at 5° off the strike of a vertical strike-slip fault. The motion is primarily near-field P and SH. The full Cagniar solution is used for sources at small ranges where it is important to accurately compute near-field terms and static effects. At larger ranges an asymptotic form of the solution can be used without introducing significant error. For the layer-over-a-half-space structure it was found that accurate computation of near-field waveforms requires the full Cagniard solution for point sources at ranges $r < 3$ km and angles $x > 45°$, where $x = \arctan(\frac{d}{r})$, d being the source depth. The generalized ray paths considered are shown in the upper right-hand corner of Figures 8 and 9. The discrete wavenumber/finite element method computes the total wavefield up to a specified frequency. There is no consideration of rays. Both near- and far-field terms are included with this method and the solutions are accurate in frequency content from zero hz. Examples of the functions $\underline{Y}_{ik}$ for the velocity gradient structure in Figure 7 computed with the discrete wavenumber/finite element method are shown in figure 10. The Green's functions in Figure 10 have been computed to a frequency of 2 hz, which is sufficient for modeling ground displacmenet. The 230°, 140°, and vertical components of displacement are shown at 5° off the strike of a vertical strike-slip fault. Some of the waveforms in Figure 10 show high-frequency oscillations which are a product of terminating the calculation at 2 hz. These oscillations do not affect our results since they have random arrival times and are smoothed out in the process of forming a finite fault.

Whether the $\underline{Y}_{ik}$ functions are calculated using the generalized ray method or the discrete wavenumber/finite element method the response of a finite fault is constructed in the same manner. A master set of Green's functions is computed for a sufficient number of ranges and depths (many more than are shown in Figures 8, 9, and 10) such that spatially adjacent Green's functions do not vary greatly in wave shape. Then for a given station location and fault geometery, the required Green's functions are interpolated from the master set to uniformly cover the fault plane. The interpolation is accomplished by lining up adjacent records on the S-wave arrival time and using a simple linear interpolation scheme (Heaton and Helmberger, 1979;

845

Hartzell et al., 1978). The gridwork spacing is continually reduced with more and more interpolated point sources until there is no further change in the sum, $\underline{U}(t)$. For the displacement synthetics in this study the final interpolated point source spacing used is no greater than 0.5 km both along the strike and down the dip of the fault.

Fault Models

This section presents several finite-fault models and discusses the synthetics obtained by the techniques outlined in the previous section. In the accompanying figures generalized ray synthetics are labeled GR and discrete wavenumber/finite element synthetics are labeled DWFE.

Uniform Rupture Model

The simplest and logically the first finite-fault model that should be investigated is a uniform rectangular fault. In this model each of the weights on the fault plane, m_{jk}, is set equal to one. Thus the moment contribution from each point on the fault is the same. Figure 11 compares synthetics for this model with the observed displacements for the three stations EL7 (El Centro array station #7), DIF (El Centro differential array), and BOC (Bonds Corner). (See Figure 1 for station locations). The epicenter is 32.63°N, 115.33°W (about 5 km south of the international border) with a hypocenter at a depth of 10.5 km. The rupture is unilateral to the north with a constant velocity of 2.7 km/sec or about 0.9 the shear wave velocity of the basement material. A circular rupture front advances from the hypocenter until it fills a rectangular region 32 km long and 10.5 km wide. The mechanism is strike-slip with a 90° dip. The strike is 143° clockwise from north (the average trend of the surface trace of the southern half of the Imperial fault). $D(t)$ is assumed to be constant over the fault plane and approximated by a triangle with a one-second duration.

Figure 11 shows synthetics for two different velocity structures; generalized ray solution for the layer-over-a-half-space model, labeled GR, and discrete wavenumber/finite element solution for the velocity gradient model, labeled DWFE. For stations near the fault trace, like EL7, the vertical synthetics for both velocity structures are dominated by the P-wave from the section of the fault lying at 45° to the station (P-wave radiation pattern maximum). The 230° component is approximately transverse to the fault and situated at an SH radiation pattern maximum for most of the fault plane. SH waves originating from the fault plane between the hypocenter and the station pile up on one another and interfere constructively in a directivity effect. After the rupture passes the station, the wavefronts are defocused, producing dispersed, long-period wavetrains of much lower amplitude. Therefore, the P-wave pulses on the vertical components are narrow because they come from a very limited area of the fault plane, and the SH waveforms are relatively narrow and simple in form because of directivity. These considerations also explain the small S-P time of only about one second for the EL7 synthetics. The larger S-P time of about 2.3 sec for the data indicates complexity not explained by a uniform rupture model.

Consider now station BOC. Although BOC lies off the fault trace it also experiences a directivity effect resulting in impulsive waveforms for both velocity models. In the case of BOC it is a vertical directivity. There is constructive addition for P and S waves that originate between the hypocenter and the surface. This vertical directivity may be partly responsible for the large accelerations recorded at BOC (770 cm/sec^2 on 230° component). However, again we note that the simple, smooth rupture model does not yield the complexities in the data. For both EL7 and BOC the synthetic waveforms (but not amplitudes) for the two velocity models are similar. For station DIF, which is further from the fault and not subject to strong directivity, the differences between the two velocity models are more apparent. The layer-over-a-half-space structure is still dominated by body-waves, whereas the velocity gradient structure has a well-developed, later-arriving surface-wave. The surface-waves are, however, significantly stronger than in the data, indicating as we concluded earlier that an important percentage of the faulting occurred deep.

The amplitudes in Figure 11 are based on a moment of 5.0×10^{25} dyne-cm. The velocity gradient structure yields SH amplitudes about a factor of two larger than those for the layer-over-a-half-space structure. Since the angle of incidence at the free surface does not affect the amplitude of SH waves, the above observation is easily traced to the difference in near-surface rigidities. The steeper angle of incidence in the velocity gradient structure tends to polarize the P-wave onto the vertical component and the SV-wave onto the 140° component. Thus, the vertical and 140° components are amplified by both the lower rigidity and the steeper incident angle. Finally, the uniform rupture model produces amplitudes which are too large (for a moment of 5.0×10^{25} dyne-cm), again indicating that more of the faulting must have occurred at depth.

Layer-Over-Half-Space Fault Model

It is instructive to discuss one finite-fault model which uses the layer-over-a-half-space velocity structure despite this model's shortcomings, since by investigating other velocity models we obtain a better understanding of the effects that a particular structure has on strong-ground motion. Figure 12 shows contoured dislocation in meters on the Imperial fault plane assuming a moment of 5.0×10^{25} dyne-cm for three different models. Model 51 was obtained using the layer-over-a-half-space structure. Models 8 WM and 9 WM were obtained using the velocity gradient structure and are discussed later. The dip of the fault plane for model 51 is 90°, rake 180° (right-lateral strike-slip), epicenter 32.63°N 115.33°W, hypocenter at a depth of 10.5 km, and unilateral rupture to the north at 3.0 km/sec. Before switching to the velocity gradient structure, model 51 was considered the best fitting solution to a subset of 5 of the strong-motion stations shown in Figure 13.

Although the synthetics in Figure 13 do not fit the observed displacements particularly well, model 51 still has several of the general characteristics of the presently preferred model, 9 WM. Most of the faulting occurs in the basement material below the sediments, there is an area of larger dislocations south of the El Centro array but north of the border, and the distribution of surface offsets is generally consistent with the observations. The region of larger dislocations below a depth of 5 km is included in model 51 to produce the previously noted arrival at the array

847

stations having an S-P time of about 2.3 sec (see Table I). But since the
layer-over-a-half-space structure gives shorter S-P travel times for a given
range compared with the velocity gradient structure, this region of greater
slip is misplaced in model 51. Using the velocity gradient structure the area
of larger dislocations shifts to the north, to under Interstate 8, leaving
behind a broader region of relatively large fault offsets (i.e. model 9 WM).
The strike of the fault is not constant in model 51. To model the previously
mentioned large P-wave amplitudes at array stations lying near the fault
strike, the region of larger dislocations in model 51 is given a strike of
155° (see Figure 12). The remainder of the fault plane has a strike of 143°,
consistent with the trend of the surface trace.

Two synthetics are shown in Figure 13 for station BOC, one with and one
without a foreshock. Station BOC seems to be modeled better with the addition
of a magnitude 5 foreshock at the hypocenter of the main shock and preceding
the main rupture by 2.0 seconds. This conclusion is also supported by the
models run with a velocity gradient. However, the term foreshock is used
rather loosely here. The actual faulting process may only involve a variable
rupture velocity; intially high, then low, then high again for the remainder
of the fault plane. The vertical components at stations DIF, EL7, and MEL for
Model 51 have large SV components (labeled in Figure 13). This SV phase is
not seen in the data. Using the Fuis et al. gradient structure, the SV phase
is shifted off the vertical component and onto the 140° component. The
synthetic labeled DWFE in Figure 13 for station EL7 uses the gradient
structure. However, there is still a large phase, labeled P_b, on the vertical
component. P_b is a P wave originating from much closer to the station where
the P-wave radiation pattern is a maximum. Obviously model 51 still does not
achieve the correct P-wave radiation distribution.

Velocity Gradient Fault Model

The preceding discussions were included in part to motivate the reasoning
which led to the presently preferred fault model, model 9 WM in Figure 12.
The model parameters are listed in Table II. Synthetics for model 9 WM are
compared with the observed displacements in Figures 14a and b, where again we
assume a triangular shaped $\dot{D}(t)$ with a one second duration. In general the
waveforms and amplitudes are fit quite well. However, the predicted
horizontal ground motion for the two stations very near the fault strike (EL7
and MEL) is too large. This discrepancy may be due to scattering and rupture
incoherencies that are not in our model. The fault plane has a strike of 143°
except for the region under station MEL, where the fault strike is varied to
produce an 'S' shape or corrugated pattern when viewed from above (see Figure
12). This complexity has been added to produce the P-waveform at EL7 and is
not strongly required or excluded by the other stations. The vertical
synthetic for MEL is missing a leading up and down swing suggesting that a
similar wiggle in the fault plane exists for the region of larger dislocations
just north of the border. In general, stations like EL7 and MEL are not
particularly useful in recovering the distribution of slip. They are too
close to the fault and therefore too sensitive to subtle changes in fault
parameters. BOC is a much more useful station. A very diagnostic array would
have stations parallel to the fault at about 5 km from the surface trace. The
localized source south of the border and just above the hypocenter in model 9
WM (see Figure 12) is a foreshock preceding the main rupture by 2.0 sec. The
moment of the foreshock is 1.0×10^{24} dyne-cm ($M_L = 5.3$). As mentioned

earlier this may not be a foreshock in the usual sense of the word. Of the stations modeled, BOC is the only one requiring the foreshock since the foreshock's displacements are very small at the other station. However, the 2.25 sec of low level accelerations following triggering of the array stations (see Figure 5) may be due partly to this foreshock.

One question of interest is how much of the observed surface slip occurred coseismically and how much occurred as sympathetic creep? Models 9 WM and 8 WM are very similar except for the amount of slip allowed in the sediments north of Interstate 8 (or station MEL). These two models produce very nearly the same displacements at all 12 stations modeled except for the two closest, EL7 and MEL. Two vertical synthetics are shown in Figure 14 for station EL7, one for model 9 WM and the other for 8 WM. The differences are not large. The data are insensitive to the exact distribution of shallow faulting as long as it is small. The data are compatible with all of the shallow surface faulting north of MEL occurring as creep. The data is also rather insensitive to the amount of deep faulting north of the El Centro array. Because the rupture on this section of the fault plane propagates away from most of the stations, the resulting amplitudes are low. However, the amount of faulting north of the array must be small compared to the amount south of the array.

The synthetics in Figure 14 are for a rupture velocity of 2.5 km/sec or about 0.8 of the basement shear wave velocity. However, the synthetics do not change a great deal when a rupture velocity of 2.7km/sec (0.9 of the basement shear wave velocity) is used. So we are limited in the resolution of the average rupture velocity to 2.5 - 2.7 km/sec. Although our preferred model uses a unilateral rupture to the north, the data we have modeled would also allow a small amount of rupture to the south. Finally, we note that most of the vertical synthetics in Figures 14a and b appear as if they would match the observations better if they were shifted to the left a small amount. This discrepancy in phasing is attributed to an incorrect Poisson ratio in the sediments, although this interpretation is subject to considerable uncertainty. Therefore, at this stage of modeling we have placed a greater emphasis on fitting the SH and P-wave portions of these motions. We adopted this position because of the strong interference between P and SV arrivals starting at the SV onset. The time separation between these arrivals is controlled by the rupture process and crustal structure. The latter structure is not well known since most refraction studies are done with P-waves. A better appreciation of the importance of shallow velocity structure on the various components of motion awaits the many aftershock studies now in progress such as Liu and Helmberger (1980).

Discussion

An important question to be asked of any fault model derived from near-field strong-motion records is how well does the moment compare with the teleseismic body-wave moment? The teleseismic body-wave moment is certainly an important datum, and the moment obtained from a near-field study should not be greatly different. Short of modeling the teleseismic body waves for the Imperial Valley earthquake, we can make a simple comparison to answer the above question. The 1968 Borrego Mountain earthquake has a similar mechanism and location to the 1979 Imperial Valley earthquake. Figure 15 compares rotated S waves (radial and transverse components) from selected WWSSN

stations for these two events. The waveforms are amazingly similar at a wide range of azimuths except for amplitude differences. The moment of the Borrego Mountain earthquake from a study of teleseismic body waves is 1.12×10^{26} dyne-cm (Burdick and Mellman, 1976). From Figure 15 it is clear when we neglect nodal components that the Imperial Valley earthquake runs consistently a factor of two smaller than the Borrego Mountain earthquake. The moment of 5.0×10^{25} dyne-cm for Imperial Valley determined in this study is very consistent with the above data. The fact that SV (radial components) is also proportionately smaller for Imperial Valley than for Borrego Mountain indicates that there is not significant normal faulting associated with the Imperial Valley earthquake.

In model 9 WM major faulting initiates at the surface and at depth just north of the border. This characteristic of the model is consistent with the observed surface faulting. Figure 16 compares the measured surface offsets for the 1979 and 1940 Imperial Valley earthquakes. The 1979 curve is based on work by Sharp et al. (1982). The 1979 offsets are zero in the epicentral region and remain so until about 5 km north of the border. At this point there is an almost step-like discontinuity, with the offsets rising to their maximum values of 60 to 70 cm. The 1940 curve is based on unpublished field notes of J. P. Buwalda and is less accurate than the 1979 curve. The 1940 event apparently ruptured primarily to the south from an epicenter about 10 km north of the border (see Figure 1). However, there is a prominent increase in the surface offsets for the 1940 earthquake in the same area as the abrupt decrease in offsets for the 1979 earthquake. Both of these rapid changes in surface offsets lie above the region of large dislocations just north of the border in model 9 WM. Hartzell (1978) modeled the El Centro displacement record for the 1940 Imperial Valley earthquake by summing aftershock records. In that study the aftershock records are treated as empirical Green's functions. It was found that a reasonable fit could be obtained to the El Centro record if the earthquake is treated as four separate events. Three of these events and the aftershock used to represent their ground motions are situated in the same general region as the localized large dislocation source 3 km north of the border in model 9 WM. Thus, this same region of the fault plane was apparently also important in 1940.

Figure 17 shows aftershock epicenters for the first 26 days following the October 15, 1979 earthquake (Johnson and Hutton, 1982). The vast majority of aftershocks occur at the very northern end of the observed ground breakage and extend further to the north. A clear exception to this pattern is the obvious pocket of aftershocks located north of the border but south of El Centro. The depths of several of these aftershocks were accurately determined by Peter German of the USGS at Caltech. All the events considered consistently fall at a depth of 8.5 ± 0.5 km. Referring to model 9WM (Figure 12), the pocket of aftershocks plots between the two maxima in dislocation in the distance range of 12 to 15 km north of the epicenter. These aftershocks may represent a readjustment to the strain field created by the flanking larger dislocations.

The large amplitude vertical accelerations recorded at the array stations are coincident in time with pulses on the vertical displacement records. The relationship is clearly seen in Figure 5 for station EL7. The same is true for station EL6 which recorded a peak vertical acceleration of 1.7g. In this paper the vertical displacement pulses at the array stations are explained by

characterized by an occasional large event, such as the 1940 and 1979 earthquakes, with creep on just the northern half of the fault. Most of the dislocation in model 9WM is concentrated on the aseismic section. The southern half of the Imperial fault apparently acts as a locked section that breaks violently. The comparison of models 9 WM and 8 WM showed that faulting north of the El Centro array is largely insignificant and may have occurred as creep. There are numerous observations of creep on the northern half of the Imperial fault and the Brawley fault (see Johnson, 1979, for a summary). In particular, surface cracks reported along the Brawley fault during the 1975 swarm, which appear very similar to those following the 1979 earthquake, are attributed to aseismic creep (Sharp, 1976; Johnson and Hadley, 1976). Model 9 WM is therefore consistent with the observed seismicity pattern and our best estimates of the mode of strain release in the Imperial Valley.

Acknowledgments

TABLE I

TIMES AT THE EL CENTRO ARRAY STATIONS

STATION	P (Vertical)	SH (Horizontal)	t (s-p)
7	2.27	4.55	2.28
6	1.36	3.64	2.28
8	2.55	5.18	2.63
5	2.18	5.09	2.91
DIF	2.55	4.91	2.36
4	2.45	4.73	2.28
3	4.18	6.18	2.00

TABLE II

MODEL PARAMETERS FOR FAULT MODEL 9 WM

Strike	143° clockwise from north, with 'corrugations'
Dip	90°
Rake	180° (right-lateral, strike-slip)
Moment	5.0×10^{25} dyne-cm
Rupture Velocity	2.5 km/sec, unilateral to the north
Epicenter	32.63°N, 115.33°W
Depth	10.5 km

References

Alekseev, A. S. and B. G. Mikhailenko (1979). Numerical modelling of transient wave fields in seismology and seismic prospecting (Vertically inhomogeneous half-space and radially inhomogeneous sphere), Siberian Branch of the Academy of Sciences of the USSR, Novosibirsk.

Alekseev, A. S. and B. G. Mikhailenko (1980). Solution of dynamic problems of elastic wave propagation in inhomogeneous media by a combination of partial separation of variables and finite difference methods, Journ. of Geophys. (submitted).

Archuleta, R. J. and P. Spudich (1981). A seismological analysis of the acceleration generated by the 1979 Imperial Valley, California earthquake, IASPEI meeting, London, Ontario.

Brady, A. G., V. Perez, and P. N. Mork (1980). The Imperial Valley earthquake, October 15, 1979, digitization and processing of accelerograph records, U.S. Geological Survey open-file report 80-703, Menlo Park, California.

Burdick. L. J. and G. R. Mellman (1976). Inversion of the body waves from the Borrego Mountain earthquake to the source mechanism, Bull. Seism. Soc. Am., 66 1485-1499.

Ebel, J. and D. V. Helmberger (1981). P-wave complexity and fault asperities: The Borrego Mountain, California, earthquake of 1968, Bull. Seism. Soc. Am., in press.

Eshelby, J. D. (1957), The determination of the elastic field of an ellipsoidal inclusion and related problems, Proc. Roy. Soc. London, Series A, 241, 376-396.

Fuis, G. S., W. D. Mooney, J. H. Healy, G. A. McMechan, and W. J. Lutter (1982). Crustal structure of the Imperial Valley region, in U.S. Geological Survey Prof. Paper No. 1254, Menlo Park, California.

Hartzell, S., G. A. Frazier, and J. N., Brune (1978). Earthquake modeling in a homogeneous half-space, Bull. Seism. Soc. Am., 68, 301-316.

Hartzell, S. (1978). Earthquake aftershocks as Green's functions, Geophys. Res. Lett., 5, 1-4

Heaton, T. H. (1978). Generalized ray models of strong ground motion, Ph.D. Thesis, California Institute of Technology, Pasadena, California.

Heaton, T. H. and D. V. Helmberger (1979). Generalized ray models of the San Fernando earthquake, Bull. Seism. Soc. Am., 69, 1311-1341.

Helmberger, D. V. and D. Harkrider (1978). Modeling earthquakes with generalized ray theory, in Modern Problems in Elastic Wave Propagation, J. Miklowitz and J. D. Achenbash, editors, John Wiley and Sons, New York.

Johnson, C. E. and D. M. Hadley (1976). Tectonic implications of the Brawley earthquake swarm Imperial Valley, California, January, 1975, <u>Bull. Seism. Soc. Am.</u>, 66, 1133-1144.

Johnson, C. E. (1979). I.CEDAR - An approach to the computer automation of short-period local seismic networks II. Seismotectonics of the Imperial Valley of Southern California, Ph.D. Thesis, California Institute of Technology, Pasadena, California.

Johnson, C. E. and K. Hutton (1982). Aftershocks and prior seismicity of the 1979 Imperial Valley earthquake of 1979, in U.S. Geological Survey Prof. Paper No. 1254, Menlo Park, California.

Kanamori, H. and J. Regan (1982). Long-period surface waves generated by the Imperial Valley earthquake of 1979, in U.S. Geological Survey Prof. Paper No. 1254, Menlo Park, California.

Keilis-Borok, V. (1959). On estimation of the displacement in an earthquake source and of source dimensions, <u>Ann. Geofis. (Rome)</u>, 12, 205-214.

Knopoff, L. (1958). Energy release in earthquakes, <u>Geophys. J.</u>, 1, 44-52.

Langston, C. A. (1978). The February 9, 1971 San Fernando earthquake: A study of source finiteness in teleseismic body waves, <u>Bull. Seism. Soc. Am.</u>, 68, 1-29.

Liu, Hsui-Lin and D. Helmberger (1980). S83, An explanation for high frequency vertical strong motions recorded in sedimentary basins, <u>EOS</u>, 61, 1036.

Mueller, C. S. and D. M. Boore (1981). Site amplification at El Centro strong motion array station #6, <u>Earthquake Notes</u>, 52, 84.

Olson, A. H. (1978). Synthesizing ground motion using a discrete wavenumber/finite element representation, <u>Trans. Am. Geophys. Un.</u>, 59, 1128.

Sharp, R. V. (1976). Surface faulting in Imperial Valley during the earthquake swarms of January - February 1975, <u>Bull. Seism. Soc. Am.</u>, 66, 1145-1154.

Sharp, R. V. <u>et al</u>. (1982). Surface faulting in central Imperial Valley, in U.S. Geological Survey Prof. Paper No. 1254, Menlo Park, California.
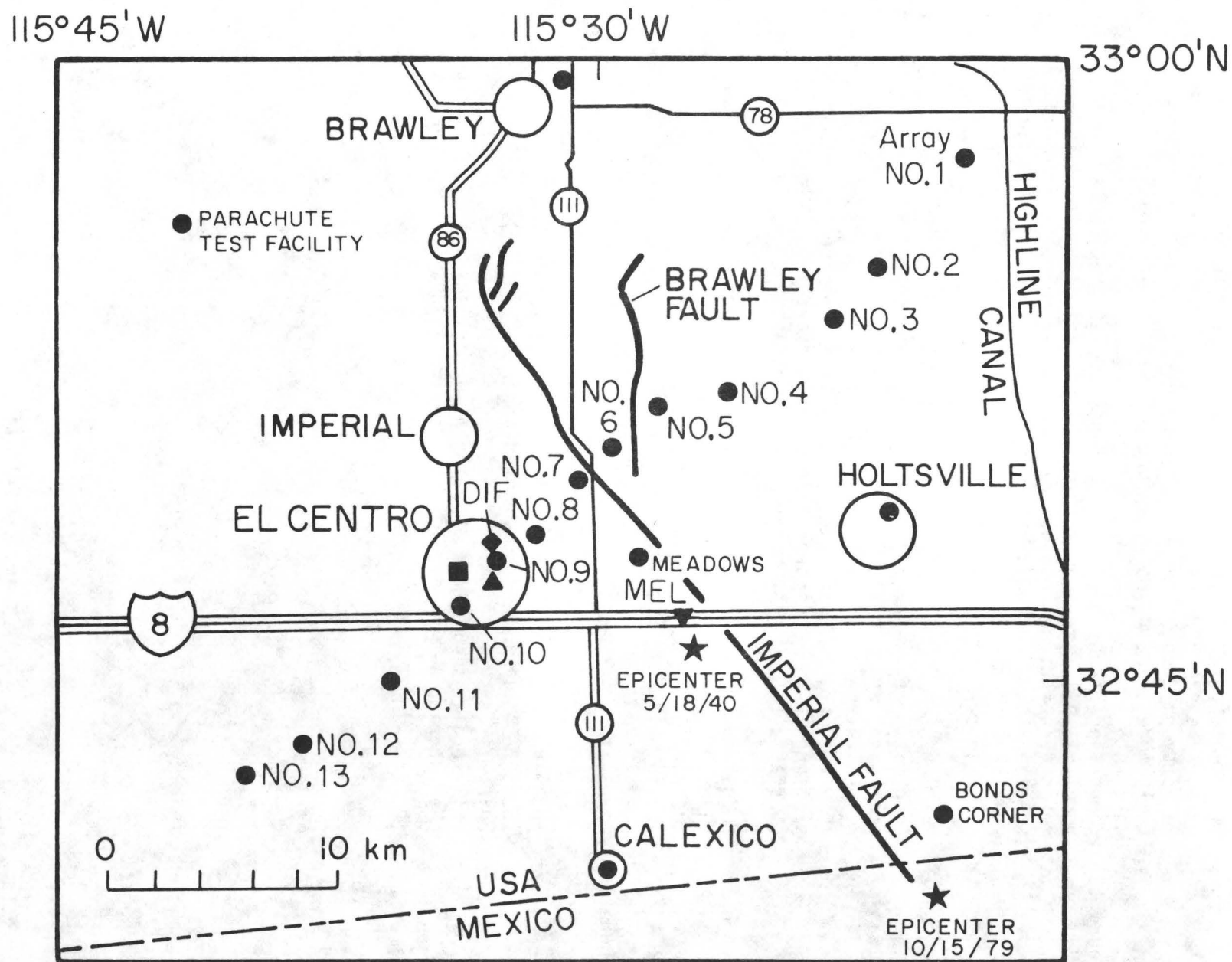
FIGURE CAPTIONS

Figure 1   Area map of the southern Imperial Valley showing the surface traces of the Imperial and Brawley faults and the locations of strong motion instruments. The El Centro array is numbered 1 through 13.
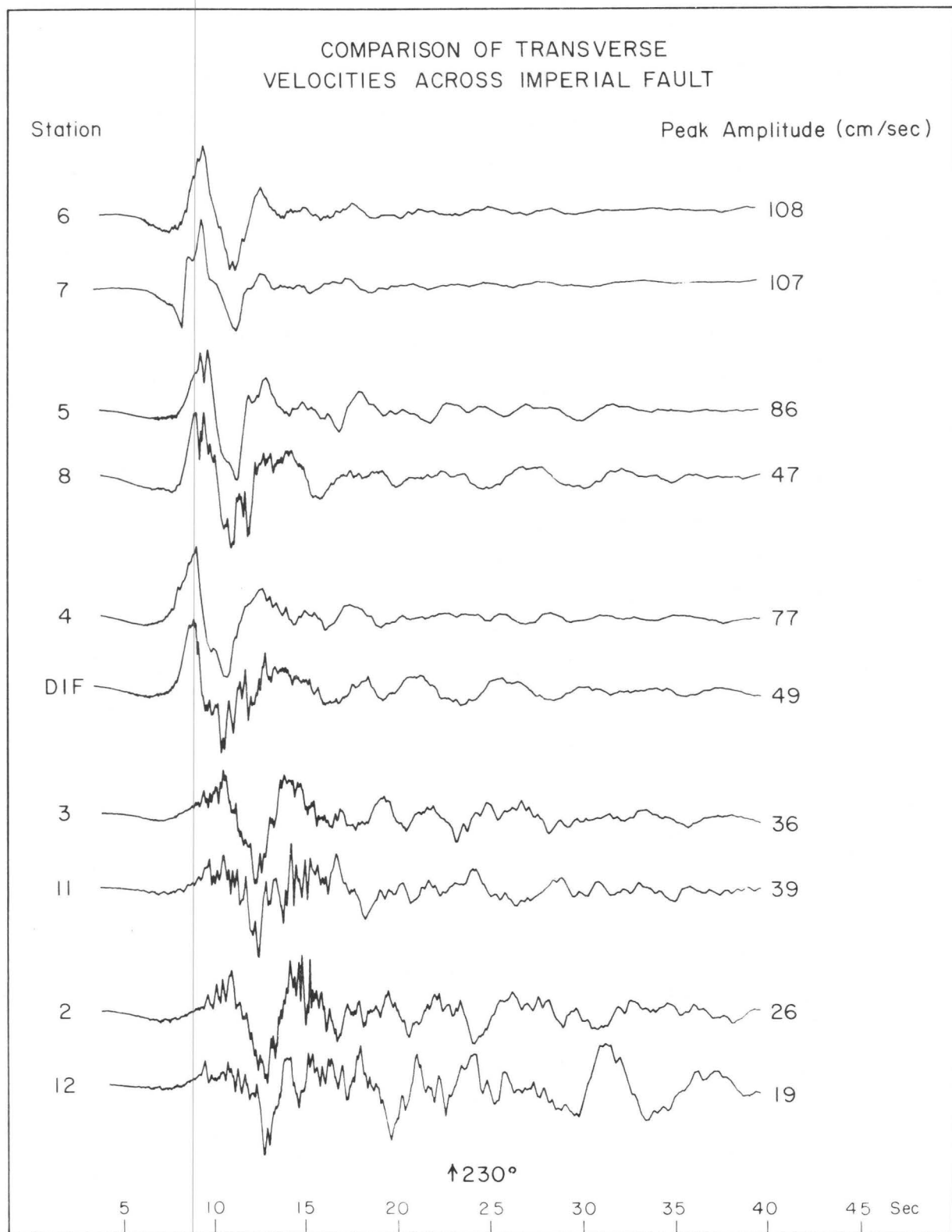
Figure 2   Comparison of transverse (SH) velocities from the El Centro array for pairs of stations on either side of the Imperial fault and approximately the same distance from the fault trace.
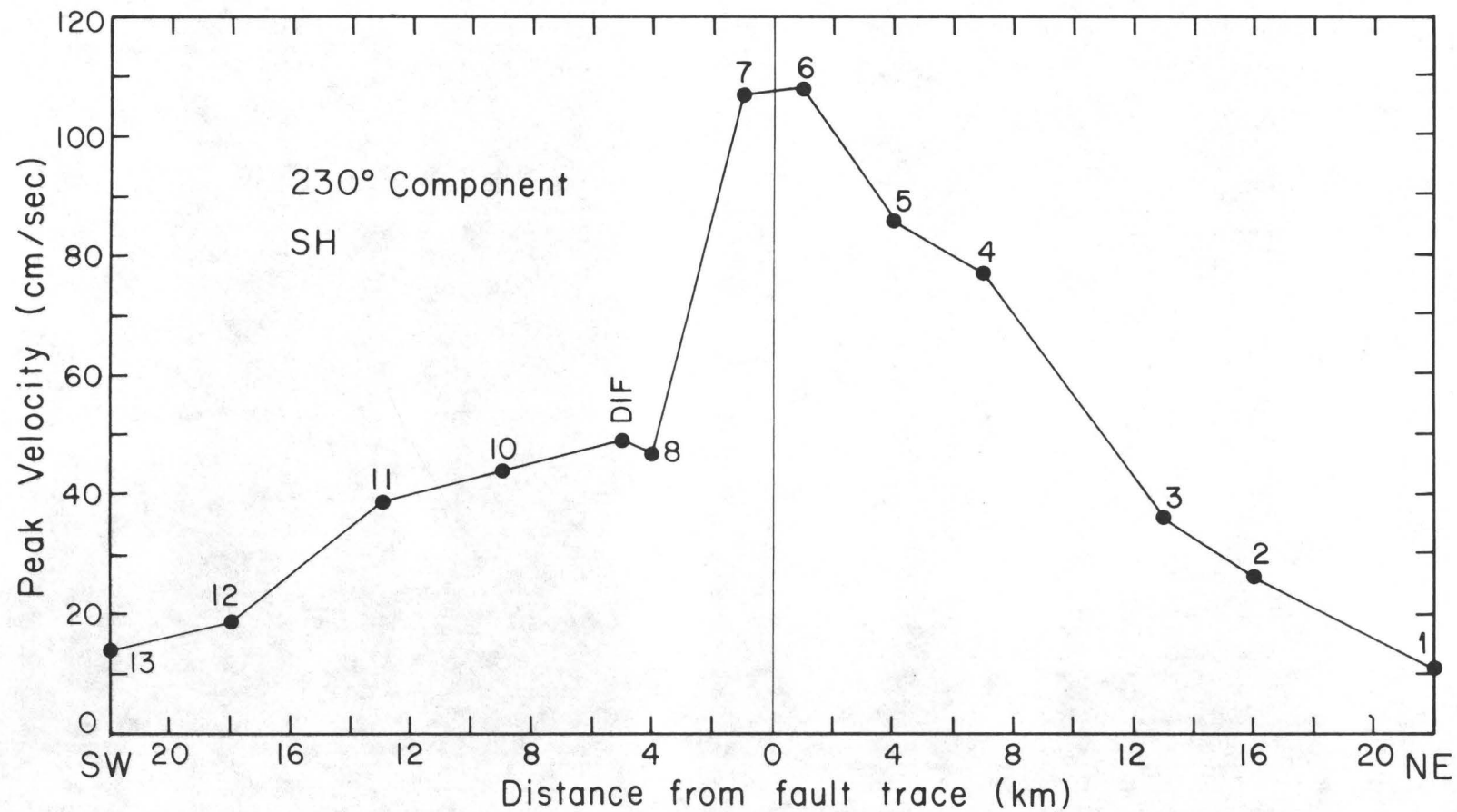
Figure 3   Peak transverse (SH) velocities for the El Centro array plotted as a function of distance from the closest point on the Imperial fault.
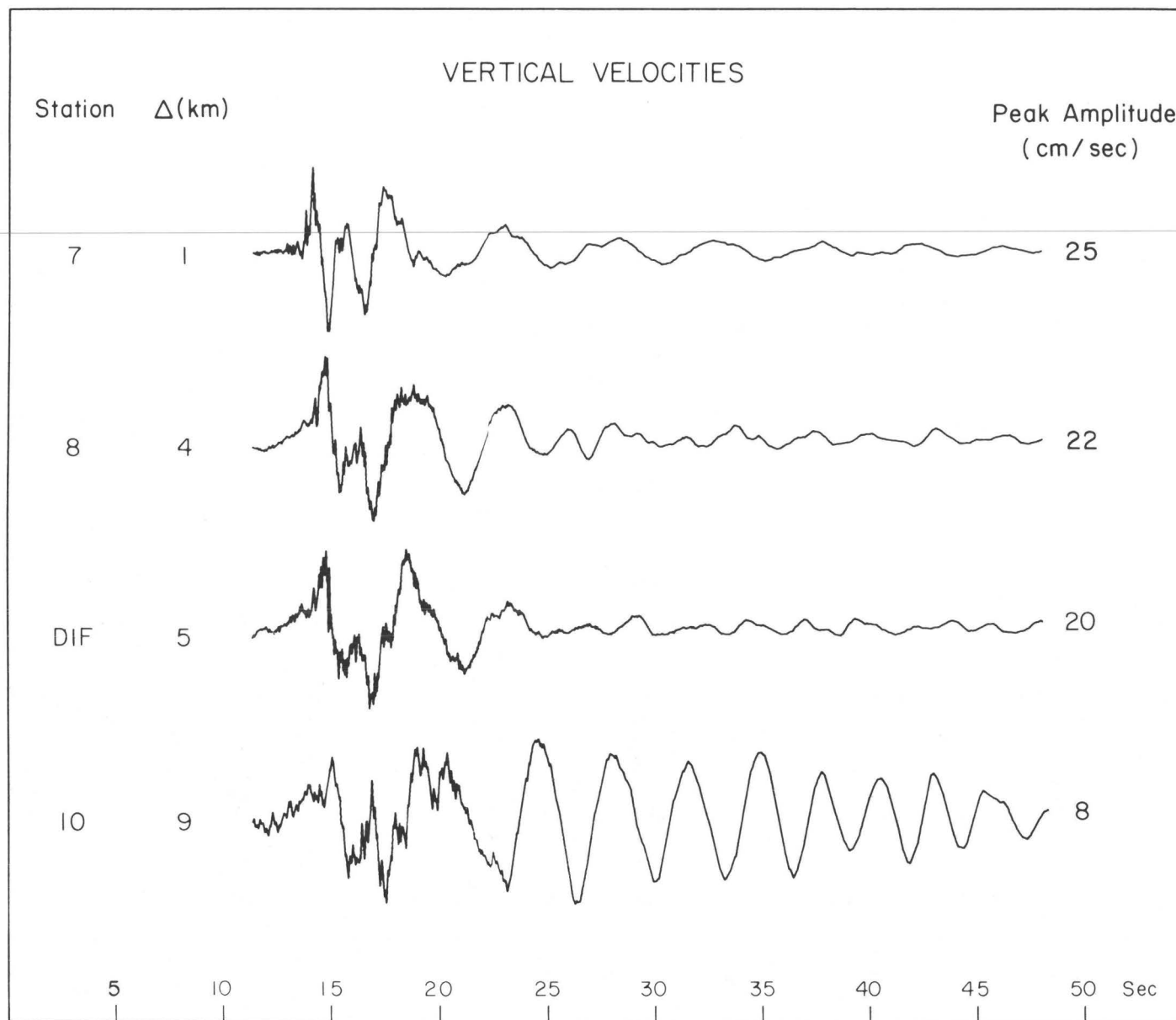
Figure 4   Vertical velocities from the El Centro array plotted as a function of distance from the Imperial fault.
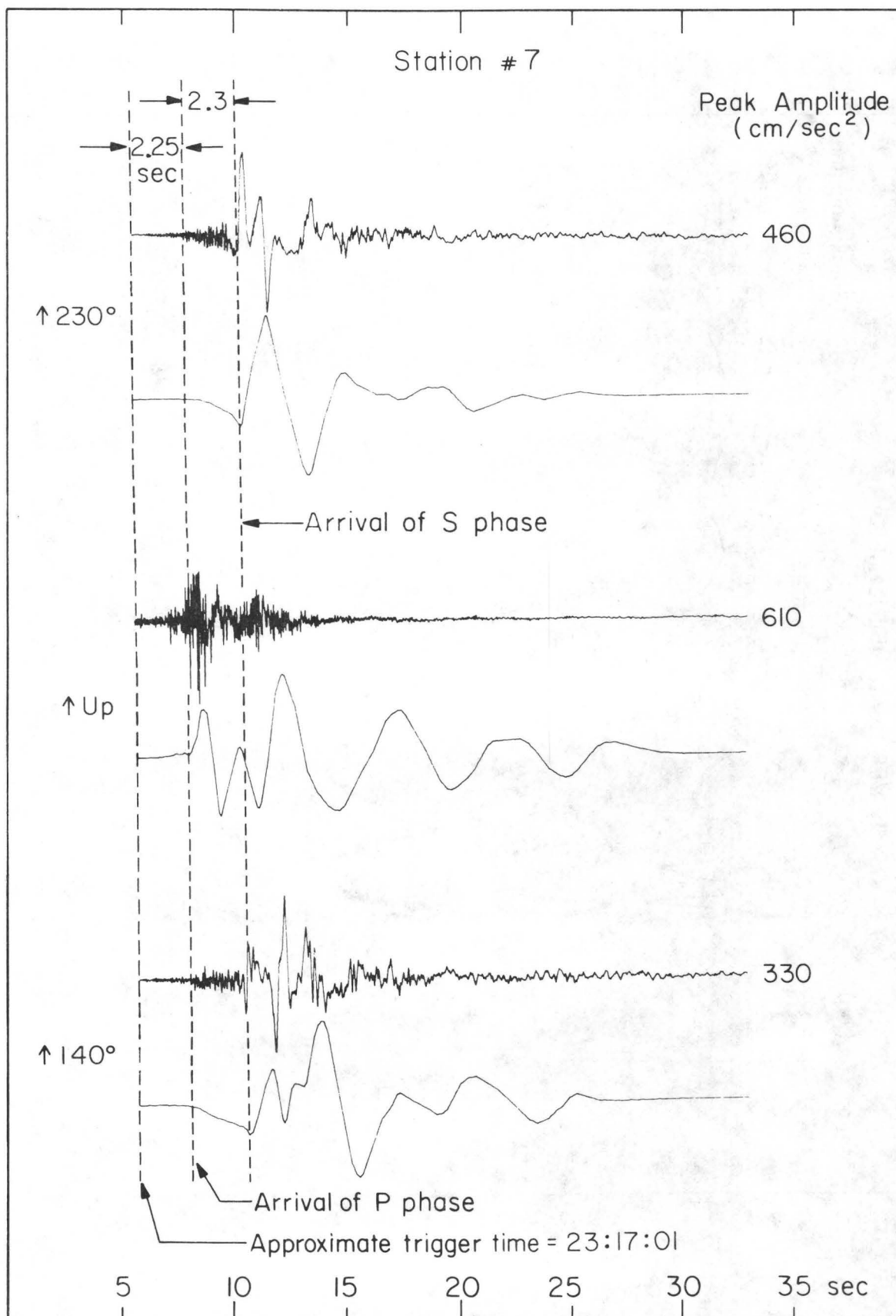
Figure 5   Detail of array station #7 (EL7, Imperial Valley College) record. The first trace is the corrected acceleration. The second trace is the ground motion as recorded by a damped harmonic oscillator with a free period of 5 sec and 0.7 of critical damping.
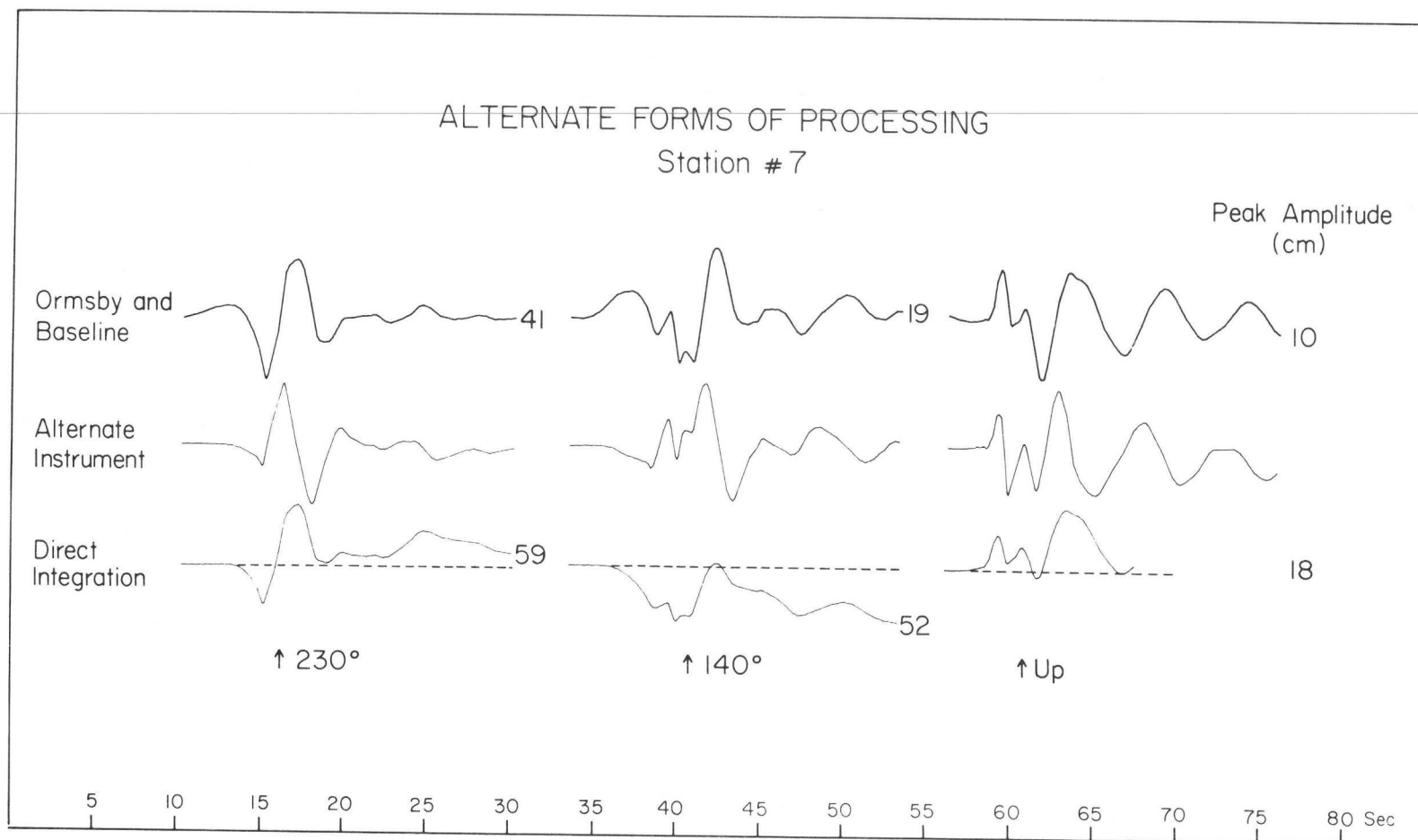
Figure 6   Comparison of displacements for array station #7 (EL7) obtained from the accelerograms by three different processing techniques.
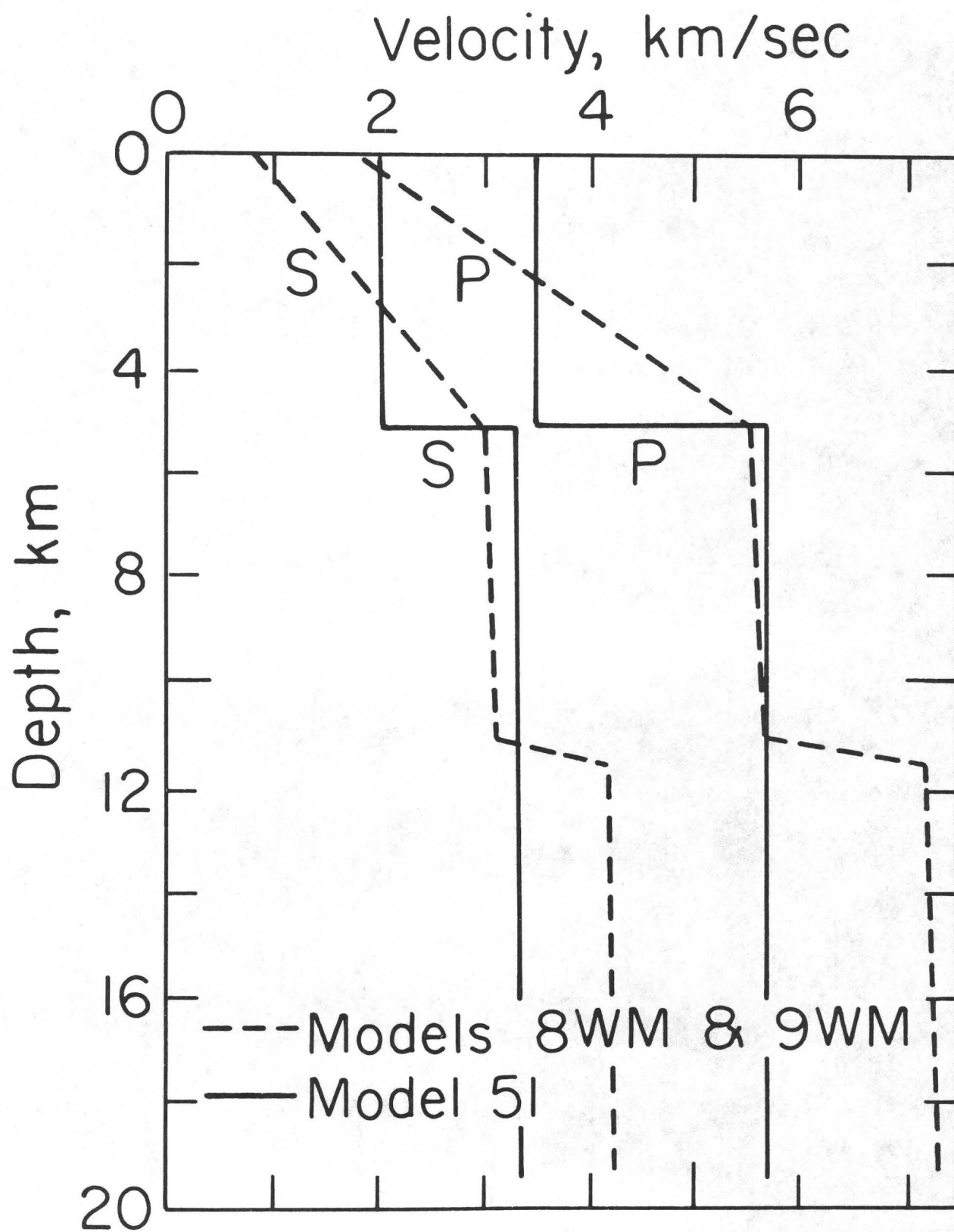
Figure 7   Two P and S velocity models for the Imperial Valley considered in this study. The gradient model is based on recent refraction profiles (Fuis et al., 1982).

Figure 8   Point source responses for a ramp dislocation using generalized rays for a strike-slip source within the top layer of the two layer velocity structure in Figure 7.

Figure 9   Point source responses for a ramp dislocation using generalized rays for a strike-slip source below the top layer of the two layer velocity structure in Figure 7.

Figure 10   Point source responses for a step dislocation using discrete wavenumber/finite elements for a strike-slip source at two different depths within the velocity gradient structure in Figure 7.

Figure 11   Comparison of observed displacements and synthetics for a uniform rectangular fault model assuming a moment of 5.0×10^{25} dyne-cm. GR: generalized ray synthetics for two layer velocity structure in Figure 7. DWFE: discrete wavenumber/finite element synthetics for velocity gradient structure in Figure 7.

Figure 12   Contoured dislocation in meters on the Imperial fault for three different fault models. Model 51 was derived using the two layer velocity structure and models 8 WM and 9 WM were devised using the velocity gradient structure in Figure 7. 9WM is the preferred fault model. The hypocenter for each model is indicated by a *.

Figure 13   Comparison of observed displacements and synthetics for fault model 51. All are generalized ray synthetics for the two layer velocity structure in Figure 7 except the one labeled DWFE for station EL7. The two synthetics for station BOC (Bonds Corner) show the effect of adding a magnitude 5 foreshock 2.0 sec before the main rupture.

Figure 14
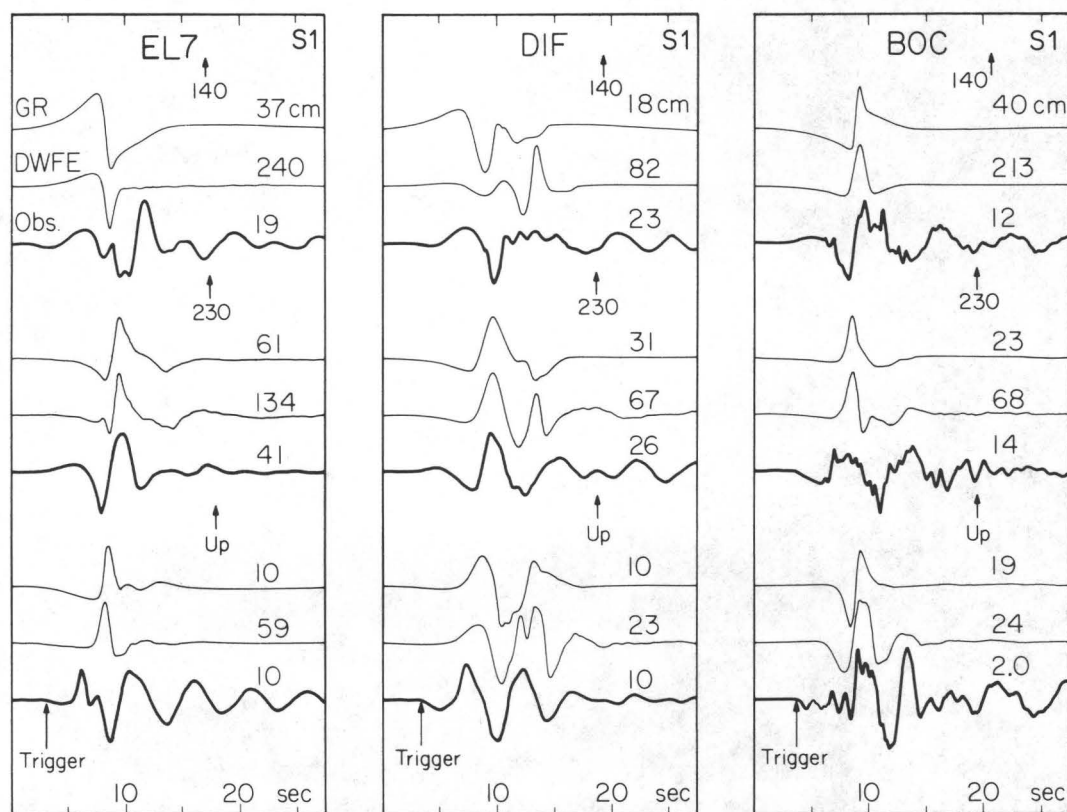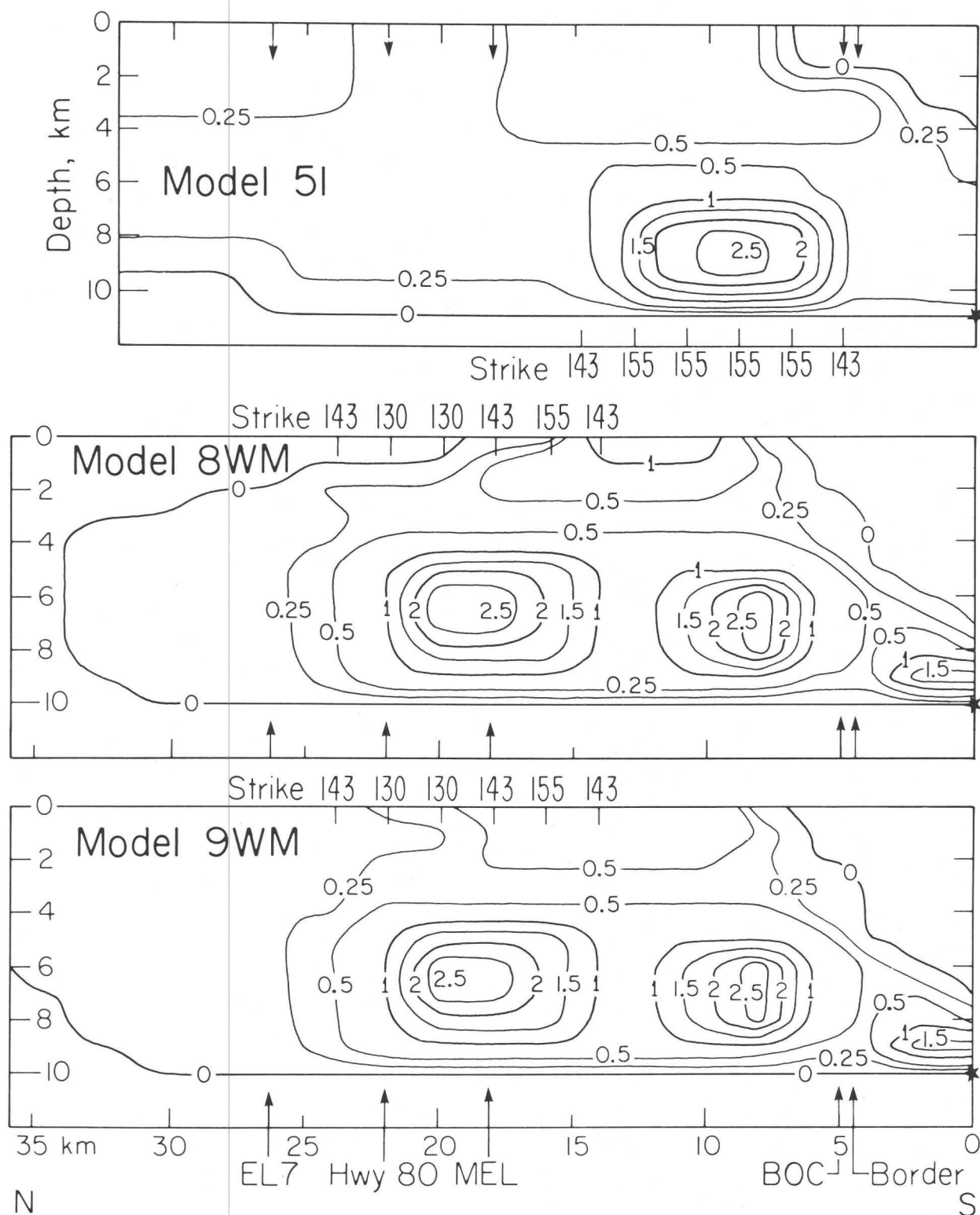a, b   Comparison of observed displacements and synthetics for the preferred fault model, 9WM. All are discrete wavenumber/finite element synthetics for the velocity gradient structure in Figure 7. (EL3-EL5, EL7, EL8, EL10, and EL11 are El Centro array stations; DIF, El Centro differential array; MEL, Meloland Overpass; BOC, Bonds Corner; CAL, Calexico; HOL, Holtville).

Figure 15   Comparison of rotated (R, radial and T, transverse) teleseismic shear waves for the Borrego Mountain (M = 1.1 x 10^{26} dyne-cm) and Imperial Valley (M = 5.0 x 10^{25} dyne-cm) earthquakes. Amplitudes are in units of 10^{-3} cm.

Figure 16   Comparison of the measured surface offsets for the 1940 and 1979 Imperial Valley earthquakes.

Figure 17   Aftershock epicenters for the first 26 days following the October 15, 1979 earthquake from Johnson and Hutton (1982).

Figure 18   Well-located epicenters (horizontal error less than 2.5 km) within the Imperial Valley for the time period 1973-1978 from Johnson (1979).

Figure 1. Area map of the southern Imperial Valley showing the surface traces of the Imperial and Brawley faults and the locations of strong motion instruments. The El Centro array is numbered 1 through 13.

Figure 2. Comparison of transverse (SH) velocities from the El Centro array for pairs of stations on either side of the Imperial fault and approximately the same distance from the fault trace.

Figure 3.   Peak transverse (SH) velocities for the El Centro array plotted as a function of distance from the closest point on the Imperial fault.

VERTICAL VELOCITIES

Station	Δ(km)		Peak Amplitude (cm/sec)
7	1		25
8	4		22
DIF	5		20
10	9		8

5   10   15   20   25   30   35   40   45   50 Sec

Figure 4. Vertical velocities from the El Centro array plotted as a function of distance from the Imperial fault.

Figure 5. Detail of array station #7 (EL7, Imperial Valley College) record.
The first trace is the corrected acceleration. The second trace is
the ground motion as recorded by a damped harmonic oscillator with
a free period of 5 sec and 0.7 of critical damping.

862

Figure 6. Comparison of displacements for array station #7 (EL7) obtained from the accelerograms by three different processing techniques.

Figure 7.   Two P and S velocity models for the Imperial
Valley considered in this study.   The gradient
model is based on recent refraction profiles
(Fuis, et al. 1982).

864

Figure 8. Point source responses for a ramp dislocation using generalized rays for a strike-slip source within the top layer of the two-layer velocity structure in Figure 7.

Figure 9. Point source responses for a ramp dislocation using
generalized rays for a strike-slip source within
the top layer of the two-layer velocity structure
in Figure 7.

Figure 10.   Point source responses for a step dislocation using discrete wavenumber/finite elements for a strike-slip source at two different depths within the velocity gradient structure in Figure 7.

Figure 11. Comparison of observed displacements and synthetics for a uniform rectangular fault model assuming a moment of 5.0×10^{25} dyne-cm. GR: generalized ray synthetics for two-layer velocity structure in Figure 7. DWFE: discrete wavenumber/finite element synthetics for velocity gradient structure in Figure 7.

Figure 12.   Contoured dislocation in meters on the Imperial
fault for three different fault models.   Model 5I
was derived using the two-layer velocity
structure and models 8 WM and 9WM were
devised using the velocity gradient structure
in Figure 7.   9 WM is the preferred fault
model.   The hypocenter for each model is
indicated by a *.
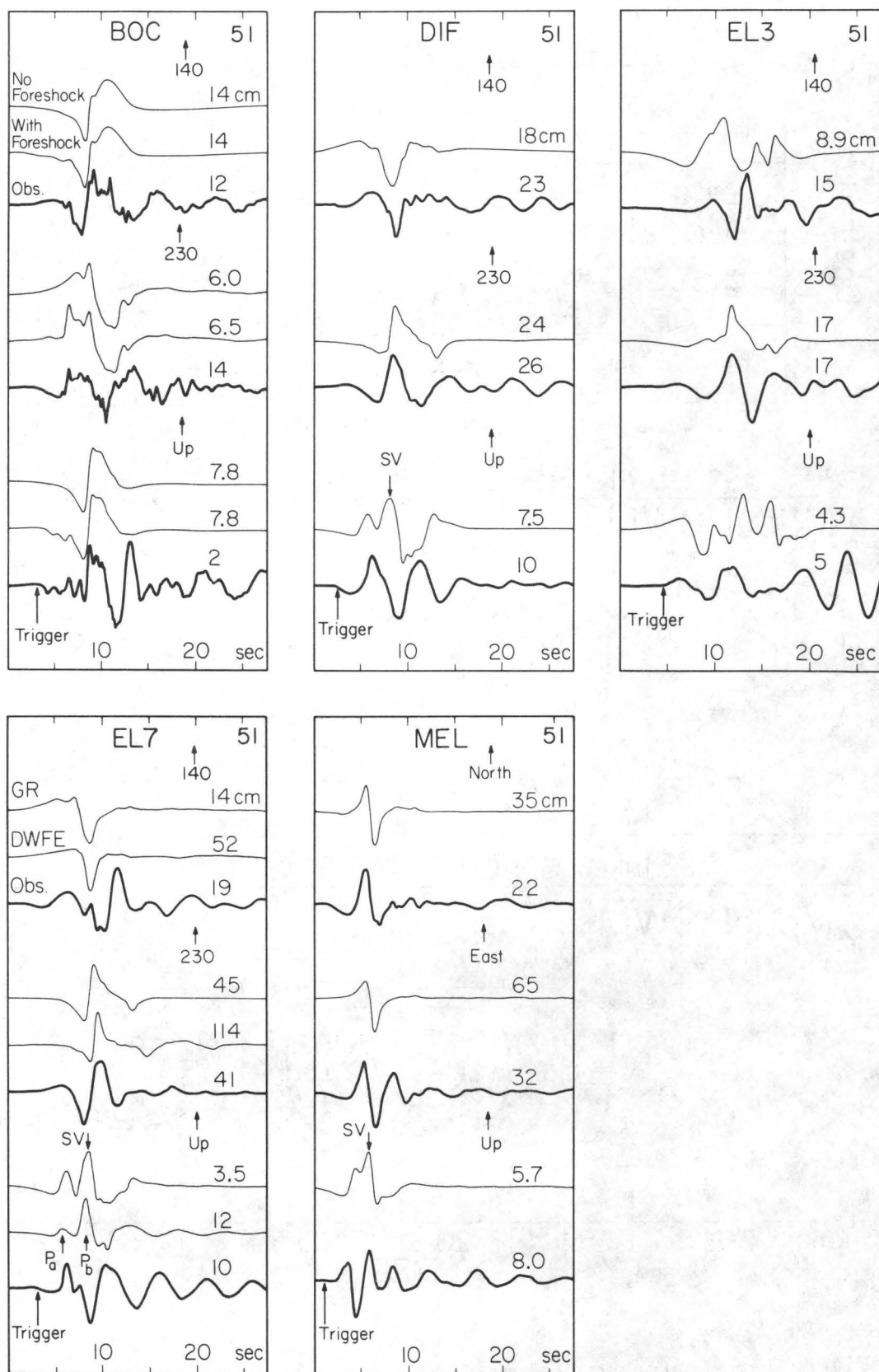
Figure 13.   Comparison of observed displacements and synthetics
for fault model 51.   All are generalized ray
synthetics for the two-layer velocity structure in
Figure 7 except the one labeled DWFE for station
EL7.   The two synthetics for station BOC (Bonds
Corner) show the effect of adding a magnitude 5
foreshock 2.0 sec before the main rupture.
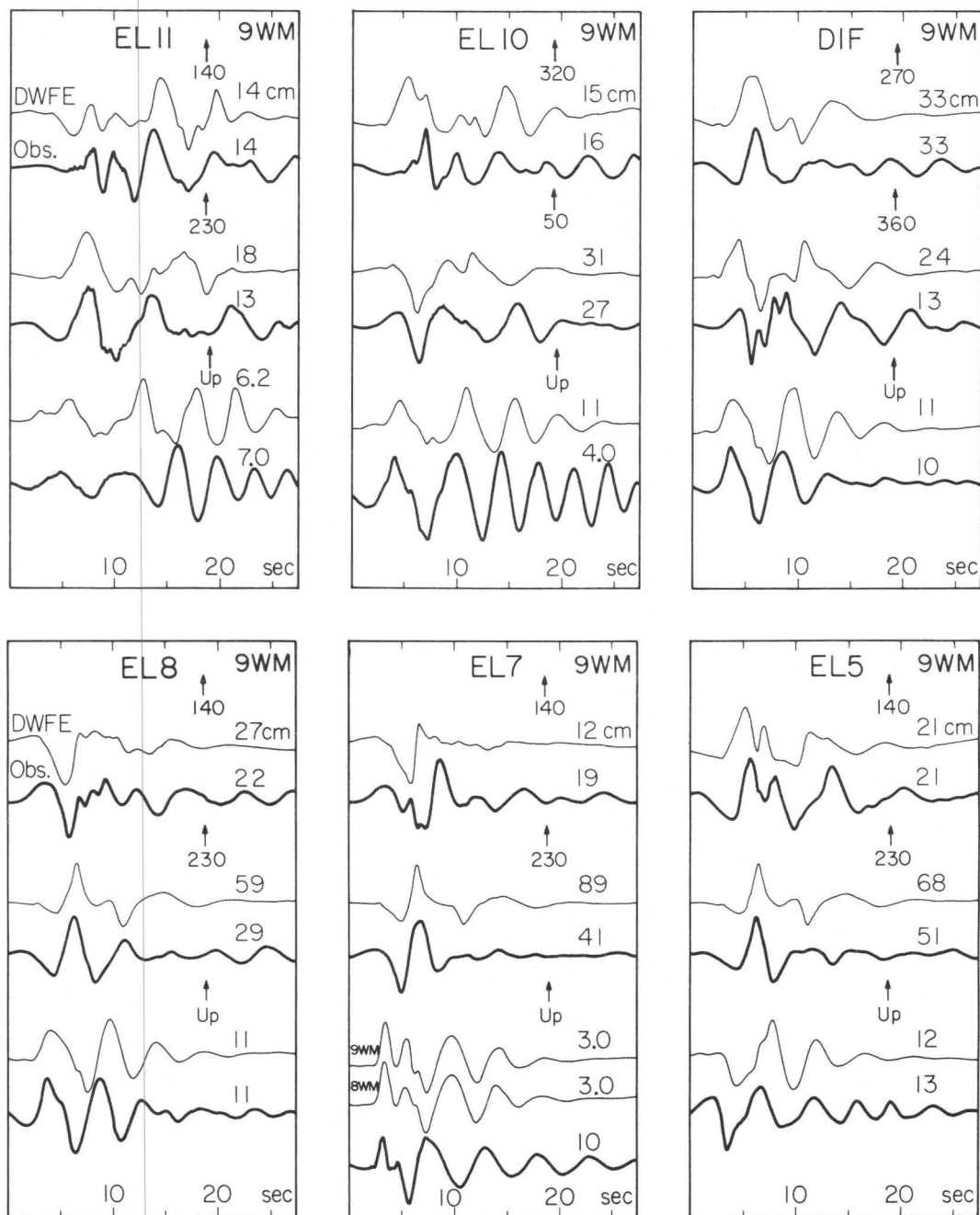
Figure 14a. Comparison of observed displacements and synthetics for
the preferred fault model, 9 WM. All are discrete wavenumber/
finite element synthetics for the velocity gradient structure
in Figure 7. (EL3–EL5, EL7, EL8, EL10 and EL11 are El Centro
array stations; DIF, El Centro differential array;
MEL, Meloland Overpass; BOC, Bonds Corner, CAL, Calexico;
HOL, Holtville).

871
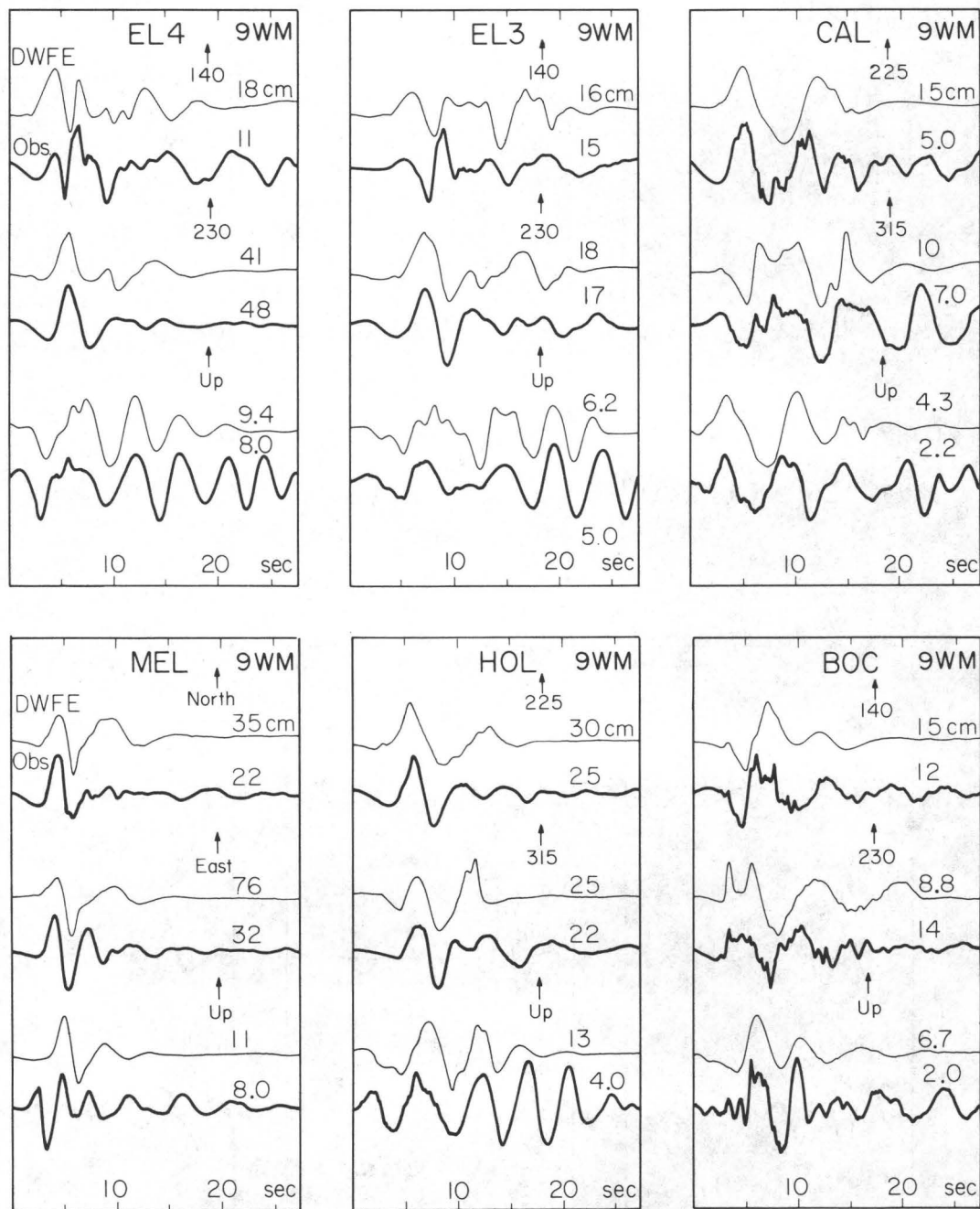
Figure 14b. Comparison of observed displacements and synthetics for the preferred fault model, 9 WM. All are discrete wavenumber/finite element synthetics for the velocity gradient structure in Figure 7. (EL3-EL5, EL7, EL8, EL10, and EL11 are El Centro array stations; DIF, El Centro differential array; MEL, Meloland overpass; BOC, Bonds Corner; CAL, Calexico; HOL, Holtville)
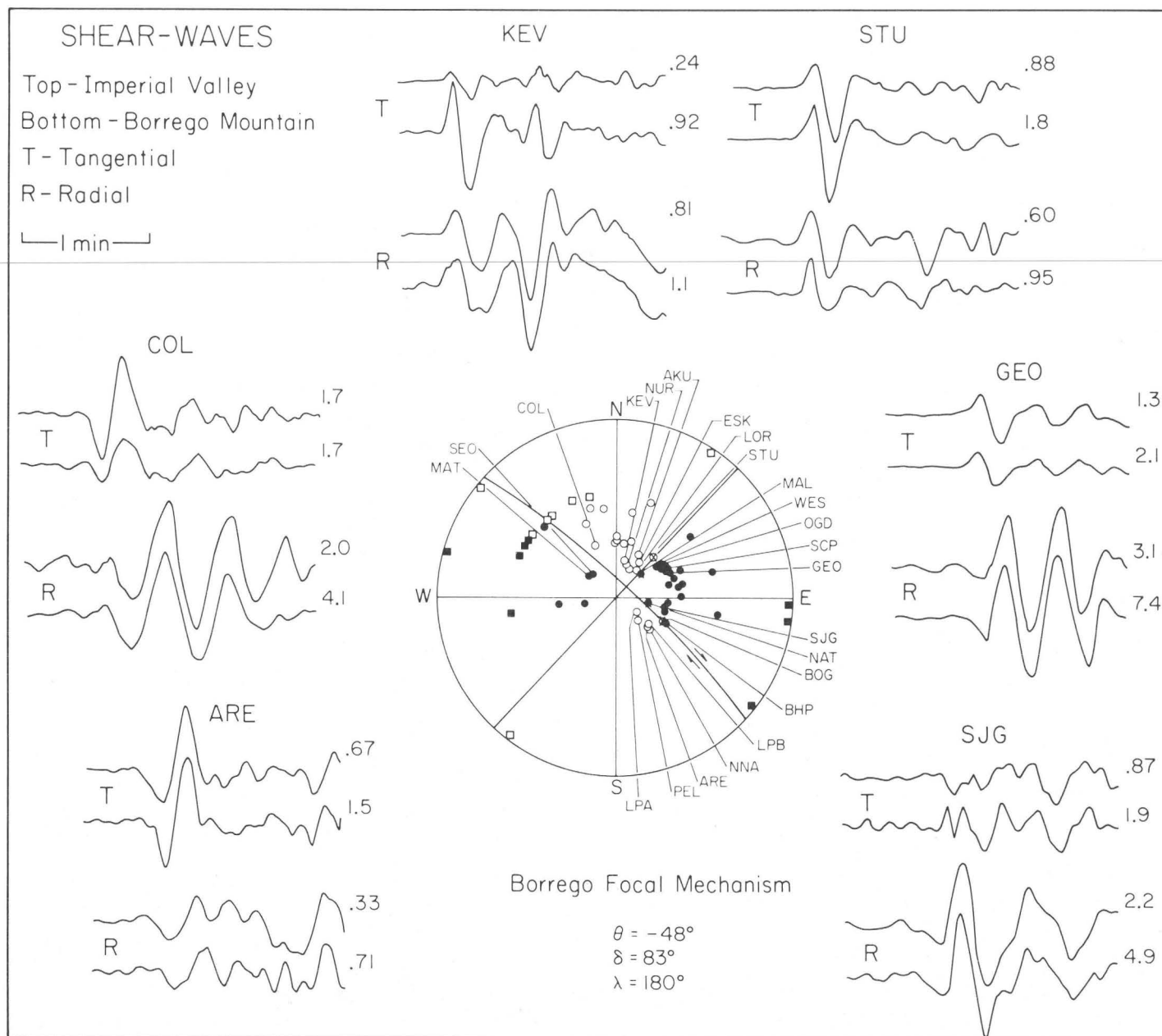
Figure 15. Comparison of rotated (R, radial, and T , transverse)
teleseismic shear waves for the Borrego Mountain
(M = 1.1 x 10²⁶ dyne-sm) and Imperial Valley
(M$_o$ = 5.0 x 10²⁵) dyne-cm earthquakes. Amplitudes
are in units of 10⁻³ cm.
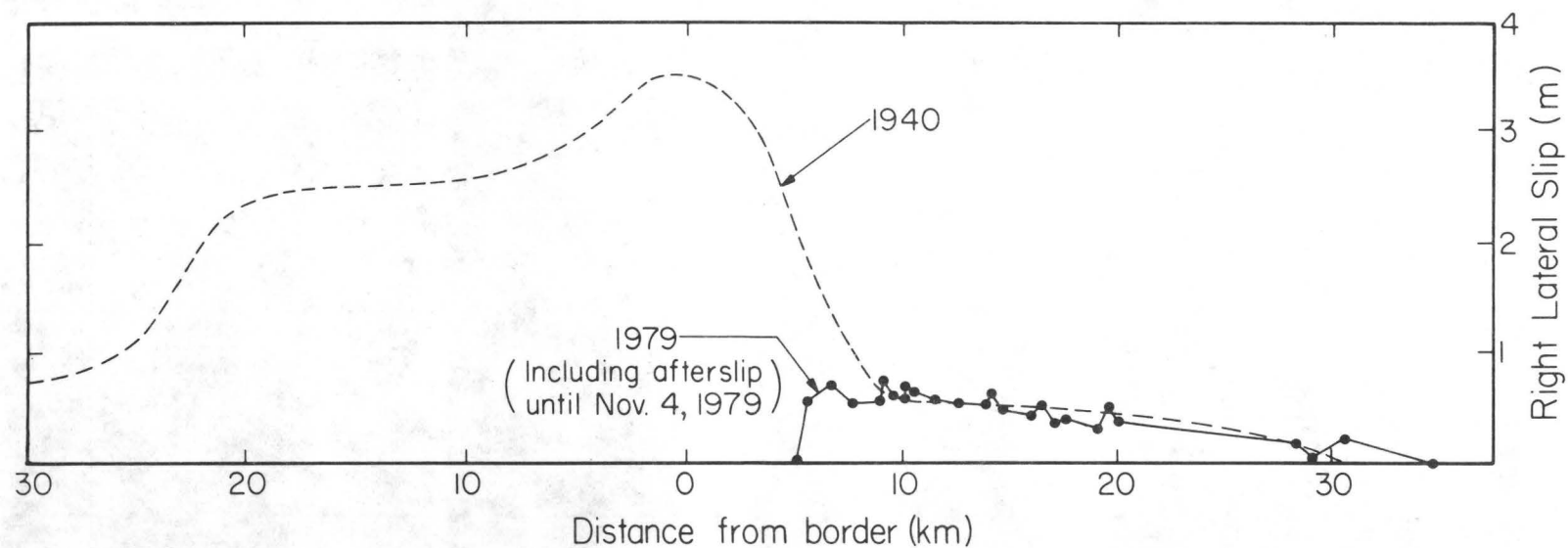
Figure 16.   Comparison of the measured surface offsets for the 1940 and 1979 Imperial Valley earthquakes.
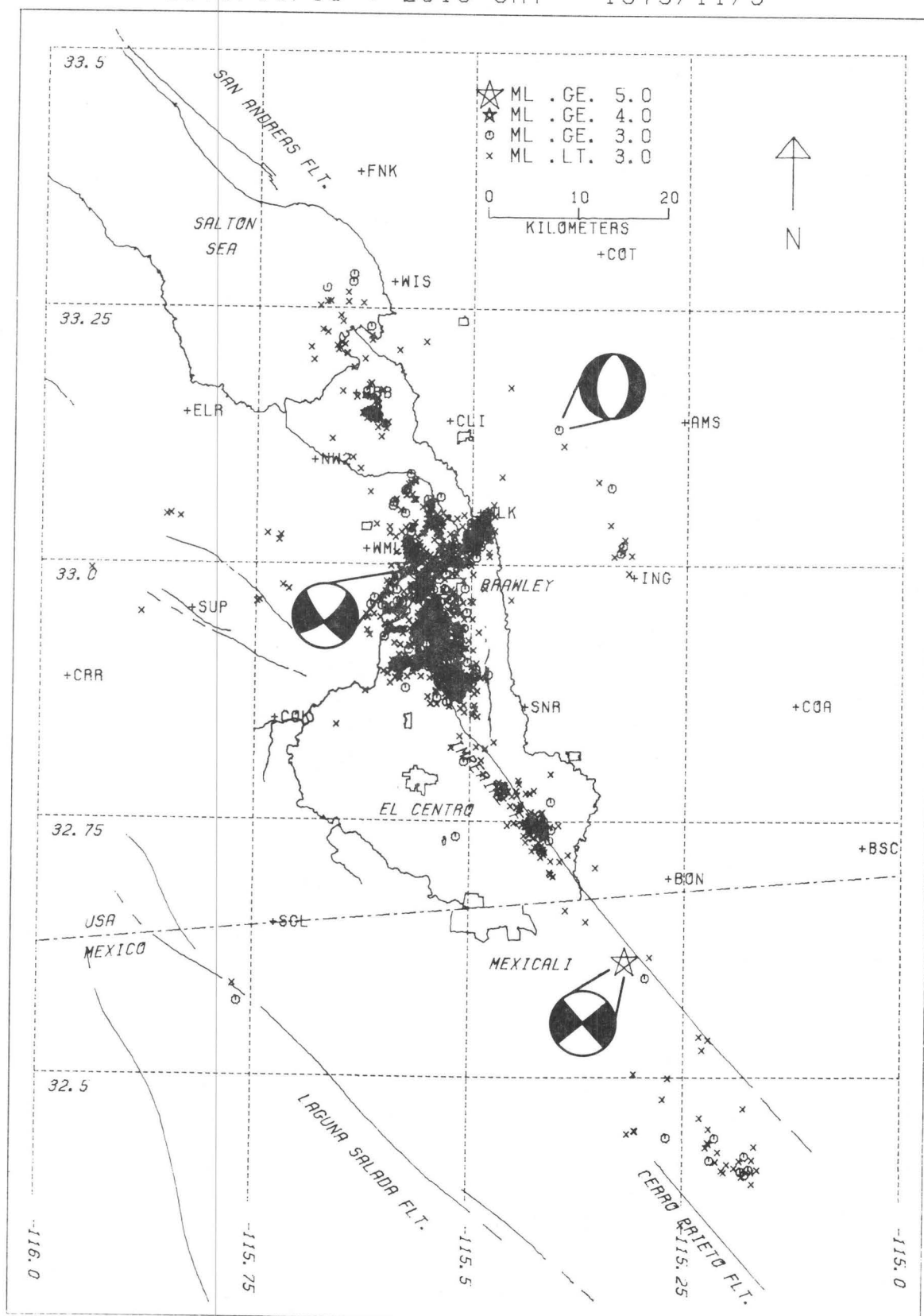
Figure 17. Aftershock epicenters for the first 26 years
following the October 15, 1979 earthquake from
Johnson and Hutton (1982).
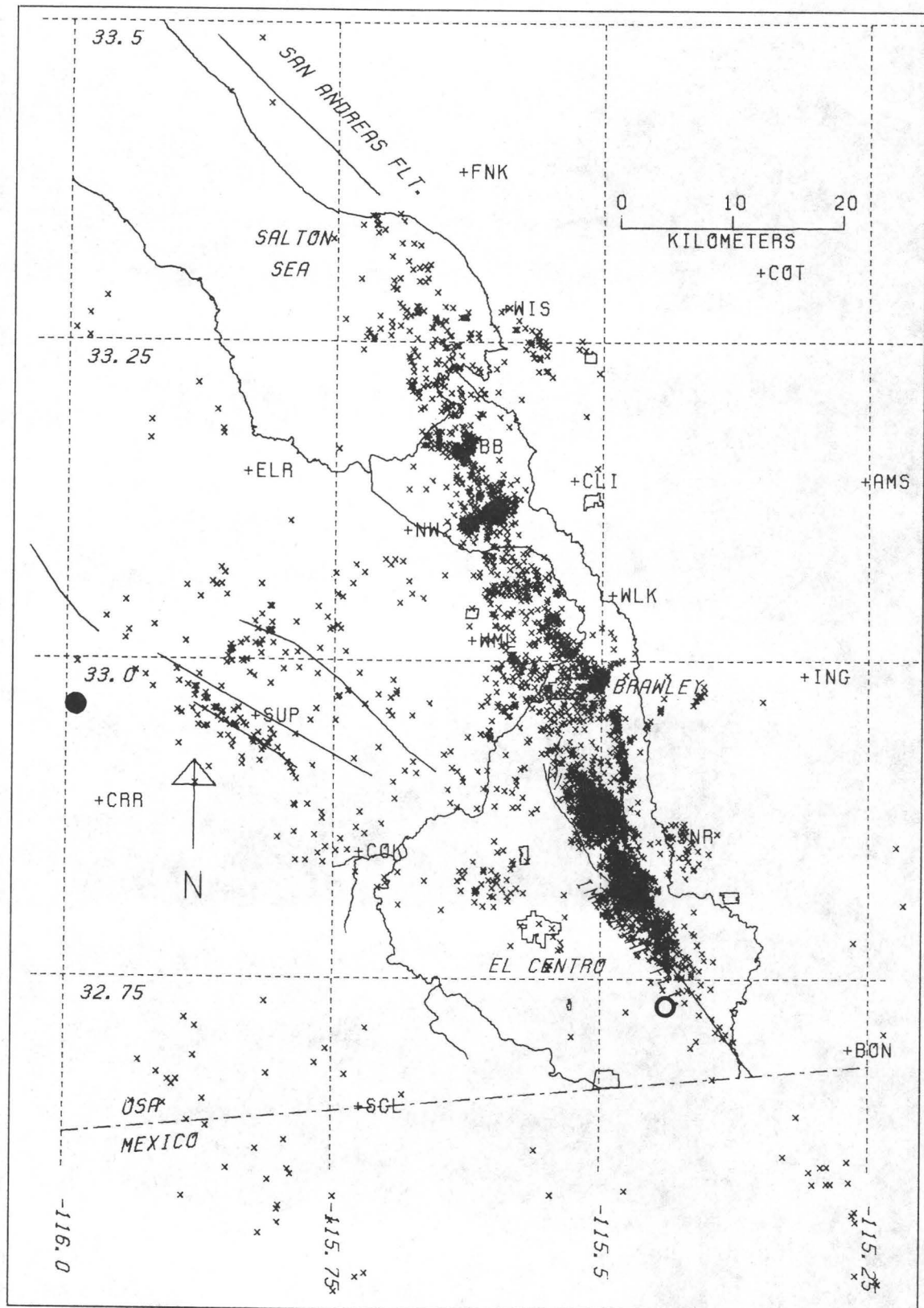
Figure 18. Well located epicenters (horizontal error less than 2.5 km) within the Imperial Valley for the time period 1973-1978 from Johnson (1979).

Finite Faults and Inverse Theory

with Applications to the 1979 Imperial Valley Earthquake*

Allen H. Olson[†] and Randy J. Apsel[††]

Abstract

Using a representation theorem from elastodynamics, subsurface slip on a known fault is formulated as the solution to an inverse problem in which recorded surface ground motion is the data. Two methods of solution are presented: the least squares method, which minimizes the squared differences between theory and data, and the constrained least squares method which simultaneously maintains a set of linear inequalities. Instabilities in the solution are effectively eliminated in both methods and the sensitivity of the solution to small changes in the data is quantitatively stated. The inversion methodology is applied to 77 components of near-field ground acceleration recorded during the October 15, 1979 Imperial Valley earthquake. The faulting is constrained to propagate bilaterally away from the epicenter at an average velocity of 90 percent of the shear wave speed on a vertical fault plane extending from the surface to ten kilometers depth. Inequality constraints are used to keep the faulting sequence physically reasonable by maintaining right lateral motion and positive slip velocity. The preferred solution is stable and provides a good fit to the data; it is also realistic and consistent with observed surface offsets and independent estimates of seismic moment.

1. Introduction

Faulting is characterized by the slipping of one side of a fault surface with respect to the other. If the earth is modeled as an elastic solid, then the displacement field due to a point dislocation can be taken as a Green's function for the earthquake faulting problem. The displacement field at all points in the earth due to an arbitrary distribution of slip on a fault is expressed as an integral over the fault surface of the slip distribution convolved with the Green's function. The slip distribution enters linearly into the integrand so that it may be obtained as the solution to a linear inverse problem in which recorded ground motion at the earth's surface is taken as data.

In order for a particular slip distribution to be an acceptable solution to the inverse problem, it must satisfy the following three conditions.

(1) The solution must explain the data.

(2) The solution must be physically reasonable (consistent with independent constraints).

(3) If more than one solution fits the data equally well, additional information must be supplied to uniquely define which solution is being obtained.

Conditions (1) and (2) simply amount to finding a realistic model which fits the data. Often, there may be many solutions which fit the data equally well. When this occurs the solution may be divided into two parts: a stable and an unstable part. The unstable part of the solution is comprised of distributions of slip which have little or no effect on the data. By definition, an arbitrary amount of the unstable part may be added to the stable part of the solution without affecting the fit to the data. In the presence of this effective nonuniqueness, condition (3) requires that additional information be supplied to uniquely define which solution is to be obtained. For example, the added information might lead to: the smallest solution (small in the sense that the integral of the slip over the fault plane is minimized); or, the slip distribution most like a preferred solution. No matter which solution is obtained, only the stable part is demanded by the data; the unstable aspects of the solution are simply not recoverable based upon the data alone.

The following discussion is divided into three major parts contained in Sections 2, 3, and 4. In Section 2, the forward problem of computing the theoretical ground motion due to earthquake faulting is reduced to specifying a set of parameters which correspond to slip across planar sections of fault surface. The slip parameters are linearly related to the ground motion data by a matrix. Two methods of inverting the matrix are presented in Section 3: the least squares method which minimizes the squared differences between theory and data and the constrained least squares method which simultaneously maintains a set of inequality constraints. A stabilizing procedure is also presented which determines the significance of particular details in the solution. In Section 4, the inversion methodology is applied to 77 components of near-field ground acceleration recorded during the October 15, 1979 Imperial Valley earthquake; four solutions are obtained which fit the data. Differences in the four solutions represent either unstable or nonphysical fault motions. The fourth solution is preferred since it: (1) provides a good fit to the data; (2) is physically reasonable; and (3) is related to the to the data in a stable manner.

2. Theoretical Formulation of the Forward Problem

2.1 A Representation Theorem in Elastodynamics

The representation theorem provides an expression for the radiation in an elastic media resulting from the creation of a discontinuity in the displacement and stress fields across a fault surface. The Green's function, $\mathbf{G}$, used in the representation is the response of the medium to a point force in the absence of discontinuities. This Green's function can be used to satisfy any boundary condition on the fault surface; hence, the elastodynamic equations need only be solved once.

A derivation of the representation theorem for general anisotropic elastic media is given by Burridge and Knopoff (1964). Since faulting is defined by the slipping of one side of a fault surface relative to the other, the representation theorem is specialized to the case where the stress field is continuous across the fault surface and only the displacement field is allowed to be discontinuous:

$$U^i(y,t) = \int_{-\infty}^{+\infty} \int_S \mathbf{n}(x)\,\mathbf{s}(x,\tau):\mathbf{G}^i(x,t-\tau;\,y)\,dx\,d\tau\,. \qquad (2\text{-}1)$$

The first integral in Eq. (2-1) is a convolution in time, t; the second is over the fault surface S. In Figure 2-1, S is illustrated as a plane striking along the x_1 axis at a dip δ from the vertical. The unit normal to the fault surface is given by the vector $\mathbf{n}(x)$ which depends upon position x. The slip vector, $\mathbf{s}(x,\tau)$, is the local discontinuity in displacement across the fault surface at time $t=\tau$ and position x. The quantity $U^i(y,t)$ is the i'th component of displacement at position y and time t resulting from the slip on S. The Green's function, $\mathbf{G}^i(x,t-\tau;\,y)$, is the second order stress tensor in the unfaulted elastic media as a function of position x and time t due to an impulsive point load applied at position y in the i'th coordinate direction at time $t=\tau$. The tensor components of $\mathbf{G}^i(x,t-\tau;\,y)$ can also be interpreted as the i'th component of displacement at position y due to a point dislocation at x. Once the Green's function is known and the slip prescribed, the theoretical ground displacements are obtained by performing the integration in Eq. (2-1). The symbol : is used to denote the inner product of the components of the two second order tensors $\mathbf{n\,s}$ and $\mathbf{G}$.

2.2 Discretization of the Fault Surface

In this study, the fault surface is divided into a set of cells, each cell being a rectilinear planar zone. Locations within each cell are assumed to undergo the same slip within a specified time shift. Within each cell, the slip is described by a two component vector in the plane of the fault having an unknown time dependence (a three component vector can be just as easily used if the fault surface is allowed to separate). The functional form of the parameterization is given in Eqs. (2-2) through (2-4).

$$\mathbf{s}(x,t) = \sum_{j=1}^{J} X_j(x) \sum_{k=-K}^{K} s_{jk} P_k(x,t) \tag{2-2}$$

$$X_j(x) = \begin{cases} 1 & \text{if } x \text{ in } j\text{'th cell} \\ 0 & \text{otherwise} \end{cases} \tag{2-3}$$

$$P_k(x,t) = F(t - T(x) + k\,\delta t) \tag{2-4}$$

The first sum in Eq. (2-2) is over the J cells representing the fault surface. The second sum defines the slip within the j'th cell: the vector s_{jk} is the slip direction of the j'th cell at the k'th time point and has two components in the plane of the fault; the function $P_k(x,t)$ contains the time dependence of the k'th slip. Each cell is allowed to slip $2K+1$ times at successive increments of δt in time; each slip varies according to the specified time function $F(t)$. The absolute time at which slip takes place within the cell is centered about $T(x)$.

Equation (2-2) simplifies if each cell is allowed to slip only once; in which case, the sum over k goes away and the slip within each cell varies as $F(t)$, progressing through the cell as a rupture front prescribed by $T(x)$. When the cells are allowed to slip more than once, $T(x)$ represents an average rupture time. By only allowing slip to occur within a prescribed time window about a predetermined average rupture time, the number of parameters is kept to a minimum. This also allows for the local rupture velocity to differ from the average rupture velocity.

By substituting Eq. (2-2) for $\mathbf{s}(x,t)$ in Eq. (2-1), the integration over x and convolution in t can be performed since the space and time dependence of the integrand is known completely.

$$U^i(y,t) = \sum_{j=1}^{J} \sum_{k=-K}^{K} s_{jk} \cdot \mathbf{g}_j^i(y,t+k\,\delta t) \tag{2-5}$$

The vector $\mathbf{g}_j^i(y,t+k\,\delta t)$ is the Green's function for the j'th cell at position y in i'th component direction. Equation (2-5) is a matrix version of the integral in Eq. (2-1). The columns of the matrix correspond to components of the Green's function vectors $\mathbf{g}_j^i(y,t+k\,\delta t)$ for fixed values of j and k. Since s_{jk} and $\mathbf{g}_j^i(y,t+k\,\delta t)$ are two-component vectors, the total number of scalar parameters is $2J(2K+1)$. The number of rows in the matrix equals the number of components (index i) being considered times the number of time points for which each component is sampled.

In practice, the integral in Eq. (2-1) is done numerically. The Green's function, $\mathbf{G}$, is sampled at a grid-work of points on the fault plane. The Green's function at a location which does not coincide

with a sample point is approximated by the Green's function at the nearest grid-point subject to a time shift; the time shift is determined according to the phase velocity of the dominant body wave (usually the S wave). This approximation is exact for nondispersive waves and is a very good approximation when one particular body wave dominates the Green's function. For a line source of uniform slip, this approximation is equivalent to convolving a single Green's function with a box car.

The integral in Eq. (2-1) is known to represent an underdetermined problem for the solution $s(x,t)$ (Backus and Gilbert, 1968). Equation (2-5) however appears to be overdetermined since the number of unknown parameters, s_{jk}, may be far less than the number of time points of observed ground motion. If the cells on the fault are made sufficiently small, then redundancies in the matrix cause the problem to be ill-conditioned, thereby allowing many solutions to Eq. (2-5). The redundancies occur for two principal reasons: (1) many columns in the matrix are simply time shifts of each other by an amount $k\,\delta t$; and (2) columns corresponding to cells which are spatially close to each other are very similar.

3. Inverse Theory for the Discrete Problem

Inverse theory for the discrete problem requires solving a system of linear equalities. In general, these equalities may be satisfied exactly or approximately, depending on whether the system is under-determined or overdetermined. Two methods of solution are presented in this section; they are, the least squares method, which satisfies the equalities by minimizing the sum of the squared differences between calculated and observed data, and the constrained least squares method which simultaneously maintains a set of linear inequalities. Measures of stability for each of these two methods are presented so that the significance of particular details in the solution can be determined with respect to possible nonuniqueness.

3.1 The Generalized Inverse and the Least Squares Solution

The system of linear equality constraints in Eq. (2-5) can be written more compactly as

$$\mathbf{A}\mathbf{x} = \mathbf{f}. \tag{3-1}$$

The vector $\mathbf{x}$ of length n corresponds to the unknown parameters; the vector $\mathbf{f}$ of length m contains the data; and the matrix $\mathbf{A}$ with m rows and n columns contains the theory relating the parameters to the data. If $m=n$ and $\mathbf{A}$ is nonsingular, then $\mathbf{x}$ is found by calculating the inverse of $\mathbf{A}$. In the presence of inconsistent data and/or a singular matrix, the exact inverse of $\mathbf{A}$ is not defined and an alternate definition of inverse is needed. One such alternative is the generalized inverse (Penrose, 1955) which always exists and includes the exact inverse as a special case.

An overview of the literature on the generalized inverse, GI, is presented in Ben-Israel and Charnes (1963). Of the many ways of defining GI, the one chosen here is attributed to Penrose (1956). The norm being used is the Euclidean norm defined by

$$\| \mathbf{x} \| = (\mathbf{x}'\mathbf{x})^{1/2} = \left(\sum_{i=1}^{n} x_i^2 \right)^{1/2} \tag{3-2}$$

in which $\mathbf{x}'$ denotes the transpose of $\mathbf{x}$.

Definition: Among all solutions $\mathbf{x}$ satisfying

$$minimum \ \| \mathbf{A}\mathbf{x} - \mathbf{f} \|, \tag{3-3}$$

there is a unique solution, $\tilde{\mathbf{x}}$, which satisfies

$$minimum \ \| \mathbf{x} \|. \tag{3-4}$$

The generalized inverse of $\mathbf{A}$, $\tilde{\mathbf{A}}$, *is the matrix which produces* $\tilde{\mathbf{x}}$ *from the data.*

$$\tilde{\mathbf{x}} = \tilde{\mathbf{A}} \mathbf{f}. \tag{3-5}$$

Note that $\tilde{\mathbf{x}}$ is: 1) the least squares solution in the presence of inconsistent data; 2) the smallest solution satisfying the data exactly for the underdetermined case; and 3) the smallest least squares solution in the presence of inconsistent data and a singular matrix. In the remaining discussion, $\tilde{\mathbf{x}}$ refers to the *GI* solution while $\mathbf{x}$ refers to other candidate solutions to Eq. (3-3).

A discussion of the construction of $\tilde{\mathbf{A}}$ is given by Lawson and Hanson (1974) in terms of orthogonal decompositions. A particular decomposition which proves useful in examining the stability of $\tilde{\mathbf{x}}$ is the singular value decomposition, *SVD*, given by

$$\mathbf{A} = \mathbf{U} \Lambda \mathbf{V}'. \tag{3-6}$$

$\mathbf{U}$ and $\mathbf{V}$ are orthogonal matrices of dimension m by n, and n by n, respectively. The matrix Λ is an n by n diagonal matrix in which the diagonal elements, λ_{ii}, are arranged in decreasing order down the diagonal. Since $\mathbf{U}$ and $\mathbf{V}$ have orthonormal columns, the inverse of each is is simply its transpose so that the *GI* of $\mathbf{A}$ is

$$\tilde{\mathbf{A}} = \mathbf{V} \Lambda^{-1} \mathbf{U}'. \tag{3-7}$$

The components of Λ^{-1} are defined by

$$\left(\Lambda^{-1} \right)_{ii} = \begin{cases} \lambda_{ii}^{-1} & \text{for } \lambda_{ii} > 0 \\ 0 & \text{for } \lambda_{ii} = 0 \end{cases}. \tag{3-8}$$

The inclusion of the second criterion in Eq. (3-8) allows for the case where the exact inverse does not exist.

The null space of $\mathbf{A}$ is spanned by the columns of $\mathbf{V}$ associated with the zero singular values. Distributions of $\mathbf{x}$ which lie in the null space vanish when multiplied by $\mathbf{A}$. The exact inverse does not exist since information about the null space can never be recovered. The *GI* does exist because it sets the null space component of $\mathbf{x}$ to zero. In the case of inconsistent data, the *GI* similarly considers only that part of the data which is in the column space of $\mathbf{A}$. In the remaining discussion, the *GI* solution is referred to as simply the least squares solution.

Although the least squares solution is unique in theory, it may be very unstable in practice since small changes in the data can often lead to large changes in the solution. One useful measure of stability is presented in Franklin (1970) where a perturbation in the data, $\delta\mathbf{f}$, is compared with the related perturbation in the solution, $\delta\mathbf{x}$. The relative change in the solution divided by the relative change in the data is

$$S = \left(\frac{\| \delta\mathbf{x} \|}{\| \mathbf{x} \|} \right) \left(\frac{\| \delta\mathbf{f} \|}{\| \mathbf{f} \|} \right)^{-1}. \tag{3-9}$$

For a stable problem, the value of S should not be much greater than one. The maximum value that S can attain is called the condition number of $\mathbf{A}$; Franklin (1970) shows that the condition number is given by the ratio of the largest to smallest singular value in Λ. The example given there is that a 3 percent change in the data could produce a 60 percent change in the solution if the condition number is 20. A condition number of 20 is not an uncommon occurrence.

Another useful measure of stability is obtained through statistics by determining the variance in the solution due to random errors of known variance, σ^2, in the data (Backus and Gilbert, 1970; Jackson, 1972; Wiggins, 1972). The covariance of the solution parameters caused by adding independent random noise to the data is

$$E|\tilde{\mathbf{x}} \tilde{\mathbf{x}}'| = \sigma^2 \mathbf{V} \Lambda^{-2} \mathbf{V}', \tag{3-10}$$

where $E|\ |$ denotes the usual expected value. Small singular values in Λ give rise to large covariances in the solution parameters since Eq. (3-10) involves taking the squared inverse of small numbers. Just as in the condition number, instability is indicated by small singular values.

One method of handling ill-conditioning is to filter the solution. Filtering eliminates the ill-conditioned part of the solution and involves a trade off between resolution and variance (Backus and Gilbert, 1970; Gilbert, 1971; Jackson, 1972; Wiggins, 1972) By filtering, linear combinations of the parameters are determined rather than determining any particular parameter uniquely. If the components of $\mathbf{x}$ correspond to values of a sampled continuous function, then the linear combinations of $\mathbf{x}$ mostly involve neighboring parameters so that the filter is performing a local average of the unknowns.

A pseudo low-pass filter, $\mathbf{V L V'}$, is defined by a set of filter coefficients in the diagonal matrix $\mathbf{L}$. The matrix $\mathbf{L}$ consists of ones in the first i diagonal entries and zeroes in the last $n - i$ entries. The filtered version of $\mathbf{x}$ is denoted by $\mathbf{y}$ where

$$\mathbf{y} = \mathbf{V L V'}\tilde{\mathbf{x}}. \tag{3-11}$$

The filter retains only that part of $\mathbf{x}$ associated with the large singular values. The components of $\mathbf{y}$ represent local averages of the components of $\mathbf{x}$ in as much as the rows of the filter matrix are concentrated about the diagonal. If $\mathbf{L}$ has all ones on the diagonal, $i = n$, then the filter is the identity matrix and no filtering is being done. The filter becomes increasingly spread about the diagonal as the number of zeroes along the diagonal of $\mathbf{L}$ is increased, thus sacrificing resolution.

Using the definition of $\tilde{\mathbf{x}}$ given in Eqs. (3-5) and (3-6), along with Eq. (3-11), the filtered least squares solution becomes

$$\mathbf{y} = \mathbf{V L \Lambda^{-1} U'f}. \tag{3-12}$$

The matrix $\mathbf{L}$ cancels the large values in $\mathbf{\Lambda}$ which arise from division by small numbers. The filter can simply be thought of as modifying the GI of Eqs. (3-7) and (3-8) by treating the small singular values as zero and not allowing them to participate in the solution. The covariance matrix for $\mathbf{y}$ is

$$E|\mathbf{y y'}| = \sigma^2 \mathbf{V L^2 \Lambda^{-2} V'}. \tag{3-13}$$

The small singular values of $\mathbf{\Lambda}$ are canceled by zeroes in $\mathbf{L}$, having the net effect of decreasing the variance. The number of nonzero values in $\mathbf{L}$ is at the discretion of the user and the transition from one to zero along the diagonal can either be abrupt or smooth just as in Fourier filtering. Any number of transitions may yield similar variances.

Another way to achieve stability in the inversion is to append equations to the original matrix $\mathbf{A}$ in such a way that only the unstable part of the solution is affected. To isolate the unstable part of the solution, a pseudo high-pass filter is defined in terms of a diagonal matrix $\mathbf{H}$ containing zeroes in the first i diagonal entries and ones in the last $n - i$ entries. The unstable part of the solution, $\mathbf{e}$, is given by

$$\mathbf{e} = \mathbf{V H V'}\tilde{\mathbf{x}}. \tag{3-14}$$

By defining $\mathbf{L}$ and $\mathbf{H}$ in this manner, the solution $\tilde{\mathbf{x}}$ to the least squares problem is viewed as the sum of two parts, a stable and an unstable part.

$$\tilde{\mathbf{x}} = \mathbf{y} + \mathbf{e} \tag{3-15}$$

If a smoother transition is desired in the filter, the only requirement for Eq. (3-15) to hold is that the diagonal elements of $\mathbf{L}$ and $\mathbf{H}$ sum to unity.

$$\mathbf{L} + \mathbf{H} = \mathbf{I} \text{ (identity)} \tag{3-16}$$

The inversion is stabilized by appending a high-passed set of equalities to the original matrix and data.

$$\begin{bmatrix} \mathbf{A} \\ k_o \mathbf{V H V'} \end{bmatrix} \{\mathbf{x}\} = \begin{Bmatrix} \mathbf{f} \\ \mathbf{b} \end{Bmatrix} \tag{3-17}$$

The augmented matrix and data will be denoted by $\mathbf{A_a}$ and $\mathbf{b_a}$ respectively. If k_o is set very large and $\mathbf{b}$ is set equal to zero, the unstable part of $\mathbf{x}$ is effectively eliminated as in the low-pass filter example above. By adjusting k_o, $\mathbf{H}$, and $\mathbf{b}$ in Eq. (3-17), the ill-conditioned vector $\mathbf{e}$ may be eliminated, made small, or used to make $\mathbf{x}$ resemble some preferred solution. Inversion of the augmented system is stable provided k_o is set large enough to result in a stable condition number.

The *SVD* of the augmented matrix, $\mathbf{A_a}$, is

$$\mathbf{A_a} = \mathbf{U_a} \mathbf{\Lambda_a} \mathbf{V'},\qquad(3\text{-}18)$$

where

$$\left(\mathbf{\Lambda_a}\right)_{ii} = \sqrt{\lambda_{ii}^2 + (k_o H_{ii})^2}\qquad(3\text{-}19)$$

and

$$\mathbf{U_a} = \begin{bmatrix} \mathbf{U}\mathbf{\Lambda_a}^{-1}\mathbf{\Lambda} \\ k_o\,\mathbf{V}\mathbf{\Lambda_a}^{-1}\mathbf{H} \end{bmatrix}.\qquad(3\text{-}20)$$

The matrix $\mathbf{V}$ is unchanged and the singular values are ordered in the diagonal matrix $\mathbf{\Lambda_a}$. The *SVD* of $\mathbf{A_a}$ is easily verified: (1) the columns of $\mathbf{U_a}$ and $\mathbf{V}$ are orthonormal; (2) the diagonal matrix $\mathbf{\Lambda_a}$ has positive elements; and (3) the equality in Eq. (3-18) is satisfied. Appending equations reduces the condition number since previously small singular values become larger in Eq. (3-19); this is a much more stable situation.

The least squares solution to the augmented system is $\mathbf{y_a}$, where

$$\mathbf{y_a} = \mathbf{V}\mathbf{\Lambda_a}^{-2}\left(\mathbf{\Lambda}\mathbf{U'}\mathbf{f} + k_o\mathbf{H}\mathbf{V'}\mathbf{b}\right).\qquad(3\text{-}21)$$

If k_o is set very large and $\mathbf{b}$ set to zero, the last $n-i$ singular values in $\mathbf{\Lambda_a}$ become very large; when these terms are inverted in Eq. (3-21), the ill-conditioned part of the solution is effectively eliminated and $\mathbf{y_a}$ takes on the same value as the filtered solution $\mathbf{y}$ in Eq. (3-12).

If $\mathbf{b}$ is set to zero, k_o set to an intermediate value between the largest and smallest singular value, and i set to zero so that the appended matrix is the scaled identity matrix; then, Eq. (3-21) reduces to the damped least squares solution of Levenberg (1944) and Neumann (1981). The damped least squares solution is $\mathbf{y_d}$, where

$$\mathbf{y_d} = \mathbf{V}\mathbf{\Lambda}\,(\mathbf{\Lambda}^2 + k_o^2\mathbf{I})^{-1}\mathbf{U'}\mathbf{f}.\qquad(3\text{-}22)$$

In damped least squares, the ill-conditioned part of the solution is suppressed while the stable part is affected by an amount determined by k_o; usually k_o is taken to be small.

3.2 The Constrained Least Squares Solution

Inequality constraints arise when bounds are placed on some aspect of the solution. These constraints can occur when the solution parameters correspond to physical quantities which may be required to be positive, or not allowed to exceed a certain maximum value. Conventional least squares as presented in Section 3.1 does not incorporate inequality constraints. The following defines an extension of the *GI* for the constrained least squares problem.

Definition: Among all solutions $\mathbf{x}$ *satisfying*

$$\mathbf{G}\mathbf{x} > \mathbf{h},\qquad(3\text{-}23)$$

and

$$minimum\ \|\,\mathbf{A}\mathbf{x}-\mathbf{f}\,\|,\qquad(3\text{-}24)$$

there is a unique solution $\tilde{\mathbf{x}}_c$ *which satisfies*

$$minimum\ \|\,\mathbf{x}\,\|.\qquad(3\text{-}25)$$

The constrained generalized inverse of $\mathbf{A}$, $\tilde{\mathbf{A}}_c$, *is the matrix which produces* $\tilde{\mathbf{x}}_c$ *from the data.*

$$\tilde{\mathbf{x}}_c = \tilde{\mathbf{A}}_c\mathbf{f}\qquad(3\text{-}26)$$

The only difference between this definition and that of Eqs. (3-3) through (3-5) is the inclusion of the

883

inequality constraints in Eq. (3-23).

A complete description and derivation of the properties of $\tilde{\mathbf{A}}_c$ is given in Lawson and Hanson (1974). The first difficulty which may be encountered is that the inequality constraints in Eq. (3-23) may be incompatible so that no solution exists. Assuming the inequalities can be satisfied, there still may be many solutions which satisfy Eq. (3-24); once again, the inverse is uniquely defined by finding the smallest solution. All of this is similar to the previous discussion except that an explicit formula relating $\tilde{\mathbf{A}}_c$ to $\mathbf{A}$ and $\mathbf{G}$ cannot be found. The method by which the solution $\tilde{\mathbf{x}}_c$ is produced from the data is an iterative one and depends upon the data $\mathbf{f}$ and constraint data $\mathbf{h}$ as well.

Lawson and Hanson (1974) show that $\tilde{\mathbf{x}}_c$ is simply the least squares solution to an unconstrained problem of smaller dimension. The dimension of the problem is reduced by satisfying a subset of the inequalities in Eq. (3-23) exactly as equalities; the particular subset to be satisfied is determined from an iterative procedure. As an example, if $\mathbf{G}$ is the n by n identity matrix and $\mathbf{h}$ is zero, the constrained generalized inverse $\tilde{\mathbf{A}}_c$ is the *GI* of a modified $\mathbf{A}$ in which certain columns of $\mathbf{A}$ have been set to zero. The components of $\tilde{\mathbf{x}}_c$ associated with the zeroed columns are zero.

Due to the iterative method of obtaining $\tilde{\mathbf{x}}_c$, the linear analysis used in section 3.1 is not tractable and a new definition of stability is needed. Stability is defined as the length of the smallest data perturbation required to change a linear combination of the parameters by a prescribed amount. If the linear combination taken involves an isolated parameter, then the measure indicates the smallest change in data needed to change that particular parameter by a prescribed amount. One parameter is said to be more stable than another if a larger data perturbation is required to change it by an equal amount. The stability measure is derived from the solution to the following problem.

Definition: Among all solutions $\mathbf{x}$ *satisfying*

$$\mathbf{G}\,\mathbf{x} > \mathbf{h}\,, \tag{3-27}$$

$$\mathbf{w}'\mathbf{x} = \mathbf{w}'\tilde{\mathbf{x}}_c + \delta x\,, \tag{3-28}$$

and

$$minimum \; \|\, \mathbf{A}\,(\mathbf{x} - \tilde{\mathbf{x}}_c)\,\| \; = \; \|\, \delta\mathbf{f}\,\| = \delta f\,, \tag{3-29}$$

there is a unique solution $\hat{\mathbf{x}}$ *which satisfies*

$$minimum \; \|\, \mathbf{x}\,\|\,. \tag{3-30}$$

In this definition, the quantities $\mathbf{G}$, $\mathbf{A}$, $\mathbf{h}$, and $\tilde{\mathbf{x}}_c$ are the elements of the constrained least squares problem given in Eqs. (3-23) through (3-26); the purpose of this definition is to test the stability of the linear combination $\mathbf{w}'\tilde{\mathbf{x}}_c$. After solving Eqs. (3-27) through (3-30), the residual vector $\delta\mathbf{f}$ is the smallest change in the data of Eq. (3-24) sufficient to increase the linear combination $\mathbf{w}'\tilde{\mathbf{x}}_c$ by an amount δx. Large values of δf indicate greater stability of $\mathbf{w}'\tilde{\mathbf{x}}_c$ than small values of δf.

For the least squares problem without inequality constraints, this stability measure can be expressed in closed form. If the linear combination being tested is the j'th parameter (*i.e.* $\mathbf{w}'$ is all zeroes except for a one in the j'th location), the data perturbation necessary to increase the j'th parameter by an amount δx is given by

$$\delta f = \left(\frac{\delta x^2}{(\mathbf{V}\,\Lambda^{-2}\mathbf{V}')_{jj}}\right)^{\!\frac{1}{2}}. \tag{3-31}$$

The expression in the denominator is also the variance in the j'th parameter due to independent errors of unit variance in the data as given in Eq. (3-10). If a general linear combination of parameters is to be tested, one can simply make a change of variables so that the j'th parameter has the value of the linear combination and Eq. (3-31) can be applied. Hence, for least squares without inequality constraints, this new definition of stability is equivalent to the more commonly used variance estimates.

A closed form solution for δf is not known when inequality constraints are maintained due to the iterative method of obtaining the solution. When analyzing the stability of the constrained least squares solution, the inverse problem of Eqs. (3-27) through (3-30) must be solved for each combination of

parameters being tested. One important feature of this stability measure is that it simply involves solving another constrained least squares problem. By virtue of the fact that the original problem can be solved, the stability analysis can be performed and requires no further expertise.

Two methods of stabilizing the solution were presented in Section 3.1: low-pass filtering (Eq. (3-11)) and augmentation of the original matrix (Eq.(3-17)). Only the augmented matrix method can be used to stabilize the constrained least squares solution since low-pass filtering generally causes the inequality constraints to be violated.

3.3 Computer Implementation of Inversion Methods

Once the matrices and data vectors are formed, the inversion follows a three step procedure designed to eliminate redundant calculations. The following discussion presumes that $m > n$ so that the system appears overdetermined.

(1) The matrix $\mathbf{A}$ and data $\mathbf{f}$ are reduced from an m by n system to the n by n system

$$\mathbf{\Lambda} \mathbf{V}'\mathbf{x} = \mathbf{U}'\mathbf{f},\qquad (3\text{-}32)$$

which has the same least squares solution as the original system.

(2) The filter $\mathbf{H}$, constant k_o, and data $\mathbf{b}$ of Eq. (3-17), are defined and appended to the reduced matrix from step (1) to stabilize the inversion. This composite system which is now $2n$ by n is once again reduced to the n by n equivalent system

$$\mathbf{\Lambda_a} \mathbf{V}'\mathbf{x} = \mathbf{\Lambda_a}^{-1} \mathbf{\Lambda} \mathbf{U}'\mathbf{f} + k_o \mathbf{\Lambda_a}^{-1} \mathbf{H} \mathbf{V}'\mathbf{b}.\qquad (3\text{-}33)$$

(3) The constrained least squares problem of (3-23) through (3-26) is solved using the reduced system of step (2). If inequality constraints are absent, the least squares solution

is obtained by multiplying Eq. (3-33) in step (2) by $\mathbf{V} \mathbf{\Lambda_a}^{-1}$ to obtain Eq. (3-21).

The number of arithmetic operations associated with each of steps (1) and (3) is proportional to the number of rows in the matrix times the number of columns squared. Hence, step (1) requires $m n^2$ operations and step (3) requires n^3 operations. Step (2) requires a negligible amount of calculation since it is known by an exact algebraic expression. Since $m > n$, the utility of step (1) is recognized when the inverse problem is to solved many times since only steps (2) and (3) need to be repeated for each subsequent inversion. This three step procedure has the added benefit that the amount of computer storage required to perform the inversion in step (3) is also reduced.

The following Fortran computer codes are used to form the inversion algorithm. The program SVDRS (Lawson and Hanson, 1974) is used to compute the *SVD*. The programs SQRDC and SQRSL (Dongarra *et al.*, 1979) are used to perform Gram-Schmidt decomposition of the $\mathbf{A}$ matrix. The constrained least squares solution is obtained using program LSI written by A. Olson based upon the text of Lawson and Hanson (1974). Routine LSI performs the appropriate transformations necessary to call programs NNLS and LDP (Lawson and Hanson 1974).

4. Application to the 1979 Imperial Valley Earthquake

In this section, near-field ground accelerations of the 1979 Imperial Valley earthquake are inverted, resulting in four solutions which fit the data. The first two solutions are obtained from least squares and demonstrate the concept of a solution's stability. The third and fourth solutions are

obtained by constrained least squares analysis; the slip velocity is constrained to be positive everywhere on the fault to ensure that the solutions are physically reasonable. It should be noted that these constraints do not allow the slip to have an over-shoot, *i.e.*, reverse direction; this type of faulting is not considered here, although it is easily accommodated in the inversion procedure by constraining only the total offset instead of the slip velocity. Finally, the stability of each of these solutions is made quantitative so that the significance of particular details in the solutions can be assessed.

4.1 Description of Fault Geometry and Station Locations

The October 15, 1979 Imperial Valley earthquake had a local magnitude $M_L = 6.6$ and occurred within the vicinity of several permanent seismic networks operating in the United States and Mexico. The magnitude, epicentral location, and origin time are given by Chavez *et al.* (1981). Figure 4-1 shows the geometry of the recording stations with respect to the epicenter and known major faults. The observed surface offset is predominantly right-lateral strike-slip with the dip-slip component of offset increasing near the northern end of the Imperial Fault. A maximum offset of 70 cm was observed beginning 10 km northwest of the epicenter on the Imperial Fault and decreasing to zero in a distance of 30 km at the fault's northern end (Sharp *et al.*, 1981). The observed offset on the Brawley Fault averaged approximately 25 cm. The orientation of surface offset with respect to epicenter location indicates that the slip on the fault proceeded to the northwest along the Imperial Fault.

A total of 30 three-component accelerometers recorded this earthquake and are listed in Table 4-1. Four of these are not used in the inversion study due to their proximity to the perimeter of the valley or other structural irregularities (e.g., Cerro Prieto is located on top of a volcano). The remaining 26 stations are those shown in Figure 4-1. Stations numbered 1 through 22 are part of a permanent array deployed by the United States Geological Survey (USGS). The station locations, component orientations, and trigger times (when available) for these 22 stations are given in Brady *et al.* (1980). Stations 23 through 29 are located in Mexico and are maintained by the University of California at San Diego (UCSD). The ground motion at these seven sites was recorded digitally and the location, component orientations, and trigger times are given in Brune *et al.* (1981). Station 30 is maintained by the California Division of Mines and Geology (CDMG) as described in McJunkin and Ragsdale (1980). A total of 77 acceleration times series from these 26 stations comprise the recorded data for the inversion study.

The Green's functions of Eq. (2-5) are calculated with the computer program PROSE, which generates the complete response of a layered visco-elastic halfspace by means of a wavenumber integral formulation and Fourier transform (Apsel, 1979). The velocity structure used is given in Table 4-2 and is based upon the interpretation by McMechan and Mooney (1980) of a recent refraction survey in the Imperial Valley conducted by the USGS (Fuis *et al.*, 1981a and 1981b). The layered velocity model is an approximation to the gradient which varies smoothly along the northwest trending axis of the valley. Since the refraction analysis only pertained to P waves, the S wave structure of Table 4-2 is conjectured based upon a P to S ratio of 1.73 at depths greater than 5.75 km, and a P to S ratio which is 3.38 at the surface of the halfspace and increases linearly with depth. The density structure in Table 4-2 is consistent with the interpretation of gravity data given in Fuis *et al.* (1981a). The ground acceleration is low-passed before inversion so that periods shorter than 3 seconds are not considered. At this low frequency and distance range, the effects of attenuation and of layering rather than gradient are negligible.

4.2 Discretization of the Fault Surface

Inversion requires a discretization of the fault surface into a set of cells as described in Section 2.2. The parameterization is totally defined by: the cell size; slip function, $F(t)$; wavefront, $T(x)$; the number of times each cell may slip, $(2K+1)$; and the time step between each slip, δt.

In this study, the Imperial and Brawley faults are approximated as vertical planes extending from zero to 10 km depth. The Imperial Fault is 50 km in length extending 40 km northwest and 10 km

southeast of the epicenter. The Brawley Fault is 10 km in length extending northward from the Imperial Fault as shown in Figure 4-1. The cells are 5 km by 5 km square. This means that there are two cells vertically on each fault, ten cells horizontally on the Imperial Fault, and two cells horizontally on the Brawley Fault. A cell dimension less than 5 km for this problem is not feasible since the number of parameters would become quite large. The data is filtered so that the shortest data wavelength is roughly 10 km corresponding to a three-second period wave in the material below 5 km depth. The smallest discretization wavelength and smallest data wavelength are therefore comparable.

The slip function, $F(t)$, is illustrated in Figure 4-2. $F(t)$ is basically a smooth step function which begins rapidly, achieving about 75 percent of the final offset in one second and terminates in 2.25 seconds. For the frequency range of the filtered data (periods greater than 3 seconds), the departure of $F(t)$ from a step function in Figure 4-2 is not significant and the reader may simply regard $F(t)$ as a step function. Each cell is allowed to slip five times at sequential delays of $\delta t = 0.75$ seconds, slipping as $F(t)$ each time. The increment of 0.75 seconds is chosen in accordance with the 3-second low-pass filtering of the data; increments in slip occurring at higher frequencies can not be resolved.

The average rupture front $T(x)$ is the arrival time of a geometrical ray wavefront defined by 90 percent of the shear wave speed (see Table 4-2 for shear wave velocity). $T(x)$ initiates at 10 km depth below the epicenter and proceeds bilaterally along the Imperial Fault. $T(x)$ on the Brawley Fault initiates when the wavefront passes on the Imperial Fault. Since the observed surface offset began abruptly at 10 km northwest of the epicenter on the Imperial Fault, a second rupture is allowed to occur here which propagates to the south and is initiated by the passing of the first rupture. This second rupture is equivalent to allowing the average rupture front $T(x)$ to proceed bilaterally from a point 10 km northwest of the epicenter on the Imperial Fault.

The number of parameters equals twice the number of cells multiplied by the number of times each cell can slip. The factor of two arises since each slip vector, s_{jk} in Eq. (2-5), has two components in the plane of the fault. There are 24 cells on the Imperial and Brawley faults combined for the initial bilateral rupture and 8 cells on the Imperial Fault for the second rupture: a total of 32 cells. Each cell is allowed to slip five times. This yields a total of $n=320$ parameters.

Before performing the inversion, both sides of Eq. (2-5) are Fourier band-pass filtered to retain only periods longer than 3 seconds and shorter than 10 seconds. Both data and Green's functions are then sampled at 0.25 second increments so that the character of the waveforms is maintained. Only the first 30 seconds of recorded ground motion is considered which results in 120 data points for each of 77 components, a total of $m=9240$ data points. Although $m>n$ and the problem appears overdetermined, there is a great deal of redundancy and the solution for the slip parameters is likely to be ill-conditioned.

For each component of acceleration used in the inversion, the maximum value is found and both data and Green's functions for that component are divided by that value. This has the effect of normalizing the problem so that the inversion is attempting to fit each component to within the same percentage. Due to the inability of the inversion to fit the motion at several stations, certain components were weighted small in the inversion; these are marked with a * in Figure 4-12. The weighting was accomplished by multiplying the rows of the matrix and the data by 0.01 for these components; all other components were not weighted and therefore have an effective weight of 1.

4.3 The Least Squares Solution

The least squares solution is defined in Eqs. (3-3) through (3-5). Figure 4-3 shows the distribution of slip which results from fitting the data without any attempt to ensure stability in the solution. The area of each triangle is proportional to the slip in a given cell and points in the direction of slip. For example, a triangle pointing to the right indicates right-lateral strike-slip motion; a triangle pointing up indicates dip-slip motion with the west side of the fault surface moving up relative to the east side.

The dynamic slip in Figure 4-3 (bottom) contains two groups of boxes, each group being five boxes high. The upper group of boxes contains the five slips in the row of cells spanning 0 to 5 km

depth on the fault surface; the static offset from 0 to 5 km depth is shown in the upper row of cells above. The lower group of boxes contains the five slips in the row of cells spanning 5 to 10 km depth; the static offset from 5 to 10 km depth is shown in the lower row of cells above. The static offset in a given cell is the vector sum of the five corresponding dynamic slip vectors.

The static offset and dynamic slip are each scaled separately according to their peak value. The peak offset in Figure 4-3 is 3.96 meters. The peak dynamic slip is 2.05 meters, occurring within a time increment of 0.75 seconds. The seismic moment is 4.04×10^{25} dyne-cm, defined as the scalar length of the vector sum of the offsets in all cells. The offset is very oscillatory with neighboring cells having offsets in opposing directions. Even the dynamic slip within a given cell oscillates, changing direction by as much as $180°$ in 0.75 seconds. Most of the energy radiating from this fault motion is simply canceling and has a minimal affect upon the fit to the data. This solution is not acceptable due to the erratic spatial and temporal variations and the significant component of left-lateral faulting on known right-lateral faults.

The erratic character exhibited in Figure 4-3 is typical of unstable solutions in which small variations in the data produce large changes in the solution. The stabilizing methodology presented in Section 3.1 is used to suppress the unstable part of the least squares solution, and in so doing, increase the misfit to the data by a small amount. Although the stabilized solution is not the best fit to the data, it is stable in the sense that it is not being controlled by small features in the data.

The condition number of the original matrix is 128 (ratio of the largest to smallest singular value) implying that a one percent change in the data could lead to a 128 percent change in the overall solution. The condition number is reduced in order to stabilize the solution by appending a set of equations to the original matrix as defined in Eq. (3-17). The filter coefficient matrix $\mathbf{H}$ is prescribed to be: zero where the singular value ratio is between 1 and 4; unity where the singular value ratio is greater than 20; and linear in between. The vector $\mathbf{b}$ is set to zero and the constant k_o is made large enough to reduce the condition number from 128 to 6. Stabilizing the matrix in this manner suppresses the unstable part of the solution associated with small singular values.

Figure 4-4 shows the stabilized least squares solution obtained using the augmented matrix and data. Both the static offset and dynamic slip are much smoother than the unstabilized solution in Figure 4-3. The peak offset decreases from 3.96 meters in Figure 4-3 to 1.31 meters in Figure 4-4; the peak dynamic slip also decreases from 2.05 meters to 0.75 meters. The seismic moment similarly decreases from 4.04×10^{25} to 3.37×10^{25} dyne-cm. While the offset and slip are smaller by a factor of three, the moment is smaller by only 20 percent. Such a small change in moment is due to the near cancellation of the unstable slip distributions. This cancellation results from the vector sum of slip vectors having opposing orientations. The small change in moment suggests, quite expectedly, that moment is a more stable quantity than offset or slip.

The geology and tectonics for the Imperial Valley indicate that faulting is predominantly right-lateral strike-slip; the dip-slip component is much smaller with the west side of the Imperial Fault moving up and the west side of the Brawley Fault moving down relative to the east side. The stabilized solution (Figure 4-4) also exhibits predominantly right-lateral offset. The dip-slip component of offset in Figure 4-4 has the wrong polarity but is much smaller in amplitude than the strike-slip component.

The dynamic slip for the stabilized solution still shows intermittent left-lateral motion, *i.e.*, reversals. Even the offset shows a few neighboring cells which moved in opposing directions, especially on the Brawley Fault. These reversals, both in static offset and dynamic slip, are no longer due to instabilities in the solution. They are a characteristic of the least squares solution to this particular data set and no further amount of stabilization can make them disappear.

Opposing static offsets along the fault contradict the expected fault motion based upon the tectonic stress field and are therefore unphysical. The interesting question remains as to whether a distribution of slip can be found which: (1) has no reversals; (2) is consistent with tectonic and geologic evidence; and (3) satisfies the recorded ground motion data. Since the ground motion data alone does not require the solution to be nonreversing, additional information must be added to the inversion to ensure this outcome as discussed in the next section.

4.4 The Constrained Least Squares Solution

By solving the constrained least squares problem of Eqs. (3-23) through (3-26), only nonreversing solutions are allowed. The inequalities of Eq. (3-23) take the form of positivity constraints for the parameters representing strike-slip motion. By keeping these parameters positive, each strike-slip parameter remains right-lateral. The dip-slip parameters for the Imperial Fault are constrained to be positive while the dip-slip parameters for the Brawley Fault are constrained negative.

The constrained least squares solution is shown in Figure 4-5. Only the data and inequality constraints are used in this inversion and no attempt is made to ensure the stability of the solution. The remarkable difference between this solution and the least squares solution (Figure 4-3) is due entirely to the inclusion of the inequality constraints in the constrained least squares inversion. The static offset is much smoother in Figure 4-5 with all cells being right-lateral and having the appropriate dip-slip component in accordance with the inequality constraints. The dynamic slip is also quite reasonable in appearance showing the coherent temporal behavior resulting from the inequality constraints.

The peak values of static offset and dynamic slip for the constrained solution (Figure 4-5) are nearly the same as the corresponding values for the least squares solution (Figure 4-3). The amount of static offset within any given cell is also nearly the same for these two solutions, although, the polarity of the offset sometimes differs significantly. The constrained solution has a moment of 1.71×10^{26} dyne-cm which is four times larger than the moment of 4.04×10^{25} in the least square solution. As was pointed out earlier, cancellation is responsible for the low value of moment in the least squares solution. The inequality constraints force the slip within each cell to be nearly parallel; hence, the amount of possible cancellation is minimized and the moment increased.

Although the constrained least squares solutions seems reasonable (Figure 4-5), it does not follow from this judgement alone that it is also stable. Certainly, the addition of the inequality constraints can only increase the stability of the solution when compared with the unconstrained solution; however, the amount of increase has yet to be determined. The constrained least squares inversion is stabilized exactly as the least squares inversion (Section 4.3, Figure 4-4). A set of equations are appended to the original matrix and the solution to the augmented system is then found. The filter coefficient matrix $\mathbf{H}$ and vector $\mathbf{b}$ are defined exactly as in Section 4.3. The constant k_o is set large enough to change the condition number from 128 to 7.

The stabilized constrained least squares solution is shown in Figure 4-6. Once again, stabilization produces significant changes in the solution. The moment is 9.13×10^{25} dyne-cm compared with 1.71×10^{26} in the unstabilized solution, nearly a factor of two smaller. The peak static offset and peak dynamic slip are also smaller by nearly a factor of two: 1.65 meters and 0.93 meters in the stabilized solution; 2.6 meters and 1.93 meters in the unstabilized solution. In the stabilized solution (Figure 4-6), the relative offset in the upper five km on the Imperial Fault is much smaller at the northern end than in the unstabilized solution (Figure 4-5).

A noticeable trend can be seen going from the upper middle to the lower right in the dynamic slip at depth on the Imperial Fault (Figure 4-6). To interpret this trend, consideration must be given to the wavefront $T(x)$ which defines the absolute time for the five point time window. Zero time for the five point time window is defined as the travel time of a wavefront initiating at the earthquake epicenter and traveling at 90 percent of the local shear wave velocity. Trends which go across the boxes from left to right correspond to slip propagating along the fault with a horizontal phase velocity equal to the wavefront $T(x)$. Trends which go from upper left to lower right correspond to slip propagating with a horizontal phase velocity greater than the wavefront $T(x)$. Similarly, trends which go from lower left to upper right correspond to phase velocities less than $T(x)$.

The bottom group of boxes contains the five slips for the single row of cells at five to ten km depth; hence, the trend corresponds to slip propagating in this depth range at a horizontal phase velocity greater than 90 percent of the shear wave speed. The actual phase velocity is between 4.0 and 5.0 km/sec which more nearly equals the compressional wave velocity. Since this is the horizontal phase velocity of slip propagation, the actual velocity may be less. For example, if the slip is propagating vertically as a plane wave the horizontal phase velocity is infinite. With only two cells in the vertical

direction on the fault, the vertical phase velocity can not be accurately determined.

Figure 4-6 (bottom) shows the right-lateral component of offset on the Imperial Fault for the stabilized solution. The dark triangular shaded region is a schematic representation of the observed surface offset (Sharp *et al.*, 1981). The consistency of the solution and observation is remarkable since the inversion is based only on the acceleration recordings. Both inversion and observation show the offset near the surface to be concentrated between 10 and 35 km north of the epicenter decaying to zero at the most northern end. The inversion shows about 70 percent more displacement in the upper five km than reflected in the observed offset at the surface. The offset between 5 km and 10 km is about twice that in the upper five km but the overall shape is very similar. It is interesting to note that no large concentrations of slip are required by the data; this is evidenced by the smooth character of the stabilized solution.

The moment estimated from long period surface waves is 6×10^{25} dyne-cm (Kanamori and Regan, 1981). Laser strain meter measurements taken at Pinon Flat Observatory approximately 140 km away indicate a moment of 9×10^{25} dyne-cm (Wyatt, 1981). The moment for the stabilized solution in Figure 4-6 is 9.13×10^{25} dyne-cm, consistent with these independent estimates of moment.

The fits to the data by the stabilized solution (Figure 4-6) are plotted geographically in Figures 4-7, 4-8, and 4-9 for the 230°, 140°, and vertical components of motion respectively. Figures 4-10 through 4-12 show the same fits in greater detail. The overall agreement in both amplitude and phase is very good. Figure 4-12 shows the detailed fit to the stations farthest south in Mexico; although there is agreement in amplitude, the fit to the phase is not very good due to the more complicated nature of the data in the south. Recordings denoted by a * in Figure 4-12 were weighted small in the inversion since their complexity was not well modeled by the inversion.

By stabilizing the solution, a certain amount of fit to the data is sacrificed. Figure 4-13 shows the fit to the 230° component of data by the unstabilized least squares solution. While the fit is nearly perfect, the corresponding solution (Figure 4-3) contains a very oscillatory slip distribution. Conversely, the distribution of slip in the stabilized constrained least squares solution (Figure 4-6) is smoothly varying while the fit to the 230° component of data (Figure 4-7) is less perfect. The amount of misfit in Figure 4-7 is not much considering the improvement in the slip distribution. Of the four slip distributions (Figures 4-3 through 4-6), the stabilized least squares solution (Figure 4-6) is preferred due to its stability, coherence, and compatibility with geologic, tectonic, and other independent observations.

4.5 Stability Analysis of Inversion Results

The condition number provides an estimate of the overall stability of the solution. In order to test the significance of particular details in the solution, stability is defined in terms of the smallest change in the data required to change the offset in a given cell by one meter (see Eqs. (3-27) through (3-30)). A cell which requires a small change in the data is less stably determined than a cell which requires a large change in data.

Figures 4-14 shows the stability results for the two least squares solutions shown in Figures 4-3 and 4-4. The most stable cell in the least squares solution is the third from the upper right corner on the Imperial Fault (Figure 4-14, top). An 8.5 percent change in the data is required to change the dip-slip component of offset in this cell by one meter, while a 3.4 percent change is required to produce an equal change in the strike-slip component. Other cells (Figure 4-14, top) contain lower values for stability, sometimes only a fraction of a percent as in the northern upper corner of the Imperial Fault. These low values correspond to the least stably determined offsets in the least squares solution.

The stability of the stabilized least squares solution is shown in Figure 4-14 (bottom). It is clear that the effect of the stabilizing procedure is to make the stability of the strike-slip and dip-slip components more nearly equal and the same in each cell. An 18 percent change in the data is required to produce a one meter change in the offset of the stabilized solution. Using this measure, the stability is improved by roughly a factor of 2 to 20 depending upon the cell. Again, improved stability is caused by suppressing the unstable slip distributions.

The stability of the two constrained least squares solutions are shown in Figure 4-15. Comparing Figure 4-15 (top) with Figure 4-14 (top), the constrained least squares solution is seen to be everywhere more stable than the least squares solution. This confirms the earlier statement that adding information to the inversion has the effect of stabilizing the solution. A 9.6 percent change in the data is required to change the dip-slip component of offset in third cell from the upper corner on the Imperial Fault (Figure 4-15, top). The cell with the most stably determined strike-slip component of offset is now near the southern upper corner of the Imperial Fault (Figure 4-15, top) requiring a 6.6 percent change in the data to produce a one meter change. Just as in least squares (Figure 4-14, top), stability varies from cell to cell.

The stability of the stabilized constrained least squares solution (Figure 4-15, bottom) is much greater than the unstabilized solution (top). The stability of the dip-slip component is nearly a constant 14.2 percent everywhere, while the strike-slip stability is almost uniformly 12.8 percent. It should be noted that more than a 14.2 percent change in the data is likely to be required to change the dip-slip component of offset in two cell simultaneously; this amount has not been determined here. The same holds for simultaneously changing the strike-slip and dip-slip components of offset in one cell.

To put the stability analysis in perspective, note that multiplying the data by two will change the solution by exactly a factor of two since the problem in linear in this regard. Since the offsets in the stabilized solutions (Figures 4-4 and 4-6) are roughly one meter, a 100 percent change in the data can therefore change the offset in every cell by roughly one meter. To change the a component of offset in only one cell by one meter will require less than a 100 percent change in the data. Hence, the 14.2 percent change in the data shown in Figure 4-15 (bottom) indicates a stable solution.

5. Conclusions

Due to the linear relation between the displacement discontinuity on a fault surface and the resulting seismic radiation, it was shown that linear inverse theory could be used to infer subsurface slip distributions on a known fault from recordings of ground motion at the Earth's surface. In order to obtain physically reasonable slip distributions, inequality constraints were satisfied in addition to the recorded data. Not only did inverse theory allow a reasonable solution to be systematically found, it provided a framework wherein the solution was decomposed into a stable and an unstable component. When many distributions of slip fit the data, differences in the solutions were found to correspond to the unstable component which is not determined by data.

Inverse theory was applied to 77 components of low frequency acceleration recorded in the near-field of the October 15, 1979 Imperial Valley earthquake. A solution was obtained in Section 4.4 which satisfies the data, is physically reasonable, and only contains the stable component of slip distribution. The seismic moment of 9.13×10^{25} dyne-cm obtained for this solution is consistent with independent estimates of moment from long period surface waves and static strain measurements. The corresponding peak offset is 1.65 meters occurring between 5 km and 10 km depth and 15 to 20 km north of the epicenter on the Imperial Fault; the offset in the upper five kilometers conforms in both amplitude and shape to observations of surface offset and has a peak value of one meter. The offset obtained was predominantly right-lateral and smoothly varying requiring no localized zones of high offset; offset on the Brawley Fault is much less than that on the Imperial Fault. The time behavior of slip was explained by a rupture front propagating at an average velocity of 90 percent of the local shear wave speed; however, over a distance of 20 to 30 km on the Imperial Fault, the horizontal propagation of slip occurred at a velocity approaching that of the compressional wave.

6. Acknowledgments

7. References

Apsel, R. J. (1979). *Dynamic Green's Functions for Layered Media and Applications to Boundary Value Problems*, Ph.D. Thesis, University of California, San Diego, Ca.

Backus, G. and F. Gilbert (1968). The resolving power of gross earth data, *Geophys. J. R. astr. Soc.*, **16**, 169–205.

Backus, G. and F. Gilbert (1970). Uniqueness in the inversion of inaccurate gross earth data, *Phil. Trans. R. Soc. Lond.*, **266A**, 123–192.

Ben-Israel, A. and A. Charnes (1963). Contributions to the theory of generalized inverses, *J. Soc. Indust. Appl. Math.*, **11**, 667–699.

Brady, A. G., V. Perez, and P. N. Mork (1980). The Imperial Valley earthquake, October 15, 1979, digitization and processing of accelerograph records, *U.S. Geol. Survey open-file report*, **80-703**, Menlo Park, Ca.

Brune, J. N., J. Prince, F. Vernon III, E. Mena, and R. Simons, (1981). Strong motion data recorded in Mexico for the 10/15/79 Imperial Valley earthquake, *U.S. Geol. Survey professional paper*, Menlo Park, Ca.

Burridge, R. and L. Knopoff (1964). Body force equivalents for seismic dislocations, *Bull. Seism. Soc. Am.*, **54**, 1875–1888.

Chavez, D., J. Gonzales, J. N. Brune, F. Vernon III, R. Simons, K. L. Hutton, P. T. German, and C. E. Johnson (1981). Mainshock location and Magnitude determination using combined U.S. and Mexican Data, *U.S. Geol. Survey professional paper*, Menlo Park, Ca.

Dongarra, J. J., J. R. Bunch, C. B. Moler, and G. W. Stewart (1979). *Linpack Users' Guide*, S.I.A.M., Philadelphia, Penn.

Franklin, J. N. (1970). Well posed stochastic extensions of ill-posed linear problems, *J. Math. Anal. Appl.*, **31**, 682–716.

Fuis, G. S., W. D. Mooney, J. H. Healey, G. H. McMechan, and W. J. Lutter (1981a). Seismic refraction studies of the Imperial Valley region, California - Profile models, a traveltime contour map, and a gravity model, *U.S. Geol. Survey open file report*, **81-270**, Menlo Park, Ca.

Fuis, G. S., W. D. Mooney, J. H. Healey, G. H. McMechan, and W. J. Lutter (1981b). Crustal structure of the Imperial Valley region, *U.S. Geol. Survey professional paper*, **1254**, Menlo Park, Ca.

Gilbert, F. (1971). Ranking and winnowing gross earth data for inversion and resolution, *Geophys. J. R. astr. Soc.*, **23**, 125–128.

Jackson, D. D. (1972). Interpretation of inaccurate, insufficient, and inconsistent data, *Geophys. J. R. astr. Soc.*, **28**, 97–109.

Kanamori, H. and J. Regan (1981). Long-period surface waves generated by the Imperial Valley earthquake of 1979, *U.S. Geol. Survey professional paper*, Menlo Park, Ca.

Lawson, Charles L. and Richard J. Hanson (1974). *Solving Least Squares Problems*, Prentice-Hall, Inc., Englewood Cliffs, New Jersey.

Levenberg, K. (1944). A method for the solution of certain non-linear problems in least squares, *Quarterly of Applied Mathematics*, **2**, 163–168.

McJunkin, R. D. and J. T. Ragsdale (1980). Compilation of strong-motion records and preliminary data from the Imperial Valley earthquake of 15 October, 1979, *California Division of Mines and Geology preliminary report 26*, Sacramento, Ca.

McMechan, G. A. and W. D. Mooney (1980). Asymptotic ray theory and synthetic seismograms for laterally varying structures: theory and application to the Imperial Valley, California, *Bull. Seism. Soc. Am.*, **70**, 2021−2035.

Neumann, G. (1981). Determination of lateral inhomogeneities in reflection seismics by inversion of traveltime residuals, *Geophysical Prospecting*, **29**, 161−177.

Penrose, R. (1955). A generalized inverse for matrices, *Proc. Camb. Phil. Soc.*, **51**, 406−413.

Penrose, R. (1956). On best approximate solution of linear matrix equations, *Proc. Camb. Phil. Soc.*, **52**, 17−19.

Sharp, R. V., *et al.* (1981). Surface faulting in central Imperial Valley, *U.S. Geol. Survey open-file report*, Menlo Park, Ca.

Wiggins, R. (1972). The general linear inverse problem: implications of surface waves and free oscillations on earth structure, *Rev. Geophys. Space Phys.*, **10**, 251−285.

Wyatt, F. (1981). Distant deformation from the Imperial Valley, California earthquake 1979, submitted to *Bull. Seism. Soc. Am.*.
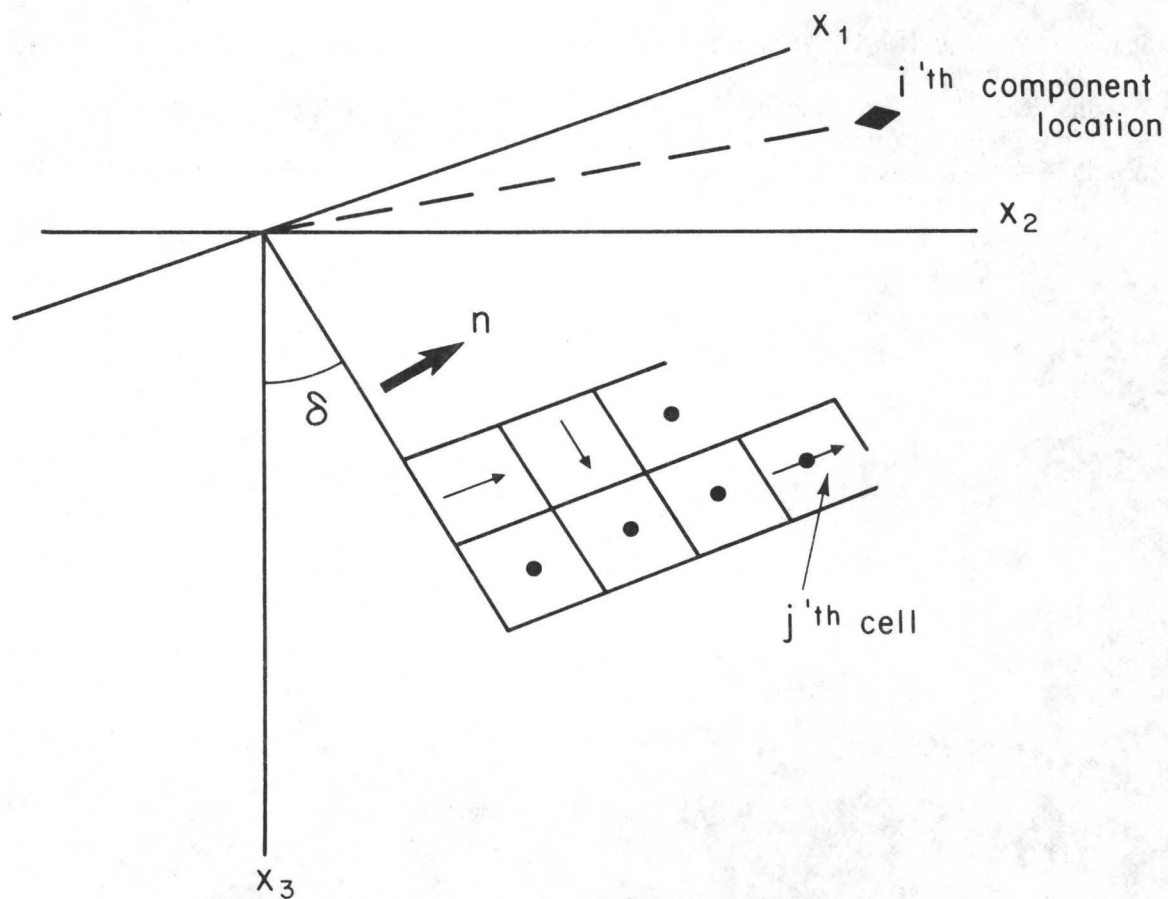
Figure 2-1. Geometry of fault surface S in an elastic halfspace. In this figure, a planar fault surface at a dip of δ from the vertical is divided into two-dimensional rectilinear cells. Each cell requires a two component vector to described the relative slip across the surface.
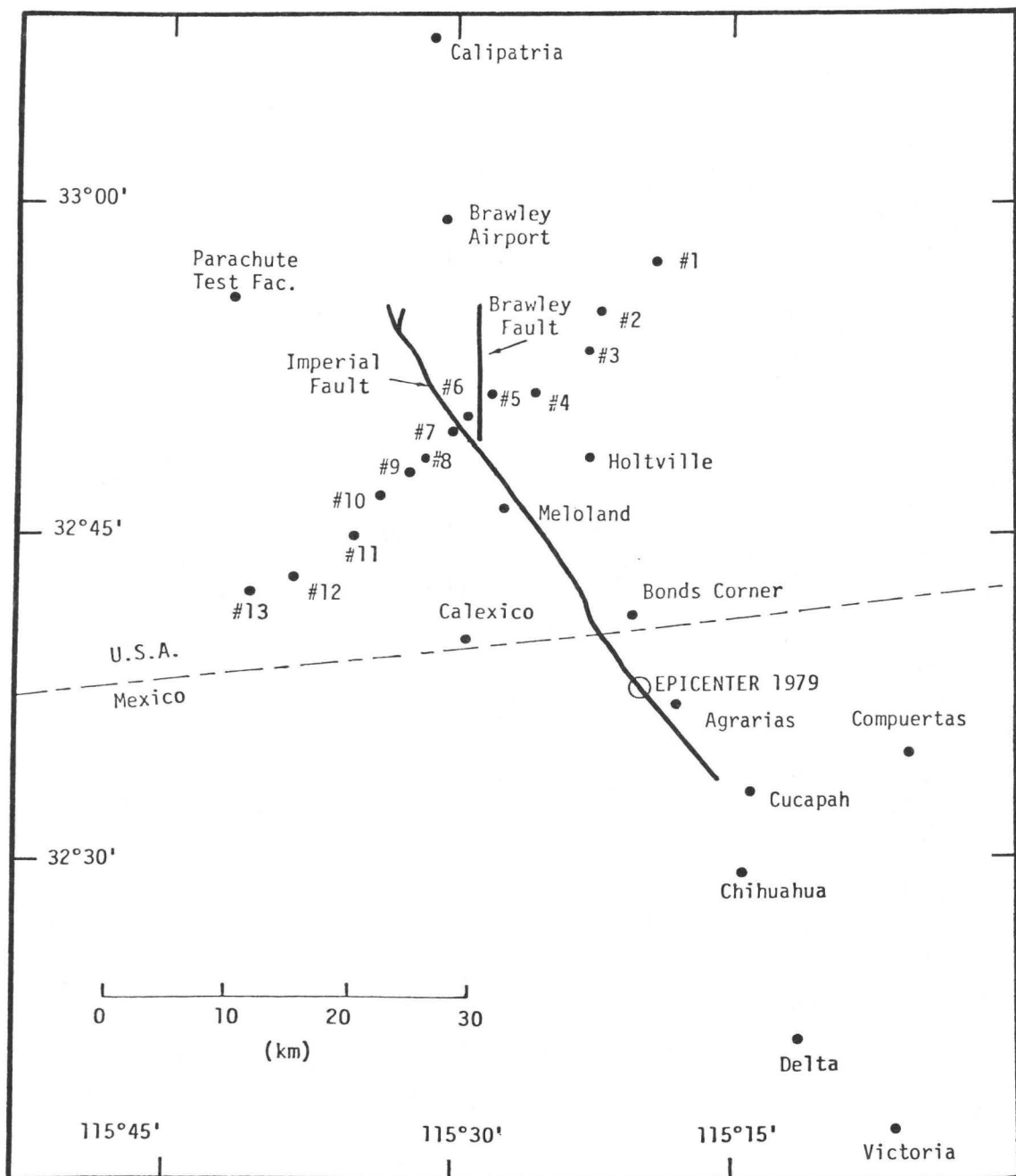
Figure 4-1. Map showing fault geometry and station locations for the October 15, 1979 Imperial Valley earthquake. The 26 stations shown are used in the inversion for the distribution of slip on the Imperial and Brawley faults.
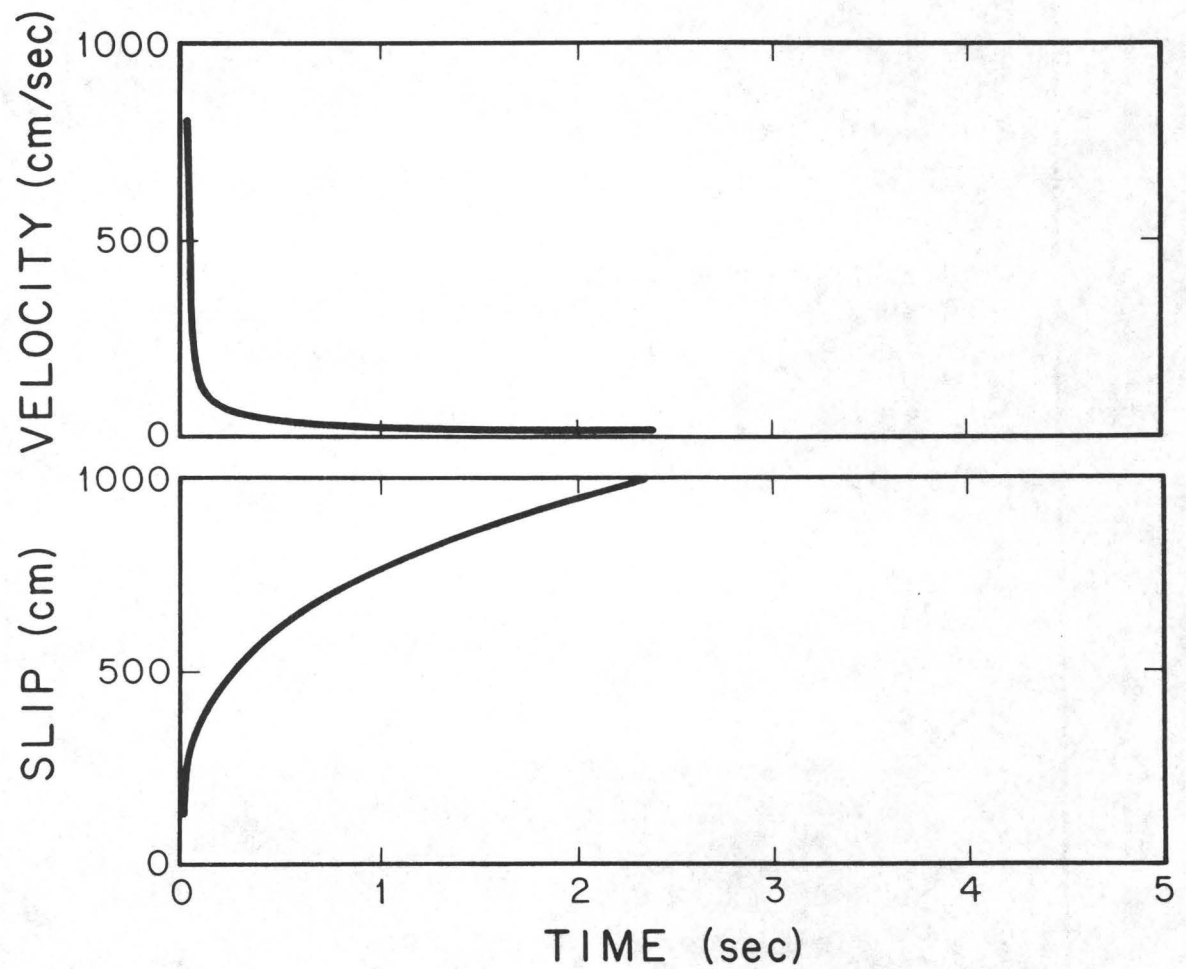
Figure 4-2. The time function $F(t)$ (bottom) and its derivative (top) used in the discretization of the inverse problem. Each point on the fault is allowed to slip a prescribed number of times, slipping as $F(t)$ each time.

LEAST SQUARES

STATIC OFFSET
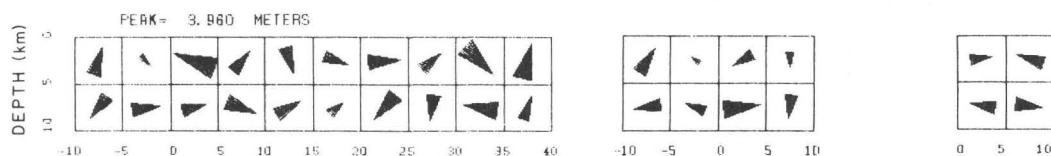
DYNAMIC SLIP
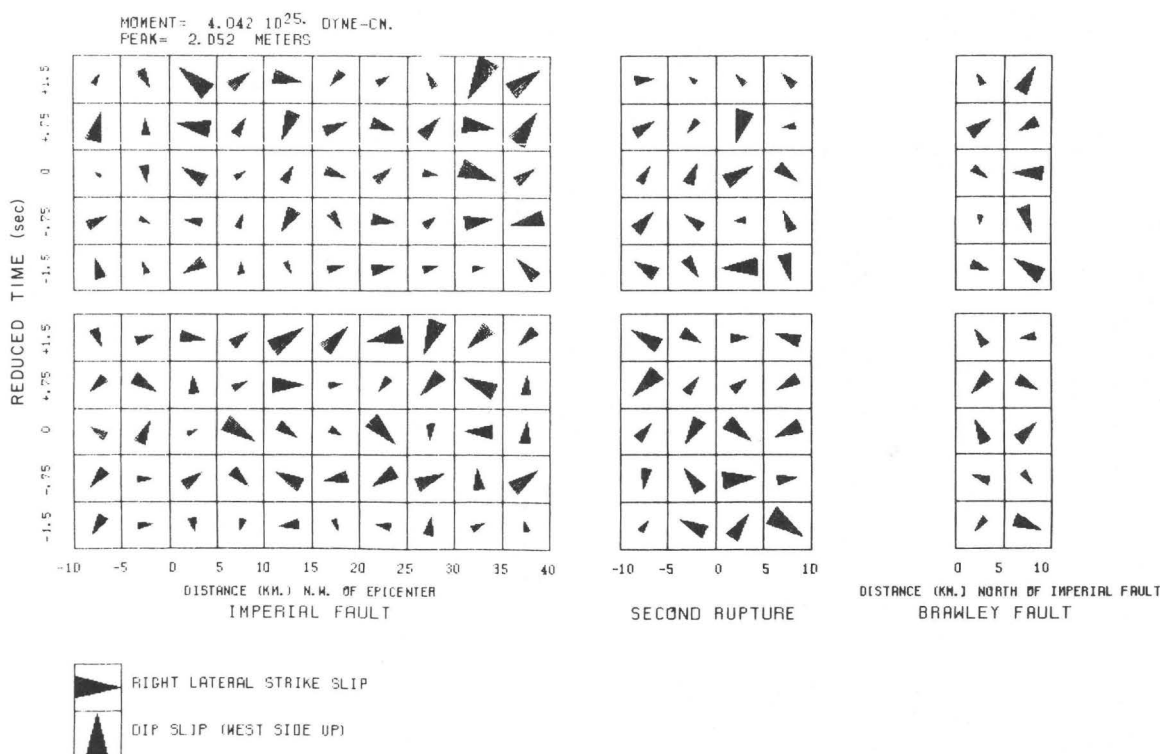
Figure 4-3. Slip on the Imperial and Brawley faults obtained by least squares inversion without stabilization. Triangles have an area proportional to the displacement, and point in the direction of slip; the peaks define the scales for static and dynamic displacements. The static offset (top) is shown for the two horizontal rows of 5 km. square cells which make up the fault surface. The two groups of boxes (bottom) contain the dynamic slip for the two rows of cells (top). The vector sum of the five sequential slips plotted vertically (bottom) equals the static offset in the corresponding cell above. Zero time for the dynamic slip is the time required by a wavefront moving at 90 percent of the shear wave velocity to travel from the hypocenter to the cell.

STABILIZED LEAST SQUARES

STATIC OFFSET

PEAK= 1.308 METERS

DYNAMIC SLIP

MOMENT= 3.372 10²⁵· DYNE-CM.
PEAK= 0.746 METERS

IMPERIAL FAULT

SECOND RUPTURE

BRAWLEY FAULT

RIGHT LATERAL STRIKE SLIP
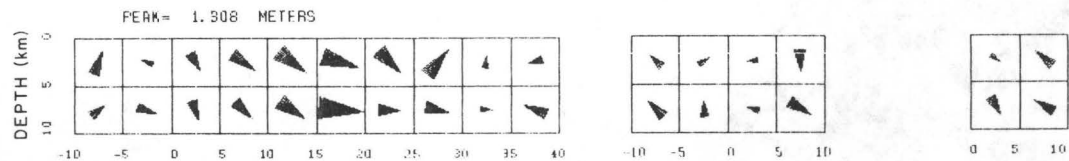
DIP SLIP (WEST SIDE UP)
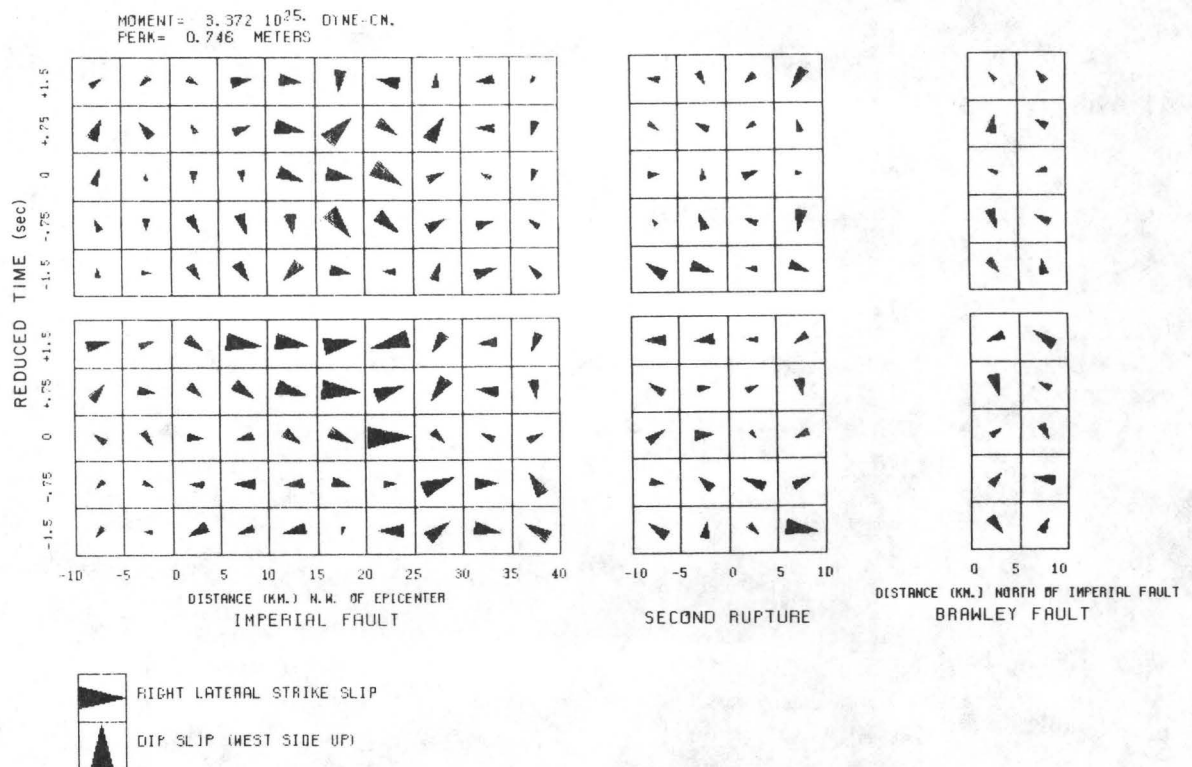
Figure 4-4. Slip on the Imperial and Brawley faults obtained by least squares inversion with stabilization (analogous to Figure 4-3 for the unstabilized solution). Stabilization provides a much smoother offset (top) and dynamic slip (bottom) than the unstabilized result in Figure 4-3; this is evidenced by the more uniform direction and amplitude of adjacent triangles.

CONSTRAINED LEAST SQUARES
STATIC OFFSET

DYNAMIC SLIP

RIGHT LATERAL STRIKE SLIP
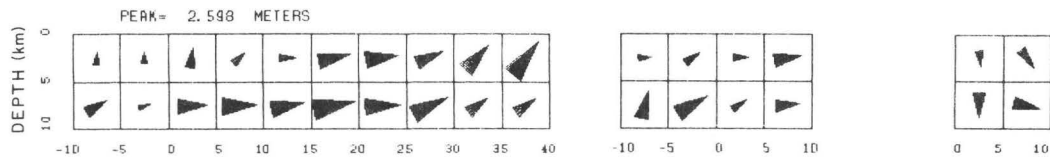
DIP SLIP (WEST SIDE UP)
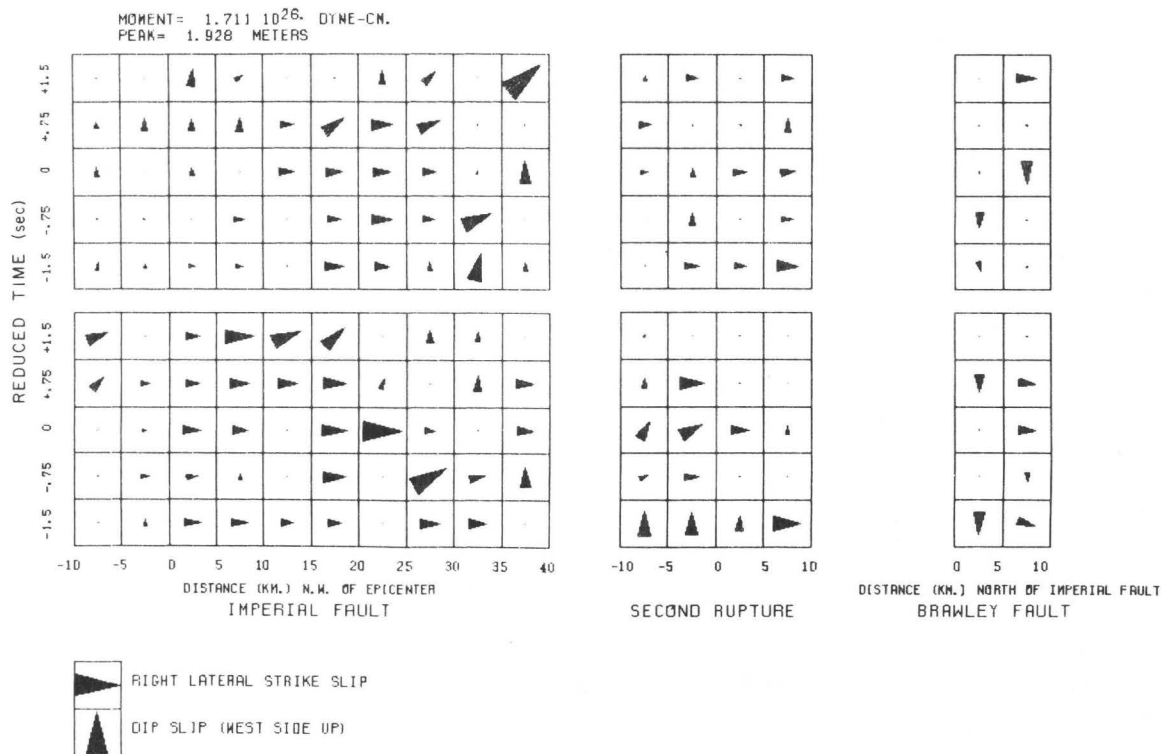
Figure 4-5. Slip on the Imperial and Brawley faults obtained by constrained least squares inversion without stabilization (analogous to the unconstrained solution shown in Figures 4-3). In this solution, the slip is constrained to be right-lateral; west side up on the Imperial Fault; and west side down on the Brawley Fault. As a result of the constraints, the dynamic slip (bottom) does not reverse direction, and the static offsets (top) in adjacent cells are not in opposing directions (compare with Figures 4-3 and 4-4).

STABILIZED
CONSTRAINED LEAST SQUARES
STATIC OFFSET
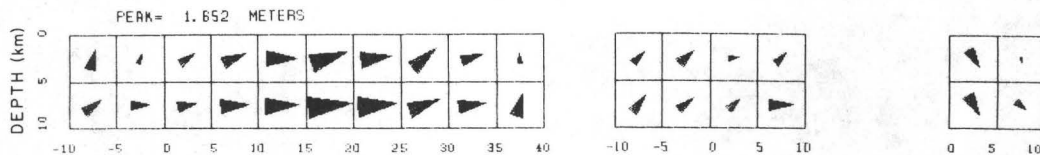
DYNAMIC SLIP
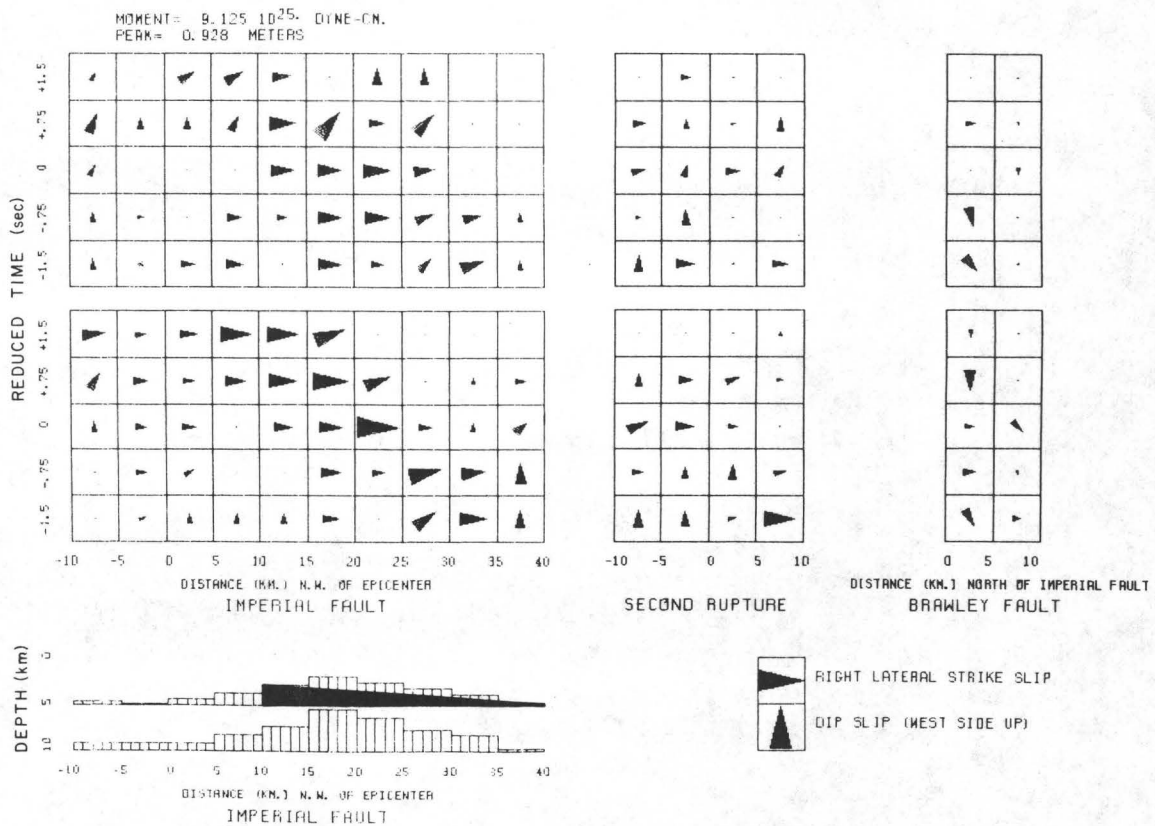
Figure 4-6. Slip on the Imperial and Brawley faults obtained by constrained least squares inversion with stabilization (analogous to the unstabilized solution in Figure 4-5). The seismic moment is much smaller than in Figure 4-5. Also, a noticable trend with a horizontal phase velocity between 4.0 and 5.0 km./sec. has emerged in the dynamic slip of the bottom row of cells on the Imperial Fault. The strike-slip component of offset on the Imperial Fault is shown in the lower left superimposed upon a shaded schematic of the observed surface offset.

STABILIZED
CONSTRAINED LEAST SQUARES
230°
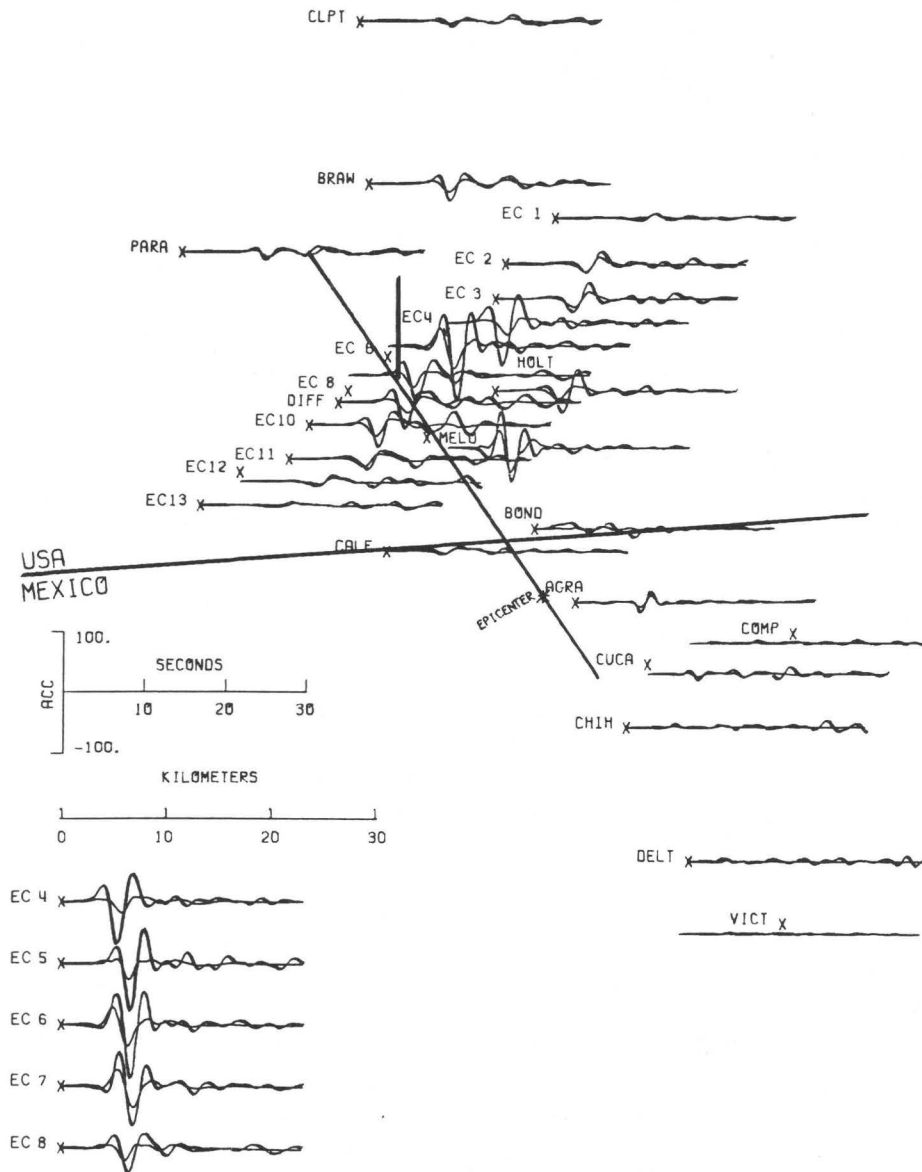
Figure 4-7. Comparison of the data (heavy line) with the fit to the data (light line) for the stabilized constrained least squares solution shown in figure 4-6. The seismograms are plotted geographically beginning at the station location marked with an X. The 230° component (perpendicular to the Imperial Fault) is shown.

STABILIZED
CONSTRAINED LEAST SQUARES
140°
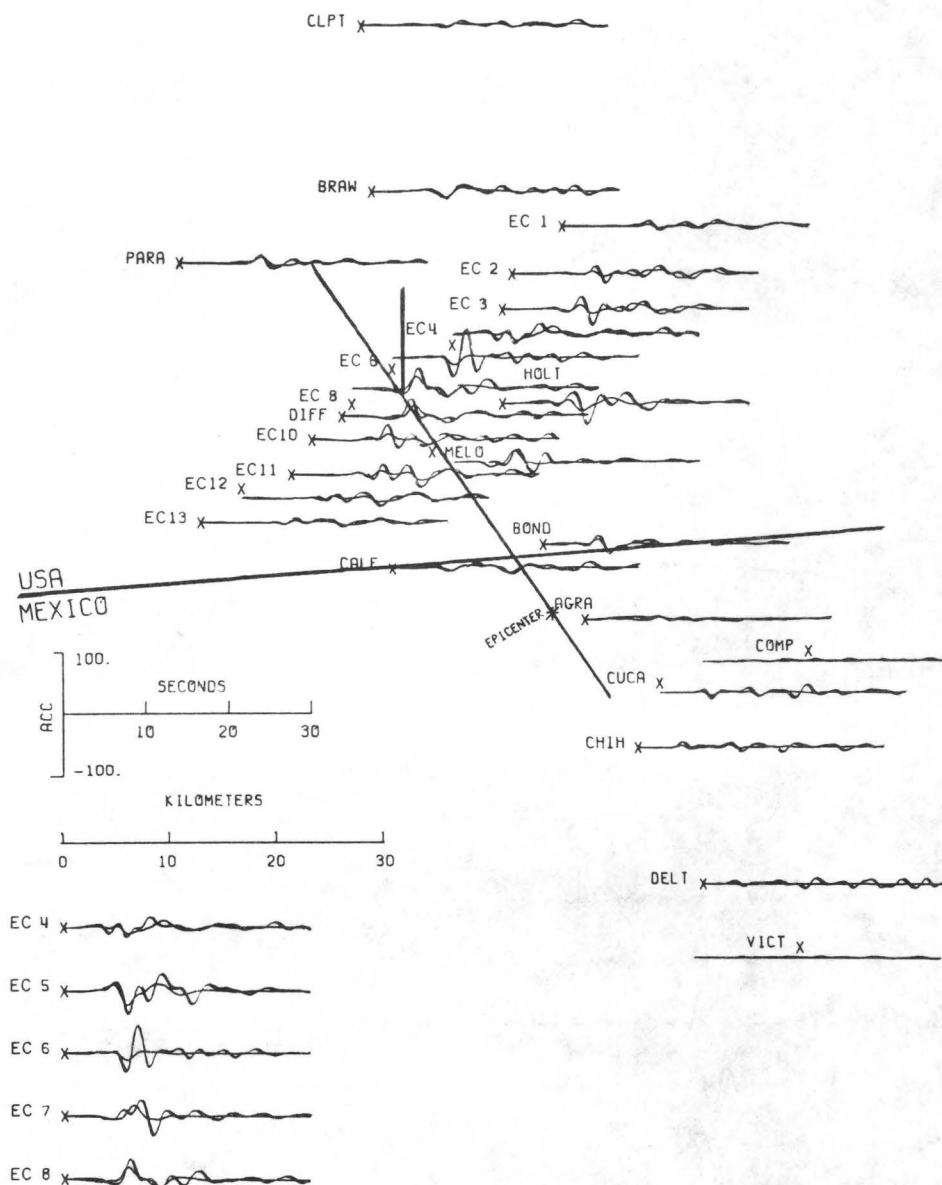
Figure 4-8. Comparison of the data (heavy line) with the fit to the data (light line) for the stabilized constrained least squares solution shown in figure 4-6 (analogous to Figure 4-7). The 140° component (parallel to the Imperial Fault) is shown.

STABILIZED
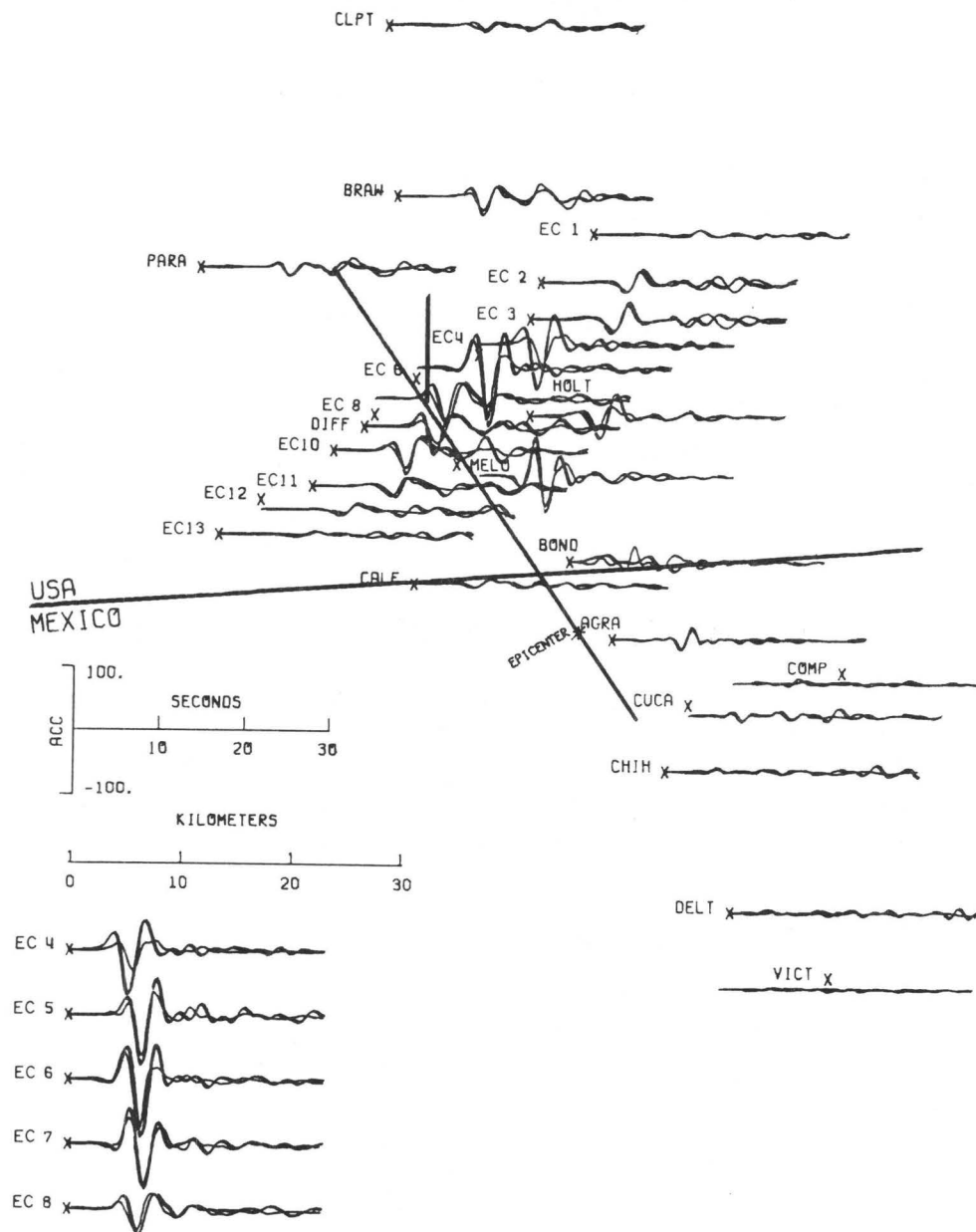# CONSTRAINED LEAST SQUARES
VERTICAL
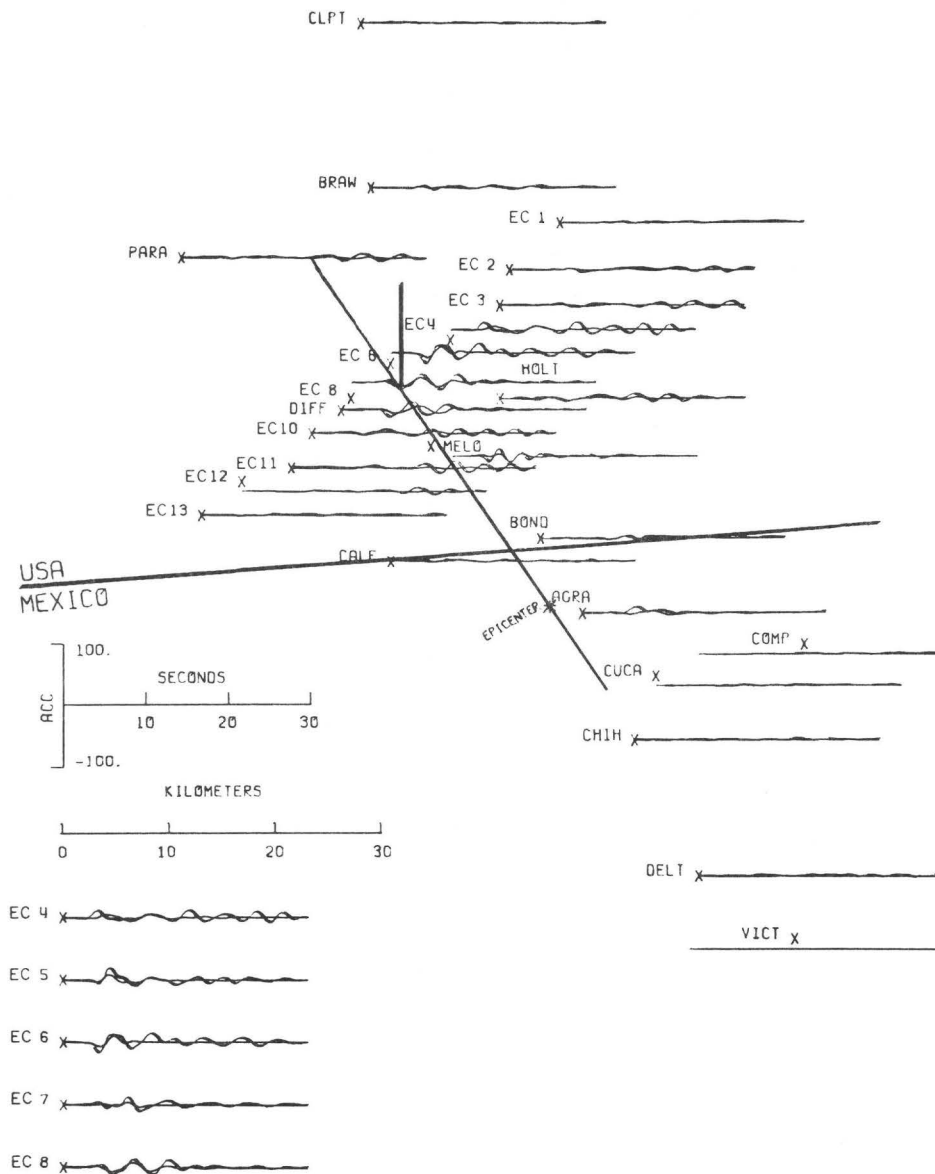
Figure 4-9. Comparison of the data (heavy line) with the fit to the data (light line) for the stabilized constrained least squares solution shown in figure 4-6 (analogous to Figures 4-7 and 4-8). The vertical component is shown with orientation given in Table 4-1.
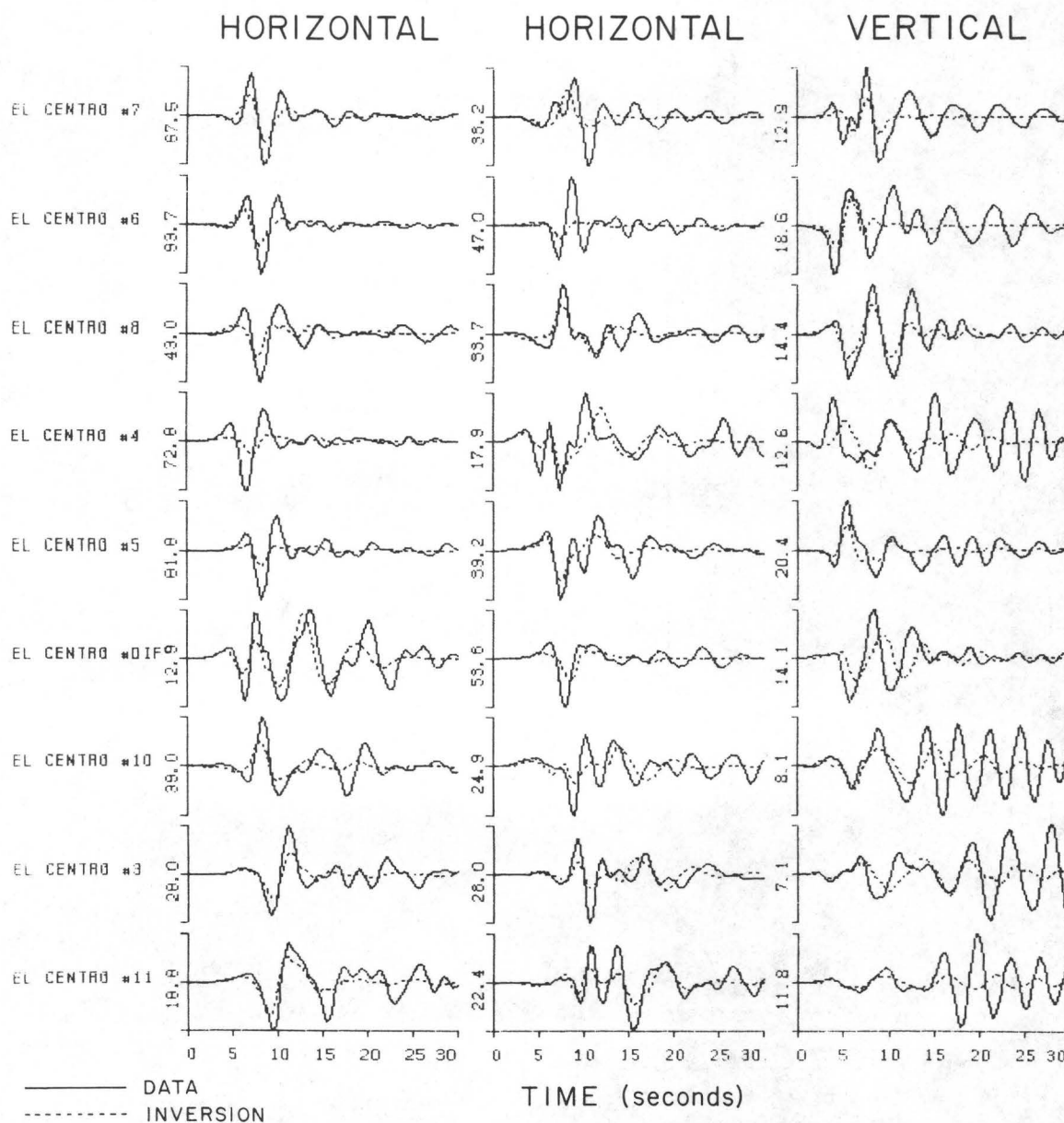
Figure 4-10. Comparison of data (solid line) with fit to the data (dashed line) by the stabilized constrained least squares solution of Figure 4-6. Nine of the stations compared in Figures 4-7 through 4-9 are shown in greater detail. Component orientations are listed in Table 4-1 with the left-most horizontal orientation in Table 4-1 corresponding to the left-most horizontal component plotted above. The numbers at the side of each component are the maximum horizontal acceleration in cm./sec.^{2}. The absolute time scale and acceleration scale pertain to both data and inversion.
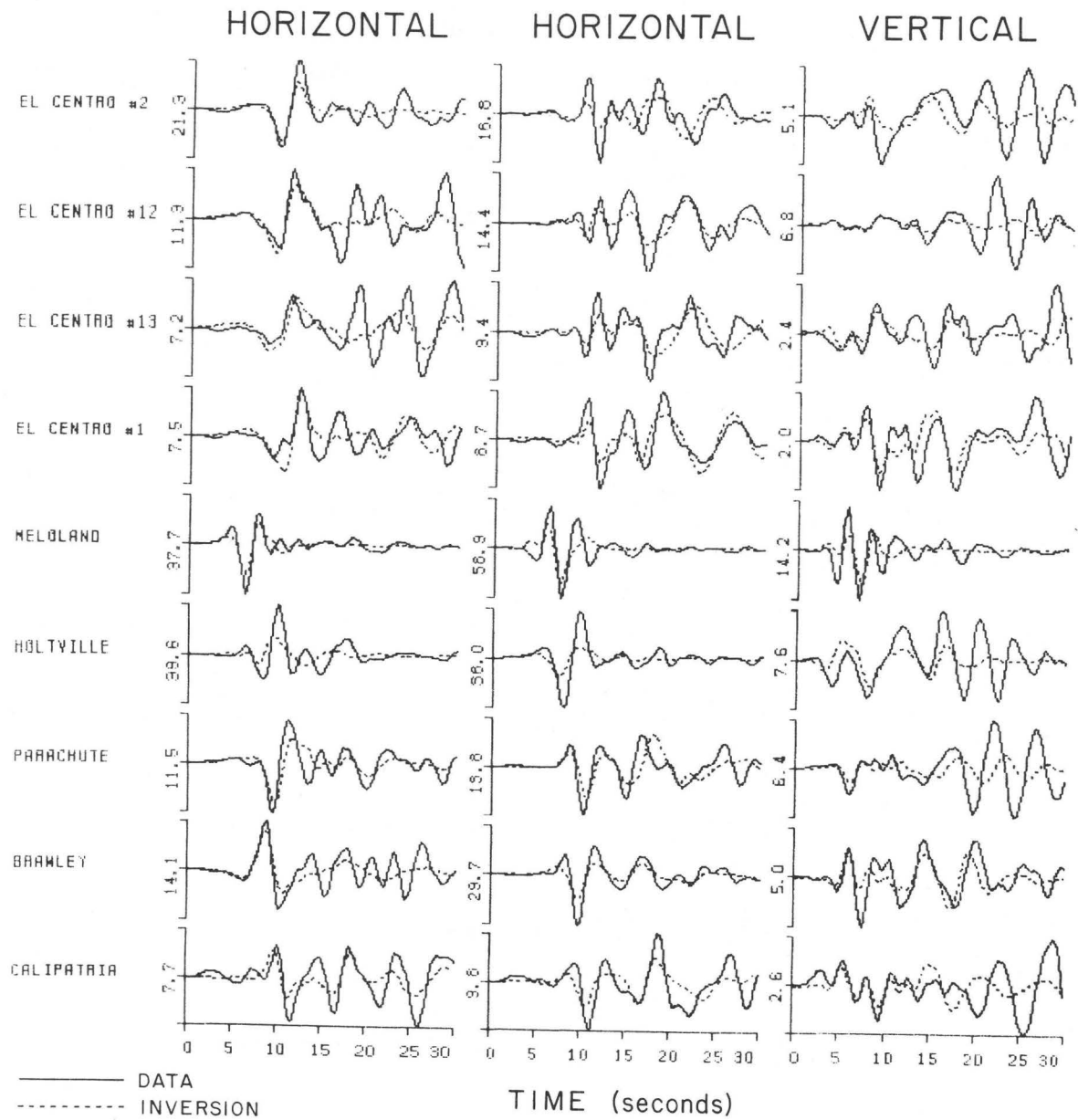
Figure 4-11. Comparison of data (solid line) with fit to the data (dashed line) by the stabilized constrained least squares solution of Figure 4-6 (analogous to Figure 4-10 for nine additional stations).
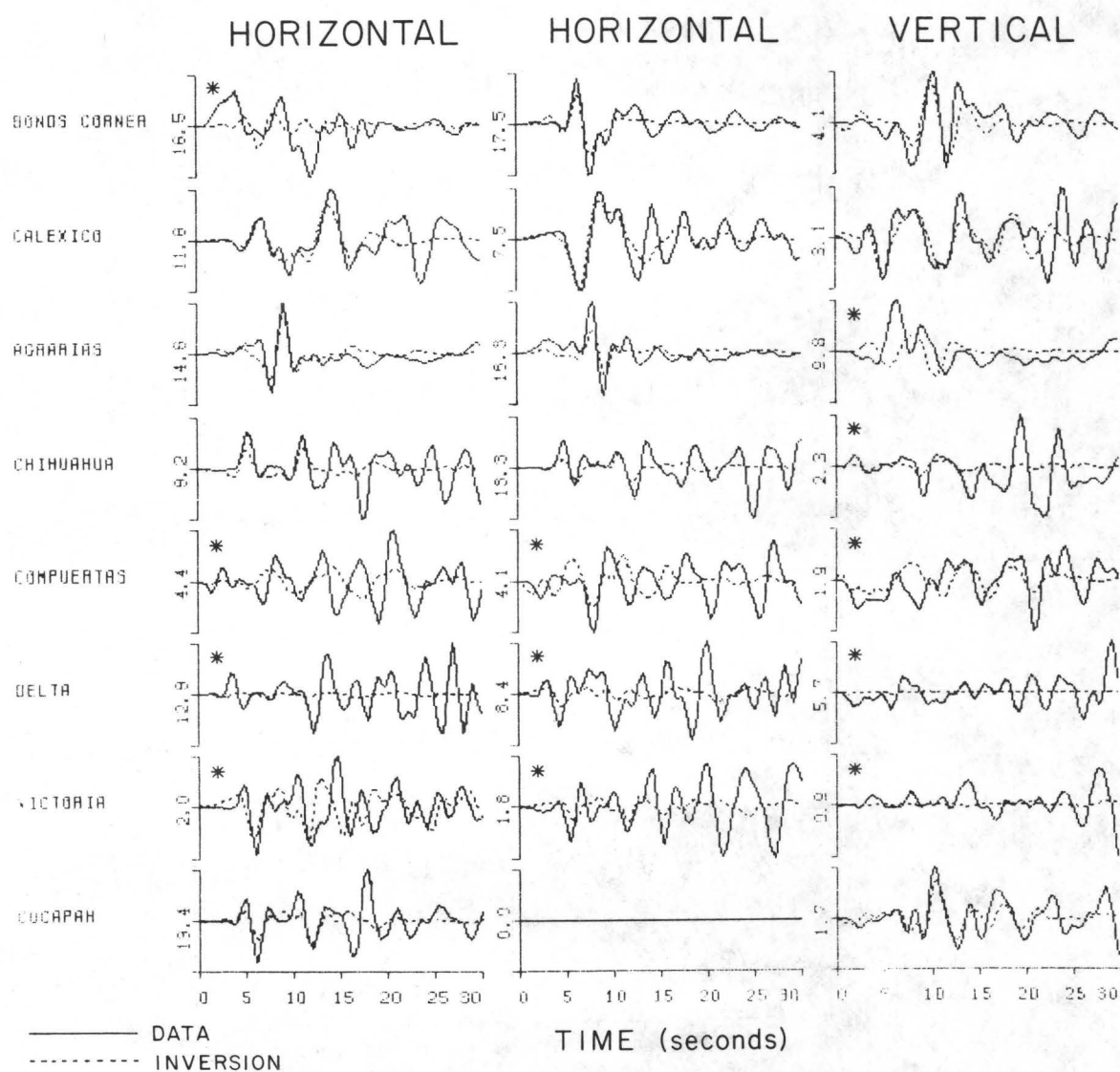
Figure 4-12. Comparison of data (solid line) with fit to the data (dashed line) by the stabilized constrained least squares solution of Figure 4-6 (analogous to Figures 4-10 and 4-11 for eight additional stations). Components marked with a * are weighted very small in the inversion and are shown for comparison purposes; these have a negligible contribution to the final solution.

LEAST SQUARES
230°

Figure 4-13. Comparison of the data (heavy line) with the fit to the data (light line) for the unstabilized least squares solution shown in Figure 4-3. The 230° component (perpendicular to the Imperial Fault) is shown. The fit is almost exact. Compare with Figure 4-7 for the stabilized constrained least squares fit to the data.

STABILITY

LEAST SQUARES

DIP SLIP OFFSET
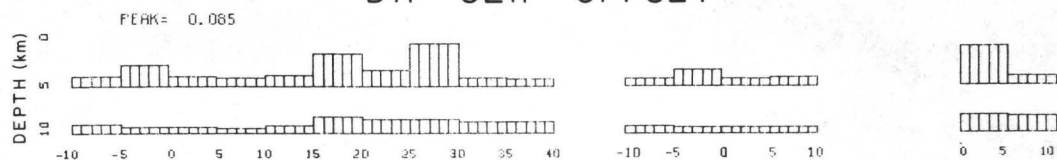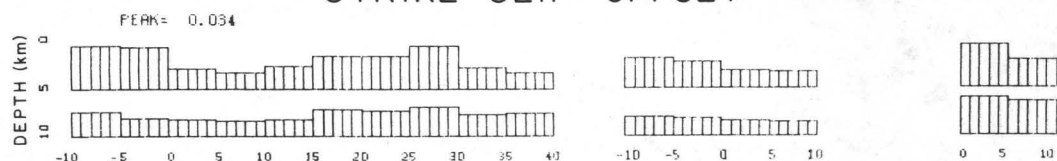
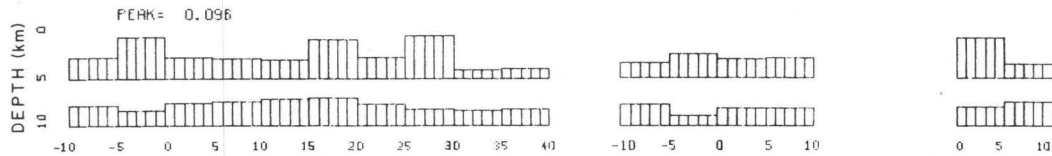### STRIKE SLIP OFFSET

STABILIZED LEAST SQUARES

DIP SLIP OFFSET
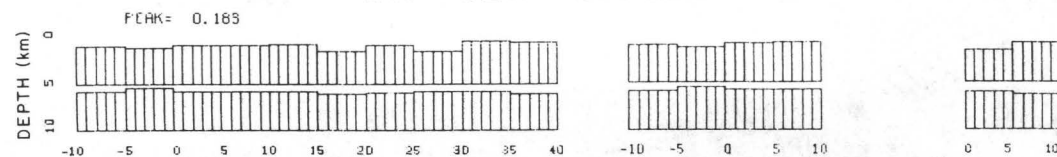
STRIKE SLIP OFFSET
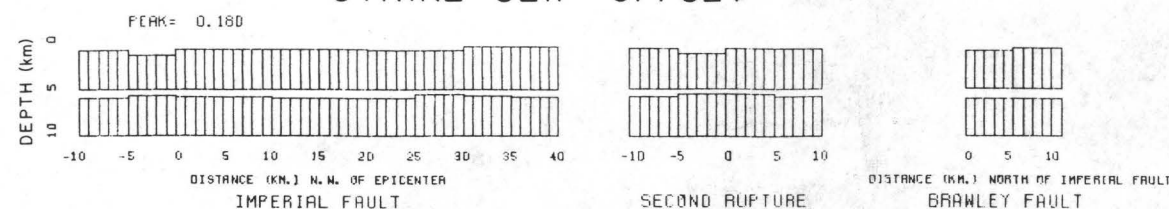
Figure 4-14. Stability analysis results for the least squares solution (Figure 4-3) and the stabilized least squares solution (Figure 4-4). The height of each box is proportional to the smallest percentage change in the data required to change a component of offset in the corresponding cell by one meter. The peak value for each component of offset is given since each of the four results shown is scaled separately. Large values depict cells with most stably determined offset. The stablilized solution (bottom) is more stable everywhere than the unstabilized solution (top), and all cells (bottom) are equally stable.
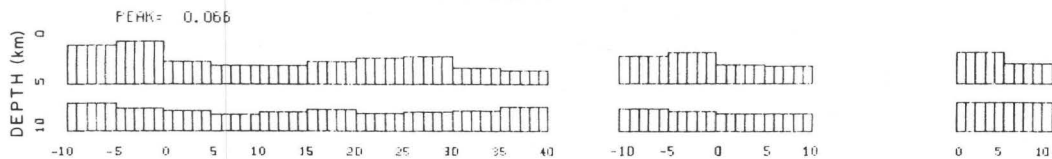
STABILITY

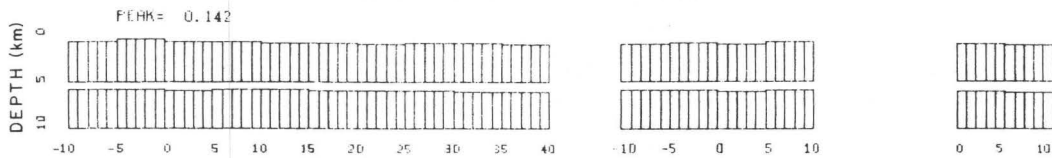## CONSTRAINED LEAST SQUARES

DIP SLIP OFFSET

STRIKE SLIP OFFSET

STABILIZED
CONSTRAINED LEAST SQUARES

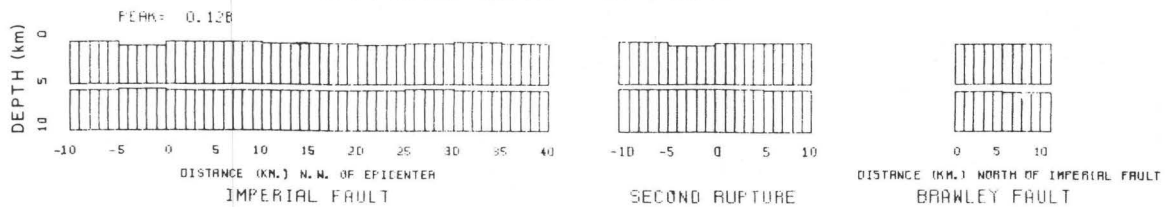### DIP SLIP OFFSET

STRIKE SLIP OFFSET

Figure 4-15. Stability analysis results for the constrained least squares solution (Figure 4-5) and the stabilized constrained least squares solution (Figure 4-6) (analogous to Figure 4-14 for the stability of unconstrained least squares). The constrained least squares solution (top) is everywhere more stable than the unconstrained least squares solution (Figure 4-14, top). Also, the stabilized solution (bottom) is more stable everywhere than the unstabilized solution (top).

Station Number	Station Name	Component Orientations*
1	El Centro #7	230°, up, 140°
2	El Centro #6	230°, up, 140°
3	Bonds Corner	230°, up, 140°
4	El Centro #8	230°, up, 140°
5	El Centro #5	230°, up, 140°
6	El Centro Diff.	360°, up, 270°
7	El Centro #4	230°, up, 140°
8	Brawley Airport	315°, up, 225°
9	Holtville Post Office	315°, up, 225°
10	El Centro #10	50°, up, 320°
11	Calexico	315°, up, 225°
12	El Centro #11	230°, up, 140°
13	El Centro #3	230°, up, 140°
14	Parachute Test Fac.	315°, up, 225°
15	El Centro #2	230°, up, 140°
16	El Centro #12	230°, up, 140°
17	Calipatria	315°, up, 225°
18	El Centro #13	230°, up, 140°
19	El Centro #1	230°, up, 140°
20	Superstition Mt.**	135°, up, 45°
21	Plaster City**	135°, up, 45°
22	Coachella Canal #4**	135°, up, 45°
23	Agrarias	183°, down, 93°
24	Cerro Prieto**	57°, down, 327°
25	Chihuahua	192°, down, 102°
26	Compuertas	195°, down, 105°
27	Delta	172°, down, 82°
28	Cucapah	85°, up, 355°
29	Victoria	75°, up, 345°
30	Meloland	0°, up, 270°

Table 4-1. List of component orientations for near-field stations recording the October 15, 1979 Imperial Valley earthquake.
  * Horizontal direction measured in degrees clockwise from North.
  ** Stations not considered in the inversion studies.
  -- Data not recorded for this component.

Layer	Thickness/ Depth (km.)		P-Wave Velocity, km/sec	S-Wave Velocity, km/sec	Density gm/cm^3
1	0.10	0.0	1.690	0.500	2.04
2	0.15	0.10	1.790	0.818	2.06
3	0.50	0.25	2.167	1.010	2.13
4	0.50	0.75	2.533	1.200	2.21
5	0.50	1.25	2.900	1.410	2.28
6	0.50	1.75	3.267	1.620	2.35
7	0.50	2.25	3.633	1.850	2.43
8	0.50	2.75	4.000	2.080	2.50
9	0.50	3.25	4.367	2.330	2.57
10	0.50	3.75	4.733	2.590	2.65
11	0.50	4.25	5.100	2.870	2.72
12	0.50	4.75	5.375	3.060	2.77
13	0.50	5.25	5.650	3.260	2.83
14	5.25	5.75	5.750	3.320	2.85
15	0.30	11.0	6.700	3.870	3.04
16	0.30	11.3	6.900	3.980	3.08
17	0.30	11.6	7.100	4.100	3.12
18	1.31	11.9	7.300	4.210	3.16
19	2.50	13.21	7.800	4.500	3.26
20	----	15.71	8.100	4.670	3.32

Table 4-2. Crustal structure consisting of homogeneous plane layers used in the calculation of theoretical Green's functions for the Imperial Valley, California.

SOURCE DYNAMICS OF THE 1979
IMPERIAL VALLEY EARTHQUAKE FROM NEAR-SOURCE
OBSERVATIONS (OF GROUND ACCELERATION AND VELOCITY)

Mansour Niazi
TERA Corporation
2150 Shattuck Avenue
Berkeley, California 94704

ABSTRACT

Two sets of observations obtained during the October 15, 1979, Imperial Valley Earthquake, M_s 6.9, are presented. The data suggest different dynamic characteristics of the source when viewed in different frequency bands. The first data set consists of the observed residuals of the horizontal peak ground accelerations and particle velocity from predicted values at epicentral distances within 50 km. The residuals are calculated from a nonlinear regression analysis of the data (Campbell, 1981) to the following empirical relationships,

$$PGA = A_1 (R + C_1)^{-d_1},$$

$$PGV = A_2 (R + C_2)^{-d_2}$$

in which R is the closest distance to the plane of rupture.

The so-calculated residuals are correlated with a positive scalar factor signifying the focusing potential at each observation point. The focusing potential is determined on the basis of the geometrical relation of the station relative to the inception point of rupture on the fault plane.

The second data set consists of the acceleration directions derived from the windowed time histories of the horizontal ground acceleration across the El Centro Differential Array (ECDA). The horizontal peak velocity residuals and the low-pass particle acceleration directions across (ECDA) require the fault rupture to propagate northwestward. The horizontal peak ground acceleration residuals and the high frequency particle acceleration directions, however, are

either inconclusive or suggest an opposite direction for rupture propagation. The inconsistency can best be explained to have resulted from the incoherence of the high frequency radiation.

A test for the sensitivity of the correlation procedure to source location was conducted by ascribing the observed strong ground shaking to a single aspeity located 12 km northwest of the hypocenter. The resulting inconsistency between the peak acceleration and velocity observations in relation to the focusing potential is accentuated. The particle velocity of Delta Station, Mexico, in either case appears abnormally high and disagrees with other observations near the southeastern end of the fault trace. From the observation of a nearly continuous counterclockwise rotation of the plane of particle motion at ECDA, the average rupture velocity during the first six seconds of source activation is estimated to be about 2.7 km/sec.

INTRODUCTION

Because of the extensive near-field instrumental coverage of the October 15, 1979 Imperial Valley earthquake, the recorded information is well suited for testing different suggestions regarding the focusing effect of near-source strong ground shaking. In this study an attempt is made to study the dynamic characteristics of the source of this earthquake by examining two sets of observations. One set consists of all the available near-source PGA and PGV information within 50 km epicentral distance. The second data set consists of the acceleration time histories obtained across (ECDA). The more coherent nature of the low frequency (f < 1 Hz) waves at ECDA allows an estimation be made of the average velocity of rupture propagation.

DATA ANALYSIS

The mean horizontal peak ground acceleration at 36 stations (72 observations) and the peak velocity at 31 stations (62 observations) located within 50 km epicentral distance are regressed by the method described by Campbell (1981) as a function of their significant distances (the distance of the closest approach of
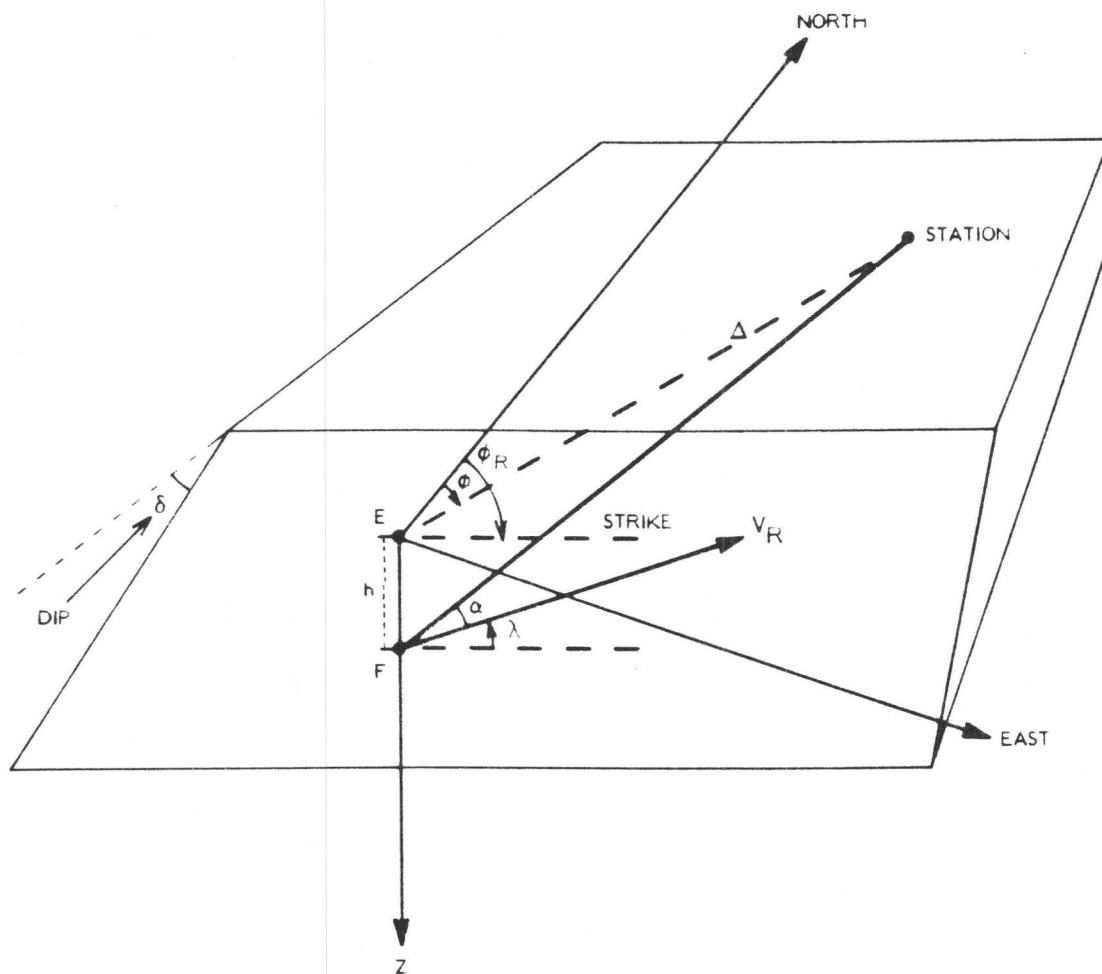
the rupture surface), and residuals from the mean are calculated at each observation point. Because, all observations are for a single earthquake, the effect of the earthquake magnitude does not enter in the analysis. The residuals are, therefore expected to agree also with those resulting from the analysis of Joyner et al. (1981), the slightly different definition of distance

notwithstanding, by using a commom formula

$$PGA = A_1 (R + C_1)^{-d_1}$$

$$PGV = A_2 (R + C_2)^{-d_2}$$

(1)

The so calculated residuals from the predicted values given by (1) are then normalized to the standard deviation σ of regression and then are correlated with the focusing potential at their respective stations. Calculation of the focusing potential based on a purely geometrical relation between a source and receiver pair is illustrated in Figure 1. A numerical value above one for this factor at a station indicates a potential for focusing at that station and a value below one suggest defocusing. In Figures 2 and 3 the correlation of the residuals with the focusing potential are shown for peak horizontal ground acceleration and velocity, respectively. Because in the calculation of focusing potential we assumed a northwesterly direction for rupture propagation, a negative slope would correspond to a negative rupture velocity equivalent to a propagation to the southeast. There is a slight suggestion of such negative slope in Figure 2. The trend is, however, clearly influenced by the high peak acceleration observations at Delta (with a residual of about 2σ). The trend almost disappears when this data point is eliminated. The observed residual for peak velocity also appears abnormally high at Delta, and is seen in Figure 3 as an outlier. Curiously, however, when this data point is disregarded in Figure 3, a positive trend clearly emerges, which suggests a predominantly northwest direction for rupture propagation.

The selection of the hypocenter as the main contributing source of the peak ground motion is not quite justifiable for extended sources. There have also been

$$\alpha = Cos^{-1}\left[\frac{\Delta Cos\phi\left(Cos\lambda\,Cos\phi_R + Cos\delta\,Sin\lambda\,Sin\phi_R\right) + \Delta Sin\phi\left(Cos\lambda\,Sin\phi_R - Cos\delta\,Sin\lambda\,Cos\phi_R\right) + h\,Sin\lambda\,Sin\delta}{\sqrt{h^2 + \Delta^2}}\right]$$

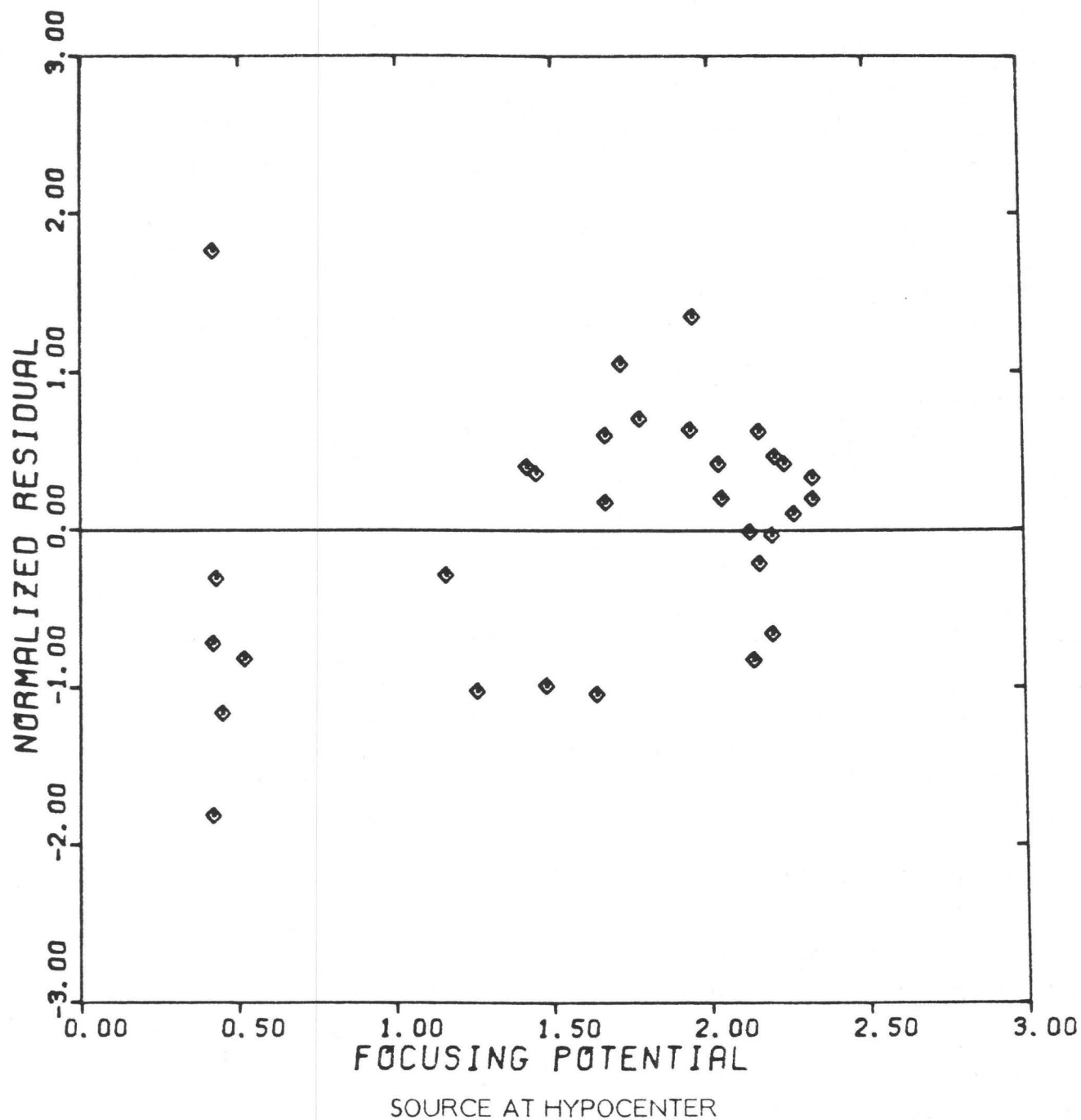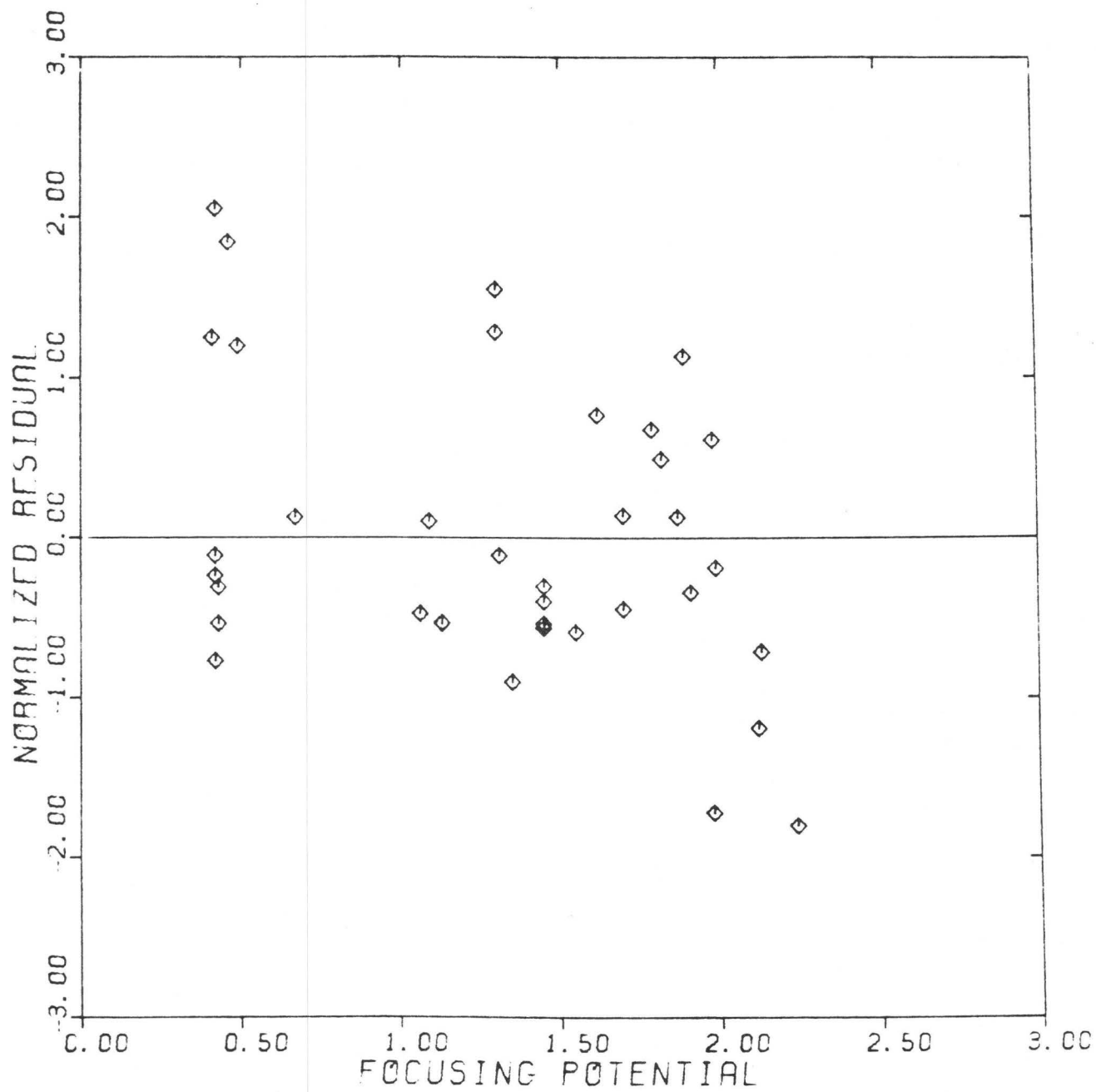DEFINE FOCUSING POTENTIAL AS $\left(\dfrac{\beta}{V_R} - Cos\,\alpha\right)^{-1}$

FIGURE 1

915

FIGURE 2

IMPERIAL VALLEY 1979 DATA
PEAK GROUND ACCELERATION

FIGURE 3

IMPERIAL VALLEY 1979 DATA
PEAK GROUND VELOCITY

917

several suggestions (Hartzell and Helmberger, 1980) for the main source of energy, asperity, for this earthquake to lie approximately 10 km to the northwest of hypocenter. We have, therefore, reanalyzed the data under the assumption of a source located about 12 km northwest of its epicenter at 32.728 degree North and 115.404 degree West. The results of new correlations for this source location are given in Figures 4 and 5, for peak horizontal acceleration and velocities, respectively. For the revised asperity location, Bonds Corner and Mexicali stations are in defocused position and thus greatly enhance the negative trends of the Figure 4, suggesting that for this geometry, the peak horizontal acceleration clearly favor a southeast direction for the rupture propagation, provided the residuals are viewed in terms of focusing effect only by disregarding the site and propagation effects. The lower frequency peak particle velocities however, still maintain their preferred northwestward propagation of the source.

The inferred inconsistency between the dynamics characteristics of the source as observed by the near-source strong ground shaking in different frequency bands is also reflected in the acceleration time histories, resulting from the P wave observations at ECDA. Analyzing the first seven seconds of the records at elements 1-4 of the array, the signal to noise ratio of P coda at element 5 is extremely low, we present the particle acceleration direction in the form of rose diagrams in consecutive 1 second windows.

Figure 6 shows these diagrams for the recorded accelerations after they were subjected to a low-pass filtering at 1 Hz. The filtered horizontal components were combined vectorially and weighted to obtain the predominant directions of particle acceleration in the form of rose diagrams each containing 1 second data, i.e., 100 digital points. There is some noise problem at the beginning of the element 4 traces. The rest of the data present remarkably similar particle motion across the array for this frequency range.

Considering the rectilinear nature of the P vibrations, the direction of the major sectors of the rose diagram would be expected to be parallel to the general direction of the recorded vibrations. They should, therefore, point to the source

FIGURE 4

IMPERIAL VALLEY 1979 DATA
PEAK GROUND ACCELERATION
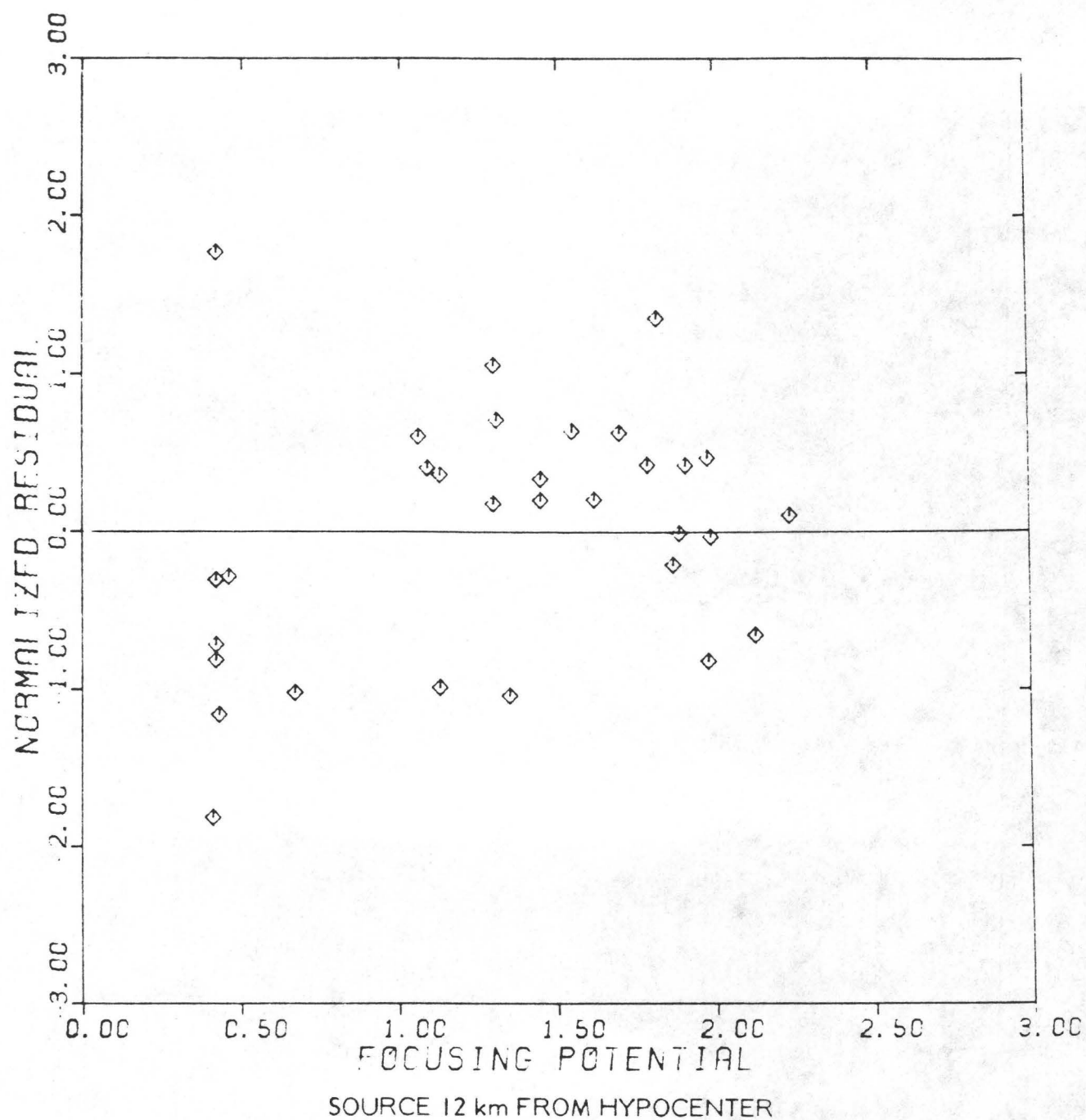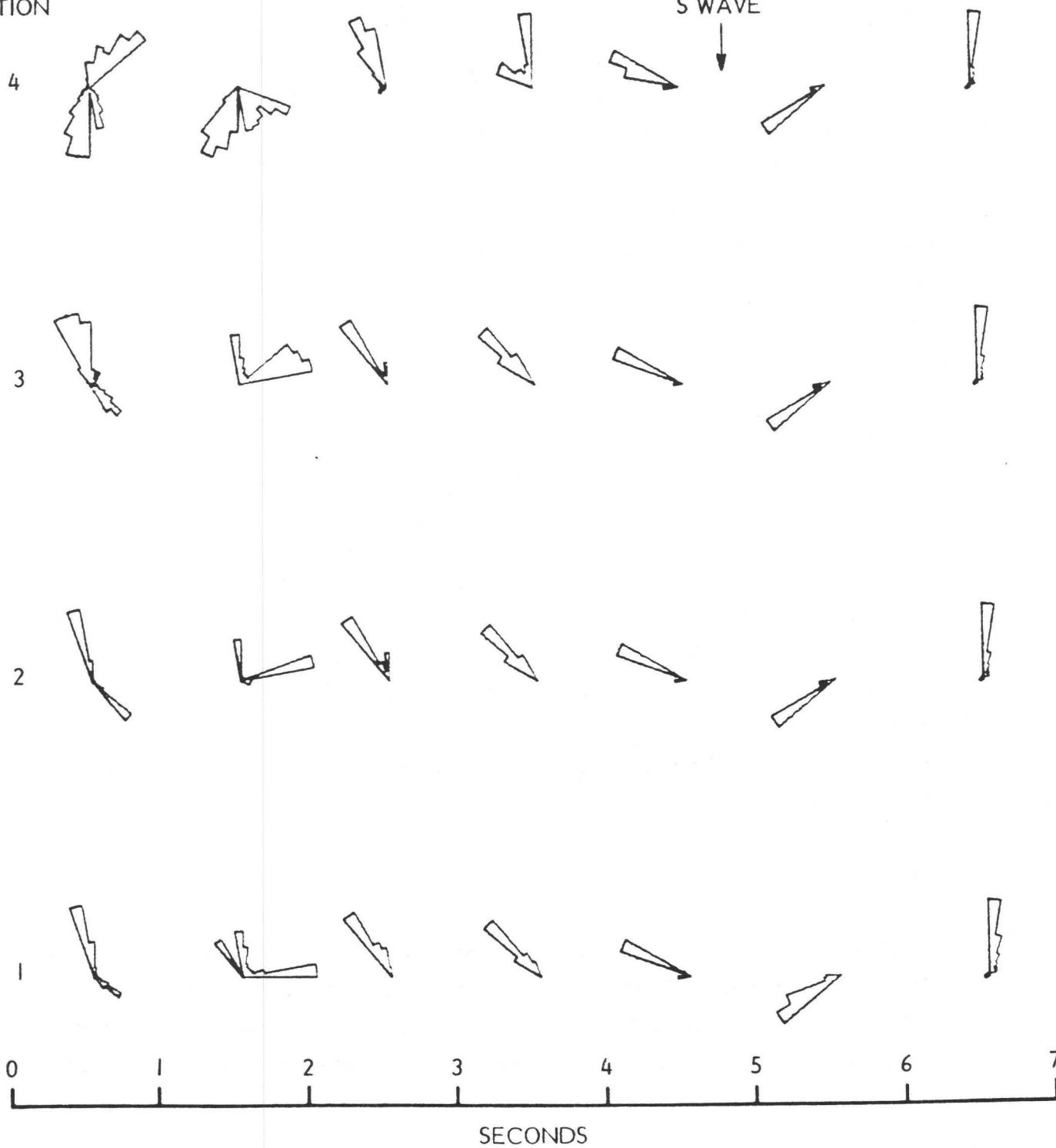
FIGURE 5

IMPERIAL VALLEY 1979 DATA
PEAK GROUND VELOCITY

FIGURE 6

DIRECTION OF PARTICLE ACCELERATION
ACROSS ECDA (f < 1 Hz)

location from which they were radiated. Thus, disregarding the burst of the superimposed energy which apparantly approached the array in an east-west direction in the second time window, the source direction, during the first five seconds of observation, is seen to progressively rotate counterclockwise by as much as 50 degrees. The later observations, though extremely coherent, are predominantly shear waves which begin at about 5 second mark into the record. Based on these observations, the coherent component of the rupture propagated about 16 km northwestward in the first 5 seconds after its inception. Allowing for the propagation time (McMechan and Mooney, 1980) from the source, the average rupture velocity is estimated to be about 2.7 km/sec (see Figure 7 for details).

A similar set of diagrams for the 1-10 Hz frequency band is presented in Figure 8. While the inferred source direction during the initial second is consistant with those of Figure 6, the rose diagrams of consequent 4 seconds appear to be marked by multisource and multipath arrivals which result in a much less coherent picture across the array. Furthermore, the sequential patterns produced by individual array elements do not convey a clear indication of a coherently propagating rupture front. Evidently, the same factors such as incoherence of high frequency vibrations and multiple source character of the source for these frequencies would mask the dynamic characteristics of the source as were revealed by the low frequency observations. (Further discussions concerning the incoherent nature of high frequency accelerations are given by Smith et al, 1981; Niazi, 1981.)

DISCUSSIONS

The two lines of evidence as presented here, suggest that because of the high frequency character of peak accelerations, it is not always expected to be influenced in a predictable manner by focusing, as observed by Boore and Porcella (1980) for the Livermore earthquakes of January 1980. The focusing effect on the peak acceleration may therefore be viewed as an additional random
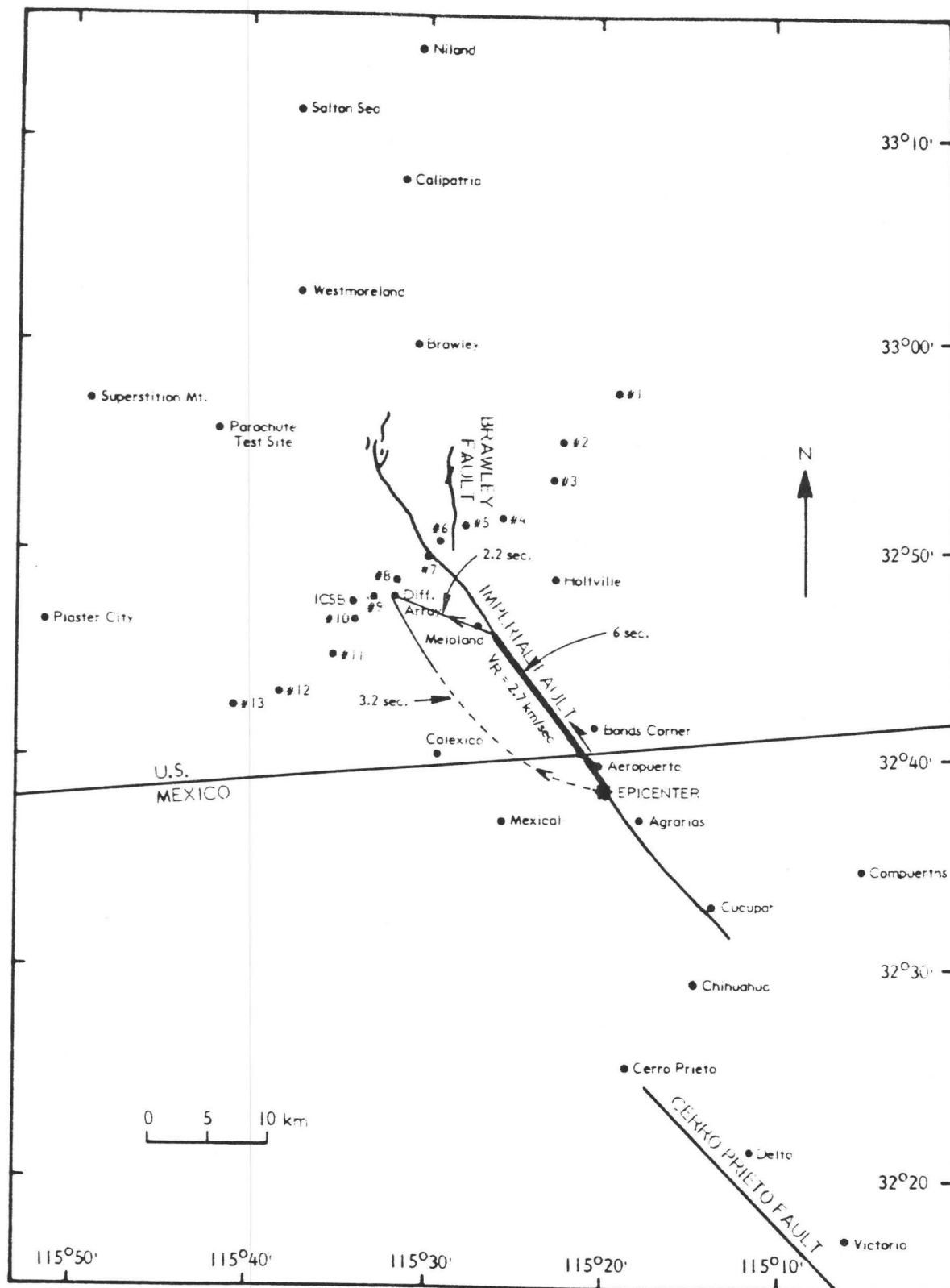
FIGURE 7

LOCATION OF RECORDING STATIONS
WITHIN THE NEAR-SOURCE REGION OF THE
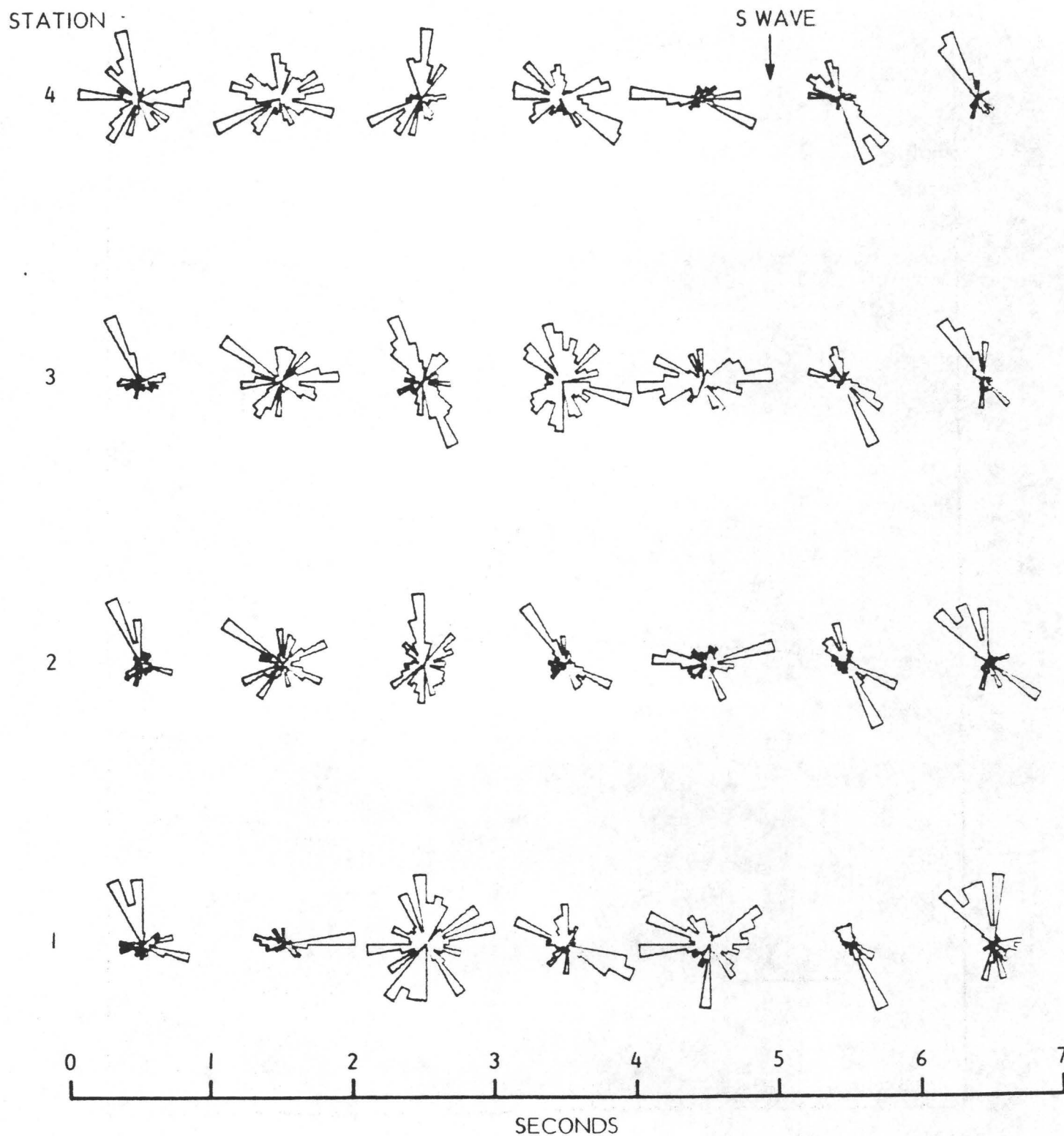IMPERIAL VALLEY EARTHQUAKE OF OCT. 15, 1979

STATION

4

3

2

1

0   1   2   3   4   5   6   7

SECONDS

FIGURE 8

DIRECTION OF PARTICLE ACCELERATION
ACROSS ECDA (1-10 Hz)

924

variable, contributing to the scatter of PGA, in much the same way as the site condition, propagation path and stress distribution may influence these observations. The source directivity, on the other hand, seems to have an observable influence on the peak ground velocity and/or low frequency acceleration amplitudes. The progressive rotation of the direction of P wave particle acceleration across ECDA, agrees with a rupture front propagating to the northwest with a rupture velocity of approximately 2.7 km/sec during the first 5 seconds of faulting associated with the 1979 Imperial Valley Earthquake.

REFERENCES

Boore, D.M. and R.L. Porcella (1980) Peak Acceleration from Strong-Motion Records: A Postscript, Bull. Seism. Soc. AM., 70, 2295-2297.

Campbell, K.W. (1981) Estimation of Peak Acceleration at Near and Far Distances for Moderate to Large Earthquakes, Bull. Seism. Soc. Am., 71:6. (In press.)

Hartzell, S.H. & D.V. Helmberger (1980) Strong ground motion modeling of the October 15, 1979 Imperial Valley Earthquake, EOS, 61, 1036.

Joyner, W.B. and D.M. Boore (1981) Peak Horizontal Acceleration and Velocity from Strong-Motion Records including Records from the 1979 Imperical Valley, California, Earthquake, Bull. Seism. Soc. Am., 71:6. (In press.)

McMechan, G.A. and W.D. Mooney (1980) Asymptotic Ray Theory and Synthetic Seismograms for Laterally Varying Structure: Theory and Application to the Imperial Valley, California, Bull. Seism. Soc. Am., 70, 2021-2035.

Niazi, M. (1981) Wave scattering as a possible cause of the observed PGA fluctuations at El Centro Differential Array during the October 15, 1979 Earthquake, Earthquake Notes, 52:1, 79.

Smith, S.W., J.E. Ehrenberg, and N. Hernandex (1981) Analysis of the El Centro Differential Array for the 1979 Imperial Valley Earthquake, Earthquake Notes, 52:1, 84.
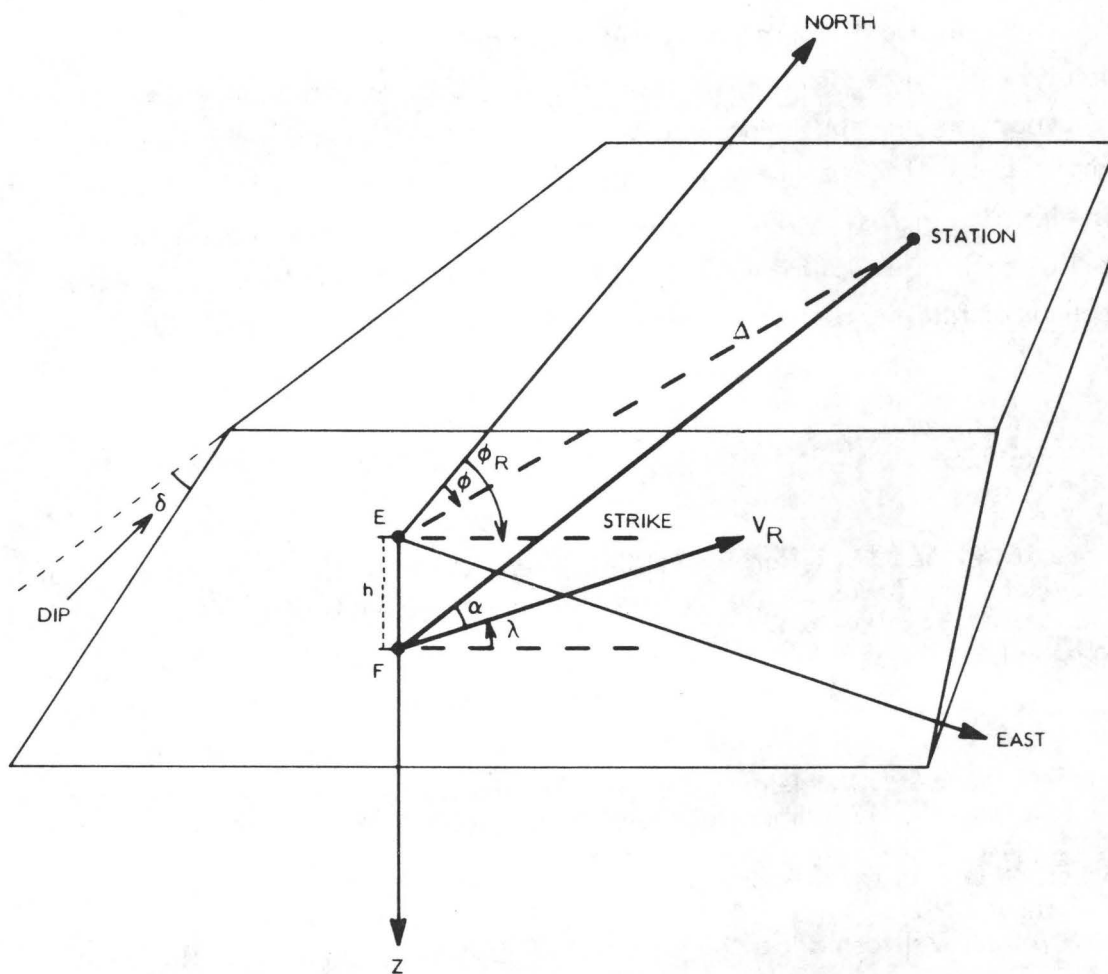
FIGURE I

GEOMETRICAL INTERPRETATION OF ANGLE α
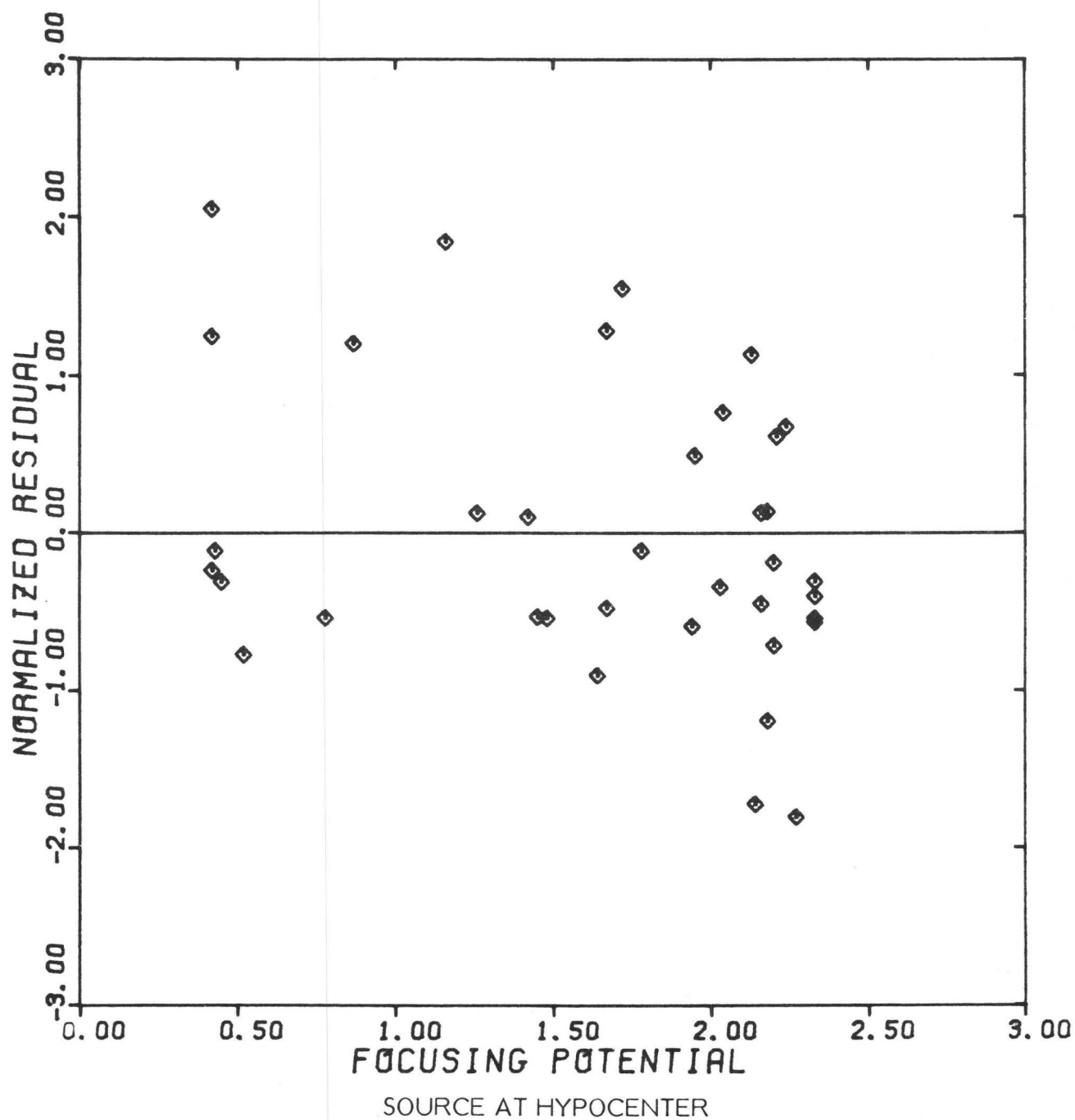SUBTENDED BETWEEN THE RAY AND DIRECTION
OF RUPTURE PROPAGATION

FIGURE 2

IMPERIAL VALLEY 1979 DATA
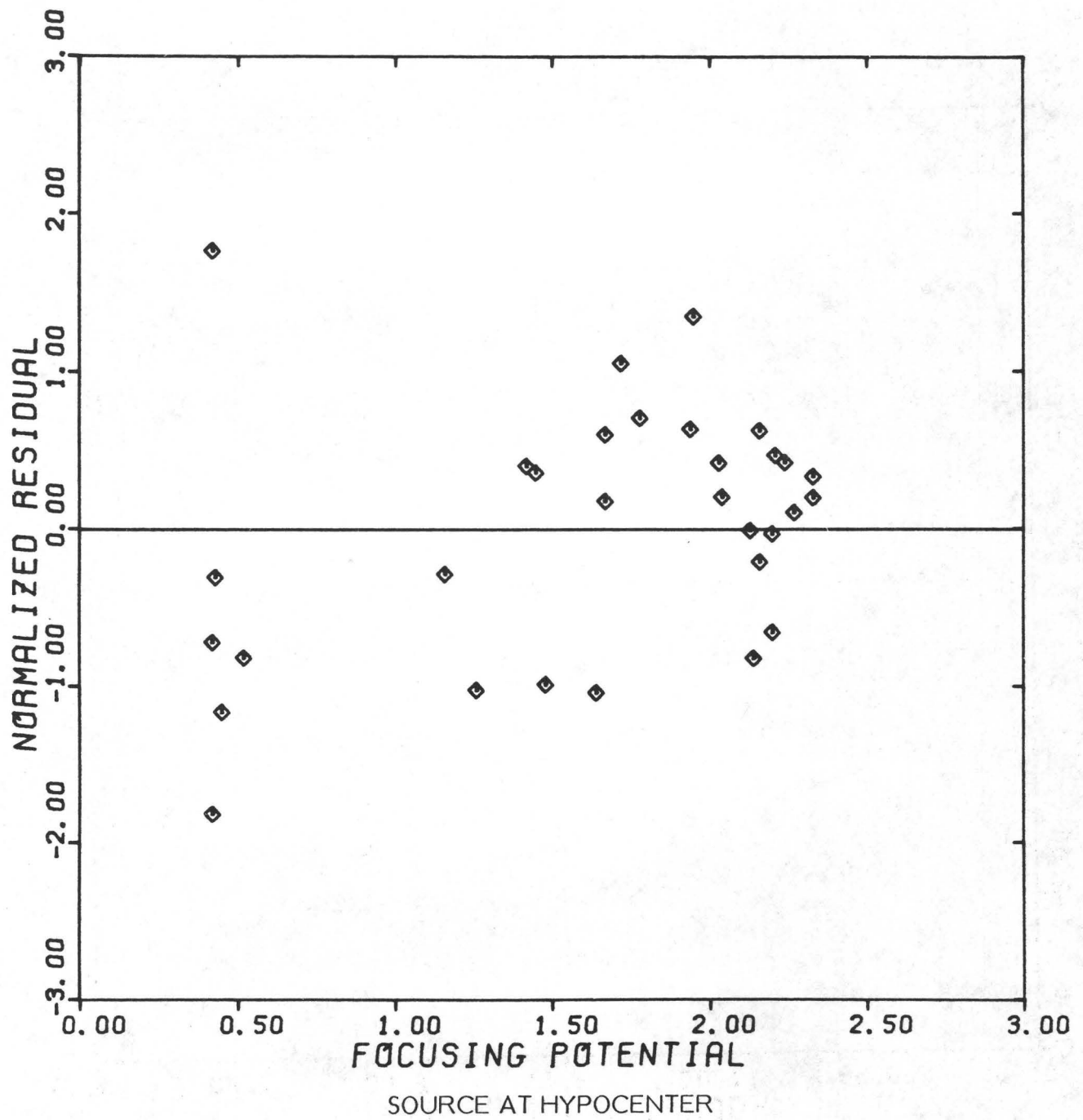PEAK GROUND ACCELERATION

FIGURE 3

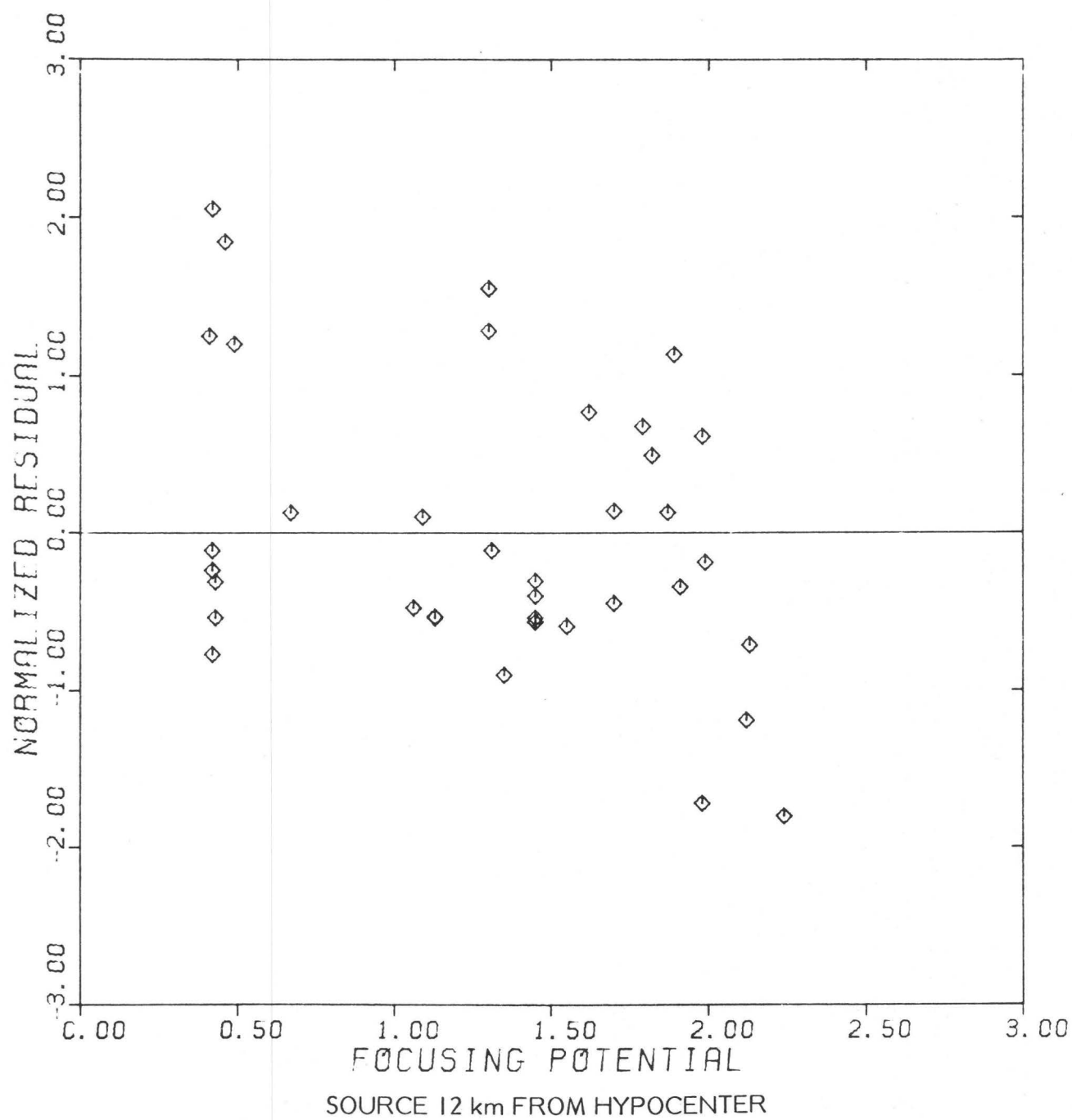IMPERIAL VALLEY 1979 DATA
PEAK GROUND VELOCITY

928

FIGURE 4

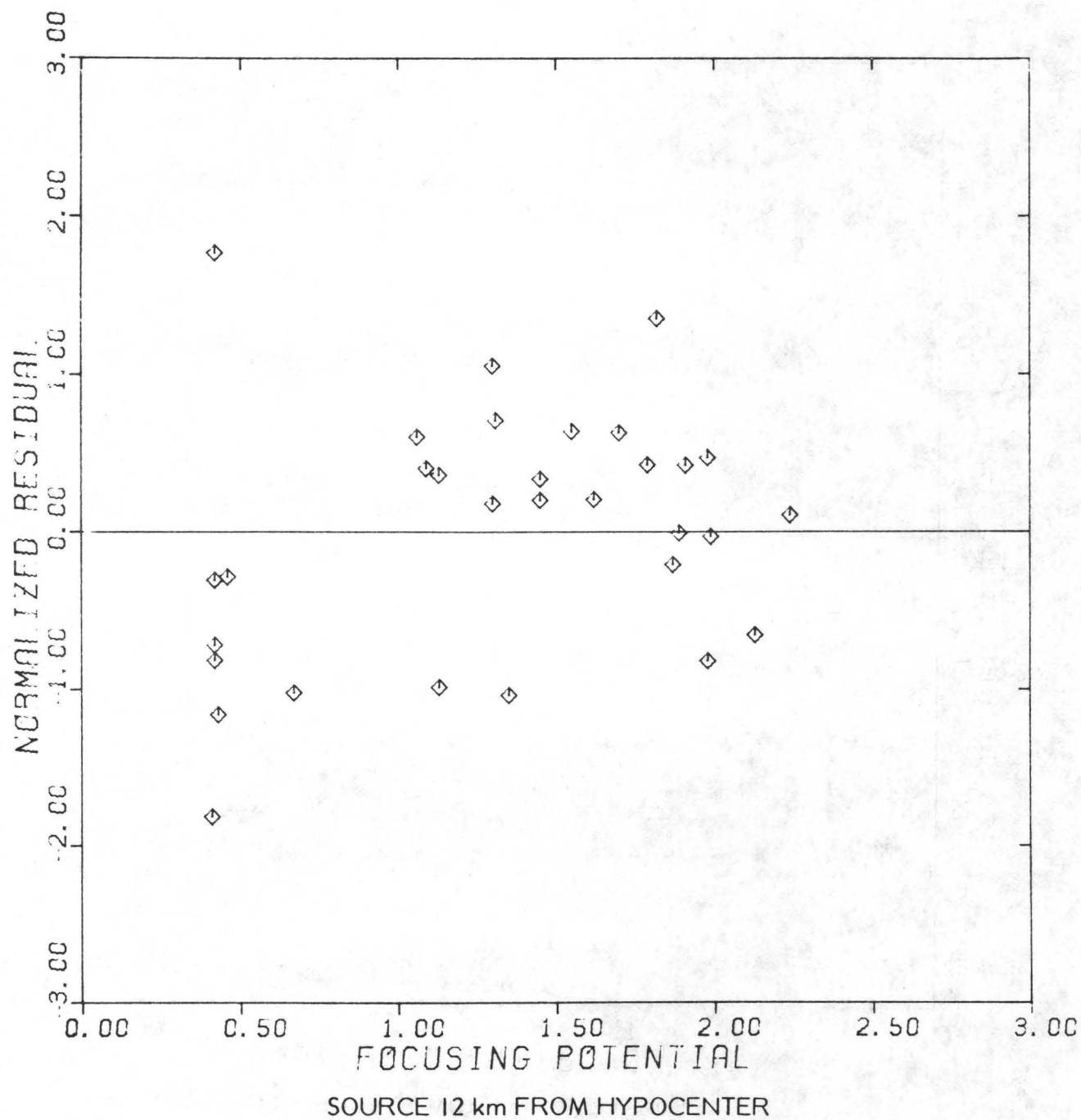IMPERIAL VALLEY 1979 DATA
PEAK GROUND ACCELERATION

FIGURE 5

IMPERIAL VALLEY 1979 DATA
PEAK GROUND VELOCITY

FIGURE 6
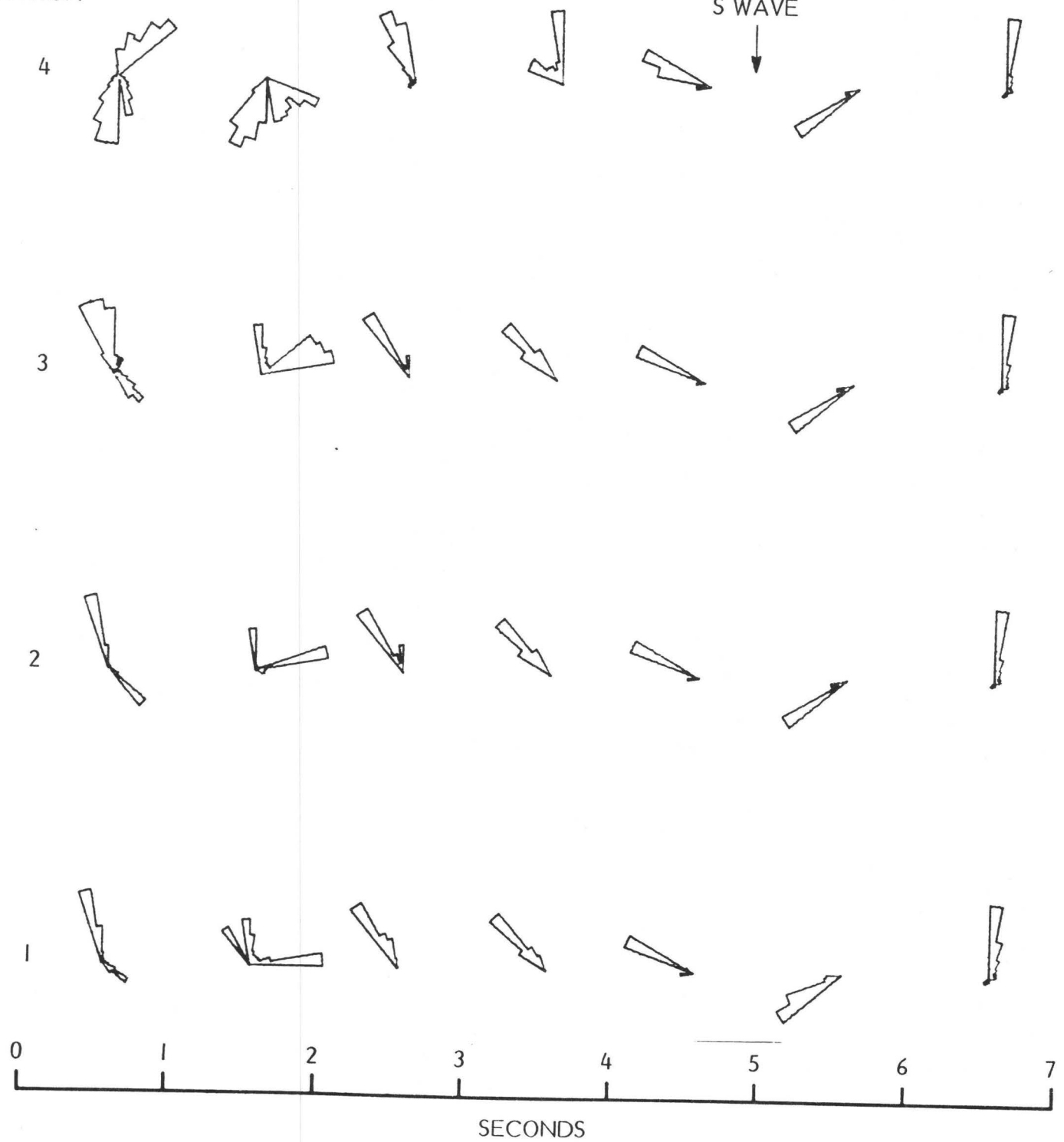
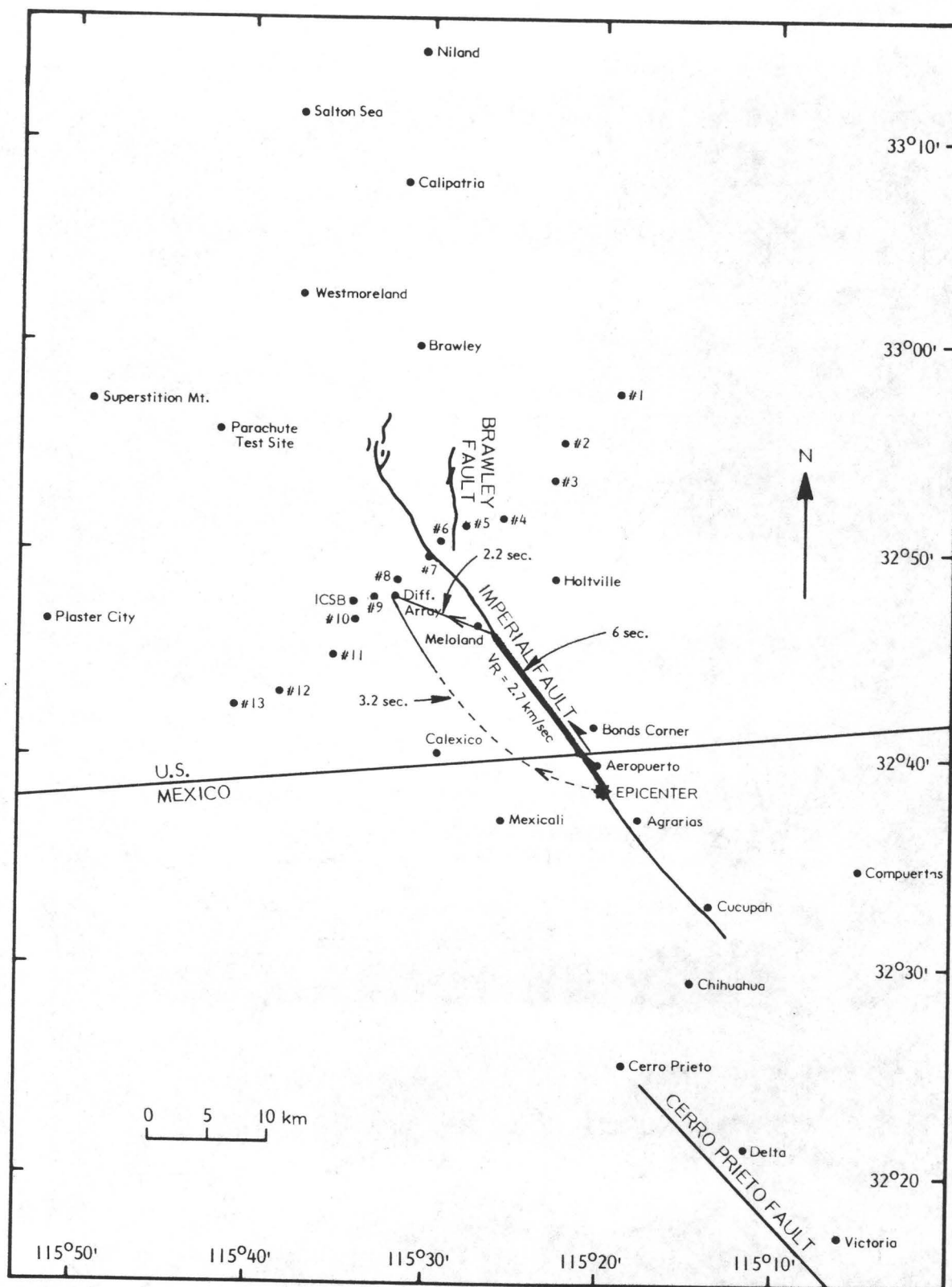DIRECTION OF PARTICLE ACCELERATION
ACROSS ECDA (f < 1 Hz)

931

FIGURE 7

LOCATION OF RECORDING STATIONS
WITHIN THE NEAR-SOURCE REGION OF THE
IMPERIAL VALLEY EARTHQUAKE OF OCT. 15, 197

STATION

S WAVE

4

3

2

1

0   1   2   3   4   5   6   7
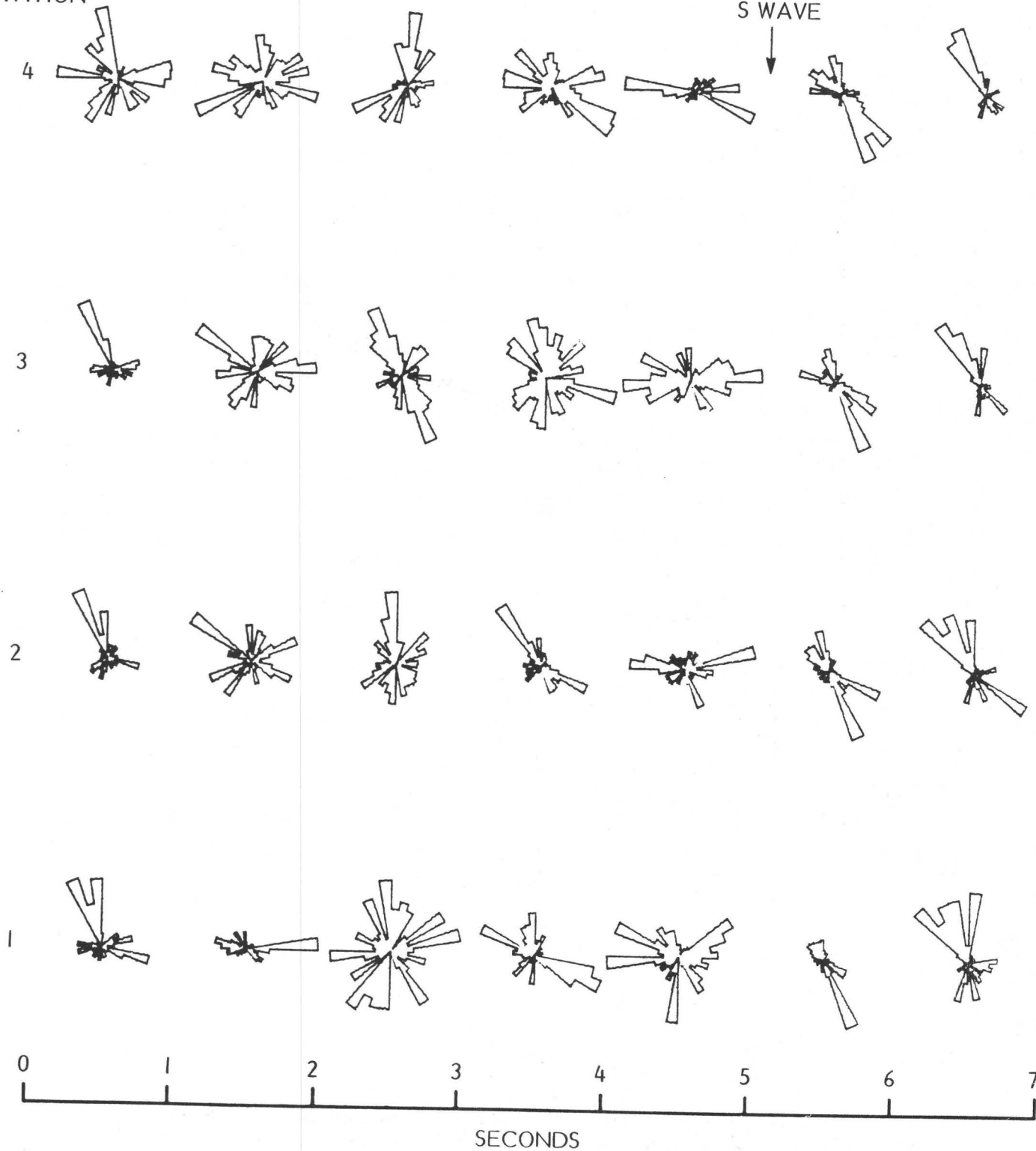
SECONDS

FIGURE 8

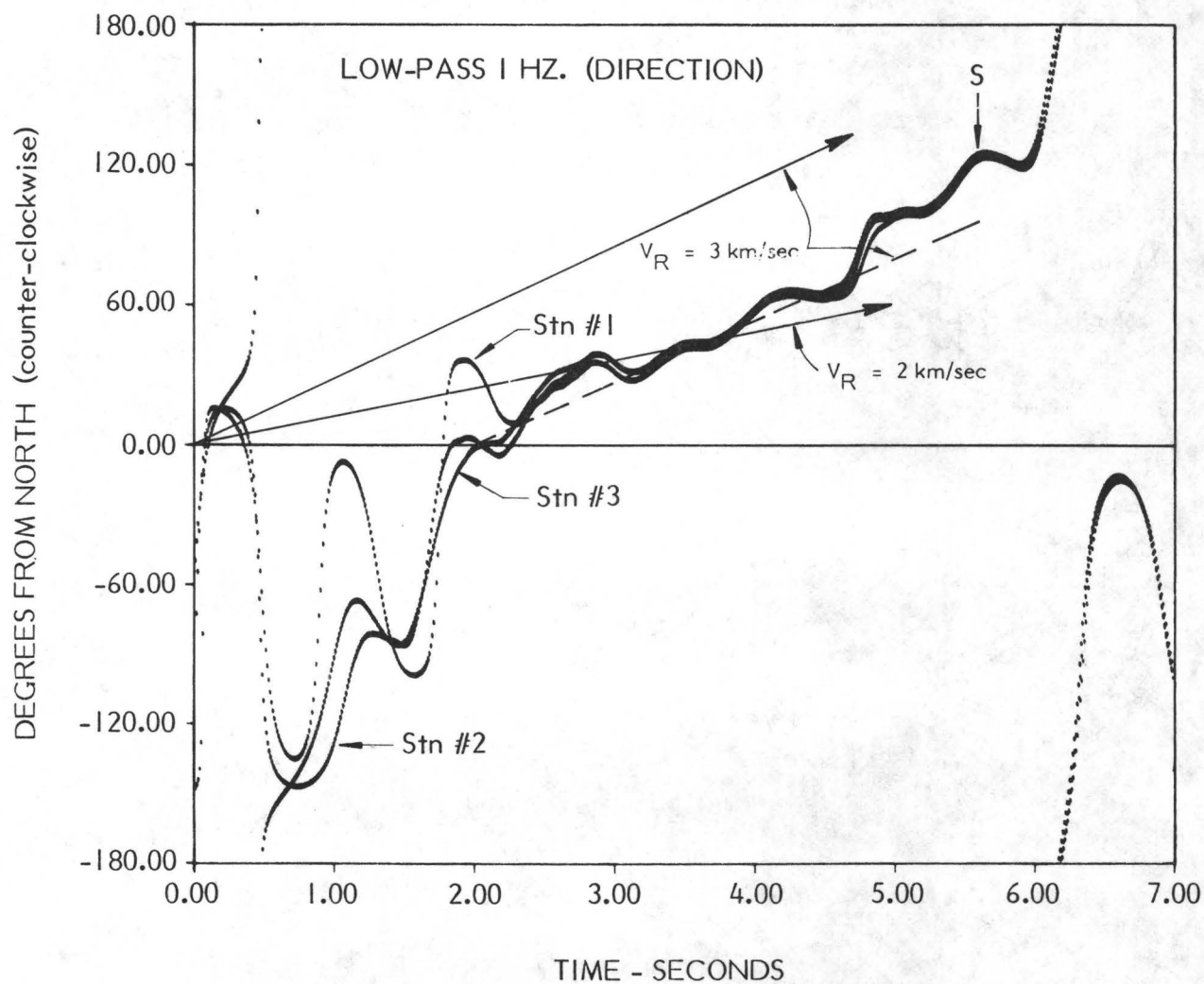DIRECTION OF PARTICLE ACCELERATION
ACROSS ECDA (1-10 Hz)

933

FIGURE 9

DETAILED VARIATION OF THE OBSERVED POLARIZATION ANGLE
OF P-WAVE CODA DURING THE FIRST FIVE SECONDS AT ELEMENTS I TO
3 OF THE ARRAY. IN COMPUTATION OF THE THEORETICAL PREDICTIONS FOR
2 AND 3 KM/SEC RUPTURE VELOCITIES, A VELOCITY OF 5.85 KM/SEC
IS ASSUMED FOR TRANSMISSION OF P-WAVES IN THE BASEMENT ROCK.

SH RAYS AND MODES IN A TWO-LAYER EARTH MODEL, WITH APPLICATION TO THE IMPERIAL VALLEY

E. Niver, A. H. Kamel and L. B. Felsen
Department of Electrical Engineering/Computer Science
and Microwave Research Institute
Polytechnic Institute of New York
Farmingdale, New York 11735
(516) 454-5073

I. BACKGROUND

Transient propagation in a stratified environment has traditionally been analyzed in terms of guided mode expansions (comprising discrete and, when appropriate, continuous mode spectra) or ray expansions (Cagniard-DeHoop techniques or Fourier inversion of harmonic ray fields). More recently, efforts have also been exerted toward direct numerical evaluation of propagation integrals. These techniques have been constrained to idealized configurations, with uniformity along the duct or layer axis. Even with these restrictions, implementation becomes difficult at the high-frequency end of the signal spectrum since a modal formulation may require consideration of very many modes while the numerical evaluation of propagation integrals may require excessive computer time. Ray methods are limited because, for long observation times, the ducting environment necessitates inclusion of many rays having undergone multiple reflection and (or) refraction. For tractability, the high-frequency mode or ray expansions are often truncated, with only a vague estimate of the truncation error. Even when these alternative methods yield comparable numerical results, the interpretation of the data derived by either method in terms of physical wave processes is obscured in view of the contribution, by superposition or interference, of many terms with comparable magnitudes.

In an attempt to deal with the difficulties noted above, we have developed a rigorously based hybrid formulation whereby the transmitted signal is expressed in terms of a judiciously chosen combination of ray fields, modal fields, and a remainder. The method is especially well suited to the high frequency regime. The number of modes and rays included in this hybrid representation is usually far less than when only modes or only rays are considered. This facilitates numerical treatment of the problem. One also gains new physical insights since the formulation implies that propagation processes characterized by rays with many reflections can be treated collectively in terms of a few modes while processes characterized by many modes can be expressed succinctly in terms of a few rays. Moreover, the procedure seeks to minimize the contribution from the remainder, usually given in computable integral form, so that the entire motion can be expressed as a mixture of ray and modal fields chosen according to criteria with poignant physical interpretation. Thus, the hybrid formulation quantifies the truncation error of a mode series in terms of rays or, equivalently, the truncation error of a ray series in terms of modes, with inclusion of a remainder that often turns out to be negligible over broad ranges of the observation parameters. Furthermore, since the number of modes in a modal expansion can now be suitably restricted, the eigenvalue problem in a complicated layered environment may often be reduced to a simpler form for the retained cluster of modes. This feature economizes on computer time and required computer capacity.

The hybrid method has first been applied to time-harmonic propagation in tropospheric ducts,[1] underwater acoustic ducts,[2] and on concave surfaces.[3] More recently, it has been applied to the study of a seismic event based on a simple model of the Borrego Mountain earthquake.[4] The model consisted of a homogeneous sedimentary surface layer above a semi-infinite homogeneous bedrock, with a line source of SH motion located in the bedrock, and the resulting SH motion observed at the earth's surface. This example demonstrated clearly the previously noted advantages of the hybrid approach. By combining rays and modes appropriately, the ray-like character of the early arrivals and the mode-like character of the late arrivals has been exploited within a single concise formulation that allows the continuous monitoring from the first arrival to long observation times and exhibits the smooth transition from the ray phase to the modal phase of the hybrid field.

II. MODELING OF THE IMPERIAL VALLEY ENVIRONMENT

The analysis summarized in Section I has now been generalized to accommodate a simple two-layer model of the Imperial Valley environment. Here, the SH line source is located in the sediment which is assumed to have an inhomogeneous velocity profile.[5] The velocity in the bedrock is assumed to be constant, with a velocity jump occurring at the sediment-bedrock interface, and the densities in the sediment and bedrock are also assumed to have the constant values ρ_1 and ρ_2, respectively (see Fig. 1). Lateral variations along z in the layer structure are ignored.

For application to underwater sound propagation, we have previously employed a velocity profile varying exponentially with depth,[6] since the wave equation in such a medium has solutions in terms of known functions (Bessel functions). In choosing a smooth canonical profile that fits the piecewise linear data in reference 5, we have therefore attempted to employ a functional dependence that permits portions of our underwater computer program to be used in the calculations. We decided on a velocity profile of the form

$$v_s(x) = \frac{v_s(0)}{[p + q \ \exp(-2x/a)]^{1/2}} \tag{1}$$

$$v_s(0) = 812.5 \ \text{m/sec}, \tag{1a}$$

$$a = 2000 \, \text{m} \, , \quad p = 0.06445 \, , \quad q = 0.93555,$$

which approximates the given data quite well (see Fig. 1) and also yields solutions of the depth-dependent portion of the SH motion in the form of Bessel or Hankel functions

$$f = H_\nu^{(1,2)}(\xi_x) \, , \quad \nu = ka \sqrt{\zeta^2 - p} \, , \quad \xi_x = kaq^{1/2} \exp(-x/a) \tag{2}$$

Here, x is the depth coordinate, ζ is the normalized wavenumber along z, and $k = \omega / v_s(0)$, with ω denoting the radian frequency. Our previous model,[6] also shown in Fig. 1, is recovered from (1) by setting $p = 0$, $q = 1$. Although this simpler model is a poorer approximation to the dashed profile in Fig. 1, we have used it for illustration in some of the numerical calculations since the resulting functions f are then more readily computable.

III. ANALYSIS

For a source in the sediment, the profile in (1) admits of surface ducted (whispering gallery) rays as well as rays reflected between top and bottom. The caustic structure for the surface ducted rays is shown in Fig. 2. By the hybrid scheme, one may employ ray-mode combinations that exclude the caustic forming ray species and fill the angular volume subtended by these with modes (Fig. 3). Thereby, one avoids the need for corrections in the simple asymptotic ray field when the observer is near a caustic, or the need for computing generalized ray integrals that are valid in the caustic transition region. Time-dependent source functions can be synthesized by exploring this option for various frequencies. The critically reflected ray and the glancing ray at the sediment-bedrock interface, for which the simple asymptotic ray solution fails (Fig. 3), can likewise be eliminated in this manner.

A. Formulation

Referring to Fig. 1 we seek a solution of the two-dimensional wave equation for SH motion caused by a time-harmonic line source at $(x', 0)$ in the sediment region (time variation $\exp(-i\omega t)$ is suppressed). In the sediment $0 < x \leq b$

$$\left[\frac{\partial}{\partial x} \mu(x) \frac{\partial}{\partial x} + \mu(x) \frac{\partial^2}{\partial z^2} + \rho_1 \omega^2 \right] u(x, z) = -\delta(x-x') \delta(z) \ , \tag{3}$$

Here, $u(x, z)$ stands for the displacement in the y-direction at the observation point (x, z), and

$$\mu(x) = v_s^2(0) \ \rho_1/n^2(x), \text{ with } n^2(x) = p + qe^{-2x/a} \ , \tag{4}$$

is Lamé's constant. In the bedrock, the motion satisfies the simpler equation (3) with $\mu(x)$ replaced by the constant μ_2, ρ_1 by ρ_2, and the right-hand side set equal to zero. The boundary conditions require continuity of stress and displacement at $x = b$, vanishing of stress at $x = 0$, and a radiation condition at $x \to +\infty$.

B. Plane Wave Spectral Representation

By plane wave spectral decomposition with respect to z, one may derive a contour integral representation for $u(x, z)$. The x-dependent functions in the integrand are solutions of the reduced equation (3) (with $\partial/\partial z \to ik\zeta$, where ζ is the normalized longitudinal wavenumber) subject to the x-domain boundary conditions. For the parameters in (4), this reduced equation is quite complicated. However, by assuming that

$$n^2(x) - \zeta^2 >> \frac{1}{(ka)^2} \left[1 - \frac{p^2 + 4pq \ e^{-2x/a}}{n^4(x)} \right] \tag{5}$$

one obtains a simplified equation which can be solved in terms of the Bessel functions in (2). Care must now be taken to keep the original integration path C_0 away from points where $\zeta \cong \pm n(x)$, which requirement is well satisfied for observation points on the surface $x = 0$ where $n(0) = 1$. Moreover, the inequality requires sufficiently high frequencies. Both of these restrictions are kept in mind when performing subsequent calculations. These difficulties do not arise

for the simpler model with $p = 0$, $q = 1$, for which simpler Bessel functions provide an exact solution.

The solution can now be constructed by standard techniques.[6] When the original integration path C_0 along the real axis of the complex ζ-plane is deformed into the contour C in Fig. 4, one obtains the desired representation for the motion $u(x, z)$

$$u(x, z) = \frac{ika}{8} \frac{n(x)n(x')}{v_s^2(0)\, \rho_1} \int_C \frac{[H_\nu^{(1)}(\xi_x) + R_u(\zeta) H_\nu^{(2)}(\xi_x)]}{1 - R_u(\zeta)R_d(\zeta)}$$

$$\cdot [H_\nu^{(2)}(\xi_{x'}) + R_d(\zeta) H_\nu^{(1)}(\xi_{x'})] e^{ik\zeta z} d\zeta \tag{6}$$

with ν and ξ_x, for any value of x, defined in (2). $R_u(\zeta)$ and $R_d(\zeta)$ are reflection coefficients at the upper and lower boundaries of the sediment, respectively,

$$R_u(\zeta) = -\frac{H_\nu'^{(1)}(\xi_o) + \frac{\sqrt{q}}{ka} H_\nu^{(1)}(\xi_o)}{H_\nu'^{(2)}(\xi_o) + \frac{\sqrt{q}}{ka} H_\nu^{(2)}(\xi_o)}, \quad R_d(\zeta) = -\frac{H_\nu'^{(2)}(\xi_b) + Y(\zeta)H_\nu^{(2)}(\xi_b)}{H_\nu'^{(1)}(\xi_b) + Y(\zeta)H_\nu^{(1)}(\xi_b)} \tag{7}$$

with a prime denoting differentiation with respect to the argument. Furthermore,

$$Y(\zeta) = i\frac{1}{n_2^2} \frac{\rho_2}{\rho_1} \frac{n^2(b)}{\sqrt{q}} e^{b/a} (n_2^2 - \zeta^2)^{1/2} + \frac{\sqrt{q}}{ka\, e^{b/a} n^2(b)} \tag{8}$$

and

$$n_2 = \frac{v_s(0)}{v_{s_2}} \tag{9}$$

Branch cuts are drawn as shown in Fig. 4 so that

$$\text{Im}\{(n_2^2 - \zeta^2)^{1/2}\} \geq 0 \tag{10}$$

on the upper Riemann sheet, thereby satisfying the radiation condition as $x \to +\infty$.

By contour deformation and manipulation of the integrand, one may derive from (6) various alternative representations.

C. Normal Modes, Leaky Modes, Plus Continuous Spectrum

Normal modes trapped in the sediment layer arise from the poles ζ_m which satisfy the resonance equation

$$1 - R_u(\zeta_m) R_d(\zeta_m) = 0 \tag{11}$$

in the interval $n_2 < \zeta_m < 1$ on the real axis.

Leaky mode poles ζ_ℓ also satisfy (11) but lie on the lower Riemann sheet $\mathrm{Im}\{(n_2^2 - \zeta^2)^{1/2}\} < 0$ in the interval $0 < \mathrm{Re}\{\zeta_\ell\} < n_2$, $\mathrm{Im}\{\zeta_\ell\} > 0$. By deforming the original contour into the contour C_B(Fig. 4) one obtains instead of the highly oscillatory integrand along C an integrand which decreases rapidly and is therefore useful for numerical or asymptotic evaluation. During this deformation one must take into account the intercepted pole singularities. One thus obtains the sum of all possible normal modes F_m, a finite number of leaky modes F_ℓ, and a branch cut integral F_c with rapidly decaying integrand. For observation points on the surface $x = 0$,

$$u(0, z) = \sum_{m=1}^{M} F_m + \sum_{\ell=1}^{L} F_\ell + F_c \tag{12}$$

where

$$F_h = \frac{\pi}{4} \frac{ka\,n(x')}{v_s^2(0)\rho_1} \frac{E(\xi_o)[H_\nu^{(2)}(\xi_{x'}) + R_d(\zeta_h) H_\nu^{(1)}(\xi_{x'})]}{\frac{\partial}{\partial\zeta}[R_u(\zeta_h) R_d(\zeta_h)]} e^{ik\zeta_h z}\bigg|_{\nu=\nu_h}, \quad h = m \text{ or } \ell \tag{13}$$

Here,

$$E(\xi_o) = H_\nu^{(1)}(\xi_o) + R_u(\zeta) H_\nu^{(2)}(\xi_o) \tag{13a}$$

and F_c is the integral in (6) (for $x = 0$), evaluated along the contour C_B. M and L indicate the number of normal and leaky modes, respectively.

The Hankel functions in (13) are approximated in terms of Airy functions (see Appendix A). The resulting formulation is employed to generate the reference solution, with which the other representations are compared. When the Airy functions are further reduced by WKB approximations, the normal and leaky mode fields due to the pole residues may be interpreted in terms of two self-consistent modal ray congruences as shown in Figure 5.

D. __Hybrid Ray-Mode Representation__

By expanding the denominator in (6) into a partial power series

$$\frac{1}{1 - R_u(\zeta) R_d(\zeta)} = \sum_{n=0}^{N} (R_u(\zeta) R_d(\zeta))^n + \frac{(R_u(\zeta) R_d(\zeta))^{N+1}}{1 - R_u(\zeta) R_d(\zeta)} \tag{14}$$

one may rewrite the motion for observation points on the surface $(x = 0)$ as

$$u(0, z) = \sum_{j=1}^{2} \left(\sum_{n=0}^{N_j} \overline{G}_{nj} + D_{N_j} \right) \tag{15}$$

where each $\bar{G}_{nj}$ denotes a generalized ray field with n reflections at the upper boundary $x = 0$,

$$\bar{G}_{nj} = \frac{ika}{8} \frac{n(x')}{v_s^2(0)\rho_1} \int_C E(\xi_o) \phi_j(\xi_{x'}) [R_u(\zeta)R_d(\zeta)]^n e^{ik\zeta z} d\zeta \qquad (16a)$$

and

$$D_{N_j} = \frac{ika}{8} \frac{n(x')}{v_s^2(0)\rho_1} \int_C E(\xi_o) \phi_j(\xi_{x'}) \frac{[R_u(\zeta)R_d(\zeta)]^{N_j+1}}{1 - R_u(\zeta)R_d(\zeta)} e^{ik\zeta z} d\zeta \qquad (16b)$$

denotes a remainder accounting for truncation of the series at $n = N$. Here,

$$\phi_j(\xi_{x'}) = R_d^s(\zeta) H_\nu^{(j)}(\xi_{x'}) \qquad (16c)$$

with $s = (1, 0)$ for $j = 1, 2$, respectively, and j identifies the ray species according to the possible departure directions of a ray from the source, as shown in Fig. 6. The summation limit N in (14) has therefore been replaced by N_j in (15). The generalized ray integrals may describe surface ducted rays as well as rays (trapped or leaky) reflected between top and bottom of the sediment (see Fig. 6). Replacing the Hankel functions in (16a) by their Debye approximations (Appendix A), one may perform an asymptotic evaluation[7] of a generalized ray integral along the path C_{nj} in Fig. 4 to find the following contributions from saddle points $\zeta_{nj}^{(1)}$ and $\zeta_{nj}^{(2)}$, and the branch point at n_2 (when intercepted during the deformation of C into C_{nj}):

$$\bar{G}_{nj} = G_{nj}^{(1)} + G_{nj}^{(2)} + G_{nj}^L U(\zeta_{nj}^{(2)} - n_2) \qquad (17)$$

where $U(\cdot)$ is the Heaviside unit function, and $G_{nj}^{(1)}$ (due to $\zeta_{nj}^{(1)}$) represents a ray whose turning point is above the lower boundary (category (1)) while $G_{nj}^{(2)}$ (due to $\zeta_{nj}^{(2)}$) represents a ray intercepting both boundaries (category (2)) as depicted in Fig. 6. Even without the Debye approximations, the integrand decays away from the saddle points along C_{nj} and therefore renders numerical evaluation of the generalized ray integrals $G_{nj}^{(1)}$ and $G_{nj}^{(2)}$ more efficient. The branch point contribution, when relevant, represents a lateral wave (refraction arrival) G_{nj}^L, as schematized in Fig. 3. Here, the rapidly convergent integrand in (16a) is evaluated along the contour C_B in Fig. 4. To simplify the notation, the ray species index j is omitted henceforth.

The remainder D_N in (16b) can likewise be made rapidly convergent[6] by deforming the contour C into the contour C_N passing through the saddle points $\zeta_N^{(r)}$, $r = 1, 2$; the integrand now decays away from the saddle points along the deformed path. During the deformation, one must extract residues due to any intercepted (normal or leaky mode) pole singularities. This yields

$$D_N = \sum_{m=1}^{M_N} \hat{F}_m + \sum_{\ell = L_{N+1}}^{L} \hat{F}_\ell + R_N \qquad (18)$$

The "incomplete" normal modes $\hat{F}_m$ and leaky modes $\hat{F}_\ell$ represent portions of the complete modes in (13):

$$\hat{F}_h = \frac{\pi}{4} \frac{ka\, n(x')}{v_s^2(0)\rho_1} \left. \frac{E(\xi_o)\phi(\xi_{x'})e^{ik\zeta_n z}}{\frac{\partial}{\partial\zeta}[R_u(\zeta_h)R_d(\zeta_h)]} \right|_{\nu=\nu_n} , \quad h = m \text{ or } \ell \qquad (19)$$

with $\phi(\xi_{x'})$ defined in (16c) and $E(\xi_o)$ in (13a). The new remainder R_N, evaluated along C_N has the form

$$R_N = R_N^{(1)} + R_N^{(2)} + R_N^L\, U(\zeta_N^{(2)} - n_2) \qquad (20)$$

For category (1),

$$R_N^{(1)} = -\frac{1}{2}\, G_N^{(1)} + \overline{R}_N^{(1)} \qquad (20a)$$

where the first term represents half of the last included surface reflected ray, and

$$\overline{R}_N^{(1)} = \frac{ika}{16} \frac{n(x')}{v_s^2(0)\rho_1} \int_{C_N} E(\xi_o)\phi(\xi_{x'})[R_u(\zeta)R_d(\zeta)]^N \cdot \frac{1+R_u(\zeta)R_d(\zeta)}{1-R_u(\zeta)R_d(\zeta)} e^{ik\zeta z} d\zeta$$

$$(21)$$

Here, the relevant position of the integration path is the one near $\zeta_N^{(1)}$. Analogous considerations, now referring to $\zeta_N^{(2)}$, apply to $R_N^{(2)}$. The last term in (20) is the branch point contribution, when required, with the integral in (21) evaluated along C_B in Fig. 4.

Substitution of (18) into (15) yields the following exact hybrid representation for the motion (omitting the subscript j on the right-hand side):

$$u(0,z) = \sum_{j=1}^{2} \left[\sum_{n=0}^{N} \overline{G}_n + \sum_{m=1}^{M_N} \hat{F}_m + \sum_{\ell=L_{N+1}}^{L} \hat{F}_\ell + R_N \right] , \qquad (22)$$

different portions of which can be expressed asymptotically, when applicable. This result can evidently be generalized to apply to any finite group of rays $\underline{N} \leq n \leq \overline{\overline{N}}$ extracted from the totality of all possible rays.

When the saddle points $\zeta_n^{(1)}$ and $\zeta_n^{(2)}$ are not too close to $\zeta_b = \sqrt{p+qe^{-2b/a}}$, one may use the isolated saddle point method to evalue (16a) asymptotically by taking the contribution from each saddle point $\zeta_n^{(r)}$, with (r) = (1) or (2), individually:

$$G_n^{(r)} \sim \sqrt{\frac{2\pi}{ka\,|q_n''(\zeta_n^{(r)})|}}\, f_n(\zeta_n^{(r)}) \exp\left\{ika\, q_n(\zeta_n^{(r)}) \pm i\pi/4\right\} \qquad (23)$$

where the upper and lower signs refer to $q_n''(\zeta_n^{(r)})$ positive and negative, respectively.

The saddle point $\zeta_n^{(r)}$ is determined from the condition

$$\frac{\partial}{\partial \zeta}\left[q_n(\zeta_n^{(r)})\right] = 0. \tag{24}$$

With $\delta(x,\zeta)$ and $S(x,\zeta)$ defined in Appendix A, one has

$$q_n(\zeta) = (2n+1)\,\delta(0,\zeta) - \sigma_r 2(n+1)\delta(b,\zeta) + \hat{m}\delta(x',\zeta) + \zeta\frac{z}{a} \tag{25}$$

and

$$f_n(\zeta) = \frac{ika\,n(x')}{8\,v_s^2(0)\,\rho_1}\,\hat{\ell}\,S(0,\zeta)S(x',\zeta)\,[1+i\overline{R}_u]\,\overline{R}_u^n\,\alpha_r^{n+s} \tag{26}$$

where $\hat{\ell} = (-i,1)$ and $\hat{m} = (1,-1)$, for $j=1,2$, respectively. Furthermore, $\alpha_r = (1,\overline{R}_d)$ and $\sigma_r = (0,1)$ for $r=1,2$. Finally,

$$\overline{R}_u = i\left(\frac{ika\sqrt{1-\zeta^2}+q}{-ika\sqrt{1-\zeta^2}+q}\right) \tag{27a}$$

and

$$\overline{R}_d = -i\left(\frac{-i\sqrt{p+q\,e^{-2b/a}-\zeta^2}+\sqrt{q}\,e^{-b/a}\,Y(\zeta)}{i\sqrt{p+q\,e^{-2b/a}-\zeta^2}+\sqrt{q}\,e^{-b/a}\,Y(\zeta)}\right) \tag{27b}$$

The ray caustics at and near the surface, depicted in Fig. 2, are determined from the simultaneous solution of (24), for category (1), and

$$\frac{\partial^2}{\partial\zeta^2}\left[q_n(\zeta_n^{(1)})\right] = 0$$

Debye asymptotics and subsequent simple saddle point evaluation fails when the two saddle points $\zeta_n^{(1)}$ and $\zeta_n^{(2)}$ approach ζ_b, which corresponds to the glancing ray in Fig. 3 or, at longer ranges, to a glancing ray with several surface reflections. One then has the option of employing numerical integration for the generalized ray integral $\overline{G}_n$ in (16a) or of replacing this ray group by a group of modes.

Similar considerations apply to the transition region $\zeta_n^{(2)} \approx n_2$ near the angle of total reflection (see Fig. 3) where the simple asymptotic evaluation of the integral for the lateral wave G_n^L and $G_n^{(2)}$ fails.

E. Numerical Results

In our numerical work, we intend to retain ray fields whenever these can be approximated by their simple asymptotic forms, and to employ the hybrid formulation to eliminate those rays which correspond to the transition regions wherein asymptotic ray theory (ART) is invalid. In performing the calculations, we have several objectives in mind. A first concern is to establish a reference solution, with which subsequent alternatives can be compared. Since (18), with (20), is an exact relation, one part of the equation can provide a check on the accuracy of the remaining part. Accordingly, we have evaluated the ray integrals numerically and compared the result with a numerical evaluation of the mode sums plus collective ray or mode remainders. Positive agreement not only proves that the ray-mode equivalences are posed properly and that the programs operate correctly, but it also establishes the validity of certain high-frequency approximations (WKB or Airy type for the depth-dependent functions), which will arise in the study of more general profiles. A second concern is to simplify evaluation of the collective remainders by utilizing asymptotic analytical evaluation of the relevant integrals. This is possible when the transition regions surrounding the spectral truncation points are isolated from other singularities in the integrands. Finally, to establish the limits of applicability of ART, one must know the width of the transition regions surrounding the troublesome rays. This can be assessed by comparing the numerically evaluated ray integrals with their ART approximations. It may be noted that all numerical evaluations of ray or remainder integrals are performed along contours in the complex plane whereon the integrands decay exponentially away from the central region near a saddle point. Therefore, to within stated accuracy, the integration routines here are much more efficient than those (for example, FFT) relying on spectral integration along the real axis where the integrands are highly oscillatory.

We wish to emphasize again that the conclusions to be reached from this investigation of the special model profiles in Fig. 1 will have a strong bearing on what one may expect under more general conditions since WKB type and related appropriate high-frequency approximations have been utilized, whenever possible, for the exact functions in Section III.

The following results have been obtained so far:

α. For the surface ducted caustic-forming rays in Fig. 3 , it has been established by comparing the numerically evaluated ray integrals with ART that ART may be inapplicable even when the observer is not near a caustic! This conclusion is in accord with previous observations[6] that rays with many surface reflections, whose trajectories lie entirely within the first two, or so, surface guided modal ducts, cannot be validated by ART. The supporting data is presented in Table I. Thus, for the rays with the largest number of reflections $(n = 3, 4)$, alternatives to ART <u>must</u> be employed. The caustics for both model profiles are shown in Fig. 2.

β. For the glancing ray transition region in Fig. 3 , the ray-mode equivalence has been expressed as follows

$$G_N^{(1)} + G_N^{(2)} = \sum_{\overline{M}_1}^{\overline{M}_2} \hat{F}_m - \frac{1}{2} G_{N+1}^{(1)} - \overline{R}_{N+1}^{(1)} - \frac{1}{2} G_{N+1}^{(2)} + \overline{R}_{N+1}^{(2)} \tag{28}$$

Results for profile 2, shown in Table II, demonstrate the inadequacy of ART and the applicability of the ray-mode equivalence.

These calculations are now being carried further to establish how the hybrid method can most effectively complement the asymptotic ray theory (ART) algorithm, the real ζ spectral integration algorithm, the normal mode algorithm, and other computational schemes now in use. Here, the hybrid approach can be employed systematically to correct failurs, as in transition regions for ART and the early arrival domain for normal modes; it will also be explored to render the overall computations for synthetic seismograms more efficient.

ACKNOWLEDGMENT

APPENDIX A

Asymptotic Representations of Hankel Functions

Uniform asymptotic formulas, in terms of Airy functions, for Bessel functions and their derivatives are as follows: [8]

$$J_{\nu}(kx) \sim \left(\frac{2}{\alpha}\right)^{1/2} \beta^{1/6} Ai\left[-\beta^{2/3}\right] \tag{A1}$$

$$J'_{\nu}(kx) \sim -\frac{1}{kx}(2\alpha)^{1/2}\beta^{-1/6} Ai\left[-\beta^{2/3}\right] \tag{A2}$$

where

$$\alpha = \begin{cases} \sqrt{(kx)^2 - \nu^2}, & kx > \nu \\[2ex] i\sqrt{\nu^2 - (kx)^2}, & kx < \nu \end{cases} \tag{A3}$$

and

$$\beta = \begin{cases} \dfrac{3}{2}\left[\sqrt{(kx)^2 - \nu^2} - \nu \arccos(\nu/kx)\right], & kx > \nu \\[3ex] -i\dfrac{3}{2}\left[\nu \ln\left(\dfrac{\nu + \sqrt{\nu^2 - (kx)^2}}{kx}\right) - \sqrt{\nu^2 - (kx)^2}\right], & kx < \nu \end{cases} \tag{A4}$$

The square roots are defined to be positive when ν is real and thereby, by analytic continuation, the behavior of the square root functions in the complex ν-plane is specified.

In the text, the asymptotic evaluations are carried out in the ζ-plane, which is defined via

$$\nu = ka\sqrt{\zeta^2 - p} \tag{A5}$$

with

$$\operatorname{Re}\sqrt{\zeta^2 - p} > 0 \quad \text{and} \quad \operatorname{Re}\sqrt{p + qe^{-2x/a} - \zeta^2} > 0 \tag{A6}$$

on the top sheet. In the ζ-plane

$$\beta = i\frac{3}{2}ka\left[\sqrt{\zeta^2 - p}\,\ln\frac{\sqrt{\zeta^2 - p} + i\sqrt{p + qe^{-2x/a} - \zeta^2}}{\sqrt{q}\,e^{-x/a}} - i\sqrt{p + qe^{-2x/a} - \zeta^2}\right] \tag{A7}$$

In the numerical computations, $\ln(\cdot)$ is taken as the principal value and $\beta^{1/n}$, where n is a positive integer, is computed as

$$\beta^{1/n} = |\beta|^{1/n} \exp i(\arg \beta + 2\pi\tau)/n \qquad \tau = 0, 1, \ldots n-1 \qquad (A8)$$

and τ equals 0 for $\mathrm{Re}(\zeta) < \sqrt{p + qe^{-2x/a}}$ and equals 1 otherwise. Similarly,

$$H_\nu^{(1),(2)}(kx) \sim \left(\frac{2}{\alpha}\right)^{1/2} \beta^{1/6} w_{1,2}(-\beta^{2/3}) \qquad (A9)$$

where

$$w_{1,2}(t) = Ai(t) \mp i\, Bi(t) \qquad (A10)$$

Debye asymptotic forms for the Hankel functions[7] in the ζ-plane (ν-plane) valid for $ka\sqrt{\zeta^2 - p} < ka\sqrt{q}\, e^{-x/a}$ ($\nu < kx$) are given by

$$H_\nu^{(1),(2)}\left(ka\sqrt{q}\, e^{-x/a}\right) \sim S(x,\zeta) \exp(\pm i\, ka\, \delta(x,\zeta) \mp i\pi/4) \quad (A11)$$

where

$$S(x,\zeta) = \sqrt{\frac{2}{\pi ka\, [p + qe^{-2x/a} - \zeta^2]^{1/2}}} \qquad (A12)$$

and

$$\delta(x,\zeta) = \sqrt{p + qe^{-2x/a} - \zeta^2} - \sqrt{\zeta^2 - p}\, \cos^{-1}\left(\frac{\sqrt{\zeta^2 - p}}{\sqrt{q}\, e^{-x/a}}\right) \qquad (A13)$$

REFERENCES

1. S. H. Cho, C. G. Migliora and L. B. Felsen, "Hybrid Ray-Mode Formulation of Tropospheric Propagation," in Proc. AGARD Symp. on Special Topics in HF Propagation (1979).

2. L. B. Felsen and T. Ishihara, "Hybrid Ray-Mode Formulation of Ducted Propagation," J. Acoust. Soc. Am., 65, pp. 595-607 (1979).

3. T. Ishihara and L. B. Felsen, "High-Frequency Fields Excited by a Source Located on a Concave Cylindrical Impedance Surface," IEEE Trans. on Antennas and Propag., AP-27, pp. 172-179 (1979).

4. A. Kamel and L. B. Felsen, "Hybrid Ray-Mode Formulation of SH Motion in a Two-Layer Half-Space," Bull. Seismol. Soc. Am. 71, pp. 1763-1781 (1981).

5. G. A. McMechan and W. D. Mooney, " Asymptotic Ray Theory and Synthetic Seismograms for Laterally Varying Structures: Theory and Application to the Imperial Valley, California, " Bull. Seismol. Soc. Am. 70, pp2021-2035 (1980

6. E. Niver, S. H. Cho and L. B. Felsen, "Rays and Modes in an Acoustic Channel with Exponential Velocity Profile," Radio Science, 16, No. 8, pp. 963-970 (1981).

7. L. B. Felsen and N. Marcuvitz, Radiation and Scattering of Waves, Prentice Hall: Englewood Cliffs, New Jersey, Chapter 4 (1973).

8. M. Abramowitz and I. A. Stegun, Handbook of Mathematical Functions, New York: Dover, pp. 368, (1972).

9. A. Kamel and L. B. Felsen, "On the Ray-Equivalent of a Group of Modes," to appear in J. Acoust. Soc. Am., (1982).
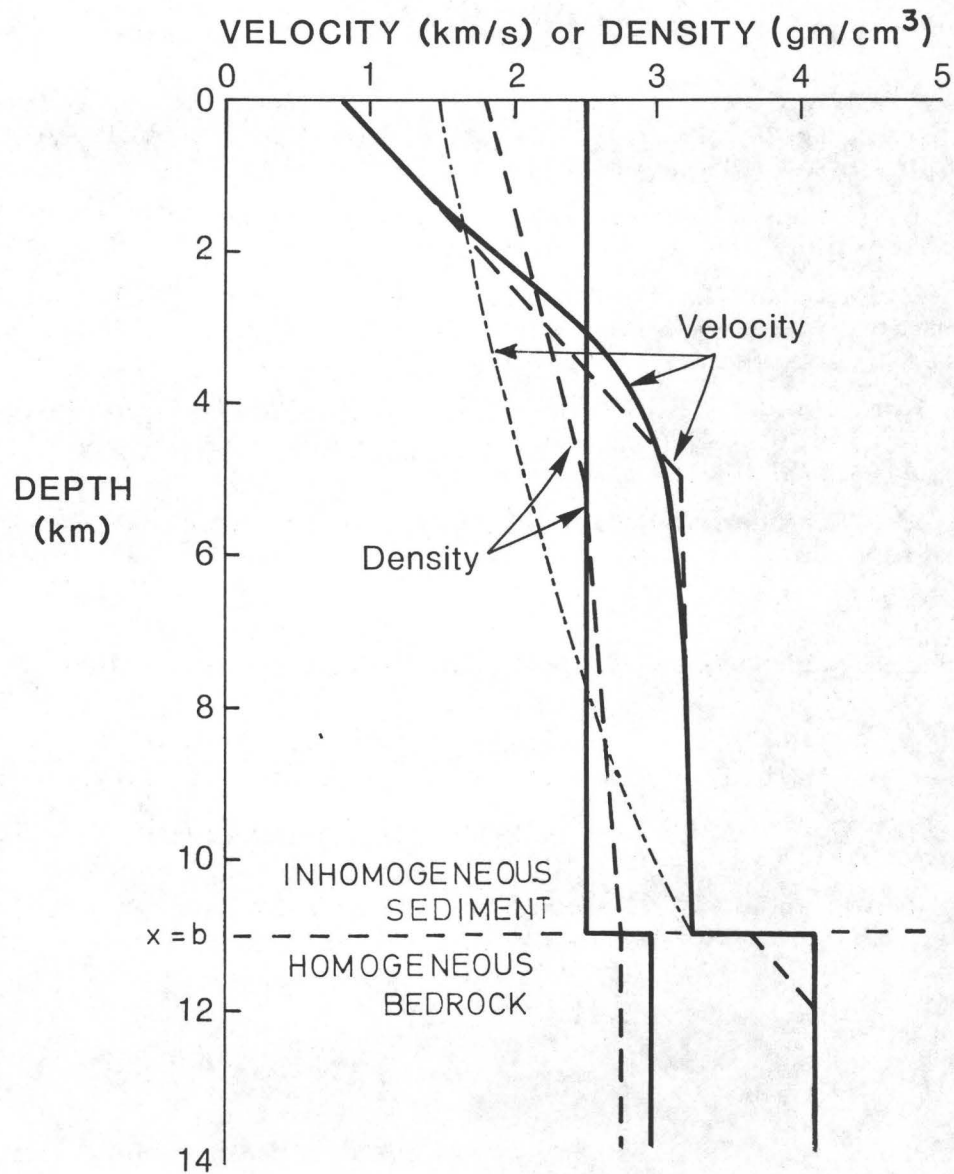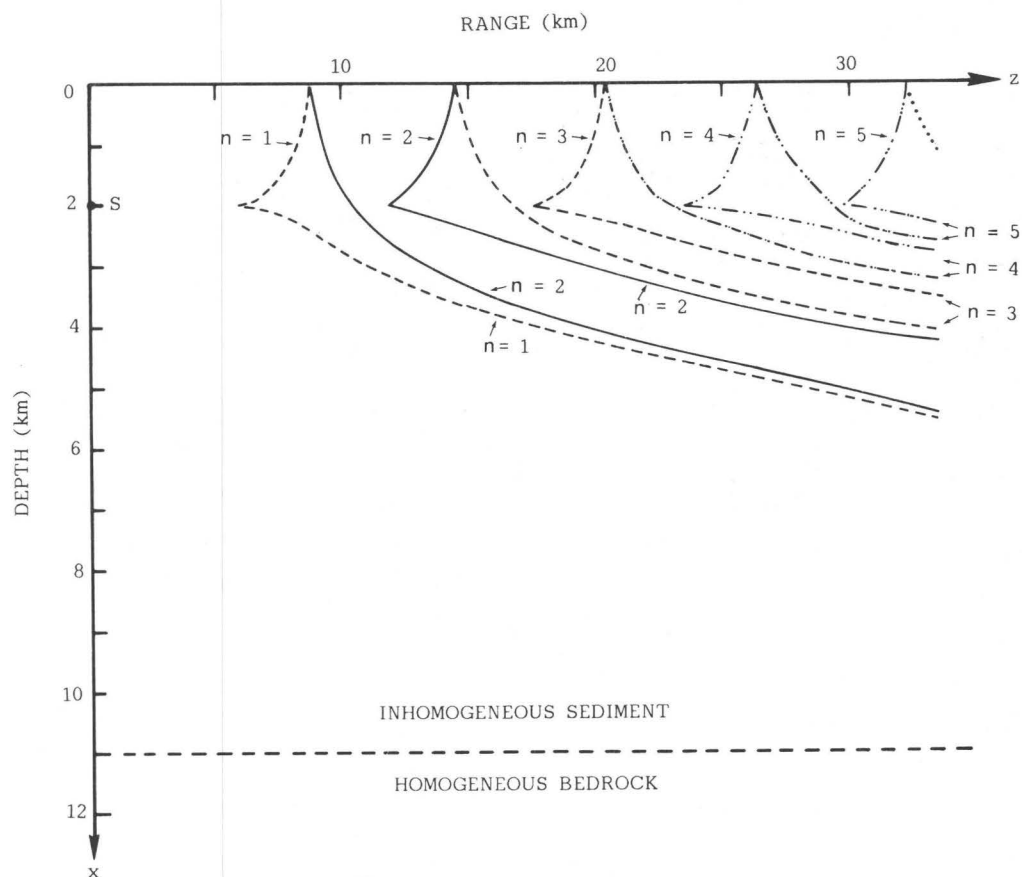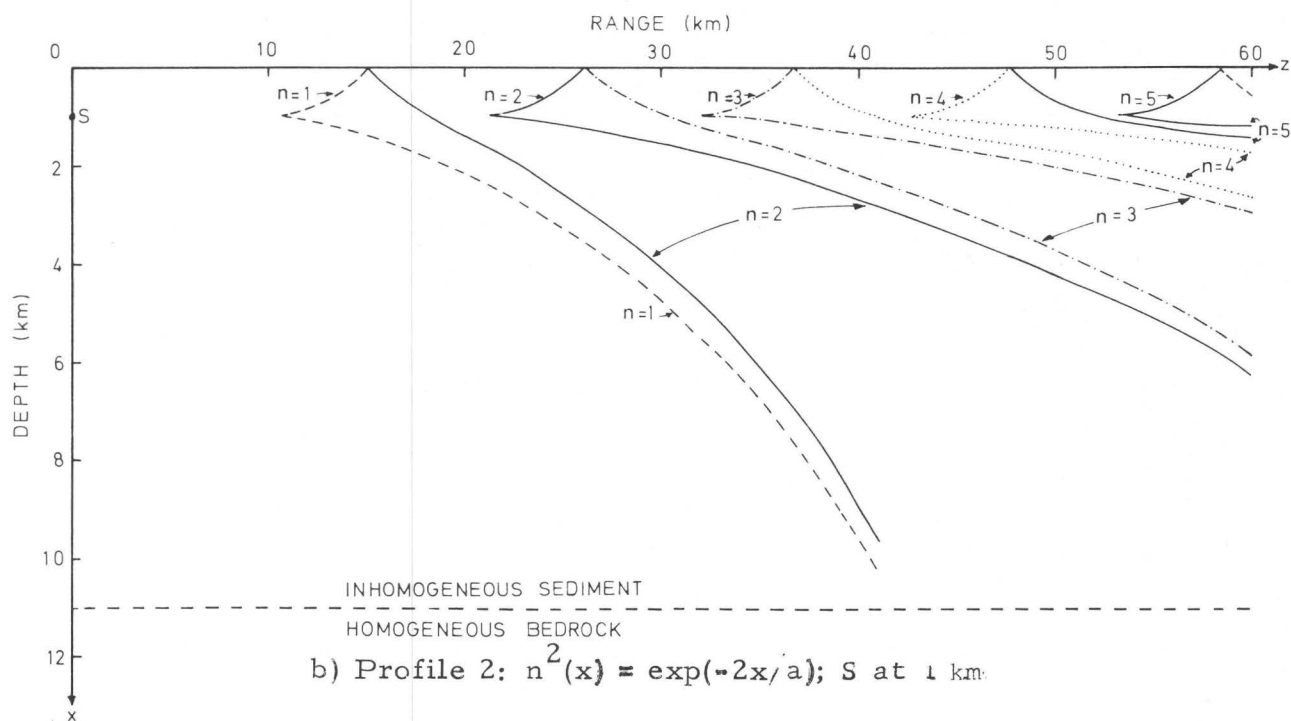
Fig. 1. SH velocity and density profiles for Imperial
Valley terrain. Dashed curves: data from
reference 5. Solid curves: proposed model
with $n(x) = [p+q\exp(-2x/a)]^{1/2}$ (profile 1).
Dot-dashed curve: simplified model with
$n(x) = \exp(-x/a)$ (profile 2).

a) Profile 1: $n^2(x) = p + q \exp(-2x/a)$; S at 2 km

b) Profile 2: $n^2(x) = \exp(-2x/a)$; S at 1 km

Fig. 2. Caustics for surface-reflected rays for the profiles in Fig. 1. n denotes the number of reflections. Although subsequent calculations are restricted to observation points on the surface, the figure contains also the submerged branches.
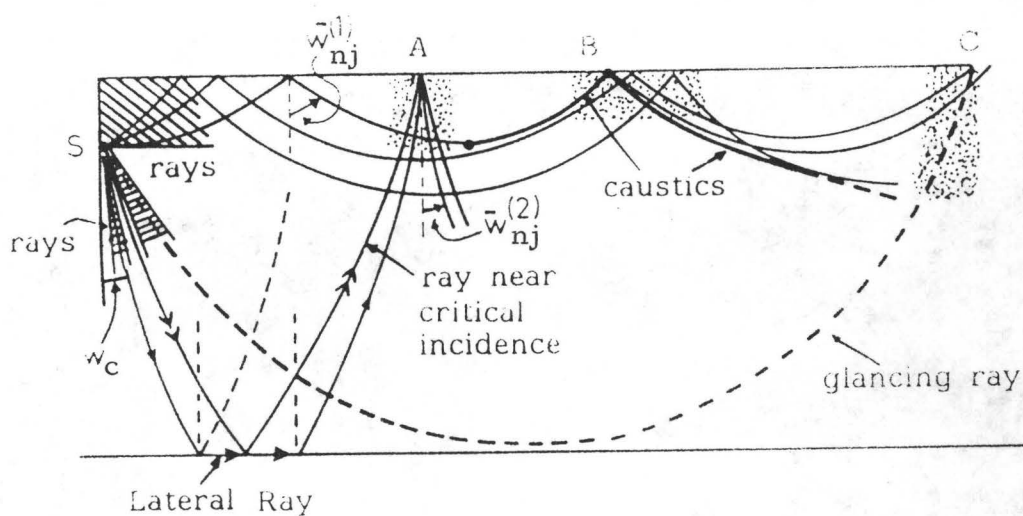
949

Fig. 3. Hybrid combinations that avoid corrections of the simple asymptotic ray field required in transition regions A, B and C. The corresponding angular intervals (shown shaded) can be filled with modes. Alternatively, the field can be evaluated by numerical integration of generalized ray integrals. Referring to (17) the ray angles $\bar{w}_{nj}^{(1),(2)}$ here and $w_{nj}^{(1),(2)}$ in Fig. 6 are related to the wave-numbers as follows $\zeta_{nj}^{(1),(2)} = n(x') \sin w_{nj}^{(1),(2)} = n(o) \sin \bar{w}_{nj}^{(1),(2)}$
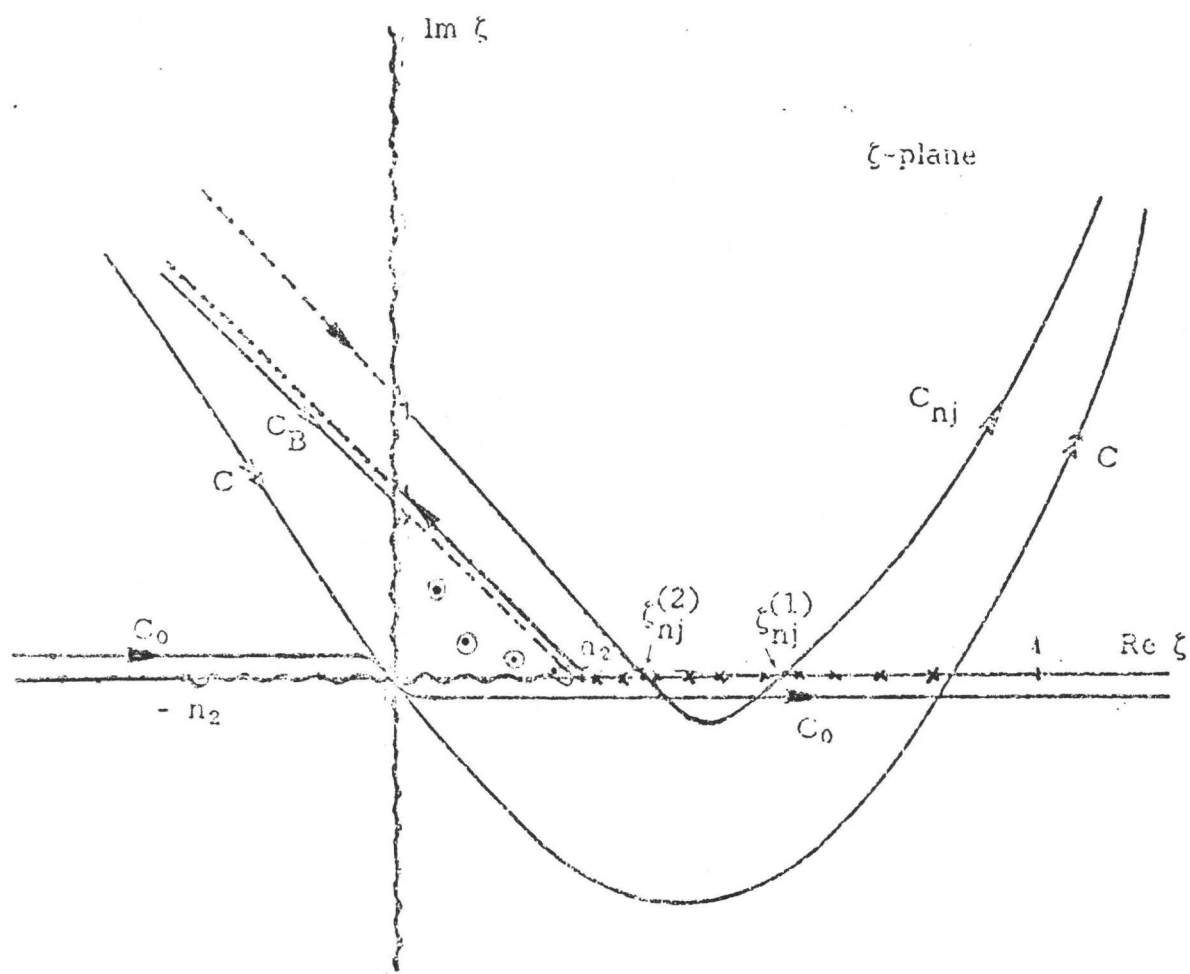
Fig. 4.   Integration paths and singularities in the complex ζ-plane. Solid curves are contours on upper Riemann sheet $\mathrm{Im}\,(n_2^2 - \zeta^2)^{1/2} \geq 0$.

xxxxx   normal mode poles (surface guided and top-bottom trapped)

⊙⊙⊙   leaky mode poles

$\zeta_{nj}^{(1)}$ and $\zeta_{nj}^{(2)}$ are saddle points for rays intercepting the upper and both boundaries, respectively. (See Fig. 6.)
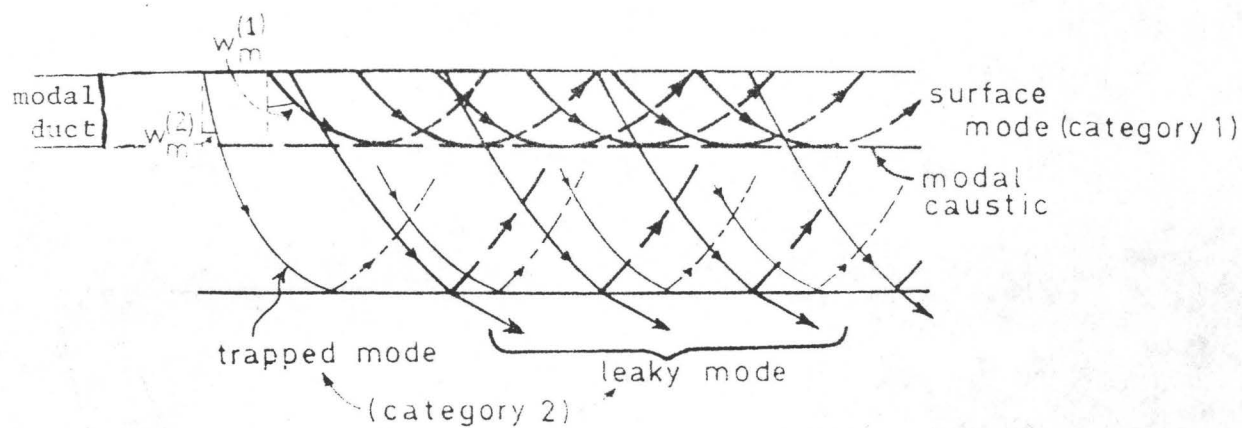
Fig. 5.   Modal ray congruences for surface guided, top-bottom trapped, and leaky modes.

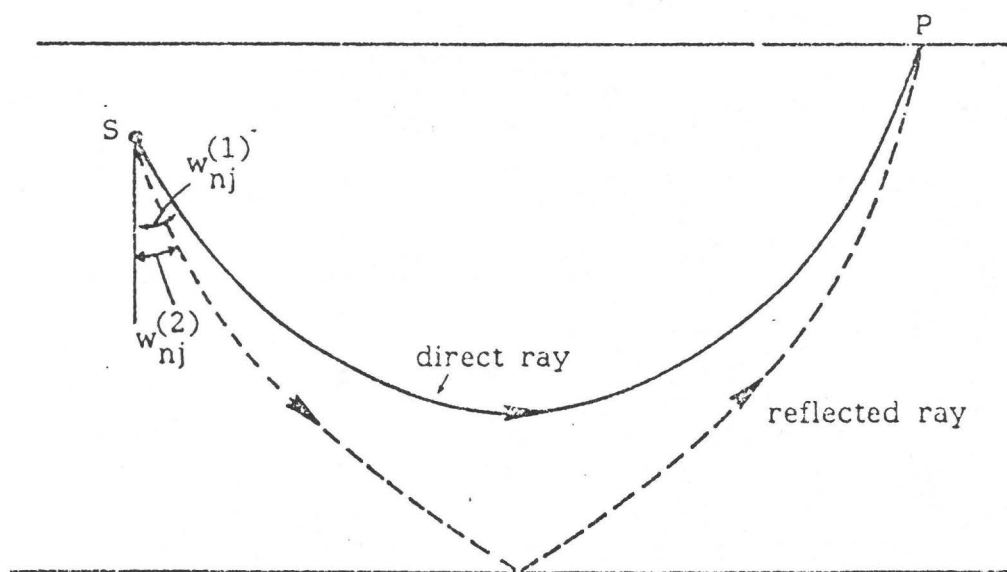Referring to (11) $w_m^{(1),(2)} = \sin^{-1}(\zeta_m^{(1),(2)}/n(o))$.

Fig. 6. Trajectories for the two different ray categories corresponding to saddle points $\zeta_{nj}^{(1)}$ and $\zeta_{nj}^{(2)}$ with $j = 1$ and $n = 0$. The ray angles $w_{nj}^{(1)}$ and $w_{nj}^{(2)}$ are obtained from the mapping $\zeta = n(x')\sin w$.

Profile 2 - Source Depth at 1 km											
		50 km		51 km		52 km		53 km		54 km	
j=1		Re	Im	Re	Im	Re	Im	Re	Im	Re	Im
n=3	$G_n^{(1)}$	0.265	0.337	0.294	0.302	0.325	0.257	0.359	0.204	0.382	0.134
	ART	0.330	0.300	0.351	0.260	0.373	0.210	0.393	0.150	0.406	0.078
n=4	$G_n^{(1)}$	-0.352	-0.284	-0.310	-0.299	-0.270	-0.315	-0.230	-0.334	-0.194	-0.350
	ART	-0.585	-0.309	-0.495	-0.374	-0.423	-0.374	-0.365	-0.392	-0.317	-0.402
	A	-0.222	-1.876	0.551	-1.921	1.206	-1.768	1.821	-1.391	2.245	-0.885
	B	-0.215	-2.065	0.531	-1.976	1.242	-1.823	1.846	-1.412	2.269	-0.944

$\} \times 10^{-11}$

Table I - Real (Re) and Imaginary (Im) Parts of Surface Field Due to Surface-Ducted Rays vs. Range (f = 1.644 Hz). Caustic locations may be inferred from Fig. 2. n = number of surface reflections. $G_n^{(1)}$ = numerical evaluation of ray integral, with Airy approximations in integrands; ART = asymptotic formula for ray integral in (23). For n = 1, 2, $G_n^{(1)}$ and ART agree to within 2%. "A" represents the numerically evaluated sum of rays with n = 3, n = 4, plus a collective formulation of all evanescent rays with n > 4. "B" represents the modal equivalent (2 Airy approximated modes) plus a collective ray remainder. The comparison between A and B indicates the validity of the modal equivalent for this group of rays. The failure of ART for n = 3, 4 is attributed to the fact that the turning points of these rays, over the given range interval, lie within the first two surface-guided modal ducts (see Fig. 5 for definition of modal duct). The widths of these ducts are 0.576 and 1.85 km, respectively. At a range of 50 km, the turning points of rays n = 3 and n = 4 are at a depth of 1.54 and 1.05 Km, respectively. The turning points of rays n = 1, 2 lie outside the first two modal ducts.

Profile 2 - Source Depth at 1 km										
	58 km		59 km		60 km		61 km		62 km	
j=1	Re	Im	Re	Im	Re	Im	Re	Im	Re	Im
ART	-0.296	-0.059	0.245	0.213	-0.158	-0.311	0.082	0.353		
LHS	-0.298	0.150	0.254	-0.005	-0.172	-0.073	0.095	0.096	-0.038	-0.089
RHS	-0.299	0.150	0.255	-0.006	-0.172	-0.073	0.097	0.097	-0.039	-0.089

$\} \times 10^{-11}$

Table II - Real (Re) and Imaginary (Im) Parts of Surface Field in Glancing Ray (N = 1) Transition vs. Range (f = 1.644 Hz) (Profile 2). LHS = numerical evaluation of ray integrals (with Airy approximated integrands) on the left-hand side (LHS) in (28); RHS = numerical evaluation of right-hand side (RHS) in (28). ART = asymptotic formula for LHS. Glancing at bottom corresponds to a range of ~ 61 km. Nine (Airy approximated) modes are required in RHS, with $\overline{M}_1 = 5$, $\overline{M}_2 = 13$. The total number of possible trapped modes is 16.

SPECTRAL ATTENUATION OF SH-WAVES ALONG THE IMPERIAL FAULT

S. K. SINGH

Instituto de Geofísica
Universidad Nacional Autónoma de Mexico, Mexico 20, D.F. México
(905) 550-5215

R. J. APSEL AND J. FRIED

Del Mar Technical Associates, P.O. Box 1083, Del Mar, CA 92014
(714) 481-9292

J. N. BRUNE

Institute of Geophysics and Planetary Physics, Scripps Institution of Oceanography
University of California, San Diego, La Jolla, CA 92093
(714) 452-2890

ABSTRACT

Spectral attenuation of SH-waves has been studied to infer Q along the Imperial Fault. The data set consists of six aftershocks of the Imperial Valley earthquake (15 October 1979, $M_L = 6.6$) digitally recorded up to a distance of 51km. Although there is large variance in Q^{-1} due to scatter in the data, Q below 3.75km appears to be a function of frequency (increasing from about 60 at 3Hz to 500 at 25Hz). High Q values obtained at high frequencies strongly suggests that scattering has not removed a significant amount of energy from the signals and, thus, the observed result, Q varying with frequency, is not due to scattering. For sources below 4km the observed average SH-wave spectral amplitudes, $A(f,R)$ along the fault can be fitted by

$$A(f,R) = \frac{S(f)}{R} e^{-\pi f t^*} e^{-\pi f t / Q(f)}$$

where f = frequency, R = hypocentral distance, $S(f)$ = source factor, $Q(f)$ = quality factor below about 3.75km, and t = travel time up to 3.75km below the surface. The value of t^* for the upper 3.75km is probably between 0.027 and 0.047 (average Q between 100 and 60) depending upon the fall off of $S(f)$ with f (f^{-3} or f^{-2}) beyond the corner frequency.

INTRODUCTION

One of the most critical parameters in simulating earthquake ground motions is the seismic quality factor, Q. Even at short distances, Q is likely to play an important role in the attenuation of seismic shear waves at frequencies above about 1Hz. Present day uncertainty in Q leads to corresponding uncertainty in the seismic design of buildings and critical structures in earthquake prone areas.

Several regressions on peak ground motion with distance have been made in the past (e.g., *Joyner and Boore*, 1981; *Boore et al.*, 1980). Attenuation of Fourier amplitude spectra with distance for California earthquakes has been studied by *Trifunac* [1976], *McGuire* [1978], and *McGuire and Hanks* [1980]. *Trifunac* [1976] reported that the attenution with distance is essentially frequency independent and thus the shape of the spectra does not vary appreciably in the distance range between about 10 and 100km. He found that the attenuation of Fourier amplitudes is adequately described by the empirical amplitude attenuation function of *Richter* [1958]. *McGuire* [1978], in a similar study but with somewhat different data set, found the attenuation of Fourier amplitudes with distance as R^{-b} where R is the hypocentral distance and b increases with frequency. The data set for these studies comes from earthquakes with $M > 5$ and from different regions of California. Thus the results from these studies provide an average attenuation relation for California.

It is reasonable to assume that large differences in upper crustal structure will result in large differences in attenuation of seismic waves. Thus, each region should be studied separately. Ideally, for a given region, the data should come from small earthquakes (so that the events could be assumed

simple point sources) recorded over large epicentral distances and the crustal structure should be known. If the crust could be approximated by horizontal layers then the theoretical spectra, calculated for different distributions Q, could be matched with data to determine the Q structure of the crust. However, since at wavelengths of interest here ($\sim$100m to 3km) the crust is likely to be laterally heterogeneous, the observed attenuation would include the effect of scattering losses as well as the effect of intrinsic Q.

In this study we present results of spectral attenuation of SH-wave along the Imperial fault. The data consists of six aftershocks ($3.0 \leqslant M_L \leqslant 3.4$) of 15 Oct 1979 ($M_L = 6.6$) earthquake which were digitally recorded up to a distance of 51km. The interpretation of the observed average spectra as a function of epicentral distance supports a frequency-dependent Q model.

DATA

Aftershock data used in this study were obtained from portable digital event recorders operated by Centro de Investigacion Cientifica y de Educacion Superior de Ensenada (CICESE), Institute of Geophysics and Planetary Physics (IGPP), Scripps Institution of Oceanography, University of California at San Diego, and U.S. Geological Survey (USGS), Menlo Park. Only those events which triggered three or more stations in an epicentral distance of at least 30km were selected. Six aftershocks ($3.0 \leqslant M_L \leqslant 3.4$) fulfilled this criterion. Table 1 gives relevant data on these events. Locations of the events and the stations are shown in Figure 1. Events 3, 7 and 9 occurred towards north, events 6 and 8 towards south, and event 12 was located near the center of the fault segment which broke during the main shock. CICESE stations utilized modified Terra Tech DCA 300 recorders whereas IGPP stations were equipped with Terra Tech DCS 302 recorders. Sensors were Kinemetric 5-sec and Geotech 1-sec seismometers. Specifications of USGS stations (Sprengnether DR100) are given by *Fletcher et al.* [1981]. Data reduction procedures for IGPP/CICESE and USGS stations are given by *Brune et al.* [1980] and *Fletcher et al.* [1981], respectively.

All stations were equipped with three-component sensors. Horizontal sensors were oriented N45°E and N45°W at all CICESE/IGPP stations and in N-S, E-W directions at USGS stations. In theory, the S-wave motion at each station can be resolved in azimuthal (SH) and radial components and, applying a radiation pattern correction, the SH motion can be reduced to the expected SH motion at a station located at the same epicentral distance along the fault. In practice, correcting for radiation pattern results in unreliable signal and is very error prone at frequencies of interest in this study ($>$ 1Hz). We find that stations which are expected to be nearly nodal for P and radial S show significant amount of energy for these phases. The same is true for stations expected to be nearly nodal for SH-wave (see also *Boore and Fletcher*, 1981, Table 7). To avoid large errors caused by radiation pattern correction, we have chosen only those stations which were located near the fault plane and, in a few cases, near the auxiliary plane. Focal mechanisms of events 7 and 9 are given by *Boore and Fletcher* [1981] and for event 12 by R. Archuleta (personal communication, 1981). Although these solutions vary slightly, they are consistent with a vertical right lateral strike-slip fault with a strike of about N33°W. We shall assume this mechanism for all six events considered here. USGS stations were rotated to obtain the SH component. For CICESE/IGPP stations N45°E component was taken as recording SH motion. N45°E is within about 15° from the true azimuthal direction for these stations and events (Figure 1). Tests with USGS data showed that rotation, generally, did not change the spectra in an appreciable manner.

About 2 to 4 seconds of S-wave signal were selected for analysis. Fourier displacement spectra were calculated after applying instrumental correction. Table 2 gives stations which provided data for each event. Spectra from IVC and HED were found to be anomalous. Signals and spectra from IVC were much lower than expected, perhaps because of instrumental problems or due to its location in a large school building. Spectra from HED appear reasonable at lower frequencies but attenuated much faster at higher frequencies than nearby stations COM and IAA. This is true for events both the the NW (events 3, 7, and 9) and to the SE (events 6 and 8) of HED. The anomalous character of the spectra may be due to local site conditions. HED was located on a sand dune. Whatever the cause of the anomalous behavior of these two stations, the data from these stations were discarded since our

interest here is in investigation of average attenuation along the Imperial fault rather than studying local site effects.

In order to obtain spectral values at the same frequency points for all stations and events, the calculated spectra were globally fit with cubic splines constrained to have continuous first and second order derivatives, and interpolated. The spectra were then smoothed by a low pass filter to remove extreme roughness yet preserving their basic character. For USGS stations only the plots of the signal and the S-wave spectra were available to us at the time of this study. The spectral amplitudes for these stations were smoothed by eye, read, fitted by global splines and interpolated.

Spectra of the selected events showed no apparent difference in the corner frequencies at the same epicentral distance range r, although amplitude levels varied. For a given event the spectra at sttions in the epicentral distance ranges $2 \leqslant r \leqslant 14$km, $22 \leqslant r \geqslant 25.5$km, $29.5 \leqslant r \leqslant 33.5$km, and $43 \leqslant r \leqslant 51$km were similar. For any given event, the recordings were available from only a few stations (Table 2). Rather than analyze individual events separately, it was decided to scale all the events so that the data could be thought of as being obtained from a single aftershock. The scale factors, given in Table 1, were obtained by shifting the spectral plots so that the spectra for stations in groups A $(2 \leqslant r \leqslant 14$km), B $(22 \leqslant r \leqslant 24.5$km), C $(29.5 \leqslant r \leqslant 33.5$km), and D $(43 \leqslant r \leqslant 51$km) of different events approximately matched. Scaled station spectra for group A are shown in Figure 2. Spectra in all groups show considerable scatter and oscillation. In order to obtain a representative spectra for each group, the logarithm of spectra in each group were averaged. Figure 3 shows these log averaged spectra along with flanking curves for ± one standard deviation. (We have also analyzed the data by taking average of the amplitudes rather than the log average. The conclusions reached in this paper are not sensitive to the choice of the averaging process.) The numbers of stations in groups A, B, C, and D are 10, 3, 8, and 5, respectively (Table 3). The average epicentral distance for stations in groups A, B, C, and D are 8, 23, 31.8, and 47.3km, respectively. The average focal depth of the events is 8.5 ± 1.4km. Narrow band filtering at $10-20$Hz verified that the high frequency part of the spectra correspond to primarily S wave energy, even at the largest distances.

INTERPRETATION

Figure 3 shows our basic data for the average attenuation of SH waves along the Imperial fault. Although the data has been obtained from different events and instruments the mean curves in these figures should represent the average characteristics of the spectra at epicentral distances of about 8, 23, 32, and 47km.

Our model for interpretation of the data is

$$A(f,R) = \frac{S(f)}{R} e^{-\pi ft/Q} \tag{1}$$

where $A(f,R)$ is the spectral amplitude at frequency f and hypocentral distance $R = (r^2 + 8.5^2)^{1/2}$, $S(f)$ = source factor, t = total travel time, and Q = quality factor. This is a very simple model valid for a point source in a homogeneous, isotropic, infinite space and *a priori* might not provide adequate description of attenuation for the complicated Imperial Valley structure [*McMechan and Mooney*, 1980]. In order to test the validity of Eq. (1) we generated synthetic SH-wave spectra using Apsel-Luco synthetic seismogram code [*Apsel*, 1979]. Calculations were made for a point dislocation, with Heaviside slip, buried at 8km and corresponding to a strike-slip faulting on a vertical fault plane. The receivers were located along the fault plane. The crustal model adopted for shear waves, based on the P-wave model of *McMechan and Mooney* [1980], is given in Table 4. The spectra were calculated at epicentral ranges corresponding to the actual earthquakes and stations (Table 3). These spectra were divided into groups A to D, smoothed and log averaged following the same procedure as used for the observed data. Two test cases were considered. In the first case Q of each layer was effectively infinite. It was found that the smoothed spectra decreased very nearly as $1/R$, independent of frequency, in epicentral range of interest. $S(f)$, as expected, was constant with frequency. This means that $1/R$ geometrical spreading assumption in Eq. (1) does not introduce an important error.

In the second test case we assigned Q to each layer according to the following relation:

$$Q = 2\pi + 10\beta^{3.5} \tag{2}$$

where β = shear wave velocity of the layer (km/sec). Calculated spectra were smoothed, log averaged, and grouped. From these average spectra at the four average epicentral distances of 8.0, 23.0, 31.8, and 47.3km, we attempted to recover the source factor $S(f)$ and Q. Taking logarithm (base 10) of both sides. EQ. (1) can be rewritten as

$$\log A(f,R) + \log R = \log S(f) - \left|\frac{1.364\,f}{Q}\right| t \,. \tag{3}$$

For each frequency we have four data points and two unknowns. Solving EQ (3) at each frequency we obtained $Q \approx 250$, independent of frequency, but the inferred source factor, $S(f)$, instead of being constant with frequency, as was actually the case, decayed rapidly with f. The reason turned out to be simple. The upper crustal layers have very low velocities (Table 4) with β increasing from about 0.5km/sec at the surface to about 2.5km/sec at 4km. For sources below 4km the waves travel nearly vertically through these layers and the travel time is essentially independent of distance. Thus the attenuation in the upper shallow layers is essentially independent of distance and the method cannot distinguish this from a variation in source spectrum. Let $t^* = \int_{\text{path}} dt/Q = t_s/Q_s$ where t_s is the vertical travel time in the upper 4km of crust and Q_s is the equivalent Q. t^* is nearly independent of R for these nearly vertically incident rays. For the Imperial Valley crustal structure, EQ. (1) can then be rewritten as

$$A(f,R) = \frac{S(f)e^{-\pi f t^*}}{R} e^{-\pi f t/Q} \tag{4}$$

where t now is total travel time minus t_s and Q is the quality factor of the half-space below the stack with $t^* =$ constant. Equation (4) can be written as

$$\log A(f,R) + \log R = \log G(f) - \left|\frac{1.364\,f}{Q}\right| t \tag{5}$$

where

$$G(f) = S(f)\,e^{-\pi f t^*} \,. \tag{6}$$

We reinterpreted the theoretical spectra for case two by including the effect of constant t^* in the upper 3.75km. For the model (Table 4) t_s is about 2.7 sec and $t^* = 0.113$. The resulting Q was about 280 with both Q and $S(f)$ independent of frequency. Predicted spectra with $t^* = 0.113$ and $Q = 280$ in Eq. (4) are in excellent agreement with the calculated average spectra of case two (Figure 4).

From the test cases we conclude the following:

(1) $1/R$ is reasonable for geometrical spreading factor for the Imperial Valley crustal structure in the epicentral range of interest in this study.

(2) For the Imperial Valley crustal structure it is reasonable to assume that the shear waves would propagate vertically in the upper 4km or so of the crust. For this reason, it is not possible to determine Q of these upper layers from sources located below 4km without making assumptions regarding the source factor $S(f)$. We can only solve for $G(f)$ in Eq. (6) and the average Q of the assumed half-space model below 4km.

(3) It is remarkable that the simple relation given in Eq. (4) predicts the average synthetic spectra of case two so well. This gives us confidence that the observed data can also be interpreted with Eq. (4).

For the interpretation of the actual observed spectra we followed the same procedure as for case two. At each frequency point, the observed averaged spectral values, $A(f,R)$, at the four epicentral ranges were used to solve for G and Q^{-1} in Eq. (5). Figures 5 and 6 show plots of $G(f)$ and Q^{-1}. Q clearly appears to be a function of frequency, increasing from about 60 at 3Hz to about 500 at 25Hz. The variance in $\log A(f,R)$ can be roughly assigned as 0.123 (s.d. $= \pm 0.35$) independent of f and R (see Figure 3). Variance in Q^{-1} corresponding to this variance in $\log A(f,R)$ was calculated. Figure 6

shows $\pm$ one s.d. curves for Q^{-1}. Large s.d. in the value of Q^{-1} implies that Q^{-1} is not well constrained.

In order to see if a constant Q below 3.75km would fit the data equally well, we solved Eq. (5) at all frequencies and ranges simultaneously constraining Q to be a constant. This resulted in a Q of about 240. Predicted spectra at the four ranges with Q as a function of frequency and $Q = 240$ are shown in Figure 3 along with observed spectra. It is not surprising that $Q(f)$ model predicts the observed average spectra better than Q = constant model, since $Q(f)$ was obtained by fitting the data at each frequency. At close distances the constant Q model underestimates the average spectra at lower frequencies, and overestimates it at higher frequencies (Group A, Figure 3a). The converse is true at far distances (Group D, Figure 3d). This can be seen more clearly in Figure 7. Neither of the two models fit the observed data well for group B (Figures 3b and 7b). This is probably because only three spectra were available in this distance range (Table 3) and two of these were from the same station (IAA). Local site conditions may have resulted in anomalous nature of the observed average spectra. Although constant Q model predicts the spectra roughly within the error of the data (except for group B were the $Q(f)$ model also does not fit well at low frequencies) the misfit to observed average data at close and far distances suggests that $Q(f)$ is a more acceptable model. Observed similar average spectral shapes at different distance ranges is best explained by frequency dependent Q below about 4km. Our experience with depth dependent Q in the second model, as discussed earlier, shows that $Q(z)$ can be approximated by an average constant Q independent of frequency. Thus variation of Q with depth is not a likely explanation for the frequency dependence of the observed Q. It is possible that the standard error in observed average data (Figure 3) would decrease if each individual spectra were heavily smoothed before averaging. This would result in smaller variance of Q^{-1}. This, however, has not been attempted here.

Further support for $Q(f)$ model comes from plots of $G(f)$ shown in Figure 5. Recall that $G(f) = S(f)\ e^{-\pi f t^*}$. If we take the constant Q assumption, $G(f)$ in Figure 5 decays as $\sim f^{-1}$ between 2 to 10Hz, and $\sim f^{-3}$ above 10Hz. Various studies on source theory suggest that $S(f)$ should fall off as $f^{-\nu}$ ($2 \le \nu \le 3$) at high frequencies (e.g., *Brune*, 1970; *Madariaga*, 1976; *Brune et al.*, 1979). This implies that the second term in $G(f)$ (involving t^*) is essentially constant, i.e. that t^* is very small ($Q > 200$). However, intuitively one would expect the upper 4km of Imperial Valley to have rather low Q. The $G(f)$ curve assuming Q a function of frequency in Figure 5 does not lead to this difficulty. Let us take the corner frequency of the events studied as 7Hz which corresponds to a source radius of about 200m according to Brune's model [*Brune*, 1970]. Assuming f^{-2} decay beyond 7Hz for $S(f)$, a $t^* \approx 0.0477$ is obtained from $G(f)$ for the $Q(f)$ model. This gives an average Q of about 60 in the upper 3.75km. If $S(f)$ is assumed to decay as f^{-3} we obtain a $t^* \approx 0.027$, the corresponding average value of Q being about 100. Thus, only a rough bound on the value of t^* between 0.027 and 0.047 is possible since it is dependent on the source function. Although t^* may also be frequency dependent we cannot resolve it from our data set.

CONCLUSIONS

Analysis of spectral attenuation of SH waves along the Imperial fault suggests a frequency-dependent Q below about 4km. The estimated Q^{-1} values shown in Figure 6 indicate that: (1) Q is very high at high frequencies $\sim 400-500$ at 20–25Hz, (2) Q values are probably lower at 5–10Hz, $\sim 70-140$, and may decrease to values lower than 30 at lower frequencies, although the standard deviations at lower frequencies ($\sim$1Hz) are too large to establish this for certain. Because of the longer wavelengths compared to path lengths at lower frequencies, the reliability of the Q determination is lower.

Although taking the extreme curve within the standard deviation bounds would allow a Q almost independent of frequency, we consider this unlikely. Even if this extreme interpretation were accepted, the conclusion that Q is very high at high frequencies would remain, and it would have to be concluded that Q is also quite high (>100) at lower frequencies.

The fact that such high values of Q were obtained at high frequencies strongly suggests that scattering has not removed significant amount of energy from the signals, and that the apparent variation of Q with frequency is not a result of scattering.

Frequency dependent Q for lithosphere from coda as well as shear waves have been reported by several authors [*Aki and Chouet*, 1975; *Rautian and Khalturin*, 1978; *Tsujiura*, 1978; *Aki*, 1980a,b]. $Q(f)$ for Imperial fault is lower than for the regions considered by these authors. It is quite reasonable to expect a lower Q long an active fault zone. *Bakun and Bufe* [1975] report Q for SH waves between 75 and 100 (1 to 12Hz) along the San Andreas fault in central California.

The attenuation in the upper 4km is essentially independent of epicentral distance since for sources below 4km the waves travel nearly vertically regardless of distance. This attenuation can be described by $e^{-\pi f t^*}$. The value of t^*, based on f^{-2} or f^{-3} model for the source radiation beyond corner frequency, lies between 0.047 (average $Q \approx 57$) and 0.027 (average $A \approx 100$). Any frequency dependence of the Q in the upper 4km cannot be resolved by the present data set.

Taking $Q(f) \approx 20f$ ($25 > f > 3$Hz) as suggested by our data, the attenuation with distance, $[e^{-\pi f t / Q(f)}]/R$, can be written as $\sim e^{-0.05R}/R$. This decay of spectral amplitudes (valid for sources below 4km) is greater than those reported by *Trifunac* [1976] and *McGuire* [1978]. It is also greater than the attenuation of peak acceleration and velocity with distance as reported by *Joyner and Boore* [1981]. The difference may be due to anomalous attenuation along the fault. Source characteristics of larger events which constitutes the data set used by these other authors may also be a factor in the difference of the attenuation, although the situation may be more complex for larger events, since at high strain amplitudes nonlinear attenuation may come into effect.

Greater resolution of Q would have been possible if we had more stations recording the same event over larger range. Obviously, understanding of high frequency seismic wave attenuation would benefit greatly by improving both the quality and the quantity of digital data from events located at different focal depths.

REFERENCES

Aki, K., 1980a. Attenuation of shear-waves in the lithosphere for frequencies from 0105 to 25 Hz. *Phys. Earth Planet. Int.* **21**, 50—60.

Aki, K., 1980b. Scattering and attenuation of shear waves in the lithosphere. *J. Geophys. Res.* **85**, 6496—6504.

Aki, K. and B. Chouet, 1975. Origin of coda waves: Source, attenuation and scattering effects. *J. Geophys. Res.* **80**, 3322—3342.

Apsel, R., 1979. Dynamic Green's functions for layered media and applications to boundary-value problems, Ph.D. thesis, University of California at San Diego, La Jolla, CA.

Bakun, W.H. and C.G. Bufe, 1975. Shear-wave attenuation along the San Andreas fault zone in central California. *Bull. Seism. Soc. Am.* **65**, 439—459.

Boore, D.M., W.B. Joyner, A.A. Oliver III, and R.A. Page, 1980. Peak acceleration, velocity, and displacement from strong-motion records. *Bull. Seism. Soc. Am.* **70**, 305—321.

Boore, D.M. and J.B. Fletcher, 1981. A preliminary study of selected aftershocks of the 1979 Imperial Valley earthquake from digital acceleration and velocity recordings, U.S.G.S. Professional Paper (in press).

Brune, J.N., 1970. Tectonic stress and the spectra of seismic shear waves from earthquakes. *J. Geophys. Res.* **75**, 4997—5009.

Brune, J.N., R.J. Archuleta, and S.H. Hartzell, 1979. Far-field S-wave spectra, corner frequencies and pulse shapes. *J. Geophys. Res.* **84**, 2262—2272.

Brune, J.N., R.S. Simons, F. Vernon, L. Canales, and A. Reyes, 1980. Digital seismic event recorders: Description and examples from the San Jacinto fault, the Imperial fault, the Cerro Prieto fault and the Oaxaca, Mexico subduction fault. *Bull. Seism. Soc. Am.* **70**, 1395—1408.

Fletcher, J.B., R.L. Zepedda, and D.M. Boore, 1981. Digital seismograms of aftershocks of the Imperial Valley, California earthquake of October 15, 1979. U.S.G.S. Open File Report 81-655.

Joyner, W.B. and D.M. Boore, 1981. Peak horizontal acceleration and velocity from strong-motion records including records from the 1979 Imperial Valley, California earthquake. *Bull. Seism. Soc. Am.* **71**, 2011—2038.

Madariaga, R., 1976. Dynamics of an expanding circular fault. *Bull. Seism. Soc. Am.* **68**, 803—822.

McGuire, R.K., 1978. A simple model for estimating Fourier amplitude spectra of horizontal ground acceleration. *Bull. Seism. Soc. Am.* **68**, 803—822.

McGuire, R.K. and T.C. Hanks, 1980. RMS accelerations and spectral amplitudes of strong ground motion during the San Fernando, California earthquake. *Bull. Seism. Soc. Am.* **70**, 1907—1919.

McMechan, G.D. and W.M. Mooney, 1980. Asymptotic ray theory and synthetic seismograms for laterally varying structures: Theory and application to the Imperial Valley, California. *Bull. Seism. Soc. Am.* **70**, 2021—2035.

Rautian, T.G. and V.I. Khalturin, 1978. The use of coda for determination of the earthquake source spectrum. *Bull. Seism. Soc. Am.* **68**, 923—948.

Richter, C.F., 1958. *Elementary Seismology*, Freeman, San Francisco.

Trifunac, M.D., 1976. Preliminary empirical model for scaling Fourier amplitude spectra of strong ground acceleration in terms of earthquake magnitude, source-to-station distance and recording site conditions. *Bull. Seism. Soc. Am.* **66**, 1343—1373.

Tsujiura, M., 1978. Spectral analysis of the coda waves of local earthquakes. *Bull. Earthquake Res. Inst.* **53**, 1—48.

TABLE 1

Aftershocks used in this study. Scaling factor refers to the factor by which S-Wave spectra of the event has been multiplied so that the events could be grouped together as one event (see text).

Event No.	Date	Time (H:M:S)	Lat. °N	Lat. °W	Depth (km)	M_L [4]	Scaling Factor
3 [1]	Oct. 18, 1979	13:20:26.61	32.872	115.513	8.8	3.2	1/2
6 [2]	Oct. 19, 1979	19:42:36.69	32.480	115.219	9.4	3.3	1
7 [1]	Oct. 20, 1979	05:04:07.43	32.912	115.540	9.0	3.0	1
8 [2]	Oct. 20, 1979	07:25:23.43	32.484	115.212	9.7	3.1	5/2
9 [2]	Oct. 20, 1979	14:52:54.93	32.884	115.499	5.9	3.3	1
12 [3]	Oct. 31, 1979	11:43:46.45	32.738	115.413	8.0	3.4	1/3

[1] Origin, location, and depth from Fletcher, et al. (1981).

[2] Origin, location, and depth from D. Chavez (personal communication, 1981).

[3] Origin, location, and depth from R. Archuleta (personal communication, 1981).

[4] M_L from C. Johnson (personal communication, 1981).

TABLE 2

Stations providing data for each event. Data from IVC and
HED were not used in analysis because of instrument problem
and/or abnormal character.

Event No.	Stations* Used in Analysis
3	TAM, IAA, COM, HED, IVC
6	TAM, IAA, COM, HED, IVC, MEQ
7	TAM, IAA, COM, HED, IVC, MEQ, FBR, SLD
8	TAM, IAA, HED, IVC, MEQ
9	TAM, IAA, COM, HED, IVC, MEQ, FBR, JMS
12	AFB, BCS, FBR, GPN, HUS, SLD

*CICESE stations: TAM, IAA, COM; IGPP stations: MEQ, IVC, HED;
USGS stations: AFB, BCS, GPN, GRS, HUS, JMS, SLD. JMS:
forced balanced accelerometer, all others velocity sensors.

TABLE 3

Epicentral distance ranges defining groups A to D
and stations contributing to data in each group

Group	Epicentral Distance Range, km	Stations (epicentral distance, km)	Average Epicentral Distance, km
A	$2 \leq r \leq 14$	TAM(10.5), TAM(10.5), FBR(4.0) SLD(8.5), FBR(2.0), JMS(6.0) MEQ(3.0), BCS(8.0), HUS(13.5) GPN(14.0)	8.0 ± 4.2
B	$22 \leq r \leq 24.5$	IAA(22.0), IAA(24.5), COM(22.5)	23.0
C	$29.5 \leq r \leq 33.5$	COM(29.5), IAA(31.5), COM(33.0) IAA(35.5), AFB(29.5), SLD(31.5), COM(29.5), IAA(31.5)	31.8 ± 2.3
D	$43 \leq r \leq 51$	TAM(43.0), MEQ(51.0), MEQ(51.0), TAM(47.5), TAM(44.0)	47.3 ± 3.8

TABLE 4

Crustal model of Imperial Valley, based on McMechan and
Mooney (1980), used in the generation of synthetic spectra.

Layer	Thickness, km	P-Wave Velocity, km/sec	S-Wave Velocity, km/sec	Density gm/cm^3
1	0.10	1.690	0.500	2.04
2	0.15	1.790	0.818	2.06
3	0.50	2.167	1.010	2.13
4	0.50	2.533	1.200	2.21
5	0.50	2.900	1.410	2.28
6	0.50	3.267	1.620	2.35
7	0.50	3.633	1.850	2.43
8	0.50	4.000	2.080	2.50
9	0.50	4.367	2.330	2.57
10	0.50	4.733	2.590	2.65
11	0.50	5.100	2.870	2.72
12	0.50	5.375	3.060	2.77
13	0.50	5.650	3.260	2.83
14	5.25	5.750	3.320	2.85
15	0.30	6.700	3.870	3.04
16	0.30	6.900	3.980	3.08
17	0.30	7.100	4.100	3.12
18	1.31	7.300	4.210	3.16
19	2.50	7.800	4.500	3.26
20	∞	8.100	4.670	3.32
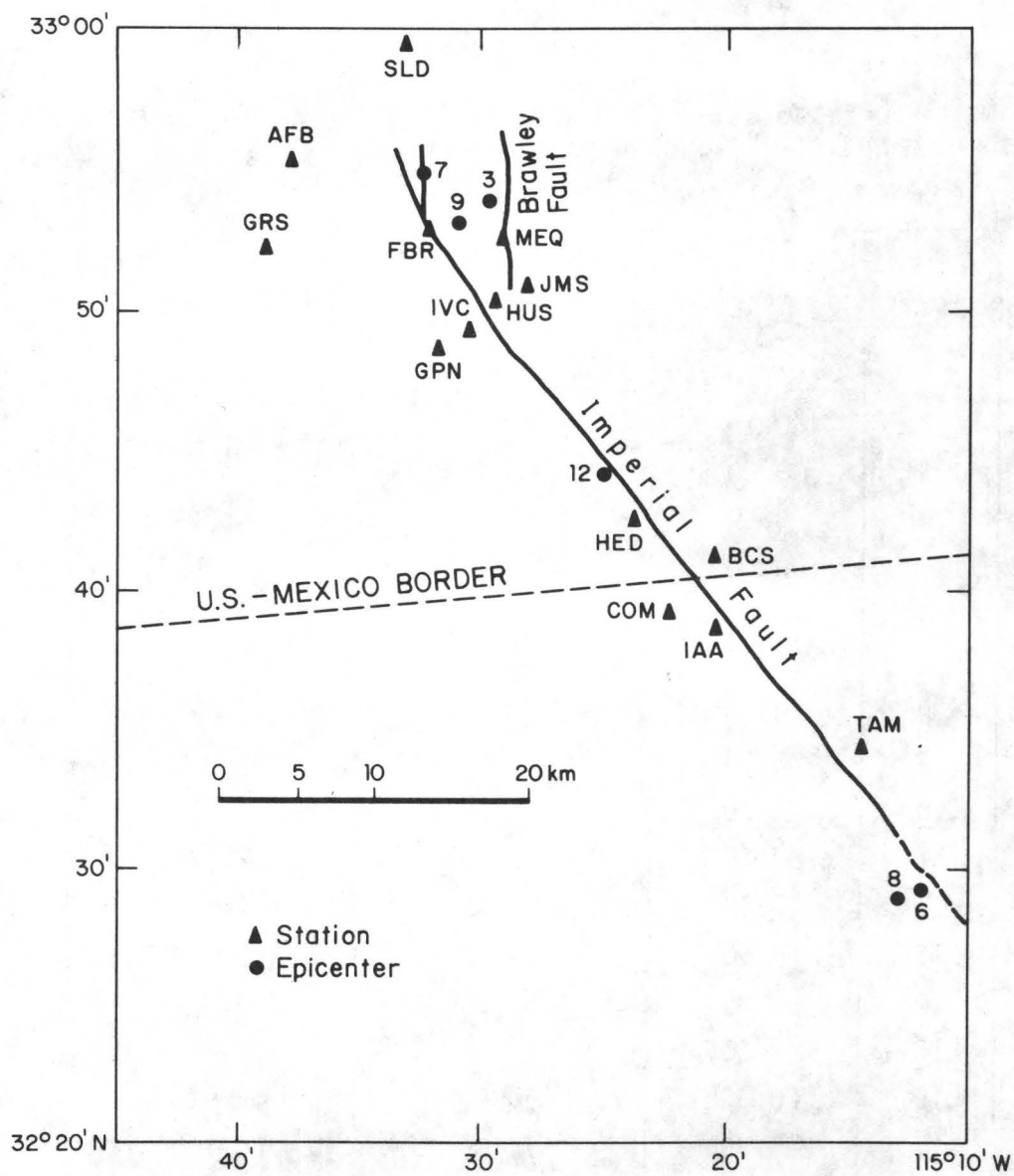
Figure 1. Location map. Epicenters and stations used in this study are shown by heavy dots and triangles, respectively.
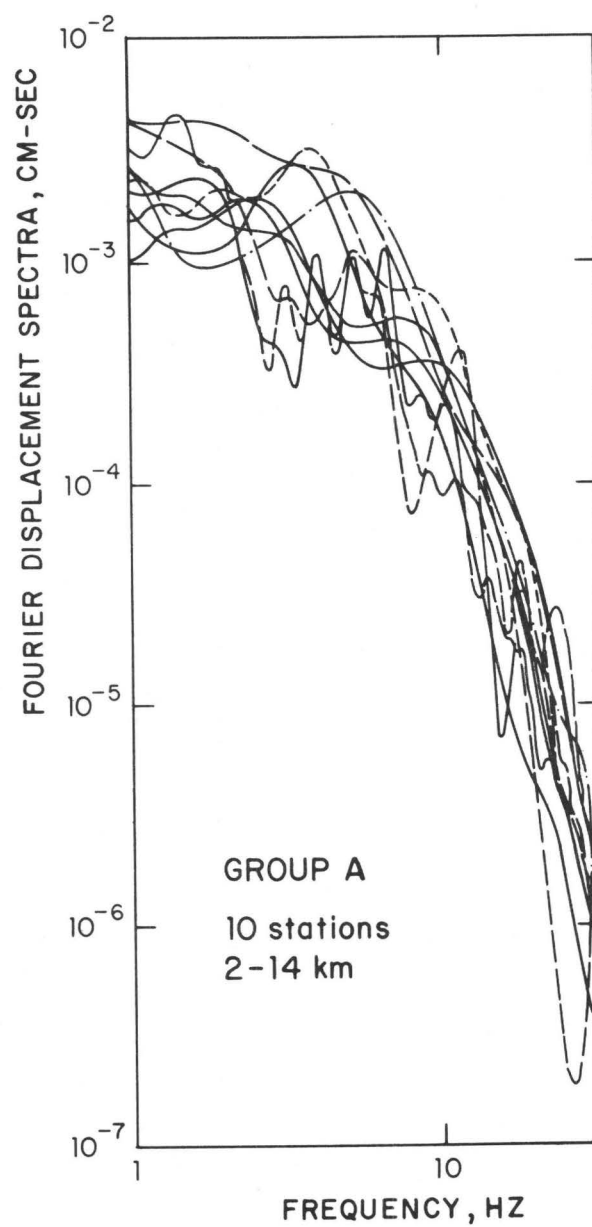
Figure 2. Fourier displacement-spectra of various events at stations in an epicentral range of 2 to 14km (Group A). Spectra of different events have been scaled (see Table 1 and text) and smoothed to remove extreme roughness. Spectra for other groups show similar scatter.
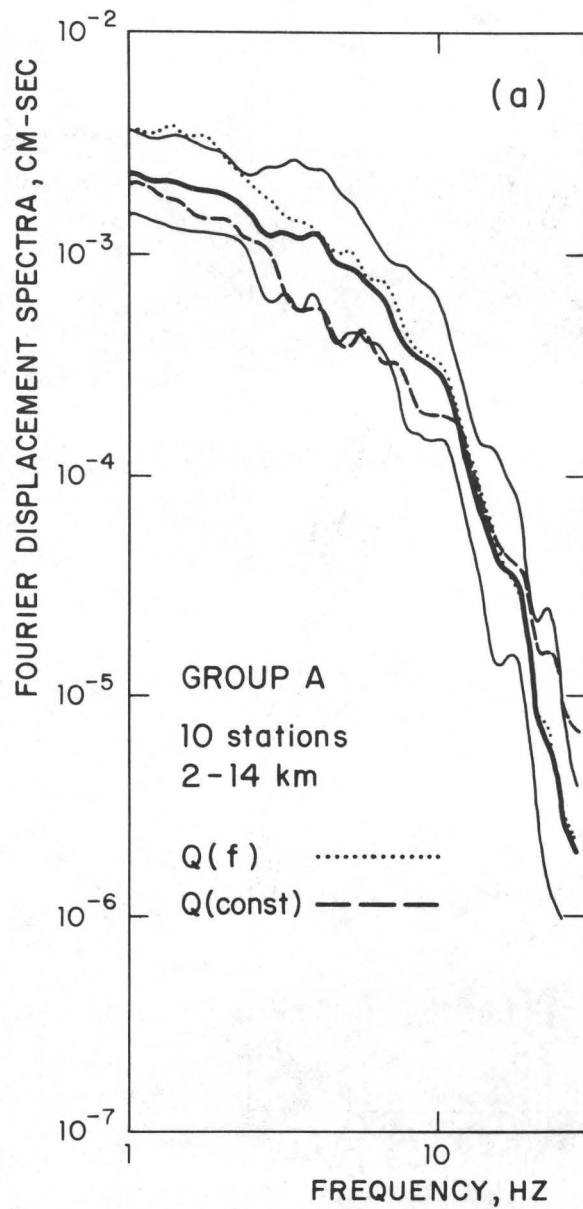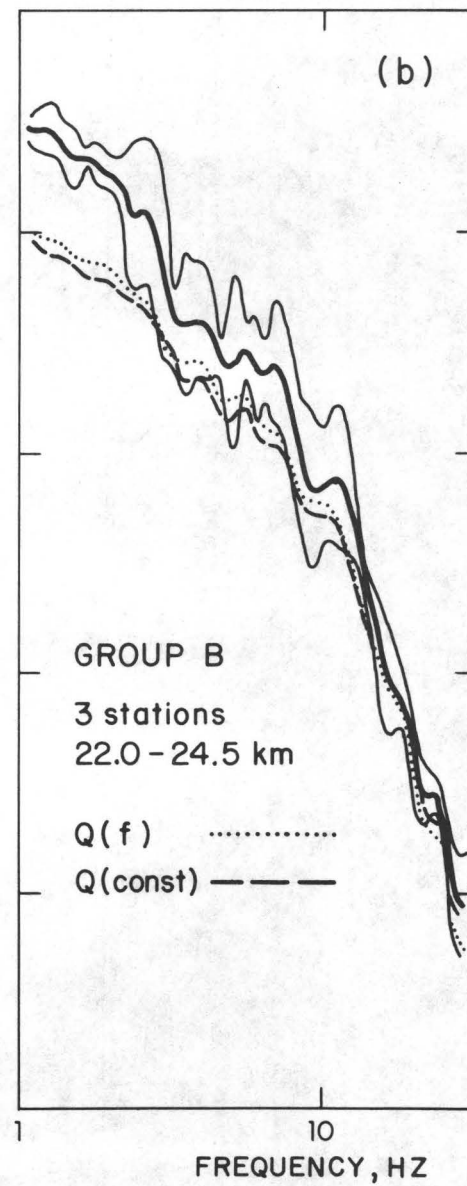
Figure 3. Log averaged spectra (thick curve) along with flanking curves (thin) for ± 1 s.d. for different groups. Also shown are predicted spectra for $Q(f)$ (model), dotted curve, and Q (const) model, dashed curve (see text). (a) Group A (2–14km). (b) Group B (22–24.5km). (c) Group C (29.5–36.5km). (d) Group D (43–51km).
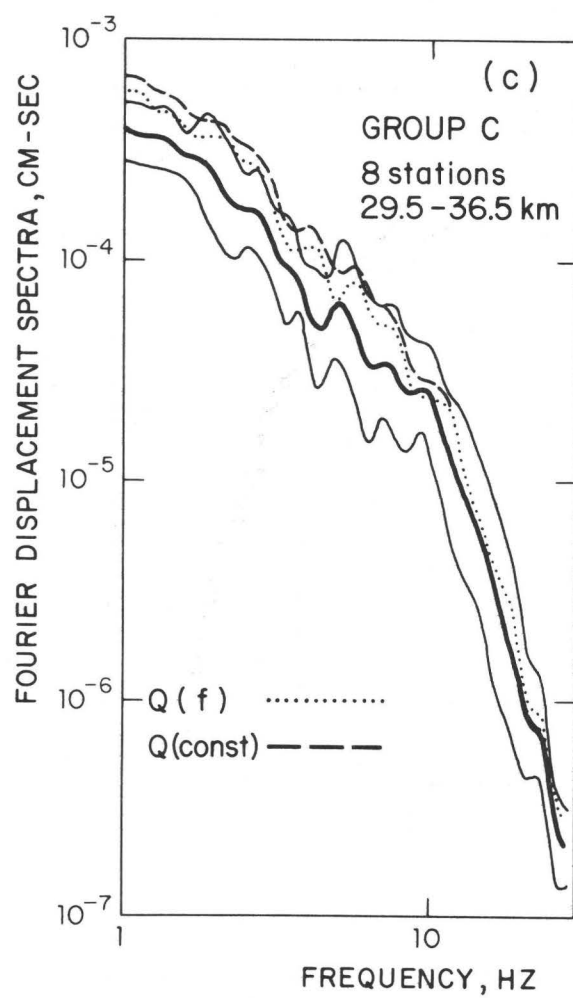
Figure 3c
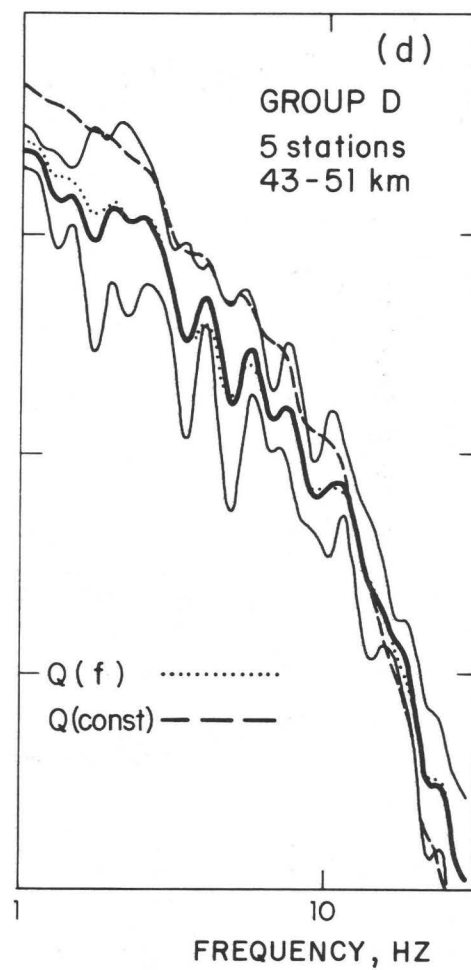
Figure 3d
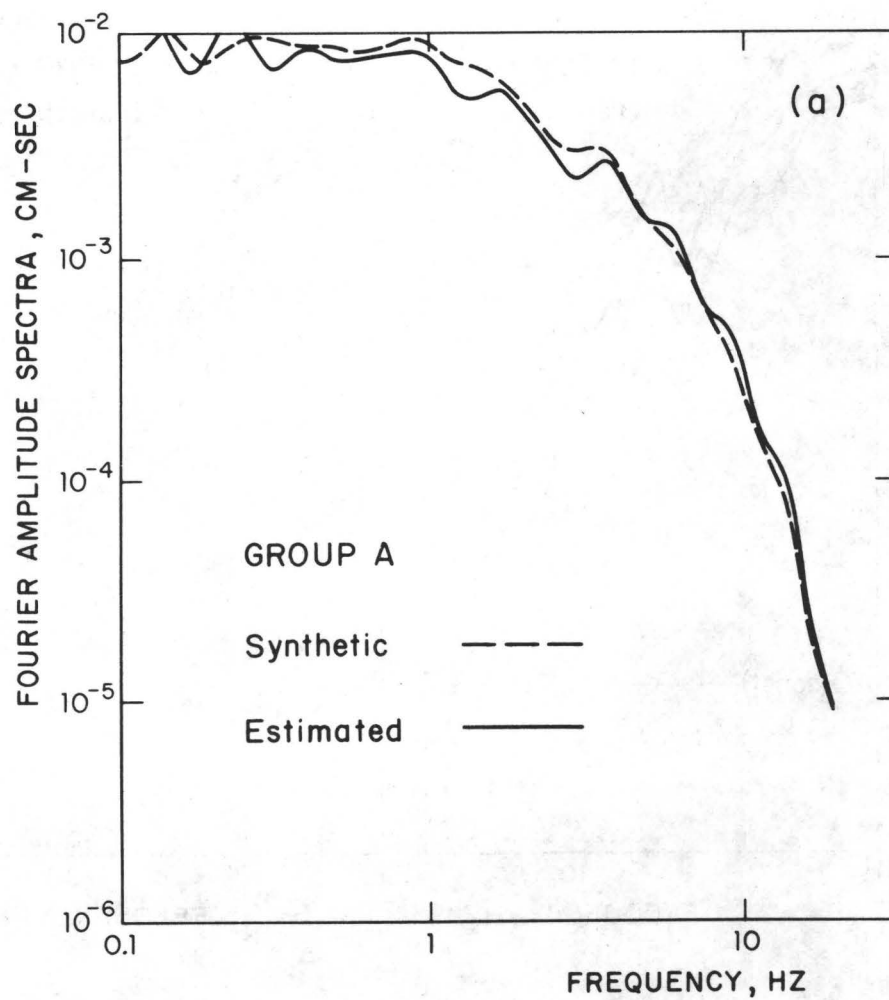
Figure 4a

Figure 4. Synthetic log average spectra for the second test model for different groups. Predicted spectra obtained from the interpretation of the synthetic spectra, based on Eq. (5), is shown. The fit is excellent. (a) Group A. (b) Group B. (c) Group C. (d) Group D.
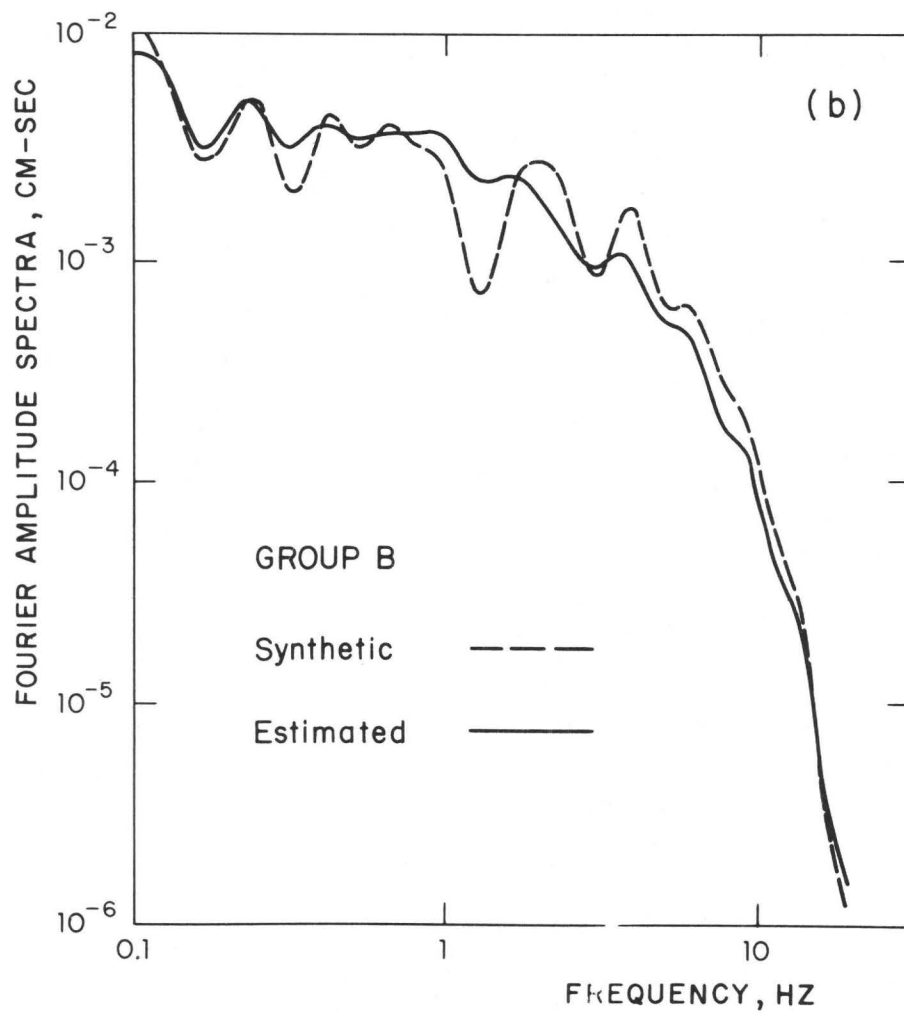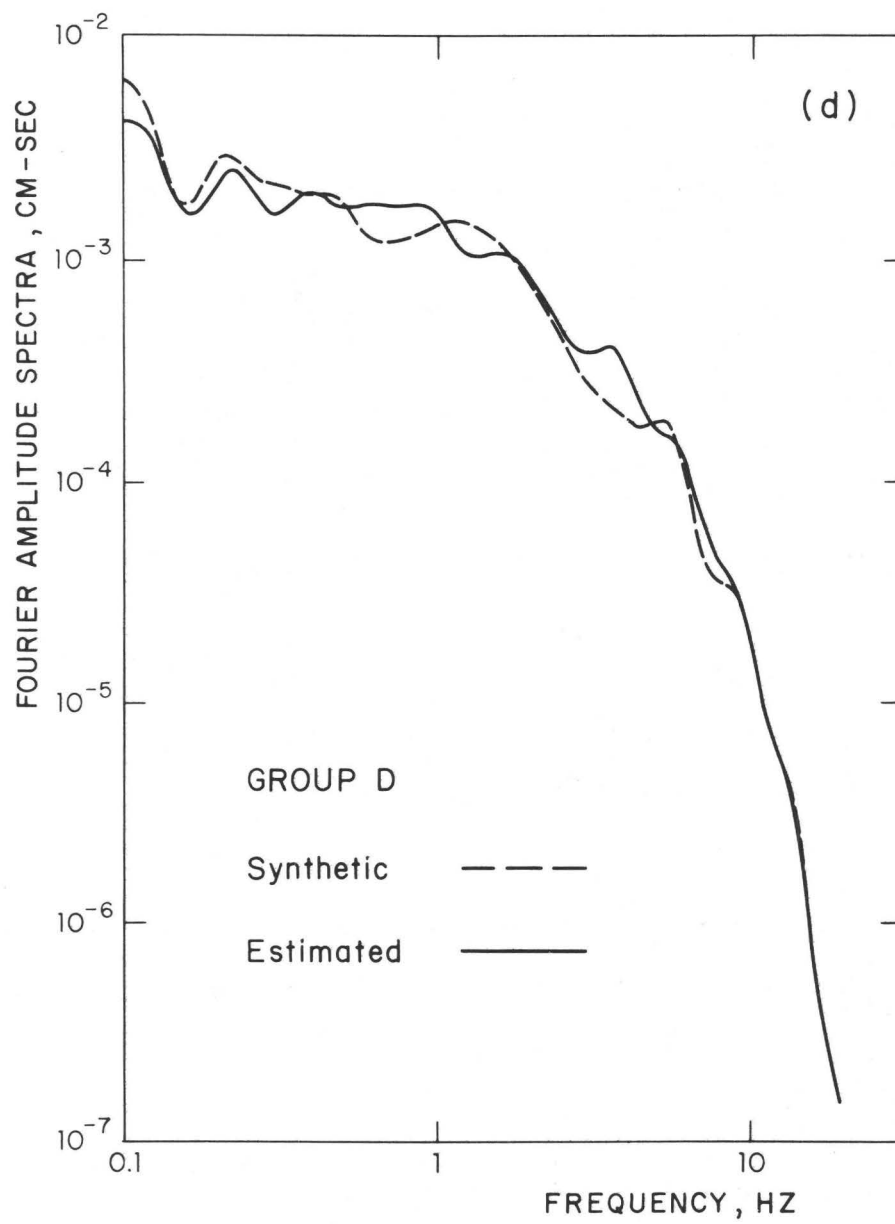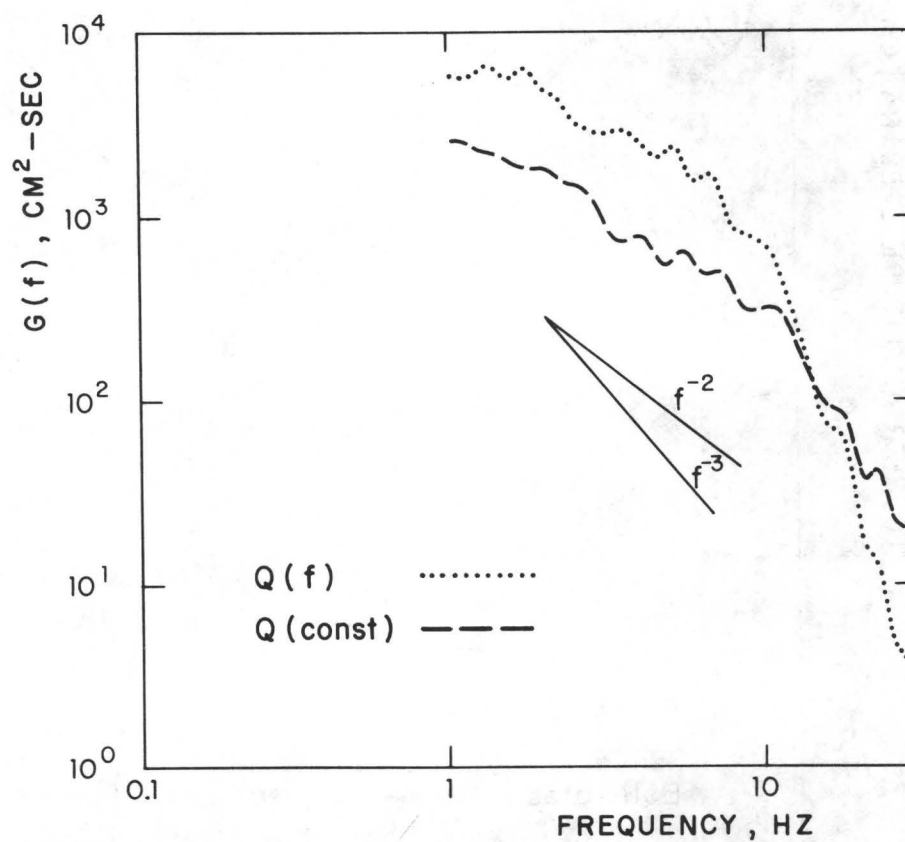
Figure 4b
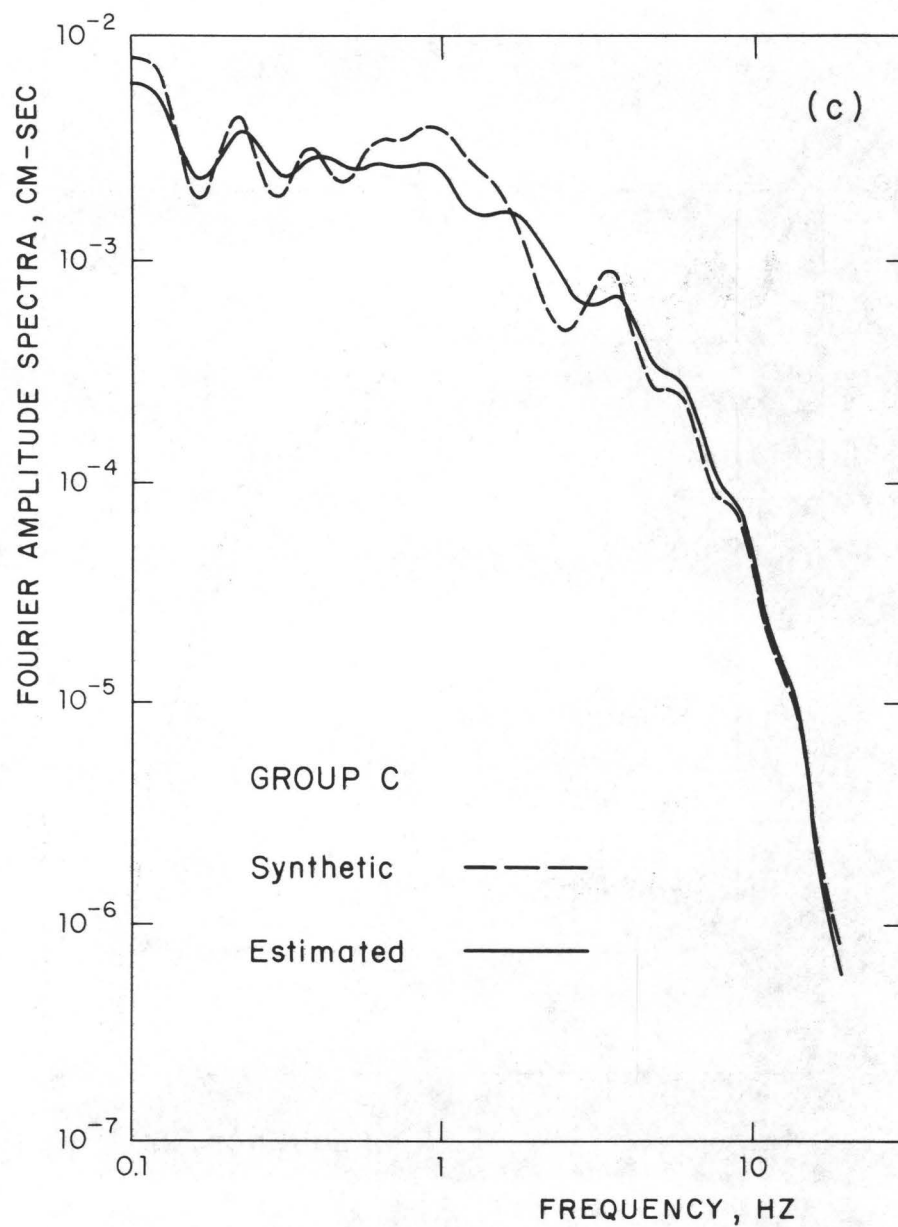
Figure 4c

Figure 4d

Figure 5. $G(f) = S(f)e^{-\pi f t^*}$ (Eq. 6) obtained from interpreting observed spectra using Eq. (5). Dotted curve $Q(f)$ model, dashed curve Q (const.) model.
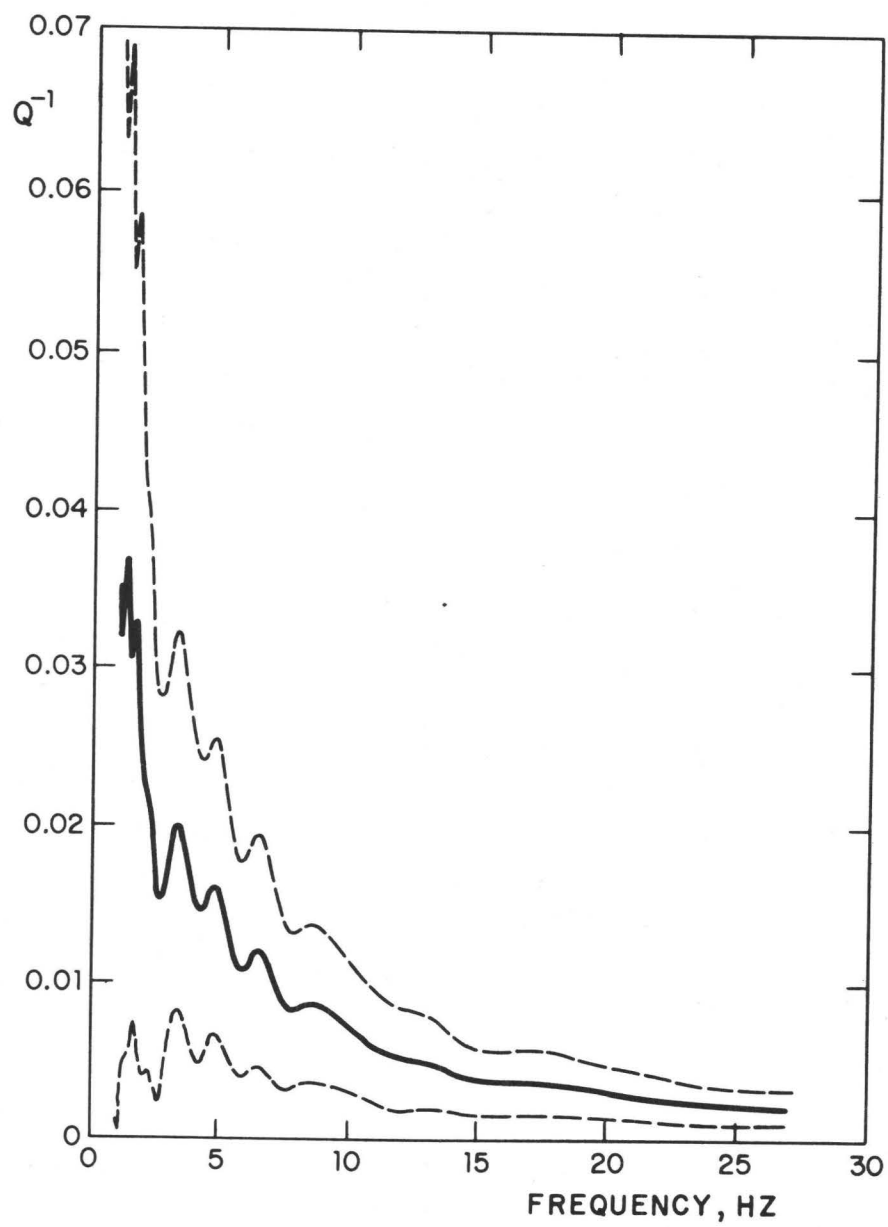
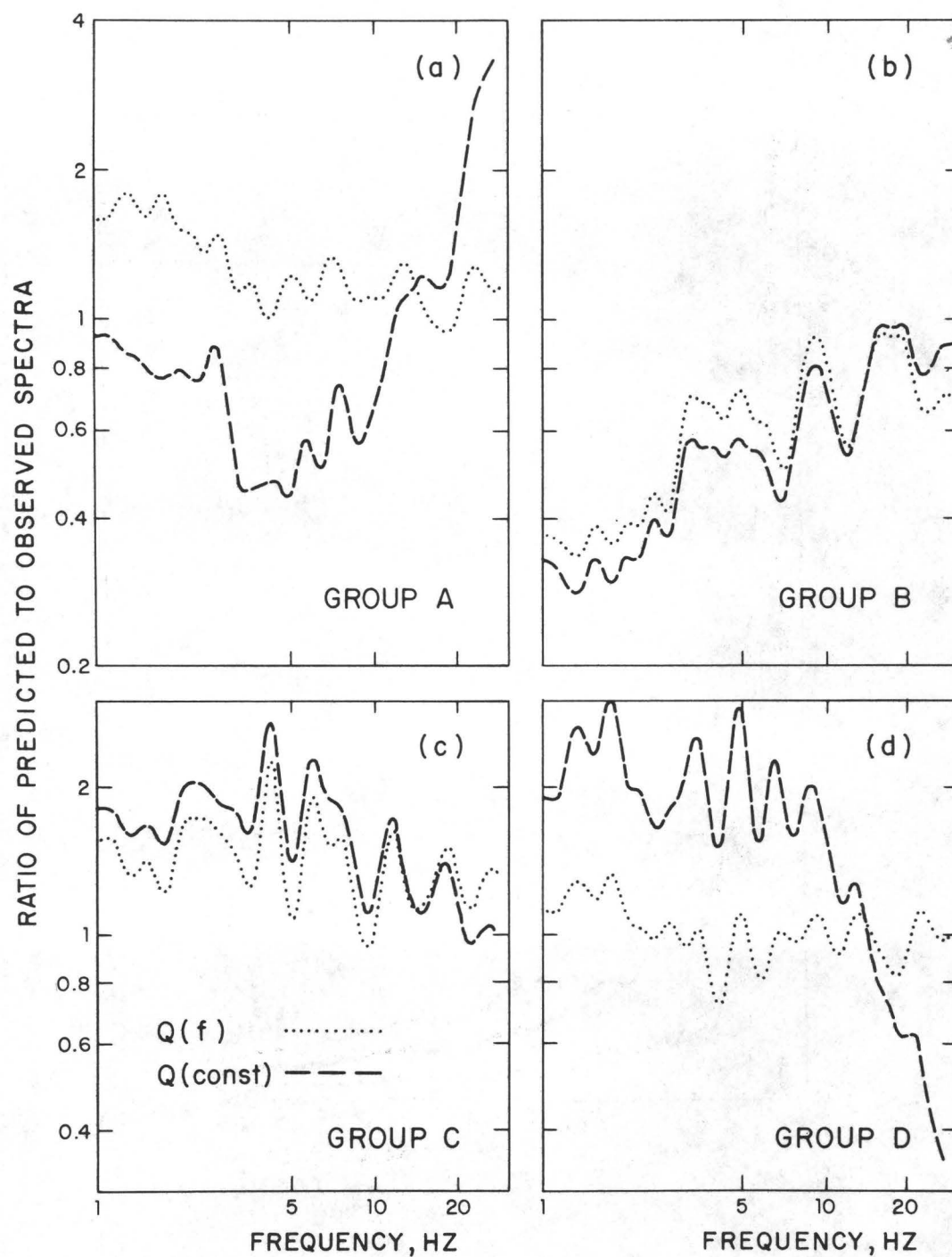Figure 6. Q^{-1} as a function of frequency (thick curve) along with $\pm$ 1 s.d. curves (thin dashed curve).

Figure 7. Ratio of predicted to observed average spectra for $Q(f)$ model (dotted curve) and Q (const.) mode (dashed curve). (a) Group A. (b) Group B. (c) Group C. (d) Group D.